

Lecture Notes in Civil Engineering

Angela Mottaeva *Editor*

Technological Advancements in Construction

Selected Papers

 Springer

Lecture Notes in Civil Engineering

Volume 180

Series Editors

Marco di Prisco, Politecnico di Milano, Milano, Italy

Sheng-Hong Chen, School of Water Resources and Hydropower Engineering,
Wuhan University, Wuhan, China

Ioannis Vayas, Institute of Steel Structures, National Technical University of
Athens, Athens, Greece

Sanjay Kumar Shukla, School of Engineering, Edith Cowan University, Joondalup,
WA, Australia

Anuj Sharma, Iowa State University, Ames, IA, USA

Nagesh Kumar, Department of Civil Engineering, Indian Institute of Science
Bangalore, Bengaluru, Karnataka, India

Chien Ming Wang, School of Civil Engineering, The University of Queensland,
Brisbane, QLD, Australia

Lecture Notes in Civil Engineering (LNCE) publishes the latest developments in Civil Engineering - quickly, informally and in top quality. Though original research reported in proceedings and post-proceedings represents the core of LNCE, edited volumes of exceptionally high quality and interest may also be considered for publication. Volumes published in LNCE embrace all aspects and subfields of, as well as new challenges in, Civil Engineering. Topics in the series include:

- Construction and Structural Mechanics
- Building Materials
- Concrete, Steel and Timber Structures
- Geotechnical Engineering
- Earthquake Engineering
- Coastal Engineering
- Ocean and Offshore Engineering; Ships and Floating Structures
- Hydraulics, Hydrology and Water Resources Engineering
- Environmental Engineering and Sustainability
- Structural Health and Monitoring
- Surveying and Geographical Information Systems
- Indoor Environments
- Transportation and Traffic
- Risk Analysis
- Safety and Security

To submit a proposal or request further information, please contact the appropriate Springer Editor:

- Pierpaolo Riva at pierpaolo.riva@springer.com (Europe and Americas);
- Swati Meherishi at swati.meherishi@springer.com (Asia - except China, and Australia, New Zealand);
- Wayne Hu at wayne.hu@springer.com (China).

All books in the series now indexed by Scopus and EI Compindex database!

More information about this series at <http://www.springer.com/series/15087>

Angela Mottaeva
Editor

Technological Advancements in Construction

Selected Papers

 Springer

Editor

Angela Mottaeva 

Moscow State University of Civil

Engineering

Moscow, Russia

ISSN 2366-2557

ISSN 2366-2565 (electronic)

Lecture Notes in Civil Engineering

ISBN 978-3-030-83916-1

ISBN 978-3-030-83917-8 (eBook)

<https://doi.org/10.1007/978-3-030-83917-8>

© The Editor(s) (if applicable) and The Author(s), under exclusive license to Springer Nature Switzerland AG 2022, corrected publication 2022

This work is subject to copyright. All rights are solely and exclusively licensed by the Publisher, whether the whole or part of the material is concerned, specifically the rights of translation, reprinting, reuse of illustrations, recitation, broadcasting, reproduction on microfilms or in any other physical way, and transmission or information storage and retrieval, electronic adaptation, computer software, or by similar or dissimilar methodology now known or hereafter developed.

The use of general descriptive names, registered names, trademarks, service marks, etc. in this publication does not imply, even in the absence of a specific statement, that such names are exempt from the relevant protective laws and regulations and therefore free for general use.

The publisher, the authors and the editors are safe to assume that the advice and information in this book are believed to be true and accurate at the date of publication. Neither the publisher nor the authors or the editors give a warranty, expressed or implied, with respect to the material contained herein or for any errors or omissions that may have been made. The publisher remains neutral with regard to jurisdictional claims in published maps and institutional affiliations.

This Springer imprint is published by the registered company Springer Nature Switzerland AG
The registered company address is: Gewerbestrasse 11, 6330 Cham, Switzerland

Contents

Content of Radionuclides in Soils of the Voronezh Region	1
Elena Mingareeva, Boris Aparin, E. Sukhacheva, Natalia Sanzharova, Margarita Lazareva, Vitaly Terleev, and Luka Akimov	
Shading System Design and Solar Gains Control for Buildings Passive Energy-Efficiency Improvement	13
Luka Akimov, Vladimir Lvov, Davide de Martino di Montegiordano, Kevin De Mei, Nikolay Osipov, Anastasia Ostrovaia, Sergei Krasnozhen, Vladimir Badenko, and Vitaly Terleev	
Features of Determining the Entrepreneur' Profit in the Agricultural Land Cadastral Valuation Under Buildings and Structures	25
Vladimir Nosov, Kirill Zhichkin, Lyudmila Zhichkina, Olga Vaganova, and Andrey Kotyazhov	
Forecasting of Thermal Regime in an Oil Mine	39
Aleksandr Galkin and Vladimir Pankov	
Influence of Forced Cooling Criteria on the Pressure Distribution Inside the Curved Ventilation Ducts of the Brake Disc	47
Pavel Polyakov, Artem Litvinov, Ruslan Tagiev, Alexey Golikov, Nina Zadayanchuk, and Ivan Yaitskov	
Modeling the Clustering of Dispersed Systems Using Dynamic Models	61
Alexey Bormotov and Anastasia Gorokhova	
Substantiation of the Method for Calculating Soil Deformation Modulus	71
Aleksandr Kalinin, Aleksandr Prolygin, and Natalya Aleksandrova	

Neural Network Model for Quality Indicators Assessment: Case of Paper Manufacturing Industry	83
Irina Rudakova, Alexey Peshekhonov, Anna Chernikova, and Svetlana Kuzmina	
Design of “Green” Roofs of Extensive Type in Various Climatic Zones of Russia	99
Elena Syssoeva and Ilya Morozov	
Results of Measuring the Thermal Concrete Properties by the Impulse Method	109
Mikhail Arkulis, Gennadii Dubskiy, Oxana Logunova, Galina Trubitsina, and Georgy Tokmazov	
The Development of Polymer Fire-Resistant Thermal Insulation Coating Filled with Anthropogenic Waste	117
Marina Ilina, Oleg Selivanov, and Ivan Kurochkin	
Seismic Vulnerability of Individual Housing: Case Study	127
Mashrap Akhmedov and Rustam Abirov	
Strength and Deformability of the Dome of the Mausoleum of Khoja Ahmed Yasawi	137
Nurakhmet Makish, Syrymgali Yerzhanov, Vladimir Lapin, and Dauren Kassenov	
Simulation Modeling Using Neural Networks to Control Complex Technical Systems	149
Tatyana Kozhevnikova and Ilya Manzhula	
Assessment of the Vulnerability of Architectural Monuments to Dangerous Natural Processes	159
Elena Arefyeva, Larisa Gorina, and Ekaterina Alekseeva	
Complex Assessment the Construction Works Quality Using BIM Technologies	171
Tatyana Rubailo, Marina Petrochenko, Anna Gorodishenina, and Yuri Lazarev	
Risk Identification and Assessment in the Design of Concrete Mixes . . .	183
Liubov Lisienkova, Liudmila Nosova, and Liudmila Komarova	
Anisotropic Characteristics of Single Jointed Rock Mass Under Uniaxial Compression	193
Long Cheng, Yaojia Sun, Jiyun Zhang, and Meng Guo	
Real Estate Public Management Quality Assessment	203
Nadezhda Kamynina, Elena Gorbashko, Irina Golovtsova, and Alexandra Titova	

Tuning the PID Controller According to the Criterion of the Maximum Phase Margin	217
Natalia Lysova, Nina Myasnikova, Dmitrii Plotnikov, and Anatolii Semenov	
Detailing the Impact Structure of the Participants of the Complex Transport Service	225
Valerii Zubkov	
Reproducibility of the Properties of Foamed Ceramics by the Processability Factor Method	235
Denis Portnyagin and Elena Loginova	
Optimized Chemical Composition of Concrete Used in Waterproof Objects	245
Ashot Antonyan	
Modelling of Ultrasonic Wave Propagation Through the Border of Two Mediums	255
Sergey Gerasimov and Tatiana Igumnova	
Clustering Methods and Time Parameterization in the Management of Port Cargo Flows	265
Oleg Chislov, Natalya Magomedova, Alexandra Kravets, Danil Bezusov, and Vyacheslav Zadorozhniy	
High Speed Transport Systems for Urban Agglomerations	279
Oleg Larin, Alexander Bokov, and Liudmila Ponimatkina	
On Some Properties of the Blow-Up Solutions of a Nonlinear Parabolic System Non-divergent Form with Cross-Diffusion	289
Alisher Matyakubov and Dilmurod Raupov	
Block Matrix for Three-Factor Analysis of Machinery Failures	303
Irina Buslaeva and Lena Yakovleva	
Research on Load-Bearing Constructions Behavior During Pit Excavation Under «Slurry Wall» Protection	313
Vasilii Komolov, Artem Belikov, and Peter Demenkov	
Assessment of Stress-Deformed State of Armocement Two-Layer Elements	325
Salis Bayramukov, Zuriat Dolaeva, and Tolya Khezhev	
Estimation Residual Resource of Unreinforced Stone Structures by Changing the Parameters Masonry	335
Dmitry Korolkov, Galina Bolodyan, and Marina Gravit	

Importance of Solar in Aeration of High-Rise Buildings in Cities of Southern Countries with Hot Climatic Condition	347
Adham Giyasov	
Effectiveness of the Use of Instrumental Measuring Tools for Cadastral Surveying	359
Anna Osennyaya, Dmitry Gura, Sergey Samarin, and Daria Bespyatchuk	
Tensoresistor-Based Microfluidics and Telemetric Strain-Gauge Lens-Less Detectors as Specialized Labs-on-a-Chip for Soil Mechanics and Foundation Monitoring	371
Feodor Orekhov and Oleg Gradov	
An Approach to Assessing Construction Enterprise Intellectual Capital in the Digital Age	381
Oksana Pirogova, Vladimir Plotnikov, and Agakhanum Yusufova	
Automatic Defect Recognition in Glass Rod Production Using Machine Vision and Deep Learning	391
Yury Matveev and Mohammed Alaqabi	
Automation of Cargo Correspondences in Railway-Water Communication	405
Nina Sirina and Valerii Zubkov	
Solving Differential Equations by Means of Mathematical Simulation in Simulink App of Matlab Software Package	417
Maria Semenova, Anastasia Vasileva, Galina Lukina, and Ulyana Popova	
Information and Intelligent Models in the Management of Transport and Logistics Systems	433
Valerii Zubkov and Nina Sirina	
A Review of the Earthquake Caused Damage on Reinforced Concrete and Masonry Buildings in Turkey	447
Başak Zengin	
Identification of Defective Supports by Visual and Instrument Aids in the Operating Environment of a Railway Power Supply Division	457
Valeriy Li, Lyudmila Demina, and Sergey Vlasenko	
Concrete Hydraulic Curing Under Different Moisture Conditions	471
Ashot Antonyan	
Parametric Model of Cement Soil	481
Nikolai Seregin	
Construction of Diagnostic Algorithms for Complex Systems	493
Dmitry Orlov, Aleksandr Michailov, Vladimir Makhov, and Igor Kazan	

Determination of the Convergence of the Behavior of a Full-Scale Model of a Tower Crane with a Real Object 503
 Lev Khakhulin, Etibar Balaev, and Vladimir Eliseev

Modeling of Parameters of Laser Surfacing Zones and Determination of Tribotechnical Properties of Coatings Obtained by Laser Additive Technologies 511
 Vladimir Biryukov

Determination of Tribotechnical Characteristics of Modified Aluminum Alloys 521
 Vladimir Biryukov, Anton Princ, Oleg Gradov, and Tatiana Bazlova

Obtaining a Coating with Increased Adhesive and Cohesive Strength for High-Speed Flame Spraying for a Pair of Materials Coating-Substrate Metal–Metal 533
 Etibar Balaev and Vladimir Eliseev

Study of the Compressive Strength of Concrete with Polypropylene Microfiber 543
 Sergey Antonov, Marina Gravit, Evgeny Meshalkin, Ivan Dmitriev, and Alexey Shchukin

Methodology for Assessing the Response Parameters of Multi-storey Buildings with Non-linear Dynamic Vibration Dampers in Case of Seismic Impacts 553
 Galina Bogdanova and Andrey Benin

Correction to: Modeling of Parameters of Laser Surfacing Zones and Determination of Tribotechnical Properties of Coatings Obtained by Laser Additive Technologies C1
 Vladimir Biryukov

Author Index 565

Content of Radionuclides in Soils of the Voronezh Region



Elena Mingareeva , Boris Aparin , E. Sukhacheva ,
Natalia Sanzharova , Margarita Lazareva , Vitaly Terleev ,
and Luka Akimov 

Abstract The results of a study of the content of natural radionuclides (NRN) (^{226}Ra , ^{232}Th , ^{40}K) and technogenic ^{137}Cs in soil samples formed on red-brown clays collected at the period of time from 1927 to 2017 are presented. Soil sections were laid on the territory of the «Kamennaya Step'» wild life sanctuary and the island oak grove “Shipov Les” under three types of land: arable land, fallow and forest (forest protection belt. For the first time, data on the specific activity of NRN (^{226}Ra , ^{232}Th and ^{40}K) was obtained in the soils of the “Kamennaya Step'” wild life sanctuary and the island oak forest “Shipov Les” before the first nuclear tests (before 1954). The highest specific activity of NRN, as well as technogenic ^{137}Cs , is observed in soils under forest, and the lowest: for radium-226 and cesium-137 in arable soils, and thorium-232 and cadmium-40 in fallow soils. ^{137}Cs was found in modern soil samples (0–20 cm), as well as in the 1962 sample (at a depth of 0–5 cm). Its specific activity varies in the range of 26.9–124.4 Bq/kg, with the highest content in soils under forest.

Keywords Natural radionuclides · Technogenic cesium · Soils · Bio resource collection of soil monoliths

E. Mingareeva · B. Aparin · E. Sukhacheva · M. Lazareva
Central Soil Museum By V.V. Dokuchaev - Branch of the Federal Research Centre V.V.
Dokuchaev Soil Science Institute, Birzhevoy proezd, 6, St. Petersburg 199034, Russian Federation

N. Sanzharova
Russian Institute of Radiology and Agroecology, Kievskoye Road, 109 km, Obninsk, Kaluga
Region 249032, Russian Federation

V. Terleev · L. Akimov (✉)
Peter the Great St. Petersburg Polytechnic University, Polytechnicheskaya, 29, St. Petersburg
195251, Russian Federation

V. Terleev
Agrophysical Research Institute, Grazhdansky pr., 14, St. Petersburg 195220, Russian Federation

1 Introduction

Cosmic radiation and radiation of natural radionuclides contained in soil, water and air constituted the natural background radiation before 1950s. In connection with nuclear tests for military purposes in the second half of the XX century, technogenic radioactive contamination has become one of the most pressing environmental problems. Regardless of the source of pollution, it always appears in the soil. Currently, considerable factual material has been accumulated on the radioactive contamination of soils in Russia and the world [1, 2]. However, this data is either strongly averaged and does not take into account territorial features (relief, landscape automorphism/hydromorphism, type of land, etc.), or relates to specific soils and regions without taking into account the lithological types of parent rocks (PP)—carriers of radionuclides [3–5].

Bioresource collection (BRC) of soil monoliths (SM) of the Central Museum of Soil Science named after V.V. Dokuchaev (CMSS) provides a unique opportunity to study environmental pollution of soils, the content of natural radionuclides (NRN) in soils under different types of land, as well as spatial and temporal variability. SM is a volumetric soil prism of an undisturbed structure with standard dimensions of $100 \times 20 \times 5$ cm.

The purpose of this work is to study the content of NRN (^{226}Ra , ^{232}Th , ^{40}K) and technogenic ^{137}Cs in soils sampled from 1929 to 2017 in the Voronezh region using the Bioresource collection of the CMSS.

2 Materials and Methods

The objects of this study were soils of different sampling periods from 7 SM and 4 sections, taken in 1929, 1947, 1952, 1960, 1970, 2011, and 2017 and included in the BRCCMSS.

Radionuclides were studied in the soils of the Voronezh region on the territory of the “Kamennaya Step” wild life sanctuary under three types of land: arable land (3 sections), protective forest belt (2 sections) and fallow (4 sections), as well as on the island oak grove “Shipov Les” (2 sections). The classification diversity of soils is represented by 4 taxonomic types [6]: chernozems (points 768, 926, 767, 1001, 1.11, 2.11), chernozems aric (points 718, 969, 3.11) in the “Kamennaya Step”, as well as mollic umbrisols (point 746) and umbrisols (point 6.17) in “Shipov Les”. All soils are formed on red-brown clays.

The “Kamennaya Step” wild life sanctuary is a unique object that has been studied by specialists of various profiles for over a century. At the initial stage, the area was comprehensively and versatile explored by an expedition headed by V.V. Dokuchaev. The natural features of the “Kamennaya Step” reflect the specificity of the Chernozem region. There are developed soils that form under meadow-steppe and steppe vegetation on carbonate red-brown clays. The plowing of the territory

began with the settlement of the area in the eighteenth century. The protective forest belt in the sanctuary was created in 1903 to combat drought, and the fallow—in 1912 to study the dynamics of vegetation without the influence of economic activity [7].

The “Shipov Les” is the largest insular oak forest in the Chernozem zone, located on the right bank of the river Osered. The forest was intensively cut down for ship-building purposes. In 1848, its first forest inventory was carried out and systematic forest management began. Modern old-growth stands are the second coppice generation of oak, and young and middle-aged stands are the third. In the “Shipov Les”, soils are formed on carbonate-free red-brown clays with minimal anthropogenic impact compared to the “Kamennaya Step”.

The first nuclear test on the European territory of Russia was carried out in 1954 at the Trotsky test site, 40 km from the city of Buzuluk. In this regard, all soil samples taken up to this time are conditionally referred to as “clean” – not contaminated with technogenic radionuclides.

NRN are inherited by soils from SM, and their distribution in the profile is related to soil processes, pH value, amount of fine fraction (fraction < 0.01 mm) and humus [8, 9].

Samples from SM and sections were taken layer by layer from depths of 0–5, 5–10 (or 0–10 cm), 10–20 and 90–100 cm. Sample preparation and subsequent analysis of the samples were carried out in the same type and according to generally accepted methods [10]. The specific activity (R_A , Bq/kg) of ERH (^{226}Ra , ^{232}Th , ^{40}K) and technogenic ^{137}Cs was determined in an air-dry sample by gamma spectrometry at the All-Russian Research Institute of Radiology and Agroecology. The measurements were carried out on a GAMMA-1P spectrometer for two measuring paths with semiconductor detectors made of ultrapure germanium manufactured by EG&G ORTEC (USA) [11]. Statistical processing of the obtained data was carried out by the method of descriptive statistics: arithmetic mean (M), standard deviation (σ), coefficient of variation (V_σ) and correlation analysis [12]. V_σ was calculated for the entire set of samples, separately for the samples: soils of “Kamennaya Step” and “Shipov Les”; timing of sampling (soils sampled before 1954 and after); by depths of sampling (taking into account the type of land). Based on the literature data and statistical processing of the obtained material, V_σ exceeding 30% was taken as an indicator of the inhomogeneity of R_A of natural radionuclides (NRN) [1]. Correlation relationships were considered significant for a sample of 43 samples at $r \geq 0.3$ ($t_{r,theoretical} = 2.02$ and confidence level 0.95) [12].

3 Results and Discussions

General Characteristics of Soils. All soils are characterized by a heavy particle size distribution. In the “Kamennaya Step”, they are light and medium-loamy, and in the “Shipov Les”, they are heavy-loamy and medium-loamy. Coarse and fine dust and silt are the predominant fractions of the granulometric composition in all studied soils. The content of physical clay (<0.01 mm) in soils of the “Kamennaya Step”

(group I) averages $65.2 \pm 5.8\%$, and the silt fraction (<0.001 mm): $32.5 \pm 8.0\%$ (Table 1). In the soils of the “Shipov Les” (group II), the content of these fractions is $58.0 \pm 10.0\%$ and $29.0 \pm 9.0\%$, respectively. In the soils of both groups, a lightening of the granulometric composition in the upper part of the profile (0–20 cm, humus horizons) is observed in comparison with the SM. The largest difference between the humus horizons and the SM is observed in the point 969 (26%) and point 746 (27%) soils, and the smallest—in the soils of the “Kamennaya Step” (points 926, 767, and 3.11). In the upper part of the soil profile (point 718, 746, 969, 1001, 1.11, 2.11, 3.11, and 6.17), the content of the sand fraction (1–0.25 and 0.25–0.05 mm) reaches 17%.

In accordance with the grouping of D.S. Orlov [13], the humus content in the upper part of the profile (0–20 cm) of soils of group I is high and very high (Table 1). The exceptions are soils: point 718 (under arable land) and point 926 (under forest). In these two soils, the humus content does not exceed 6.1%. The amount of humus in the soils of the “Kamennaya Step” varies from 5.6 to 12.8% ($M = 8.0 \pm 2.3\%$). The average humus content in the soils of the “Shipov Les” is higher ($M = 9.3 \pm 7.6\%$) than in the soils of group I, with a wider range—from low (3.3%) to very high (17.9%). In PP samples, the amount of humus varies within 0.3–1.6%, with the highest amount in the soil under the forest (point 2.11).

The soils of group I have a neutral and alkaline reaction of the environment, and soils of group II are slightly acidic and neutral. In all soils, with the exception of the modern soil from “Shipov Les” (point 6.17), the pH values in the upper part of the profile are lower in comparison with the parent rock. The pH at a depth of 90–100 cm varies between 7.8–8.4 in the “Kamennaya Step” and 6.5–6.6 in the “Shipov Les”.

The Content of Radionuclides. Radium-226. The range of specific activity (R_A) ^{226}Ra in the soil samples of the Stone Steppe is wider (7.5–59.5 Bq/kg) than in the soils of the “Shipov Les” (23.7–41.4 Bq/kg), with a higher average R_A in the latter (Table 1). The range in soil samples taken before 1954 turned out to be narrower (7.5–35.0 Bq/kg), and the average R_A value is lower ($M = 20.4 \pm 8.8$ Bq/kg) in comparison with soils sampled after 1954. The lowest average content is observed in soils under arable land. In soils under fallow and forest, the average R_A values are similar.

In samples from SM of “Kamennaya Step”, R_A of radium-226 is less (7.5–31.9 Bq/kg, $M = 19.1 \pm 7.4$ Bq/kg) than in the “Shipov Les” (26.0–34.4 Bq/kg, $M = 30.2 \pm 5.8$ Bq/kg). This nature of the radium content is retained in the humus horizons (0–20 cm) of soils at wider ranges: 7.6–59.5 Bq/kg, $M = 26.2 \pm 11.5$ Bq/kg for group I and 28.3–41.4 Bq/kg, $M = 31.0 \pm 7.6$ Bq/kg—group II. The average R_A of radium-226 in the humus horizons is higher than in the SM for the soils of both groups, with a minimal (insignificant) difference between the values in the soils of group II.

The coefficient of variation (V_σ) for ^{226}Ra exceeded the 30% threshold in almost all considered samples. It was below 30% only for soils sampled after 1955 (total

Table 1 General characteristics of soils (along the profile) by the content of natural radionuclides and physical and chemical properties

Research objects (number of samples, pcs.)	NRN	Mean value (M) and standard deviation (σ) Bq/kg	Specific activity range (R_A)	Coefficient of variation ($V\sigma$) %	Humus content in humus horizons %	PH range of aqueous suspension		Fraction content range	
						<0,001 mm %	<0,01 mm		
Soils of the "Kamennaya Step" (36)	^{226}Ra	24.4 ± 11.1	7.5–59.5	45.3	5.1–12.8	6.3–8.4	12–45	52–77	
	^{232}Th	39.3 ± 11.0	17.0–59.1	27.9					
	^{40}K	505 ± 128	154–728	25.3					
Soils of oak groves "Shipov Les"(7)	^{226}Ra	30.8 ± 7.0	23.7–41.4	22.8	3.3–17.9	5.6–6.9	16–43	44–71	
	^{232}Th	48.9 ± 13.5	38.0–63.9	27.6					
	^{40}K	680 ± 96	591–830	14.2					
Soils sampled before 1954 (20)	^{226}Ra	20.3 ± 8.8	7.5–35.0	43.4	5.1–8.4	6.3–8.4	12–41	52–76	
	^{232}Th	42.5 ± 10.6	25.5–59.1	25.0					
	^{40}K	556 ± 118	290–728	21.2					
Soils sampled after 1954 (23)	^{226}Ra	30.2 ± 10.2	16.0–59.5	33.7	3.3–17.9	5.6–8.4	16–45	44–77	
	^{232}Th	39.4 ± 12.9	17.0–63.9	32.7					
	^{40}K	514 ± 154	154–740	29.9					
Soils under arable land (12)	^{226}Ra	18.7 ± 9.0	7.5–36.0	48.0	5.1–7.8	6.7–8.4	12–41	52–74	
	^{232}Th	41.8 ± 11.8	25.5–59.1	28.2					
	^{40}K	502 ± 120	290–714	23.9					
Fallow soils (16)	^{226}Ra	27.3 ± 12.1	12.7–59.5	44.4	5.9–12.1	6. 3–8.1	22–43	57–77	
	^{232}Th	35.7 ± 11.0	17.0–50.0	30.8					
	^{40}K	485 ± 133	154–645	27.4					
Soils under forest (protective forest belt) (15)	^{226}Ra	29.0 ± 7.9	16.1–41.4	27.1	3.3–17.9	5.6–8.4	16–45	44–75	
	^{232}Th	45.3 ± 11.2	33.0–63.9	24.7					
	^{40}K	609 ± 129	430–830	21.2					

sample, depths 0–10 and 10–20 cm), in soils under fallow at a depth of 90–100 cm and soils under forest (total sample, depths 0–10 and 10–20 cm).

Thorium-232. The range of ^{232}Th content in samples from “Kamennaya Step” is wider (17.0–59.1 Bq/kg) than in samples from “Shipov Les” (38.0–63.9 Bq/kg), with a higher average R_A value in soils of group II (Table 1). The R_A range of the radionuclide in soil samples taken before the first nuclear tests is narrower (25.5–59.1 Bq/kg) than in soils collected after 1954 (17.0–63.9 Bq/kg). At the same time, the average radionuclide content in soils of group I, soils before 1954 and modern soils are similar (the difference does not exceed 3.5 Bq/kg) (Table 1). In the soils of the “Shipov Les”, the average R_A is significantly higher. According to the type of land, the lowest average content is observed in soils under fallow lands, and the highest in soils under forest.

The R_A of thorium-232 in SM samples from the “Kamennaya Step” varies in a wider range than in samples from “Shipov Les” (24.3–48.4 Bq/kg, $M = 37.4 \pm 10.3$ Bq/kg and 45.0–63.9 Bq/kg, $M = 54.5 \pm 11.6$ Bq/kg, respectively). The average specific activity is lower in soils of group I. This character of the content of thorium-232 is retained in the humus horizons: 17.0–59.1 Bq/kg, $M = 39.9 \pm 11.2$ Bq/kg and 38.0–55.5 Bq/kg, $M = 46.7 \pm 13.9$ Bq/kg, respectively. In the soils of the “Kamennaya Step”, the higher average R_A is confined to the humus horizons, and in the soils of the “Shipov Les”, on the contrary, to the parent rock.

The calculation of V_σ for ^{232}Th showed an excess of the 30% threshold only in the samples: modern soils (the entire population and depth of 0–5 cm), fallow (total sample and depth of 0–10 cm) and arable (90–100 cm depth) soils.

Potassium-40. The range of $R_A^{40}\text{K}$ in soil samples of group I is wider (154–728 Bq/kg) than in group II (591–830 Bq/kg). The average radionuclide content is higher in the soils of the “Shipov Les” (Table 1). The ranges and mean values of $R_A^{40}\text{K}$ in soils of different sampling periods (before and after 1954) are close. In absolute terms, in soils sampled before the first nuclear tests, the range is narrower, and the average content is higher (290–728 Bq/kg, $M = 556 \pm 118$ Bq/kg) than in modern soils (154–740 Bq/kg, $M = 514 \pm 154$ Bq/kg). The lowest average content of potassium-40 is observed in soils under fallow lands, and the highest in soils under forest.

In samples from SM of “Kamennaya Step”, the range of $R_A^{40}\text{K}$ is wider, and the average content is lower (290–517 Bq/kg, $M = 440 \pm 74$ Bq/kg) than in the samples from “Shipov Les” (591–740 Bq/kg, $M = 666 \pm 90$ Bq/kg). In the humus horizons of group I, the range is wider, and the average content is lower than in the “Shipov Les”: 154–728 Bq/kg, $M = 528 \pm 135$ Bq/kg and 593–830 Bq/kg, $M = 686 \pm 101$ Bq/kg, respectively. The average specific activity of potassium-40 in the humus horizons is higher than in the SM. The difference between the average R_A in humus horizons and SM in the soils of the “Shipov Les” is only 20 Bq/kg.

V_σ by ^{40}K exceeds the indicator by 30% only in 2 samples: Soil samples taken after 1955 from a depth of 10–20 cm and fallow soils (samples from a depth of 0–10 cm).

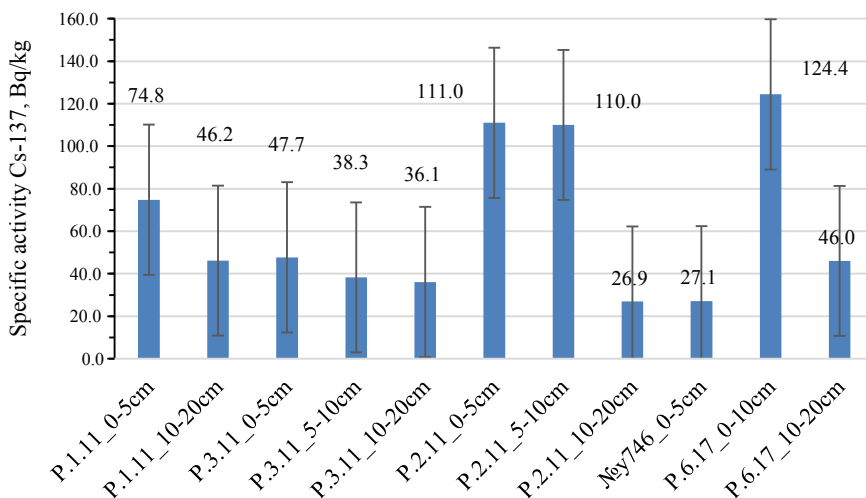


Fig. 1 The specific activity of ^{137}Cs in the humus horizons* of the studied soils. * The graph shows data only for samples in which ^{137}Cs was detected

Cesium-137. The technogenic radionuclide was found only in modern soils (2011 and 2017) at a depth of 0–5, 5–10 (or 0–10) and 10–20 cm, as well as in the soil from the “Shipov Les” of 1962 (point 746) at a depth of 0–5 cm (Fig. 1). The activity of the radionuclide in this sample is one of the lowest. The range of R_A ^{137}Cs varies within 26.9—124.4 Bq/kg ($M = 66.1 \pm 35.3$ Bq/kg), while the soil from the “Shipov Les” (point 6.17) has the highest R_A compared to all soils, see Fig. 1.

Calculation of V_σ in samples in which the content of technogenic ^{137}Cs was noted showed significant spatial heterogeneity for the entire set of data (53.4%) and for a depth of 0–10 cm (40.9%). At a depth of 10–20 cm, it is below 30%. In soils under forest, V_σ is the highest—58.2%. V_σ in fallow and arable soils is less than 30%.

4 Discussion

The study of R_A NRN in various types of soils of the “Kamennaya Step” and “Shipov Les” is a difficult task due to the peculiarities of the conditions of soil formation and anthropogenic impact on them. Soils, with a close location of the study areas and the same genetic type of SM, differ in the content of NRN.

The relationship between the content of NRN and the fractions of the granulometric composition is manifested in 2 aspects: firstly, the mineralogical composition is associated with the granulometric composition—a potential carrier of NRN, and secondly, the sorption capacity is associated with it. Coarse fractions (physical sand) are represented by primary minerals, and silty fractions are secondary clay minerals—the main sorbents of the NRN [3, 8]. The content of NRN in soils correlates with

the fractions of the granulometric composition. A significant inverse relationship for ^{226}Ra was revealed only with a fraction of 1–0.25 mm ($r = -0.35$), ^{232}Th with a fraction of <0.001 mm ($r = -0.31$), and ^{40}K with <0.01 mm ($r = -0.31$). For radium-226 and potassium-40, a non-linear relationship was also noted with the content of fractions 0.05–0.01 mm (power-law, $r = 0.41$; linear, $r = 0.26$) and silt (logarithmic, $r = -0.30$; linear, $r = -0.29$), respectively. A direct relationship between the RA of thorium-232 and potassium-40 was noted with the coarse dust fraction ($r = 0.31$ and 0.57, respectively). A good illustration of the relationship is the combination of particle size distribution and RA NRN in soils in the graph (Fig. 2, 3, 4).

Soils under the fallow: Nos. 1–4—point 768 (1929), samples 0–5, 5–10, 10–20 and 90–100 cm; 5–8—point 767 (1947); 9–12—point 1001 (1970); 13–15—point 1.11 (2011), samples 0–10, 10–20 and 90–100 cm. Soils under arable land: 16–19—point 718 (1929); 20–23—point 969 (1952); 24–27—point 3.11 (2011). Soils under forest: 28–31—point 926 (1947); 32–35—point 2.11 (2011); 36–39—point 746 (1962); 40–42—point 6.17 (2017).

The distribution of radionuclides in the soil profile is associated with soil acidity. According to [8, 14, 15], the strongest sorption of ^{232}Th is observed in soils with neutral and weakly alkaline medium reactions, and the least in acidic ones. The reaction of the environment in the studied soils varies over a wide range (5.6–8.4). It is

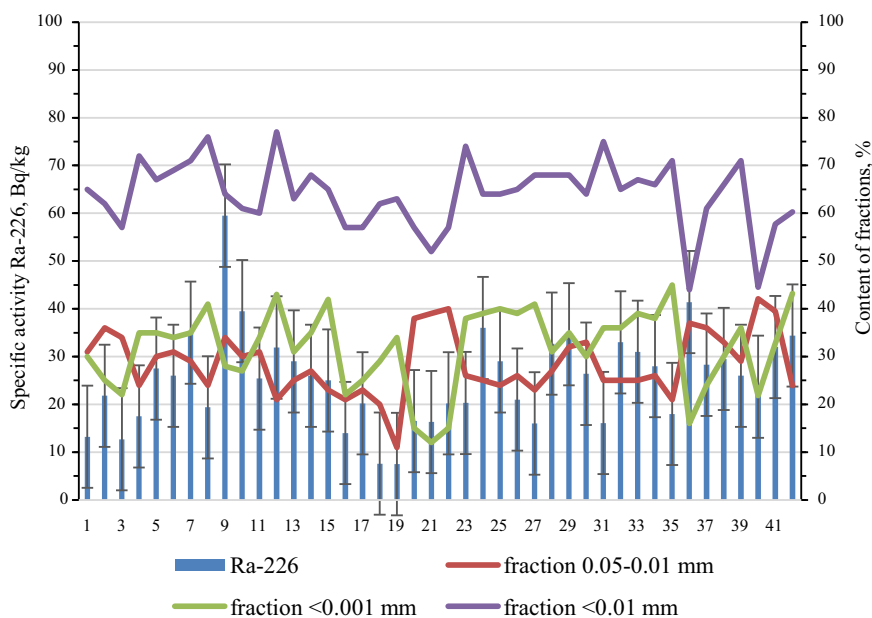


Fig. 2 Specific activity of ^{226}Ra in soils and the content of the main fractions of particle size composition and humus. * The scatter of the values indicated on the histograms characterizes the value of the standard deviation calculated for the population of data for a particular horizon

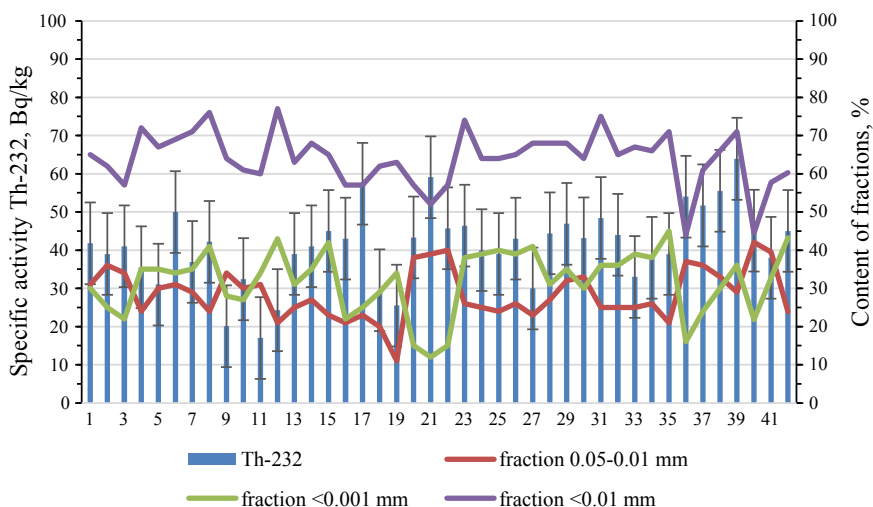


Fig. 3 Specific activity of ^{232}Th in soils and the content of the main fractions of particle size composition and humus

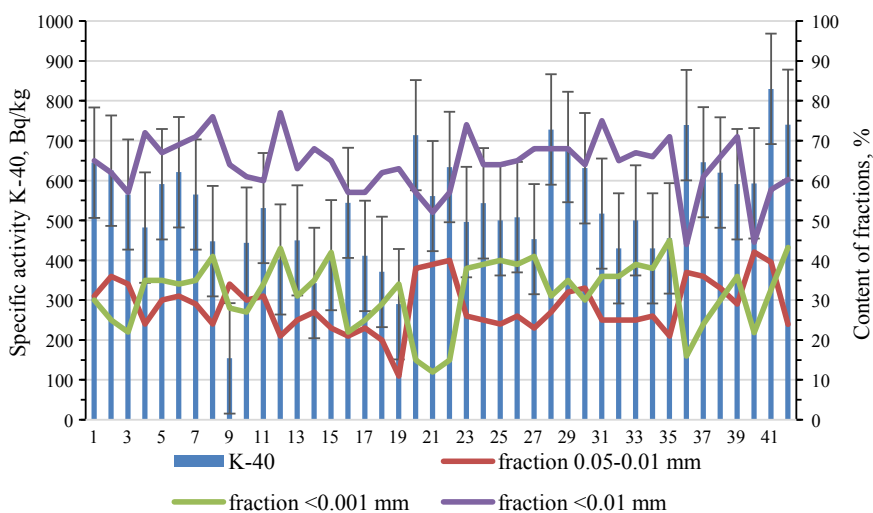


Fig. 4 Specific activity of ^{40}K in soils and the content of the main fractions of particle size composition and humus

associated with the presence of carbonates in the SM and soil processes. Calculations of the correlation relationships between R_{ANRN} and pH showed a significant relationship for ^{226}Ra ($r = -0.40$) and ^{40}K ($r = -0.33$). No significant relationship was found for ^{232}Th . Probably, this is due to the fact that all the samples under study have a pH above 3.5 [9].

Humic substances affect the NRN activity by sorption and the formation of organic-mineral complexes. They either themselves are collectors of radionuclides, or act as sorbents and form mobile compounds with them [8]. In their presence, the mobility increases and the efficiency of radium absorption decreases, complexation of thorium with organic ligands takes place [8]. Probably, this is due to the ratio of humic acids and fulvic acids in humus. Humic acids are soluble in alkalis and inactive, while fulvic acids are soluble in water and easily migrate along the profile. The soils of the “Kamennaya Step” are characterized by the humate type of humus, and the “Shipov Les” is of the fulvate-humate type [16]. A significant relationship (direct) between the humus content and R_A NRN is noted only for radium-226 ($r = 0.45$). This can be explained by the fact that ^{226}Ra is present in nature in a dispersed state and is practically not included in the composition of individual minerals, and in soils it has the greatest migration ability [3, 8, 9].

Comparison of data on ranges and average values of activity in the studied soils, sampled before and after 1954, with the data given in Sources and Effects of Ionizing Radiation (^{226}Ra —average specific activity 35 ± 4 Bq/kg, with a typical range of 17–60 Bq/kg; ^{232}Th — 30 ± 3 Bq/kg, 11–64 Bq/kg; ^{40}K — 400 ± 24 Bq/kg, 140–850 Bq/kg) [1, 5], showed a difference only in average R_A . Thus, the content of ^{226}Ra in the studied soils is lower, while ^{232}Th and ^{40}K are, on the contrary, higher.

The soils sampled before the first nuclear tests have narrower ranges of NRN content compared to those taken after 1954. The difference in the average values of R_A between soils of different sampling periods for ^{226}Ra is 9.9 Bq/kg, ^{232}Th —3.1 Bq/kg, and ^{40}K —42 Bq/kg. The difference in the average R_A ^{232}Th and ^{40}K for the soils sampled before and after 1954 is within the limits of σ . The soils sampled before 1954 have $V_\sigma > 30\%$ only in terms of the radium-226 content ($V_\sigma = 43.4\%$). In modern soils (sampled after 1954), V_σ in ^{226}Ra decreases (33.7%), while ^{232}Th (32.7%) and ^{40}K (29.9%), on the contrary, increases.

According to the content of NRN in soils under different types of land, the following features are noted. The highest average R_A ^{226}Ra is characteristic of soils under forest, and the lowest, under arable land. At the same time, the average content in soils under fallow and arable land is similar. The highest average R_A ^{232}Th and ^{40}K is also observed in soils under forest, but the lowest for fallow lands. Probably, this is due to the removal of NRN and other elements in arable soils, a change in the type of humus from humate to fulvate-humate in soils under protective forest belts and the restoration of natural processes in fallow soils [3, 8, 9, 14–16].

The average content of the technogenic radionuclide ^{137}Cs changes in the same sequence as that of ^{226}Ra . Its widest range, as well as the highest content, is noted in soils under forest ($M = 74.2 \pm 43.2$, 26.9–124.4 Bq/kg), and the lowest—under arable land ($M = 40.7 \pm 7.3$, 36.1–47.7 Bq/kg). The soils under the fallow occupy an intermediate position ($M = 60.5 \pm 16.8$, 46.2–74.8 Bq/kg). This may be due to the return of the technogenic radionuclide with litter in the forest and its constant removal with agricultural products.

5 Conclusion

For the first time, data on the specific activity of NRN (^{226}Ra , ^{232}Th and ^{40}K) was obtained in the soils of the “Kamennaya Step” reserve and the island oak forest of “Shipov Les” before the first nuclear tests (before 1954): ^{226}Ra : 20.3 ± 8.8 (7.5–35.0) Bq/kg;

^{232}Th : 42.5 ± 10.6 (25.5–59.1) Bq/kg;

^{40}K : 556 ± 118 (290–728) Bq/kg.

The specific activity of NRN in the studied soils of the “Kamennaya Step” (chernozems and chernozems aric) and “Shipov Les” (molic umbrisols and umbrisols) differs from the averaged data (without division into genetic soil types) given in the report “Sources and effects of ionizing Radiation” [1, 5]. The soils of the “Kamennaya Step” reserve differ most strongly in radium, and the soils of the “Shipov Les” oak forest differ in thorium and potassium.

Comparison of the average R_A NRN in the upper part of the soils (0–5, 5–10 or 0–10 and 10–20 cm) and in the parent rock (90–100 cm) revealed a higher content of NRN in the upper part of the profile in the soils of the “Kamennaya Step”. In the soils of the “Shipov Les”, the difference between humus horizons and SM is insignificant (within σ) for ^{226}Ra and ^{40}K . The specific activity of ^{232}Th is higher in SM.

Comparison of the NRN content in soils sampled before and after 1954 showed a higher average R_A in modern soils only for radium-226. At the same time, in modern soils, the ranges of all NRNs are wider than in soils sampled before 1954.

The highest specific activity of NRN, as well as technogenic ^{137}Cs , is noted in soils under forest, and the lowest: for radium-226 and cesium-137 in arable soils, and thorium-232 and cadium-40 in fallow soils.

Significant correlations between the NRN content were revealed for ^{226}Ra with a humus content ($r = 0.45$) and a fraction of 1–0.25 mm ($r = -0.35$), as well as with pH ($r = -0.40$). R_A ^{232}Th correlated only with fractions of particle size distribution—coarse dust ($r = 0.31$) and silt ($r = -0.31$). For ^{40}K , significant relationships were manifested with pH ($r = -0.33$) and fractions of coarse dust ($r = 0.57$) and physical clay ($r = -0.31$). Nonlinear correlations were found for ^{226}Ra with coarse dust (power-law, $r = 0.41$; linear, $r = 0.26$) and ^{40}K —with silt (logarithmic, $r = -0.30$; linear, $r = -0.29$).

Technogenic ^{137}Cs was found only in the humus horizons of modern soils (2011 and 2017), as well as in the soil (point 746) from the “Shipov Les” of 1962 selection. R_A ^{137}Cs varies in a wide range of 26.9–124.4 Bq/kg ($M = 66.1 \pm 35.3$ Bq/kg), with the most severe contamination of soils in the Spike Wood (point 6.17).

References

1. Sources and effects of ionizing Radiation. United Nations Scientific Committee on the Effects of Atomic Radiation. Report to the General Assembly, with annexes. V.1. Sources. United Nations, N.Y. (2008)
2. Silant'ev AN, SHkuratova IG, Bobovnikova CI (1989) Vertical migration in soils of radionuclides precipitated as a result of the accident at the Chernobyl nuclear power plant. *At Energ* 66(3):194–197
3. Barsukov AO, YAzykeev DV (2012) Horizontal and vertical migration ⁴⁰K, ¹³⁷Cs, ²²⁶Ra, ²³²Th I ²⁴¹Am on the cultivated slope agrolandscapes of the Penza region of varying degrees of steepness. *Izvestia of the Penza State Pedagogical University named after. V.G. Belinskogo* 29:369–374
4. Buraeva EA et al (2013) Content and distribution of natural radionuclides in different types of soil in the Rostov region. *Mod Prob Sci Educ* 4:1–9
5. Perevolockij AN, Perevolockaya TV (2014) About the content ⁴⁰K, ²²⁶Ra i ²³²Th in the forest soils of the Republic of Belarus. *Radiat Biol Radioecol* 54(2):193–200
6. IUSS Working Group WRB 2015 (2014) World Reference Base for Soil Resources 2014, update 2015 International soil classification system for naming soils and creating legends for soil maps. World Soil Resources Reports No. 106. FAO, Rome
7. Dokuchaeva VV (2009) Diversity of soils of the Kamennaya Steppe. *Nauch. Trudy. Pochv. in-t im*
8. Rachkova NG, Shuktomova II, Taskaev AI (2010) The state of natural radionuclides of uranium, radium, and thorium in soils. *Eurasian Soil Sci* 43(6):651–658
9. Titaeva NA (2000) Nuclear geochemistry (2nd volume). *Izd-vo MGU*
10. Vorob'eva LA (2006) Theory and practice of chemical analysis of soils. *GEOS, Monografiya*
11. Activity of radionuclides in counting samples (2014) Measurement methodology for gamma spectrometers using software «SpectralLine». *Mendeleevo*
12. Popov AI, Igamberdiev AM, Alekseev YUV (2009) Statistical processing of experimental data. *SPb.: Izd-vo SPbGU*
13. Gagarina EI, Abakumov EV (2012) Soil-forming rocks with elements of quaternary geology. *SPb.: Izd-vo SPbGU*
14. Aparin BF, Mingareeva EV, Sukhacheva EY, Sanzharova NI (2017) Concentrations of radionuclides (²²⁶Ra, ²³²Th, ⁴⁰K, and ¹³⁷Cs) in chernozems of Volgograd region sampled in different years. *Eurasian Soil Sci* 50(12):1395–1405
15. Mingareeva E et al (2020) Content of radionuclides (²²⁶Ra, ²³²Th, ⁴⁰K, ¹³⁷Cs) in soils of the North-West region of Russia formed on three types of soil forming rocks. In: *E3S web of conferences*, vol 175, p 09018
16. Orlov DS, Grishina LA (1981) Workshop on Humus Chemistry. *MGU*

Shading System Design and Solar Gains Control for Buildings Passive Energy-Efficiency Improvement



Luka Akimov , Vladimir Lvov , Davide de Martino di Montegiordano , Kevin De Mei , Nikolay Osipov , Anastasia Ostrovaia , Sergei Krasnozhen , Vladimir Badenko , and Vitaly Terleev 

Abstract In this article authors discuss a design of static shading that has its aim to fulfill several important requirements in order to provide a building's envelope design optimization. The demonstrated shading system design meets all the necessary requirements for comfort conditions in the space, that include efficiency of shading for mitigation of harmful (excessive) solar gains (that may lead to space overheating and increase in cooling loads) and acceptable amount of useful light entering the space. To design such static shading authors followed several crucial steps that are discussed in detail. The steps are further summarized in a design workflow. The shading is validated to ensure comfortable thermal conditions and visual comfort inside the space under investigation by the use of specific software. The importance of introduction of digital twin technology to the passive energy-efficient design of buildings by means of passive control of thermal and visual conditions with the use of shading systems is as well discussed.

Keywords Energy efficiency · Daylight · Visual conditions improvement · Solar control · Shading design · Digital twin · IESVE

L. Akimov (✉) · A. Ostrovaia · S. Krasnozhen · V. Badenko · V. Terleev
Peter the Great St. Petersburg Polytechnic University, Polytechnicheskaya,
29, St. Petersburg 195251, Russian Federation

L. Akimov · V. Lvov · D. de Martino di Montegiordano · K. De Mei
Politecnico di Milano, 32 Piazza Leonardo da Vinci, 20133 Milan, Italy

V. Lvov
Bureau of Technics-Project, 25ZH Tsvetochnayast., Saint-Petersburg 196084, Russian Federation

D. de Martino di Montegiordano
Maffeis Engineering, 26 via Mignano, 36020 Solagna, Italy

K. De Mei
Stahl + Weiß PartGmbH, Basler Straße 55, 79100 Freiburg im Breisgau, Germany

N. Osipov
Lenmorniiproekt, 3 Mezhevoy kanal st., Saint Petersburg 198035, Russian Federation

V. Terleev
St. Petersburg State Agrarian University, Peterburgskoe shosse,
2, St. Petersburg-Pushkin 196601, Russian Federation

1 Introduction

The nowadays trend of energy-efficient buildings design is driven by the need of sustainable architectural design that may solve different important environmental and ecological issues, such as decrease in CO₂ emission rates, decrease of water and soils contamination [1–3] that may influence soil hydro-physical properties [4–10] and many others. Building façade is the main component that regulates heat and mass transfer between indoor and outdoor environments, proper design of which is the key parameter to sustainable energy-efficient design. All the loads, that buildings are subjected to, such as heating, cooling and ventilation are regulated by building envelope [11–13].

Based on the orientation of the façade, curtain wall systems or large glass windows can be significantly affected by direct solar radiation [14]. Effective daylighting saves energy and improves the quality of the visual environment; reducing reduces operating costs and enhancing occupant satisfaction. Daylight can reduce the amount of electric light needed to adequately illuminate a workspace which as well results in reduction of energy costs. However, allowing too much light associated with solar radiation can have a negative effect onto space subjected to light. It may result into undesirable heat gain that may increase cooling loads [15]. Additionally, uncontrolled solar radiation greatly affects building loads, as well as the visual conditions in the occupied zone [16–18]. Thermal and visual discomfort can noticeably reduce the productivity and well-being of occupants [19]. For this reason, shading device design, that is aimed to control incoming solar radiation, plays an important role in questions of reducing harmful solar gains [20].

The issue of optimization of a building's energy performance draws attention to new types of interactive and adaptive building envelopes—for example, dynamic facades [21–23]. However, being such an interesting and promising technology for lowering the building's energy consumption as well as regulating indoor comfort, it still remains a challenge to assess the performance of adaptive facades, leading to difficulties for efficient design, operation, and maintenance [21, 24–26].

The static shading solar control remains a classical and reliable option, However, its design is a complex procedure that depends on such parameters as efficiency of shading for mitigation of harmful solar gains, acceptable amount of useful light entering the space (visual comfort), structural design of shading bearing structures (cantilever length), control of thermal bridges and other parameters. In this paper we introduce a design of static shading that meets all the necessary requirements for comfort conditions in the space. We followed the workflow that would ensure an adequate static shading design to meet all the important requirements. In our study we provide a daylight conditions verification for the designed shading system. The provided methodology would be useful for designers and engineers in static shading design.

2 Materials and Methods

In this section we introduce the climatic conditions and the description of the building as well as the software that we used in the static shading design workflow.

For the purpose of the analysis of visual performance of shading in terms of DF, we used IESVE (IES virtual environment) 2017, feature pack 04. IESVE is an in-depth suite of integrated analysis tools for the design and retrofit of buildings, as well as the investigation of techniques for energy use optimization of buildings [27].

To analyze weather conditions and sun path, we used Climate Consultant v.6.0.15. Climate Consultant is a simple-to-use, graphic-based computer program that helps engineers understand the climatic conditions for the development of energy optimization strategies. It uses annual 8760 h EPW format climate data [28].

2.1 Building Description

The reference building, where we applied the shading strategy is an office building with daily operating hours from 8am to 6 pm. It consists of 5 floors, 4 m height each (measuring from the floor level to the ceiling level). The building has 2 blocks connected with each other by the tunnel. In Fig. 1 we demonstrate the geometry of the

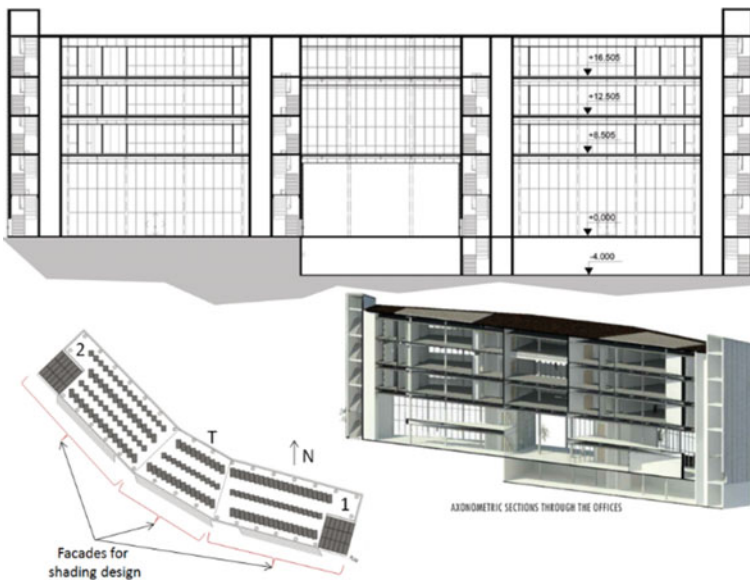


Fig. 1 The building geometry and orientation (1 and 2 are correspondent Block numbers, T stands for tunnel)

building and indicate the facades to which we are going to apply shading strategies. These facades perceive the most solar gains being southeast oriented.

Block 1 facade under consideration is oriented south-west with an inclination of 16° to west from south; block 2 facade under consideration is oriented south-west with an inclination of 46° to west from south.

For the daylight availability inside the building's spaces estimation we are using a raw building carcass opening, meaning that no windows are modelled in our geometry.

2.2 Building Site Climatic Conditions

The building is located in Milan, Italy, that is characterized by humid subtropical climate or mild temperate climate (Cfa) according to Koppen climates classification [29]. This climate is characterized by hot and humid summers, and cold to mild winters. In Fig. 2 we demonstrate the shadow and sun position throughout the year on the building's site, we can see that the building site is exposed to direct sun with very little shadow intersection.

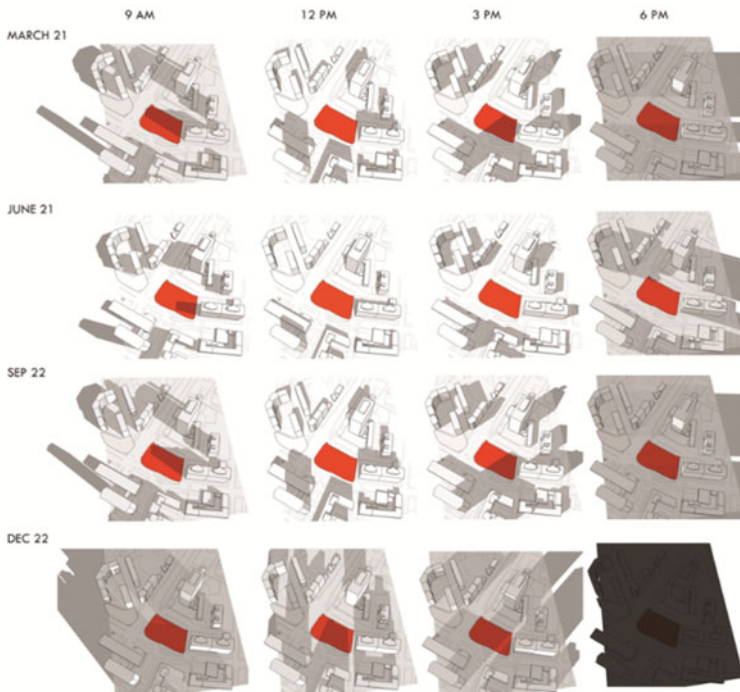


Fig. 2 Sun position and shadow analysis on the building site

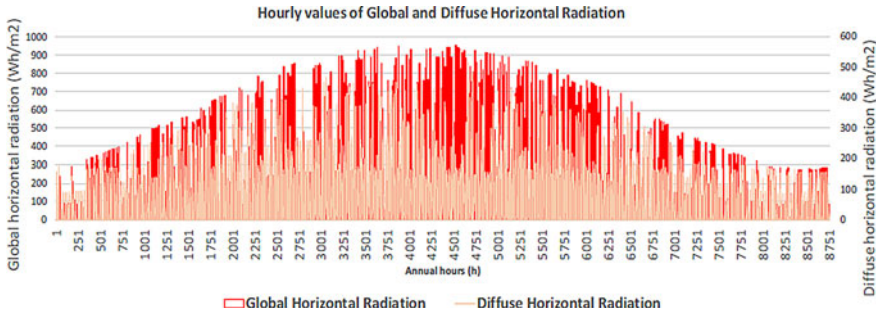


Fig. 3 Global and diffuse horizontal radiation hourly data of the site location (based on.epw weather data)

In the graph present in Fig. 3 we provide global and diffuse horizontal radiation hourly data, the data is taken from.epw weather data [30].

As we can see from the graph, total solar horizontal radiation average value in the area of Milano is 147.4 W/m^2 with maximum of 952 W/m^2 . The diffused horizontal solar radiation average value is 73.8 W/m^2 . The area of Milano perceives a good amount of solar gains that can be either used in the passive strategies design or become harmful and lead to the increased demand in cooling loads. This data is needed for further solar control design.

3 Results and Discussion

In our design we tried to apply shading that will mitigate as much harmful solar gains as possible respecting the adequate dimension of overhang and vertical fins from structural point of view and without limiting illuminance parameters for comfort occupancy of the envelope (daylight factor).

3.1 Block 1 South Facing Façade Shading Design

Block 1 façade under consideration is oriented south-west with an inclination of 16° to west from south (see Fig. 1 and discussion in Sect. 2.1). Since the block 1 façade is mostly south oriented, only horizontal shading devices are necessary to mitigate harmful solar radiation inside the building.

With the use of Climate Consultant and Sun Shading chart (see Fig. 4) we are able to calculate the horizontal shading angle that allows us to mitigate harmful solar gains as much as possible.

In Fig. 4 the harmful solar gains and corresponding number of hours when the shading is needed is indicated with red dots.

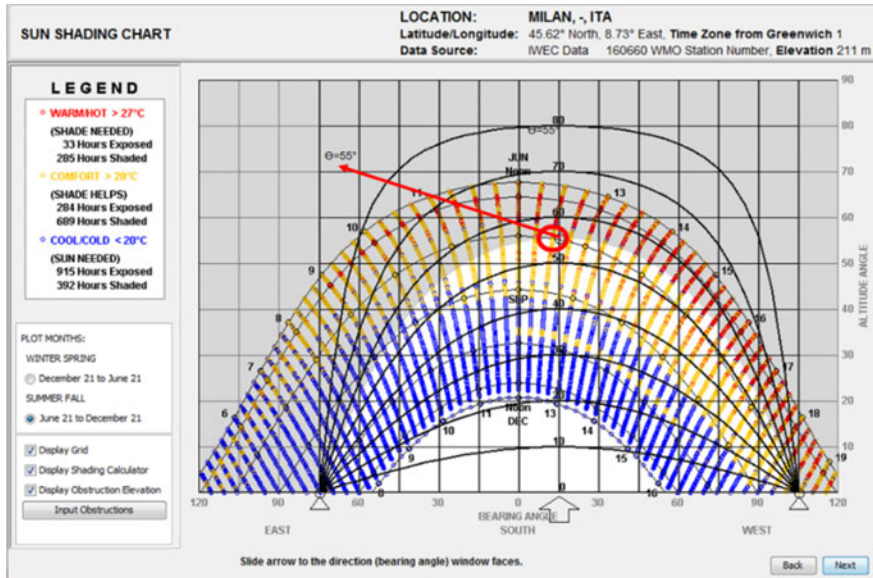


Fig. 4 Sun shading chart for Block 1 façade (south-facing façade) shading design

The bearing angle of our façade is 16° from south to west. To guarantee a minimum exposure to harmful solar gains inside the building (55° from Fig. 3), it is necessary to adopt a horizontal overhang of 1.40 m. We decided to incline it by 15° to reduce its length without affecting the efficiency of the shading system. With this system we guarantee a mitigation of 90% of harmful solar radiation hours in the Block 1 during fall and summer periods.

3.2 Block 2 South-West Facing Façade Shading Design

Block 2 façade under consideration is oriented south-west with an inclination (façade bearing angle) of 46° to west from south. According to Fig. 5, since the façade is facing south and west, the horizontal and vertical shading devices are necessary to mitigate solar radiation inside the building.

To cut a considerable amount of harmful solar gains coming from west exposure, we decided to place vertical fins that would shade solar gains coming from west. We have to cut solar gains coming from bearing angle of 61° onwards towards west. That gives us information that we have to shade 15° exposure towards west from façade bearing angle (46° from Fig. 5).

As in Sect. 3.1, to guarantee a minimum exposure to harmful solar gains inside the building (55° from Fig. 5), it is necessary to adopt a horizontal overhang of 1.40 m. Additionally, from Fig. 5 it is required to place 0.55 m long vertical fins rotated 45°

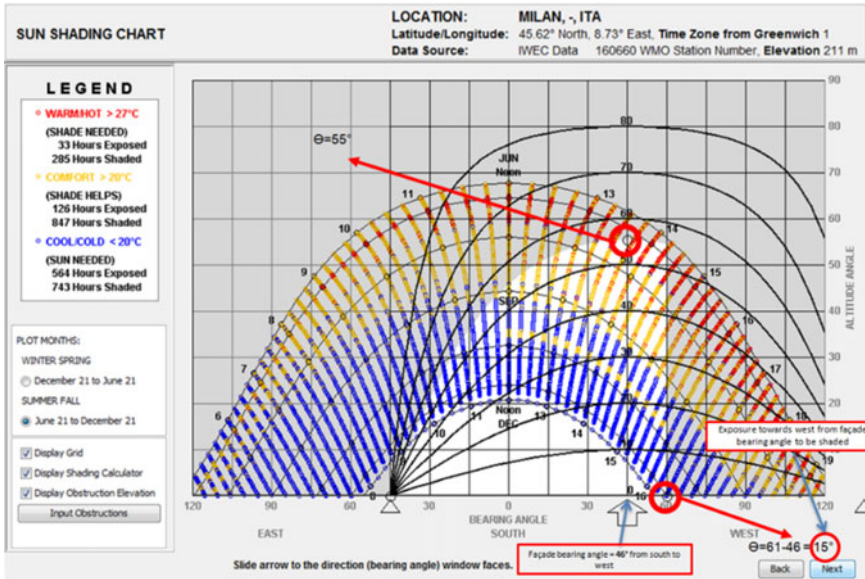


Fig. 5 Sun shading chart for Block 2 façade (south and west-facing façade) shading design

every 1 m, in this case we are able to cut all the harmful solar gains coming from 15° west exposure.

Finally, we decided to use 1.2 m overhangs inclined 15°, one per floor, and 0.55 m long vertical fins rotated 45°, one every 1 m. With this system we guarantee a mitigation of 90% of harmful solar radiation hours in the Block 2 during fall and summer periods.

3.3 Tunnel South-West Facing Façade Shading Design

The tunnel façade under consideration is oriented south-west with an inclination (façade bearing angle) of 30° to west from south. According to Fig. 6, applying the same logic as in Block 2 (Fig. 5), the horizontal and vertical shading devices are necessary to mitigate solar radiation inside the building.

The same as in the cases of Blocks 1 and 2, to mitigate harmful solar gains coming from south exposure, we have decided to use 1.2 m horizontal overhangs inclined 15° one per floor. To mitigate harmful solar gains coming from west exposure, we have decided to use 0.45 m long (in plan) vertical fins inclined 45° from vertical axes in plan view, one every 1 m. In this case we can manage to cut harmful solar gains coming from 30° exposure towards west from façade bearing angle to mitigate as much solar gains as possible (comes from the analysis of Sun shading chart on Fig. 6).



Fig. 6 Sun shading chart for Tunnel façade (south and west-facing façade) shading design

With this system we guarantee a mitigation of 90% of harmful solar radiation hours in the Tunnel during fall and summer periods.

In Table 1 we demonstrate the schemes of the designed overhangs on the façades of Blocks 1 and 2 and Tunnel. Overhang is indicated with red line, the transparent part of the façade is indicated with blue line. In Fig. 7 the render of the final shading system solution is present.

Table 1 Shading systems schemes

Blocks 1, 2 and Tunnel horizontal overhang	Block 2 vertical fins	Tunnel vertical fins



Fig. 7 The render of final shading system design attached to building blocks

3.4 Daylight Performance Verification

The above mentioned steps of static shading system design can be very beneficiary in terms of energy-efficiency management, especially in cases where the mitigation of solar gains is a must (climates with very high amount of solar radiation). However, shading system can drastically influence a visual performance of the internal space of the building. In order to verify whether our design provides an adequate visual performance, we performed a simulation to determine if the light inside our building meets the requirements set by EN12464-1 “Light and lighting. Lighting of work-places”.

For the sake of daylight performance verification, we use a classical daylight metric that is called “daylight factor” (DF). The daylight factor is conceived as a means of rating daylighting performance *independently* of the actually occurring, instantaneous sky conditions [31]. It is defined as the ratio of the internal horizontal illuminance E_{in} at some arbitrary point in a space to the unobstructed (external) horizontal illuminance E_{out} from a hemisphere of sky [32]. The higher the DF, the more natural light is available in the room. Equation 1 is the DF expression [33]:

$$DF = 100 E_{in}/E_{out} \quad (1)$$

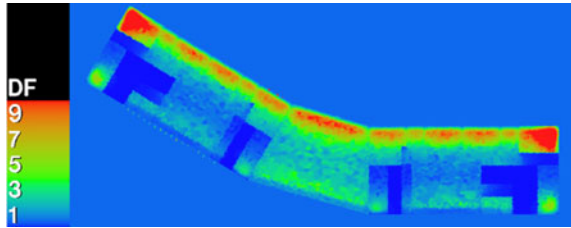
Where:

E_{in} is the internal illuminance at a fixed point,

E_{out} is the external horizontal illuminance under an overcast or uniform sky, as defined by the Commission Internationale de l’Eclairage (CIE).

[34] determines the comfortable range of daylight factor between 2 and 5% for working/studying activities. If DF is lower than 2, the working space is not adequately

Fig. 8 DF of the analyzed space (IESVE presentation)



lit—artificial lighting is required; if DF is over 5—Well lit—artificial lighting generally not required, except at dawn and dusk—but glare and solar gain may cause problems.

Our goal was to shade the space from harmful solar gains that are associated with overheating and visual comfort issues such as glare that are predominant in summer.

DF estimation may provide better idea regarding visual comfort conditions, and its estimation is present in Fig. 8.

As we can see, with the use of the designed static shading the average daylight factors inside the offices are in the range of 2 and 5. Hence, we can conclude that the total average DF is within the acceptable limit.

4 Conclusion

In this paper we introduced a design of static shading that meets all the necessary requirements for comfort conditions in the space: efficiency of shading for mitigation of harmful solar gains and acceptable amount of useful light entering the space (visual comfort). To do so, we followed several crucial steps that could be summarized in a design workflow:

1. Climatic conditions of building site analysis: for shading design it includes solar radiation analysis and shading analysis.
2. Sun shading chart analysis to define harmful solar gains and approaches for their mitigation.
3. Shading design that meets the considerations derived from the analysis mentioned in steps 1 and 2.
4. Check of daylight availability of the space with the use of designed shading. In case the daylight availability is insufficient, return to step 2.

Additionally, it is important to mention that in cases where it is difficult to meet both comfortable thermal conditions and visual comfort by means of static shading system, it may be considered to apply a dynamic shading system to an envelope. Dynamic facades respond to an environmental condition change (amount of daylight, outdoor temperature or other environmental conditions) [35, 36]. To control the performance of such façade, the adoption of digital twin technology [37] might be useful. Since the comfort inside the building space is a complex multi-parametric

problem, the design of a system that might forecast changes that might occur in the space under consideration is beneficiary. It might help to make decisions that would ensure thermal and visual comfort of the occupants, which is a question of the further research on digital twins' applicability.

Acknowledgements The research is partially funded by the Ministry of Science and Higher Education of the Russian Federation as part of World-class Research Center program: Advanced Digital Technologies (contract No. 075-15-2020-934 dated 17.11.2020).

References

1. Andrianova MJ, Vorobjev KV, Lednova JA, Chusov AN (2014) A short-term model experiment of organic pollutants treatment with aquatic macrophytes in industrial and municipal waste waters. *Appl Mech Mater* 587–589:653–656
2. Bondarenko EA, Il'ina KH, Andrianova MJu, Chusov AN (2017) Main inorganic ions and electric conductivity of polluted urban streams. *Mag Civil Eng* 68(08):37–44. <https://doi.org/10.5862/MCE.68.4>
3. Andrianova MJ, Bondarenko EA, Krotova EO, Chusov AN (2014) Comparison of chemical and optical parameters in monitoring of urban river Okhta. In: 2014 IEEE workshop on environmental, energy, and structural monitoring systems proceedings, pp 1–5
4. Poluektov RA, Oparina IV, Terleev VV (2003) Three methods for calculating soil water dynamics. *Russ Meteorol Hydrol* 11:61–67
5. Terleev V et al (2016) Modelling the hysteretic water retention capacity of soil for reclamation research as a part of underground development. *Procedia Eng* 165:1776–1783
6. Terleev V et al (2017) Hysteretic water-retention capacity of sandy soil. *Mag Civil Eng* 70:84–92
7. Terleev V et al (2019) Models of hysteresis water retention capacity and their comparative analysis on the example of sandy soil. In: Murgul V, Pasetti M (eds) International scientific conference energy management of municipal facilities and sustainable energy technologies EMMFT 2018. Springer, Cham, pp 462–471. https://doi.org/10.1007/978-3-030-19868-8_46
8. Terleev V et al (2019) Improved hydrophysical functions of the soil and their comparison with analogues by the Williams-Kloot test. In: Murgul V, Pasetti M (eds) International scientific conference energy management of municipal facilities and sustainable energy technologies EMMFT 2018. Springer, Cham, pp 449–461. https://doi.org/10.1007/978-3-030-19868-8_45
9. Terleev V et al (2018) Five models of hysteretic water-retention capacity and their comparison for sandy soil. In: MATEC web conference, vol 193, p 02036
10. Dunaieva I et al (2019) GIS services for agriculture monitoring and forecasting: development concept. In: Murgul V, Pasetti M (eds) International scientific conference energy management of municipal facilities and sustainable energy technologies EMMFT 2018. Springer, Cham, pp 236–246. https://doi.org/10.1007/978-3-030-19868-8_24
11. Petritchenko MR, Kotov EV, Nemova DV, Tarasova DS, Sergeev VV (2018) Numerical simulation of ventilated facades under extreme climate conditions. *Mag Civil Eng* 77:130–140
12. Baranova D, Sovetnikov D, Borodinecs A (2018) The extensive analysis of building energy performance across the Baltic Sea region. *Sci Technol Built Environ* 24:982–993
13. Zemitis J, Terekh M (2018) Optimization of the level of thermal insulation of enclosing structures of civil buildings. In: MATEC web conference, vol 245, p 06002
14. Yan S, Li X, Wang B, Lyu W (2019) Free-running temperature of room equipped with pipe-embedded double skin façade: a case study in Guangzhou. *Sci Technol Built Environ* 25:1132–1142

15. Kubba S (2012) Handbook of Green Building Design and Construction: LEED, BREEAM, and Green Globes. Butterworth-Heinemann
16. Eltaweel A, Su Y (2017) Parametric design and daylighting: a literature review. *Renew Sustain Energy Rev* 73:1086–1103
17. Hafiz D (2015) Daylighting, space, and architecture: a literature review. *Enquiry ARCC J Architect Res* 12
18. Ricci A, Ponzio C, Gaspari J, Naboni E (2019) A study on the impact of climate adaptive building shells on indoor comfort. *JFDE* 7:27–40
19. Al horr Y, Arif M, Katafygiotou M, Mazroei A, Kaushik A, Elsarrag E (2016) Impact of indoor environmental quality on occupant well-being and comfort: a review of the literature. *Int J Sustain Built Environ* 5:1–11
20. Tablada A, Zhao X (2016) Sunlight availability and potential food and energy self-sufficiency in tropical generic residential districts. *Sol Energy* 139:757–769
21. Konstantoglou M, Tsangrassoulis A (2016) Dynamic operation of daylighting and shading systems: a literature review. *Renew Sustain Energy Rev* 60:268–283
22. Fiorito F, Sauchelli M, Arroyo D, Pesenti M, Imperadori M, Masera G, Ranzi G (2016) Shape morphing solar shadings: a review. *Renew Sustain Energy Rev* 55:863–884
23. Couvelas A, Phocas M, Maden F, Matheou M, Ölmez D (2018) Daylight performance of an adaptive façade shading system integrated on a multi-storey office building
24. Attia S, Bilir S, Safy T, Struck C, Loonen R, Goia F (2018) Current trends and future challenges in the performance assessment of adaptive façade systems. *Energ Build* 179:165–182
25. Attia S (2018) Evaluation of adaptive facades: the case study of Al Bahr Towers in the UAE. *QScience Connect* 2017:6
26. Attia S, Bashandy H (2016) Evaluation of Adaptive Facades: The Case Study of AGC Headquarter in Belgium. Ghent University
27. IES Virtual Environment (IESVE). <https://www.iesve.com/software>. Accessed 14 Apr 2021
28. Climate Consultant. <https://climate-consultant.informer.com/6.0/>. Accessed 14 Apr 2021
29. Peel MC, Finlayson BL, McMahon TA (2007) Updated world map of the Köppen-Geiger climate classification. *Hydrol Earth Syst Sci* 11:1633–1644
30. EnergyPlus official web-site. <https://energyplus.net/weather>. Accessed 14 Apr 2021
31. Tzempelikos A, Athienitis AK (2007) The impact of shading design and control on building cooling and lighting demand. *Sol Energy* 81:369–382
32. Mardaljevic J, Christoffersen J (2017) ‘Climate connectivity’ in the daylight factor basis of building standards. *Build Environ* 113:200–209
33. Kubba S (2010) Indoor Environmental Quality. LEED Practices, Certification, and Accreditation Handbook, pp 211–269
34. Yarham RE, Wilson J (1999) CIBSE lighting guide: daylighting and window design. Lighting Guide LG10
35. Loonen RCGM, Trčka M, Cóstola D, Hensen JLM (2013) Climate adaptive building shells: state-of-the-art and future challenges. *Renew Sustain Energy Rev* 25:483–493
36. Luible A (2014) Memorandum of Understanding for the implementation of a European Concerted Research Action designated as COST Action TU1403: Adaptive Facades Network. COST Action TU1403
37. Rasheed A, San O, Kvamsdal T (2020) Digital twin: values, challenges and enablers from a modeling perspective. *IEEE Access* 8:21980–22012

Features of Determining the Entrepreneur' Profit in the Agricultural Land Cadastral Valuation Under Buildings and Structures



Vladimir Nosov , Kirill Zhichkin , Lyudmila Zhichkina ,
Olga Vaganova , and Andrey Kotyazhov 

Abstract Currently, there is an acute problem of acquiring agricultural land for the production, storage and primary processing of agricultural products and determining the value of these sites. The use of the allocation method to determine the value of land under production facilities is fraught with a number of difficulties. Based on this, it is proposed to determine the value of the plot as the sum of the value of the land plot, calculated according to the value of the surrounding land, plus a certain amount of added value arising from the synergistic effect of joint investments in the creation of a single real estate object. Several possible variants of such calculations were considered in the work. As a result, it was found that the market value of the land is made up of the market value of the surrounding land (as a complete analogue of the assessed plot) and a coefficient equal to the rate of return on invested capital. In this case, the market (in this case—cadastral) value of the acquired land can be obtained from the results of the assessment of the first type of land use.

Keywords Entrepreneur's profit · Agricultural land · Cadastral valuation · Buildings · Full replacement cost

V. Nosov · A. Kotyazhov
K.G. Razumovsky Moscow State University of Technologies
and Management, Moscow 109004, Russia

K. Zhichkin (✉) · L. Zhichkina
Samara State Agrarian University, Kinel 446552, Russia

O. Vaganova
Yuri Gagarin State Technical University of Saratov, 410054 Saratov, Russia

V. Nosov
Peoples' Friendship University, Moscow 117198, Russia

1 Introduction

The third type of permitted use includes agricultural land occupied by buildings, structures, structures used for the production, storage and primary processing of agricultural products [1–3].

In the rural industrial real estate market, only single objects are circulating (land plots with buildings and structures located on them), and the overwhelming majority of objects are located on the settlements lands. Separate plots for industrial real estate (outside settlements) are not for sale or offered for sale [4–8].

This situation is easy to explain. In the Samara region, outside the settlements, there is an excess of agricultural land, which is quite simple to purchase for construction by objects used for the production, storage and primary processing of agricultural products. That is, there is a buyer's market here, which, although dictating prices, is ready to pay for building land somewhat more expensive than the surrounding area (agricultural land or non-arable land) [9, 10]. The excess of the land value under production facilities over the value of surrounding land is ensured by the possibility of supplying communications, lower transport costs, and the availability of labor. In this situation, it is also necessary to take into account the influence of a nearby large settlement [11–15].

There are very few such plots on the open land market (both for sale and for rent) in the Samara region—single offers of agricultural land for building near large settlements. This implies a low possibility of determining the market value by comparative or income approach. This forces the appraiser to turn to indirect methods for determining the land market value [16–19].

The use of the allocation method to determine the land value under production facilities (the value of the building itself is deducted from the value of a single object, the remainder of the value refers to the land) faces the following difficulties that cannot be eliminated in the cadastral (mass) valuation:

- establishment of the exact full replacement cost of construction of buildings on the estimated site (there is no information about the design features of the facilities);
- determination of the exact value of physical and economic wear and tear [20–22].

If we assume that the minimum market value of buildings outside settlements in rural areas fluctuates in the range of 500–1000 rubles/m², then the estimated cost of the occupied land (for example, in the Bezenchuksky district) in the amount of 2–3 rubles/m² is far beyond the calculation accuracy of both full replacement cost of construction (PVS) and all types of wear.

2 Methods and Materials

Based on the foregoing, we suggest, it was decided not to use the allocation method to establish the market value of the third type permitted use land plots.

In this regard, the following calculation logic is used:

- historically, before the formation of a building or structure, there was free land (most often near the settlement border);
- on this land, an entrepreneur performed work to create an improvement and a single object was formed.

Thus, the assessment consists subject of a land plot (part of the surrounding area), as well as buildings and structures as part of the future business [23].

The owner who provided (sold) a land plot for this object can rightly claim a part of the future profit, which arises from the synergistic effect when two assets are added—land and improvements [24, 25]. A fair distribution of this asset-sharing gain can be estimated by the amount the parties contribute to the joint venture [26–29].

Thus, the value of the land plot under the object (improvement) can be estimated as the sum of the land plot value, calculated from the value of the surrounding land, plus a certain amount of added value arising from the joint investments synergistic effect in the single real estate object creation [30, 31].

In addition, abstract-logical and statistical methods were used in the study. In particular, we used absolute, relative and average values. The research results are presented in tabular and graphical forms.

3 Results and Discussion

In an active market, the value of the synergistic effect is defined as the difference between the initial investment in the project and the object selling cost on the market. In the market absence (i.e., the opportunity absence to sell an object), the synergetic effect can, in a first approximation, be equated to the entrepreneur's profit—theoretically, the object being sold should bring some kind of profit, otherwise it was not worth building.

Calculation of the entrepreneur's profit. Option 1. The value of the enterprise's profit can be calculated by analyzing the economic results of the agricultural enterprises activities in the Samara region. According to the official data of the territorial body of the Federal State Statistics Service for the Samara region on the enterprises profitability engaged in agricultural production, the following information was revealed.

The overall profitability (by the type of activity "Agriculture, hunting, forestry in 2010, taking into account small businesses) is 5%.

The profitability (loss ratio) of non-current assets is 1.4%.

In addition, we studied the annual balance sheets, forms No. 2 and profit and loss statements for 2008–2010 for a number of agricultural enterprises in the Samara region.

Based on these documents, the activities of these enterprises were analyzed and conclusions about profitability were drawn. The return on net assets indicator reflects the return on capital invested in the company. In fact, this is similar to the

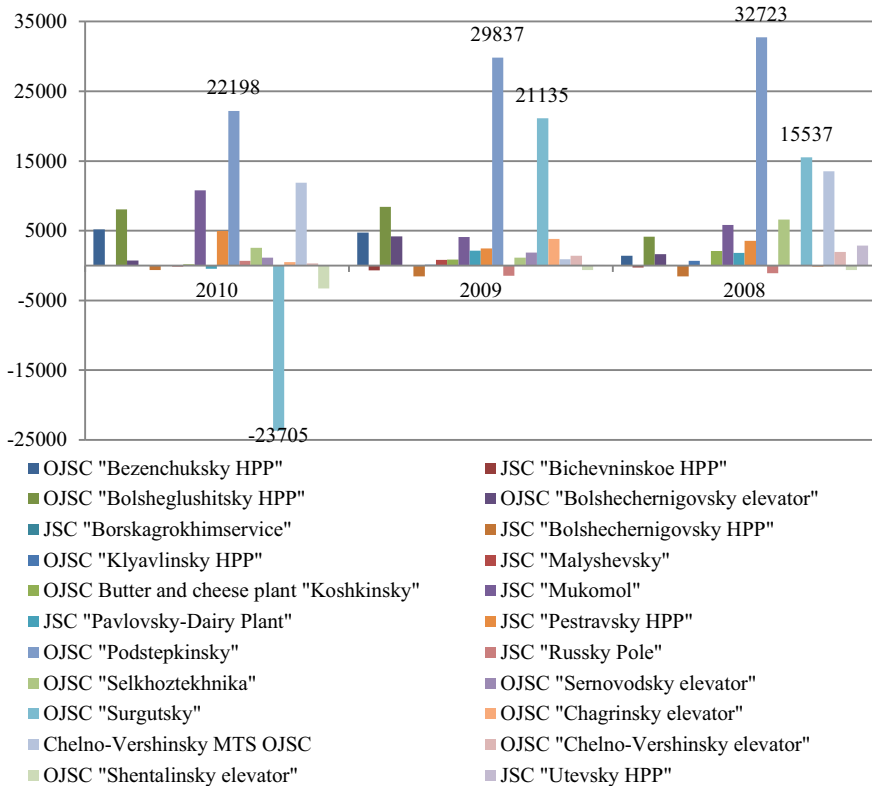


Fig. 1 Net profit (loss) of the reporting period, thousand rubles

entrepreneurial profit concept. Information on these enterprises is shown on Fig. 1 and 2.

Analyzing the data of balance sheets and profit and loss statements, the enterprises net assets profitability for 2008–2010 was calculated. From the data on Fig. 1 and 2, it can be seen that enterprises numbered 2, 6, 11, 13, 14, 21 are either clearly unprofitable, or gross errors were made in the financial statements.

Enterprises numbered 4, 7, 8, 9, 16, 17, 18 have very low profitability. A prudent entrepreneur with such a profitability will abandon the activity, preferring an alternative investment of funds, for example, in a bank deposit, which is more profitable and carries less risks, therefore the analysis includes the following enterprises indicated on Fig. 3.

The average return on net assets left over for the analysis of the nine businesses is 27%.

The entrepreneur’s profit (return on net assets) according to the first calculation method is 27%.

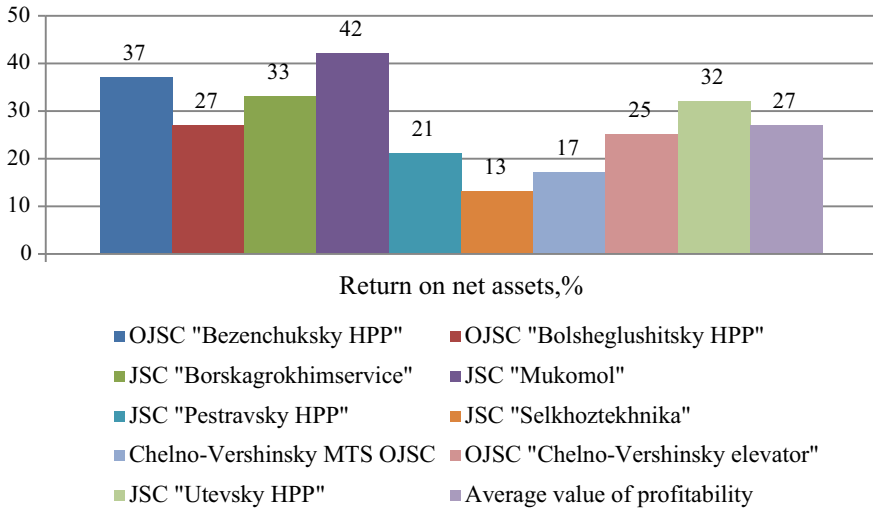


Fig. 3 The average return on net assets

construction project is not less than the profit from an alternative project that has the same level of risk and the same duration as and new construction [15].

The formula for calculating the entrepreneur’s profit can be calculated:

$$PP = n * \frac{Y_a}{2} (1 + n * \frac{2Y_a}{3} + C_0 (1 + \frac{2}{3} * n^2 * Y_a^2)) \tag{1}$$

where PP—the developer’s profit, %;

C₀—the share of the advance payment in the total amount of payments;

n—the number of construction years (period);

Y_a—the annual rate of return on invested capital.

The construction period n is determined according to Building Codes and Regulations 1.04.03-85 “Standards for the duration of construction and backlog in the construction of enterprises, buildings and structures”, for an approximately identical object.

The calculation method for determining the duration of the construction of objects n is based on the functional dependence of the construction period on the cost of construction and installation works.

For the main industries, this dependence is expressed as functions:

$$n = A_1\sqrt{C} + A_2C; \tag{2}$$

$$n = A_1\sqrt{C} + A_2; \tag{3}$$

Table 1 Calculation of the investment risk premium

Risk factors	Recommended premium range	Accrued premium	Explanations
Clientele diversification	0–4%	2.00%	The circle of buyers and users of real estate is wide, the risk is not high
Industrial and territorial diversification	0–3%	3.00%	The industry is strictly tied to the territory, the range of services is narrow—the risk is maximum
Revenues: profitability and predictability	0–4%	4.00%	In crisis and post-crisis periods, the uncertainty is great, the risk is maximum ñ
Financial structure	0–5%	2.50%	Depends on the company, the average is used
Company size	0–3%	1.50%	Depends on the company, the average is used
Quality of management	0–5%	2.60%	Affects all areas of company activity, the premium is calculated as the average of the previous awards
Other risks	0–5%	2.50%	Depends on the company, the average is used
Total premium		18.10%	

$$n = A_1C + A_2, \quad (4)$$

where C —the volume of construction and installation work, million rubles, at prices in effect since 1984;

A_1, A_2 —parameters of the equation, determined from statistics.

The ratio of C_0 is assumed to be 0.50 based on the assumption that the investor initially advances in construction 50.0% of the work total cost. The annual rate of return Y_a is set at 30%, which roughly corresponds to the estimated capitalization ratio for similar properties, taking into account the typical investment risks and the 10-year return on capital (Ring method).

The rate of return on invested capital for the construction industry was calculated on a cumulative basis. In this case, to build the rate, the risk-free rate of return is taken as a basis, and then premiums for special risks of the activity are added to it. The long-term GKO-OFZ rate was taken as the risk-free rate, the list and range

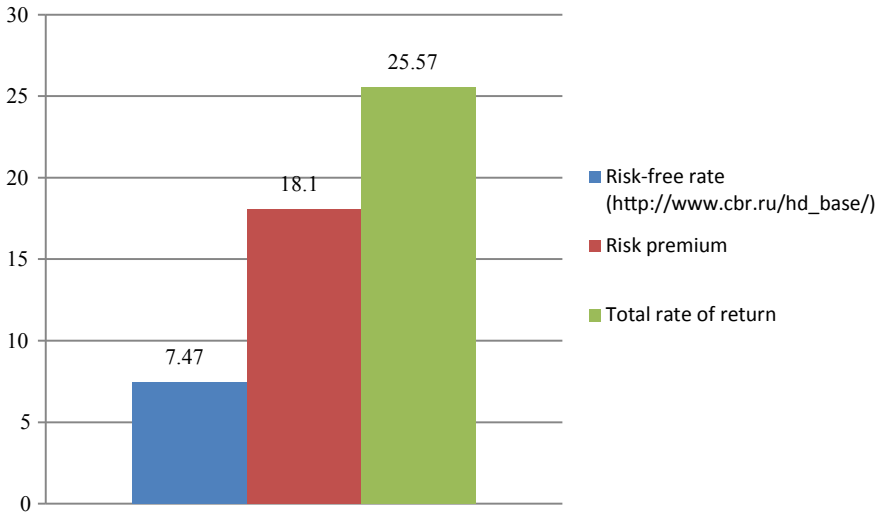


Fig. 4 Calculation of the rate of return on invested capital

of risk premiums—based on research materials from the Institute for Economic Development of the World Bank.

Based on the calculations performed, we take the rate of return on invested capital to calculate the entrepreneur's profit in the construction industry at 25.57% (Table 1, Fig. 4).

Both methods of calculating the entrepreneur's profit magnitude showed similar results, therefore, for further calculation, we take the average value—26.28%.

Thus, a project each co-investor for the agricultural facility construction can count on receiving its part of the synergistic effect (equal to the entrepreneur's profit) in the amount of 26.28%.

To confirm this assumption, we will carry out two simple calculations of the construction cost of conditional agricultural production facilities and determine the share of the synergistic effect attributable to each co-investor.

The cost calculation was performed using Consolidated Indices of Construction Costs. The aggregated indicators given in the collections are compiled in prices and rates of the base period—1969.

The calculation is carried out according to the formula:

$$CC = C_v * V_{zd} * I_1 * I_2 * I_3 * PP * VAT \quad (5)$$

where: CC—replacement cost (construction cost) at the date of assessment;
 C_v —the replacement cost of 1 m³ of the assessed object in the base period 1969;
 V_{zd} —the volume of the evaluated object;
 I_1 —index of the rise in construction and installation costs by 1.01.84—1.2;

Table 2 Calculation of the cost of building a cowshed

Assessment object	Double row cowshed
Capital group	2
Climatic region	2
Total area of the assessment object, m ²	1 000.00
Construction volume of the assessment object, m ³	4 600.00
Year built	2010
No. of Consolidated Indices of Construction Costs collection and tables	Col. № 26, table 3
An analogue characteristics from Consolidated Indices of Construction Costs	DOUBLE ROW COWSHED. Buildings without an attic space (combined coverage). Roofing roofing material for reinforced concrete. Capital group II. Central heating, ventilation, plumbing, sewerage, hot water supply, electric lighting and concrete feeders with a wooden stall frame are taken into account
Unit of measurement	m ³
Replacement cost according to the collection, rubles/m ³	14.1
Correction factor for climatic region	1.00
Correction factor for capital group	1.00
Correction factor for building volume	1.00
Other amendments	1.00
Adjusted cost of the aggregated indicator, rubles/m ³ in 1969 prices	14.1
The same, in prices of 1984 (Resolution of the State Construction Committee of 11.05.83, coefficient 1.2)	16.92
The same, in 1991 prices (Letter of the State Construction Committee of 6.09.90, No. 14-D. Coefficient 1.6)	27.07
Construction and installation work index from 1991 to the date of assessment (Index of rise in the cost of construction and installation works as of the assessment date. Data from the Center for Pricing in Construction)	63.687
Aggregated indicator at current prices, rubles/m ³	1 724
Total for the subject of assessment, rubles	1 724 134
The same, taking into account unforeseen costs 2%, rubles	1 758 617
The same, with VAT (replacement cost excluding depreciation), rubles	2 075 168

Table 3 Calculation of profit for the owner of the land under the cowshed

№	Parameter	Indicator
1	Density of construction of cowshed	46%
2	Built-up area under the cowshed, m ²	1 000.00
3	The area required for the normal functioning of the cowshed, m ²	2 174
4	The cost of agricultural land, rubles/m ² (conditionally)	2.0
5	Cost of land under the cowshed, rubles	4 348
6	Cowshed construction cost, rub	2 075 168
7	Total cost of creating a single object, rubles	2 079 516
8	Share of land in the total value of the property	0.002090787
9	Investor profit 26.28% as a synergistic effect, rubles	546 497
10	Share of profit for the land owner, rubles	1 143
11	Market value of the land allocated for the cowshed, rubles/m ²	2.53

I_2 —index of the rise in the cost of construction and installation work on 1.01.91—1.6;

I_3 —the index of the rise in the cost of construction and installation work on the date of assessment—63.687;

PP—the entrepreneur's profit;

VAT—value added tax (Table 2).

For the normal functioning of this building, a land plot is required, the area of which is determined taking into account the normative building density (Building Codes and Regulations II-97-76 “General plans of agricultural enterprises”). For cowsheds, the ratio of the building area and the standard area of the required land plot is on average (for buildings for cattle keeping) 46%.

The increase in the value of land due to the influence of the synergistic effect was 26.28% (Table 3).

Second calculation. For the normal functioning of this object, a land plot is required, the area of which is determined taking into account the normative building density (Building Codes and Regulations II-97-76 “General plans of agricultural enterprises”).

For greenhouses, the ratio of the building area and the standard area of the required land plot is on average 55%.

The increase in the land value from the influence of the synergistic effect was also 26.28% (Tables 4, 5).

Table 4 Calculation of the cost of building a greenhouse

Assessment object	Greenhouse
Capital group	2
Climatic region	2
Total area of the assessment object, m ²	1 010.00
Construction volume of the assessment object, m ³	4 000.00
Total building area, m ²	1 010.00
Construction volume of the building, m ³	4 000.00
Year built	2010
No. of Consolidated Indices of Construction Costs collection and tables	Col. № 26, section 2, table 149 a
Characteristics of an analogue from Consolidated Indices of Construction Costs	Greenhouse for growing vegetables. Belt foundations made of concrete blocks and monolithic concrete; precast concrete slab walls; roof-covering-metal glazed structures; dales asphalt and unpaved; concrete pools. Capital group I. Central heating, air heating, underground pool heating, humidification system, irrigation water supply system, technological pipelines and electric lighting are taken into account
Unit of measurement	m ²
Replacement cost according to the collection, rubles/m ³	45.3
Correction factor for climatic region	1.00
Correction factor for capital group	1.00
Correction factor for building volume	1.00
Other amendments	1.00
Adjusted cost of the aggregated indicator, rubles/m ³ in 1969 prices	45.3
The same, in prices of 1984 (Resolution of the State Construction Committee of 11.05.83, coefficient 1.2)	54.36
The same, in 1991 prices (Letter of the State Construction Committee of 6.09.90, No. 14-D. Coefficient 1.6)	86.98
Construction and installation work index from 1991 to the date of assessment (Index of rise in the cost of construction and installation works as of the date of assessment. Data from the Center for Pricing in Construction)	63.687
Aggregated indicator at current prices, rubles/m ³	5 539

(continued)

Table 4 (continued)

Assessment object	Greenhouse
Total for the assessment subject, rubles	5 594 633
The same, taking into account unforeseen costs 2%, rubles	5 706 526
The same, with VAT (replacement cost excluding depreciation), rubles	6 733 700

Table 5 Calculation of profit for the owner of the land under the greenhouse

№ п/п	Parameter	Indicator
1	Density of construction of greenhouse	55%
2	Built-up area under the greenhouse, m ²	1 010.00
3	The area required for the normal functioning of the greenhouse, m ²	1 836
4	The cost of agricultural land, rubles/m ² (conditionally)	2.0
5	The cost of the land under the greenhouse, rubles	3 673
6	Greenhouse construction cost, rub	6 733 700
7	Total cost of creating a single object, rubles	6 737 373
8	Share of land in the total value of the property	0.000545128
9	Investor profit 26.28% as a synergistic effect, rubles	1 770 582
10	Share of profit for the land owner, rubles	965
11	Market value of land allocated for a greenhouse, rubles/m ²	2.53

4 Conclusion

As a result of the study, it was found that for agricultural land used for the production, storage and primary processing of agricultural products, the use of the allocation method to determine the value of a given land plot is associated with a number of difficulties. Based on this, it is proposed to determine the value of the plot as the sum of the value of the land plot, calculated according to the value of the surrounding land, plus a certain amount of added value arising from the synergistic effect of joint investments in the creation of a single real estate object. Several possible variants of such calculations were considered in the work. As a result, it was found that the market value of the land is made up of the market value of the surrounding land (as a complete analogue of the assessed plot) and a coefficient equal to the rate of return on invested capital.

We have confirmed the assumption that the land owner that will be built up, as a co-investor of the project, has the right to add to the value of the land in the amount of the rate of return on invested capital—26.28%.

In this case, the land market value is made up of the market value of the surrounding land (as a complete analogue of the assessed plot) and a coefficient equal to the rate of return on invested capital, i.e. for this assessment—1.2628.

$$\text{Ccad} = \text{Csur} \bullet 1,2628 \quad (6)$$

The market (in this case, the cadastral) value of the surrounding land can be obtained from the results of the first type use lands assessment (arable land, pastures, hayfields).

References

1. Abramov VL, Kodirov FA, Gibadullin AA, Nezamaikin VN, Borisov OI, Lapenkova NV (2020) Formation of mechanisms for ensuring the sustainability of industry. In: Journal of physics: conference series, vol 1515, p 032025. <https://doi.org/10.1088/1742-6596/1515/3/032025>
2. Lakomiak A, Zhichkin KA (2019) Photovoltaics in horticulture as an opportunity to reduce operating costs. A case study in Poland. In: Journal of physics: conference series, vol 1399, p 044088. <https://doi.org/10.1088/1742-6596/1399/4/044088>
3. Staselko EA, Erdniev OV, Balinova TA et al (2019) Principles of cadastral valuation and usage of water reservoirs in the Republic of Kalmykia. In: IOP conference series: materials science and engineering, vol 663, p 012050. <https://doi.org/10.1088/1757-899X/663/1/012050>
4. Bykova E, Sishchuk J (2015) The state real estate cadaster in Russia - problems and perspectives. ZFV - Zeitschrift fur Geodasie Geoinformation und Landmanagement 140(1):22–26
5. Zhichkin K, Nosov V, Lakomiak A, Zhichkina L (2020) Cadastral valuation of lands dedicated to perennial plantings: features and practice. In: E3S web of conferences, vol 177, p 04002. <https://doi.org/10.1051/e3sconf/202017704002>
6. Tyutyunikov A, Pashuta A, Zakshevskaya T (2019) On the issue of assessing the value of agricultural land in the region based on its economic potential. In: IOP conference series: earth and environmental science, vol 274, p 012012. <https://doi.org/10.1088/1755-1315/274/1/012012>
7. Zhichkin K, Nosov V, Zhichkina L, Tkachev S, Voloshchuk L (2020) Prediction methodology for potential damage from misuse of agricultural lands. In: E3S web of conferences, vol 161, p 01060. <https://doi.org/10.1051/conf/202016101060>
8. Sadridinov MI, Mezina TV et al (2020) Assessment of technological development and economic sustainability of domestic industry in modern conditions. In: IOP conference series: materials science and engineering, vol 734, p 012051. <https://doi.org/10.1088/1757-899X/734/1/012051>
9. Kilić J, Rogulj K, Jajac N (2019) Fuzzy expert system for land valuation in land consolidation processes. Croatian Oper Res Rev 10(1):89–103. <https://doi.org/10.17535/crorr.2019.0009>
10. Cay T, Uyan M (2013) Evaluation of reallocation criteria in land consolidation studies using the Analytic Hierarchy Process (AHP). Land Use Policy 30(1):541–548. <https://doi.org/10.1016/j.landusepol.2012.04.023>
11. Zhichkin K, Nosov V, Zhichkina L, Grigoryeva O, Kondak V, Lysova T (2020) The impact of variety on the effectiveness of crop insurance with state support. In: IOP conference series: earth and environmental science, vol 433, p 012004. <https://doi.org/10.1088/1755-1315/433/1/012004>
12. Awasthi MK (2014) Socioeconomic determinants of farmland value in India. Land Use Policy 39:78–83. <https://doi.org/10.1016/j.landusepol.2014.04.002>
13. Zhichkin K, Nosov V, Zhichkina L, Zhenzhebir V, Rubtsova S (2020) The agricultural crops production profitability in modern conditions. In: E3S web of conferences, vol 175, p 13008. <https://doi.org/10.1051/e3sconf/202017513008>
14. Bastian CT, McLeod DM et al (2002) Environmental amenities and agricultural land values: a hedonic model using geographic information systems data. Ecol Econ 40(3):337–349. [https://doi.org/10.1016/S0921-8009\(01\)00278-6](https://doi.org/10.1016/S0921-8009(01)00278-6)

15. Beckmann MJ (1971) An input-output model of a von Thünen economy. *Ann Reg Sci* 5(1):6–10. <https://doi.org/10.1007/BF01288108>
16. Borchers A, Ifft J, Kuethe T (2014) Linking the price of agricultural land to use values and amenities. *Am J Agr Econ* 96(5):1307–1320. <https://doi.org/10.1093/ajae/aa041>
17. Burt OR (1986) Econometric modeling of the capitalization formula for farmland prices. *Am J Agr Econ* 68(1):10–23. <https://doi.org/10.2307/1241645>
18. Chicoine DL (1981) Farmland values at the urban fringe: an analysis of sale prices. *Land Econ* 57(3):353–362. <https://doi.org/10.2307/3146016>
19. Delbecq BA, Kuethe YH, Borchers AM (2014) Identifying the extent of the urban fringe and its impact on agricultural land values. *Land Econ* 90(4):587–600. <https://doi.org/10.3368/le.90.4.587>
20. Huang H, Miller GY, Sherrick BJ, Gómez MI (2006) Factors influencing Illinois farmland values. *Am J Agr Econ* 88(2):458–470. <https://doi.org/10.1111/j.1467-8276.2006.00871.x>
21. Livanis G, Moss CB, Breneman VE, Nehring RF (2006) Urban sprawl and farmland prices. *Am J Agr Econ* 88(4):915–929. <https://doi.org/10.1111/j.1467-8276.2006.00906.x>
22. Ma S, Swinton SM (2011) Valuation of ecosystem services from rural landscapes using agricultural land prices. *Ecol Econ* 70(9):1649–1659. <https://doi.org/10.1016/j.ecolecon.2011.04.004>
23. Zhichkin K, Nosov V, Zhichkina L (2021) The express method for assessing the degraded lands reclamation costs. In: Mottaeva A (ed) Proceedings of the XIII international scientific conference on architecture and construction 2020: commemorating the 90th anniversary of Novosibirsk state university of architecture and civil engineering. Springer, Singapore, pp 483–492. https://doi.org/10.1007/978-981-33-6208-6_47
24. Ivanova IA, Pulyaeva VN, Vlasenko LV, Gibadullin AA, Sadriddinov MI (2019) Digitalization of organizations: current issues, managerial challenges and socio-economic risks. In: *Journal of physics: conference series*, vol 1399, p 033038
25. Plantinga AJ, Lubowski RN, Stavins RN (2002) The effects of potential land development on agricultural land prices. *J Urban Econ* 52(3):561–581. [https://doi.org/10.1016/S0094-1190\(02\)00503-X](https://doi.org/10.1016/S0094-1190(02)00503-X)
26. Plantinga AJ, Miller DJ (2001) Agricultural land values and the value of rights to future land development. *Land Econ* 77(1):56–67
27. Shi YJ, Phipps TT, Colyer D (1997) Agricultural land values under urbanizing influences. *Land Econ* 73(1):90–100. <https://doi.org/10.2307/3147079>
28. Baimisheva TA, Kurmaeva IS, Gazizyanova YY, Baimeshev RH, Aishesheva GA (2019) IOP conference series: earth and environmental science, vol 315, p 22090. <https://doi.org/10.1088/1755-1315/315/2/022090>
29. Vitaliano DF, Hill C (1994) Agricultural districts and farmland prices. *J Real Estate Finan Econ* 8(3):213–223. <https://doi.org/10.1007/BF01096992>
30. Morkovkin DE, Kolosova EV, Sadriddinov MI, Semkina NS, Gibadullin AA (2020) Organizational and management mechanisms for the digital transformation of economic activities. In: *IOP conference series: earth and environmental science*, vol 507, p 012023. <https://doi.org/10.1088/1755-1315/507/1/012023>
31. Dibrova ZhN, Nosov VV, Ovchenkova GS, Pilyugina AV, Erkovich EA (2018) The main directions of the solution of the problem of food security in Russia. *Int J Mech Eng Technol* 9(12):387–394

Forecasting of Thermal Regime in an Oil Mine



Aleksandr Galkin  and Vladimir Pankov 

Abstract The aim of the present work was to assess the influence of oil freely flowing in a groove on the formation of the thermal regime of the haulageway of the oil mine and to justify the necessity (in case that this source of heat proves to be significant) of development of new technical solutions to decrease its intensity. To assess the significance of this heat source in the mine working on the increase of the air temperature, the gradients of thermal stream in the mine working with the presence of the oil flowing in the soil of the mine working and without it were compared. For the purpose of describing the process of formation of thermal conditions in the mine, a mathematical model was built and a system of differential equations was analytically solved. The absolute and relative error in predicting the magnitude of the thermal stream and temperature at the end of the mine was determined. The thermal stream and temperature at the end of the mine working was determined. According to the formulas obtained, variant calculations were carried out, the results of which are presented in the form of 3D graphs. It was found that errors in determining the thermal stream gradient, i.e. degree of heating of the mine air can reach significant values in practically important cases. If the thermal exchange of the oil flow with the air is not considered, the error in determination of the thermal flow gradient can be as high as 1.5–2.2. Importantly, the error cannot be included in the safety factor.

Keywords Error · Forecast · Heat sources · Mining · Oil mine · Temperature conditions

1 Introduction

A significant attention is dedicated in the scientific and engineering community to the issue of thermal regime regulation in deep mining drifts and mine workings. This

A. Galkin (✉)

Melnikov Permafrost Institute of the Siberian Branch of the Russian Academy of Sciences, Merzlotnaya, 36, 677010 Yakutsk, Sakha Republic, Russia

V. Pankov

North-Eastern Federal University, Belinskogo, 58, 677027 Yakutsk, Sakha Republic, Russia

issues is especially relevant for the coal mines in China, Poland, Ukraine and gold mines in South Africa. For example, in some South African mines mining works are conducted on levels where the natural temperature of the rocks exceeds 50 °C. In these countries a sufficient amount of experience of mitigating the negative effects of high temperatures in mine workings has been collected. Usually, social methods, such as decreasing the length of the workers' shifts, and technical methods, such as increased ventilation, use of cooling devices, thermal insulation of the mine workings, special individual protection means for the underground workers, are applied to reduce the adverse effects of high temperatures. To coordinate the research and exchange the experience on normalization of microclimate in the deep coal mine workings and drifts the specialists in this issue are united in various international mining thermal physics bureaus. The issue is also current for Russia. In the last decades, the Russian mining industry has been going in the direction of moving underground works and mining to greater depths. The temperature of rocks in some of these mine workings reaches up to 30 °C. This is typical for the diamond mines in the Republic of Sakha (Yakutia) and for mine workings in Norilsk which mine polymetallic and nickel ores. In these mines, the works take place at the depths of 1200–1300 m in adverse climatic conditions. It is known that adverse climatic conditions at the workplaces not only decrease the productivity of the personnel but also have negative effects on the health of the workers [1–5]. All the researchers note a significant decrease in the labor efficiency of the underground workers at high surrounding environment temperatures. The radiative heat exchange of the human with the environment poses the highest danger for the work in underground conditions. Special devices were developed fully assess the degree of influence of the convective and radiative components of heat exchange on the human at different air humidity levels. On the basis of complex scientific research, the normative requirements which determine the permitted parameters of the mine air, usually temperature, humidity and speed of the air, were developed. If the actual parameters in the mine workings do not correspond to the normative parameters, conducting mining works is prohibited. Different countries apply different normative requirements. In Russia, the maximum speed of air is set at 8 m/s and the temperature should not exceed 26 °C. The Yaregskoye viscous oil reservoir serves as the object of research in the present article. It is located in central Russia in the Republic of Komi, a region of Russia. The deposit is located at the depth of 130–220 m in sandstone grounds. The oil reservoir of a stratal type has a height up to 87 m and the dimensions are 36 km length and 3–6 km width. Despite the fact that the reservoir is located in a temperature zone where the rocks temperature does not exceed 10–12 °C, the temperature conditions in the mine workings themselves are very adverse. It is a unique reservoir developed using a shaft method with a preliminary heating of the rocks of the oil strata with water vapor whose temperature is around 170–190 °C. The technology of viscous oil mining has been in use for around 80 years and consists of the following. At the first stage, the part of the stratum to be developed is treated with vapor until it reaches temperature of 70–80 °C. At the second stage, water is used to push the oil out of the heated stratum into the underground mine workings from where it is delivered to the surface through a vertical shaft. The duration of the first stage is 6–8 months. The

average temperature of the stratum increases to 30–40 °C. The technology currently used to extract the viscous oil of the Yaregskoye oil field, whereby the oil is extracted employing a tunnel method of oil mining, permits a free trickling (flow) of the oil in an open groove in the soil of the tilted surface of the oil field mine working to the point of collection from where the oil is pumped further. During this process, both because of the thermal exchange between the mine air and the rocks, which contain the haulageway, and the thermal exchange between the air and the oil stream, the air is heating intensively and at the end of the haulageway, the air temperature exceeds the values permitted by safety norms and sometimes reaches temperatures of up to 30–35 °C. The principal difference of the oil shafts thermal regime from the deep coal shafts is the absence of the thermal equalizing wrapper around the transportation mine workings.

These conditions require introduction of energy-expensive measures for cooling the air and normalization of the parameters of microclimate in the mines. An analysis of literature on the topic confirms that normalization of thermal conditions in the mine workings is an important and a current task for the oil mines of the Yaregskoye oil field [6–9]. For the purposes of justification and choice of rational technical solutions to normalize the thermal conditions in the mines it is necessary to determine the impact of individual components of thermal exchange on the rise in air temperature [9–12].

The aim of the present work was to assess the influence of oil freely flowing in a groove on the formation of the thermal regime of the haulageway and to justify the necessity (in case that this source of heat proves to be significant) of development of new technical solutions to decrease its intensity.

2 Methods

For the assessment of the importance of this heat source in the mine working for the overall rise in air temperature the following mathematical model was used. The gradients of thermal stream in the mine working with the presence of the oil flowing in the soil of the mine working and without it were compared. Based on the previously determined dependencies [13, 14], equations of thermal balance for the two cases considered can be written in the following form:

$$\partial(GJ) = \alpha_1 u_1 (T_1 - t) \partial l + \alpha_2 u_2 (T_2 - t) \partial l \quad (1)$$

$$\partial(GJ) = \alpha_1 u_1 (T_1 - t) \partial l + \alpha_2 u_2 (T_2 - t) \partial l \quad (2)$$

$$\partial(GJ) = \alpha_1 u_0 (T_1 - t) \partial l \quad (3)$$

The following designations were chosen: G —mass air expenditure in the working, kg/s; G_2 —mass oil expenditure in the working, kg/s; J —enthalpy of the humid air, J/kg; J_2 —enthalpy of the oil, J/kg; α_1 —heat reflection coefficient from the air to

the rocks, $W/(m^2/kg)$; α_2 —heat reflection coefficient from the air to the oil flow, $W/(m^2/kg)$; u_0 —perimeter of the mine working, m; u_1 —perimeter of the mine working without accounting for the width of the groove for their oil flow, m; u_2 —width of the groove for the oil flow, m; T_1 —temperature of the wall of the mine working, K; T_2 —temperature of the oil inside the mine working, K; t —air temperature inside the mine working, K; l —the length of the mine working, m.

The first equation characterizes the thermal exchange of the air in the mine working with the presence of the flowing oil. The second equation describes the change in the temperature of the flowing oil due to the thermal exchange with the air. The third equation describes the thermal exchange in the mine working without including the thermal exchange with the oil flow. The relative error, received during the determination of the gradient of the thermal stream in the mine working if the oil flow is not accounted for, can be determined according to the following formula:

$$\varepsilon = abs(k(1 - \theta)) \quad (4)$$

where

$$\theta = (T_2 - t)/(T_1 - t) \text{ and } k = u_2/u_1 \quad (5)$$

In this case, there is no need to solve the Eqs. (1) to (3). In order to determine the error itself in determination of the temperature at the end of the mine working it is necessary to solve the Eqs. (1) and (2). The temperature of the oil flow will be considered nearly constant along the length of the mine working, equal to the average of the temperatures at the beginning and the end of the mine working. For the purposes of the aims of this work, there will be no effect on the result, since we are interested in the possible range of the change in the error values which will be received as a result of variant calculations. The left part of the Eqs. (1) and (2) can be written in the following form [10, 15]:

$$\partial(GJ) = G(c_p + rn\varphi)\partial t \quad (6)$$

The solution of the equations will be presented in the form:

$$\begin{aligned} t_{k1} &= T_1 + (t_0 - T_1) \exp(-\beta) \\ t_{k2} &= T_3 + (t_0 - T_3) \exp(-\beta). \end{aligned} \quad (7)$$

$$\begin{aligned} \text{where } \beta &= \alpha_1 u_1 l / G(c_p + rn\varphi); \\ T_3 &= k(T_1 - T_2) \end{aligned} \quad (8)$$

Here, the following designations are used: t_{k1} —temperature of air at the end of the mine working with presence of the oil flow, °C; t_{k2} —temperature of the air in the end of the mine working without the oil flow, °C; t_0 —temperature of the air at the beginning of the mine working, °C; c_p —the total thermal capacity of the air, $J/(kg K)$;

r —temperature of steam creation, J/kg; n —coefficient of linearization determined according to the tables in [10], 1/K; φ —relative air humidity in the mine working, without units. β, T_3 are intermediary parameters determined according to the formula (8).

The relative error in determination of the temperature, or, in other words, the precision of the forecast of the temperature without accounting for the effects of the oil flow on the formation of the thermal regime in the mine working, was determined according to the following formula:

$$\varepsilon = abs(1 - t_{k2}/t_{k1}) \tag{9}$$

3 Discussion of Results

On the basis of the formulas established, variant calculations were conducted. The results of these variant calculations are presented in the form of 3D charts in the Figs. 1 and 2. Figure 1 shows the change in the error in determination of the thermal flow gradient dependent on the coefficient k , characterizing the width of the oil flow groove relative to the perimeter of the mine working and the parameter θ , which is a unitless temperature value determined using the formula (5). As can be seen in the graph, the error significantly increases as the value of the unitless parameter θ increases. The value of the parameter θ is dependent on the temperature of the flowing oil: the higher is the temperature of the oil, the bigger the value of the parameter. Similarly, the higher is the value of the parameter k , that is, the wider the groove, the higher the value of the error. In general, those can be viewed as obvious facts that follow from an elementary analysis of the formula (4).

In this case, however, we are interested not in the qualitative view but a quantitative one. What applies is that the errors in determination of the thermal flow gradient, that is, the degree to which the temperature of the air in the mine working can rise, can

Fig. 1 Change in error in determination of the thermal flow gradient in the mine working dependent on the width of the groove and temperature of the oil

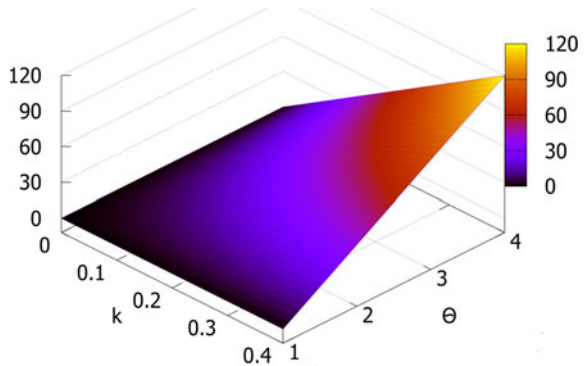
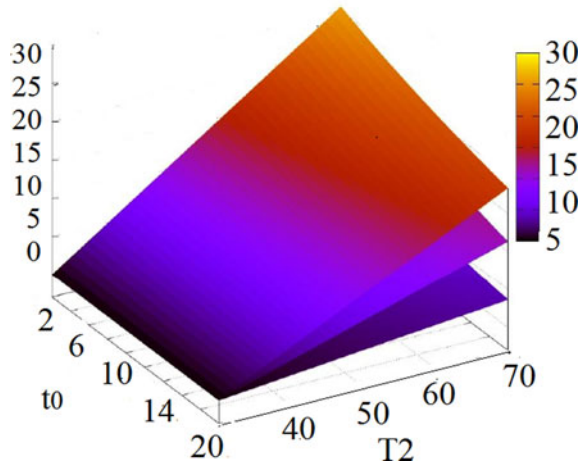


Fig. 2 Change in the error in determination of the air temperature in the working when the thermal exchange with the oil flow not considered



reach significant values in practical cases. As follows from the graph, if the thermal exchange of the oil flow with the air is not considered, the error in determination of the thermal flow gradient can be as high as 1.5–2.2. Importantly, the error cannot be included in the safety factor.

That is, we are underestimating the value of the thermal stream, which means the temperature of the air in the mine working is also underestimated. Because the deviations of these values are significant, there is a risk of allowing a mistake in justification and choice of the methods and means of normalizing the parameters of microclimate in the oil mine workings.

On Fig. 2 are represented the 3D graphs showing the error in determination of the air temperature in the mine working when the influence of oil flow on the change in the air temperature along the length of the mine working is not considered. The calculations were conducted for the typical parameters, which are a part of the formulas (7) and (8).

It can be observed from the graphs that the error in determination of the temperature at the end of the mine working can reach values significantly higher than those permitted in the engineering practice (typically, the value of the error permitted is up to 10%). Different planes in the picture relate to the different values of the parameter β which characterizes the air expenditure in the mine working and its length.

The given parameter was changing from 0,1 to 0,9 in the calculations and, as can be seen in the graphs, it has a significant influence on the relative error in determination of the air temperature in the mine working. This parameter also has an influence on the air temperature in the end of the mine working and is decisive. However, the task here was not to find the absolute temperature but a relative error in determination of the temperature. Thus, if the error is 25%, then, at the end of the mine working, if the temperature is, for example, +10 °C, the value of the error will be +2,5 °C. In case that the temperature is +20 °C, the absolute error will be 5 °C. To demonstrate how important this is: using a simplified model that does not include the influence of

the oil flow on the thermal exchange processes, using formula (7), it was determined that the temperature at the end of the haulageway is equal to $+26\text{ }^{\circ}\text{C}$. That is, it corresponds to the safety standards and there is no need to employ any measures for the normalization of microclimate in the mine working. But based on the graphs it can be determined that the relative error in these conditions is 25%. This means that the expected air temperature will be $32.5\text{ }^{\circ}\text{C}$. This is almost $7\text{ }^{\circ}\text{C}$ higher than permitted by the safety standards. It becomes obvious that the accurate forecast and assessment of the influence of separate heat sources, determining the formation of the thermal regime in the mine workings, is an important scientific and practical task. Its solution allows to make correct engineering decisions to normalize the thermal regime in the mine workings of the oil shafts. In particular, in this specific example, it is necessary to reduce the level of impact the oil flowing in open grooves has on the heat exchange with the ventilation stream. It is possible to achieve this through a change in the technology of oil transportation itself, for example to change to transportation in thermally insulated pipelines laid in the mine workings. The other option is to insulate the grooves themselves using thermal protective screens. The choice of one or the other solution should be made on the basis of comparison of economic costs of their practical implementation.

4 Conclusion

In forecasting thermal conditions in the oil mines it is necessary to carefully analyze the influence of all heat sources on the final result. Dependencies to determine the relative error in determination of the temperature gradient and the temperature itself at the end of the haulageway, caused by not considering the thermal exchange of the mine air with the oil flowing in an open groove, were established. It was established that transportation of oil in open grooves in the soil of the mine working has a significant influence on the level of thermal exchange with the ventilation air. For typical cases, this heat source can constitute up to 30% of the total thermal exchange in the mine working. An important factor in normalization of the parameters of microclimate is the development of technological and technical solutions to decrease the influence of this heat source (for example, thermal insulation of the grooves) or exclusion of this heat source (for example, transportation of oil in insulated pipes) from the thermal exchange processes in the mine workings. Further research should be directed towards the assessment of energy and economic efficiency of the use of various methods of normalizing thermal conditions in the mine workings of oil mines.

References

1. Alabyev VR, Kruk MN, Korobitsyna MA, Stepanov IS (2018) Influence of environmental technologies on the economic component in the normalization of thermal conditions in oil-stores. *J Environ Manag Tourism* 1:75–81
2. Chebotarev AG (2018) The state of the working conditions and prevalence of occupational disease among the workers of mining enterprises. *Proc Min Inst* 1:92–95
3. Chebotarev AG, Afanasyeva AF (2012) Physiological-hygienic assessment of microclimate at workplaces in tunnel and open pit mines and methods of prevention of its adverse impact. *Min Ind* 6:34–40
4. Dyadkin YD (1968) Basics of thermal physics for mines of the North, Nedra, Moscow
5. Epstein Y, Moran DS (2006) Thermal comfort and the heat stress indices. *Ind Health* 3:388–398
6. Galkin AF (2015) Thermal conditions of the underground town collector tunnel. *Metall Min Ind* 8:70–73
7. Galkin AF (2015) Thermal control in mine openings. *Metall Min Ind* 2:304–307
8. Hunt AP, Parker AW, Stewart IB (2013) Symptoms of heat illness in surface mine workers. *Int Arch Occup Environ Health* 5:519–527
9. Martynov AA, Maleev NV, Yakovenko AK (2011) A program to calculate the air temperature in deep coal mines. *Coal of Ukraine* 34–36
10. Nikolaev AV (2016) A method of ventilation of tilted blocks of oil mines increasing the efficiency of underground oil mining. *Oil Enterp* 11:133–136
11. Nor MA, Nor EV, Tshadaya ND (2017) Sources of heating microclimate in development of highly viscous oil deposits using the thermal tunnel method. *Proc Min Inst* 225:360–363
12. Parsons K (2006) Heat stress standard ISO 7243 and its global application. *Ind Health* 3:368–379
13. Rudakov ML, Korobitsyna MA (2019) On the possibility of normalization of air temperature in the drilling galleries of the mine tunnels. *Occup Saf Ind* 8:66–71
14. Scherban AN, Kremnev OA, Zhuravlenko VY (1977) A handbook on regulation of thermal regime of mine tunnels, Nedra, Moscow
15. Voropayev AF (1979) Thermal conditioning of mine air in deep mine tunnels, Nedra, Moscow

Influence of Forced Cooling Criteria on the Pressure Distribution Inside the Curved Ventilation Ducts of the Brake Disc



Pavel Polyakov , Artem Litvinov , Ruslan Tagiev , Alexey Golikov , Nina Zadayanchuk , and Ivan Yaitskov 

Abstract To control the processes of reducing the thermal load in the working vapors of the friction unit, it is necessary to understand the influence of the criteria on the cooling process. For the use of forced cooling systems, it is necessary to systematize and evaluate the effect of its design and operational parameters. These parameters include system pressure and angle of attack. In addition to these factors, the location of the air supply can be directly an optimization parameter. The paper presents a theoretically grounded model of pressure distribution inside the curved ventilation ducts of the left and right brake discs. The distribution model justifies the use of forced cooling systems, since the inversion of pressure inside the ventilation ducts during forced cooling does not make it possible to make frequent changes in air masses. This pressure distribution model offers a choice of air source location with minimal resistance to braking.

Keywords Ventilation device · Pressure · Brake disc · Angle of attack · Pressure coefficient

1 Introduction

A fairly wide range of studies has been devoted to friction units. Special attention is paid to the problem of the influence of the geometric parameters of the ventilation apparatus on the deformation and on the mass of the brake disc [1]. The stresses and mass in the brake disc are important parameters that affect the reliability and metal consumption of the entire assembly as a whole. The team of the author proposed a

P. Polyakov (✉) · A. Litvinov (✉) · R. Tagiev · A. Golikov
Kuban State Technological University, Krasnodar, 2a, Moskovskaya st., Krasnodar 350020, Russia

N. Zadayanchuk
Kuban State University, Krasnodar, 149 Stavropolskaya, st., Krasnodar 350040, Russia

I. Yaitskov
Rostov State Transport University, Rostovskogo Strelkovogo Polka Narodnogo Opolcheniya, d. 2, Rostov-on-Dons, Russia

thermal model of a friction pair of a ventilated brake disc, which gives an understanding of the thermal loading of the friction unit, taking into account long-term operation [2]. In [3], a method for designing the profile of friction pairs of friction units with the task of uniform distribution of contact stresses over the contacts of the friction lining is proposed. The solution to this problem makes it possible to subsequently obtain a uniform temperature distribution over the area of the friction pad, but it does not solve the problem of heat removal from friction pairs. Works that analyze thermal loading and methods for its reduction using heat pipes [4] or using a developed ventilation apparatus with a porous medium core [5, 6] received wide coverage. These works deserve attention, but the application of the results obtained is possible when using forced cooling. In [7], an improved modification of the blades of the brake disc ventilation apparatus is proposed in order to increase heat removal from friction pairs. In work [8], the analysis of various configurations of curved channels of a ventilated brake disc at the speed of air flows with forced cooling is carried out. Curved ventilation ducts in brake discs are becoming more common, but the most widespread is the ventilation apparatus with radial ducts. In [9], a method was proposed for evaluating the brake disc cooling system. It would be advisable to consider how its parameters change in the context of one ventilation duct of the brake disc.

Modern ventilated disc brakes are available with and without a variety of ventilation duct configurations. The configurations of the ventilation ducts of the brake disc can be radial and curved (Fig. 1 a, b, c).

As a ventilation device of the brake disc, ribs connecting the two halves of the working surfaces of the disc are used. These ribs have different cross-sectional geometries and locations inside the ventilation apparatus (Fig. 2 a, b). The most widely used radial ventilation ducts (for cars from economy to business class).

Brake discs with curved ventilation ducts are used for sports cars, wheel friction assemblies that accumulate a huge amount of thermal energy. It is the ventilation device that helps dissipate the thermal energy that is generated as a result of braking.

With forced cooling, air flows from the gap between the brake disc and the wheel hub. Passing through the ventilation device, it cools the non-working surfaces of the brake disc and exits between the gap of the brake disc and the wheel disc. Depending on the direction of action of the ambient air currents, the outflow process

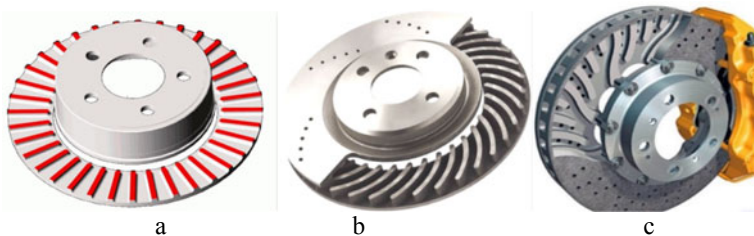


Fig. 1 Configurations of ventilation ducts of brake discs: a - radial; b - curvilinear; c - with a complex configuration

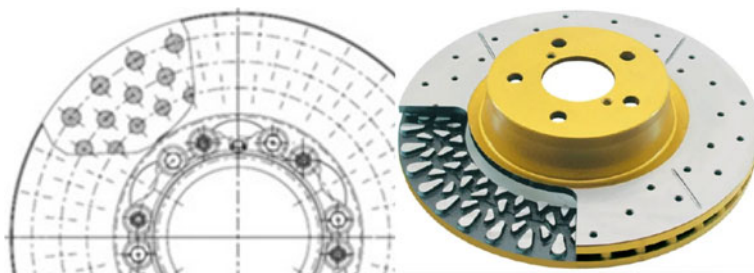


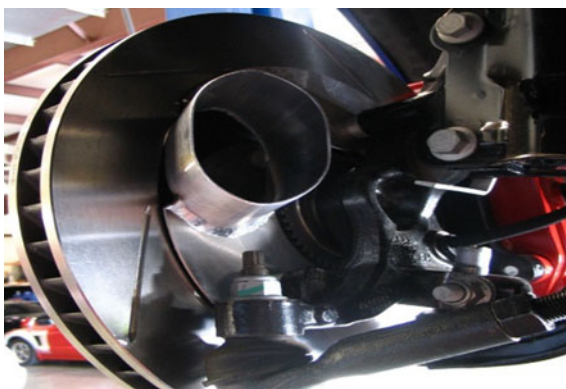
Fig. 2 The ribs of brake discs with different cross-sections: a - round; b - in the form of “kangaroo paws”

may be insufficiently intense. To increase the intensity of air permeability through the ventilation device of the brake disc, various devices are used to inject cooling air into the cavity of the ventilation device. The cooling mode of the brake discs is called forced cooling. An example of such a cooling mode is the mono-air supply system through the brake shield to the ventilation apparatus (Fig. 3).

The disadvantage of this system of forced cooling of the brake disc is the uneven loading of the ventilation ducts with cooling air. It is possible to correct this drawback by using a distributed cooling air supply system to the vehicle ventilation apparatus. Numerous studies in the field of forced cooling of friction units allow us to speak about the effectiveness of the developed systems. However, there is a significant gap in the study of the effect of forced air supply location on the performance of the ventilator.

Optimization parameters for forced cooling systems of friction units are the number and location of air supply nozzles, as well as the angle of its attack. This article examines the influence of the nozzle position of the forced cooling system and the angle of attack on the pressure distribution in curved ventilation ducts. The main elements of the developed model are ventilation ducts and a partition between

Fig. 3 Forced cooling by means of a mono-supply of cooling air to the brake disc ventilator



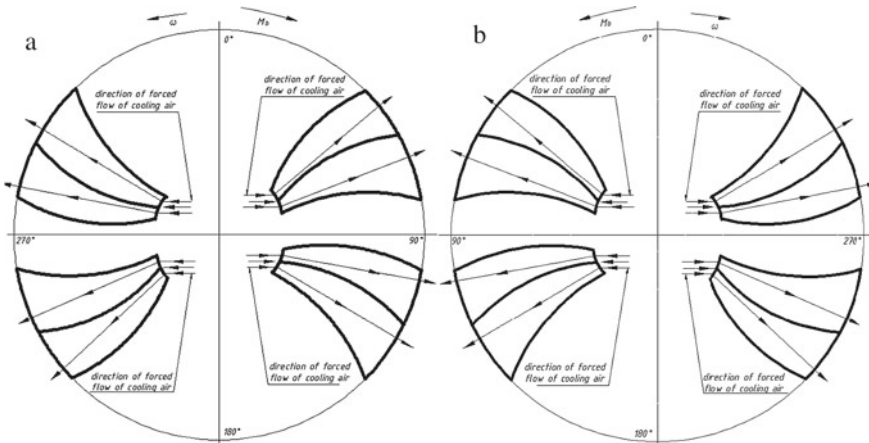


Fig. 4 Scheme of operation of the forced cooling system of the ventilation device for the left (a) and right (b) brake discs

them. The baffle is a thin, freeform profile placed in the air stream. Let us take the angle of attack equal to α .

The forced cooling system of the ventilated brake disc is divided into four sectors. Each sector has a source for air supply. For a ventilator with curved ventilation ducts, the configurations of the left and right brake discs are different. A diagram of a ventilation device with a forced cooling system for the left and right brake discs is shown in Fig. 4 a, b. We represent each sector using a polar coordinate system, where the polar radius is limited by the radius of the outer surface of the brake disc. For simplicity, we will assume that the brake disc sectors are limited to 90° .

2 Materials and Methods

One of the main operating parameters of the ventilation device is pressure. Assuming that, from all sources of forced cooling, air comes out with equal pressure. To determine the most efficient location of the air supply source, it is necessary to develop a pressure distribution model within the ventilation ducts and between adjacent ventilation ducts. Adjacent ventilation ducts were chosen as the central subject of the study, because with a distributed air supply, air can only enter two adjacent ducts separated by a partition. When the forced cooling source is removed, the distributed cooling air supply loses its effectiveness.

To model a complex system with curved ducts, it is necessary to resort to considering a more simplified system with radial ventilation ducts. To do this, consider two sectors (from 0 to 90°) and (from 90 to 180°) of the computational model (Fig. 5 a, b).

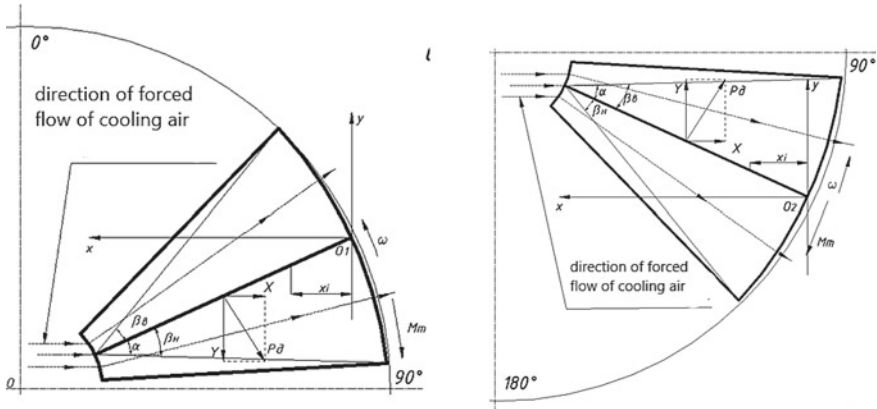


Fig. 5 Calculated pressure diagram on the surface of the brake disc ventilation apparatus a - sector from 0 to 90° b - sector from 90 to 180°

In each sector of the computational model, two radial channels of the brake disc ventilation apparatus are considered, opposite which an air flow source is installed. As an example, consider a sector limited to values from 0 to 90°. When the air flow passes through the ventilation ducts, a zone of increased resistance to air flow is formed on top of the rib, while a free flow zone of cooling air is formed under the rib of the ventilation duct.

The angles of air flow distribution for the upper and lower ventilation duct will be determined from the condition of the air flow around the plate in the aerodynamic flow:

$$\beta_H = \beta_G = \frac{\chi+1}{4} \alpha \left\{ 1 + \sqrt{1 + \left[\frac{4}{(\chi+1)\alpha Re} \right]^2} \right\}, \tag{1}$$

where χ is the isentrop index; α —angle of attack of the air flow, deg.; Re is the Reynolds number.

The pressure coefficient in the upper ventilation duct will be positive and equal to:

$$\overline{p_G} = 2\alpha\beta_G, \tag{2}$$

Whereas the pressure coefficient for the lower ventilation duct will be negative and determined by the formula:

$$\overline{p_H} = -2\alpha\beta_H, \tag{3}$$

Substituting the values of the pressure coefficient in the formula (1), we obtain:

$$\overline{p}_e = \frac{\chi+1}{2} \alpha^2 \left\{ 1 + \sqrt{1 + \left[\frac{4}{(\chi+1)\alpha Re} \right]^2} \right\}, \tag{4}$$

$$\overline{p}_H = -\frac{\chi+1}{2} \alpha^2 \left\{ \sqrt{1 + \left[\frac{4}{(\chi+1)\alpha Re} \right]^2} - 1 \right\}, \tag{5}$$

Since the pressure in the lower and upper ventilation ducts is distributed unevenly, the pressure coefficients at all points of the upper and lower ventilation ducts will vary from the parameter x . To determine the pressure difference between the ventilation ducts, it is necessary to position the rib of the ventilation ducts in the coordinate axes with the center $O1$.

Let us assume that the shape of the partition of the ventilation ducts is given by the equations: for the left (Fig. 6 a, b) and right (Fig. 7 a, b) brake discs, the geometry of curved ventilation ducts

Fig. 6 Calculation diagram of pressure on the surface of the ventilation apparatus with curved ventilation ducts of the left brake disc: a - sector from 0 to 90° b - sector from 90 to 180°

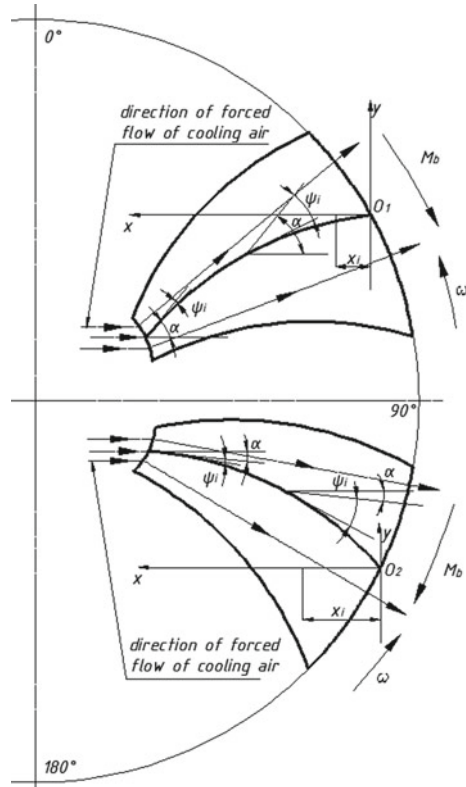
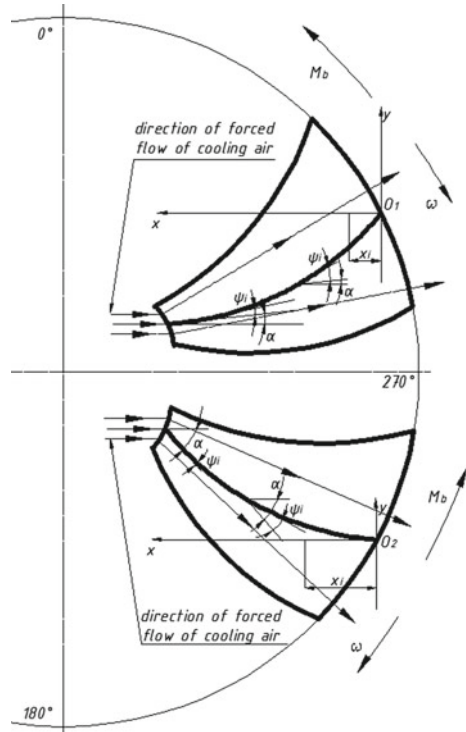


Fig. 7 Calculation diagram of pressure on the surface of the ventilation apparatus with curved ventilation ducts of the right brake disc: a - sector from 0 to 90° b - sector from 90 to 180°



$$y_1 = f_1(x), \tag{6}$$

for the right brake disc geometry of curved ventilation ducts:

$$y_2 = f_2(x), \tag{7}$$

where y_1 and y_2 are the ordinates of the surfaces of the partitions of the ventilation ducts for the left and right brake discs, respectively.

Let us denote the angles of inclination of the surfaces of the partitions of the ventilation ducts in the section x_i with respect to the tangent surface through ψ_i . Similarly to radial channels, we accept the condition that the thickness of the partition is much less than its diameter $\delta \ll d$:

for the left brake disc of curved ventilation ducts:

$$\psi_1 = -\frac{dy_1}{dx}, \tag{8}$$

for the right brake disc geometry of curved ventilation ducts:

$$\psi_2 = -\frac{dy_2}{dx}, \tag{9}$$

The local angles of attack of the air flow on the surfaces of the partitions of the ventilation ducts are determined by the sum:

$$\alpha_{xi} = \alpha_i \pm \psi_i, \quad (10)$$

To determine the pressure coefficients at the points of the ventilation ducts for the left and right brake discs, we set the following requirement. We will assume that the pressure at each point of the baffle of the curved channel will be the same as on the surface of the baffle of radial ventilation ducts, in a streamlined flow with the same Re number, but substituted at an angle of attack equal to the local angle of attack at this point.

Therefore, to calculate the pressure coefficients at the points on the surface of the partitions of curved ventilation ducts, one can use the dependences for the pressure coefficient of the radial ducts (4) and (5), taking in them the angle α equal to the local angle of attack α_i .

In the sector from 0 to 90° for the left brake disc, the pressure coefficients for curved ventilation ducts are determined from the dependence:

bottom

$$\overline{p}_u = -\frac{\chi+1}{2}(\alpha-\psi_i)^2 \left\{ 1 + \sqrt{1 + \left[\frac{4}{(\chi+1)(\alpha-\psi_i)\text{Re}} \right]^2} \right\}, \quad (11)$$

upper

$$\overline{p}_e = \frac{\chi+1}{2}(\alpha-\psi_i)^2 \left\{ \sqrt{1 + \left[\frac{4}{(\chi+1)(\alpha-\psi_i)\text{Re}} \right]^2} - 1 \right\}, \quad (12)$$

In a similar sector for the right brake disc, the pressure coefficients for curved ventilation ducts are:

bottom

$$\overline{p}_u = -\frac{\chi+1}{2}(\alpha+\psi_i)^2 \left\{ 1 + \sqrt{1 + \left[\frac{4}{(\chi+1)(\alpha+\psi_i)\text{Re}} \right]^2} \right\}, \quad (13)$$

upper

$$\overline{p}_e = \frac{\chi+1}{2}(\alpha+\psi_i)^2 \left\{ \sqrt{1 + \left[\frac{4}{(\chi+1)(\alpha+\psi_i)\text{Re}} \right]^2} - 1 \right\}, \quad (14)$$

In the sector from 90 to 180° for the left brake disc, the pressure coefficients for curved ventilation ducts are determined from the dependence:

bottom

$$\overline{p_H} = \frac{\chi+1}{2} (\alpha+\psi_i)^2 \left\{ 1 + \sqrt{1 + \left[\frac{4}{(\chi+1)(\alpha+\psi_i)\text{Re}} \right]^2} \right\}, \quad (15)$$

upper

$$\overline{p_G} = -\frac{\chi+1}{2} (\alpha+\psi_i)^2 \left\{ \sqrt{1 + \left[\frac{4}{(\chi+1)(\alpha+\psi_i)\text{Re}} \right]^2} - 1 \right\}, \quad (16)$$

In a similar sector for the right brake disc, the pressure coefficients for curved ventilation ducts are:

bottom

$$\overline{p_H} = \frac{\chi+1}{2} (\alpha-\psi_i)^2 \left\{ 1 + \sqrt{1 + \left[\frac{4}{(\chi+1)(\alpha-\psi_i)\text{Re}} \right]^2} \right\}, \quad (17)$$

upper

$$\overline{p_G} = -\frac{\chi+1}{2} (\alpha-\psi_i)^2 \left\{ \sqrt{1 + \left[\frac{4}{(\chi+1)(\alpha-\psi_i)\text{Re}} \right]^2} - 1 \right\}, \quad (18)$$

In dependencies (13), (14), (15) and (16), it is shown that the local angles of attack of curved ventilation ducts are the sum of the angle of attack of the air flow and the angle of inclination of the surface of the partitions of curved ventilation ducts. It can be clearly seen from the design diagrams that the closer to the periphery of the brake disc, the more value will be exerted by the angle of inclination of the surfaces of the partitions.

From dependencies (11), (12), (17) and (18) the local angles of attack are formed by the difference between the angle of attack of the air flow and the angle of inclination of the surface of the partitions of curved ventilation ducts. Analyzing the design schemes, it can be concluded that the local angle of attack to the periphery of the brake disc decreases, due to the increase in the angle of inclination of the surfaces of the partitions.

The pressure drop between the lower and upper ventilation ducts is expressed as the difference:

$$d(p_6 - p_n) = (\overline{p_6} - \overline{p_n}) \frac{dx \rho v^2}{d_k^2}, \quad (19)$$

where v is the speed of the cooling air flow during forced cooling, m/s; ρ is the density of the air flow during forced cooling, kg/m³; d_k —the diameter of the ventilation duct in the section x .

Substitute dependencies (11), (12), (13), (14) into formula (6) and we obtain that the pressure drop is determined for the left brake disc:

$$d(p_6 - p_n) = \frac{dx \rho v^2}{d_k^2} (\chi + 1) (\alpha - \psi_i)^2 \sqrt{1 + \left[\frac{4}{(\chi+1)(\alpha-\psi_i)Re} \right]^2} \quad (20)$$

for the right brake disc:

$$d(p_6 - p_n) = \frac{dx \rho v^2}{d_k^2} (\chi + 1) (\alpha + \psi_i)^2 \sqrt{1 + \left[\frac{4}{(\chi+1)(\alpha+\psi_i)Re} \right]^2} \quad (21)$$

If we take into account the sector limited from 90 to 180°, then the value of the pressure drop for the left brake disc will be determined from the formula:

$$d(p_6 - p_n) = -\frac{dx \rho v^2}{d_k^2} (\chi + 1) (\alpha + \psi_i)^2 \sqrt{1 + \left[\frac{4}{(\chi+1)(\alpha+\psi_i)Re} \right]^2} \quad (22)$$

for the right brake disc:

$$d(p_6 - p_n) = -\frac{dx \rho v^2}{d_k^2} (\chi + 1) (\alpha - \psi_i)^2 \sqrt{1 + \left[\frac{4}{(\chi+1)(\alpha-\psi_i)Re} \right]^2} \quad (23)$$

The minus sign indicates the inversion of the pressure drop when the position of the partition of the ventilation ducts changes relative to the center of rotation of the disk.

To determine the direction of action of the pressure drop in the ventilation ducts, it is advisable to turn to the vector value, namely the resulting force (Fig. 8 a, b).

Then the elementary resulting force of the air flow P_{res} is determined by the formula:

$$dP_{res} = d(p_6 - p_n)S = \frac{dx \rho v^2}{d_k^2} S (\chi + 1) \alpha_{xi}^2 \sqrt{1 + \left[\frac{4}{(\chi+1)\alpha_{xi}Re} \right]^2} \quad (24)$$

where S is the area of the partition of the ventilation ducts, m².

It is expedient to expand the elementary force along the projection along the axes. Taking at small angles of attack, the projection of the elementary force (Y) on the Y axis:

$$dY = dP_{res} \cos \alpha_{xi} = dP_{res}. \quad (25)$$

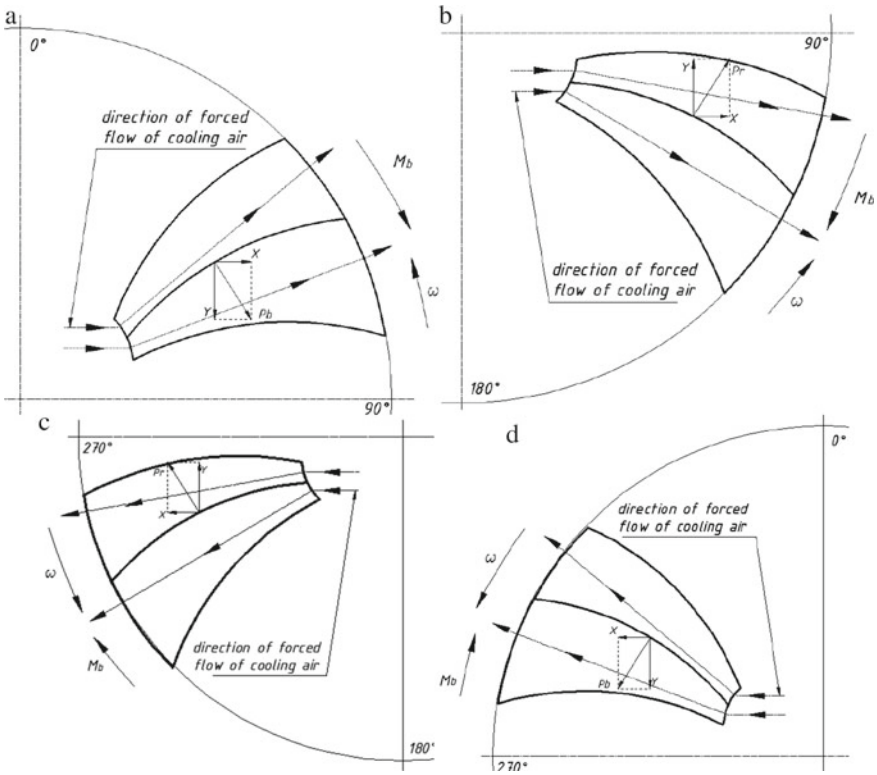


Fig. 8 The resulting force from the sector of the left brake disc (a - from 0 to 90°; b - from 90 to 180°; c - from 180 to 270°; d - from 270 to 360°)

Whereas the horizontal projection (X) will be determined by the formula:

$$dX = dP_{res} \sin \alpha = dP_{res} \alpha. \tag{26}$$

If the direction of action of the projection of the elementary force on the Y-axis coincides with the direction of action of the braking torque, then it is auxiliary to braking (Pb). In the opposite case, the projection is the resistance force (Pr).

In a similar way, it is possible to construct the resulting forces for the sectors limited by values from 180 to 270° and from 270 to 360° (Fig. 8 c, d).

For the right brake disc, an inversion of the resultant force is also observed, which, when passing through a sector limited to 90°, is converted from an auxiliary force to a resistance force.

To confirm the theoretical studies, a model of the ventilation apparatus of the right brake disc was developed, consisting of several curved ventilation ducts of a passenger car brake disc (Fig. 9).

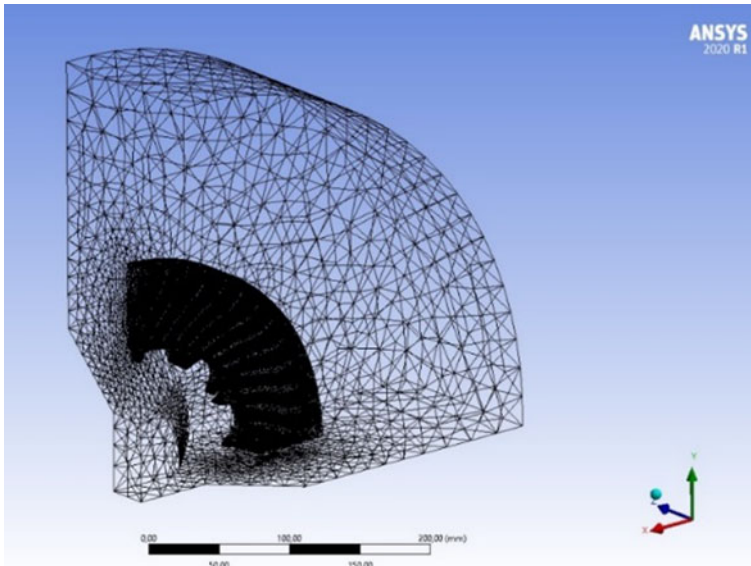


Fig. 9 Investigated part of the disk during blowing

The ICEM-CFD ANSYS module was used to generate the mesh and simulations were performed in ANSYS Fluent. The main goal of this study is to understand the pressure distribution in radial ventilation ducts. As an example, the right brake disc with curved channels was chosen; for a complete picture, the ventilation channels had an unequal cross-sectional diameter along the entire length. Ambient pressure and temperature are assumed to be 101,325 Pa and 300 K. The simulation is carried out under the assumption that the outer surfaces of the brake disc have a constant temperature of 700 K. The angular rotation speed of the brake disc segment is 800 rpm.

A three-dimensional model with three cooling vanes was selected to analyze the pressure drop across the ventilation ducts. As in the calculation model presented above, the position of the ventilation ducts in two sectors of the right brake disc was considered (a—from 0 to 90°; b—from 90 to 180°). The air flow source was brought to the inlets of the ventilation ducts at an angle of attack equal to 5°, with a speed equal to 40 m/s. The pressure drop in the first sector varied from -1.37 MPa to 0.954 MPa (Fig. 10 a).

3 Conclusion

The results of computer simulation clearly show when the ventilation ducts are in the sector from 0 to 90°, the pressure at the inlet of the upper ventilation duct will

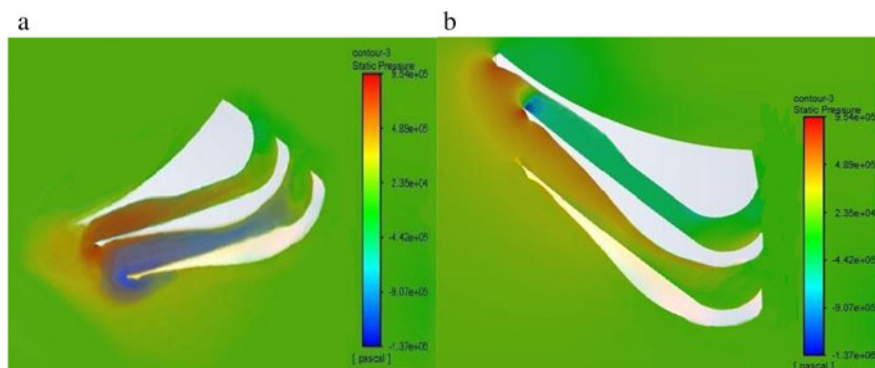


Fig. 10 Model of pressure distribution inside the ventilation ducts of the right brake disc, depending on the location of the air flow source (a - sector of the brake disc from 0 to 90°; b - sector from 90 to 180°)

be excessive and along the length of the ventilation duct towards the periphery of the ventilation disc will gradually decrease. In the lower ventilation duct, a vacuum is observed along the entire length of the ventilation duct. At the beginning of the lower ventilation duct, a zone of increased vacuum is formed.

In the sector from 90 to 180°, the pressure distribution is inverted, as a result of which there is a rarefied air zone in the upper ventilation duct (Fig. 10 b). The largest part is concentrated at the beginning of the channel inlet. Whereas a pressure gradient appears in the lower ventilation duct near the inlet. But throughout the entire length of the channel, the pressure begins to decrease closer to the periphery of the brake disc. As in the computational model, the pressure gradient is inverted depending on the position of the rib of the ventilation ducts, depending on the source of the air flow.

In general, computer simulations have confirmed theoretical studies on the distribution of pressure in the ventilation ducts of the brake disc, depending on the position of the baffle of the ducts, depending on the location of the source of forced cooling.

Summing up, we can draw the following conclusion: the criteria for optimizing the forced cooling system are the angles of attack of the air flow, the geometry of the ventilation ducts and the location of the air flow source relative to the ventilation ducts. The result of computer simulation is the distribution of pressure inside the ventilation ducts, the pressure difference between the lower and upper ducts, and a constant inversion of the air pressure, which can lead to a deterioration in the filling of the ventilation duct with cooled air.

References

1. Indira R, Bharatish A (2020) Optimization of ventilated brake disc rotor geometry for enhanced structural characteristics. *J Meas Eng* 8:98–106. <https://doi.org/10.21595/jme.2020.21399>

2. Polyakov PA, Tagiev RS, Fedotov ES, Polyakova EA, Moskalenko MB (2020) Development of a thermal model of a brake disc of a friction unit. *Bull Irkutsk State Tech Univ* 24(150):64–76. <https://doi.org/10.21285/1814-3520-2020-1-64-76>
3. Polyakov PA, Litvinov AE, Polyakova EA, Fedotov ES, Tagiev RS (2020) Design of surface profile of pairs of friction unit. In: *IOP conference on series: materials science and engineering*, 2020, 6. <https://doi.org/10.1088/1757-899X/843/1/012001>
4. Qifei J, Wang L, Shuia Y (2020) Thermal analysis of ventilated brake disc based on heat transfer enhancement of heat pipe. *Int J Thermal Sci* 155:106356. <https://doi.org/10.1016/j.ijthermalsci.2020.106356>
5. Mew T, Kang K, Kienhofer F, Kim T (2015) Transient thermal response of a highly porous ventilated brake disc. *Proc Inst Mech Eng J Automobile Eng* 229:674–683. <https://doi.org/10.1177/0954407014567516>
6. Yanab H, Zhangbc Q, Lubc T (2016) Heat transfer enhancement by X-type lattice in ventilated brake disc. *Int J Thermal Sci* 107:39–55. <https://doi.org/10.1016/j.ijthermalsci.2016.03.026>
7. Nejat A, Aslani M, Mirzakhilili E, Najian R (2011) Asl heat transfer enhancement in ventilated brake disk using double airfoil vanes. *J Thermal Sci Eng Appl* 3:10. <https://doi.org/10.1115/1.4004931>
8. Polyakov PA, Volchenko NA, Fedotov ES, Tagiev RS, Denisenko VA (2019) Development of a model of the ventilation apparatus for disc-shoe brakes of cars. In: *Mechanics, equipment, materials and technology: international. scientific-practical conference Krasnodar*, pp 252–261
9. Litvin AE, Polyakov PA, Polyakova EA, Tagiev RS, Fedotov ES, Golikov AA (2020) Development of a methodology for evaluating the cooling system of brake discs. *Bull ISTU named after M. T. Kalashnikov* 23(1):14–22. <https://doi.org/10.22213/2413-1172-2020-1-14-22>

Modeling the Clustering of Dispersed Systems Using Dynamic Models



Alexey Bormotov and Anastasia Gorokhova

Abstract A mathematical method for modeling the processes of structure information of dispersed systems and composite materials is proposed using dynamic models that take account of energy, structural and rheological features of interparticle interaction. The conditions of the processes of spontaneous formation of floccules and clusters are considered. Mathematical models of clusters structure formation in dispersed systems are constructed, the parameters of clusters and the prescription-technological conditions of their formation are determined. Control possibility of the processes of disperse systems structure formation in order to obtain the optimal parameters of the structure and properties of composite materials on the basis of the proposed models and mathematical methods is shown.

Keywords Composite materials · Mathematical modeling · Rheology · Optimization of properties

1 Introduction

Composite materials (CM) by their nature are referred to dispersed systems, which are obtained by combining a viscous matrix (binder) and finely ground dispersed phases of various nature (fillers). This circumstance must be considered in the mathematical modeling of the processes of structure formation of CM. Composite materials with special or extreme properties are just such systems. Using the optimal recipe and technological parameters, the fabrication of products requires low energy costs.

The structure formation of composites filled with dispersed minerals is determined by interactions between structure-forming elements—flocules and clusters, as well as processes occurring on the surfaces of these conglomerates and in binder

A. Bormotov (✉)

Penza State Technological University, Baidukova pr., Gagarina St., 1a, 11, 440039 Penza, Russia

A. Gorokhova

Penza State University of Architecture and Construction, Germana Titova St., 28, 440028 Penza, Russia

interlayers. The thickness of the binder interlayer and the size of dispersed conglomerates have a decisive effect on the rheological properties of composites and on the structure and performance properties of composite materials [1–7].

The emergence of new systemic properties in composites, as complex technical systems, is associated with the emergence of new formations—flocules (clusters), which distinguishes composites from a mechanical mixture of components, and is the main factor in the quality of modeling the composites structure formation [3].

One of the most important scientific and technical problems of great practical importance is the development of methods for mathematical modeling of the mechanism of structure formation (flocculation) in order to obtain the specified structure and properties of CM.

2 Research Methods and Principles

In order to perform adequate mathematical modeling of the processes of structure formation of composite materials, it is necessary to have an adequate mathematical description of the physical and technological parameters of the formation of the structure of composite materials in a formalized form.

Obtaining a mathematical description of the processes of structure formation of composite materials was carried out by the analytical method and by the method of computer modeling. Methods of modeling dynamic and kinematic modes of floccule formation were used as analytical methods. Such methods are characterized by the presence of a cumbersome mathematical apparatus. At the same time, these methods can be used to assess the adequacy of the numerical modeling results. The advantage of analytical methods is the possibility of mathematical and imitation modeling of flocculation processes, which largely determines the operational properties of the composite material [4].

To model the structure formation of dispersed filled systems, the methods of system analysis and the theory of optimal control were used on the basis of analytical, rheological, energy, structural, cybernetic and informational approaches. To simulate many combinations of structure-forming factors, the author's method of joint solution of analytical dependences of interactions of structure-forming elements and numerical computer modeling of the mathematical description of the conditions of flocculation was used.

3 The Main Results

As known, the evolution of structure formation of dispersed systems is determined by interphase interactions between structure-forming elements [5]. In a composite filled with dispersed minerals one of the basic structural units is a spontaneously arising floccular or cluster conglomerate. The article proposes a mathematical description

of filled composites, the structure formation processes of which can be described by a system of equations:

$$m_i \frac{d^2 \vec{r}(t)}{dt^2} - k_i \cdot \left(\frac{d\vec{r}(t)}{dt} - \vartheta_i \right) = -\Delta U_i, i = \overline{1, N} \tag{1}$$

here m_i – mass of the i -th particle; $r_i = (x_i, y_i, z_i)$ – radius vector of coordinates of the i -th particle; N —number of filler particles; k – efficient determined by the dissipative properties of the dispersed filler, v_i – the velocity of the dispersion environ at the point r_i ; U_i – energy potential at point r_i , in the general case, is depended on the parameters of the dispersion environ and on the relative position of all other particles of the system.

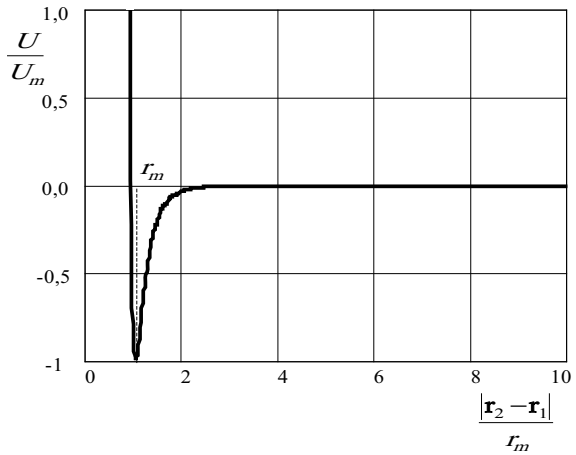
The left side of Eq. (1), which is the difference between the forces of inertia and viscous friction, is unchanged in shape for any dispersed system. The expression for the gradient on the right-hand side of (1) turns out to be complex and ambiguous for each individual case.

The potential of interparticle interaction in Eq. (1) includes many terms, but the contribution to the overall result of most of them is one or two orders of magnitude less than the contribution of the first two [6]. Let us take a binary potential for a system with a single equilibrium in the form:

$$U(r_1, r_2) = \frac{\alpha}{|r_2 - r_1|^{12}} - \frac{\beta}{|r_2 - r_1|^6} \alpha > 0 \beta > 0 \tag{2}$$

Expression (2) contains two independent parameters, the numerical values of which depend on the following parameters (Fig. 1):

Fig. 1 Accepted binary potential of particle interaction



- The distance $r_m = |\mathbf{r}_2 - \mathbf{r}_1|$, corresponding to the equilibrium coordinate for which it characteristically is $\nabla U|_{r=r_m} = \mathbf{0}$;
- The size of potential well $U_m = -U(r_m)$, measured from zero energy level.

The values of the parameters in Eq. (2) are related to the indicated quantities by the following relations:

$$\alpha = U_m r_m^{12}, \beta = 2U_m r_m^6. \quad (3)$$

The physical and mechanical properties of a binder—a matrix obtained by combining mineral or organic binders with finely ground fillers—depend on the formation of their optimal structure. An increase in the macro-properties of the binder matrix depends on the parameters of the binder structure, on the type and rate of surface phenomena at the interface, as well as on the amount of filler v_f , its dispersion S_{sp} and the physicochemical activity of the surface of fillers and aggregates. For lyophilic systems, optimization of the CM filling can be carried out by changing v_f and S_{sp} , the ratio of which makes it possible to calculate the average thickness of the interlayer of the binder between the filler particles h . The achievement of the calculated thickness of the binder layer depends on the duration of the dispersion process, and is not determined by surface phenomena [7]:

$$h = \frac{6}{\rho_f S_{sp}} \left(\sqrt[3]{\frac{\eta_f}{v_f}} - 1 \right), h = \frac{1 - v_f}{v_f} \frac{1}{S_{sp} \rho_f} \quad (4)$$

here ρ_f , S_{sp} , v_f —density, specific surface area, volume fraction of filler material respectively; η_f —maximum packing density of particles.

Researches show that the boundary or solvation layer of a binder is formed when the components of the binder are combined at the interface. This layer is characterized by a dense and ordered arrangement of the structural elements of the binder and large oligomer molecules. The rheological properties of mixtures and the physico-mechanical properties of CMs depend on the thickness of the solvation layer, the structure of the layer, and the strength of adhesion of the solvation shell to the surface of the particles of the dispersed phase. However, the boundary layer also determines the aggregate stability of the dispersion system, on which the possibility of the formation of clusters in the structure of the composite depends. As the studies of the authors show, if the thickness of the binder layer is many times greater than the thickness of the solvation shell, then spontaneous formation of clusters is not possible due to the negligible effect of the surface energy of the particles of the dispersed phase.

It is proposed to determine the thickness of the solvation shell on the basis of rheological, energetic, structural approaches.

Rheological approach is based on Einstein's law:

$$h_c = 2 \sqrt[3]{\frac{\eta_{un} \infty}{2, 5 v_f}} - \frac{3}{S_{un} \rho_f}, \text{ or } h_c = \frac{1}{\rho_f S_{un}} \left(\frac{K_1}{K_0} - 1 \right), \quad (5)$$

here $\eta_{un\infty} = \frac{\eta_{\infty} - \eta_0}{\eta_0}$ —reduced viscosity; K_I, K_0 —coefficients determined by the viscosities of a dispersed system in which the environ doesn't form at all or forms a solvation shell of an infinitely small thickness on the particle surface.

The energy approach is to take into account the Van der Waals interaction of molecules:

$$h_c = \sqrt[3]{\frac{\pi \rho_m \chi_m |B_{mf} \rho_f - B_m \rho_m|}{6C_p}}, \text{ and } h_c = C \left(1 - \frac{T}{T_{cr}}\right)^{-\frac{1}{6}}, \quad (6)$$

here $C_p = \frac{\rho_h - \rho_m}{\rho_m}$; ρ_m —binder density; ρ_m —binder density at thickness h ; χ_m —isothermal compressibility of the binder; B_m and B_{mf} —Van der Waals interaction constants of the binder molecules with each other and with the structural elements of the other phase respectively; T_{cr} —critical temperature of structure formation.

The structural approach is based on taking into account the processes occurring at the interface:

$$h_l = \frac{8\pi^2 \sigma_m}{RT(\rho_f - \rho_m) \ln\left(\frac{\rho_f}{\rho_m}\right)}, \text{ and } h_l = \frac{const}{(\rho_f - \rho_m)^2 \ln\left(\frac{\rho_f}{\rho_m}\right)}, \quad (7)$$

here σ_m —surface tension of the binder.

From (5)...(7) it follows that at a noticeable distance from T_{cr} values of h_l are in the interval $10^{-7} \dots 10^{-9}$ m. Moreover, for substances consisting of complex molecules, the thickness h_l is close to $10^{-7} \dots 10^{-8}$ m; for substances consisting of simple molecules—close to 10^{-9} .

As practice shows, the use of formulas (5) ... (7) is associated with difficulties in instrumental determination of quantities. The processes occurring at the phase interface cannot be estimated.

The authors propose a method for determining h_l , devoid of these disadvantages. It is based on an energetic approach. Namely, when the surface of a solid is wetted, energy is released equal to:

$$U_{wet} = S\sigma_l \cos \theta \quad (8)$$

here σ_l —surface tension; θ —contact angle of solid surface wetting; S —wetted surface area. This energy is spent on the formation of a solvation layer with a number of molecules $N = \frac{U_{wet}}{RT} N_A$, here N_A —Avogadro's constant; RT —thermal energy of 1 mol of binder.

The thickness and mass of the solvation layer are determined as:

$$h_l = \frac{m_l}{\rho_l S}, m_l = \frac{N}{N_A} M, \quad (9)$$

here m_c, ρ_c —layer mass and density respectively, M —molecular weight of the binder.

Table 1 Maximum thickness of the solvation layer $h_{l,max}$, nm [8]

Binder type	Temperature, °C				
	25	50	75	125	150
Sulfuric astringent	–	–	–	2.12	2.02
Epoxy phenolic aldehyde resin	14.6	13.4	12.5	–	–
Phenol formaldehyde resin	13.4	12.4	11.5	–	–

Relations (8) and (10) determine the coefficients in the expression for the potential. From (7), (8) and (9), we obtain:

$$h_l = \frac{\sigma_l \cos \theta}{RT} \frac{M}{\rho_l} \quad (10)$$

From (10) we find that the thickness of the binder interlayer increases with an increase in the molecular weight, molecular size, and surface tension of the binder. Also, an increase in the wettability of the filler surface with a binder affects the increase in the thickness of the solvation layer. A decrease in the thickness of the binder layer is observed with an increase in the temperature and density of the layer. These provisions are confirmed by experimental data. [8, 9].

With preliminary calculations, it is possible to take $\rho_l = \rho_m$. The maximum thickness of the solvation layer is then determined by (10):

$$h \frac{\sigma_l \cos \theta}{RT} \frac{M}{\rho_{m l,max}} \quad (11)$$

The values of the thickness of the solvation layer for some binders are given in Table 1.

The calculated values of $h_{l,max}$ coincide with the experimental data, and formula (11) can be used to study the processes of structure formation (flocculation) of CM [8, 9].

4 Discussion

For a theoretical system of two particles in the absence of external forces, taking into account their significant distance from each other ($|\mathbf{r}| \gg r_m$), in expression (1) the second term is significant for the potential; the first can be discarded.

Modeling of structure formation was carried out in a rectangular coordinate system. The origin of coordinates was located at the place of the first particle, and the direction of the abscissa axis was chosen in the direction of the vector \mathbf{r}_{12} . With low friction, equal (2) can be written in the form:

$$m\ddot{x} = U_m \frac{d}{dx} \left(\frac{x_m^6}{x^6} \right) \tag{12}$$

here U_m —potential well depth ($U_m > 0$), x_m —its position.

Next:

$$\frac{m\dot{x}^2}{2} = U_m \left(\frac{x_m}{x} \right)^6 + C \tag{13}$$

We take the moment of particle contact as the reference point, and change the reference direction to the opposite. Then the constant of integration $\dot{x}|_{x=\infty} = 0$ and

$$\frac{m\dot{x}^2}{2} = U_m \left(\frac{x_m}{x} \right)^6 \tag{14}$$

As you can see, with increasing time t , both parts of (14) increase (the potential energy of interaction of particles transforms into kinetic energy), the distance x between particles decreases.

From (14) we have:

$$x^4 = 4x_m^3 \sqrt{\frac{2U_m}{m}} t + C \tag{15}$$

Consequently, the time of “spontaneous” formation of floccules in the CM (the time of movement of a particle from point $x = x_1$ to point $x = x_2$ ($x_1 > x_2$)) is determined in the form:

$$\Delta t = \frac{1}{4x_m^3} \sqrt{\frac{m}{2U_m}} (x_1^4 - x_2^4) \tag{16}$$

which rapidly increases with the increase in the initial distance between the particles (in proportion to the fourth power of the distance).

The calculated values of Δt , obtained in accordance with (16) for particles with a diameter of 1 mcm, are shown in Table 2. Was accepted: $x_m = h_{c,max}$, $U_m = N k T$, here $h_{l,max}$ —determined by (4) the maximum thickness of the solvation layer, N —number of molecules in the solvation layer, k —Boltzmann constant, T —temperature.

Table 2 Estimation of clustering time, years

Binder type	Initial distance between particles, mcm				
	1	5	10	50	100
Sulfuric astringent	1	500	10,000	$5 \cdot 10^6$	10^8
Epoxy resin	3 days	5	100	$5 \cdot 10^4$	10^6

The values given in Table 2 are the lower limit of the clustering time (without taking into account the repulsive forces and dissipative properties of the system). The exact experimental values will be higher than those given in Table 2.

Let us show the possibility of the formation of a linear cluster due to the capture of particles in the process of mixing the composition. We choose the coordinate system so that the only nonzero term remains on the right-hand side. Neglecting the forces of inertia, the law of motion of a particle can be represented as:

$$k(\dot{x} - \dot{x}_e) = -\frac{\partial}{\partial x}U \quad (17)$$

here \dot{x} and \dot{x}_e —particle velocity and dispersion environ respectively.

The point corresponding to the maximum force value $|\nabla U|$:

$$\frac{\partial}{\partial x}\nabla U = U_m \frac{\partial^2}{\partial x^2} \left(\left(\frac{x_m}{x} \right)^{12} - 2 \left(\frac{x_m}{x} \right)^6 \right) = 12U_m \frac{x_m^6}{x^8} \left(13 \left(\frac{x_m}{x} \right)^6 - 7 \right) \quad (18)$$

Equating the derivative to zero, we get:

$$x_f = x_m \sqrt[6]{13/7} \quad (19)$$

The value of the force acting on a particle at a point $x = x_f$:

$$F|x = x_f = \frac{72U_m}{13x_m} \sqrt[6]{\frac{7}{13}} \quad (20)$$

Equating the force of viscous friction acting on a particle from the side of the dispersion environ with the force acting on the particle from the side of the field of another particle, we obtain the limiting value of the velocity of the dispersion environ at which cluster formation is still possible:

$$\dot{x} \frac{12}{13} \sqrt[6]{\frac{7}{13}} \frac{U_m}{\pi \eta R x_m} \frac{U_m}{\eta R x_{m,e,max}} \quad (21)$$

here R —particle radius, η —environ viscosity. Limiting speed values calculated in accordance with (21) are given in Table 3.

Table 3 Estimation of the limiting velocity of the dispersion environ, mm/sec

Binder type	Particle diameter, mcm				
	0.1	0.5	1	5	10
Sulfuric astringent	$1.3 \cdot 10^6$	$2.6 \cdot 10^5$	$1.3 \cdot 10^5$	$2.6 \cdot 10^4$	$1.3 \cdot 10^4$
Epoxy resin	1.7	0.34	0.17	0.03	0.02

5 Conclusions

From the presented results it follows that the formation of clusters in the process of mixing the composition due to the capture of particles in high-viscosity systems does not occur, because the forces of viscous friction acting on the particle from the side of the dispersion medium lead to the destruction of clusters. However, the formation of clusters in low-viscosity filled systems is possible when energy is supplied from the outside, i.e. with various methods of energetic pumping of the system—intensive stirring, heating, shaking, ultrasonic treatment, etc.

Analysis of the results allows us to conclude that the spontaneous formation of flocculas from macroscopic (more than 1 μm) particles is also not possible. In systems consisting of particles, the linear dimensions of which, as well as the inter-particle distance between which are comparable to the value of $h_{l,max}$ —the formation of floccules and floccular conglomerates is possible.

Equation (16) is one of the components of the generalized model of structure formation of dispersed-filled systems [7] and makes it possible to estimate the time of “spontaneous” formation of floccules in a composite material during controlled multicriteria synthesis of composites with given structure parameters.

The developed method of simulation modeling of flocculation in dispersed systems makes it possible to take into account the influence of the main recipe and technological factors on the process of structure formation of composites. The adequacy of the obtained analytical solutions is confirmed by numerical solutions obtained for known composite materials with an error of no more than 5% [8–10].

References

1. Ebeling V, Engel A, Feistel R (2001) Physics of evolutionary processes. URSS Publishing House, Moscow
2. Bobryshev AN, Kozomazov VN, Babin LO, Solomatov VI (1994) Synergetics of composite materials. NPO ORIUS, Lipetsk
3. Bormotov AN, Proshin AP, Korolev EV, Danilov AM, Garkina IA (2003) Development and quality management of building materials with adjustable structure and properties for radiation protection. In: Proceedings of the II international conference “identification of systems and control tasks SICPRO’03”. Publishing house of the V A Trapeznikov Institute of Control Sciences of the Russian Academy of Sciences, Moscow, pp 2437–2460
4. Proshin AP, Danilov AM, Korolev EV, Smirnov VA (2003) Dynamic models in the study of clustering in composite materials. Limit systems. Izvestiya vuzov. Building. Publishing house of the Novosibirsk State University of Architecture and Civil Engineering, Novosibirsk, vol 3, pp 32–38
5. Proshin AP, Danilov AM, Garkina IA, Bormotov AN, Solomatov VI (2001) Theoretical aspects of the synthesis of polymer composite materials for protection from radiation Izvestiya VUZov. Building and architecture. Publishing house of the Novosibirsk State University of Architecture and Civil Engineering Novo-Siberian, vol 6, pp 7–9
6. Melker AI, Vorobieva TV (1997) Self-organization and formation of helicoidal structures of polymers. Solid State Phys (Ioffe Physicotech Inst RAS, 39(10):1883–1889

7. Bormotov AN (2011) Mathematical modeling and multicriteria synthesis of composite materials for special purposes, Ph.D. thesis, Penza, PSTU
8. Bormotov AN (2012) Polymer composite materials for radiation protection. Ph. Paleotype, Moscow
9. Proshin AP, Korolev EV, Bormotov AN, Figovsky OL (2005) The extra-heavy concrete for protection from radiation. In: Proceedings of the international conference on role of concrete in nuclear facilities 2005 international congress – global construction: ultimate concrete opportunities. Ser. “Role of concrete in nuclear facilities – proceedings of the international conference”, University of Dundee, Concrete Technology Unit. Dundee, Scotland, pp 69–76
10. Proshin AP, Korolev EV, Bormotov AN (2011) Mathematical modeling and multicriteria synthesis of composite materials, Ph. PSTU, Penza

Substantiation of the Method for Calculating Soil Deformation Modulus



Aleksandr Kalinin , Aleksandr Prolygin , and Natalya Aleksandrova 

Abstract The purpose of the article is to analyze methods for calculating the deformation modulus of subgrade soils based on the results of stamp tests. To perform a comparative analysis, stamp tests of a subgrade model built in a soil channel were carried out. During the tests, the load was applied in steps, and the stamp settlement was measured upon completion of deformation stabilization from each step. The criterion for the stabilization of deformation was a decrease in the speed to 0,02 mm/min and the time of application of the load, which should be not less than 120 s. Further, the calculations of the soil deformation modulus were carried out using various methods regulated by the standards of the Russian Federation. The results of calculating the deformation modulus are grouped into data samples, which are processed by methods of mathematical statistics. During data processing, each sample is checked for gross errors. The data samples were checked for belonging to the same general population. To check whether three samples belong to one general population, the Kruskal W.H. and Wallis W.A. criterion was applied. Based on this comparison, we obtained judgments about the significance of the differences in the samples. As a result, to determine the deformation modulus of soil and road pavements made of granular materials, a way for calculating the deformation modulus by a method that assumes a non-linear dependence of deformations from pressures described by a polynomial of the second degree is recommended.

Keywords Road pavement · Soil-crushed-stone loayer · Deformation modulus

1 Introduction

Currently, the preliminary standards of the Russian Federation divide automobile public roads into two groups: public roads and low-traffic intensity roads. Two different techniques are used to design road pavements for low-traffic intensity roads. For the design of non-rigid road pavements of the capital and lightweight type with

A. Kalinin (✉) · A. Prolygin · N. Aleksandrova
The Siberian State Automobile and Highway University, Prospekt Mira, 5, Omsk Oblast,
644080 Omsk, Russia

an improved surface, the traditional method is used, according to which the strength calculation is performed using three criteria. These criteria are the calculation of the structure as a whole for the permissible elastic deflection and checks for the resistance to fatigue failure from bending of monolithic layers and shear resistance in the subgrade soil. Non-rigid road pavements of transitional and lower types are designed according to the criteria of strength and operational reliability. Strength calculation is performed on the basis of elastoplastic deformation, ensuring the total deformation modulus on the coating surface is not less than the required value. The calculation for operational reliability is performed by determining the depth of the rut and comparing its value with the permissible value. The need for differences in the calculations of layers made of monolithic and granulated materials of elastic deflection was discussed in the work [1]. In this paper, it is noted that the traditional method for calculating the total modulus of elasticity is based on solving the theory of plate bending. Therefore, both layers of grainy materials and layers of granulated materials and sands are endowed with the ability to work for bending. In reality, granulated materials and soils operate under triaxial compression, which requires calculating the displacement of their surface by integrating vertical deformation over the layer thickness or the depth of the soil half-space [1–4].

Of course, solving the problems of improving calculation methods, bending asphalt concrete layers, and layers of granulated materials, as well as subgrade soils, it is necessary to use the knowledge of different sections of mechanics. Calculations of pavements with asphalt concrete pavement and layers of monolithic materials develop:

- by creation of methods for calculating changes in evenness under the influence of frost heaving of soils [5];
- by improvement of fatigue theories by applying models of nonlinear damage accumulation in concrete [6] and asphalt concrete [7–9];
- by development and improvement of mechanical-empirical methods for calculating the depths of ruts [10–12].

The problem of pavement layers made of granulated materials is the formation of ruts, which are formed due to the accumulation of residual deformations in these layers and soils of the subgrade. Therefore, the improvement of calculations of pavements with layers of such materials is carried out by the development of methods for calculating residual deformations [13–16] or improvement of calculation methods for shear strength [17] with the refinement of the parameters of the Mohr—Coulomb criterion and the development of mathematical models linking cohesion and the angle of internal friction with humidity [18].

The problem of rutting is relevant for pavements on roads with low traffic intensity. Such roads have pavements, usually of a transitional or lowest type. The pavements of such roads are often made of granulated materials. To reduce the intensity of accumulation of residual deformations in crushed stone layers, they are reinforced with geosynthetic materials [19–24].

For the construction pavements of transitional types, local materials are used [25], including industrial waste [26, 27] and reused materials [28], soils and materials

stabilized and reinforced with polymer additives and binding material [29–34]. In pavements of the lowest type, it uses soil-crushed stone mixtures [35, 36].

The design of lowest and transitional type road pavements on roads with low traffic intensity requires the use in calculation the deformability parameters of materials and soils. This parameter is the modulus of deformation, which is similar to the modulus of elasticity, but characterizes elastoplastic deformation. To calculate the value of the modulus of deformation of materials, the data of tests of the road structure, performed on the surface of the layer from the test material and on the surface of the layer underlying the test layer, are used. Often the underlying layer is a soil half-space, that is, a subgrade.

Several methods of testing road structures are currently in use. In [37], it was shown that some methods are well suited for testing pavements with asphalt concrete, while others are good for testing soils and layers from granulated materials. Moreover, to calculate the deformation modulus of soils and the total deformation modulus on the surface of a layer of granulated material, different methods are used, according to which different values of the calculated deformation characteristic are obtained. Therefore, the works aimed at substantiating the method for calculating the deformation modulus are acquiring acute relevance. This justification is the goal of our study.

2 Materials and Methods

To solve the set tasks, stamp tests of the subgrade soil, fill up in the tray of the soil laboratory, were performed. The tests used a standard stamp setup with a hydraulic jack, an electronic dynamometer and a rigid round stamp with a diameter of 33 cm. In the course of the experiment, five points of the subgrade soil were tested. The thickness of the subgrade model is 1,2 m, which is comparable to four stamp diameters. In order to avoid the influence on the values of the settlement of the soil massif, the concrete bottom of the tray, the maximum value of the pressure from the stamp is limited to 0,25 MPa. Such a limitation is permissible by the preliminary national standard of the Russian Federation PNST 311-2018. The requirements of this standard were taken as the basis for performing experiments, in accordance with the requirements, the size of the steps was assigned during loading and subsequent unloading of the subgrade model. In Fig. 1 shows a stamp setup which includes a load plate (stamp) a hydraulic jack, a deflectometer equipped with an indicator, as well as an illustration of the application of a load with control of its value using an electronic dynamometer.

Table 1 shows formulas for calculating the modulus of deformation and elasticity, regulated by the standards of the Russian Federation.

The load from each stage was maintained for the time required to stabilize the settlement. This time was determined by reducing the deformation rate of the subgrade to a value of 0,02 mm/min, but not less than 2 min. Upon completion of

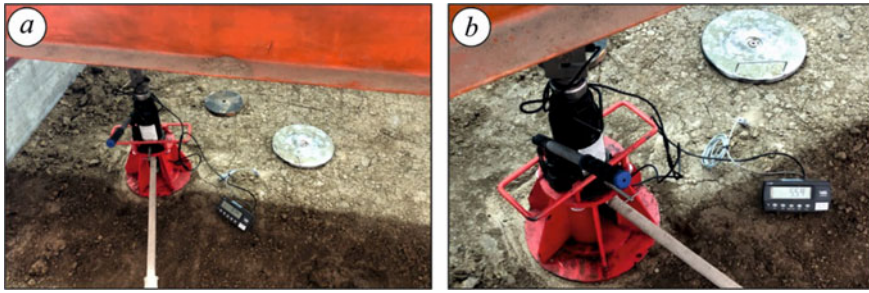


Fig. 1 Stamp tests: *a*—placement of a stamp, jack, deflectometer and dynamometer; *b*—load application and control of its value using a dynamometer

Table 1 Formulas for calculating settlements and deformation modulus of soils, regulated by state and preliminary national standards of Russia

Standard	Characteristic	Calculation formulas
GOST 20,276-2012	Deformation modulus E_d	$E_d = (1 - \mu^2) \cdot K_{h/D} \cdot K_1 \cdot D \frac{\Delta p}{\Delta S_z}$
PNST 371-2019	Relative settlement of the subgrade soil	$\lambda = \frac{S_z}{D}$,
	Modulus of deformation of the subgrade soil E_d	$E_d = \frac{p}{\lambda}$;
PNST 311-2018	Subgrade soil settlement	$S_z = a_0 + a_1 \cdot p_0 + a_1 \cdot p_0^2$;
	Deformation modulus E_d	$E_d = \frac{0,75 \cdot D}{a_1 + a_2 \cdot p_{max}}$
	Elastic modulus E_d	$E_{el} = \frac{0,75 \cdot D \cdot p_{max1}}{S_{el}}$

where $K_{h/D}$ —coefficient depending from the relative value of the penetration of the stamp during the test (at $h/D = 0$, as well as when tested in pits and faces, $K_{h/D} = 1$); K_1 —coefficient taken for a rigid round stamp equal to 0,79; Δp and ΔS_z —increments of pressure and settlement respectively; where λ —the required amount of relative deformation, the value of which is taken in the range $\lambda = 0,01 \dots 0,02$ for subgrade soils and $\lambda = 0,04 \dots 0,08$ for road pavement; a_0 , a_1 and a_2 —constant of polynomial of the second degree; p_{max} —the maximum value of the pressure transmitted by the stamp to the subgrade or road surface when measured, MPa; p_{max1} —maximum pressure value reached during loading stage, MPa

the deformation stabilization, the next load step was applied, waiting for the settlement to stabilize. The load was applied until the pressure from the stamp reached 0,25 MPa. Then unloading was performed.

The test results at each of the five points were presented as a graphical dependence of elastoplastic and reversible deformation from pressure. Such dependences are shown in Fig. 2.

The calculation of the deformation modulus was carried out according to the formulas presented in Table 1. Explanation of the calculation of the modulus of soil deformation according to the formulas of Table 1 are shown in the form of graphic illustrations in Fig. 3. In Fig. 1a shows the dependence of settlement from pressure

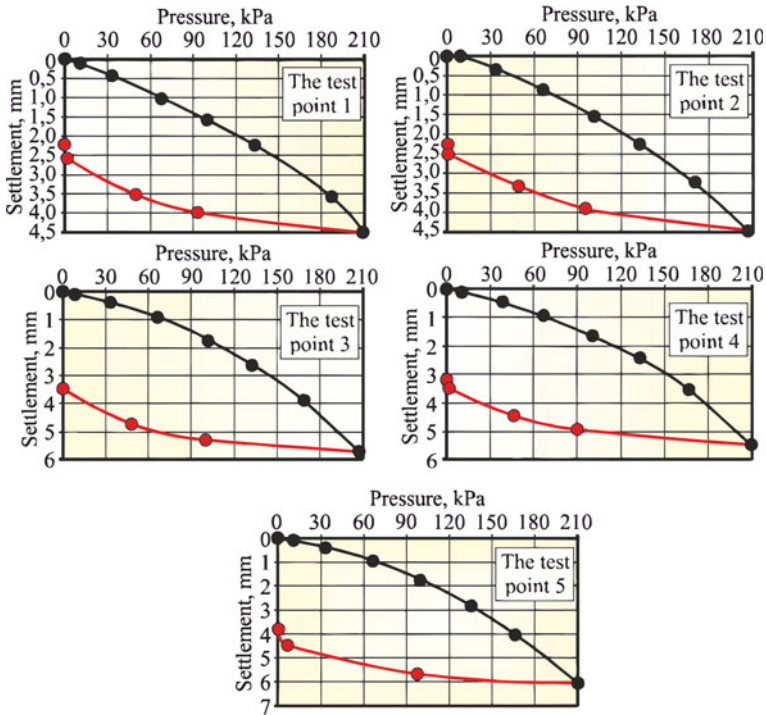


Fig. 2 Dependence of settlement from pressure

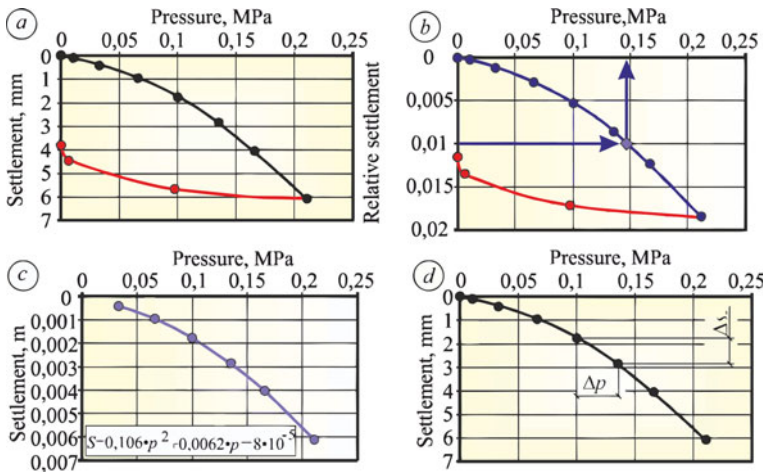


Fig. 3 Illustrations for calculating the deformation modulus: *a*—dependence of settlement from pressure at test point 5; *b*—dependence of the relative settlement from pressure and determination of the pressure corresponding to the value of the relative settlement 0,01; *c*—approximation of the dependence of settlement from pressure by a polynomial of the second degree; *d*—illustration of determining the increment of settlement and pressure from the *i*-th stage of loading

for test point 5. This dependence is identical to the dependence shown in Fig. 2. To calculate the deformation modulus according to the PNST 371-2019 method, it is necessary to calculate the relative settlements λ , determined by the ratio of settlement S_z to the diameter of the stamp D . The calculated values of the relative settlements are used to plot the graph, illustrating the dependence of such relative settlements from pressure. This graph is shown in Fig. 1b. Using such a graph, the pressure is determined that corresponds to the required value of the relative settlement, which is taken in the range $\lambda = 0,01 \dots 0,02$. In Fig. 1b, it is assumed that the required value of the relative settlement is $\lambda = 0,01$. Then the pressure corresponding to the value $\lambda = 0,01$ can be easily determined from the graph, it is approximately $p \approx 0,15$ MPa. Further, according to the formula Table 1 the value of the deformation modulus is calculated. Analyzing this method, we note that with a nonlinear dependence of the relative settlement from pressure with an increase in the required value of the relative settlement λ from 0,01 to 0,02, the calculated value of the deformation modulus will decrease.

When calculating the deformation modulus by the PNST 311-2018 method, the dependence of the settlement from pressure must be approximated by a polynomial of the second degree, as shown in Fig. 1c. In this case, the first two points of the graph are not taken into account in the approximation. Of these two points, the first point is the origin, and the second connects the least settlement with the minimum pressure applied to load the subgrade at the start of the test. As a result of the approximation, the values of the coefficients of the second degree polynomial are calculated. According to the data in Fig. 1c, the values of these coefficients are: $a_0 = 8 \cdot 10^{-5}$, $a_1 = 0,0062$ and $a_2 = 0,106$. The values of the coefficients a_1 and a_2 are used to calculate the deformation modulus, and the calculation is performed according to the corresponding formula of Table 1. In Fig. 1d illustrates the determination of the deformation modulus according to the GOST 20,276-2012 method. According to this technique, it is first necessary to determine the pressure increments from the load steps Δp_i and the corresponding increments of the settlement ΔS_{z_i} . Further, for the corresponding pressure increments Δp_i and settlement ΔS_{z_i} according to the formula in Table 1, the deformation modulus E_{d_i} are calculated. This technique is characterized by a decrease in the value of the modulus of deformation when using in the calculation increments of pressure Δp_i and settlement ΔS_{z_i} , corresponding to an increase in settlement.

Taking into account the specifics of calculating the deformation modulus according to the methods GOST 20,276-2012 and PNST 371-2019, which consists of the dependence of the deformation modulus value from settlement, we have calculated the average values of these deformation characteristics. When using the PNST 371-2019 technique, the maximum value of the deformation modulus E_{dmax} was first calculated, which corresponds to a relative settlement $\lambda = 0,01$. Then the minimum value of the modulus of deformation E_{dmin} was calculated, it is obtained either at a relative settlement $\lambda = 0,02$, or at the maximum value of the relative settlement λ_{max} , measured during testing, less than 0,02, but greater than 0,01, that is $0,01 < \lambda_{max} \leq 0,02$. The calculation of the average value of the deformation modulus by the PNST 371-2019 method was carried out according to the formula:

$$E_d = \frac{E_{dmin} + E_{dmax}}{2}. \quad (1)$$

When calculating the deformation modulus according to the GOST 20,276-2012 method, the deformation modulus were calculated for each stage of the load E_{dj} , using the increments of settlement and pressure corresponding to this stage. At the final stage, the calculation of the deformation modulus value averaged over the settlement was performed. In this case, we used the formula:

$$E_d = \frac{\sum_{j=1}^n E_{di} \cdot \Delta S_j}{\sum_{j=1}^n \Delta S_j}. \quad (2)$$

3 Results

The test results were presented as samples of deformation modulus. The total number of samples is equal to the number of methods for calculating the deformation modulus, that is, 3 samples. Each sample consisted of five private values of the deformation modulus obtained by calculation using experimental data at the corresponding measurement points. Each data sample was checked for gross errors using a standard dropout criterion. In addition, by comparing the coefficient of variation with its limiting value, a rough estimate of the applicability of the normal distribution law of a random value was made. At the final stage, the calculated values of the deformation modulus are determined, calculated by different technique. The results of statistical processing are shown in Table 2.

From the analysis of the data Table 2 it follows that the average and calculated values of the deformation modulus calculated by the formulas of different standards, differ significantly. Therefore, when determining the deformation characteristics, it is necessary to substantiate the method for calculating the deformation modulus from the measured settlements and pressures.

For such substantiate, let us check three samples for belonging to the same general population. Since the number of private values of the deformation modulus in all samples is the same, for our purposes we can use the rank criterion W.H. Kruskal, W.A. Wallis [38]. The criterion W.H. Kruskal, W.A. Wallis [38] is a nonparametric alternative to the Fisher criterion. This criterion is based on the assessment of the differences between c medians ($c > 2$) and is a generalization of the Wilcoxon rank criterion [39].

When applying the criterion [38], it is necessary to replace the observations in the samples with their combined ranks. The first rank corresponds to the smallest observation, and the last rank corresponds to the largest observation. If some values are repeated, they are assigned the average of their ranks.

Application of W.H. Kruskal, W.A. Wallis [38] is based on the calculation of the statistics H . The calculation is made according to the formula:

Table 2 Results of statistical processing

Statistical characteristic		The value of the characteristic when applying the method of calculating the deformation modulus		
		GOST 20,276-2012	PNST 371-2019	PNST 311-2018
Private value of the deformation modulus by test points E_{di} , MPa	1	9.9	16.5	12.1
	2	9.7	16.3	11.7
	3	7.4	14.2	9.2
	4	7.8	14.6	10.2
	5	7.1	13.2	8.7
Average value E_d , MPa		8.4	15.0	10.4
Standard deviation S , MPa		1.3	1.4	1.5
Highest value $ E_d - E_{di} $, MPa		1.5	1.8	1.7
The value of the statistical criterion v at the number of determinations $n = 5$ and two-sided confidence coefficient $F = 95\%$		1.92	1.92	1.92
Criterion value $v \cdot S$		2.5	2.7	2.9
Criterion fulfillment $ E_d - E_{di} > v \cdot S$		No	No	No
Conclusion about the presence of gross errors in the sample		No mistakes	No mistakes	No mistakes
The coefficient of variation V , %		15.7	9.4	14.4
Criterion fulfillment $V < V_{lim}$, $V_{lim} = 30\%$		Yes	Yes	Yes
Conclusion on the applicability of the normal distribution law of a random value		Yes	Yes	Yes
Coefficient t_α with the number of degrees of freedom $K = 4$ and two-sided confidence coefficient $F = 95\%$		2.78	2.78	2.78
Calculated value	Minimal	6.7	13.2	8.5
	Maximum	10.0	16.7	12.2

$$H = \left[\frac{12}{n \cdot (n + 1)} \cdot \sum_{j=1}^c \frac{T_j^2}{n_j} \right] - 3 \cdot (n + 1), \quad (3)$$

where n —total number of observations in samples, n_j —number of observations in the j -th sample ($j = 1, 2, \dots, c$), T_j —sum of ranks j -th sample.

The private values of the deformation modulus and the corresponding ranks are given in Table 3, in which also calculates sums of rank for each sample.

After assigning the ranks presented in Table 3, and calculating their sum in each sample: $T_1 = 19$; $T_2 = 36$; $T_3 = 65$ ranks are checked. To do this, check the fulfillment of the equation:

Table 3 Private values of deformation modulus and their corresponding ranks

Sample 1 (GOST 20,276-2012)		Sample 2 (PNST 311-2018)		Sample 3 (PNST 371-2019)	
E_{di} , MPa	Rank	E_{di} , MPa	Rank	E_{di} , MPa	Rank
7.1	1	8.7	4	13.2	11
7.4	2	9.2	5	14.2	12
7.8	3	10.2	8	14.6	13
9.7	6	11.7	9	16.3	14
9.9	7	12.1	10	16.5	15
T_1	19	T_2	36	T_3	65

$$\sum_{j=1}^c T_j = \frac{n \cdot (n + 1)}{2}. \tag{4}$$

After checking, make sure that

$$\sum_{j=1}^c T_j = 19 + 36 + 65 = 120; \quad \frac{15 \cdot (15 + 1)}{2} = 120$$

Therefore, the ranks are assigned correctly, you can calculate the statistics H .

$$H = \left[\frac{12}{15 \cdot (15 + 1)} \cdot \left(\frac{19^2}{5} + \frac{36^2}{5} + \frac{65^2}{5} \right) \right] - 3 \cdot (15 + 1) = 10,82$$

The critical value of the Kruskal—Wallis criterion at a significance level of $\alpha = 0,05$ for the case of comparing 3 samples with five private values of observations in each sample is $H_\alpha = 5,78$.

Since the condition $H \geq H_\alpha$ ($10,82 > 5,78$) is satisfied, we reject the null hypothesis about random differences in the samples according to the level of the studied sign. Therefore, the samples cannot be combined into one population.

4 Discussion

As a result of the performed experiments and statistical processing of their experimental data, it was found that the samples of the private values of the deformation modulus calculated using three different methods, have significant differences. Application of the Kruskal—Wallis criterion showed that the compared samples cannot be combined into one population therefore, it is necessary to choose a method for calculating the soil deformation modulus. From the analysis of the methods for calculating the modulus of deformation, it follows that the calculation according to the formulas PNST 311-2018 is based on the nonlinear dependence of settlement from

pressure, which is a polynomial of the second degree. The constant coefficients of this polynomial are easily determined by regression analysis.

In this regard, to calculate the deformation modulus, we recommend using the methodology regulated by PNST 311-2018. Statistical processing of the experimental data allows us to define the mathematical expectation of the deformation module and its calculated value. In this case, in order to improve the reliability of the calculation of road pavements, the minimum calculated value of the deformation modulus can be taken.

References

1. Chusov VV, Aleksandrova NP, Ignatov VF (2019) Calculation of road clothes by elastic deflection criteria taking into account damage to asphalt concrete. *IOP Conf Ser: Mater Sci Eng* 687(2):1–7
2. Hirakawa D et al (2008) Relationship between sand ground stiffness values from FWD and from plate loading tests. *Jpn Geotech J* 3(4):307–320
3. Kongkitkul W et al (2010) Evaluation of static-equivalent stiffness by a simple falling weight deflectometer. *ATRANS Res* 2(1):1–14
4. Aleksandrov AS, Semenova TV, Aleksandrova NP (2020) Calculation of residual deformations of granulated materials from exposure to repeated loads. *Mater Sci Forum* 992:828–835
5. Churilin V, Efimenko S, Matvienko O et al (2018) Simulation of stresses in asphalt-concrete pavement with frost heaving. In: *MATEC web of conferences*, vol 216, pp 1–9
6. Chen Y, Chen X, Bu J (2018) Nonlinear damage accumulation of concrete subjected to variable amplitude fatigue loading. *Bull Polish Acad Sci: Tech Sci* 66(2):157–163
7. Xu X (2019) New damage evolution law for steel-asphalt concrete composite pavement considering wheel load and temperature variation. *Materials* 12:3723
8. Aleksandrov A et al (2018) Ways of application of the provisions of mechanics of bodies with cracks to the calculation of asphalt concrete on strength and plasticity. In: *MATEC web of conferences*, vol 239, pp 1–8
9. Aleksandrova N, Chusov V, Stolbov Y (2020) Damage accumulation in asphalt concrete under compression. *Adv Intell Syst Comput* 982:908–918
10. Rodezno MC, Kaloush K (2011) Implementation of asphalt-rubber mixes into the mechanistic empirical pavement design guide. *Road Mat Pavement Design* 12(2):423–439
11. Li Q et al (2011) Mechanistic-empirical pavement design guide (MEPDG): a bird's-eye view. *J Mod Transp* 19(2):114–133
12. Gercog VN, Dolgikh GV, Kuzin NV (2015) Calculation criteria for road pavement evenness. Part 1. Substantiating the flatness standards of asphalt pavement. *Mag Civ Eng* 5(57):45–57
13. Salour F, Erlingsson S (2016) Characterisation of permanent deformation of silty sand subgrades from multistage RLT tests. In: *3rd international conference on transportation geotechnics (ICTG 2016)*, procedia engineering, vol 143, pp 300–307
14. Salour F, Erlingsson S (2017) Permanent deformation characteristics of silty sand subgrades from multistage RLT tests. *Int J Pavement Eng* 18(3):236–246
15. Rahman MS, Erlingsson S (2015) Predicting permanent deformation behaviour of unbound granular materials. *Int J Pavement Eng* 16(7):587–601
16. Chen X, Chen L, Zhang J (2020) Permanent deformation behavior of coarse-grained residual subsoil under large amplitude loading cycles. In: Tutumluer E., Chen X., Xiao Y. (eds) *Advances in environmental vibration and transportation geodynamics*. Lecture notes in civil engineering, vol 66. Springer, Singapore

17. Aleksandrov A, et al (2018) The application of the principles of the theory of shakedown to the calculation of pavement layers of granular materials in shear. In: MATEC web of conferences, vol 239, pp 1–8
18. Zheng S et al (2018) Characterization of the undrained shear strength of expansive soils of high water content. In: MATEC web of conferences, vol 206, pp 1–5
19. Matveev SA et al (2020) The geogrid-reinforced gravel base pavement model. *Mag Civ Eng* 94(2):21–30
20. Matveev SA, Martynov EA, Litvinov NN (2014) Determine the reinforcement effect of gravel layer on a sandy foundation. *Appl Mech Mater* 662:164–167
21. Matveev SA, Martynov EA, Litvinov NN (2014) Effect of reinforcing the base of pavement with steel geogrid. *Appl Mech Mater* 587–589:1137–1140
22. Madjadoubbaye J, Camela WR (2019) reinforcement of flexible pavements by the use of geogrid: case of the road Mbalmayo - Ebolowa. *Civ Eng Res J* 8(5):134–138
23. Adams CA, Amofa NY, Opoku-Boahen R (2014) Effect of geogrid reinforced subgrade on layer thickness design of low volume bituminous sealed road pavements. *Int Refer J Eng Sci (IRJES)* 3(7):59–67
24. Murad AQ (2017) Application of geosynthetics in pavement design. *Int Res J Eng Technol (IRJET)* 4(7):1–7
25. Gyulzadyan H, Voskanyan G, Ter-Simonyan V (2014) Exploration results of applying limestone powder in crushed-stone-sand mixtures for road pavement layers. *Adv Mater Res* 1020:31–36
26. Lytkin AA (2020) Study of the transport loads influence on the nature of belite sludge hardening in pavement. *Mater Sci Forum* 992:79–85
27. Iлина ON, Ilin IB (2019) Road organo-mineral mixtures based on oil sludge. *Mag Civ Eng* 92(8):115–126
28. Dolinsky YA, Starkov GB, Matveev SA (2020) Experience in repairing highways using cold regeneration technology in the Altai Republic. In: International science and technology conference FarEastCon-2019, IOP conference series: materials science and engineering, vol 753, pp. 1–5. IOP Publishing Ltd.
29. Naeini SA, Naderinia B, Izadi E (2012) Unconfined compressive strength of clayey soils stabilized with waterborne polymer. *KSCE J Civ Eng* 16(6):943–949
30. Ismaiel HAH (2013) Cement kiln dust chemical stabilization of expansive soil exposed at El-Kawther Quarter, Sohag Region Egypt. *Int J Geosci* 4:1416–1424
31. Thomas A, Tripathi RK, Yadu LK (2018) A laboratory investigation of soil stabilization using enzyme and alkali-activated ground granulated blast-furnace slag. *Arab J Geosci* 43:5193–5202
32. Satyanarayana Reddy CNV, Prasad ACSV (2014) Performance studies on cement stabilized gravelly soil exposed to sulfate environment. *Indian Geotech J* 45(2):217–224
33. Rudgalskiy D et al (2020) Strength indices of sand reinforced by foamed bitumen. In: International scientific conference energy management of municipal facilities and sustainable energy technologies EMMFT 2019, journal of physics: conference series, vol 1614, pp 1–9. IOP Publishing Ltd.
34. Vdovin EA, Stroganov VF (2020) Properties of cement-bound mixes depending on technological factors. *Mag Civ Eng* 93(1):147–155
35. Aleksandrov A, Chusov V, Prolygin A (2021) Dependence of the deformation modulus of soil-crushed-stone layer from the content of crushed stone. *Lect Notes Civ Eng* 130:367–381
36. Dolgih G, Aleksandrova N, Prolygin A (2021) Experimental study of the deformation properties of soil-crushed-stone samples under compression. *Lect Notes Civ Eng* 130:518–532
37. Rudgalskiy P et al (2020) The effect of networks cracks on the strength of pavement. In: International scientific conference energy management of municipal facilities and sustainable energy technologies EMMFT 2019, journal of physics: conference series, vol 1614, pp 1–13. IOP Publishing Ltd.
38. Kruskal WH, Wallis WA (1952) Use of ranks in one-criterion variance analysis. *J Am Stat Assoc* 47(260):583–621
39. Wilcoxon F (1945) Individual comparisons by ranking methods. *Biom Bull* 1(6):80–83

Neural Network Model for Quality Indicators Assessment: Case of Paper Manufacturing Industry



Irina Rudakova , Alexey Peshekhonov , Anna Chernikova ,
and Svetlana Kuzmina 

Abstract Analysis of roll products at the final stage of production is the main stage for identifying defects, disrupted integrity or homogeneity, etc. Paper production is a typical example of such an operation in an industrial setting. It is proposed to use the results of the assessment for opacity, described by several standardized and statistical estimates, as the main characteristic for the quality of paper products. Studies of the dependence of the quality of the paper web on the production conditions and the properties of raw materials produce considerable variance, so that it is impossible to make accurate predictions. For this reason, we used a neural network modeling technology to develop an intelligent system for monitoring the quality of the paper web. Online quality control allows to assess the efficiency of the paper machine and rapidly adjust the manufacturing execution system. Special technologies such as computer vision systems can be introduced for this purpose, making it possible to make a transition from subjective assessment of the structure and defects of the paper web to obtaining objective quantitative estimates of these indicators. We considered a procedure for determining the estimates of structural heterogeneity of the paper web at the final stage of its production. We suggest to expand the classification of finished product samples by using neural fuzzy interpolation of linguistic values of such indicators. The approach introduced is aimed at improving the efficiency of the production process.

Keywords Paper production · Quality assessment · Structural heterogeneity · Opacity control · Formation · Neural-fuzzy systems · Neural network model · Neural network classifier

I. Rudakova · A. Peshekhonov
Saint-Petersburg State Institute of Technology, Moskovsky prospect,
26, 190013 St. Petersburg, Russia

A. Chernikova
Peter the Great St. Petersburg Polytechnic University, Polytechnicheskaya,
29, 195251 St. Petersburg, Russia

S. Kuzmina (✉)
Saint Petersburg Electrotechnical University, ul. Professora Popova
5, 197376 St. Petersburg, Russia
e-mail: snkuzmina@etu.ru

1 Introduction

Forming and dewatering a paper web is one of the most critical stages in the production of quality paper. The main goal of the process is to obtain a paper web with a mostly homogeneous structure. Studies on this subject were carried out by numerous scholars and research teams. We considered the main approaches to tackling the problem of increasing the accuracy and stability of the technological process of paper production at the stages of preparation and forming, as well as the issue of obtaining an extremal dependence for non-uniform opacity of the paper depending on the rate of mass filling on the pulp feed rate [1]. Our study was aimed at obtaining the physico-chemical and physico-mechanical characteristics of raw materials that can improve the binding capacity of fibers and stabilize the formation and dewatering of the paper web [2]. The homogeneity of the opacity was assessed by different technical methods of control [3], and a system for visualizing and analyzing the homogeneity of the structure of a paper sheet was tested [4]. Several studies discussed the applications of neural network modeling technologies, including diagnostic systems [5], decision support systems [6], forecasting systems [7], and monitoring and fault detection systems [8].

Considerable attention is paid to the problems faced by industrial enterprises in the field of paper production and the results achieved in eliminating these problems. Diverse solutions were offered for real issues in the paper industry, including mathematical approaches, experience and challenges [9]. A typology was constructed for cutting and packaging problems [10]. A procedure for optimizing the cutting plan for the paper industry was proposed [11], as well as an integrated solution for assignment, sequencing and cutting problems in paper production planning [12]. Optimization of the complex problem of lot sizing and cutting stock in the paper industry was offered in topic [13]. Integration of two-dimensional cutting stock and lot sizing problems was carried out in article [14]. For example, a study by Sahnó J., Shevtshenko Ed., Karaulova T., Tahera Kh. [15] introduces a novel approach to using the Six Sigma DMAIC (Define, Measure, Analyse, Improve, Control) methodology. This approach combines different tools and techniques into a single structure consisting of five steps. As another example, Rajnoha R., Gálová K., Rózsa Z. [16] is dedicated to searching for industrial engineering practice that can affect the overall economic performance, making it possible to understand whether the effect of these practices is extended to all sectors in the Czech Republic or only to specific ones. An algorithm for problems with constrained extrema is presented in topic [17]. The problems, modeling methods, and potential solutions are described in [18]. The impact of digitization on the development of modern metrology is considered in [19], while a paper by Okrepilov V.V., Kuzmina S.N., Makarov V.L., Bakhtizin A.R. [20] ideals with the peculiarities of using supercomputer technologies for modeling socio-economic systems.

At the same time, the most crucial issues involving the quality of paper production are related to the quality standards imposed by regulatory documents.

Heterogeneity of the structure is largely a subjective indicator of the quality of the paper web, as it is often assessed by opacity. According to GOST R 53,636-2009, opacity is an indicator characterizing the uniformity of distribution of the constituent components in paper in the form of areas with unequal opacity, visible on a sheet of paper in transmitted light. The GOST does not define the numerical characteristics of the opacity. From a technological standpoint, 'poor' paper opacity is due to uneven distribution of the paper pulp over the area of the sheet, which is a consequence of flocculation of fibers during the forming process. Paper with an unsatisfactory opacity is usually uneven in thickness and is characterized by low aesthetic properties, poor printability and an increased tendency for surface warping [21].

The opacity is determined by brightly illuminate the paper sample, and then capturing its digital image. Such criteria OST 13-299-87 are used for numerical assessment:

Forming index is the ratio of height to width of the histogram of points (ordinate) with different brightness (abscissa);

Heterogeneity of opacity is the standard deviation of the brightness of the points;

Light transmission is the ratio of the mean brightness to the brightness of the light source;

Directional heterogeneity is the dependence of the luminous flux on the coordinate along the web. It is calculated in the longitudinal and transverse directions;

Heterogeneity of pulp distribution is the sum of excess (flocs) and deficiency (voids) of pulp in the sample.

Another term adopted to characterize the heterogeneity of the structure of the paper web is formation, which is assessed by two indicators, namely, intensity and scale. The intensity is characterized by the magnitude of the change in the local mass of the paper, and the scale is characterized by the size of the zones of increased (flocs) and reduced (voids) mass. Flocs mainly contain long fibers, while densely compressed 'fines' are concentrated in the voids. Uneven filling of the paper sheet with respect to density generates secondary defects, for example, low mechanical strength, reduced air permeability, low absorbency, printing defects (such as spotting), low whiteness [1], uneven surface coloration of the paper. There is currently no GOST for assessing formation as an indicator of the quality of the paper web. This confirms that this indicator is extremely difficult to objectively describe and digitize.

2 Generation of the Data

Analyzing several studies on the subject [1], we found that formation depends both on the operating modes selected at different stages of the paper production process (speed of the paper machine, drying parameters, slope of the hydrofoils, dewatering, the degree of beating of the paper pulp, etc.), and on the parameters of the raw material (composition of the paper pulp, such as needles, leaves, wood pulp, rejects, the type of semi-finished wood product; presence of flocculating and deflocculating agents).

The reason for growing research in this area is that technical means for monitoring the heterogeneity of the structure of the paper web need to be introduced in the industry, which is to say that a transition has to be made from subjective assessment of formation to potentially obtaining objective quantitative estimates of this indicator. Various companies offer analysis of opacity and formation based on a number of specific estimates, such as: forming index, specific perimeter, standard deviation, coefficient of variation, average size of heterogeneity, correlation function.

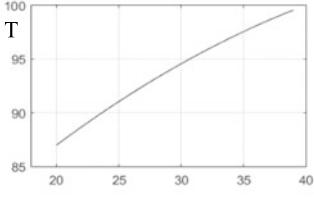
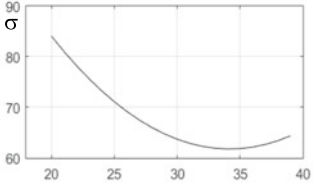
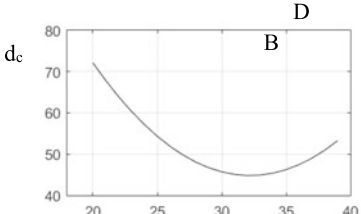
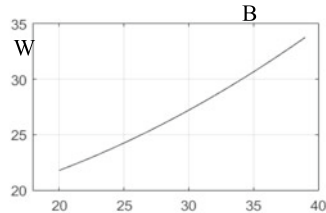
The relationship of the **structure of** and the **operating parameters** that govern it with the **quality** achieved was established in several studies. For example, [2] established the connection between quality, firstly, with the number of fibers of different lengths: samples with higher quality have a very high quantitative content of fine fibers (up to 1 mm), about 80%; secondly, with the degree of beating (DB) and the composition of the species, since samples with higher degrees of beating and higher contents of hardwood have higher quality, which, as we can observe, also contributes to production of finer fibers.

The **opacity** can be used to characterize **the structure of the finished product**. This is confirmed by [3], assessing the influence of such parameters as the degree of beating (DB), the content of the filler and the sizing agent on the quality indicators for the opacity of cardboard and paper web. The relationship between DB (measured in Schopper-Riegler degrees) and several key indicators for the quality of the paper macrostructure, expressed in relative units, is shown in Table 1.

As indicated in the studies on statistical assessment of the quality characteristics of the paper web, as well as in other works, the form of correlation dependences for different types of roll products does not allow an unambiguous classification from unsatisfactory to good opacity, ranking the quality indicators from minimum to maximum. The distribution of fibers of the paper web macrostructure largely depends on the conditions of the process and the characteristics of the raw material. Most of the standardized quality indicators are determined by laboratory methods and are not suitable for online assessment of the paper web, in contrast to the opacity, which can be used to characterize the homogeneity of the structure and, accordingly, the quality of the web. Since modern paper machines are equipped with systems for monitoring the image of the finished web for opacity, for example, the Cognex system, we formulated a task to develop a classifier based on generalization of statistical data, because Cognex's list of algorithms for processing statistical data does not include the classification of paper opacity.

A classification system for quality of paper web quality should be based on sample sets ranked according to degree of similarity to the required macrostructure of the paper. The initial data consisted of paper samples that were each subjected to illumination with constant intensity; next, the images were taken with a resolution capturing all the features of the macrostructure. The video control system for calculating histograms of brightness (intensity) distribution uses grayscale (depth of 8 bits per pixel) with 256 shades of gray (0 for black, 255 for white). The entire brightness range from 0 to 255 is divided into 16 sections: 4 sections of light pixels, 8 sections of gray pixels and 4 sections of dark pixels, with the percentage of pixels in each section returned.

Table 1 Relationship of paper quality indicators

Indicator	Calculated expression for indicator	Functional relationship
Light trans- mission	$T = \frac{\sum_{i=1}^n I_i}{nI_0}$ <p data-bbox="331 402 639 578"> I_0 is the brightness of incident light; I_i is the brightness of light passed through the point i; n is the number of points in the sample </p>	 <p style="text-align: center;">D B</p>
Opacity	$\sigma = \sqrt{\frac{1}{n-1} \sum_{i=1}^n (I_i - I_c)^2}$ $I_c = \frac{1}{n} \sum_{i=1}^n I_i$	 <p style="text-align: center;">D B</p>
Geometric mean heteroge- neity	$d_c = \frac{I_{long} - I_{tr}}{2}$ <p data-bbox="331 901 639 1012"> I_{long}, I_{tr} are the average lengths of heterogeneities in the longitudinal and transverse cross-sections </p>	 <p style="text-align: center;">D B</p>
Heterogenei- ty of pulp distri- bution	$W = \frac{M_E}{M_D}$ <p data-bbox="331 1125 639 1241"> M_E is the total volume of excess pulp M_D is the total volume of deficient pulp </p>	 <p style="text-align: center;">D B</p>

The following indicators, modified with respect to the standardized versions, were used for quantitative assessment of the paper opacity/

1. Coefficient of variation

$$VAR = \frac{\sigma}{M}, \tag{1}$$

where σ is the standard deviation of brightness;
 M is the mathematical expectation of brightness.

2. Pearson's skewness measure of a unimodal distribution

$$AS = \frac{M - \text{mod}}{\sigma}, \quad (2)$$

where mod is the mode (maximum of the brightness distribution density).
 This indicator implicitly reflects the excess or deficiency of flocs (accumulations of large fibers) and voids (accumulation of fines).

3. Relative areas of voids and flocs. An image with an 8-bit resolution is used to set the brightness of the holes (about 255) or floccules (less than 128); the number of pixels with a given brightness level on the histogram is then estimated.

Then the relative area of the flocs is

$$SF = \frac{C_F * 100}{C_0}, \quad (3)$$

the relative area of the voids is

$$SF = \frac{C_p * 100}{C_0}, \quad (4)$$

where SF and SP are the relative areas of flocs and voids;
 C_F , C_P are the numbers of pixels of flocs and voids;
 C_0 is the total number of pixels in the image.

The analysis of the paper samples obtained as reference was carried out by experts and is subjective in nature. The experts assigned the samples to the categories with 'good' (GO), 'satisfactory' (SO) and 'poor' (PO) opacity. To verify the reliability of expert assessments, a 3D image of typical samples for each rank was obtained with the PaperForming software (certificate of registration 2,013,619,551) (Fig. 1).

In contrast to the sample with GO, pronounced areas with voids and flocs can be observed in the images with PO. The sample with SO has areas of distributed voids, and this peculiarity of the paper web can be traced mainly by the calculated brightness indicators. Evidently, there is no clear correlation between the quantitative values of the indicators and the results of laboratory analysis performed by experts; this means that approaches related to pattern recognition have to be introduced to solve the problem. Figure 2 shows a graphical interpretation of statistical data describing 24 paper samples, categorized into three different opacity categories. Analyzing the distribution of values selected as the main 4 quality indicators and comparing the obtained with sets with expert assessments, we can see that the deviations of individual indicators (for example, AS) compensated by the uniform distribution of the macrostructure allow to classify the sample as GO.

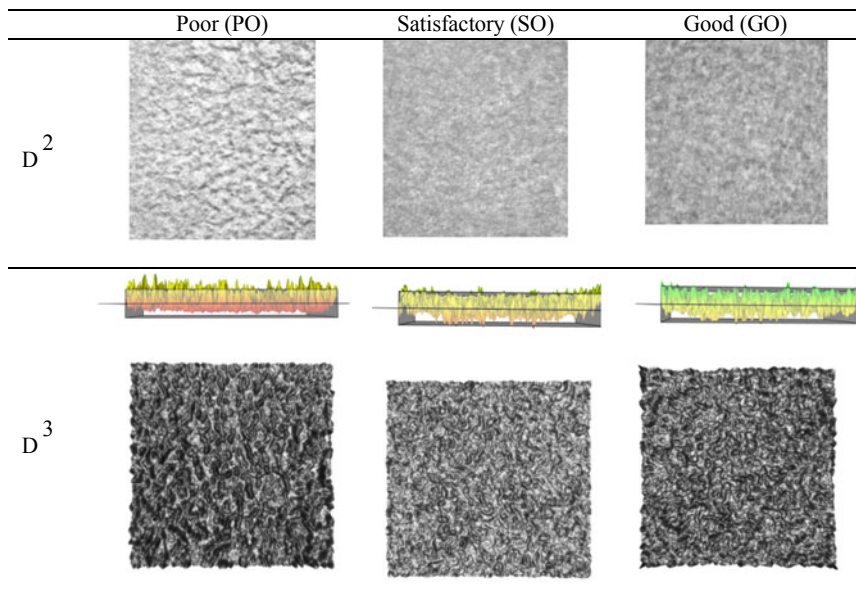


Fig. 1. 2D and 3D images of paper samples with GO and PO quality characteristics

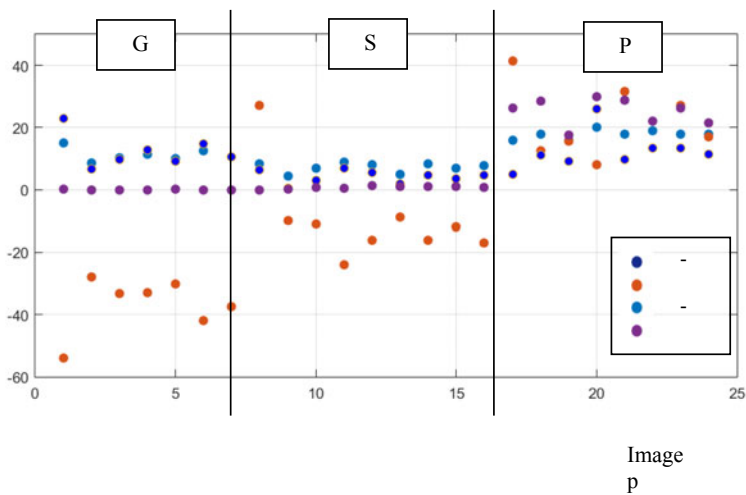


Fig. 2 Graphic interpretation of results of expert assessments for paper web samples

A promising direction in development of models designed to classify specific samples using an augmented array of statistical data as the basis are neural network technologies. A neural network model designed to rank patterns given on a set of 4 statistical indicators is based on typical topologies [5], constructed, in particular, for solving classification problems [6] and pattern recognition from an incomplete image:

- multilayer feedforward network learning by the backpropagation scheme (BPN),
- radial basis function network (RBF),
- probabilistic neural network (PNN),
- neural network with the compositional rule of fuzzy inference

While the structure of the BPN network can be used by selecting the number of layers, assigning the number of neurons in the layer and studying the operation of the network with different types of activation functions, the topology of RBF and PNN networks is generated based on dimension and correlation of data in the training set. However, an aspect that has to be taken into account for this problem is that as the samples accumulate, the training set expands, and the number of network neurons changes during retraining. In this case, the RBF and PNN topologies adapt to expansion of the set during training. As evident from Table 1, the composition of the quality indicators for roll products can be different, and there is no clear distribution of the variation ranges that can be correlated with the classification into PO, SO or GO. In addition to opacity, it should be borne in mind that defects (folds, creases, breaks, etc.) periodically appear on the surface of roll products, and in this case a section of the web should be allocated to cut out the defective part. It is impossible to compose a typical image for each type of defect, so it is advisable to use a different neural network model for initial recognition of the defect before assessing the opacity of the product.

Classifying potential defects, for example, as spots or holes allows to subsequently use linguistic representation of the calculated quality indicators. The combination of a large positive value of AS with an increased value of SP and an increased value of the mean geometric heterogeneity in the longitudinal cross-section may indicate a crease or a spot. For example, if we rely on the characteristics defined above, clear values of the indicators VAR, SP, SF after fuzzification are described by a set of membership functions with respect to three linguistic values (terms): ‘small’, ‘medium’, ‘large’ or μ_M , μ_C , μ_B , and the skewness measure AS by the terms: ‘negative’, ‘zero’, ‘positive’ or μ_O , μ_H , μ_I . Samples of paper web with pronounced defects are accumulated unevenly, and as the material is collected, the membership functions characterizing the terms of linguistic representations of estimates have to be adjusted. In this case, a promising approach is to use a hybrid system of fuzzy inference and neural network modeling [22]. The structure of such a network for the problem of defect recognition is shown in Fig. 3.

To ensure that the neural network model is flexible and that the pool of recognized defects is expanded as statistical data is accumulated, a system is chosen that consists of two levels of autonomous neural network modules. The fuzzification operation is implemented by a neural network based on a single-layer perceptron NSF1—NSF4,

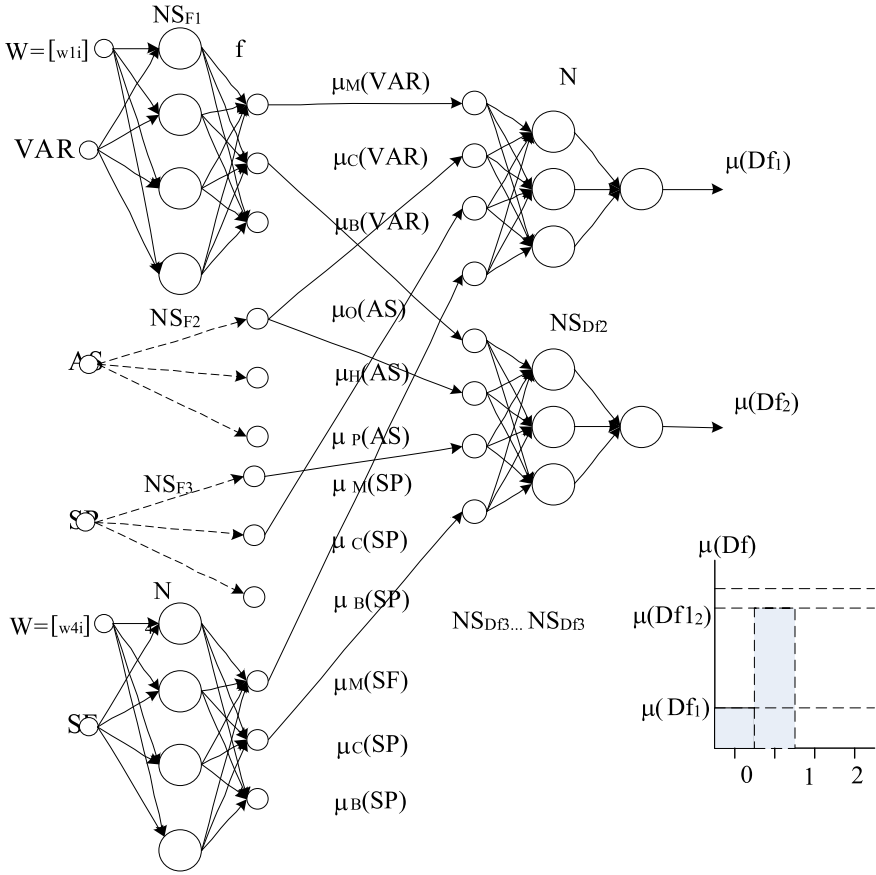


Fig. 3 Modular structure of neural network-based classifier of paper web defects

which allows to independently adjust the parameters of the membership function. To represent the bell-shaped membership function, it is proposed to use the typical structure of an artificial neuron (Manoshin D.A. 2019) with a sigmoidal transformation function

$$f = \frac{1}{1 + \exp(-g(x + w))} \tag{5}$$

where g is the weighting factor of the total signal at the input of the conversion function, w is the weighting factor for the offset, x is the input clear value of the indicator.

Implementing the fuzzification operation on typical structures of neurons does not impose serious restrictions on the choice of the design environment for such a system. In addition, transition to a fuzzy representation eliminates the need for preliminary

normalization of the initial data. Thus, the space of the variables describing the image is expanded to 12 by converting them into membership functions of linguistic values (terms) of indicators.

The second level of neural network models is associated with identifying the degree of similarity of the observed image with the descriptions of the defects input in the model. A classical feedforward network with one hidden layer, nonlinear neurons (sigmoidal transformation function) on the hidden layer and a linear function with constraints on the output layer is selected as the topology of local networks NS_{Df_j} . Thus, combining the terms of indicators characteristic for a certain defect Df_j generates a neural network module NS_{Df_j} for calculating the degree to which the analyzed image belongs to the given type of defect $\mu(Df_j)$.

The results yielded by the classifier are shown in Fig. 3 in the form of a histogram. If none of the classifier outputs exceeded the threshold for defect detection, $\mu(Df_j) > \mu_{\max}$, then the operation categorizing the observed fragment of the web by opacity is performed; otherwise, the observed area is classified as broke and is removed at the stage when the slitte starts to operate.

3 Results

The simulation was performed in the MatLab environment using the nntool procedure. An array of expected outputs with the dimension of 24×3 was generated for the training set with the dimension of 24×4 (quantitative indicators of the opacity), shown in Fig. 2. Each output takes a value of either 0 or 1, depending on whether the specific image from the training set matches or does not match one of three levels of paper quality: PO, SO, GO. To identify whether the topologies listed in clause 2 could be used, models of a neural network classifier for opacity were developed based on three structures of BPN, RBF and PNN networks.

The neural network model based on BPN included varying numbers of layers L and numbers of neurons N on hidden layers using a sigmoidal activation function. Developing the neural network, we considered structures that yielded the minimum training error with a relatively small number of epochs in case of training by the Levenberg–Marquardt algorithm. The histogram of the mean error values for all network outputs with the training set for varying L and N fed to the input is shown in Fig. 4. Each structure was retrained 5 times until the minimum training error was reached.

$$\Delta = \frac{1}{24} \sum_p^{24} = 1 \left(0.2 \sum_k^5 = 1 \left(\sum_{j=1}^3 |F_j(p) - U_j| \right) \right) \quad (6)$$

It is evident from the generalized results that the distribution of the data from the training set data is best fitted by the model with two hidden layers and with the number of neurons in the first layer equal to 5. The limited dimension of the training set drastically deteriorates the results with an increase in the number of hidden layers.

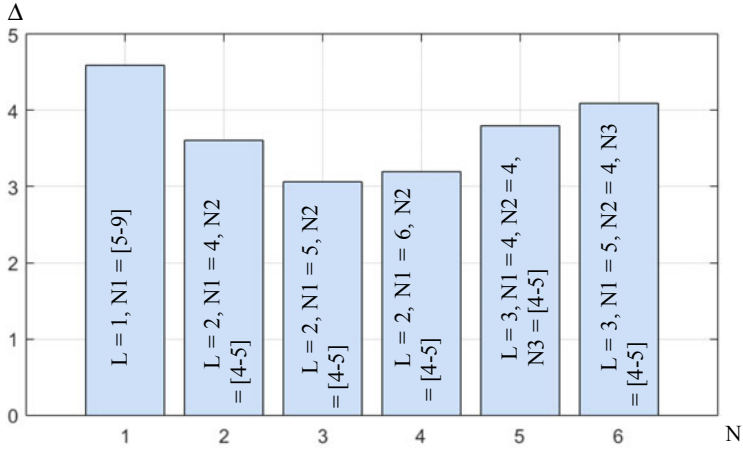


Fig. 4 Analysis of results obtained by fitting the BPN network structure

To test the selected topologies, we used a new test set (Fig. 5) of 6 samples, including all three categories of paper.

As shown in Fig. 6, the classifier based on the BPN network produces errors both in recognizing the test patterns and those in the training set, most often in the SO and PO categories. The transition to partitioning the space of variables by hyperspheres in RBF and PNN networks allows to construct a clear classification on the training array, but the space of states is not described with sufficient completeness for the RBF network, which results in significant errors during testing (Fig. 7).

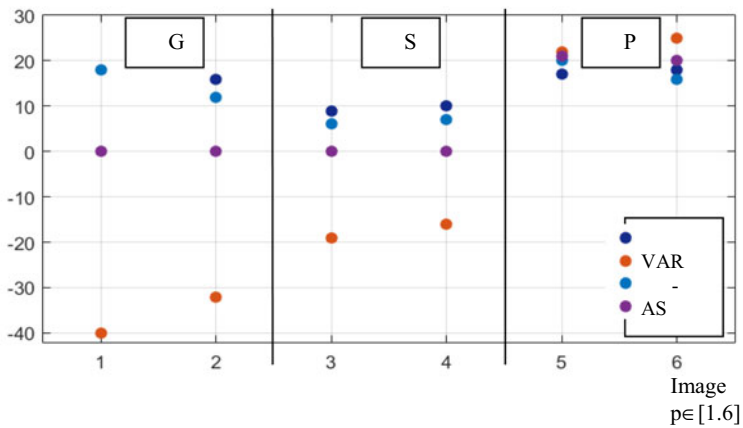


Fig. 5 Distribution of samples from the test set

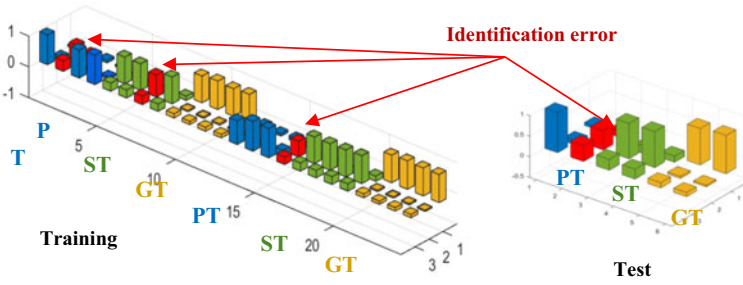


Fig. 6 Results for adjusting the classifier based on BPN network with training and test sets fed to the input

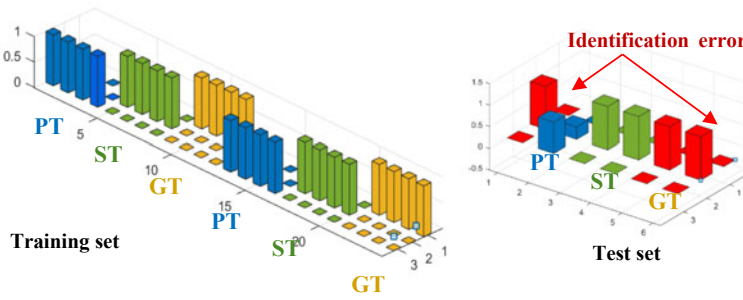


Fig. 7 Results for adjusting the classifier based on RBF network with training and test sets fed to the input

The choice of class by the degree of similarity in terms of the Gaussian density function implemented in the PNN alleviates the situation of a limited data set and makes it possible to clearly recognize both the patterns of the training set and the test patterns (Fig. 8).

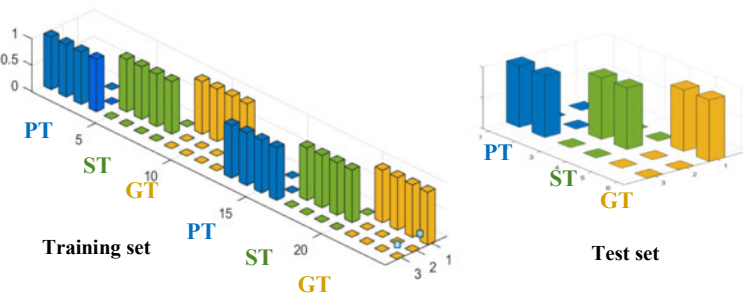


Fig. 8 The results of adjusting the classifier based on the RBF network with the training and test sets fed to the input

4 Discussion and Conclusion

Assessing the technical capabilities of modern systems for controlling the quality of paper, we can conclude that introducing machine vision systems at the final stage of roll production is feasible not only from an economic standpoint. Modern systems developed make it possible to monitor opacity not only in offline mode but also for an online image of the paper web. Using the calculated generalizing indicators, such as AS, VAR, SP, SF reduces the dimension of the problem and the execution time of the identification algorithm at the current time step. Using empirical expert information makes it possible to increase the range for identification of product quality by detecting frequently occurring defect zones in the paper web. As confirmed by the results of the studies carried out, the optimal implementation of the basic classifier by opacity allowing to determine the quality of the resulting product is based on a probabilistic neural network (PNN), since there is no guarantee within the problem solved that the training set will uniformly cover all spaces for each of the categories GO, SO and PO.

Possible practical applications of the developed classifier are not limited to quality control [9]. Structures of neural network classifiers of paper web have been developed not only for monitoring opacity but also a number of other specific defects of the paper web. The results obtained by automatic quality analysis can be used to generate tasks for the control system of a slitter to guarantee that the sections identified as defective are removed from the finished product [5]; another potential application is organizing feedback for the main indicator of product quality and adjusting the algorithm for controlling the paper machine (PM) to prevent low-quality products from being manufactured in the future. Thus, if stable deviations are detected in the quality of the paper web and their possible cause is identified, the output mechanism of the manufacturing execution system (MES) corrects the system's operating parameters in online mode. The block diagram of such a system is shown in Fig. 9.

This paper describes the general concept of the second part of the system, namely, the recognition of defects in the paper web. Practical implementations are complicated because it is difficult to accumulate a sufficient number of patterns (images) that have been assessed by experts to generate a training set. The same type of defect can take considerably different forms, so the set of the main indicators is expanding. Additionally, the likelihood of a false detection of foreign objects accidentally appearing in the video frame should be assessed. Diverse studies exploring the mutual influence of the operating parameters of paper machines and the variation of the quality indicators of the finished product do not provide clear mathematical models, so it seems reasonable to extend the research into developing algorithms for calculating corrective actions in order to organize feedback loops.

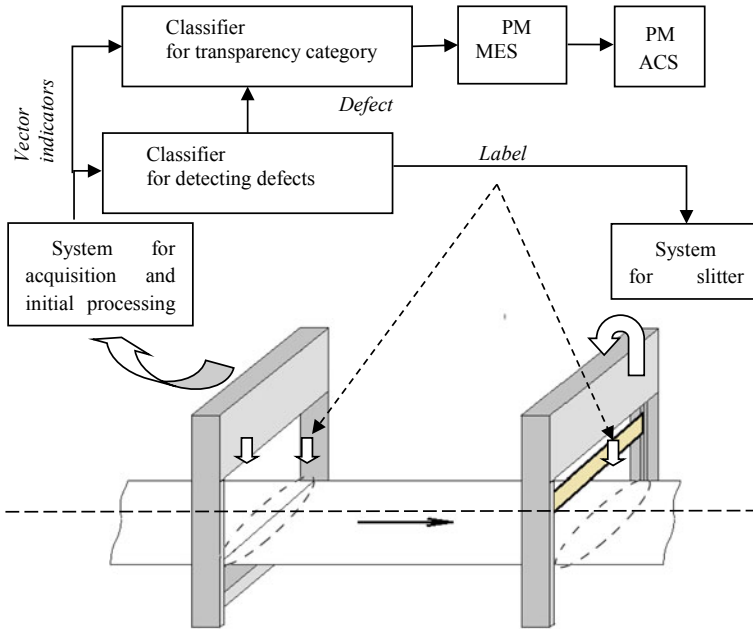


Fig. 9 Structure of operational control system for paper production process

Acknowledgements The paper was prepared with the financial support of the Russian Foundation for Basic Research in the framework of research under the project of the RFBR No. 19-010-00968

References

1. Revunov MS (2018) Improving the stabilization system of paper flow parameters using the cross-correlation algorithm. *Measur Monitor Control Control* 4:24–34
2. Osovskaya II, Antonova VS (2020) The influence of surface destruction on the hydrophilicity and ability to form connections of the cellulose fibers. *Chem Plant Raw Mater* 1:315–320
3. Gerasyuta SM, Smolin AS, Ivanova EI, Kanevskaya VS (2016) Investigation of the coefficient of variation and the average size of the heterogeneity for various types of paper on the AP-2 collet analyzer. In: *Proceedings of the St. Petersburg forestry academy*, vol 217, pp 238–247
4. Abramova VV, Gurev AV (2017) Evaluation of macrostructure forming uniformity of copy paper. *High Educ News For Mag* 4:172–186
5. Manoshin DA (2019) Artificial intelligence programming. *Colloquium-J* 12(36):121–135
6. Zhou Y (1998) Fuzzy -timing Petri net model for distributed multimedia synchronization. In: *Proceedings of the 1998 IEEE Conference on Systems, Man and Cybernetics*, Lolla, California, 11–14 October, pp 244–249
7. Koutsoukos X, Antsaklis PJ, Stiver JA, Lemmon MD (2000) Supervisory control of hybrid systems. *Proc IEEE* 5:1026–1049
8. Qian Y, Li XX, Jiang YR (2003) An expert system for real-time fault diagnosis of complex chemical processes. *Expert Syst Appl* 24:425–432

9. Kallrath J, Rebennack S, Kallrath J, Kusche R (2014) Solving real-world cutting stock-problems in the paper industry: mathematical approaches, experience and challenges. *Eur J Oper Res* 238:374–389
10. Dyckhoff H (1990) A typology of cutting and packing problems. *Eur J Oper Res* 44:145–159
11. Harjunkoski I (2008) Qualitätsbasierte Schnittplanoptimierung in der Papierindustrie, at *Automatisierungstechnik*, vol 2, pp 31–44
12. Correia MH, Oliveira JF, Ferreira JS (2012) Integrated resolution of assignment, sequencing and cutting problems in paper production planning. *Int J Prod Res* 50(18):5195–5212
13. Poltroniere SC, Araujo SA, Poldi KC (2016) Optimization of an integrated lot sizing and cutting stock problem in the paper industry, vol 17, pp 305–320
14. Silva E, Alvelos F, Valerio de Carvalho JM (2014) Integrating two-dimensional cutting stock and lot-sizing problems. *J Oper Res Soc* 65:108–123
15. Sahno J, Shevtshenko Ed, Karaulova T, Tahera Kh (2015) Framework for continuous improvement of production processes. *Econ Eng Decis* 26
16. Rajnoha R, Gálová K, Rózsa Z (2018) Measurement of impact of selected industrial engineering practices on companies' economic performance. *Econ Eng Decis* 29
17. Khapaev MM, Tsygankov AA (1997) An algorithm for the constrained extremum problems. *Comput Math Model* 8:322–325
18. Scheithauer G (2008) Zuschnitt und Packungsoptimierung. *Problemstellungen, Modellierungstechniken, Lösungsmethoden*, p 132
19. Chernikova A, Kondrashkova G, Bondarenkova I, Kuzmina S (2019) Digitization and axiomatics in modern metrology. *IOP Conf Ser: Mater Sci Eng* 497:012130
20. Okrepilov VV, Kuzmina SN, Makarov VL, Bakhtizin AR (2015) *Economy of region*, vol 2, pp 301–313
21. Gomm JB (1998) Adaptive neural network approach to on-line learning for process fault diagnosis. *Trans Inst Measur Control* 20:144–152
22. Rudakova IV, Chernikova AV (2016) Intelligent monitoring system of quality indicators of paper web. *Mathematical methods in engineering and technology - MMTT-29: collection of articles*, pp 103–107
23. Venkatasubramanian V, Rengaswamy R, Yin K, Kavuri SN (2003) A review of process fault detection and diagnosis: Part I: quantitative model-based methods. *Comput Chem Eng* 27:293–311
24. Zhou YF, Hahn J, Mannan AS (2003) Fault detection and classification in chemical processes based on neural networks with feature extraction. *ISA Trans* 42:651–664

Design of “Green” Roofs of Extensive Type in Various Climatic Zones of Russia



Elena Sysoeva  and Ilya Morozov 

Abstract “Green” roofs minimize the impact of construction on nature and the climate, prevent an increase in the deficit of the country’s resource potential, contributing to the improvement of the health of citizens. The article offers an assessment of the possibility of introducing “green” roofs on the territory of Russia in different climate zones, taking into account their features in the summer and winter periods. The paper analyzes ways to eliminate the constraints of operating a system solution for creating territorial biodiversity programmes. The assessment of the possibility of the “green” roof in megacities was carried out. Based on the calculations made, an estimate of the energy efficiency of the considered solution was obtained. On the basis of a theoretical study, the design of landscaping in the regions of Russia was considered on the example of the Ryazan region, taking into account the territorial and spatial assessment using the method of correlation and regression analysis. In this paper, a model of multiple regression is obtained. The analysis revealed that among the 10 factors considered, only 4 of them have the greatest impact on the demographic situation of the region. The problems in the regulatory and technical system of “green” construction in Russia are identified. A list of questions has been compiled, the answers to which should be contained in new versions, developed regulatory and methodological documents.

Keywords “Green” roofs · Landscaping · “Green” construction · Extensive type · Thermal protection · Energy efficiency · Energy saving

1 Introduction

In the interests of all countries of the world, it is necessary to develop a set of measures to improve the environmental situation. Territorial urban boundaries are steadily increasing, and their own peripheries are expanding [1]. Reporting statistics provided by the United Nations (UN) predict an increase in urbanization in developed

E. Sysoeva (✉) · I. Morozov
National Research Moscow State University of Civil Engineering, Yaroslavskoe Shosse, 26,
129337 Moscow, Russia
e-mail: SysoevaEV@mgsu.ru

© The Author(s), under exclusive license to Springer Nature Switzerland AG 2022
A. Mottaeva (ed.), *Technological Advancements in Construction*, Lecture Notes in Civil Engineering 180, https://doi.org/10.1007/978-3-030-83917-8_9

countries to 83% by 2030, which will result in environmental problems at the global level [2, 3]. At the moment, urbanization is proportional to the market demand for the purchase of new residential space. UN data shows that about 40% of the world's primary energy needs are spent on building construction and maintenance, and they account for about 33% of the greenhouse gas emissions. It is possible to limit global warming by reducing the consumption of energy resources [4, 5]. The development of measures for the implementation of programs and the use of environmentally friendly components will be the result of reducing the energy consumption of buildings. Roofs make up a significant part of the urban space. The construction of new buildings with the use of a green roof or the reconstruction of existing ones will restore the "green" zone on the built-up plot of land. Designed and installed "green" roofs will have a positive impact on the urban environment and will hinder the development of the urban heat island [6–9].

The use of grass and plants of different densities and types on the roof can be traced in different climatic conditions. The main functional purpose has always remained the same: a heat-insulating element with the ability to reduce the consequences of exposure to high temperatures. "Green roofs" were valued for the excellent insulating qualities of the combined plant and soil layers (turf). In cold climates, they helped to retain heat in the building, and in warm climates, on the contrary, they protected from heat [10–14].

Rooftop landscaping is not just one of the five famous points of new architecture, but an entirely new and fundamental spatial theme that explores the relationship between architecture and nature [15].

One of the first architects who identified the importance of "green" roofs primarily as a means of resisting the negative influence of evolution was Friedrich Stovasser. In nature, the Austrian architect and artist saw the source of universal harmony and believed that it should be protected from the worst enemy – people. Friedrich Stovasser sought to ensure that the time spent in his buildings imitated the period spent in nature. Trees, in his opinion, were an integral part of human structures, so in his works he preferred to include trees and shrubs on the roofs [16, 17].

Opting flat roof in the late XIX century and early XX century were caused by the presence of successful works and theoretical writings of prominent architects and urban planners, among whom was the Frenchman Le Corbusier and the American Wright [18].

The "green" roof is one of the most fruitful themes of Le Corbusier's legacy, which manifests itself in modern architectural developments. The famous French architect has implemented a large number of projects using "green" roofs, ranging from small villas to impressive complexes, including a grand ensemble of gardens on the roofs of administrative buildings in the Indian city of Chandigarh. In 1929, the "Villa Savoy" was built, classified at the beginning of the twenty-first century as a UNESCO World Architectural Heritage, which also had a "green" roof with access to the garden [19].

In other countries, the architects of the "new" wave followed the example of Le Corbusier. In 1903, a house with roof landscaping was built in Paris according to the project of the Perret brothers. A non-standard solution of the "green" roof, including a

restaurant, was implemented in Cologne according to the project of Walter Gropius, and in America Frank Lloyd Wright designed a restaurant with operated “green” roofs in Chicago [20, 21].

In his designs, architect Frank Lloyd Wright envisioned landscaping on the roof, thus following the philosophy of organic architecture. He noted that “a good building does not disturb the landscape, it makes the landscape more beautiful than it had been before this building was built.” Frank Lloyd Wright used “green” roofs in several construction projects, such as “Hollyhock House”, “Cheney House”, “Falling Waters” [22].

The beginning of the modern era was marked by great changes in both Russian and world architecture. The history of roof gardening in Russia dates back to the XVII century, when Metropolitan Jonah ordered the creation of a garden on the second floor of the Rostov Kremlin. Landscaping of the roof in most cases was created in the boyar estates and estates of the higher clergy. For their beauty and originality, they were given the name “Red”.

The period of the second half of the XVIII century was characterized by raging fires. Architect N. A. Lviv paid special attention to the owners of wooden houses to the use of lawn and grass coverings. In 1772, S. F. Ushakov wrote a treatise on the use of such a variant of the roof design [11, 23, 24].

A variant of the modern version of “green” roofs is a layer-by-layer system located above the roof to maintain the nutrient medium (substrate) and vegetation. The system solution is widely used in Germany. In recent years, the United States has been actively implementing a green roof [25–28].

2 Materials and Methods of Research

At the research stage, heat engineering calculations of two coatings were performed. The task was to determine the possibility of operation of the “green roof”, located in different climatic regions of Russia. The influence of seasonal temperatures on the green surface was estimated for 6 different cities located in different climatic zones: Rostov-on-Don (IIIV), Moscow (IIV), St. Petersburg (IIV), Astrakhan (IVG), Sochi (IVB) and Khanty-Mansiysk (ID).

The construction of the “traditional” flat roof is represented by the following layers: reinforced concrete floor slab, vapor barrier, thermal insulation (for each city the value differs in view of the climate), cement-sand screed and waterproofing. As a study of “green” design was made system solution “T-Roof Greene”, which includes: reinforced concrete slab, econobridge layer of expanded clay gravel, reinforced cement-sand screed, bitumen primer Technicol No. 01, Technoelast EPP, Technoelast green P, needle-punched geotextile Technicol, extruded polystyrene Technicol Carbon Prof 300, geotextiles heat-treated, shaped Planter geo membrane, the substrate Circum. A visual structural structure of the “traditional” and “green roof” is shown in Fig. 1 and Fig. 2.

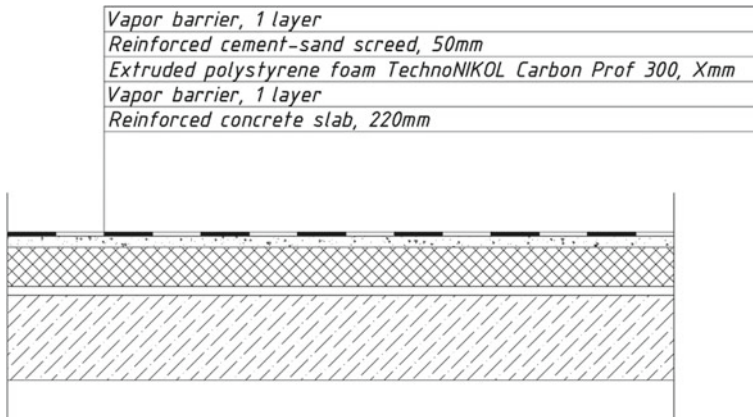


Fig. 1 “Traditional” roof layers

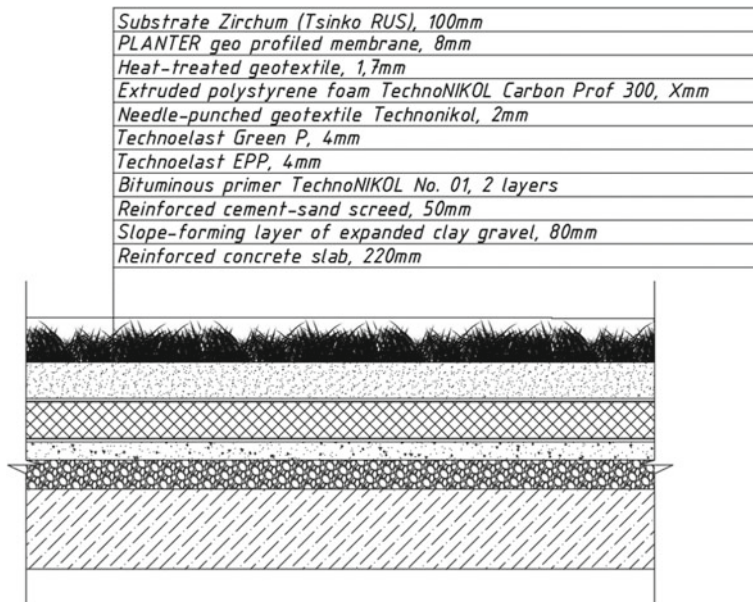


Fig. 2 “Green” roof layers

On the basis of theoretical research, taking into account the territorial-spatial assessment using the method of correlation and regression analysis, a primary review of the possible situation in the Ryazan region is performed. As independent variables, we used demographic-population growth (X1) and environmental parameters, such as the amount of emissions (X2), air pollutants coming from stationary sources; the volume of polluted wastewater discharge (X3); reforestation and greening of roofs

(X4); artificial reforestation (crop creation, X5); number of dead forest stands (X6), including conifers (X7); total area of urban land in front of the city limits (X8); total area of green spaces (X9); removal of municipal solid waste (X10). The dependent variable was the total population (Y). The calculation was performed using the MS Office Excel 2016 program.

3 Results and Discussion

The results of the comparative heat engineering calculation showed different results for each climatic zone of Russia.

For some districts (IIIV, IIV, IVG, IVB), the reorganization of the “traditional” roof into an extensive type of greening coating demonstrated a positive effect, resulting in a twofold reduction in the thickness of the thermal insulation layer (Khanty-Mansiysk) and an increase in energy efficiency by 22.26% (Astrakhan). For another area (ID), the smaller thickness of the insulation could not provide more heat transfer resistance than it was before the installation of the system solution. The energy efficiency values of the building from the installation of the “green roof” for other climatic zones are shown in Fig. 3.

Next, the demographic situation in the period 2001–2021 was considered (Fig. 4). Having a total number of observations of $n = 21$ with a significance level of 0.05, the critical value is 2.093. After checking, factors X1, X3, X4, X6, X7, X10 were excluded. Their significance is minimal. Using as the initial data independent variables that satisfy the significance condition: the number of emissions, air pollutants (X2), artificial reforestation (X5), the total area of urban land in front of the city

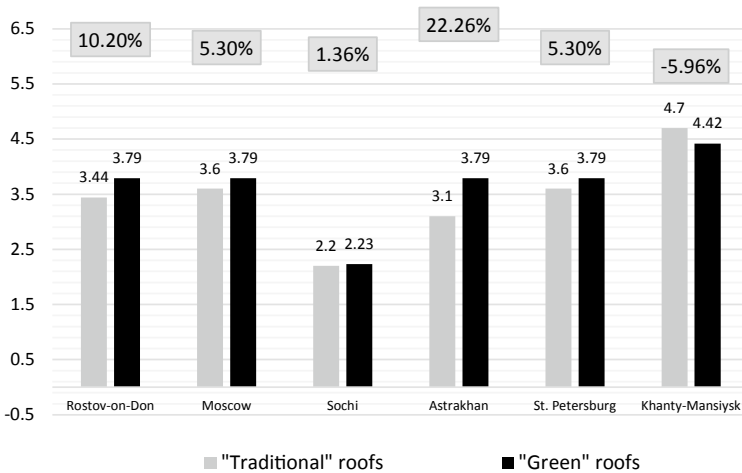


Fig. 3 Diagram of the energy efficiency of the “green roof” device in 6 different climatic regions of Russia

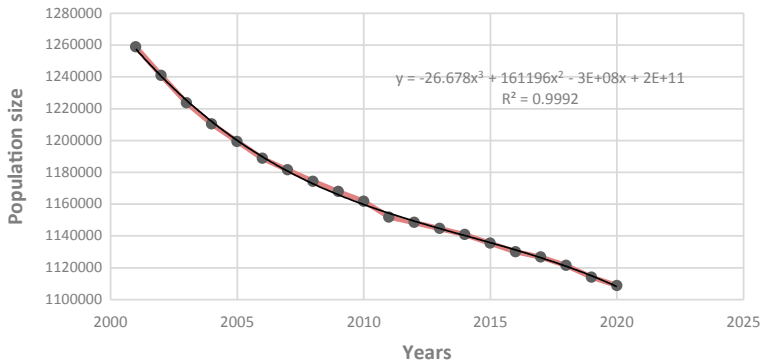


Fig. 4 Dynamics of population change in the Ryazan region 2001–2020

limits (X8), the total area of green spaces (X9), we performed a regression analysis of the initial data using the “Data Analysis” package.

As a result, the following mathematical model of multiple regression in natural form (1) was obtained:

$$\bar{y} = 618331.6 + 2.64 \cdot x_2 + 38.91 \cdot x_5 - 15.21 \cdot x_8 + 107.16 \cdot x_9, \quad (1)$$

where \bar{y} is the predicted value of the parameter, pers.; x_i are independent variables.

Interpretation of the equation parameters: after obtaining the final statistical criteria, a mathematical model can be described. The analysis revealed that in 80.1% of cases the final result depends on the factors included in the initial data, and only in 19.9% of cases on the unaccounted-for ones. As a result of repeated correlation, all 4 coefficients affect the dependent variable Y. Equation (1) shows that artificial reforestation and the creation of additional areas with green spaces can increase the size of the regional population.

A positive coefficient of 2.64 indicates that an increase in emissions of harmful substances will not negatively affect the growth of the demographic curve. If the values of X5, X8 and X9 are fixed at the average levels, its influence is minimal and will be offset by the factors of reforestation and landscaping area. An increase in the area of urban land will lead to a decrease in population growth, as evidenced by the coefficient -15.21. This can be explained by the fact that when an additional territory is included in the total area, the proportion of the population whose growth decreases annually is also taken into account. Thus, the factor (X8) leads to a demographic decline.

To date, GOST 58,875-2020 does not address all issues related to the installation of “green” roofs in Russia. The issue of thermal protection of buildings remains open and requires the creation of additional regulatory requirements and methods of thermal engineering design. The mass introduction of “green” technologies on the roofs of buildings in megacities and regions will be in the case when the design rules will be systematized for each climate zone of Russia separately.

Countries with extensive experience in using the system solution have support at the legislative level. In Russia, each climate zone requires the development of technical guidelines for the planning, design and commissioning of “green” roofs, at a minimum:

- comparison of heat engineering calculations for the winter and summer seasons in each climatic zone of Russia;
- performing strength calculations taking into account snow and wind loads in winter;
- determination of the degree of permissible wind loads for different climatic regions and different elevations due to the presence of lifting forces to which the roof is exposed;
- stability of the “green” structure in seismically active areas.

Statistics on the operation of “green” roofs in different climatic zones of Russia, even at the theoretical level, are not available, in this case, construction companies can not take on the risks of implementing the concept of landscaping in future projects.

Financial incentives should be provided for the widespread use of green roofs.

4 Conclusion

Thus, the design of “green” roofs contributes to a comprehensive solution of the environmental problems that have arisen. The research work revealed the following:

1. The adopted extensive type of landscaping can be installed in five of the six considered climatic regions of Russia, while providing the required resistance to heat transfer R_{req} ;
2. Depending on the climatic zones, the green coating device can increase the energy efficiency of the building in the range from 1.36 to 22.26%;
3. With an increase in energy efficiency, adding a larger amount of substrate, it is possible to achieve an economic effect by reducing the amount of thermal insulation material in the structure, which will minimize subsequent economic costs.

A more detailed analysis of the design of “green” roofs in the regions of Russia was carried out on the example of the Ryazan region, which belongs to the climate zone IIV, and allowed:

1. Establish the relationship between the design of “green” roofs and demography: identify the most influential factors on the level of population;
2. Derive a multiple regression equation using correlation and regression analysis, which shows the average effect of each of the selected factors (X_n) on the final result of the independent variable (Y);
3. By using factors and regressive models to predict the effectiveness of the use of “green” roofs as a way to reduce the negative impact on the environmental

situation of the city in the coming years, as well as to get the opportunity to reduce the percentage of population decline.

References

1. Solomon BD, Krishna K (2011) The coming sustainable energy transition: history, strategies, and outlook. *Energy Pol* 39(11):7422–7431
2. Osmundson T (1999) *Roof gardens: history, design, and construction*. W.W. Norton, New York
3. Antrop M (2004) Landscape change and the urbanization process in Europe. *Landsc Urban Plan* 67(1–4):9–26
4. Dutil Y, Rousse D, Quesada G (2011) Sustainable buildings: an ever evolving target. *Sustainability* 3(2):443–464
5. De Fino Mariella, Sciotti Alba, Cantatore Elena, Fatiguso Fabio (2017) Methodological framework for assessment of energy behavior of historic towns in Mediterranean climate. *Energy Build* 144:87–103
6. Cascone S, Sciuto G (2018) Recovery and reuse of abandoned buildings for student housing: a case study in Catania Italy. *Front Arch Res* 7(4):510–520
7. Fotopoulou A, Semprini G, Cattani E, Schihin Y, Weyer J, Gulli R, Ferrante A (2018) Ferrante Deep renovation in existing residential buildings through façade additions: a case study in a typical residential building of the 70s. *Energy Build* 166:258–270
8. Cascone S (2019) Green roof design: state of the art on technology and materials. *Sustainability* 11(11):3020
9. Ilyichev VA, Emelyanov CG, Kolchunov VI, Bakaeva NV (2019) Innovative technologies in the construction of cities. Biosphere compatibility and human potential. DIA Publishing House, Moscow
10. Ilichev VA, Kolchunov VI, Bersenev AV, Pozdnyakov AL (2009) Some points of designing of settlements from the point of biospheric compatibility concept. *Acad Archit Constr* 1:74–80
11. Kok KH, Mohd SL, Chow MF, Zainal Abidin MR, Basri H, Hayder G (2016) Evaluation of green roof performances for urban storm water quantity and quality controls. *Int J River Basin Manag* 14(1):1–7
12. Sysoeva EV, Gelmanova MO (2018) Principles of sustainable development when designing “green roof” on public buildings/roofs. *Constr Reconstr* 2:105–112
13. Abass F, Ismail LH, Wahab IA, Elgadi AA (2020) A review of green roof: definition, history, evolution and functions. *IOP Conf Ser: Mater Sci Eng* 713:012048
14. Peck SW, Callaghan C, Bass B, Kuhn M (1999) *Greenbacks from green roofs: forging a new industry in Canada*. Canada Mortgage and Housing Corporation, Ottawa
15. A guide for landscaping and improvement of operated roofs of residential buildings, underground and semi-underground garages, civil defense facilities and other structures. https://zna.ytovar.ru/gost/2/PosobiePosobie_po_ozeleneniyu.html. Accessed 20 Feb 2021
16. Como A, Smeragliuolo Perrotta L, Forni I (2015) Le Corbusier roof-spaces. In: *Le Corbusier 50 years later valencia (spagna) editorial universitat politecnica de valencia*. Polytechnic University of Valencia, Valencia, pp 441–460
17. Berndorfer E et al (2007) Green roofs as urban ecosystems: ecological structures, functions, and services. *Bioscience* 57(10):823–833
18. Radosavljevic J, Vukadinovic A, Đorđević A, Malenović-Nikolić J, Vasovic D (2017) Acta technica corviniensis – Bulletin of Engineering Green roofs. *Acta technica corviniensis – Bull Eng* 10(1):135–138
19. Radushinsky D, Nguyen TN, Nguyen VL, Gubankova M, Thi Mai Huong D, Fatkullina A (2019) The ecological approach to the city-planning in modern megalopolises. *E3S Web Conf.* 91(4):05026

20. Lugovaya KV, Denisenko YuS, Smekhota LA (2018) Green roofs of residential buildings. *Young Res Don* 3(12):72–75
21. Corbusier Le (1960) *L'Atelier de la recherche patiente*. Éditions Vincent Fréal, Paris
22. Grub H (1988) Greenery between the houses. Ideas, concepts, examples of the introduction of elements of nature into the production environment. Ipobank, Munich
23. Miaomoao H (2011) Promoting green roofs in China: a comparison of green roof policies in the United States (U.S.) and China A Thesis Presented to the Graduate School of the University of Florida in Partial Fulfillment of the Requirements for the Degree of Master of Science in Architectural Design. University of Florida, Gainesville
24. Mohd Razali SF, et al (2021) An evaluation of hydrological simulation of extensive green ICCOEE2020. LNCS, vol 132. Springer, Singapore, pp 47–55
25. Li Y, Babcock R (2014) Green roofs against pollution and climate change. A review. *Agron Sustain Dev* 34(4):695–705
26. Konyuhov V, Gladkih A, Galyautdinov I, Kiseleva T (2019) Ecological architecture: the green roofs. *IOP Conf Ser: Earth Environ Sci* 350:012035
27. Teotónio I, Silva C, Cruz C (2021) Economics of green roofs and green walls: a literature review. *Sustain Cities Soc* 102781
28. Bochkova IY, Tulush MD (2020) About extensive green roofs . *Forest Bull* 24(5):5–11

Results of Measuring the Thermal Concrete Properties by the Impulse Method



Mikhail Arkulis , Gennadii Dubskiy , Oxana Logunova ,
Galina Trubitsina , and Georgy Tokmazov 

Abstract The purpose of the study is to determine the thermo-physical characteristics of heavy concrete by pulse heating of different density samples by electromagnetic radiation with a flat temperature front with adjustable duration and duty cycle of the thermal pulse. It was proved, that heat conductivity and heat capacity of concrete essentially depend on humidity of concrete specimens, a distribution of components of cement stone filler, temperature and porosity of specimens. Specimens' porosity was determined by value of maximum moisture content. It was found that all thermo physical characteristics increase nonlinearly with increasing moisture content, reaching saturation at maximum moisture content. The physical nature of the thermo physical properties is described in terms of the solid state model. An elastic porous, structure less model of concrete consisting of several phases is proposed. The authors of the work proposed a methodology for determining the thermo physical parameters of the components of heavy concrete and implemented on an experimental stand. The results of research on the test bench have shown that the values of characteristics increase nonlinearly with humidity. Authors proposed algorithm of determination of generalized thermo physical characteristics of heavy concrete taking into account its component composition.

Keywords Concrete · Thermal properties · Pulse heating method · Concrete model

1 Introduction

To date, heavy concretes are the most relevant and are used in the construction of prefabricated structures and monolithic buildings [1–3]. The popularity of this material is determined by its unique strength after drying, affordability, high density, practicality and durability [4–6]. In order to ensure the above properties, the problem of studying the thermo-physical characteristics of heavy concretes becomes relevant.

M. Arkulis · G. Dubskiy · O. Logunova (✉) · G. Trubitsina
Nosov Magnitogorsk State Technical University, Lenin st, 38, 455000 Magnitogorsk, Russia

G. Tokmazov
Admiral Ushakov State Maritime University, Lenin st, 93, 353918 Novorossiisk, Russia

Analysis of conducted researches of heat conductivity, heat capacity and diffusivity of heavy concretes shows that numerical values of these properties have the following variation [7–12]: heat conductivity - $\lambda = 1,251,76 \text{ W/(m}\cdot\text{gr)}$; specific heat capacity - $c_p = 7201,76 \text{ J/(kg}\cdot\text{gr)}$; diffusivity factor - $a = (1,242,45)10^{-6} \text{ m}^2/\text{s}$. Variation of values is connected by that concrete is a non-uniform firm mass with non-uniform distribution on volume of a cement stone, rubble and sand, and also a total volume of micropores and a residual moisture in them [3, 7]. Therefore, the test specimens cut from the concrete volume block but at different locations have different values of thermo physical properties.

In addition, the measurement method and calculation procedure for these characteristics are not described. The lack of this information makes it difficult to assess their validity, as the quantity and quality of the assumptions and assumptions that are incorporated in the measurement method and calculation procedure used are unknown.

2 Theoretical Justification

In order to measure the thermo-physical characteristics of M250 heavy concrete, a pulse heating method was used to heat the samples.

The authors have introduced the following assumptions for the conditions mentioned above:

- 1) the body is regarded as a flat semi-infinite specimen along the applicates axis;
- 2) the heat flux is directed along the applicate axis and is uniformly distributed;
- 3) the process is stationary.

The method is based on the unsteady thermal conductivity equation for a limited volume body:

$$\frac{\partial T(x, y, z, t)}{\partial t} = a \nabla^2 T(x, y, z, t), \quad (1)$$

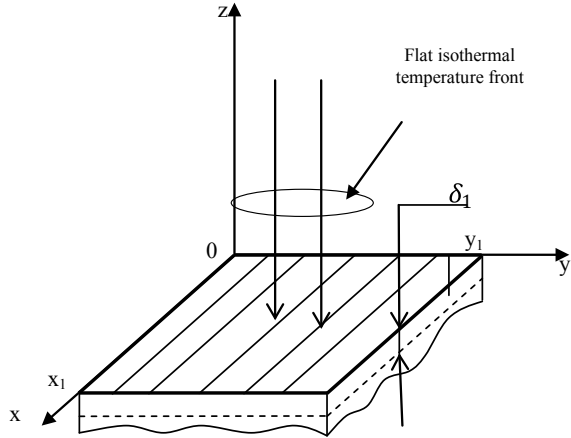
where a – diffusivity, m^2/s ; $T(x, y, z, t)$ – temperature distribution function, K; t – time, s. Initial and boundary conditions of the first and second kind are defined for Eq. (1). A thermal energy pulse q with a flat thermal front in the XY plane is incident on the surface of a flat semi-infinite specimen in the Z direction (Fig. 1). At $t = 0$ we obtain the initial condition (2):

$$T(x, y, 0, 0) = T_0, \quad (2)$$

with a boundary condition (3):

$$\lambda \left. \frac{\partial T}{\partial t} \right|_{z=\delta} = q. \quad (3)$$

Fig. 1 Implementation scheme pulse heating method



The solution of Eq. (1) with (2) and (3) in mind is as follows:

$$\Delta T = T - T_0 = \frac{q}{2c\rho\sqrt{\pi a}} \int_0^{t_0} e^{-\frac{z^2}{4a(t-\tau)}} \cdot \frac{d\tau}{\sqrt{t-\tau}}, \tag{4}$$

where c – specific heat capacity, $J/(kg \cdot K)$; ρ – sample density, kg/m^3 ; τ – is the delay time of temperature front propagation, s.

If we differentiate (4) by time and equate it to zero we obtain the equation at the extremum of the excess temperature dependence $\Delta T_{max}(t)$ at the depth $z = \delta_1$, where the measuring thermocouple is located. The solution to the extremum equations is as follows:

$$\ln \frac{\tau_{max}}{\tau_{max} - \tau_n} = \frac{\delta^2}{a} \left(\frac{1}{\tau_{max} - \tau_n} - \frac{1}{\tau_{max}} \right), \tag{5}$$

where τ_{max} – time of reaching the maximum $\Delta T(\delta, t)$, s; δ – depth of the thermo couple from the irradiated surface of the sample M ; τ_n - time of the energy pulse (energy flow), s.

Ratio (5) allows us to obtain the value of the thermal conductivity coefficient:

$$a = \delta^2 \left(\frac{1}{\tau_{max} - \tau_n} - \frac{1}{\tau_{max}} \right) : \ln \frac{\tau_{max}}{\tau_{max} - \tau_n}. \tag{6}$$

3 Description of Experimental Studies

An experimental setup at the physics department of Nosov Magnitogorsk State Technical University was developed and built to conduct research. Five cylindrical samples, 22 mm in diameter and 25 mm in height, were made for investigation. Samples were cut out with diamond hollow drill from different places of the monolithic flat block of concrete. Two thermocouples mounted in the sample were used to measure thermal conductivity according to the scheme shown in Fig. 2.

The schematic diagram of the installation, which implemented the pulse method of heating the samples to determine the specific heat capacity, thermal conductivity and thermal diffusivity coefficients, is shown in Fig. 3.

Fig. 2 Layout of thermo couples Thermo couples in a concrete sample

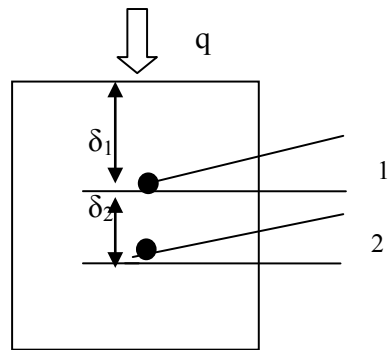
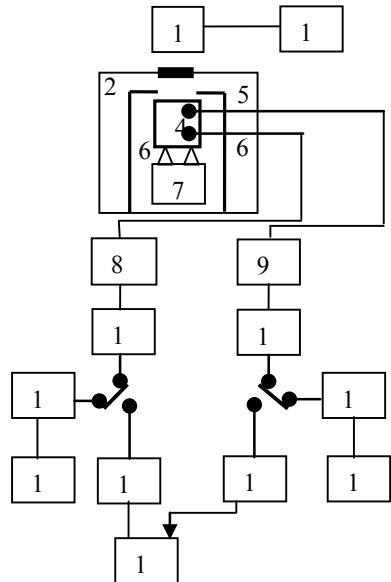


Fig. 3 Schematic diagram of experimental setup for investigation of thermo physical characteristics of solid nonmetals: 1 - pulse energy source with adjustable pulse duration; 2 - operating vacuum chamber; 3 - protective cylinder with diaphragm; 4 - sample under study; 5, 6 - chromel–alumel thermocouples; 7 - sample holder; 8, 9 - DC potentiometers PP-63; 10, 11 - voltage amplifiers U2-11; 12,13 - voltage dividers P5/1; 14,15 - two-coordinate recorders KSP-4; 16,17 - analog–digital converters; 18 - personal computer; 19 - power supply and control of pulse power source



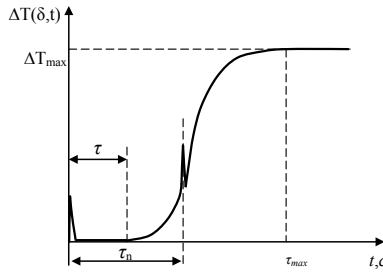


Fig. 4 Experimental time dependence of sample temperature at point $z = \delta_1$, where τ_{max} is time of maximum temperature achievement at point $z = \delta_1$, τ_n is duration of heat flux, falling on plane $(x_1, y_1, 0)$, τ_3 is time delay of thermal front moving from plane $(x_1, y_1, 0)$, τ_n to $z = \delta_1$

Experimental variation of $\Delta T(\delta, t)$ is shown on Fig. 4. Taking into account the cylindrical shape of the sample, we obtain that:

$$\lambda = \frac{\cdot \delta_2}{\Delta T \cdot S}, \lambda = \frac{\cdot \delta_2}{\Delta T \cdot S}, \lambda = \frac{\cdot \delta_2}{\Delta T \cdot S}, \tag{7}$$

where τ_{lag} – Fig. 2. Layout of thermocouples thermocouples in a concrete sample. delay time of temperature front arrival with temperature T_0 to the point with coordinate $z = \delta$, where $T(\delta, \tau_{lag}) = T_0 \cdot e^{-\delta}$, c ; P – radiation power, W ; $\Delta T = T_{max1} - \Delta T = T_{max2}$ - difference of maximum temperatures determined by experimental curves (Fig. 4) $T(\delta_1 + \delta_2; \tau_{max2})$, K ; ρ – density of heavy concrete with known humidity, kg/m^3 .

Each value of a , λ and c_p was the average of five values at a given moisture content. The magnitude of the power of the light flux incident on the sample was measured using a Luxmeter U-116 with a photocell F55C and then converted into energy.

Five measurements were made on each sample and each value of a , λ and C_p is the average of 25 measurements. The experiments were carried out for samples with different weight moisture content. The results of the measurements are shown in the table.

For the dried samples at $T = 200 \text{ }^\circ\text{C}$ for three hours the average thermal diffusivity was $1, 21 \times 10^{-6} m^2/s$. The moisture content of the samples was calculated with respect to the original samples obtained from a concrete block dried under natural conditions for one hundred and thirty days. The thermal properties presented in the table were measured with an accuracy of at least one per cent.

Although concrete is a solid, it has no structure in the long-range order aspect. Therefore, classical solid theory, based on phonon and electron subsystems involved in the phenomena of heat transfer and energy storage involving the non-stationary Boltzmann equation with the introduction of the relaxation time concept, is not applicable to it. Concrete is a solid conglomerate consisting of cement stone, aggregate in the form of crushed rock of different nature, sand and other additives. The volume

of concrete is randomly distributed with an indeterminate number of pores occupied by moisture. On this basis, the authors assume that heat transfer in a given material is possible due to: the phonon mechanism, concentrated in local areas having a near-order structure; the convection mechanism due to the presence of micropores with air and moisture; the radiative mechanism according to Stephan-Boltzmann law.

The thermal properties presented in the table are measured with an accuracy of at least one percent. The obtained data analysis shows that the thermal properties of heavy concrete depend on: density; moisture (porosity); temperature. The physical nature of the thermo-physical properties is generally described on the basis of the solid-state model (Table 1).

For crystalline solids having a long-range order, the description of these properties is based on phonon and electron subsystems involved in the phenomena of heat transfer and energy storage involving the non-stationary Boltzmann equation with the introduction of the relaxation time concept.

For illustrative purposes Fig. 5 shows a dependence graph of the thermal diffusivity on the humidity of the samples.

Table 1 Thermo physical characteristics of M250 heavy concrete

Wetness, %	Density, kg/m ³	Thermal diffusivity, m ² /s	Conductivity, W/(m·gr)	Capacity, J/(kg·gr)
0.00	2108	1.26	2.29	863
1.00	2112	1.28	2.35	872
2.00	2118	1.95	3.63	880
3.00	2120	2.38	4.49	890
4.75	2127	3.26	6.27	905
5.00	2129	3.55	6.85	907

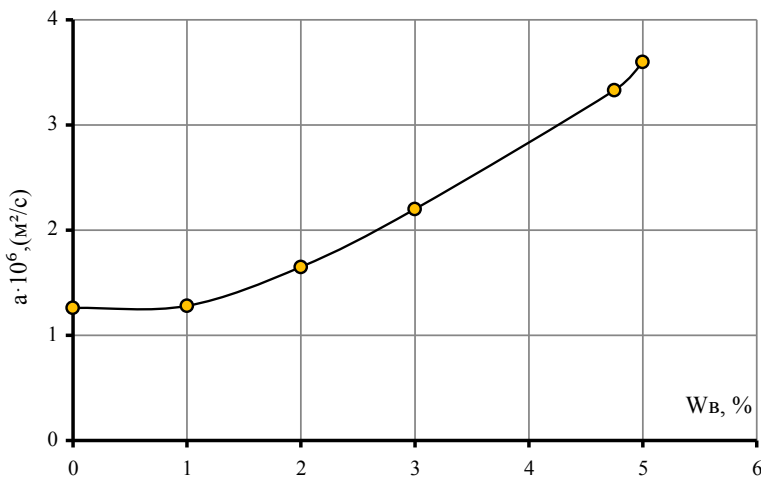


Fig. 5 Dependence of thermal conductivity on moisture content of M-250 heavy concrete

In this case, such a representation is impossible because concrete, although a solid body, is structure less, i.e. lacks long-range order. It is a solid conglomerate consisting of cement stone, aggregate of different nature, sand and other additives, as well as an indefinite number of micropores randomly distributed over the concrete volume. Some of the micropores are occupied by moisture.

Considering the list of mechanisms of heat transfer in heavy concretes, we shall introduce an algorithm for calculation of generalized thermo physical characteristics:

1. determine the total thermal resistance of the concrete according to Mattison's rule:

$$r_{0\delta} = \sum_{i=1}^N r_i, r_i = \frac{1}{\lambda_i}, \quad (8)$$

where r_i – thermal resistance of the i -th mechanism; N – machine number; λ_i – thermal conductivity coefficient of the i -th appliance;

2. determine the heat capacity of the heavy concrete:

$$C_0 = \sum_{i=1}^N k_i c_i, \quad (9)$$

where k_i – is the weight coefficient of contribution of the i -th component of heavy concrete; c_i is the heat capacity of that component in the temperature range ΔT , J/K;

3. to determine the value of the thermal conductivity coefficient for heavy concrete:

$$a_0 = \frac{\sum_{i=1}^N \lambda_i}{\sum_{i=1}^N \rho_i k_i c_i}, \quad (10)$$

where ρ_i – is the density of the i -th component of concrete, kg/m^3 .

A promising line of work is to supplement the above algorithm and flesh out the nature of the above mechanisms.

4 Conclusions

1. The authors of work proposed the definition method for thermo physical parameters of heavy concrete components and implemented on the experimental stand. Results of research on the stand showed that values of characteristics increase nonlinearly depending on moisture content.

2. The authors proposed determination algorithm of generalized thermo physical characteristics of heavy concrete taking into account its component composition.
3. Under conditions of the model adaptation to new concrete grades, the calculation methods can be transferred to the new grades.

References

1. Ban CC et al (2021) Modern heavyweight concrete shielding: principles, industrial applications and future challenges; review. *J Build Eng* 39:102290. <https://doi.org/10.1016/j.jobbe.2021.102290>
2. Siliev AS, Latina SV (2013) Necessity of automation of heavy concrete composition design. *Mod Sci-Intensive Technol* 7–1:59
3. Zelenkov DS, Polukhina NA, Podtelkov VV (2007) Obtaining of porous concretes on heavy aggregates. *Build Mater* 11:60–62
4. Polyakov VS, Padokhin VA, Akulova MV, Syrbu SA (2012) Improvement of strength properties of heavy concretes by chemical admixtures based on ϵ -caprolactam oligomers. In: *Proceedings of higher educational institutions. Series: chemistry and chemical technology*, vol 55, no 8, pp 118–121
5. Shapovalov NA, Kosukhin MM, Slusar AA, Mukhachev OV (2002) Heavy concretes on carbonate aggregate of improved quality. *Build Mater* 1:8–9
6. Chulkova IL (2012) Automated calculation of heavy concrete composition and prediction of its properties. *Bull Siberian State Autom Road Acad* 6(28):108–114
7. Bagaev II, Logunova OS (2020) Storage of key features of images of sulfur imprints in the mathematical structure form. Paper presented at the 2020 international multi-conference on industrial engineering and modern technologies, FarEastCon 2020. <https://doi.org/10.1109/FarEastCon50210.2020.9271243>
8. Tueva TV, Sudnitsina VV (2009) Influence of fine aggregate on heat conductivity of light and heavy concretes. *Bull Cherepovets State Universit* 2(21):121–123
9. Arkulis M, Logunova O, Dolgushin D (2018) Influence of magnetic field on formation of short range order regions in liquid metals: fluctuation hypothesis. <https://doi.org/10.4028/www.scientific.net/KEM.777.316>
10. Dubskiy GA, Vdovin KN, Nefediev AA, Dubskaya TY (2007) Experimental installation for investigation of thermo physical properties of solids by method of periodic heat waves (in Russian). *Vestnik of Nosov Magnitogorsk State Tech Univ* 4(20):81–88
11. Torchinskii VE, Logunova OS, Sibileva NS, Romanov PY (2018) Genetic algorithm modification: Addition of the population improvement stage. Paper presented at the ACM international conference proceeding series, pp 286–290. <https://doi.org/10.1145/3209914.3209928>
12. Verzhinskaya AB (1964) Investigation of thermo physical characteristics of materials in the form of plates and coatings by the constant power source method. *IPZh* 17(4):58–66

The Development of Polymer Fire-Resistant Thermal Insulation Coating Filled with Anthropogenic Waste



Marina Ilina , Oleg Selivanov , and Ivan Kurochkin 

Abstract The research presents the development results of the polymer coating possessing good insulation and fire-resistant properties, containing electroplating production waste from the machine-building enterprise. This coating is designed for thermal insulation and fire protection of concrete and metal surfaces of various construction structures and industrial equipment. The coating is developed basing on siloxane rubber, catalyst K-18, hollow carbon microspheres and anthropogenic waste-electroplating sludge, used as flame retardant additive. The hollow carbon microspheres provide the increase in coating strength and thermal insulation properties. The electroplating sludge in the amount of 5–15 wt.p. facilitates self-extinguishing effect of thermal insulation coating, reducing the burning time without deterioration of the operational properties – strength, adhesion, while solving another important task-safe disposal of electroplated sludge. The studies have shown that this composition allows producing relatively inexpensive, but quite effective polymer coating characterized by good thermal insulation, fire-resistance and physico-mechanical properties.

Keywords Polymer thermal insulation coating · Siloxane rubber · Hollow carbon microspheres · Electroplating sludge · Flame retardant · Thermal conductivity coefficient · Strength · Self-extinguishing effect · Safe disposal

1 Introduction

Nowadays composite polymer materials are widely used in various industries [1–3]. Their application as thermal insulation coating for concrete and metal surfaces of building structures and industrial equipment is of great interest.

They provide good thermal insulation properties, good corrosion protection, proper adhesion to the surface, low water absorption, easy coating application and good external aesthetic appearance [4–6]. At the same time, the polymer coatings flammability is their significant disadvantage. To reduce the polymer coatings

M. Ilina · O. Selivanov (✉) · I. Kurochkin
Vladimir State University, Gorkogo Street 87, 600000 Vladimir, Russia

flammability and to enhance the self-extinguishing effect, in case of their ignition, flame retardants are introduced into their composition, which can be in the form of various organic and inorganic compounds (antimony trioxide, aluminum diethyl phosphinate, ammonium salts of sulfuric and phosphoric acid, bromine, chlorine and organophosphate compounds, metal hydroxides and oxides, etc.) [7–9]. The effectiveness of halogen-containing flame retardants is increasing in the series $F < Cl < Br < I$. Bromine-containing flame retardants surpass chlorine-containing flame retardants in effectiveness, since their combustion products are less volatile. Chlorine-containing flame retardants emit chlorine at a wide temperature range, so its content in the gas phase is low, and bromine-containing flame retardants decompose at a narrow temperature range, thus providing bromine optimal concentration in the gas phase. The chlorine-containing flame retardants application has recently significantly reduced due to their compounds toxicity.

Most halogen-containing flame retardants are used in the form of synergistic mixtures with antimony oxides. Antimony oxide does not delay combustion, as it melts above the ignition temperature of most plastics. However, when mixed with halogen-containing compounds, antimony oxide forms antimony halides and oxyhalides, which at the ignition temperature are in gaseous state and dilute the combustible gases. When choosing halogen-containing flame retardants, halogen radicals are essential to be formed at the same temperature as the combustible polymer pyrolysis products. Thus, free radical scavengers will be in gaseous phase simultaneously with the fuel, ensuring maximum efficiency of the flame retardant. Nitrogen-phosphorus-containing compounds are considered to be effective from the point of view of fire protection providing, capable of decomposing to form phosphoric acid when heated. The flame retardant effect of phosphoric acid primarily depends on the abrupt change in thermal transformation mechanism of carbohydrate part of polymer material, resulting in the reduction of effective activation energy of dehydration process. The initial temperature decreases, the formation rate and the released water amount increase.

Halogenated, metallic, and phosphorus-containing flame retardants have proven their effectiveness, but they are known to be seriously harmful to human health and environment, so the new types of flame retardants are being developed, for example, based on carbon materials such as graphene, carbon nanotubes, and carbon black [10]. The flame retardants significantly complicate the ignition of polymer thermal insulation coatings, reduce the fire propagation speed, and promote self-extinguishing. However, the main disadvantage of the currently used flame retardants is their high cost. The possibility of using electroplating sludge as flame retardant additive for the polymer thermal insulation coating of machine-building waste is being considered in this study.

The electroplating sludge, used as flame retardant additive, will reduce the cost of thermal insulation coating and at the same time provide safe disposal of man-made waste.

To improve thermal insulation, strength properties and to reduce the polymer coating density in polymer composite materials, various types of microspheres are used – glass, aluminum silicate, phenol–formaldehyde, carbon, etc. Herewith, the

key condition for achieving the optimal physical and mechanical properties of the polymer thermal insulation coatings is the uniformity of microspheres distribution in size, shape and strength. The spherical shape of such fillers causes new certain functions and properties differing from the other filler properties, including: uniform stress distribution around the spherical inclusions and good dimensional stability, no orientation effects, high isotropy.

Beside the effects, associated with their spherical shape, the most important function of microspheres is to reduce the density of polymer composite materials, containing spherical shells.

The research objective is to study the flame-retardant and physico-mechanical properties of the polymer thermal insulation coating developed on the basis of siloxane rubber, catalyst K-18, hollow carbon microspheres and flame retardant additive – electroplating sludge.

2 Materials and Research Methods

Siloxane rubber was presented by phenylmethylsiloxane rubber SKTNF grade A (TU 38.103129-77) of low-molecular weight. Technical indicators of SKTNF rubber of A grade are presented in Table 1.

Materials, produced on the basis of A grade SKTNF rubber are resistant to temperatures from $-90\text{ }^{\circ}\text{C}$ to $+300\text{ }^{\circ}\text{C}$. They possess high hydrophobicity, chemical inertia, vibration resistance, resistance to biological effects (fungi and microorganisms), resistant to adverse factors - ultraviolet, ozone, various types of oxidizing agents, etc.

Catalyst K-18 (TU 6-02-805-78), tin diethyl dicaprilate solution in ethyl silicate-32, was used for curing the siloxane rubber. To improve thermal insulation properties of the developed polymer coating, hollow carbon microspheres (HCM) were

Table 1 Technical indicators of SKTNF rubber of A

Indicators	A grade SKTNF rubber
Exterior	Colorless liquid No mechanical impurities. Opalescence is possible
Conditional viscosity by VZ-1 viscometer (nozzle 5.4 mm), s	Max 90
Mass loss, % wt, max	5.0
Viability, min, min	40
Tensile strength, kgf/cm ² , min	20
Relative elongation, %, min	70
Relative residual elongation, %, max	4
Frost resistance coefficient for elastic recovery after compression by 20% at $-70\text{ }^{\circ}\text{C}$, min	0.6

Fig. 1 Electroplating sludge before drying and grinding



used, obtained by pyrolysis of phenol–formaldehyde hollow microspheres in argon medium at the temperature of 1200 °C during 4 h. The carbon microspheres, produced basing on this technology, were characterized by bulk density of 0.09 g/cm³, 90% or more carbon concentration in the material of the microspheres wall, while highly porous structure is formed (the specific surface area ranks 120 m²/g), the microspheres wall thickness is 1–4 μ.

The size of the resulting microspheres ranged from 20 to 100 μ.

It is worth noting that during the carbon microspheres production, some part of them becomes defective: as a result of oxidative erosion, micropores are formed in the cell wall, and a part of microspheres is destroyed. The latter are removed by sieving, and the defective microspheres are removed by flotation fractionation, for example in acetone. Despite the presence of micropores in the carbon microspheres shells, they are more durable in comparison, for instance, with glass microspheres without such micro defects. Thus, at gas (nitrogen) pressure of 7 MPa, 43% of glass microspheres and only 5% of carbon microspheres are destroyed.

In this study the flame retardant additive was represented by electroplating sludge (ES), formed during the effluents chemical treatment from electroplating production by lime milk at one of the machine-building enterprises in Vladimir. Depending on its composition and neutralization method, electroplating sludge refers to the 2–3 hazard class and belongs to anthropogenic waste [11, 12]. In order to reduce the electroplating sludge amount and re-use it as a secondary raw material, technologies are currently being developed for its application as a useful target additive into the various construction materials [13–16], including polymer thermal insulation coatings [17].

The electroplating sludge composition includes the following metal hydroxides: Zn(OH)₂, Ni(OH)₂, Cu(OH)₂, Fe(OH)₃, Ca(OH)₂, CaO and SiO₂ oxides. Prior the application electroplating sludge was dried at T = 130 °C and subjected to fine grinding in the ball mill. The resulting fine powder had grinding degree max 40 μ (according to GOST 6589-74). Figure 1 exhibits electroplating sludge before drying and grinding, Fig. 2 shows it after drying and grinding operations.

Fig. 2 Electroplating sludge after drying and grinding



The electroplating sludge was analyzed using “Spectroscan MAX-G” spectrometry X-ray fluorometer. The elemental composition of electroplating sludge is shown in Table 2.

The standard methods have been applied to determine the physical and mechanical characteristics of the developed coating. Thermal conductivity coefficient has been determined in compliance with GOST 23,630-79 using IT- λ -400 device. Calorimeter is the basis of IT- λ -400 device, while the metal core of calorimeter consists of the heating block, base, calorimeter, copper rod and adiabatic shell. The temperature difference is measured every 25 °C (the rod temperature) during heating at the sample and calorimeter, proportional to the number of galvanometer scale divisions.

The compressive strength has been determined in compliance with GOST 8462-85. The polymer coating adhesive strength has been determined applying adhesive meter PSO-MG4 by anchor-steel cylinder method of 20 mm diameter, glued with high-strength adhesive onto the composition coating the glass substrate.

Table 2 Elemental composition of electroplating sludge

Element (in oxide or hydroxide composition)	Quantity, %
Zn	10.96
Cu	1.68
Ca	32.84
Ni	1.35
Co	0.01
Fe	6.84
Mn	0.22
Cr	4.91
Si, O, H	Others

3 Results and Discussion

The analysis of electroplating sludge elemental composition revealed that zinc, iron, chromium and calcium hydroxides are present in electroplating sludge in the biggest amount. In case of the sudden exposure to high temperatures (for example, fire), metal hydroxides contained in the electroplating sludge are decomposing into metal oxides and water, and decomposition reaction is endothermic, which is cooling the coating polymer structure to the temperature below the ignition point. The formed water vapor contributes to the combustible gases dilution, released during the polymer combustion, oxygen action weakening and combustion rate decrease. The calcium oxide in the form of inert fine powder creates heat-insulating layer helping to stop burning of the ignited sections of the polymer coating. The effectiveness of the metal hydroxides impact is directly proportional to their content in polymer, but the content increase exceeding 50% is undesirable, since the composition viscosity is acutely increasing, and physical and mechanical properties of polymer coating are deteriorating. Hollow carbon microspheres have been chosen in this study as carbon microspheres are characterized by better strength, heat resistance and good adhesion to polymer binders.

The hollow carbon microspheres in the formulation of the developed thermal insulation coating provide the improvement of the coating strength properties, as carbon microspheres have more rough surface in comparison, for example, to the glass or ceramic microspheres, thus contributing to the increase in the intermolecular bonding forces between the carbon microspheres surface and siloxane rubber. Various functional groups are located on the micropores surface of carbon microspheres, serving as the activation centers of intermolecular chemical interaction with the polymer binder, thus significantly strengthening the polymer matrix structure of the coating. Thus, hollow carbon microspheres introduction into the composition can significantly increase the coating strength characteristics.

More over hollow carbon microspheres are characterized by low thermal conductivity coefficient, so their usage provides the produced coating with higher thermal insulation properties.

In our study, the samples of thermal insulation coatings were prepared in compliance with the following technology: hollow carbon microspheres, electroplating sludge, and catalyst K-18 were introduced into siloxane rubber in turn, according to the developed recipes. The compositions were thoroughly mixed and applied to the substrate. The drying period lasted 24 h at the temperature of 25 °C.

The compositions for thermal insulation coating samples and their physical and mechanical characteristics are presented in Table 3.

When electroplating sludge in the composition amounts over 15 wt.p., the coating adhesive properties are deteriorating, the composition viscosity is increasing and the possible technological defects are increasing as well. When less than 5 wt.p. of electroplating sludge is introduced, self-extinguishing effect of thermal insulation coating is reduced, and less sludge is disposed. The hollow carbon microspheres

Table 3 Compositions content for the thermal insulation coating samples and their physical and mechanical characteristics

Sample №	Compositions, wt.p.				Coating physical and mechanical characteristics				
	SKTNF	K-18	HCM	GS	Compressive strength limit, kg/cm ²	Thermal conductivity, W/m °C	Burning time after the end of flame exposure, s	Adhesive strength, kg/cm ²	
1	50	2.0	60	5	18	0.10	10	6	
2	20	1.8	40	15	16	0.12	6	5	
3	80	2.2	20	10	12	0.13	8	3	

introduction into the composition in the amount less than 20 wt.p. does not significantly increase the coating strength and thermal insulation properties, the increase in their content to more than 60 wt.p. in the composition causes the increase of the composition viscosity, the possibility of more technological defects, deterioration of coating adhesion to the treated surface, due to the decrease of the polymer binder amount.

To assess the physical and mechanical properties of the developed thermal insulation coating, we have compared its characteristics with the well-known thermal insulation coating, containing siloxane rubber SKTNF, hollow glass microspheres, catalyst K-18 and boron nitride flame retardant additive [18]. The manufacturing technology of the known thermal insulation coating included the application of several layers of the composition, containing the binder and the filler on to the surface, with the intermediate each layer drying and final thermal treatment of the coating. Initially, the surface was covered with the thermal insulation layers of the composition, containing siloxane rubber SKTNF 30–60 wt.p., glass microspheres 40–70 wt.p., and afterwards the fire-resistant layers of the composition containing siloxane rubber SKTNF 20.0–79.5 wt.p., glass microspheres 20.0–60.0 wt.p., boron nitride 0.5–20.0 wt.p. Each intermediate layer was dried at 20–80 °C, and finally the coating was thermally treated at 80–150 °C, and the total thickness of fire-resistant layers did not exceed 3 mm.

The comparative characteristic of physical and mechanical properties of the known thermal insulation coating and the developed one based on the composition containing 20–80 wt.p. of siloxane rubber, 20–60 wt.p. of hollow carbon microspheres, 1.8–2.2 wt.p. K-18 catalyst and 5–15 wt.p. of galvanic sludge as the flame retardant additive is presented in Table 4.

The table proves that the developed thermal insulation coating is characterized by better physical and mechanical parameters than the known thermal insulation coating.

Thus, the developed coating possesses good thermal insulation and strength characteristics, short burning time due to the self-extinguishing effect, herewith the problem of safe disposal of electroplating sludge is being solved.

Table 4 Physical and mechanical characteristics of the and developed thermal insulation coating

№	Characteristic	Value	
		Known	Developed
1	Compressive strength limit, kg/cm ²	11	12–18
2	Thermal conductivity coefficient, W/m °C	0.15	0.10–0.13
3	Burning time after the flame exposure, s	–	6–10
4	Adhesive strength, kg/cm ²	2	3–6

References

1. Hsissour R, Seghiri R, Benzekri Z, Hilali M, Rafik M, Elharfi A (2021) Polymer composite materials: a comprehensive review. *Compos Struct* 262:113640. <https://doi.org/10.1016/j.compositestruct.2021.113640>
2. Asghar S, Syed HK, Bin LK, Khan IU, Salman S (2021) Multifunctional polymer matrix composites. *Ref Module Mater Sci Mater Eng* 24. <https://doi.org/10.1016/B978-0-12-819724-0.00024-0>
3. O'Lenick AJ Jr (2007) Silicone polymers: new possibilities in nanotechnology. *ACS Symp Ser* 961:165–175. <https://doi.org/10.1021/bk-2007-0961.ch009>
4. Sun G, Yang L, Liu R (2021) Thermal insulation coatings based on microporous particles from pickering emulsion polymerization. *Prog Org Coat* 151:106023. <https://doi.org/10.1016/j.porgcoat.2020.106023>
5. Tao Y, Mao Z, Yang Z, Zhang J (2020) Preparation and characterization of polymer matrix passive cooling materials with thermal insulation and solar reflection properties based on porous structure. *Energy Build.* 225:1103619. <https://doi.org/10.1016/j.enbuild.2020.110361>
6. Wang F, Wei H, Liu C, Sun H, Zhu Z, Liang W, Li A (2019) Monolithic nanoporous polymers bearing POSS moiety as efficient flame retardant and thermal insulation materials. *React Funct Polym* 143:104345. <https://doi.org/10.1016/j.reactfunctpolym.2019.104345>
7. Yan D, Stoliarov SI, Kraemer RH (2019) Pyrolysis model development for a polymeric material containing multiple flame retardants: relationship between heat release rate and material composition. *Combust Flame* 202:43–57. <https://doi.org/10.1016/j.combustflame.2019.01.003>
8. Nabipour H, Wang X, Song L, Hu Y (2020) Metal-organic frameworks for flame retardant polymers application: a critical review. *Compos Part A Appl Sci Manuf* 139:106113. <https://doi.org/10.1016/j.compositesa.2020.106113>
9. Wypych G (2021) Selection of flame retardants for different polymers. In: *Handbook of flame retardants*, pp 89–226. <https://doi.org/10.1016/B978-1-927885-69-7.50009-9>
10. Araby S, Philips B, Meng Q, Ma J, Laoui T, Wang CH (2021) Recent advances in carbon-based nanomaterials for flame retardant polymers and composites. *Compos Part B Eng* 212:108675. <https://doi.org/10.1016/j.compositesb.2021.108675>
11. Vorob'eva AA, Shakhova VN, Pikalov ES, Selivanov OG, Sysoev ÉP, Chukhlanov VYu (2018) Production of facing ceramic with a glazing effect based on low-plastic clay and technogenic waste from vladimir oblast. *Glass Ceram* 75(1-2):51–54
12. Sukharnikova MA, Pikalov ES, Selivanov OG, Sysoev ÉP, Chukhlanov VY (2016) development of a batch composition for the production of construction ceramic based on raw material from Vladimir Oblast: clays and galvanic sludge. *Glass Ceram* 73(3–4):100–102
13. Vilarinho I, Carneiro J, Pinto C, Labrincha J, Seabra MP (2021) Development of coloured stoneware bodies through the incorporation of industrial Cr/Ni electroplating sludge. *Sustainability* 13(4):1999. <https://doi.org/10.3390/su13041999>
14. Vitkalova I, Torlova A, Pikalov E, Selivanov O (2019) The development of energy efficient facing composite material based on technogenic waste. *Adv Intell Syst Comput* 983:778–785
15. Vitkalova I, Torlova A, Pikalov E, Selivanov O (2018) Development of environmentally safe acid-resistant ceramics using heavy metals containing waste. *MATEC Web Conf* 193:03035
16. Chukhlanov VYu, Selivanov OG, Trifonova TA, Ilina ME, Chukhlanova NV (2017) Thin-layer thermal insulation coatings based on high-filled spheroplastics with polyorganosiloxane binder. *IOP Conf Ser Earth Environ Sci* 90:012061. <https://doi.org/10.1088/1755-1315/90/1/012061>
17. Vitkalova I, Torlova A, Pikalov E, Selivanov O (2018) Industrial waste utilization in the panels production for high buildings facade and socle facing. In: *E3S Web of Conferences*, 02062
18. Epifanovsky IS, Dimitrienko YuI, Polezhaev YuV, Medvedev YuV, Mikhatuliy DS (1995) RF Patent No. 2039070. *Byull. Izobret*, No. 4

Seismic Vulnerability of Individual Housing: Case Study



Mashrap Akhmedov  and Rustam Abirov 

Abstract Analysis of associated risk is necessity condition for development of mitigation strategy of disasters consequences. Central Asian region is located on earthquakes prone area. Destructive earthquakes with intensity of 8 points and higher may happen in this area. Uzbekistan is the most populated country in the region. Rapid urbanization processes in Central Asian region is natural trend as in the rest of the world. This leads to increasing risk of natural disasters especially of seismic ones. Along with using modern concepts in civil engineering, considerable part of habitants is living in individual housing and remain in cities. At some locations it is also has trend for expansion. For vulnerability mitigation of residents during seismic event is the most important to provide housing safety measures. Thus different types of researches widely provided for seismic prone regions [1–6] around the world. However, any region has its own specific features and Central Asia is no exclusion.

Keywords Strength · Building · Vulnerability · Earthquake · Damages

1 Introduction

The great importance have the problem of the growing earthquake risk for cities located in seismic prone territories world-wide and urgency of mitigation measures.

The city of Tashkent, one of large cities in Central Asia, is located in ancient oasis along the great Silk Road. Nowadays territory of the city more than 35 thousands hectares, its population is about 3 million residents.

Due to high rate of demography the seismic risk problems have a great importance for Uzbekistan especially for urban zones [7, 8] with dense building with

M. Akhmedov (✉)

Institute of Mechanics and Earthquake Engineering, Dormon yoli 33, Tashkent, Uzbekistan
e-mail: instmech@academy.uz

R. Abirov (✉)

AKFA University, 17 Kichik Xalqa Yo'li, Tashkent, Uzbekistan

individual aseismic traditional structures. In this regard first of all the great importance is assessment of stability for individual self-made, one and two story residential structures have to be provided. On this base some measures for strengthening of traditional housing are investigated and developed in this issue. The principal seismic design philosophy including financial and technical capabilities of the population for strengthening of such type of housing, including RC structures, is described here. As the case study was investigated situation in Tashkent city - capital of Uzbekistan. It is a large diversified industrial center producing about quarter of industrial production of the country.

The city has about 40,000,000 square meters of residential space, that is in average one citizen has 13,3 m² of dwelling space.

So, the problem of earthquake safety is a topical one for this region and for Tashkent especially. Vital activity of the city is provided with a complicated system of lifelines and infrastructure. And the local authority paid considerable attention to the problem for years. However, detailed analysis shows that despite of constant attention to the problem of seismic safety and considerable achievements on the way of preparedness to future disastrous earthquakes, the city of Tashkent might not be considered as ready in full for probable future large earthquakes.

The dwelling stock in Tashkent is presented by different structural types of buildings. Nowadays the individual residential buildings of Tashkent are made up of traditional 1–2 storied houses, built with local materials (adobe, airbricks, etc.) and burned bricks. Many houses confer an oriental view to the city and as thus have a historical value. By local authority inventory the individual residential houses classifies these buildings according to three following types according to their main design [9]:

Type I - Buildings made by weak local materials (such as adobe and wooden framework) *sinch* and *pakhsa*.

Type II - Buildings mainly made by air bricks.

Type III - Buildings made by burned bricks with RC inclusions.

Figure 1 shows the buildings distribution according to seismic zone within the city. More than half of the buildings are located in 9-point seismic intensity zone by MSK scale. One should also notice that the majority of the buildings of type I and II were built up to 50–100 years ago. Although life time for so structures initially proposed up to 30 years, these buildings are still in use. These buildings are particularly subject to losing their strength and therefore their response on seismic impact is not sufficient by present safety standards. In case of seismic event the individual residential buildings are exposed to characteristic supplementary damages as much as dilapidated housing [9].

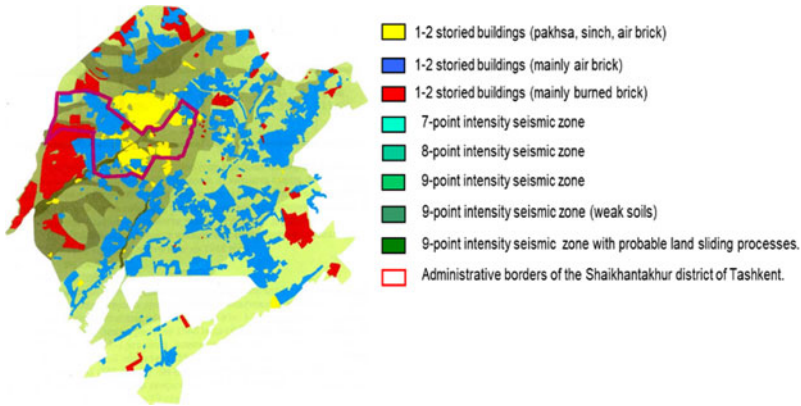


Fig. 1 Disposition of individual housing according to seismic zones in Tashkent

The territory of the Tashkent city covers an area of 32850 ha, over 15570 ha (47.4%) are occupied by residential buildings. According to Fig. 2 the number of structures from weak local materials constructed before 1966 Tashkent earthquake are presented.

Individual housing occupies more than 30% of the territory (Fig. 3). Nowadays 1–2 storied individual buildings built with weak local materials make up 3% of the territory of the city, (air bricks buildings up to 20%, burned bricks buildings up to 7%). The houses are localized in 7, 8 and 9 point intensity seismic zones. It is important to underline the soil conditions because old part of city located along river beds with soil alluvium.

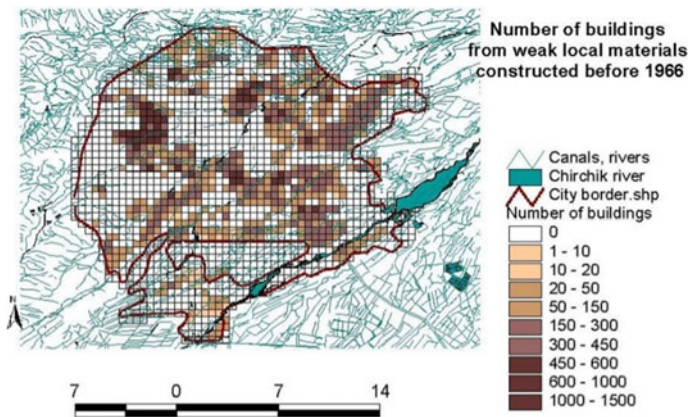


Fig. 2 Density location of dwelling stock from weak materials in Tashkent

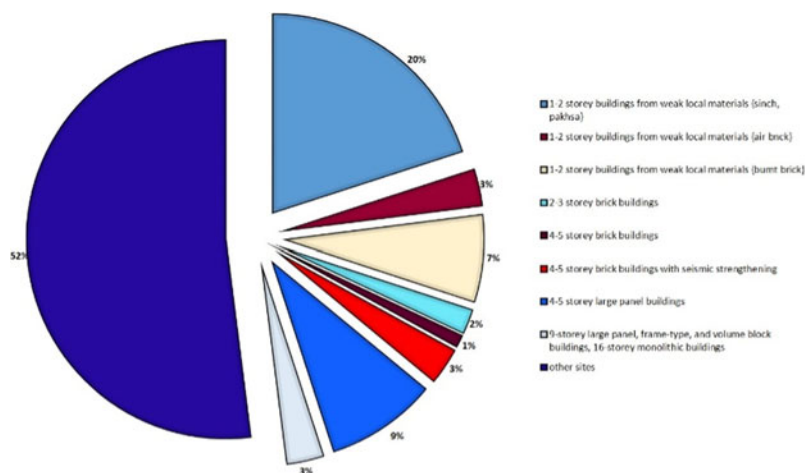


Fig. 3 Territory of city occupied by the residential buildings of various types

2 Main Part

According to Table 1 until 1966 year in Shaykhantakhur district there were only 9% of individual houses built by burned bricks, 33.7%-made by air bricks, and 30.3% of buildings with wooden framework filled with adobe (guvala) or air bricks (sinch). Today we can observe a trend (according to second part of Fig. 3) as the quantity of houses from burned bricks has increased up to 4 times and the quantity of buildings with wooden framework filled by adobe (guvala) or air bricks (sinch) has been reduced:

- 12% of the city area were built before 1948
- 18% - before 1966
- 70% - before 2000

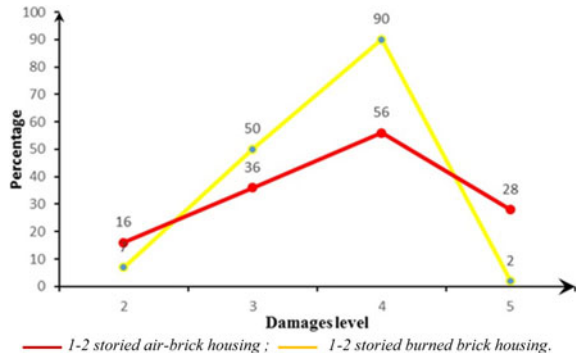
Table 1 shows distribution of houses with traditional 1–2 storied shape in Shaykhantakhur district (one of the administrative district of the city).

Figure 4 shows the distribution of the damages caused by 1966 Tashkent destructive earthquake for the 1–2 storied individual buildings (8-point intensity

Table 1 Traditional housing

Period	All houses	1-storey	2-storey	Burned bricks	Air bricks	Adobe (Pakhsa)	Wooden framework (Sinch)
26.04.1966	5948 100%	5832 98.1%	114 1.9%	528 9%	2008 33.7%	1495 25%	1801 31.3%
01.01.2001	10,115 100%	7786 72%	2329 23%	3731 35.2%	3221 31.8%	1598 15.6%	1679 16.4%

Fig. 4 Disposition of 1–2 storied buildings’ damage degree during the Tashkent earthquake



in epicenter). In 198 out of 682 cases are investigated 1–2 storied air brick buildings the collapse of walls occurred (28%), in 380 cases large cracks and considerable falling were indicated (56%) and 104 buildings (16%) have been slightly damaged. This corresponds to 2, 4 and 5 level of damages. In 1251 investigated buildings by burned bricks a collapse occurred only in 19 cases (1.4%).

An analysis of the damages can be given according to the following scale:

1. level - good visible cracks all over the partitions and wall’s stucco, vertical cracks at wall connections, weakening of pilings from ventilation and chimney canals and of canals for electricity leads, horizontal cracks in piers, cracks in framework, where the cracks disclosure is not bigger than 0.5 mm. Horizontal and obliquely cracks in chimney pipes and rafter support;
2. level – crumbling and falling of wall’s stucco and ceilings, partial collapse of the partition and of plastic cornices, inclined and intersected transparent cracks in partition, in piers and main walls, partial damage of wall’s pilings in places of leaning of floor beam, vertical and transparent cracks disclosure is not bigger than 2–5 mm. partly collapse of pipes;
3. level – exfoliation of brick-partitions, full collapse of piling, plastic cornices and framework, transparent, slope and X-formed flaws till 4–5 mm in piers, displacement and partial destroys of rafter support and opening of apertures. Multitude of slope and transparent horizontal flaws in under apertures and upper apertures parts of the wall with a displacement of crosspiece and piling, the full vertical tearing away of wall parts, displacement of girders (joists), X- formed diagonal flaws in dumb walls, the tearing of external walls away from internal ones and displacement of corner-parts of walls, full destruction of pipes, the width of the flaws in main constructions are from 2–3 up to 15–20 mm;
4. level – the full collapse of partitions, partial destruction of carrying and external self-carrying walls, the severance of aseismic girdles; a serious displacement and partial destruction of girdles;
5. level – destruction of some parts or total collapse of building.

Brick, clay-blocks and “pakhsa” houses mostly affect the 2nd grade of damage by 6 points intensity earthquake, and by 7 points intensity earthquake they fully lose



Fig. 5 Damaged individual residence after 1966 event (01.05.1966 photo by G.Zelma)

their bearing capability. However, if the historical building technologies are used then these houses can endure 7 or sometimes even 8 points intensity earthquakes.

Houses with wooden framework (Sinch) and filled by adobe (Guvala) or air bricks become rather safe constructive system, which is capable to endure 8 points intensity earthquake (Fig. 5). Wide spread was observed non-structural damage excludes damage to the building structure also. Such damage occurs frequently even under moderate intensities of earthquakes like cracking and overturning of masonry parapets, roof chimneys, etc., falling of plaster from walls and ceiling. Failure due to shear was characterized by diagonal cracks mainly due to diagonal tension.

On Fig. 6 presented instrumental measured epicenters of earthquakes in Tashkent. Last destructive earthquake in Tashkent has taken place in 1966 and 67% of individual buildings were damaged [10]. About 4 millions square meters of residential area was damaged and the thousands of the people became homeless (Fig. 7). After Chatkal earthquake in 1946, when in Tashkent the power of earthquake completed 6 points intensity, there was marked serious damage to the houses. Nazarbek earthquake [11] aftermath had the similar results.

In case of new buildings in residential sector, aseismic legislative measures are not completely provided, the building technology is broken, the ground condition is not considered.

Based on the results of the analysis of earthquake repercussions, records of the damages by the scale from 1 to 5 and construction experience in the individual housing sector in seismic regions Table 2 is filled in. This table shows the damages of individual buildings caused by local weak materials according to the graphic.

From the analysis of the graph drawn below we may argue that buildings made of burned bricks if constructed according to the aseismic construction rules (local building codes), will not get irreparable damage at a strongly possible scenario of a major earthquake. Additionally, buildings made of sinch can sustain an 8-point

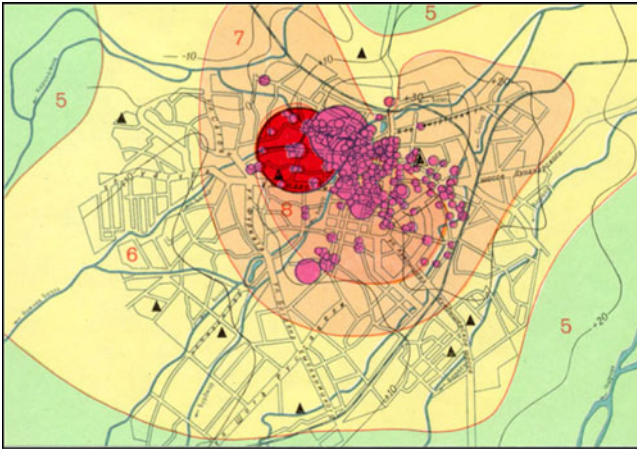


Fig. 6 The epicenters of main earthquakes and its aftershocks by V.Ulomov

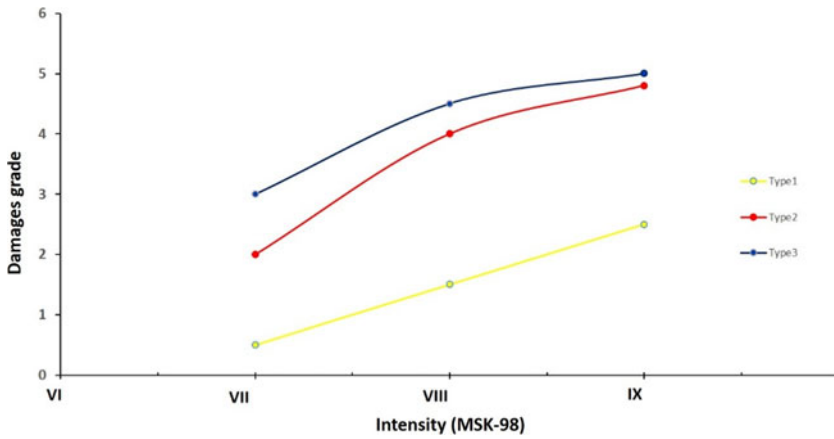


Fig. 7 Vulnerability curves for residential houses from local weak materials

Table 2 Damages of individual buildings caused by local weak materials

The type of individual houses	Damage degree by earthquake intensity		
	7-point	8-point	9-point
I	3-4	4-5	5
II	2-3	4-5	5
III	2-3	3-4	4

intensity earthquake and will not collapse, but the houses made of air bricks and pakhsa would be demolished anyway.

3 Conclusion

Due to the lack of data from the past earthquakes and insufficient quality of instrumental data it is impossible to provide deep sophisticated vulnerability analysis of individual housing during earthquakes. Nevertheless, some data allows us to provide preliminary analysis of present situation and to develop the measures of vulnerability mitigation for dwelling stock. It is first stage for general associated risk analysis due earthquakes. Based on this analysis it is possible to develop the strategy for urban land use planning and approach to avoid human losses during strong seismic activities, including reliable assessments for preparedness to emergency actions.

Obviously, buildings in fired bricks, solid concrete blocks and hollow concrete or mortar blocks are much strong rather adobe. The creation of tensile and shearing stresses in walls of masonry buildings is the primary cause of different types of damage.

The general principles and most details of aseismic design of brick or adobe buildings are applicable to those using other rectangular masonry units such as solid blocks of mortar, concrete, or stabilized soil, or hollow blocks of mortar, or concrete having adequate compressive strength. Besides the main principles as structural design and using of aseismic belts at building process, some measures for individual housing have to be developed. These measures have to be applicable and available for widespread use in practice. So, for aseismic strengthening we have to keep in the mind the next rules and options: correct choice of site locations (land use planning); taking into account soil conditions; foundation isolation and design rules; material's quality, operating rules. In some cases wrong operating rules for existing aseismic structures lead for vulnerability increasing for so buildings. Following so simple rules is path for more safety and resilience life.

References

1. Necevska-Cvetanovska G, Apostolska R (2012) Methodology for seismic assessment and retrofitting of RC building structures. In: 15th World Conference on Earthquake Engineering (15WCEE)
2. Apostolska R, Shendova V, Necevska-Cvetanovska G (2020) The need of integrated renovation of the existing building stock in North Macedonia. *Eur J Environ Civ Eng*
3. Tolles EL, Kimbro EE, Ginell WS (2002) Planning and Engineering Guidelines for the Seismic Retrofitting of Historic Adobe Structures
4. Shrestha H, Pradhan S, Guragain R (2012) Experiences on retrofitting of low strength masonry buildings by different retrofitting techniques in Nepal. In: 15th World Conference on Earthquake Engineering, Lisbon, Portugal

5. Arya AS (2000) Non-engineered construction in developing countries Bull. New Zeal. Soc. Earthq. Eng.
6. Ishiyama H, Mizutani T (2018) Seismic renovation of brick building by usage of bamboo. In: WCTE 2018 - World Conference on Timber Engineering
7. Abirov RA (2016) The seismic risk mitigation problems in urban areas of Central Asia. In: International Disaster Reduction Conference, Davos
8. Akhmedov M, Abirov RA (2006) The vulnerability of residential buildings and measures for seismic risk reduction. The experience in Uzbekistan. In: International Disaster Reduction Conference, Davos
9. Erdik M, Rashidov T, Safak E, Turdukulov A (2005) Assessment of seismic risk in Tashkent, Uzbekistan and Bishkek, Kyrgyz Republic. Soil Dyn Earthq Eng 25:473–486
10. Raskazovskiy VT, Rashidov TR, Abdurashidov KS (1967) The consequences of earthquake in Tashkent, FAN. Tashkent
11. Rashidov TR, Khojimetov GK, Shamsiev Ush (1981) The consequences of Nazarbek earthquake. In: Building and Architecture in Uzbekistan No. 10

Strength and Deformability of the Dome of the Mausoleum of Khoja Ahmed Yasawi



Nurakhmet Makish , Syrymgali Yerzhanov , Vladimir Lapin ,
and Dauren Kassenov 

Abstract For the first time, a study of the strength and deformability of the dome of the “Kazanlyk” room of the Mausoleum of Khoja Ahmed Yasawi, included in the World Heritage List by the United Nations Educational, Scientific and Cultural Organization, was carried out. The mausoleum was built in the fourteenth century. A visual inspection of the technical condition of the dome was carried out, instrumental records of micro-oscillations were obtained, and a computational and analytical assessment of the bearing capacity of the structures of a decorative dome under seismic and static influences was carried out. The technical condition of the dome is not satisfactory, there are multiple cracks along the outer surface of the dome. The technical condition of the wooden beams is not satisfactory. The presence of rotten beams, in places where they are embedded in masonry, and the presence of beams affected by fungi and insects, weaken the bearing capacity of the decorative dome. When calculating for seismic impact, the seismicity of the construction site was taken equal to 7 points. The calculation was carried out using the finite element method. Two variants of the calculation were performed - without damage and taking into account the modeling of a horizontal crack between 16 and 17 rows of stalactites with a length of $\frac{1}{4}$ of the dome perimeter. It was found that presence of a crack affects the strength and deformation characteristics of the dome. The displacement values, taking into account the simulation of the crack, changed - the maximum displacement value increased 2.7 times from 0.0256 mm to 0.0629 mm.

Keywords Historical monument · Period of oscillation · Earthquake resistance · Strength · Deformability

N. Makish · S. Yerzhanov · V. Lapin (✉) · D. Kassenov
Kazakh Research and Design Institute of Construction and Architecture, 21 Solodovnikova,
050046 Almaty, Kazakhstan

N. Makish
e-mail: nmakish@mail.ru

1 Introduction

There are 229 ancient architectural monuments on the territory of the Republic of Kazakhstan, 5 of which are included in the UNESCO World Heritage List. The most significant is the Mausoleum of Khoja Ahmed Yasawi, which since 2003 has been included in the World Heritage List by the United Nations Educational, Scientific and Cultural Organization (UNESCO) based on the criteria of value specified in the “Convention on the Protection of the World Cultural and Natural Heritage.”

The problem of preserving historical monuments is one of the important tasks of preserving the historical memory of the population of the countries of the world. A significant number of studies have been devoted to the scientific analysis of the problem [1–11].

For example, an analysis of the seismic vulnerability of the masonry of historic buildings located in the center of Lucca (Italy) was carried out in [3]. The analysis revealed some problematic issues typical for this type of building structure, such as poor wall joints and poor quality of the type of masonry.

In [8] the issues of protection of monuments of wooden architecture of Siberia are considered by methods of wood modification. It provides an overview of protective compositions based on organic silicon compounds, which are applied to the surface of wood with grinding and can be used as effective protective agents. In [11], the issues of the vulnerability of destruction of thin masonry structures in towers, the seismic behavior of historical stone towers are considered, and one of the methods of strengthening such structures is carried out.

The mausoleum of Khoja Ahmed Yasavi is located in the southeastern part of the city of Turkestan. Around the city of Turkestan there are seismogenic zones of the Karatau region - North Kirghiz, Baikadam, Glavnaya Karatau, Chudinskaya, Syrdarya, East Kyzylkum, Kumkol, Bastarau [12]. For instance, the Bakadam seismogenic zone is characterized by earthquakes with $K = 9-11$ and source depths within 15–20 km.

The aim of this study is to assess the technical condition of the dome room “Kazanlyk” with the development of preliminary recommendations for its strengthening. It is necessary to investigate the strength and deformability of the dome.

Scope of work:

- visual inspection of the dome with photographs of structural elements and damage;
- instrumental records of microseismic vibrations of the dome;
- computational and analytical assessment of the bearing capacity of decorative dome structures under seismic impact;
- engineering analysis of design solutions, assessment of the technical condition of the supporting structures for the dome;
- development of preliminary recommendations to ensure the operational reliability of the dome structures.

2 Method and Subject of Research

Research methods are visual inspection, experimental measurement of the vibration characteristics of a decorative dome.

A theoretical study of the strength and deformability of the dome is carried out using the LIRA SAPR application package, which implements the finite element method.

2.1 *Geotechnical Conditions of the Construction Site*

Geomorphologically, the site is a relatively flat foothill plain of the Syr Darya river valley, which is characteristic of the construction site of the city of Turkestan. The relief of the site is relatively flat, with a slight slope from east to west and southwest. During the survey, general construction work was carried out along the perimeter of the structure in question.

In terms of lithology, the site is composed of alluvial-proluvial deposits of the Middle-Upper Quaternary age, consisting of a layer of loess loam, light brown, porous, relatively homogeneous, of solid consistency, in the bottom with inclusions of pebbles up to 10%, thickness 1.5–3.2 m and pebble with sandy aggregate up to 30%, less often with sandy loam aggregate, exposed up to 12.5 m thick. The pebble fragments are represented by rounded sedimentary rocks, sometimes there are interlayers of conglomerates up to 20 cm thick in a volume of up to 10%. The occurrence of the above soil layers is relatively horizontal. The boulder-pebble soil from above is covered with sandy loam deposits with a thickness of 1–2 m. The thickness of the boulder-pebble soil is up to 500 m and increases towards the top of the fan.

In hydrogeological terms, the area is confined to the valley of the Syr-Darya river and the “Arys-Turkestan” canal has a significant impact on the hydrogeological regime.

Loess-like loam - homogeneous (with a small inclusion of pebbles up to 10% in the bottom of the layer), highly porous, solid, low-moisture, subsiding.

Pebble soil with sandy and sandy loam aggregate up to 10%, low moisture above the groundwater level and water-saturated in the aquifer (below the groundwater level).

Due to the fact that at the base of the structure there are loess soils, in the analysis of the soil base, the fund materials of the Institute for the city of Turkestan were used. The analysis of the physical and mechanical characteristics of soils was carried out on the basis of detailed studies of soils at the base of the mausoleum of Khoja Ahmet Yasawi. The properties of the soil at the base of the mausoleum were studied several times in the second half of the twentieth century.

2.2 Object of Study

The Kazanlyk dome is part of the construction of the mausoleum of Khoja Ahmed Yasawi. The mausoleum was built in 1389–1399 over the burial place of Khoja Ahmed Yasawi (Fig. 1).

The inner diameter of the brick dome is 18.2 m. The base of the dome is at an elevation of 25.5 m from the earth's surface, the top is at an elevation of 36.5 m (Fig. 2).

The dome is lined with ring (wedge) masonry of baked bricks on gypsum-cement mortar.

The thickness of the dome at the base is 1.2 m, in the upper part - 0.5 m. The dome rests on girder sails installed on the brick walls of the building 3.0 m thick.

Above the sails, the cylindrical part of the dome with a height of 2.8–2.9 m has the shape of a false octagon, which decorates the cylindrical part with a decorative octagonal prism, hidden from the inside by stalactite decor (decorative dome).

The masonry of the dome is hidden from the inside with ganch decor - spatial systems of stalactites (decorative dome).

Structurally, stalactites are attached to the dome with wooden beams, cantilevered into the dome's brickwork. Timber beams are installed in height in increments of approximately 50 cm. Wooden beams are mostly circular, but there are some rectangular beams. Beam diameter, on average, is 15 cm.

Fig. 1 Mausoleum of Khoja Ahmed Yasawi



Fig. 2 Brick dome of the Kazanlyk room



The average thickness of the walls of the decorative stalactite dome is approximately 20 cm (based on materials from Mankovskaya L.). The length of the generatrix of the stalactite (decorative) dome is 11 m.

3 Results

3.1 Inspection Results

As a result of the survey of the building of the stalactite dome, the following was established:

- The outer covering of the brick dome was restored and lined with a glazed ceramic coating in 2019–2020, no damage in the form of cracks or deformations is observed;
- no restoration work was carried out on the inside of the brick dome;
- measurements of the crack opening width were made (Figs. 3 and 4), in the body of the brick dome from the inside, in places, vertical cracks with an opening width of up to 15 mm were observed;

Fig. 3 Measurements of crack opening width



Fig. 4 Vertical crack with an opening width of at least 1 mm

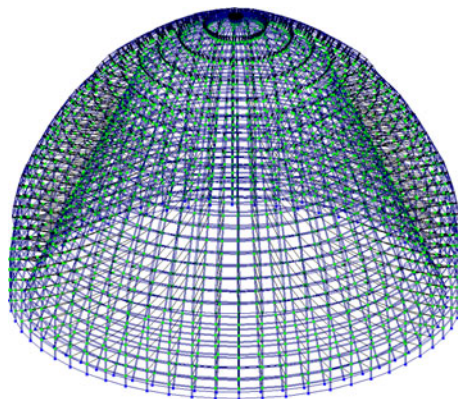


Fig. 5 Wooden beams after impacts during operation



- in the body of the stalactite dome, from the outside, there are numerous cracks with an opening up to 2 cm wide;
- in the process of observing the decorative dome, beacons were installed on cracks on the surface of stalactites, both from the inside and from the outside;
- gypsum beacons are dated 08/18/2010, mechanical beacons with graduation scales are not dated;
- on gypsum beacons, the crack opening width is insignificant (hairline cracks);
- on mechanical beacons, the crack width is not increased, except for one beacon, where the opening width increased by 2 mm;
- an insignificant part of wooden beams is exposed to rotting, as well as being exposed to insects and possibly infected by bacteria or fungi (Fig. 5);
- for the stability and rigidity of wooden beams, brick pillars are installed vertically between them closer to the decorative dome;
- some brick pillars have collapsed;
- to determine the strength of the brick, an assessment was carried out by a non-destructive testing method using IPS-MG 4.03 (shock pulse method) in accordance with GOST 22,690;
- according to the results of a random check of bricks, the strength is in the range from 14.0 MPa to 28.6 MPa, with an average value of 21.2 MPa, which corresponds to the brick grade M175-M200;
- the strength of the decorative dome material was not determined;
- in the body of the brick of the main dome, as well as in the body of the decorative dome in the inter-dome space, traces of the selection of cylindrical shapes were found to determine the physical and mechanical characteristics or the chemical composition of materials;
- To determine the actual dynamic characteristics of the decorative dome (amplitude, period, acceleration and vibration frequency), full-scale experimental work was carried out to record micro-seismic vibrations;
- during the tests, a digital recording station RSM-8 was used, equipped with seismic receivers SPM-16;
- a vibratory road roller was used as a source of vibrations, which was located at a distance of 12 m from the western wall of the mausoleum;
- tests were carried out in three stages: 1st stage - measurement of accelerations in three levels of stalactite (lower, middle and upper) in orientation (x), directed

Fig. 6 Finite elements scheme of decorative dome of the room “Kazanlyk”



along the short axis of the main building of the mausoleum; in the middle and in the upper level, vertical acceleration (z) was measured; the sensors were installed on a stalactite on the north side; 2nd stage - the orientation of the sensors is changed to (y), i.e. 90° from position (x), while the location of the sensors does not change; position (y) corresponds to the long axis of the main building of the mausoleum; in the middle and lower levels, vertical acceleration (z) was measured; the sensors were in the same places on the north side; 3rd stage - measurement of accelerations near the skating rink and near the wall of the mausoleum on a rigid concrete area connected to the piles in orientation (x) and (y); near the wall, vertical acceleration (z) was also recorded.

3.2 Analytical Assessment

The design scheme of a dome made of masonry and decor made of stalactites is taken in the form of a spatial system (Fig. 6).

The base of the dome is rigidly pinched.

The calculation was performed for the main and special combination of loads in accordance with the current regulatory documents of the Republic of Kazakhstan using the spectral method of dynamic calculation and an application package that implements the finite element method.

In the calculation, the seismicity of the site was taken equal to 7 points for type II soils in terms of seismic properties.

Horizontal seismic loads were assumed to act in the direction of the longitudinal axis.

Self-weight loads of structures are taken in accordance with the presented materials.

The coefficients for determining the design seismic loads, as well as the coefficients of the combinations of efforts, are taken taking into account the constructive solution, the degree of responsibility, soil conditions from the requirements of the

current regulatory documents of the Republic of Kazakhstan. For the design seismicity of 7 points for the II type of soils according to seismic properties, the following values of the coefficients are taken:

- class of responsibility for the purpose - IV;
- class of responsibility by number of storeys - II (middle-rise buildings);
- responsibility of the building horizontally $\gamma_{Ih} = 1.5$;
- responsibility of the building along the vertical $\gamma_{Iv} = 1.5$;
- coefficient of behavior in determining horizontal seismic loads $q = 4.0$;
- coefficient of behavior in determining vertical seismic loads $q = 1.5$;
- acceleration a_g is 0.08 (in fractions of g);
- maximum value of the period $T_c = 0.72$;
- oscillation period of the linear system $T = 0.039$ s.

Deformation moduli, volumetric weights and Poisson's ratios are taken from reference materials.

Calculation data are preliminary. To obtain more accurate results, it is necessary to carry out detailed experimental studies to determine the actual physical and mechanical characteristics of materials.

Based on the results of verification calculations, the following conclusions were made:

The value of permissible stresses in the decorative dome is taken as for brickwork - 1 MPa.

The calculated value of the maximum stress according to the color palette is 13.4 t/m^2 (0.134 MPa).

The stress in the section is $1 \text{ MPa} \times 0.2 \text{ m} = 0.2 \text{ MPa} > 0.134 \text{ MPa}$. The load-bearing capacity of the decorative dome material is ensured.

The maximum displacement value is 0.0692 mm, which is less than 1/500 of the structure's height ($1080 \text{ mm}/500 = 2.16 \text{ mm} > 0.0692 \text{ mm}$).

When simulating a crack in the dome, the stress pattern changed. The maximum stress value increased by 22% at the beginning and end of the horizontal crack.

The pattern of displacements, taking into account the simulation, also changed, the maximum value of displacements increased 2.7 times from 0.0256 mm to 0.0629 mm.

4 Discussion

According to the results of visual inspection, the technical condition of the brick dome is unsatisfactory, the presence of cracks indicates the processes of deformation of the dome, caused, most likely, by deformations of the dome supports (sails and walls of the main building of the mausoleum).

The technical condition of the decorative dome is not satisfactory, as evidenced by multiple cracks along the outer surface of the dome.

The technical condition of the wooden beams is not satisfactory.

The presence of rotten beams, in places where they are embedded in masonry, as well as the presence of beams affected by fungi and insects, weaken the bearing capacity of the decorative dome.

The presence of a horizontal crack between the 16th and 17th rows of stalactites with a length of $\frac{1}{4}$ of the dome perimeter confirms the fact of subsidence of the western pylon of the dome.

To assess the bearing capacity of the dome, verification calculations were performed. The physical and mechanical characteristics of the materials of the brick and decorative domes were taken from the reference materials. To determine the actual characteristics of materials, it is necessary to conduct appropriate experimental studies of full-scale samples.

According to the results of verification calculations, the bearing capacity of the decorative dome is ensured without damage modeling. When modeling one horizontal crack in the body of the decorative dome, the stress pattern changed significantly.

In the research work, the full-scale dynamic characteristics of the decorative dome were determined.

The results of the experimental data obtained indicate that the model of the dome of the design scheme does not accurately reflect the actual stiffness characteristics of structures and materials of domes and wooden beams (deformation modules, the presence of cracks, the accuracy of the geometric model, etc.).

The calculated acceleration in the verification calculations was taken equal to 80 cm/s^2 .

During experimental work, the accelerations near the source of oscillations were 203 cm/s^2 .

In this case, the design model is represented only by brick and decorative domes rigidly clamped at the base with wooden cantilever beams between the domes. In reality, the dome rests on the construction of the mausoleum with powerful walls and additional structural elements.

In the future, it is necessary to perform a calculation for the effect of real earthquake accelerograms. According to [12], the Kyzyl-Kum seismogenic zone is the closest to the city of Turkestan. According to instrumental observations, earthquakes with an energy class of $K = 9-15$ occurred within the Kyzylkum zone. The seismic potential of the zone is estimated as with magnitudes $M = 6.5$ southwest of the intersection with the West Syrdarya zone and as $M = 5.5$ northeast of this node.

5 Conclusion

1. The technical condition of the brick and decorative domes according to the results of visual inspection is unsatisfactory.
2. According to the results of verification calculations performed by the finite element method according to the reference values of the physical and mechanical characteristics of a dome made of masonry and a decorative stalactite dome, the

deformations of the dome at acceleration values at the base of 80 cm/s^2 are less than $h/500$ (h is the height of the decorative dome). This result appears to be an optimistic estimate of the dome's seismic resistance.

3. The results of dynamic tests showed that the model of the dome of the design scheme does not accurately reflect the actual stiffness characteristics of structures and materials of domes and wooden beams (deformation modules, the presence of cracks, the accuracy of the geometric model, etc.).
4. Recommendations for further research:
 - it is necessary to install an engineering and seismometric service station equipped with a digital instrumentation and measuring system (for example, [13–16]), which will register in real time the vibrations of the ground and structural elements of the mausoleum under natural (seismic) and man-made influences, including acoustics, and will also register the stress–strain state of structures;
 - it is necessary to study the physical and mechanical characteristics and analyze the composition of materials for dome structures, as well as assess the effect of aging on their strength characteristics;
 - it is necessary to carry out a comprehensive calculation of the entire building of the Mausoleum of Khoja Ahmed Yasawi, taking into account the real picture of the weakening of structures (cracks, gouges, etc.), with modeling of the bases and foundations;
 - an extended detailed survey of all load-bearing structures of the building of the mausoleum of Khoja Ahmed Yasawi should be performed, including the determination of the strength characteristics of materials and the dynamic characteristics of structures.
5. It is recommended to use fluoroplastic tapes to strengthen the weakened and damaged elements of the brick structures of the mausoleum of Khojaa Ahmed Yasawi [17, 18]. It is also possible to use seismic isolation systems [19–22].
6. Fiber-reinforced polymer sheets (FRP) can be used to reinforce damaged timber structures [23].

Acknowledgements The authors express their gratitude to the staff of the Institute LLP “Kazrestavratsiya” for help in the study of this object.

References

1. Betti M, Borghini A, Boschi S, Ciavattone A, Vignoli A (2017) Comparative seismic risk assessment of Basilica-type churches. *J Earthquake Eng.* <https://doi.org/10.1080/13632469.2017.1309>
2. Bergamasco I, Gesualdo A, Iannuzzo A, Monaco M (2018) An integrated approach to the conservation of the roofing structures in the Pompeian domus'. *J Cult Herit.* <https://doi.org/10.1016/j.culher.2017.12.006>

3. Boschi S, Borghini A, Pintucchi B, Zani N (2018) Seismic vulnerability of historical masonry buildings: a case study in center of Lucca. *Procedia Struct Integrity* 11:169–176. <https://doi.org/10.1016/j.proestr.2018.11.023>
4. Frunzio G, Di Gennaro L (2018) Seismic structural upgrade of historical buildings through wooden deckings strengthening: the case of study of Palazzo Ducale in Parete, Italy. *Procedia Struct Integrity* 11:153–160. <https://doi.org/10.1016/j.proestr.2018.11.021>
5. Gavarini C (2001) Seismic risk in historical centers. *Soil Dyn Earthq Eng* 21(5):459–466. [https://doi.org/10.1016/S0267-7261\(01\)00027-6](https://doi.org/10.1016/S0267-7261(01)00027-6)
6. Mosoarca M, Onescu I, Onescu E, Anastasiadis A (2020) Seismic vulnerability assessment methodology for historic masonry buildings in the nearfield areas. *Eng Fail Anal* 115:104662. <https://doi.org/10.1016/j.engfailanal.2020.104662>
7. Branco M, Guerrero LM (2011) Seismic rehabilitation of historical masonry buildings. *Eng Struct* 33(5):1626–1634. <https://doi.org/10.1016/j.engstruct.2011.01.033>
8. Krutasov BV, Molchanov VS, Krutasova IB (2016) Silicon-organic modifying additives for protection of wooden architecture monuments of Siberia. *Procedia Eng* 150:1563–1566. <https://doi.org/10.1016/j.proeng.2016.07.117>
9. Bernardini W (2004) Hopewell geometric earthworks: a case study in the referential and experiential meaning of monuments. *J Anthropol Archaeol* 23(3):331–356. <https://doi.org/10.1016/j.jaa.2004.06.01>
10. Aldrebi ZA (2018) Monitoring and certification of the most famous architectural monuments in Syria. In: *Proceedings of Petersburg Transport University, PGUPS, Saint-Petersburg*, vol 15, no 2, pp 302–310
11. Aldrebi ZA (2020) Historical masonry towers: overview, seismic vulnerability, behavior during an earthquake, seismic strengthening. *Earthq Eng Constr Saf* 6:49–66. <https://doi.org/10.37153/2618-9283-2020-6-49-66>
12. Kurskeev AK, Timush AV, Shatsilov VI, Sydykov A (2000) Seismic zoning of the Republic of Kazakhstan. *Euro*
13. Zhang X, Zhang Q, Wang M et al (2017) Development of a full-wave form voltage and current recording device for multichannel and current recording device for multichannel transient electromagnetic transmitters. *Geosci Instrum Methods Data Syst* 6:495–503. <https://doi.org/10.5194/gi-6-495-2017>
14. Yang L, Stehly L, Paul A (2018) Working Group High-resolution surface wave tomography of the European crust and uppermost mantle from ambient seismic noise. *Geophys J Int* 214(2):1136–1150. <https://doi.org/10.1093/gji/ggy188>
15. Qiao S, Duan H, Zhang Q et al (2018) Development of high-precision distributed wireless microseismic acquisition stations. *Geosci Instrum Methods Data Syst* 7:253–263. <https://doi.org/10.5194/gi-7-253-2018>
16. Groukamp L, Rossow JJ, Fourie CJS, Cormbrinck L (2011) Foundation requirements for a lunar laser ranger facility at Matjiesfontein, South Africa. *Afr J Geol* 114(3/4):573–576. <https://doi.org/10.2113/gssajg.114.3-4.573>
17. Mrozek M, Mrozek D (2020) Analysis of location of composites reinforcements of masonry structures with use topological optimization. *Appl Eng Sci* 3:1000015. <https://doi.org/10.1016/j.apples/2020.100015>
18. Kubica J, Galman-Seweryn I (2017) Comparison of two ways of AAC block masonry strengthening using CFRP strips - diagonal compression test. *Procedia Eng*. 193:42–49. <https://doi.org/10.1016/j.proeng.2017.06.184>
19. Bulat AF, Dyrda VI, Lysytsya MI, Grebenyuk SM (2018) Numerical simulation of the stress-strain state of thin-layer rubber-metal vibration absorber elements under nonlinear deformation. *Strength Mater* 50(3):387–395. <https://doi.org/10.1007/s11223-018-9982-9>
20. Dyrda VA, Kobets A, Bulat AF, et al (2020) Present problems of vibration isolation in heavy mining machines at long-term cyclic loads. In: *E3S Web of Conference*, vol 168, p 00042. <https://doi.org/10.1051/e3sconf/202016800042>

21. Lapin V (2020) Comparative analysis of the effect of seismic isolation by means of stations of engineering seismometric service on buildings. In: 16th World Conference on Seismic Isolation, Energy Dissipation on Active Vibration Conference of Structures, pp 325–332. <https://doi.org/10.13753/2686-7974-2019-16-482-527>
22. Bulat AF, Dyrda VI, Grebenyuk SN, Klimenko MI (2019) Determination of effective characteristics of the fibrous viscoelastic composite with transversal and isotropic components. *Strength Mater* 51(2):183–192. <https://doi.org/10.1007/s11223-019-00064-x>
23. Corradi M, Vemury CM, Edmondson V, Poologanathan K, Nagaratnam B (2021) Local FRP reinforcement of existing timber beams. *Compos Struct* 258:113363. <https://doi.org/10.1016/j.compstruct.2020.113363>

Simulation Modeling Using Neural Networks to Control Complex Technical Systems



Tatyana Kozhevnikova and Ilya Manzhula

Abstract As a result of the research, a combined neural network method, models and modeling tools for the operational control of complex technical systems have been developed and investigated. The analysis of existing methods, models and software for operational management of complex technical systems; the requirements for the developed methods, models and software for managing these systems have been substantiated. A combined neural network method for modeling complex technical systems based on a hierarchical neural network model is proposed, combining the capabilities of analytical and neural network approaches and allowing to significantly increase the efficiency of operational management (quality and efficiency of management decisions), as well as the flexibility of modeling and the possibility of operational management of calculation of structural and parametric optimization of the model based on information about the system obtained in real time. A hierarchical neural network model for the operational control of complex technical systems has been developed, consisting at the lower level of a set of interconnected neural network models corresponding to the elements of the modeled system, and a supervisor at the upper level designed to identify structural errors at the lower level of the model. A method of decision support for managing complex technical systems in real and pseudo-real time, based on the proposed hierarchical neural network model, is proposed. Software tools for combined neural network modeling and decision support have been developed for the operational control of complex technical systems.

Keywords Simulation modeling · Complex technical system · Neural network · Logical system model · Algorithm · Regression

1 Introduction

Operational management of complex technical systems is an activity that consists in the development of control actions and their implementation, aimed at effectively

T. Kozhevnikova · I. Manzhula (✉)
Computing Center FEB RAS, Kim Yu Chen Street, 65, 680000 Khabarovsk, Russia

achieving the goal of the system in real or pseudo-real time. The need for modeling in the operational management of complex technical systems is due to the complexity of the control object, large financial and time costs, and sometimes the impossibility of its direct study [1, 2].

Research in this area is based on the works of many Russian scientists V.P. Tarasik, A.I. Galushkina, A.A. Vavilova, N.P. Buslenko and others.

The features of complex technical systems are:

- the complexity of the structure, multicomponent, a large number of parameters;
- dynamic changes in the structure;
- incomplete initial information;
- variety of impacts on the system, their probabilistic and non-stochastic nature;
- the presence of complex nonlinear relationships between parameters;
- the need for prompt management decisions;
- limited opportunities for experimental research.

The limited possibilities for the experimental study of complex systems makes the development of methods for their modeling urgent. Often, specialists are not able to cover all events and phenomena, as well as all possible combinations of them in the process of functioning of such systems. As a result, the creation of a common model is almost impossible.

One of the ways to overcome the barrier of complexity is to decompose such a system into relatively less complex components and study these components taking into account their interaction.

Such subsystems can be described using systems of equations, the solution of which is time consuming, and the results, due to the incompleteness of the initial information, can only be approximated to the processes occurring in the subsystems. Nevertheless, the results of solving systems of equations can be used for the initial training of a set of neural network models of subsystems that have the ability to fine-tune the features of these subsystems.

This approach makes it possible to form a library of pre-trained typed neural network models of subsystems of a complex technical system.

Thus, the task of research and development of a combined neural network method, models and control tools for complex technical systems is relevant and practically significant. Therefore, on the basis of all of the above, it is possible to formulate the purpose of the study: the development of a combined neural network method, models and tools for the operational management of complex technical systems to improve the efficiency of operational management of complex technical systems.

The scientific novelty of the work lies in the developed hierarchical compositional neural network model for the operational control of complex technical systems, based on the principle of two-level construction with the use of a supervisor at the upper level to control structural errors of the model and parametric adjustment of neural network models of system elements when changing the modes of its operation at the lower level.

2 Methods for Managing Complex Technical Systems

The following main approaches to the management of complex technical systems can be distinguished: management based on expert assessments, management using a system model, a combination of these approaches.

The essence of the method of expert assessments is that experts conduct an intuitive-logical analysis of the problem with a quantitative assessment of judgments and formal processing of the results. The generalized opinion of experts obtained as a result of processing is accepted as a solution to the problem. When controlling on the basis of a model obtained in advance and verified by the results of normal operation of the control object in an accelerated, machine-like, time scale, the model parameters are repeatedly changed [3].

Complex systems tend to involve greater responsibility for decisions within their control loop. To increase the reliability of the decision to control such a system, it is possible to use a combination of model control and control based on expert assessments. In this case, with the help of a computer experiment on the model, multiple variations of the controlled parameters of the model are carried out, and then the expert decides on the choice of the final control action [4].

Let us single out two classes among the approaches to modeling complex technical systems: traditional modeling methods and neural network methods for modeling systems.

The traditional methods of modeling systems include: simulation modeling, correlation analysis and regression analysis [5].

Among the neural network architectures for modeling systems, consider the following: multilayer perceptron, generalized feedforward networks, Jordan and Elman networks, recurrent networks with a time delay, Hopfield associative memory, self-organizing feature maps, radial basis functions, principal component analysis, adaptive resonance theory [6].

3 Development of a Combined Neural Network Method and Models for Operational Control of Complex Technical Systems

In the general case, the implementation of modeling is associated with the solution of a number of scientific and technical problems: the identification of objects, the choice of the type of model, the construction of models and their computer implementation, the interaction of the researcher with the model during the experiment, and others.

One of the main requirements for a model is its adequacy to a real system, which is achieved through the use of models with different levels of detail, depending on the features of the structural and functional organization of the system and the objectives of the study [7].

One of the ways to solve the problem of modeling a complex technical system is the decomposition of such a system into relatively simple components and their study, taking into account their interaction [8].

To apply this method, it is necessary, first of all, to make sure that the system can be decomposed into parts, and there is a possibility of sufficiently accurate modeling of each element of the system, then build adequate models of these elements and combine them into a single model of the system.

The need for modeling in the operational management of complex technical systems is due to the complexity of the control object, large financial and time costs, and sometimes the impossibility of its direct study [1, 2].

Usually system modeling is broken down into the following steps:

1. Gathering information about the system.
2. Allocation of elements (subsystems) of a complex system.
3. Visual modeling of the structure of the system (formation of a logical model of the system).
4. Simulation of the system based on systems of equations (formation of a parametric model of the system).
5. Modeling a complex system based on neural network models of its elements (formation of a compositional neural network model).
6. Modeling a complex system using a single neural network (formation of a neural network model-supervisor).

For the implementation of all stages of the method and the construction of logical, parametric and hierarchical compositional neural network models, the corresponding specialized software modules are being developed.

As a result of using the proposed method, a hierarchical compositional neural network model is created, designed for modeling, assessing the state and predicting the state of a technical system in real time.

Intermediate stages of modeling are used to build a compositional neural network model capable of giving an operational forecast about the state of a technical system in real or pseudo-real time.

The proposed combined method for modeling a complex technical system can be displayed in the form of a diagram presented in Fig. 1 [9, 10].

We describe the main steps of the algorithm in more detail.

Gathering Information About the System. This stage is important for the successful modeling of the system. Errors made when collecting information can nullify all efforts to obtain an adequate result from the model [11, 12]. To successfully build a model of a complex technical system, you need to collect and systematize the following information:

- about the structure of the system;
- about possible states of the system;
- about the inertia of the system;
- about the hierarchy of the system;

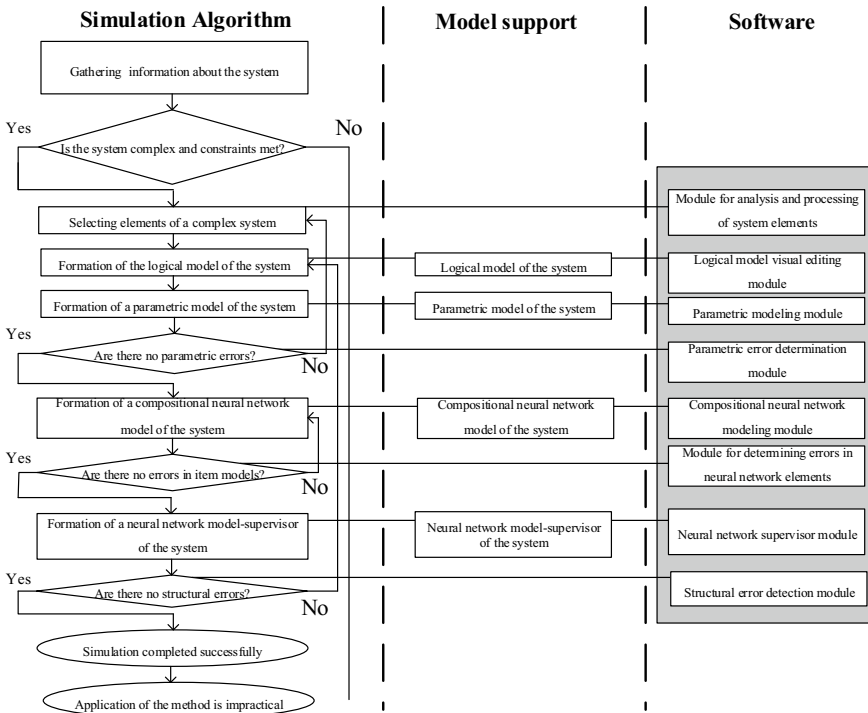


Fig. 1 Stages of a combined neural network method for modeling complex technical systems

- about the elements that are constituent parts of the system;
- about the relationships between the elements of the system;
- about the properties of the modeled system;
- about the characteristics of the environment that affect the functioning of the system.

To collect this data, knowledge about the regularities of the functioning of the system, available data from environmental monitoring stations, reference data are used; the necessary experimental studies are planned and implemented [13, 14].

Checking the system for the applicability of the modeling method. After collecting the initial data on the modeled system, it is necessary to determine whether it meets the criteria of a complex technical system and whether the proposed modeling method is applicable to it.

From the characteristics of a complex technical system, the following signs follow, by which it is possible to determine the applicability of the modeling method.

First, the system under consideration can be decomposed into a finite number of parts - subsystems. The upper subsystems can be thought of as systems for the lower level subsystems.

Secondly, the system is an integral complex of interconnected and interacting components. In this case, the subsystems considered earlier pass, as it were, into the category of the external environment, that is, for the subsystem under consideration, we have input signals determined by the previously considered subsystem.

Thirdly, the system forms a unity with the environment of functioning, that is, it is subject to influences from the environment and itself influences it [15].

Selecting Elements of a Complex System. Using the collected data, a complex technical system can be decomposed into a finite number of subsystems; each such subsystem (of the highest level) can, in turn, be decomposed into a finite number of simpler subsystems, etc., up to obtaining subsystems of the lower level - elements of a complex system that are either objectively not subject to decomposition, or can be described system of equations with sufficient accuracy [3].

Building a Compositional Neural Network Model of a Complex Technical System. To ensure the operation of the system model in real time, each of its elements is described by a separate neural network, representing the neural network model of the system element.

The inputs and outputs of such neural network models are connected in series based on the incidence matrix obtained earlier.

Another advantage of using neural networks to describe system elements is the ability to use additional data about the elements without a complex mathematical description of the mutual influence of these data [6, 7].

As such additional data, you can use the time of operation of the element, the number and type of recorded breakdowns, additional difficult formalized data on the state of the environment, etc.

An algorithm for the process of preparing neural network models of elements and forming a compositional neural network model is shown in Fig. 2.

To form a library of neural network models of system elements, neural networks, which are the basis of these models, must be trained and simulate the behavior of the corresponding elements with sufficient accuracy.

The training is carried out by the method of back propagation of the error [8].

For the initial training of neural network models, it is necessary to use the results of solving equations for various initial conditions.

Such training allows to establish only the basic boundaries for the neural model and is not able to train the neural network model to the required accuracy.

To obtain a neural network model of a complex system, the elements represented by neural network models must be connected in accordance with the visual model of the system, and, therefore, the incidence matrix in such a way that the output parameters of the previous neural network model are used as input parameters of the next model. Consequently, the inputs of the resulting system will be the inputs of the first elements, and the outputs will be the outputs of the latter.

The resulting compositional model, due to the neural network representation of its elements, is suitable for use in real time [13].

To ensure the required accuracy of modeling, additional training (fine tuning) of neural network models of system elements included in the compositional model

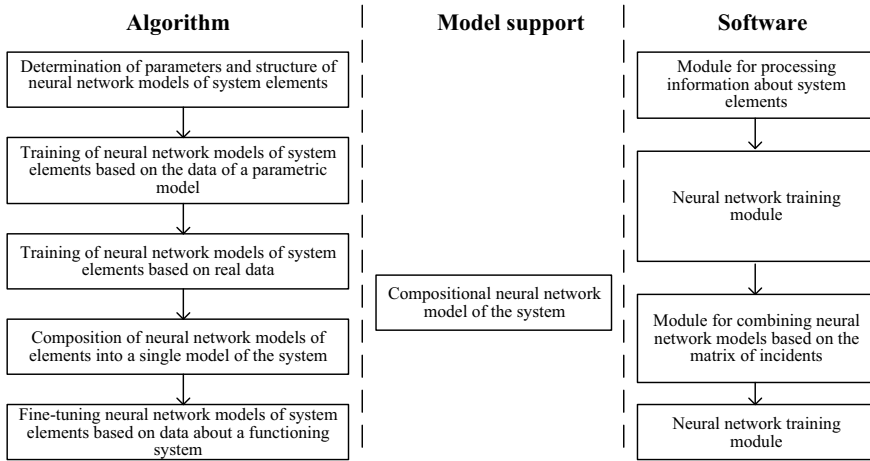


Fig. 2 Algorithm of the process of constructing a compositional neural network model of the system, the required model support and software

should be constantly carried out using real data on the functioning of a complex technical system and information about the state of the environment.

As a result of training on the basis of real data, we will receive trained classes of neural network models suitable for use as plug-in elements for structural changes in the model of a complex technical system [9].

To check the correctness of training neural network models, it is necessary to use additional data sets to check the correctness of training, as well as to compare the resulting technological parameters with the maximum permissible for a given simulated element of the system [10, 11].

If the results of modeling go beyond the boundaries of technological parameters, the stage of forming the library of neural network models should be repeated.

The correctness of connections between neural network models is quite difficult to check without special tools. This can be a supervisor neural network.

The algorithm for the process of building a neural network supervisor is shown in Fig. 3.

The inputs of such a network are the input parameters of all neural network models, and the outputs are the output parameters of the system.

With the correct connection of all structural parts of the compositional model, the outputs of the last structural element should coincide with the outputs of the supervisor [9, 13].

It is difficult to use such a neural network model as the main one in a situation of constant changes in the structure of the system, but by retraining it at specified intervals, it is possible to identify the appearance of errors in connecting elements in a system which formed by simple neural network models [14].

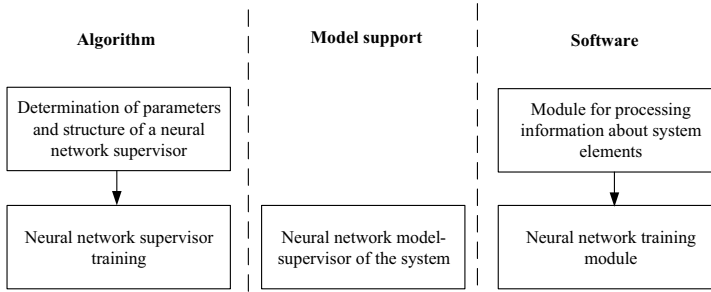


Fig. 3 Algorithm of the process of constructing a neural network supervisor of the system model, the required model support and software

For the practical implementation of the developed methods of combined neural network modeling of complex technical systems, as well as support for decision-making in the operational management of complex technical systems, software tools have been developed for the construction and use of the necessary model support [15].

Software tools for combined neural network modeling and decision support have been developed for the operational management of complex technical systems, including:

- module for analyzing system elements, designed for processing data about system elements, regression analysis of the influence of a parameter on the functioning of elements, forming a database on the parameters of elements;
- logical modeling module designed for visual editing of a logical model, forming a matrix of incidents for a logical model;
- module of parametric modeling, designed for constructing systems of equations, solving systems of equations, determining parametric errors;
- module for building, training and using a compositional neural network model, designed to build neural network models, combine (composition) neural network models based on the matrix of incidents, train neural network models, determine errors in neural network modeling;
- module for building, training and using a neural network - supervisor, designed to build a neural network - a supervisor, train a neural network - a supervisor, identify structural errors of a compositional neural network model;
- decision support module based on data obtained from the compositional model.

4 Conclusion

As a result of the study, the goal was achieved and the scientific problem was solved, which consists in the development and study of a combined neural network method, models and modeling tools for the operational control of complex technical systems.

The analysis of existing methods, models and software for operational management of complex technical systems is carried out; the requirements for the developed methods, models and software tools for managing these systems have been substantiated.

A combined neural network method for modeling complex technical systems based on a hierarchical neural network model is proposed, which combines the capabilities of analytical and neural network approaches and makes it possible to significantly increase the efficiency of operational management (quality and efficiency of management decisions), as well as the flexibility of modeling and the possibility of operational management of calculation of structural and parametric optimization of the model based on information about the system obtained in real time.

A hierarchical neural network model for the operational control of complex technical systems has been developed, consisting at the lower level of a set of interconnected neural network models corresponding to the elements of the modeled system, and a supervisor at the upper level, designed to identify structural errors at the lower level of the model.

A method of decision support for managing complex technical systems in real and pseudo-real time is proposed, based on the proposed hierarchical neural network model.

Software tools for combined neural network modeling and decision support have been developed for the operational management of complex technical systems, including:

- module for analyzing system elements, designed for processing data about system elements, regression analysis of the influence of a parameter on the functioning of elements, forming a database on the parameters of elements;
- logical modeling module designed for visual editing of a logical model, forming a matrix of incidents for a logical model;
- module of parametric modeling, designed for constructing systems of equations, solving systems of equations, determining parametric errors;
- module for building, training and using a compositional neural network model, designed to build neural network models, combine (composition) neural network models based on the matrix of incidents, train neural network models, determine errors in neural network modeling;
- module for building, training and using a neural network - super-visor, designed to build a neural network - a supervisor, train a neural network - a supervisor, identify structural errors of a compositional neural network model;
- decision support module based on data obtained from the compositional model.

References

1. Law AM, McComas MG (2001) How to build valid and credible simulation models. In: Proceedings of the 2001 winter simulation conference, pp 22–29
2. Perakath B (2000) A model-based approach for component simulation development. In: Proceedings of the 2000 winter simulation conference, pp 1831–1839
3. Kryzhanovsky BV, Litinskii LB, Mikaelian AL (2004) Vector-neuron models of associative memory. In: Proceedings of international joint conference on neural networks, Budapest, pp 909–1004
4. Carson JS (2002) Model verification and validation. In: Proceedings of the 2002 winter simulation conference, pp 52–58
5. MacGarry K, Wermter S (1999) Hybrid neural system: from simply coupling to fully integrated neural network. *Neural Coupling Surv* 2:62–93
6. Majors M, Stori J, Cho DI (1994) Neural network control of automatic systems. *IEEE Control Syst* 14(3):31–36
7. Pavlovsky YuN, Belotelov NV, Brodsky YuI (2008) *Simulation modeling*. M.: Academy
8. Moser JG (1992) Integration of artificial intelligence and simulation in comprehensive decision - support systems. *Simulation* 47:6
9. Fujimoto RM (2003) Distributed simulation systems. In: Chick S, Sánchez PJ, Ferrin D, Morrice DJ (eds) Proceedings of the 2003 winter simulation conference, pp 124–134
10. Girossi F, Jones M, Poggio T (1995) Regularization theory and neural networks architectures. *Neural Comput* 7:219–269
11. Beck MB et al (1993) Construction and evaluation of models of environment system. *Modeling Change in Environmental System*, Chichester
12. Bagrodia R, Meyer R et al (1998) Parsec: a parallel simulation environment for complex systems. *IEEE Comput* 31(10):77–85
13. Balci O (1986) Credibility assessment of simulation results. In: Proceedings of the 1986 winter simulation conference, pp 39–44
14. Diamantras KI, Kung SY (1996) *Principal component neural networks*. Wiley, New York
15. Fogel D, Fogel L, Porto V (1990) Evolving neural networks. *Biol Cybern* 63:487–493

Assessment of the Vulnerability of Architectural Monuments to Dangerous Natural Processes



Elena Arefyeva , Larisa Gorina , and Ekaterina Alekseeva 

Abstract Objects of the cultural heritage of the Republic of Tatarstan are under the negative impact of natural and man-made factors. According to experts, as well as statistical data, the state of the state-protected architectural monuments of the Republic is characterized as satisfactory. Exogenous geological processes play the main role in their destruction. The dynamics of the development of such processes in the historical territories of the republic testifies to the need to develop a rational solution in order to increase the sustainability of architectural monuments. The prevailing danger in built-up historical areas is the flooding of cultural heritage sites, initiating karsts, landslides, erosion, etc. The use of standard drainage methods in historical areas can lead to destruction and deformation of architectural monuments. In the work, the authors propose the use of a criterion - the threshold of hydrogeological danger, the critical level of groundwater, which is determined for each object and section of the built-up area. In order to determine the critical and limiting levels of groundwater for various buildings, a typology of objects was developed depending on the properties of the bases and the material of the foundation. This typology makes it possible to determine the critical and limiting levels of groundwater and drainage rates, taking into account the depth and base material of the foundations of architectural monuments, will also allow to approach each object individually when developing dewatering measures, which must be carried out in relation to objects of high cultural and historical value.

Keywords Historical and cultural territories · Monuments of history and culture · Dangerous natural and techno-natural natural processes · Hazardous natural processes · Cultural layer of the earth · Vulnerability of objects · Stability of objects · Increasing the stability of objects

E. Arefyeva · E. Alekseeva (✉)

Kazan National Research Technical University Named After A.N. Tupolev-KAI, K. Marksa Street, 10, 420111 Kazan, Russia

L. Gorina

Togliatti State University, Belorusskaya Street, 14, 445020 Tolyatti, Russia

1 Introduction

The problem of preserving architectural monuments dates back more than a decade. Thousands of specialists in various fields of science around the world are engaged in the support, restoration and reconstruction of cultural heritage monuments. Specialists in the field of engineering geology and geotechnics occupy a special place among them. This is due to the fact that the ancient architects, guided by the principle of “as measure and beauty will say”, chose places for construction that are currently exposed to dangerous natural and techno-natural processes. The structures, which were destined to stand hundreds, and sometimes many hundreds of years from the date of construction, have recently been particularly affected by various negative processes that negatively affected their safety. Observations of the state of architectural monuments in the Republic of Tatarstan show that such objects are highly susceptible to destruction as a result of adverse natural influences [1]. These impacts negatively affect the preservation of cultural heritage sites, and lead not only to their destruction, but also to their possible loss. Exogenous geological processes (EGP) pose the greatest threat to cultural heritage sites. To date, the following types of EGP are developed on the territory of the Republic of Tatarstan: gully erosion, landslide processes, karst-suffusion processes, subsidence phenomena, as well as the process of flooding. Architectural monuments and historical areas affected by EGP are becoming increasingly vulnerable to climate change. Therefore, it is required to develop management decisions that increase the resistance of such objects to EGP. To obtain management decisions, mathematical modeling is used, a methodology has been developed and software has been developed. The geofiltration equation (the Boussinesq equation) with the corresponding boundary and initial conditions is used as a basic model describing the flooding process.

2 Materials and Methods

2.1 Analysis of the Main Dangerous Natural Processes on the Territory of the Republic of Tatarstan

One of the most large-scale and active modern relief-forming processes on the territory of the Republic of Tatarstan is gully erosion. The area occupied by the ravines is 41.8 thousand hectares. The study of the dynamics of the development of ravines showed that a significant part of the ravines has reached the limit of its development and is in the stage of stabilization [2]. Most (up to 60%) stable ravines are in the Predkamye (geographical area of the Republic of Tatarstan). About 10% of the ravines are classified as growing. If earlier the main reason for the formation of ravines was the agricultural activity of people (the expansion of arable land), now the share of ravines is increasing due to the construction of roads, pipelines and new housing in settlements.

The total area of development of landslides in the Republic of Tatarstan is 0.28% of the total area of the territory, since landslides are mainly actively developing in the narrow coastal strip of the Kuibyshev and Nizhnekamsk reservoirs. The intensity of the development of the landslide process is determined, first of all, by geological, geomorphological and hydrogeological conditions [3]. Areas with an active development of the landslide process are most often confined to the ravine and coastal slopes of the Kuibyshev and Nizhnekamsk reservoirs, with steepness from 100 to 300, composed of clays and marls, with interlayers and lenses of watered sands. The largest old landslide manifestations on the coastal slopes of reservoirs are in a stable state, and 15–20% are in the stage of periodic activation. This applies to landslide bodies identified in the towns of Tetyushi, Chistopol, and urban-type settlement Kamskoe Ustye and Rybnaya Sloboda. The development of ravine erosion, and with it the landslide process in the middle part of ravines (expansion of ravines) under the influence of anthropogenic load, is typical for Kazan, Chistopol, Tetyushi, urban-type settlement Kamskoe Ustye. The trigger factor for the formation of landslides is most often a change in hydrological and hydrogeological conditions on the territory of a settlement [4].

Also, with an increased amount of spring precipitation, the activity of the landslide process in local areas of Kazan, Chistopol, Tetyushi, urban-type settlement Kamskoye Ustye was marked by a high activation of the process.

The area of development of karst-suffusion processes is only 0.15% of the total area of the Republic. The total area of variously karst territories is about ~25% of the territory of the Republic. Kazan, Almetyevsk, Zelenodolsk, Urussu and other towns fall into the emergency zone from the karst process. Many karst researchers believed that with the rise of the Kuibyshev reservoir, karst-suffusion processes in the zone of influence of the reservoir should attenuate, since the basis of erosion will decrease, and in some areas the karst thickness will be below the flooding level [5]. But the example of the Pre-Volga region (geographical area in Russia) of the Republic shows the opposite picture, for the period from 1997–2005 there were 5 major failures. The nature of the activation of karst-suffusion processes in the Pre-Volga region, apparently, is associated with significant and constant fluctuations in the level of the Kuibyshev reservoir. A new karst sinkhole was recorded in the Buinsky district in the autumn of 2017.

In an explicit form, the process of flooding and waterlogging in the territory of the Republic is less pronounced and therefore has an indicator of an average degree of damage (2.01%). However, flooding initiates a number of other dangerous exogenous processes, and also leads to a decrease in the bearing capacity of the soil of the foundations of structures, subsidence phenomena. Therefore, the zoning of the historical territories of the Republic of Tatarstan for flooding is a priority task.

Currently, in the coastal strip of the Kuibyshev reservoir, the ground water mirror has risen in the area of the cities of Zelenodolsk by 8–9 m, Kazan – by 11 m, Bolgar – by 18 m. Along the Kama River, the rise in the ground water level was 10 m near the town of Chistopol, near the mouth of the river. Vyatka – 7.5 m, along the Vyatka River near Mamadysh – 4 m. The territories of the towns of Mamadysh

are particularly susceptible to flooding. Kazan and Zelenodolsk, located on the first above-floodplain terrace of the Volga.

Local areas in Kazan (Druzhba settlement, Pervomaysky settlement), Tetyushi and Chistopol (city center) are susceptible to technogenic (anthropogenic) flooding. Such areas of local flooding are associated with violations of the hydrological and hydrogeological regime in the city as a result of economic activities [6].

2.2 Analysis of the Vulnerability of Architectural Monuments and Historical Territories of the Republic of Tatarstan to Dangerous Natural Processes

Currently, there is a significant increase in the anthropogenic load on the geological environment [7] near historical territories, due to: an increase in the density of building and the complication of the urban structure, the growth of cities and settlements “up” and “down”, conflict situations of development [8].

Analyzing the list of hazardous natural processes typical for the territory of the Republic of Tatarstan, as well as the general features of engineering and geological conditions, we can say that Kazan, Tetyushi, urban-type settlement Kamskoye Ustye, where buildings from the seventeenth century to our time are presented, are subject to a large extent to EGP.

These settlements in 2000, by a resolution of the Cabinet of Ministers of the Republic of Tatarstan, were included in the List of Historical Places of the Republic of Tatarstan, which have architectural monuments, urban planning ensembles and complexes that are monuments of history and culture, as well as preserved natural landscapes and an ancient cultural layer of the earth, representing archaeological and historical value.

Here are some typical examples of the violation of the general state of architectural monuments of the Republic during their flooding, which resulted in various EGP in the form of karsts, landslides and soil erosion [9, 10]. In particular, the Bolgar State Historical and Architectural Museum-Reserve and the State Historical and Architectural Museum-Reserve (Bolgar) and the Kazan Kremlin Art Museum-Reserve (Kazan), for which the federal protection category is established, have a significant negative impact due to flooding by groundwater. And moderate flooding occurs on the territory of the Yelabuga State Historical, Architectural and Art Museum-Reserve (Yelabuga).

Another example, after the creation of the Kuibyshev reservoir, the frequency of karst sinkholes increased in places of their former manifestation in the historical part of the city of Kazan on Ostrovsky Street, Sverdlov Street, Butlerov Street, on the lake Sredniy Kaban, in the Observatory, Kremlevskaya Street, as well as the sinkholes under the “Passage” building near the Black Lake Park.

In the area of Zilant Mountain (Zilantovaya Gora), there was also a karst sinkhole, where the Zilant (Zilantov) Monastery (1681, rebuilt in the XVIII-XIX centuries) is located - an object of cultural heritage of regional significance.

So in 2010, as a result of the formation of karst, a collapse of soil occurred on The 1st of May Square near the walls of the Kazan Kremlin. As a result, the water supply was damaged. To find out the reasons and prevent further soil collapse, the asphalt pavement had to be opened. As it turned out, the water pipe with a diameter of 150 mm was damaged by soil. Due to the fact that the historical part of the city is located on the hills, in particular, the Kremlin, there are karst cavities, the waters of the Volga and its tributary, the Kazanka River, and are close. This also caused the inclination of the Söyembikä Tower on the territory of the Kazan Kremlin.

The most dangerous processes that increase due to climate change [11, 12] and the exposure of historical territories to these processes are shown in Table 1.

Table 1 Exposure of historical territories of the Republic of Tatarstan to exogenous geological processes

EGP type	EGP area from the entire area of the Republic of Tatarstan, %	Most affected settlements/areas	Exposure of individual architectural objects of the Republic of Tatarstan to EGP
Landslide	0.28	Kazan, Tetyushi, Chistopol; urban-type settlement Kamskoye Ustye and Rybnaya Sloboda	Hotel of the Noble Assembly, The Molostovs' estate in Dolgaya Polyana village
Karst-suffusion	0.15	Kazan, Tetyushi, Almetyevsk, Zelenodolsk, Urussu, Buinskiy district	Museum-reserve "The Kazan Kremlin", Bell towers of Saints Peter and Paul Cathedral and Saint Nikolsky Cathedral, Zilantov monastery, Alexandrovsky Passage, Bell towers of Saint Nikolsky Cathedral and Saints Peter and Paul Cathedral
Flooding and waterlogging	2.01	Kazan, Bolgar, Tetyushi, Chistopol, Yelabuga, Mamadysh, Zelenodolsk	Historical center of Chistopol, Bolgar Museum-Reserve, Museum-reserve "The Kazan Kremlin", Yelabuga State Historical, Architectural and Art Museum-Reserve, Volga-Kama Nature Reserve

Considering that not only architectural monuments, but also archaeological monuments are located in historical territories, the use of approaches for dewatering (in case of flooding), acceptable for conventional built-up areas, needs some adjustment, taking into account the specifics of the territories.

2.3 Methods for Developing a Rational Solution Aimed at Increasing the Resistance of Architectural Monuments and Historical Territories to Dangerous Exogenous Processes

EGP action on historical territories creates a high potential danger for architectural objects and increases their vulnerability in the zone of influence of these processes. This predetermines the need to develop a rational solution for the organization of preventive and protective measures aimed at increasing the stability of objects.

As shown in, in built-up areas, the main unfavorable process is groundwater flooding of territories and structures. Flooding, being a latent, hidden process, initiates other dangerous exogenous processes, such as landslides, karsts, subsidence, etc. The usual protective and preventive measures used against flooding and restoring the ecological balance of the territory are various types of drainages, waterproofing systems, and systems for regulating surface runoff. But there is one significant nuance in the application of standard drainage methods in historical areas. Namely, the presence of a cultural layer for which water is a preservative. The cultural layer contains unique archaeological exhibits and is the most valuable archaeological material, and moist soils ensure the preservation of objects of the cultural layer. In addition, the moisture content of the soil ensures the safety of the wooden base, and its drainage leads to rotting and additional deformations and destruction of buildings.

On the other hand, for the operation and preservation of buildings, the building itself, the basement and other buried premises, as a rule, must be dry. And the use of standard drainage measures leads to even greater deformations due to the destruction of the wooden base and the loss of an invaluable cultural layer [13]. So, drainage can cause a negative drainage effect, suffusion, subsidence of the surface, overdrying of the soil and further deformation of buildings.

An important solution for soft regulation is the use of a criterion - the threshold of hydrogeological danger, the critical level of ground water, determined for each object and part of the built-up area. The presence in built-up areas of objects with different requirements for ensuring their safe operation (degree of drainage), also due to different depths of basements, the presence of a cultural layer, led to the need to develop criteria for optimal drainage and derive dependencies for critical (H_{kr}) and limit (H_{pr}) groundwater levels: formalized requirements to avoid going over the upper boundary, as well as requirements not to go beyond the lower boundary (for a wooden base of a building ($H_{br/pr}$)). Exceeding the limit is a warning of a hazard, and the critical is already a danger [14].

To determine the critical and limiting levels of groundwater for various buildings, a typology of objects was developed depending on the properties of the foundations of the foundation and the material of the foundation [15].

In the historical territories, 4 main classes of objects were identified according to the requirements for drainage: these are objects that allow and do not allow a humid state of buried structures and basements, and among these groups there are objects located on a stone or wooden base (Fig. 1).

The typology of objects performed by the properties of foundations made it possible to determine the critical and limiting levels of groundwater and drainage rates, taking into account the depth and material of the foundations of the objects, the presence of basements, the effective zone of the capillary border, and the seasonal excess of levels. It is important that fluctuations in the groundwater level relative to the critical level do not exceed the effective height of the capillary rise, within which the soil is saturated with water and ensures the preservation of the cultural layer and the wooden base. The flexibility of regulation provides the condition for the groundwater level to be within the capillary border zone.

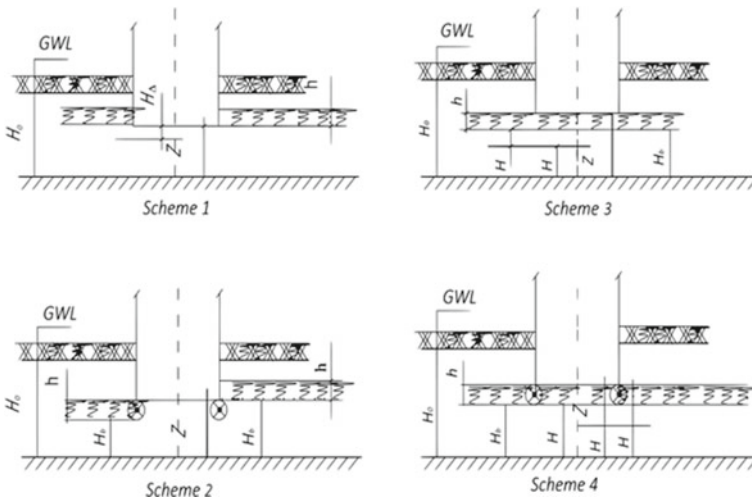


Fig. 1 Schematic representation of different types of building foundations in historical areas. Scheme 1 - the object admits humidification, but not flooding of the basement, the foundation is located on a stone foundation; Scheme 2 - the object allows humidification, but not flooding of the basement, is located on a wooden base; Scheme 3 - the object does not allow humidification, the foundation is located on a stone foundation; Scheme 4 - the object does not allow humidification, is located on a wooden base. Where H_n - limiting groundwater level (GWL) for objects (upper limit), H_{br} - limiting groundwater level for the wooden base of the building; H_o - the first level; Z_n - distance to the foundation from the water barrier; H_n - capillary border; H_n – permissible range of level fluctuations for the object, $H_{n+(-)}$ excess (decrease) over the average annual level). *Source* [10]

For solutions of flexible regulation of the groundwater regime, mathematical modeling has been carried out, a software and computer complex has been developed. The software and computer complex is based on a method for solving extreme problems to determine the parameters for regulating the groundwater regime, which allow maintaining the groundwater level in the permissible safe range, with minimal drainage of the cultural layer and maximum drainage of the soils of the foundations of structures. The calculation of the groundwater level with control parameters (drainage, pumping specified in the form of boundary conditions and a source function with an opposite sign) is performed using the Boussinesq equation (this is a parabolic partial differential equation, on the basis of which geofiltration with the corresponding boundary and initial conditions is simulated). The optimal criterion is the volume of the drained prism of the cultural layer and the drained area of the buried premises. Optimization criteria are formulated in the form of functional. The minimization of the functional determines the degree of proximity of the calculated reduced values of the ground water level with the help of control actions to the set value. The optimal solution that provides the minimum functionality of the optimization goal and is the desired optimal control parameter, which physically corresponds to the selected position of the drain or the pumped volume of water.

To develop optimal solutions by regulating the groundwater regime, an appropriate technique has been developed. The technique includes a sequence of actions: introduction of initial information about the protected object, setting the boundaries of the area, initial and boundary conditions; fulfillment of the predicted position of the groundwater level (solution of the direct problem of geofiltration) and calculation of optimization criteria; determination of the optimal position of the groundwater level; determination of the optimal position of drains, their mode of operation and calculation of optimization criteria for the foundation of the building and adjacent soil (cultural layer); the choice of a compromise option (in the case of two opposite criteria - the Pareto solution); visualization of the result, comparison of different variants of the obtained solutions.

The quality of regulation of the groundwater regime is described by a criterion - a functional that must be minimized on the set of calculated values of the groundwater level that satisfy the selected model - differential equations describing the filtration process to drains and a number of restrictions - inequalities determined by the limiting or critical levels for objects and territories: [10]

$$J^l(h, u) = J_n^l + J_k^l, l = 1, 2, \dots \quad (1)$$

where J_n^l – the functionality responsible for the non-flooding of the object;

$$J_n^l = A^h \int_Q (h(x, T, u) - h_n(x))^2 dx \quad (2)$$

where A^h – some weighting factor; Q – area of integration (in the linear case, $Q = (x_1, x_2)$ is the location of the drains); $h(x, T, u) - h_n(x, T, u)$ - the groundwater level

obtained as a result of calculations with the regulating parameter u ; T – the time by which it is required to carry out water reduction; u – regulation vector (adjustable drain parameters - depth, water flow in them); $h_n(x)$ – function of the permissible groundwater level for the object;

J_k^l – functional responsible for preventing the exit of the GWL beyond the lower boundary:

$$J_k^l = A_{k1}^h \int_{Q1} (h(x, T, u) - h_k(x))^2 dx + A_{k2}^h \int_{Q2} (h(x, T, u) - h_k(x))^2 dx, \quad (3)$$

where A_{k1} , A_{k2} - some weighting factors; $h_k(x)$ – function of the permissible groundwater level to ensure that it does not go beyond the lower boundary.

Minimization of the functional $J(h, u)$ determines the degree of proximity of the calculated lowered values of the groundwater level with the help of regulating actions to a given position, and with the condition of the presence of an admissible limiting lower boundary, ensures that the GWL does not go beyond the lower boundary.

In this case, the dynamics of the groundwater level is described by the one-dimensional or two-dimensional Boussinesq equation.

3 Results

The results of applying this approach can serve as a basis for making decisions on preventing emergencies, improving environmental safety during flooding for various objects of the technosphere, including objects of high cultural and material value, potentially dangerous and critical objects in the Republic of Tatarstan.

The developed typology of objects according to the admissibility of the level of humidification will allow to approach each object individually when developing water reduction measures, which must be carried out in relation to objects of high cultural and historical value (Fig. 2).

In the case of opposite drainage requirements, the compromise position of the drainage depth is determined by the intersection of the curves of the functional of the optimization criteria for the object and the cultural layer (for the test example).

Figure 3 shows a graphical solution for determining the optimal position of the drain (for a test example), providing optimal values for the optimization criteria.

The point of intersection of the curves describing the criteria of an architectural monument and the criteria responsible for the preservation of the cultural layer shows the optimal position of the drain in depth.

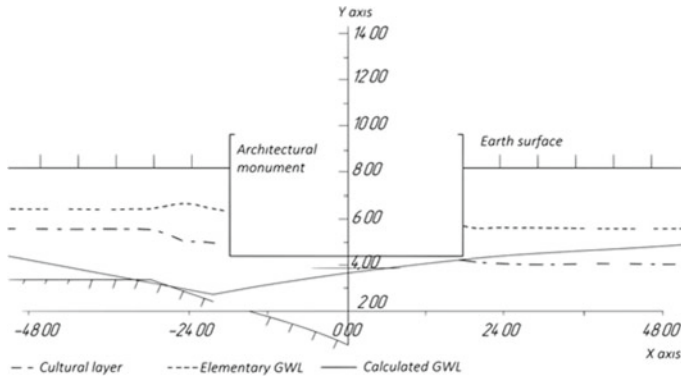
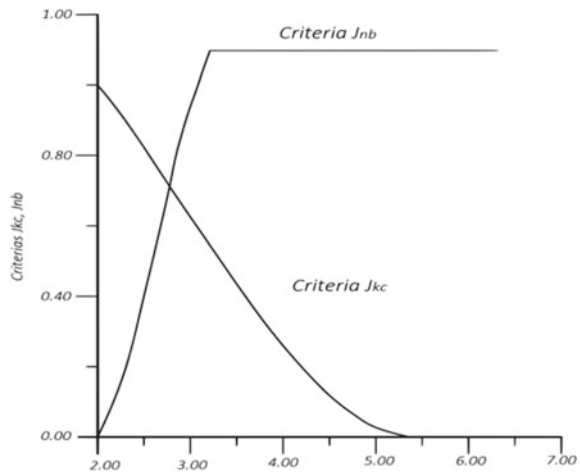


Fig. 2 Variant of calculation of drainage systems for an architectural monument. — initial groundwater level; - - - - the level of the cultural layer; - drawdown curve. *Source* [10]

Fig. 3 Determination of a rational solution - the optimal position of the drain, ensuring the minimum drainage of the cultural layer and the foundation of the building. *Source* [10]

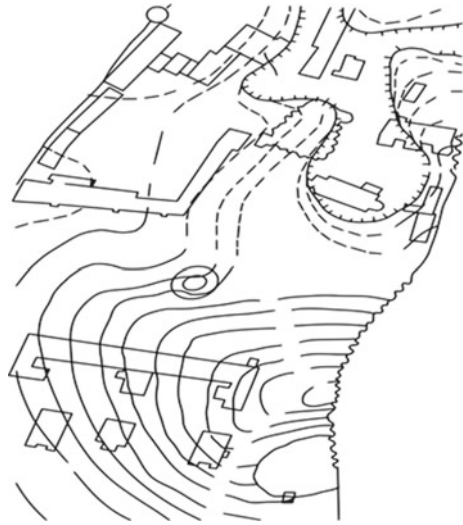


4 Discussion

The methods and algorithms proposed in the paper were used and tested as a justification for the development of design solutions for the prevention of emergencies on the territory of the Novgorod Kremlin.

So, for the flooded territory of the Novgorod Kremlin, the usual water-reducing works turned out to be unacceptable, since there are powerful layers of the cultural layer (the tenth century layer is located at a depth of 6.6 m, the eleventh century layer at a depth of 5.9 m, the fifteenth century - 1.4 m). The cultural layer contains unique archaeological exhibits and is the most valuable archaeological material. Moistened soils ensure their safety (Fig. 4).

Fig. 4 a) Fragment of a map of the contours of a water table of the territory of the Novgorod Kremlin; b) A variant of the calculation of drainage systems for the object of the Novgorod Kremlin. *Source* [10]



The methodology proposed in this paper supports the development of management decisions also in the presence of conflicting requirements for dehumidification standards and water reduction regimes.

5 Conclusions

Considering that the processes of flooding will only intensify due to climatic changes and initiate other hazardous exogenous natural processes in the territory of the Republic of Tatarstan, the relevance of applying the approach of optimal regulation of the groundwater regime in historical territories is beyond doubt. To increase the sustainability of architectural monuments and at the same time, ensuring the preservation of the cultural layer, it is advisable to carry out the calculations of drainage systems taking into account the compliance with the drainage norms specially defined for each architectural monument. Based on the calculated criteria reflecting the drainage of the architectural monument and the volume of the drained cultural layer, decision-makers determine a compromise option for the location of the drain.

References

1. Novoselov Yu, Bratan S, Bogutsky V (2016) Analysis of relation between grinding wheel wear and abrasive grains wear. *Procedia Eng* 150:809–814. <https://doi.org/10.1016/j.proeng.2016.07.116>

2. Anderson R, Rowntree K, Le Rouxa J (2021) An interrogation of research on the influence of rainfall on gully erosion. In: CATENA 206, p 105482. <https://doi.org/10.1016/j.catena.2021.105482>
3. Palamakumbura R, Finlayson A, Ciurean R, et al (2021) Geological and geomorphological influences on a recent debris flow event in the Ice-scoured Mountain Quaternary domain, Western Scotland. In Proceedings of the Geologists' Association, 10 June 2021. <https://doi.org/10.1016/j.pgeola.2021.05.002>
4. Thirarda G, Grandjean G et al (2020) Hydrogeological assessment of a deep-seated coastal landslide based on a multi-disciplinary approach. *Geomorphology* 371:107440. <https://doi.org/10.1016/j.geomorph.2020.107440>
5. Gutareva OS, Kozyreva EA, Trzhtsin'skiy YuB (2009) Karst under natural and technogenically modified conditions in Southern East Siberia. *Geogr Nat Resour* 30(1):40–46. <https://doi.org/10.1016/j.gnr.2009.03.009>
6. Morway E, Niswonger R, Triana E (2016) Toward improved simulation of river operations through integration with a hydrologic model. *Environ Model Softw* 82:255–274. <https://doi.org/10.1016/j.envsoft.2016.04.018>
7. Borella J, Quigley M, Riley M et al (2020) Influence of anthropogenic landscape modifications and infrastructure on the geological characteristics of liquefaction. *Anthropocene* 29:100235. <https://doi.org/10.1016/j.ancene.2020.100235>
8. Romanovsky VL, Alekseeva EI, Gorina LN (2020) Conducting a comparative analysis of the system state options under various external influences. *IOP Conf Ser Mater Sci Eng* 962:042035. <https://doi.org/10.1088/1757-899X/962/4/042035>
9. Makarov SA, My O (2009) Extreme manifestations of fluvial processes under natural-technogenic conditions. *Geogr Nat Resour* 30(1):21–25. <https://doi.org/10.1016/j.gnr.2009.03.005>
10. Gan F, He B, Qin Z, Li W (2020) Role of rock dip angle in runoff and soil erosion processes on dip/anti-dip slopes in a karst trough valley. *J Hydrol* 588:125093. <https://doi.org/10.1016/j.jhydrol.2020.125093>
11. Eisenhauer D (2020) Climate change; adaptation. In: *International Encyclopedia of Human Geography*, 2nd edn, pp 281–291. <https://doi.org/10.1016/B978-0-08-102295-5.10756-5>
12. Amanambuae A, Obareind O et al (2020) Groundwater system and climate change: present status and future considerations. *J Hydrol* 589:125163. <https://doi.org/10.1016/j.jhydrol.2020.125163>
13. Walsh-Korb Z, Avérous L (2019) Recent developments in the conservation of materials properties of historical wood. *Prog Mater Sci* 102:167–221. <https://doi.org/10.1016/j.pmatsci.2018.12.001>
14. Arefyeva EV, Muravyeva EV (2019) The issues of sustainability of historical and cultural areas associated with their periodic under flooding and solutions. In: *International Conference on Construction, Architecture and Technosphere Safety*. IOP Conf Ser Mater Sci Eng 687
15. Langridge R, Fencl A (2020) Implications of climate change to groundwater. In: *Encyclopedia of the World's Biomes*, pp 438–453. <https://doi.org/10.1016/B978-0-12-409548-9.12021-4>

Complex Assessment the Construction Works Quality Using BIM Technologies



Tatyana Rubailo , Marina Petrochenko , Anna Gorodishenina ,
and Yuri Lazarev 

Abstract The construction quality a complex issue. All construction process participants must follow national standards, rules and regulations. The article conducts a study of construction quality assessment, analysis of factors affecting its parameters and consideration of possibility to improve its quality by implementation of complex quality indicator. The main aim of this work is to form a methodology for obtaining and assessing a complex construction quality indicator, an efficiency improvement technical and organizational solutions. It was developed a mathematical model that allows to determine the impact of individual factors on the complex construction quality indicator. An automated control system for construction and installation works based on BIM technology was developed. The complex assessment and calculation algorithms allow to determine impact assessment of individual factors of construction works on the complex construction quality indicator. This method allows to unify the approach to the automation process of investment-construction projects and to establish a consistent approach on creation the integrated model of construction and installation work.

Keywords Construction and installation work · BIM · Construction quality assessment

1 Introduction

The concept of construction quality assurance implies the solution of a wide range scientific, practical and engineering tasks, as well as implementation a number of complex organizational and engineering measures aimed at implementation of investment and construction programs. It leads to an increase of economic potential and living conditions improvement.

Currently, in the context of constantly improving technologies, it is required to develop the new methods for quality assessment of construction materials and

T. Rubailo · M. Petrochenko · A. Gorodishenina (✉) · Y. Lazarev
Peter the Great St. Petersburg Polytechnic University (SPbPU), 29 Politechnicheskaya
street, St. Petersburg 195251, Russian Federation

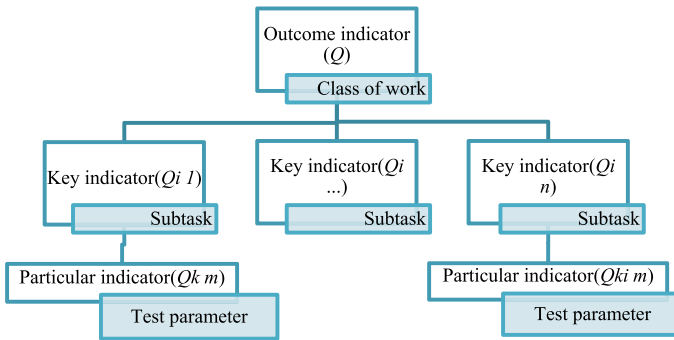


Fig. 1 Hierarchical structure of quality indicator system

construction compounds. It is necessary to adjust the construction standards base and implementation of new technologies for construction practice.

The basis of today's construction quality control system is the ISO 9000 series standard [1–3].

There is no common methodology for construction quality assessment in the industry, which would take into account the specifics of the factors affecting quality in general. Facility acceptance and control is carried out basing on compliance with the project requirements and standards in aggregate.

A. H. Baiburin proposed to assess the construction quality by evaluating the quality system of the construction itself, as well as the quality of technological processes applied in construction and installation works and the quality of structures [4–6]. Any of these factors includes several assessed factors. The block diagram for a comprehensive quality assessment of construction and installation work is shown in the Fig. 1.1 [7].

According to specialists, construction quality should be assessed on the following construction stages:

- during building design stage the following should be assessed: decisions made in the course of drafting projects, its constructability, implementation of project documentation, quality indicators, the company reputation developing the project;
- during construction stage, the following should be assessed: the process control system, the quality control in the company in accordance with which an analysis is carried out and manufacturing defects are detected, the presence or absence of a regulatory framework on the basis of which an assessment is made;
- at the stage of completion of construction the following should be assessed: work and services in facility acceptance, premarket maintenance and sale;
- during building operation stage, the following should be assessed: a thorough analysis and assessment of developed and implemented measures, which result in possibility to achieve lasting preservation of quality of constructed objects.

Modern information systems considerably solve the problem of construction quality assessment and increases the efficiency of interaction between constructing organizations [8–11].

BIM control tools are much more effective: model quality verification and volume uploading tools allow the customer to audit the model for possible bottlenecks (such as standards compliance, interdisciplinary checks), as well as quickly receive information about volumes, compare several design versions [12–18].

In this connection, it becomes necessary to introduce relevant automated technologies linked to BIM of 4D and 5D levels at the stage of construction quality control. Information technologies will help to organize construction successfully, significantly reduce the amount of human labor and digitalize paperwork.

2 Materials and Methods

The term ‘quality’ refers to two components: the standards compliance and the absence of defects. The quality of work performed during each construction stage affects the overall quality of constructed building. The implementation quality of an investment and construction project depends on the quality of each type of work.

In order to provide an integrated approach to construction management and ensure the quality of implementation using the information model, it is necessary to develop a methodology that meets the following aims:

- justification the methodological study scheme for assessing complex indicator of construction and installation works;
- selection, structuring and ranking factors influencing the quality of the object;
- creation the mathematical apparatus for determining the value of a multivariate criterion;
- formation the methodology for calculating a complex indicator of the construction and installation works quality;
- practical testing and implementation of proposed solutions based on real objects.

We determined the basic principles and approaches for managing the construction quality, which are supposed to be used in the formation a complex assessment of the construction quality [19]:

1. Systematic fundamentals – this methodological approach allows to define the tasking, the solution of which will make it possible to focus on quality in the work of construction control. This approach is based on step-by-step disaggregation of the problem into certain elements, followed by numerical evaluation of the importance of these elements.
2. Mathematical modeling methods and qualimetry – the assessment of the construction works quality is a certain essence of an object in the system a science as qualimetry, which studies the methods of quantitatively assessing the quality parameters for various objects, regardless their purpose.

The qualimetric analysis method consists of several stages:

- the required number of experts calculation, group selection;
- determination the object properties that affect its quality with its further structuring into a hierarchical tree, taking into account the weight characteristics of each object.
- Expert assessment methods – a complex of mathematical, statistical and logical procedures, the use of which allows to obtain data from experts, analyze and generalize it in order to determine the correct decision on the required issue.

3 Results and Discussion

In order to conduct a complex assessment the construction works quality, it is necessary to develop a mathematical model that allows to assess the quality of every particular work, and then to create a final complex assessment of each type of work [20]. Effectiveness evaluation of the construction and installation works is presented in the hierarchical structure form of the quality indicator system for general construction works in Fig. 1.

There are three hierarchical levels in this system:

- 1) Particular indicator Q_{ki} – describes compliance with the standards of the controlled parameter;
- 2) Key indicator Q_i – describes the quality of work;
- 3) Outcome indicator Q – describes overall work efficiency.

In order to validate the overall work efficiency assessment, we suggest to use quantitative characteristics in the context of two categories as part of the initial data, the current and reference state of the work performed.

At the first stage of efficiency calculation, the value of the relative particular indicators is determined based on the absolute values for the current and reference state of the work performed.

In the case when with an increase in a particular indicator, the efficiency of functioning increases, it is necessary to use the ratio of the current state to the reference state, in another case, the inverse value is used:

$$Q_{ki} = \begin{cases} \frac{q_{ki}}{q_{ki}^b}, & \text{if } \frac{\partial Q_i}{\partial q_{ki}} > 0; \\ \frac{q_{ki}^b}{q_{ki}}, & \text{otherwise.} \end{cases} \quad (1)$$

where:

Q_{ki} - particular indicator i type of work to the controlled parameter of k ;

q_{ki} - current status the work performed;

q_{ki}^b - reference status the work performed.

It is important to note the specific feature the calculating the Q_i value. It is necessary to take into account the correspondence the weight coefficient with the relative

particular indicator. Accounting for this dependence is regulated using thresholds or relevant values.

A detailed mathematical model based on a certain functional correspondence, allowing to obtain Q_i values:

$$Q_i = \sum_{k=1}^m Q_{ki} \cdot a_{ki} \quad (2)$$

\sum - the sum of all i properties, that characterize the assessed object quality;
 m - the total number of controlled parameters, that characterize the assessed work quality;

a_{ki} - a weighting coefficient, that determines the influence quantity the controlled parameter quality on the key indicator, the value is determined using expert assessments.

If the value of $Q_i \geq 0.8$ - the work quality is considered acceptable.

If the value is $0.5 \leq Q_i < 0.8$, corrections and improvements are required to ensure the appropriate work quality.

If the value of $0.5 \leq Q_i$ - the quality does not match, the work requires rework.

Thus, a complex assessment of the construction works quality (Q) is calculated by the formula:

$$Q = \sum_{i=1}^n Q_i \cdot b_{ki}; \quad (3)$$

$i = 1, 2, \dots, n;$

where:

Q_i – key indicator for quality assessment of one of the i control types;

\sum - the sum of all i properties, that characterize the assessed object quality;

n – the total number of works characterizing the quality of the assessed stage.

Let us consider the case applying the methodology for ensuring the quality of general construction works using a model for the concrete construction.

To ensure quality control based on the developed mathematical model, it is necessary to assign the controlled parameters (Table 1).

In order to create quality assessment sheets for the type of work under consideration, we use the cloud solution BIM 360 Field.

When creating a checklist template, we indicate: a work subtask (key indicator Q_i) with a list of test parameters (individual parameter Q_{ki}) and possible assessment value, then we add the next test parameters and sections (Fig. 2).

Further, based on the data obtained, using the developed mathematical model, it is necessary to calculate the key indicators with consideration to the weight coefficients for each work subtask and determine the outcome indicator.

As a result of expert survey, the controlled parameters for each type of work were assigned points on a scale from 0 - 5.

To determine the significance of each parameter, we calculate the weight each of them, from the point of view the impact on the complex quality indicator, within the

Table 1 Test parameters of concrete works

Outcome indicator (<i>Q</i>)	Key indicator (<i>Qi</i>)	Particular indicator (<i>Qki</i>)
Concrete works	A.Assembly of the reusable formwork	A1. Compliance the size dimensions the formwork with the design. A2. The formwork position relative to the alignment axes in plan and vertical, incl. the design marks designation of the top of the structure to be concreted inside the formwork surface. A3. Correct installation and reliability of strengthening plugs and embedded parts, as well as the entire system in general.
	B.Installation of reinforcement	B1. Compliance the position the installed reinforcement products with the design. B2. The size of the concrete cover. B3. Reliability of fixing reinforcement products in the formwork. B4. The quality of the frame nodes welding.
	C.Concrete laying	C1. Actual concrete strength. C2. The quality of structure surface, its geometric dimensions, compliance with the design position of the entire structure, as well as holes, channels, openings, embedded parts.

framework an extended mathematical model. To do this, we use the mathematical statistics principles - the variational method.

The base-line data for this method will be a statistical sample from Table 2.

This formula (4) allowed to calculate the arithmetic mean of the variation series at the first stage:

$$\bar{u} = \frac{1}{m} \sum_{k=1}^m \frac{y^k}{\sum_{k=1}^m y^k}$$

1 QA_Assembly of the reusable formwork		3 Items
Add description (optional)		
1.1 QA1_Compliance of the size dimensions of the formwork with the design		Numeric
Description:		
Estimate the relevance of the controlled parameter to the standard from a scale of 0 to 1		
<input type="text" value="Type a number"/>		
1.2 QA2_The position of the formwork relative to the alignment axes in plan vertical, incl. designation of the design marks of the top of the structure to be concreted inside the formwork surface		Numeric
Description:		
Estimate the relevance of the controlled parameter to the standard from a scale of 0 to 1		
<input type="text" value="Type a number"/>		
1.3 QA_Correct installation and reliability of strengthening plugs and embedded parts, as well as the entire system in general		Numeric
Description:		
Estimate the relevance of the controlled parameter to the standard from a scale of 0 to 1		
<input type="text" value="Type a number"/>		

Fig. 2 Checklist of reusable formwork assembly

where y^k – points, awarded to the k parameter; m – the number of expert groups.

Total weight of all coefficients is equal to 1 (Table 3).

Let us summarize the obtained values in the Table 4:

We represent the obtained values in the form of a radar chart (Fig. 3).

The obtained values exceed the required minimum, which is sufficient to consider the quality of each type of work as appropriate.

The final indicator of the quality of concrete work is calculated by the formula 3:

$$Q = (0.801 + 0.802 + 0.849) \cdot 0.333 = 0.816$$

The results obtained indicate that the quality of work meets the accepted requirements and allows to proceed to subsequent work.

As a result the final assessment the work quality, it can be considered completed and proceed to drawing up the work performed acts.

Table 2 Table of expert assessments

Formwork assembly					
Expert	A1	A2	A3	Total	
1	3	4	5	12	
2	4	4	5	13	
3	3	5	3	11	
4	4	4	4	12	
5	5	4	5	14	
Reinforcement works					
Expert	B1	B2	B3	B4	Total
1	4	5	5	4	18
2	4	4	5	5	18
3	5	4	5	5	19
4	5	5	4	4	18
5	3	5	4	5	17
Concrete laying					
Expert	C1	C2		Total	
1	4	3		7	
2	4	4		8	
3	5	5		10	
4	4	5		9	
5	5	4		9	

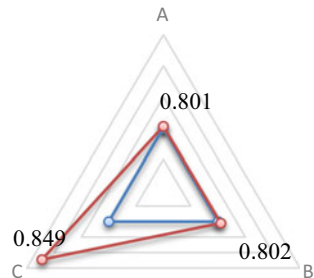
Table 3 Table of weight coefficients

Formwork assembly					
Expert	A1	A2	A3	Total	
1	0.250	0.333	0.417	1	
2	0.308	0.308	0.385	1	
3	0.273	0.455	0.273	1	
4	0.333	0.333	0.333	1	
5	0.357	0.286	0.357	1	
Total	1.521	1.715	1.764	5	
a_{ki}	0.304	0.343	0.353	1	
Reinforcement works					
Expert	B1	B2	B3	B4	Total
1	0.222	0.278	0.278	0.222	1
2	0.222	0.222	0.278	0.278	1
3	0.263	0.211	0.263	0.263	1
4	0.278	0.278	0.222	0.222	1
5	0.176	0.294	0.235	0.294	1
Total	1.162	1.282	1.276	1.279	5
a_{ki}	0.232	0.256	0.255	0.256	1
Concrete laying					
Expert	C1	C2		Total	
1	0.571	0.429		1	
2	0.500	0.500		1	
3	0.500	0.500		1	
4	0.444	0.556		1	
5	0.556	0.444		1	
Total	2.571	2.429		5	
a_{ki}	0.514	0.486		1	

Table 4 Table of quality indicators (Q_i)

Q_i	№	Q_{ki}	a_{ki}	$Q_{kj} \cdot a_{ki}$
A	A1	0.8	0.304	0.243
	A2	0.7	0.343	0.240
	A3	0.9	0.353	0.318
$Q_i = \sum_{k=1}^m Q_{ki} \cdot a_{ki}$				0.801
B	B1	0.7	0.232	0.163
	B2	0.9	0.256	0.231
	B3	0.8	0.255	0.204
	B4	0.8	0.256	0.205
$Q_i = \sum_{k=1}^m Q_{ki} \cdot a_{ki}$				0.802
C	C1	0.8	0.514	0.411
	C2	0.9	0.486	0.437
$Q_i = \sum_{k=1}^m Q_{ki} \cdot a_{ki}$				0.849

Fig. 3 Key indicators of quality assessment



4 Conclusions

As a result of the work, it was proposed a method for ensuring the quality of construction and installation works using automated technologies and a method for complex quality assessment. This method makes it possible to unify the approach to the process of automation investment and construction projects, to establish a unified approach to creating an integrated construction and installation work model by forming an interactive model, fixing the amount of work performed, systematizing and analyzing

the data obtained, visualization, and executing the final report with a final quality assessment the works performed.

The developed methodology for ensuring the construction works quality using information modeling can be recommended for the successful implementation of an investment and construction project for quality control engineers, customer services, subcontractors and general contractors.

References

1. ISO 9001:2015 (2015) Quality management systems. Requirements
2. ISO 9000:2015 (2015) Quality management systems. Fundamentals and vocabulary
3. Sinelnikov A, Strelets K (2008) Analysis of the adaptation of the international standard GOST R ISO 9001–2001 of the quality management system to the building complex of the Russian Federation. XXXVI Week Sci SPbPU 1:160–162
4. Baiburin AKh (2012) Comprehensive quality assessment of civic buildings construction considering the factors affecting their safety. Dissertation, Saint Petersburg
5. Baiburin AKh (2015) Ensuring the quality and safety of constructed civic buildings: a scientific publication. ASV Publ, Moscow
6. Baiburin AKh, Golovnev SG (2006) Quality and safety of constructional technologies. Monograph, SUSU, Chelyabinsk
7. Lukmanova I, Nezhnikova E (2013) Comprehensive assessment of quality management systems in construction. Mod. Probl. Sci. Educ. 10:1791–1795
8. Rauzana A (2017) Implementation of quality management system in construction. Am. J. Eng. Res. 6(12):173–179
9. Lukichev S, Romanenko M (2016) Problems of introduction of system of quality management in Russia. Actual Probl. Humanitarian Natural Sci. 6:113–116
10. Nezhnikova E (2013) Problems of creation and functioning of quality management systems. Mod.s Probl. Sci. Educ. 6:958–962
11. Song C, Liu Y, Zhou C, Wen L, Zhao Y (2018) Problems and countermeasures in construction quality management of house building engineering. Smart Constr. Res. 2(1):18–27
12. Eastman C, Teicholz P (2011) BIM Handbook: A Guide to Building Information Modeling for Owners, Managers, Designers, Engineers and Contractors, New Jersey, p 648
13. Van Nederveen GA, Tolman FP (1992) Modelling multiple views on buildings. Autom Constr 1(3):215–224
14. Nawari N (2012) BIM standard in off-site construction. J Archit Eng 18(2):107–113
15. Peterson F, Hartmann T, Fruchter R, Fischer M (2010) Teaching construction project management with BIM support: experience and lessons learned. Autom Constr 20(2):115–125
16. Hardin B (2009) BIM and Construction Management: proven tools, methods, and workflows. Indianapolis, p 364
17. Azhar S, Khalfan M (2012) Maqsood T Building information modeling (BIM): now and beyond. Australasian J Constr Econ Build 12(4):15–28
18. Eroshkin SY, Kallaur GY, Papikian LM (2016) Lean construction and BIM: complementing each other for better project management. Rev. Bus. Econ. Stud. 4:17–22
19. Achkar EA (2016) BIM-Integrated approach to construction quality management. Enabling information and knowledge management during the execution phase of a project life cycle. Eindhoven University of Technology Graduation program: Master of Construction Management and Engineering December 8th
20. Lapidus AA, Shesterikova IV (2019) Mathematical model for assessment the potential of the high-rise apartment buildings complex quality index. E3S Web of Conferences 91, 02025. <https://doi.org/10.1051/e3sconf/20199102025>

Risk Identification and Assessment in the Design of Concrete Mixes



Liubov Lisienkova , Liudmila Nosova , and Liudmila Komarova 

Abstract This paper investigates the process of designing concrete mixtures based on a risk-oriented approach. For the risk identification and assessment on the stage of heavy concrete mix composition design, an expert method (Failure mode and effects analysis, FMEA) has been used. Based on the results of an expert survey and an analysis of regulatory documents, potential risks of the design stage have been identified. In the experimental part of the work, the quantitative characteristics of failures (priority number of risk) have been determined, taking into account their significance in terms of consequences, the probability of occurrence and the probability of detection. As a result, it was possible to identify failures that have the highest priority risk number and occur at the stages of determining the consumption of Portland cement, fine aggregate fractions, water-cement ratio of the concrete mixture, and the quality factor of the coarse aggregate. The results have been further used to optimize the composition of the concrete mixture.

Keywords Concrete mixes · Risk identification · Risk assessment · FMEA analysis

1 Introduction

Errors in the design of the concrete mix composition lead to decrease in the quality indicators of the finished concrete mix as well as negatively affects the strength characteristics of reinforced concrete structures. Consequently, a problem arises related

L. Lisienkova (✉)

Moscow State University of Civil Engineering, National Research University, 26, Yaroslavskoe shosse, Moscow 129337, Russia
e-mail: lisienkova@ngsu.ru

L. Nosova (✉)

South Ural State Humanitarian and Pedagogical University, 69, Lenin Avenue, Chelyabinsk 454080, Russia
e-mail: nosova@cspu.ru

L. Komarova

Moscow Polytechnic University, 38, Bolshaya Semyonovskaya Ulitsa, Moscow 107023, Russia

to quality control of the design process for the composition of concrete mixtures. A properly selected composition is the basis for ensuring the required strength of concrete and reinforced concrete structures [1].

The production process of reinforced concrete structures is impossible without the stage of designing the composition of the concrete mixture. In the Russian Federation, the design of the composition is carried out in accordance with the requirements of GOST 27,006–2019 “Concrete. Rules for the selection of the composition”. At the stage of designing the composition of the concrete mixture, it is necessary to take into account the degree of the human factor influence. For example, an error in determining the workability of a mixture can lead to further delamination [2].

In Russia, the production process of concrete mixes is regulated by a standard GOST 7473–2010 “Concrete mixes. Specifications” and contains the following operations:

- dosing of bulk materials;
- mixing of bulk materials with the addition of water;
- unloading the finished mixture.

Usually while concrete mix production, special technological equipment is used, for example, continuous concrete mixers [3]. A sudden failure of such equipment entails a number of consequences: the additional cost of restoration work, processing or disposal of concrete mix, and an increase in delivery times. Equipment failures at the production stage leads to the discrepancy between the quality indicators of the finished mixture and the requirements of regulatory documents, as well as negative effects on the strength characteristics of concrete [4].

In Russia, the production process and quality control of reinforced concrete structures is carried out based on the standard 130.13330.2018 “Production of precast concrete structures and products. Building code (SNiP) 3.09.01–85 “. Recommended equipment is used at each stage of the production of structures. For example, the stage of concrete mixture compaction is performed using deep vibrators, which increases the possibility of technical risk [5].

Technical risk is determined by the production process maturity of reinforced concrete structures [6]. Minimization of this risk is possible with some preventive measures, namely [7]:

- regular maintenance of technological equipment;
- compliance with safety measures when using the equipment;
- scheduled preventive maintenance, etc.

Common practice of production of reinforced concrete structures in Russian Federation shows that, to some extent, the implementation of preventive measures is ignored, which entails the emergence of new risks [8].

The concrete mix is a key component in the production of reinforced concrete structures and buildings. Inconsistencies that arise during the design of the mixture significantly affect the strength characteristics of the finished reinforced concrete. To identify risks, it is necessary to highlight the stages of designing a concrete mixture. A

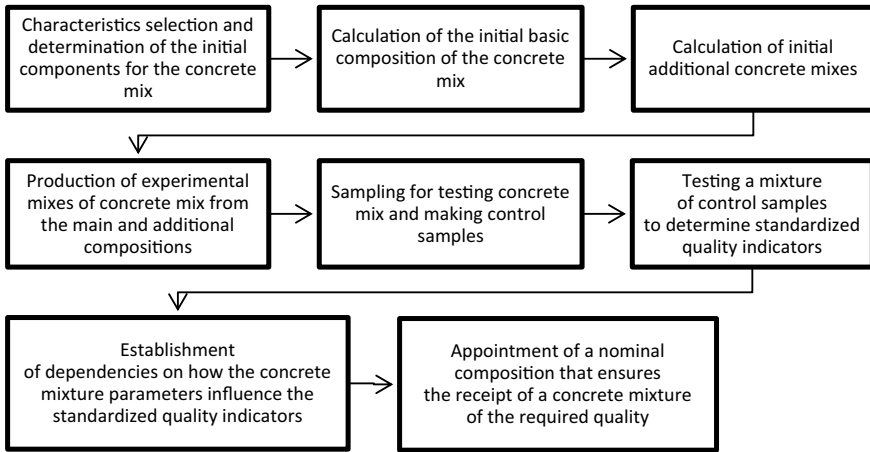


Fig. 1 The process of concrete mix design

decomposition scheme of the concrete mix design process based on GOST 27,006–2019 “Concrete. The rules for the selection of the composition” is presented in Fig. 1.

2 Methods and Materials

The concrete mix is a fundamental component in the production of reinforced concrete structures. Errors and inconsistencies arising during the design of the mixture significantly affect the strength characteristics of the finished reinforced concrete.

The object of this study is a heavy concrete mixture “BST B22.5 P2F200 W8”, the design and preparation of which is carried out in accordance with the requirements of a standard “GOST 27,006–2019 Concretes. Composition selection rules” and “GOST 7473–2010 Concrete mixtures. Technical conditions”.

To ensure the compliance of the strength characteristics of the ready-made concrete with the requirements of “GOST 26,633–2015 Heavy and fine-grained concretes. Technical conditions”, it is necessary to control the process of selection of the composition and quality indicators of the concrete mix [9]. The strength of reinforced concrete structures made of heavy concrete “BST B22.5 P2F200 W8” must be at least 28.9 MPa.

Table 1 shows the quality indicators of the concrete mixture gained through its hardening.

The analysis of the regulatory documentation showed that the quality indicators of the heavy concrete mixture and the strength characteristics of the finished reinforced concrete directly affected by the design process of the composition.

Table 1 Concrete mix quality indicators (GOST 7473–2010)

Quality indicator	Guideline values	Allowed deviation of the guideline value
Average density, kg/m ³	2000–2500	±20
Cone draft, cm	5–9	±1
Delamination of concrete mix (no more that %)	Water separation: 0,4 Solution separation: 3	Water separation: ± Solution separation: ±
Porosity, %	3–4	±1

The main components of the concrete mixture “BST B22.5 P2F200 W8” are a hydraulic binder (Portland cement PC400), water (free of alkalis and acids), granite crushed stone and clean sand, acting as coarse and fine aggregates, respectively.

Inconsistencies arising in the determination of the components of the concrete mixture significantly affect the strength of the ready-mixed concrete. Thus, it is necessary to identify the reasons for the occurrence of failures in the design process [10] and justify the monitoring the following parameters commonly used for concrete mix quality control [11]:

- a coefficient of quality of coarse aggregate;
- a water-cement ratio of the concrete mixture;
- a consumption rate of coarse and fine aggregate, kg/m³;
- a consumption rate of Portland cement, kg/m³;
- an activity level of Portland cement, MPa;
- a fraction of fine aggregate, mm.

To identify and assess risks in the design of the composition of the heavy concrete mixture, the expert method “Failure mode and effects analysis (FMEA)” [12] has been used in accordance with a standard “GOST R 51,901.12–2007 (IEC 60,812: 2006) Risk management. Method of analysis of types and consequences of failures”.

Basic principles of FMEA analysis are [13]:

1. Teamwork. Usually a multifunctional expert group of specialists carries out FMEA. The effectiveness of such a method is directly proportional to the professional level, practical experience and the coordination of experts’ actions.
2. Hierarchy. Decomposition of the concrete mixture design process helps identifying any deviations.
3. Iterative approach. This method of detecting and assessing risks is systematic, it is resumed when new factors appears;
4. Data logging. Analysis of the types and consequences of potential failures and its results should be documented.

Figure 2 is a flow chart describing the FMEA analysis procedure.

The method for analyzing the types and consequences of failures is characterized by the following estimates of possible failures:

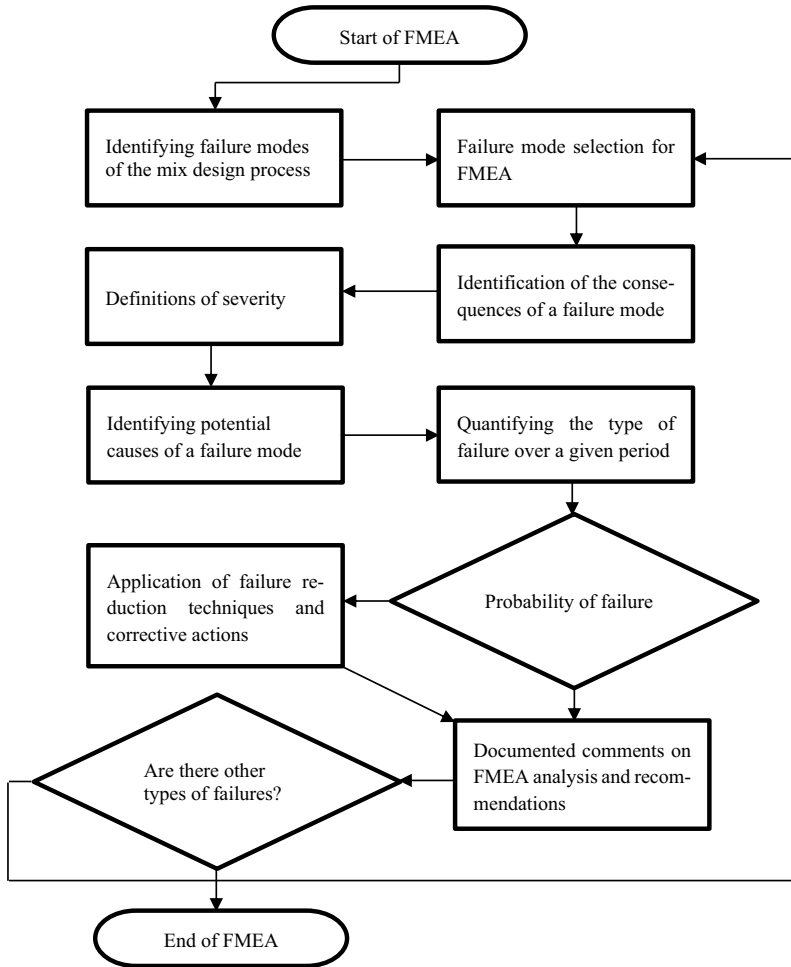


Fig. 2 FMEA analysis procedure

- the rank of significance (S) is a point score characterizing the parameter of the severity of the consequences of inconsistencies in the design process of the composition of the concrete mixture;
- the rank of occurrence (O) is a point score characterizing the frequency of causes of inconsistencies in the design process of the composition of the concrete mixture;
- the rank of detection (D) is a point score characterizing the ability of an existing control to detect potential causes of nonconformity.

In Table 2, based on a standard “GOST R 51,901.12–2007 (IEC 60,812: 2006) Risk management. The method of analysis of types and consequences of failures” provides a qualimetric scale [13] for assessing possible failures.

Table 2 Qualimetric scale for assessing possible failures

Rank of significance (S)	Rank of occurrence (O)	Rank of detection (D)
1—no significance	1—unlikely to occur	1—almost inevitable detection
2—very minor significance	2, 3—low probability of occurrence	2—a very high chance of failure detection
3—minor significance		3—a high chance of failure detection
4—very low significance	4, 5, 6—moderate probability of occurrence	4—a moderately high chance of failure detection
5—low significance		5—a moderate chance of failure detection
6—moderate significance		6—a small chance of failure detection
7—high significance	7, 8—high probability of occurrence	7—a very small chance of failure detection
8—very high significance		8—unlikely to detect a failure
9—very high significance with additional alert	9, 10—almost inevitable occurrence	9—almost unlikely to detect a failure
10—highest significance		10—impossible to detect a failure

The multiplication of three ranks from Table 2 allows determining the quantitative characteristics of failures (priority risk number) [14] in the design process of the concrete mix composition in terms of their consequences significance, the probability of occurrence and the probability of detection.

The priority risk number is determined using the formula:

$$\text{Priority risk number} = S * O * D, \quad (1)$$

where S is the rank of significance, O is the rank of occurrence, D is the rank of detection.

3 Results

The results of the FMEA analysis carried out by a group of experts, with an indication of the scores, are given in Table 3.

Based on the experience of experts and analysis of regulatory documents, Table 4 presents potential failures at the design stage of the concrete mix. According to experts, potential failures (Table 4) can affect the quality indicators of the concrete mix and the strength characteristics of the finished reinforced concrete structures.

4 Discussion and Conclusion

Based on the FMEA analysis results, the main factors have been identified that lead to the inconsistency of the concrete mixture with the requirements of regulatory documents, unreasonable overrun of components, which can ultimately lead to a decrease in the strength characteristics of finished reinforced concrete structures. Table 5 shows the factors with its priority risk number, which was calculated using the formula (1).

The factors mentioned above directly affect the performance of the concrete mix, the strength characteristics of the finished reinforced concrete structures and are the starting point for quality control. Incorrect quantification of factors will lead to inconsistencies in the next stages of the design process.

- The following steps in the design process were not included in Table 5:
- production of experimental concrete mixes (Priority risk number = 300);
- sampling and testing of concrete mix (Priority risk number = 288);
- statistical analysis of the results (Priority risk number = 84).

Previous experiments have shown that a high priority risk number is caused by the fact that the stages of making experimental mixes, sampling and testing concrete mix include many factors and have a high severity parameter of the consequences

Table 3 Qualimetric scale for assessing possible failures

Design stage of the concrete mix composition	Failure occurrence	Failure reasons	Failure consequences	S	O	D	Priority risk number
Quality factor specification of coarse aggregate	Decrease of quality factor	Human factor	Reduced strength of concrete structures	7	3	7	147
Water-cement ratio specification	Increase of the water-cement ratio	Human factor	Increased delamination of concrete mix	9	2	6	108
Specification of Portland cement consumption for the preparation of 1 m ³ of concrete mixture	Overconsumption of Portland cement	Human factor	Overestimation of the tempering strength of concrete	8	2	5	80
Specification of coarse and fine aggregates consumption	Reduced aggregate consumption	Human factor	Overconsumption of Portland cement and a decrease in the strength of concrete structures	7	3	2	42
Specification of the activity of Portland cement	Decreased activity of Portland cement	Breakage of a hydraulic press	Understating of Portland cement grade and reduced strength of concrete structures	6	3	1	18
Specification of fine aggregate fractions	Reduce of fine aggregate fractions	Human factor	Overconsumption of Portland cement for the preparation of 1 m ³ of concrete mixture	9	3	5	135
Production of experimental mixes of concrete mix	Violation in manufacturing technology	Human factor	Non-compliance with the requirements of a standard "GOST 7473–2010"	10	5	6	300
Sampling and testing of concrete mix	Violation in test technology	Human factor	Increased porosity of the concrete mix	8	6	6	288
Manufacturing and testing of control concrete samples	Violation of a hydraulic press operation	Breakage of the indicating device of the hydraulic press	The compressive strength of concrete is set incorrectly	10	7	1	70

(continued)

Table 3 (continued)

Design stage of the concrete mix composition	Failure occurrence	Failure reasons	Failure consequences	S	O	D	Priority risk number
Establishment of dependencies on how the concrete mixture parameters influence the standardized quality indicators	Error in the selection of statistical methods for results processing and optimization	Human factor	The composition does not provide a concrete mix of required quality	6	7	2	84

Table 4 Potential failures at the design stage of the mixture composition

Design stage of the concrete mix composition	Normative documents and standards	Failure consequences
Quality factor specification of coarse aggregate	GOST 27,006–2019 GOST 8269.0–97	Reduced strength of concrete structures
Specification of water-cement ratio specification	GOST 27,006–2019	Increased delamination of concrete mix
Specification of Portland cement consumption for the preparation of 1 m ³ of concrete mixture	GOST 27,006–2019 Building code (SNiP) 82–02-95	Overestimation of the tempering strength of concrete
Specification of coarse and fine aggregates consumption	GOST 27,006–2019	Overconsumption of Portland cement and a decrease in the strength of concrete structures
Specification of the activity of Portland cement	GOST 310.1–76	Understating of Portland cement grade and reduced strength of concrete structures
Specification of fine aggregate fractions	GOST 27,006–2019	Overconsumption of Portland cement for the preparation of 1 m ³ of concrete mixture
Production of experimental mixes of concrete mix	GOST 7473–2010	Non-compliance with the requirements of standard “GOST 7473–2010”
Sampling and testing of concrete mix	GOST 10,181–2014	Increased porosity of the concrete mix
Manufacturing and testing of control concrete samples	GOST 10,180–2012	The compressive strength of concrete is set incorrectly
Establishment of dependencies on how the concrete mixture parameters influence the standardized quality indicators	GOST 27,006–2019 GOST 310.1–76 GOST 7473–2010 GOST 10,181–2014 GOST 10,180–2012	The composition does not provide a concrete mix of required quality

Table 5 Investigated factors with their priority risk number

Design stage of the concrete mix composition	Name of the factor	Units	Priority risk number
Quality factor specification of coarse aggregate	Quality factor	–	147
Specification of fine aggregate fractions	Fine aggregate fraction	mm	135
Specification of water-cement ratio specification	Water-cement ratio	–	108
Specification of Portland cement consumption for the preparation of 1 m ³ of concrete mixture	Portland cement consumption	kg/m ³	80

of non-conformities 10 and 8, respectively. Determination of the variation range for these factors requires further research in this direction.

References

1. Kett I (2009) Engineered concrete: mix design and test methods. CRC Press
2. Day K (2003) Concrete mix design. CRC Press, Quality Control and Specification (with CD ROM)
3. Dils J, Schutter G, Boel V (2012) Influence of mixing procedure and mixer type on fresh and hardened properties of concrete: a review. *Mater Struct* 45(11):1673–1683
4. Sekar T, Ganesan N, Nampoothiri NVN (2011) Studies on strength characteristics on utilization of waste materials as coarse aggregate in concrete. *Int J Eng Sci Technol* 3(7):5436–5440
5. Sonebi M, Bassuoni M, Yahia A (2016) Pervious concrete: mix design, properties and applications. *RILEM Technical Letters* 1:109–115
6. Schneider M (2015) Process technology for efficient and sustainable cement production. *Cem Concr Res* 78:14–23
7. Siddika A, Mamun MAA, Ferdous W, Alyousef R (2020) Performances, challenges and opportunities in strengthening reinforced concrete structures by using FRPs—a state-of-the-art review. *Eng Fail Anal* 111, 104480
8. Gravit M, Dmitriev I, Ishkov A (2017, October) Quality control of fireproof coatings for reinforced concrete structures. In: *IOP conference series: earth and environmental science*, vol 90, no 1. IOP Publishing, p 012226
9. Kishchynskyi S, Nagaychuk V, Bezuglyi A (2016) Improving quality and durability of bitumen and asphalt concrete by modification using recycled polyethylene based polymer composition. *Procedia Eng* 143:119–127
10. Bourchy A, Barnes L, Bessette L, Chalencon F, Joron A, Torrenti J (2019) Optimization of concrete mix design to account for strength and hydration heat in massive concrete structures. *Cement Concr Compos* 103:233–241
11. Ivanovna LV, Viktorovna ML, Viktorovich TR (2016) Method of assessment quality protective and decorative coating concrete cement. *Case Stud. Constr. Mater.* 4:81–84
12. Stamatis DH (2003) Failure mode and effect analysis: FMEA from theory to execution. Quality Press
13. Azgaldov G, Kostin A (2011) Applied qualimetry: its origins, errors and misconceptions. *Benchmarking: An Int J*
14. Xiao N, Huang HZ, Li Y, He L, Jin T (2011) Multiple failure modes analysis and weighted risk priority number evaluation in FMEA. *Eng Fail Anal* 18(4):1162–1170

Anisotropic Characteristics of Single Jointed Rock Mass Under Uniaxial Compression



Long Cheng , Yaojia Sun , Jiyun Zhang , and Meng Guo 

Abstract Jointed rock mass has special discontinuous structure, which shows complex anisotropic mechanical properties. In order to grasp the complex mechanical properties, a group of joint rock specimens with different dip angles were made by similar ratio to carry out uniaxial compression tests, and the peak strength of the rock specimens and their variation with dip angles β were obtained. The peak failure modes of the specimens were analyzed. The results show that the mechanical properties of the specimens are controlled by joint surface and rock block. Compared with the intact specimens, the mechanical parameters of the joint specimens are all reduced to varying degrees, and the compressive strength of the joint specimens is U-shaped with the joint inclination Angle, and the minimum value appears in the specimens with the joint inclination Angle of 60° . When the joint dip Angle is $\beta = 0^\circ \sim 30^\circ$, the fracture failure along the axial stress direction occurs. When the joint dip Angle is $\beta > 45^\circ$, the rock begins to slip along the bedding plane. When the joint inclination Angle is $\beta = 90^\circ$, splitting failure along the bedding plane occurs. The research results can provide reference for engineering deformation and stability analysis of jointed rock mass.

Keywords Jointed rock mass · Uniaxial compression · Anisotropy · Mechanical properties

1 Introduction

Most of the rock masses in the surface of the earth have formed various primary or secondary structural planes, such as bedding, joints, foliations, folds, weak planes, etc., in the long geological history. These rocks with dominant planes of directional and regular distribution can be regarded as the generalized stratified rock masses. The deformation and strength of layered rock mass are obviously anisotropic under the

L. Cheng (✉) · J. Zhang · M. Guo
School of Civil Engineering, Henan Polytechnic University, Jiaozuo, China

Y. Sun
Zhejiang Zhongcheng Construction Co., Ltd., Shaoxing, China

influence of the dip Angle, which brings great difficulties to the practical engineering design and the stability evaluation of layered rock mass. The geometrical parameters of rock mass discontinuities, such as occurrence (strike, dip, dip Angle), shape, elongation, density, and opening, etc. have an important influence on their mechanical properties.

Rajendra et al. [1] conducted true triaxial tests on cube model specimens with three groups of joints, and studied the post-peak zone characteristics of the joint specimens. The results showed that the strain hardening, strain softening and plastic characteristics of the joint specimens depended on their geometric structure and stress state. Chen xin et al.[2] fissure containing a set of well versed in preset cubes cast joint specimen was carried out under uniaxial compression test, the results show that with the joint connectivity rate increases, the ductility of the joint specimen stress–strain curve, and studies have also shown that increase with the connectivity rate than through joint specimens [2, 3], the peak strength and elastic modulus decreases gradually. Wasantha et al. [4] conducted uniaxial compression tests on non-perforated cylindrical cement mortar joint specimens, and the results showed that joint position, inclination Angle and track length all had influences on uniaxial compressive strength. Zhang Bo et al. [5] conducted uniaxial compression tests on crab-filled rectangular joint specimens and studied cracks The effect of filling or not on the mechanical properties indicates that the peak strength and post-peak plastic deformation capacity of the joint specimens with filling are enhanced. Liu Hongyan et al. [6] conducted uniaxial compression tests on cylindrical joint models, and the results showed that joint dip Angle, joint penetration degree, number of joint groups, load strain rate, length-diameter ratio of specimens, thickness and type of joint filling material were closely related to failure mode and peak strength of jointed rock mass. Guo Zhihua et al. [7] used FLAC3D to simulate the triaxial loading characteristics of combinations with different soft and hard interval thicknesses, and studied the relationship between the equivalent elastic modulus and the dip Angle of soft strata. Wang Anming et al. [8] carried out finite element analysis on mechanics and deformation characteristics of bedded salt rock with mudstone interlayer, and studied the distribution characteristics of stress field and displacement field under single triaxial loading. Tien[9] studied the failure process and failure mode of composite rock samples in single triaxial loading tests, divided the failure modes of composite rock samples under different confining pressures into two categories: slip along the weak plane and non-slip along the weak plane, and conducted a more in-depth and systematic study on the mechanical properties and failure mechanism of composite rock samples.

Through the past research, joint on the mechanics and deformation characteristics of rock mass has the influence, in this paper, the strength of a group of seven different Angle with different single prefabricated through joint specimen was carried out under uniaxial compression test, analysis of the relationship between the stress and strain, deformation characteristics, strength characteristics and strength parameters and the anisotropic characteristics of failure mode, finally the correctness of the test results are verified through the theoretical calculation. The research results can

Table 1 Physical and mechanical parameters of rock-like materials

$\rho(\text{g.cm}^{-3})$	σ_c (MPa)	$E_c(\text{GPa})$	ν	$c(\text{MPa})$	$\Phi(^{\circ})$
0.19	34.42	9.87	0.19	8.65	33.9

provide reference for engineering deformation and stability analysis of layered rock mass. Specimen design and test scheme.

1.1 Sample Design

Due to the great dispersion of natural jointed rock mass, rock-like materials were used in this test. At present, there is no strict definition of the concept of composite rock strata. Due to the lack of target prototype, similarity theory was not considered in the process of formulation. Taking into account the strength range prepared by the laboratory and the degree of difficulty in coring, the strength of the composite rock is estimated to be about 34.42 MPa. Physical and mechanical parameters are shown in Table 1.

A layered cuboid test block was obtained by layered casting. In order to distinguish the rock strata, an appropriate amount of ink was added to the lower rock strata to adjust the color. Then through the Angle of the core, and finally cut, polished. Standard rock-like samples are obtained as shown in Fig. 1.

1.2 Test Scheme

In the test, the joint dip Angle β was defined as the Angle between the joint surface and the horizontal plane, which was divided into 0° , 15° , 30° , 45° , 60° , 75° and 90° , a total of 7 angles. The inclination angles of each joint are shown in Fig. 1. RMT-150B electro-hydraulic servo rock mechanics test system is adopted as the test equipment. The maximum axial load applied can reach 1000 kN., high test accuracy, stable performance. The axial displacement control was adopted during the test, and the rate control was 0.002 mm/s. The axial force, axial displacement and circumferential displacement of the sample were collected during the loading process.

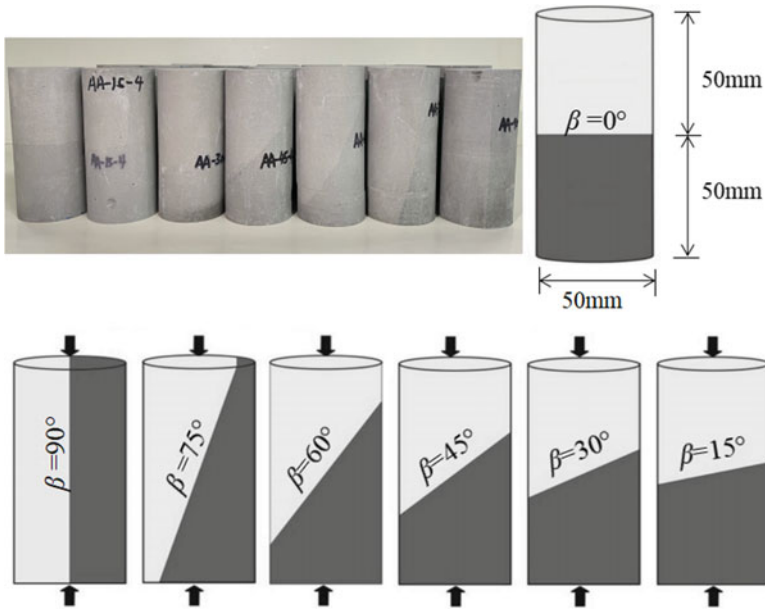


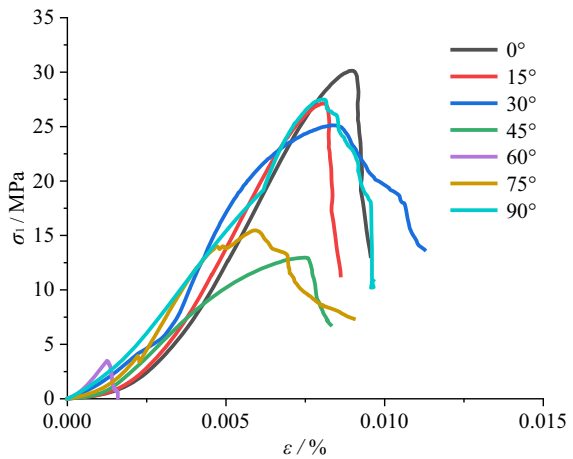
Fig. 1 Uniaxial compression specimen

2 Analysis of Anisotropy of Stratified Rock Mass

2.1 Characteristics of Stress–Strain Curve

Figure 2 shows the stress–strain curves of specimens with different joint inclination

Fig. 2 Stress–strain curves of jointed rock masses under uniaxial compression



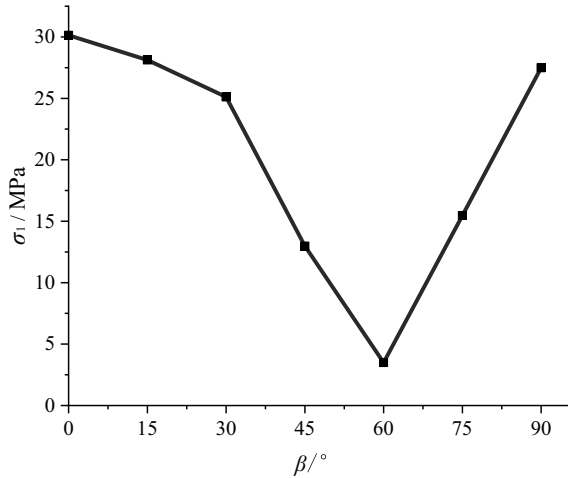
angles under uniaxial compression. The uniaxial compression stress–strain curves of the specimens with inclination angles of seven joints are shown in different colors. For $\beta = 0^\circ, 15^\circ, 30^\circ$ and $\beta = 90^\circ$ specimens, the axial compression at the initial loading stage results in a larger normal deformation and a longer concave stage in the stress–strain curve. With the increase of axial load, the bedding plane is further compressed and gradually closed. The stress–strain curve develops almost linearly, and the sample begins to enter the stage of linear deformation.

The failure mode is tensile splitting along the axial compression direction, and the stress drops rapidly after reaching the peak point, showing the characteristics of single peak point and rapid release of post-peak stress. The failure process is similar to that of brittle rock. For the sample of $\beta = 45^\circ, 60^\circ$, due to its large bedding dip Angle, the sample directly produces bedding slip failure, which is manifested as no cracks on the surface of the test block, that is, no tensile splitting failure occurs. The upper test block slides rapidly along the bedding plane and completely separates from the lower test block, and there is no obvious damage to the upper and lower rock masses. For the samples of $\beta = 75^\circ$, the stress–strain curves are obviously different from those of $\beta = 45^\circ, 60^\circ$, showing the characteristics of multiple peaks. The reason is that the laboratory compression test adopts the loading mode of fixed lower end and pressurized upper end, and the boundary conditions of the rock samples during the test make it impossible for the samples to completely slip along the bedding plane. The failure mode of rock mass specimens is splitting failure or splitting failure as the main failure mode, and the stress peak value of the failure is much higher than that of the rock mass specimens with complete shear failure and shear failure as the main failure mode.

2.2 Peak Strength

The variation curve of peak strength of jointed specimens with interface dip Angle is shown in Fig. 3. It can be concluded that the strength characteristics of jointed rock mass are jointly determined by rock formation fabric and interface dip Angle. With the increase of joint inclination Angle, the peak strength of joint specimens showed a U-shaped trend of decreasing first and then increasing, showing significant anisotropy. When the joint dip Angle is small ($\beta = 0^\circ, 15^\circ, 30^\circ$), the strength of the joint rock mass depends on the strength of the rock mass itself, which is manifested as the fracture failure of the whole specimen after passing through the joint. When the joint inclination Angle reaches $45^\circ, 60^\circ$ and 75° , the rock mass failure is sliding along the bedding plane, and the sample strength depends on the bonding strength of the joint plane. When the joint inclination Angle reaches 90° , the tensile splitting failure mainly occurs along the joint direction, and its strength depends on the rock mass strength.

Fig. 3 Relationship between peak load and Angle of jointed rock masses under uniaxial compression



2.3 Failure Characteristic Analysis

Figure 4 is the failure characteristic pattern diagram of the specimens with different joint inclination angles. It can be seen that at a lower joint inclination Angle (WW), the failure mode of the specimens is splitting failure, and longitudinal cracks appear along the surface of the cylinder, with severe damage degree. The main crack is shear crack. The failure mode of WW specimens is shear-induced fractures, which are mainly distributed along joints. For the WWW sample, the failure slippage along the joint is accompanied by a small number of splitting cracks, which is caused by the boundary stress conditions. The failure mode of the specimen under uniaxial loading is tensile fracture along the joint plane.

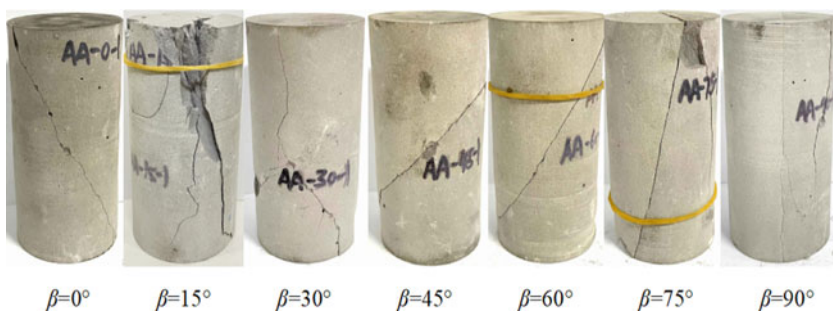


Fig. 4 Failure modes of jointed rock masses

3 Analysis of Mechanical Effect of Joint Surface

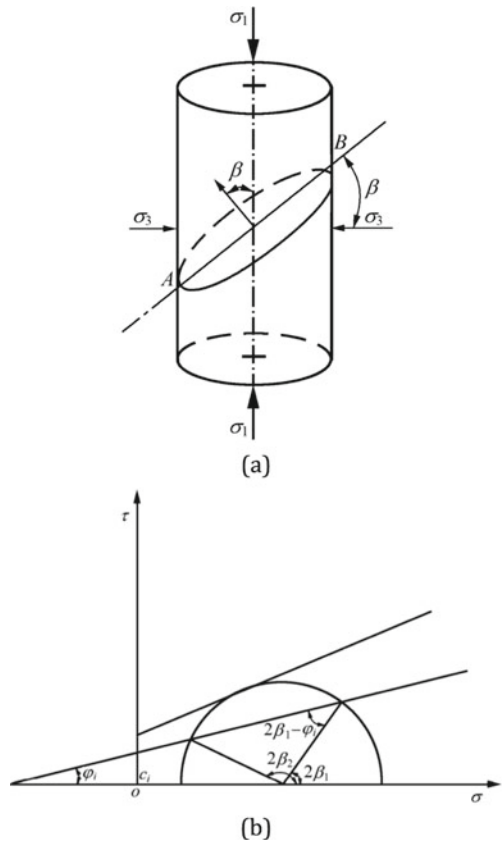
Jaeger et al. [10] used the Mohr–Coulomb criterion to describe the rock mass damaged by sliding along the weak plane. In the rock mass as shown in Fig. 5, a group of structural planes AB is developed. Assuming that the included Angle between AB and the largest main plane is β , according to the molar stress circle theory, the normal stress and shear stress acting on AB plane are respectively:

$$\left. \begin{aligned} \sigma &= \frac{\sigma_1 + \sigma_3}{2} + \frac{\sigma_1 - \sigma_3}{2} \cos(2\beta) \\ \tau &= \frac{\sigma_1 - \sigma_3}{2} \sin(2\beta) \end{aligned} \right\} \quad (1)$$

Assuming that the shear strength τ of the structural plane obeying the Moor-Coulomb criterion, as:

$$\tau_i = \sigma \tan\phi_i + c_i \quad (2)$$

Fig. 5 Theoretical diagram of single structural plane



Substituting (1) into (2), the condition of shear failure along structural plane AB can be obtained, as follows:

$$\sigma_1 - \sigma_3 = \frac{2(c_i + \sigma_3 \tan \phi_i)}{(1 - \tan \phi_i \cot \beta) \sin(2\beta)} \quad (3)$$

where, c_i and ϕ_i are the cohesion force and internal friction Angle of the structural plane respectively; $\phi_i < \beta < 90^\circ$.

According to (3), the strength of rock mass varies with the dip Angle of the structural plane. When $\beta \rightarrow 90^\circ$ or $\beta \rightarrow \phi_i$, $(\sigma_1 - \sigma_3) \rightarrow \infty$ or $\sigma_1 \rightarrow \infty$, the rock mass will fail through the structural plane. Only when $\beta_1 \leq \beta \leq \beta_2$, the rock mass fails along the structural plane. It is well explained that there are two failure modes of anisotropic rock mass with a set of discontinuities: sliding along the discontinuities and failure through the discontinuities in the rock.

By rewriting Eq. (3), the triaxial compression strength of rock mass can be obtained as:

$$\sigma_{1m} = \sigma_3 + \frac{2(c_i + \sigma_3 \tan \phi_i)}{(1 - \tan \phi_i \cot \beta) \sin(2\beta)} \quad (4)$$

Let $\sigma_3 = 0$, the uniaxial compressive strength of rock mass can be obtained:

$$\sigma_{mc} = \frac{2c_i}{(1 - \tan \phi_i \cot \beta) \sin(2\beta)} \quad (5)$$

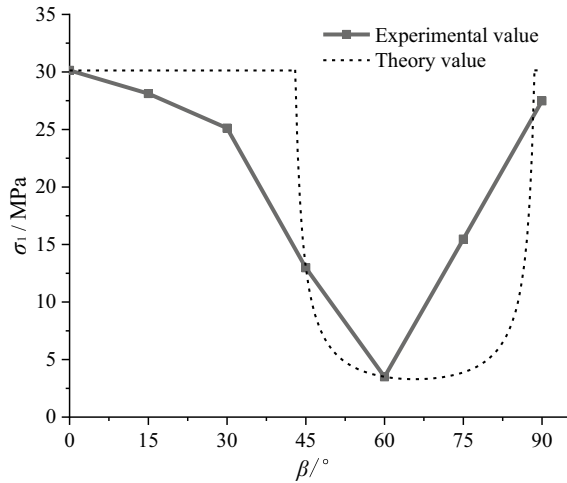
According to Mohr's circle equation, it can be obtained:

$$\beta_1 = \frac{\phi_i}{2} + \frac{1}{2} \arcsin \left[\frac{(\sigma_1 + \sigma_3 + 2c_i \cot \phi_i) \sin \phi_i}{\sigma_1 - \sigma_3} \right] \quad (6)$$

$$\beta_2 = 90^\circ + \frac{\phi_i}{2} - \frac{1}{2} \arcsin \left[\frac{(\sigma_1 + \sigma_3 + 2c_i \cot \phi_i) \sin \phi_i}{\sigma_1 - \sigma_3} \right] \quad (7)$$

According to the samples $\beta = 45^\circ, 60^\circ$ in the complete slip mode in the test, c and ϕ values at the interface of the samples in group AA and group AB can be calculated respectively. Compared with the critical angles β_1 and β_2 , the theoretical values and experimental values are shown in Fig. 6. It can be seen that the theory can better predict the strength of jointed rock masses.

Fig. 6 Comparison of theoretical and experimental values of jointed rock mass strength



4 Conclusion

1. The failure modes of jointed rock mass are sliding along the joint plane and shear failure through the joint, respectively. The mechanical properties of the failure modes are determined by the joint plane, rock block and the stress state.
2. The stress–strain curve and peak strength of joint specimens also have anisotropic characteristics and correspond to their failure modes. The theory of single weak plane can predict the strength of single joint specimens well.
3. The failure modes of jointed rock mass under uniaxial compression can be mainly divided into the following categories: ① At $\beta = 0^\circ \sim 30^\circ$, the specimen forms throughout the whole. The fracture surface of the sample directly penetrates the bedding; ② at $\beta = 45^\circ \sim 75^\circ$ slip failure occurs in the bedding of the sample; ③ At $\beta = 90^\circ$, the tensile splitting failure occurs mainly along the direction of bedding.

References

1. Tiwari RP, Rao KS (2006) Post failure behaviour of a rock mass under the influence of triaxial and true triaxial confinement. *Eng Geol* 84(3–4):112–129
2. Chen X, Liao ZH, Liao DJ (2011) Experimental study of effects of joint inclination angle and connectivity rate on strength and deformation properties of rock masses under uniaxial compression. *Chin J Rock Mech Eng* 30(4):781–789
3. Chen X, Liao ZH, Peng X (2012) Deformability characteristics of jointed rock masses under uniaxial compression. *Int J Min Sci Technol* 22(2):213–221
4. Wasantha PLP, Ranjith PG, Viete DR et al (2012) Influence of the geometry of partially-spanning joints on the uniaxial compressive strength of rock. *Int J Rock Mech Min Sci* 50:140–146

5. Zhang B, Li SC, Zhang DF (2012) Uniaxial compression mechanical property test fracture and damage analysis of similar material of jointed rock mass with filled cracks. *Rock Soil Mech* 33(06):1647–1652
6. Liu HY, Huang HS, Li KB (2013) Test study of strength and failure mode of pre-existing jointed rock mass. *Rock and Soil Mech.* 34(5):1235–1241
7. Guo ZH, Sheng Q, Mei S et al (2004) Numerical simulation test on macro mechanics parameters of layered composite rock masses. *Chin J Rock Mech Eng* 23(S2):4902–4906
8. Wang AM, Yang CH, Huang C et al (2009) Numerical experiment study of deformation and mechanical properties of layered salt rock. *Rock Soil Mech.* 30(07):2173–2178
9. Tien YM, Kuo MC, Juang CH (2006) An experimental investigation of the failure mechanism of simulated transversely isotropic rocks. *Int J Rock Mech Min Sci* 43(8):1163–1181
10. Jaeger JC (1960) Shear failure of anisotropic rocks. *Geol Mag* 97(01):65–72

Real Estate Public Management Quality Assessment



Nadezhda Kamynina , Elena Gorbashko , Irina Golovtsova ,
and Alexandra Titova 

Abstract Public Real Estate industry is becoming more competitive part of the economy of the state influencing its inclusive and sustainable growth and overall well-being. This study proposes a methodology for assessing the quality of the Real Estate public management on the basis of multivariate analysis and mathematical methods followed by the establishment of the instrumental assessing model. The quality indicators of Real Estate Organisations (REO) public management are designed in accordance with the fundamental Total Quality Management principles and consider the interests of multiple stakeholders, national and regional aspects. The model was applied to estimate the quality of public REO management in Russian regions and thus allowed to construct a matrix of priorities where indicators are ranked according to the importance and achieved results. The reported study was funded by RFBR, project number 20–010-00-571 “The Impact of Digital Transformation on Improving the Quality and Innovation of Services”.

Keywords Quality assessment · Public management · Real estate · Multivariate analysis · Integrated indicators

1 Introduction

Real Estate (RE) is one of the principal tangible assets of any country constituting its population welfare and ensuring sustainable economic growth. RE acts as a basis for meeting the needs of all members of the society. Effective and efficient RE disposal at all levels of administration requires management decisions related to Real Estate Organizations (REO) to be evidence-based [1]. RE management is directed at the design, adoption and implementation of the decisions that provide the full use of the

N. Kamynina

Moscow State University of Geodesy and Cartography, 4, Gorokhovskiy Pereulok,
105064 Moscow, Russia

E. Gorbashko · I. Golovtsova · A. Titova (✉)

Saint Petersburg State University of Economics, 21, Sadovaya Street,
191023 St. Petersburg, Russian Federation

e-mail: alexandra_titova@list.ru

RE as a consumer good, as well as the investment and material asset. According to previous research well-functioning RE management expects the realization of the following tasks:

- cost optimization for the maintenance of the REO management system;
- decisions quality improvement;
- REO database design;
- REO facilities monitoring [2];
- quality improvement and range of services expansion in order to raise RE customer satisfaction [3–8].

REO management should ensure customer satisfaction at all stages of the RE life cycle, including construction, operation and liquidation [9].

In previous studies property management is defined as a structured process aimed at ensuring the best value for money from property assets while serving the strategic needs of the state; a structured, holistic and integrating approach aimed at harmonizing and managing the requirements to the service provisions and the effective property asset management in order to achieve business goals within the framework of the central government [4, 8, 9, 11, 12]. The concept of “quality” in relation to any object (products, services, processes, management and others) represents the degree to which the characteristics of the object correspond to the requirements. In the “industry aspect”, the category of REO public management quality and the components of “inherent characteristics”, “requirements” is based on the provisions of the basic theories of state and municipal management, the budget process, real estate management, that underlie and determine the very essence of REO public management.

Based on results of previous studies we determine following control elements for REO public management: a goal-setting system, formed as a landmark of the desired object state; management principles containing rules, requirements, patterns of the management process; management objects and subjects structure and their interconnections, including types and legal forms of organizations, system design, management structures and processes, authority and responsibility; methodology, technology and management tools; the formation of management functions, including strategic, tactical and operational planning; organization, motivation, accounting, control and updating (feedback and regulation) of the management action [4, 13–15]. However, the detailed target characteristics of REO public management and methods for the quality assessment of REO public management results, including methods regarding the stakeholders’ satisfaction with quality and ensuring sustainable development of the state, are considered fragmentarily in a limited amount of works.

It is necessary to understand that the REO quality management assessment system is greatly determined by the national context, not only the legal basis, but also by the historical and geographical aspect. Models of the systems aimed at the formation of REO public management (REO PM) quality include the specifics of regional real estate management of countries [2, 3, 7, 10, 14, 16], i.e. do not take into account the level management of RE on the scale of the country as a whole [2, 4, 7, 17]. For example, in Russia, there is a very large area, a significant number of subjects,

in addition, the territories are unevenly developed, a fairly significant part of the REO facilities are abandoned and not operating at the moment. The situation is also complicated by the hysterical aspect, namely the speed and haphazard transition of a huge number of objects from the state to private hands during the period of perestroika. At the moment, a comprehensive study has not been implemented to consider all levels of RE management in the Russian Federation. The studied sources do not provide a holistic methodology for assessing the quality of REO public management.

We consider that further research on the methodology and methods for assessing the quality of public REO management should be conducted on the basis of multivariate analysis and mathematical methods followed by the establishment of the instrumental assessing model in order to develop solutions for REO optimization for the sustainable development of the state [1, 4, 10]. It is proposed to build the quality indicators of REO public management in accordance with the fundamental Total Quality Management (TQM) principles: the quality REO management principles; quality policy that meets the requirements of consumers and all stakeholders; elements of the high-quality REO public management model; feedback from consumers and stakeholders on their satisfaction formation; quality standards for results and public administration processes; a set of methods and tools for quality management.

2 Methodology and Methods

2.1 REO Public Management Quality Indicators

Utility and quality are not identical, but interrelated categories. The utility of the studied object is what, in fact, is required by the consumer, whereas the quality reflects the degree of perfection, and these categories are in dialectical unity, that is, on the one hand, utility is a measure of quality and the increment of utility in accordance with the requirements corresponds to higher quality, and on the other hand, higher quality will reflect higher utility. The REO public management can be presented as a kind of public good, in which consumers, the owners of Real Estate and other interested parties, feel the need. The relationship between the categories of benefits, needs, utility, cost and quality of REO public management is presented in Fig. 1.

Taking into account the performance indicators of the public management [2, 3, 6, 18] we group consumers and stakeholders in the following groups:

- Consumers - recipients of the REO facilities public management results, including: owners of real estate, namely owners of local REO objects (enterprises and institutions), owners of real estate in the regions, including federal and municipal entities and the state as a whole, as the owner of federal property, moreover, the owners of both REO individual objects, and land - property complexes

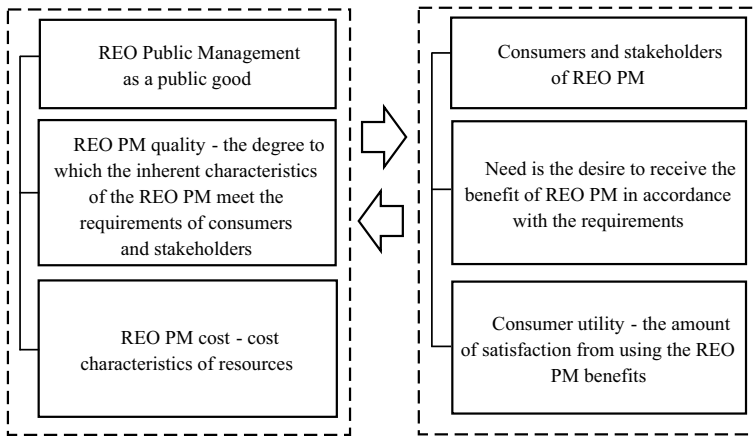


Fig. 1 Relationship categories

and individuals; organizations - consumers, managing structures of REO, participants in the real estate market and various structures as recipients of products and services of REO public management and regulation;

- State authorities at all levels of government, including the management structures of such bodies, regulating the real estate system;
- Partners and suppliers - organizations involved in the implementation of REO public management, which may include, for example, organizations in the construction industry, agriculture, various forestry and water management organizations, real estate market participants and many other partners, including those related to land management, repair and maintenance of REO facilities, investment, insurance, assessment of cadastral value and others;
- Employees of organizations and public servants of the authorities, conducting work related to the REO public management;
- The society and the international community on international property rights, consumer protection, transparency, anti-corruption and other norms.

Further we propose following expectations and requirements of REO PM stakeholders:

- for consumers there is a specificity of management levels: for example, with direct management, at the micro level - consumers need to increase the utility of REO to obtain financial or other effects, and at the regional or state level, the growth of national wealth in terms of its real estate for solving sustainable development problems and growth in budget revenues related to real estate; and it is also important for consumers to receive benefits (effects) from state legal and organizational regulatory functions and services in the field of REO, ensuring the achievement of its utility;

- for the state, as a regulator of relations between REOs, represented by state authorities, agencies and other governing structures, it is important to comply with established state standards when managing REOs within the framework of resource and budgetary opportunities to ensure sustainable development of the state;
- for the business community and any other partners and suppliers in REO public management, reliability in obligations and mutual benefit are needed;
- the international community must comply with international standards, for example, regarding property, and the development of cooperation;
- for REO employees - internal motivation is necessary to achieve performance results.

Based on this list of stakeholders' needs, we propose to divide the quality indicators of REO public management into three groups according to their role in shaping the management utility. The first group of indicators of the socio-economic utility of the REO public management is determined by the effects of the real estate use in economic turnover and social processes (I_{se}), including utility in the following areas:

I_{se} 11 - direct use of real estate in economic circulation and the provision of public services;

I_{se} 12 - capital construction of REO facilities, repair and maintenance of REO facilities;

I_{se} 13 - real estate market development and real estate operations;

I_{se} 14 - social effects from the formation of housing and land for the population;

I_{se} 15 - construction of roads, infrastructure and other structures;

I_{se} 16 - conservation of ecology, land and mineral resources, culture, world heritage;

I_{se} 17 - increase budget revenues related to real estate;

I_{se} 18 - land use;

I_{se} 19 - growth in the value of land - property complexes of regions, organizations and national real estate.

The second group of indicators reflects the legal component (I_{lc}) of REO public management:

I_{lc} 21 - the level of ensuring the rule of law in the regulation of REO and property rights protection;

I_{lc} 22 - the adequacy of the legal norms on real estate base;

I_{lc} 23 - the level of ensuring relations of property rights, real estate transactions, property rights separation;

I_{lc} 24 - the level of privatization and nationalization regulation;

I_{lc} 25 - accountability and anti-corruption.

The third group of indicators reflects the organizational usefulness of the REO PM (I_{org}) and includes:

I_{org} 31 - level of information transparency;

I_{org} 32 - the general level of cadastral registration;

- I_{org} 33 - digitalization level of cadastral registration;
- I_{org} 34 - compliance of the parameters of the public services provision with standards and requirements;
- I_{org} 35 - the convenience of receiving services for RE;
- I_{org} 36 - the level of state real estate organizational regulation.

2.2 REO Public Management Quality Indicators

The quality of the REO public management as a complex socio-economic object (SEO) is a multi-level system characterized by many indicators of various nature, thus there are found some difficulties in assessing the quality of SEO requiring the use of complex digital assessments. The theory of multidimensional and qualimetric quality assessments is considered in sufficient detail in the scientific literature, however, developments for an integrated quality indicator of SEO, based on a large data set and taking into account the significance of indicators, are still insufficient. It is proposed to find an integral SEO quality indicator in a combination of several approaches: 1) the approach used by Azgaldov G.G., Saati T. and their followers related to the formalization of the definition of the integral (complex) SEO quality by constructing a mathematical qualimetric model that allows to calculate the value of integral quality based on knowledge of the primary (single) indicators spectrum as a linear convolution of single indicators with specific weights, reflecting socio-economic significance; 2) the approach used in the research of S. Ayvazyan and his followers, where the definition of complex quality indicators as a posteriori indicators is carried out on the basis of a large number of statistical a priori indicators based on mathematical methods (for example, modified principal components and etc.) that do not require expert interventions. Each approach individually has its own advantages and disadvantages, however, combined application, allows us to get a more objective result.

The first approach uses the classical qualimetric method for calculating a comprehensive assessment, taking into account the weight of quality indicators as a weighted average:

$$q_k = \sum_{j=1}^n K_{jk} \cdot w_j \quad (1)$$

where q_k – comprehensive assessment of the SEO k -th component quality;

K_{jk} – the value of a single quality indicator of an individual j -th property of the k -th object;

w_j – the weight of the j -th property quality indicator.

One of the difficult tasks with this approach is the establishment of weighting coefficients, which is usually assigned with the help of experts and can be regarded as the disadvantage of this approach. There are many ways to establish specific weights. The most famous is the Saati T. hierarchy analysis method, where alternatives are

evaluated and the pairwise comparisons method is applied ensuring the establishment of the studied indicators by the degree of their influence on the general characteristic, and the ranking of elements is done by constructing a matrix of pairwise comparisons and processing matrices to find the main proper vectors. Another common method may be the full ranking of all indicators and the assignment of points, and the specific weights in this case are established in accordance with the principle of increasing points λ_{ij} for a higher rank, and are determined by the arithmetic mean of the points scored to the total number of possible points according to the formula (2):

$$w_j = \sum_{i=1}^n \lambda_{ij} / (\sum_{i=1}^n \sum_{j=1}^m \lambda_{ij}) \tag{2}$$

where w_j – the specific weight of the indicator,

λ_{ij} – set points scored in accordance with the rank for the indicator, i - the number of experts from 1 to m ; j is the number of indicators from 1 to n .

According to the second approach, the procedure for constructing a synthetic posteriori quality indicator of an object by finding the main components consists of the following steps:

1. The sample covariance matrix S is defined:

$$S = (S_{jk}) = \begin{pmatrix} S_{11} & \dots & S_{1p} \\ \vdots & \ddots & \vdots \\ S_{p1} & \dots & S_{pp} \end{pmatrix} \tag{3}$$

where the matrix elements are found by the following formulas (4) and (5):

$$S_{jj} = S_j^2 = \frac{1}{n-1} \sum_{i=1}^n (y_{ij} - \bar{y}_j)^2 = \frac{1}{n-1} (\sum_{i=1}^n y_{ij}^2 - n\bar{y}_j^2) \tag{4}$$

$$S_{jk} = \frac{1}{n-1} \sum_{i=1}^n (y_{ij} - \bar{y}_j)(y_{ik} - \bar{y}_k) = \frac{1}{n-1} (\sum_{i=1}^n y_{ij}y_{ik} - n\bar{y}_j\bar{y}_k) \tag{5}$$

The largest eigenvalue is determined λ_1 of matrix S , as the largest root of the characteristic equation $|S - \lambda I| = 0$.

Solving the equation $(S - \lambda_1 I)a_1 = 0$, eigenvector is determined a_1 of matrix S , corresponding to the largest eigenvalue. Vector a_1 will be the coefficient vector of the first principal component $z_1 = a_1'y$.

For each i -th object, the value of the modified first main component is calculated, which is taken as an integral indicator and is calculated by the formula:

$$q_i = \sum_{j=1}^p a_j^2 y_{ij} \tag{6}$$

where y_{ij} – j - attribute of i -object; $i = 1, 2, \dots, n$.

The advantage of the second approach is the construction of a synthetic indicator on objective trends, because the modified first main component, as well as the first main component, most accurately recovers the values of particular criteria y_{ij} by the value of the integral indicator of the object quality. In addition, the modified first main component simplifies the interpretation of the integral quality indicator of the object due to the fact that the values of the integral indicators q_i vary within the same measurement scale as the unified values of particular criteria y_{ij} . This statement follows from the following property of the main components:

$$\sum_{j=1}^p a_j^2 = 1 \quad (7)$$

The combination of methods consists in the fact that estimates of synthetic indicators in the selected measurement scale can be used in qualimetric models taking into account socio - economic significance. Thus, the methodology for the formation of the quality assessment of complex SEO is implemented by applying several approaches, including approaches based on the methods of modified principal components in determining synthetic indicators of the lower level of the hierarchy, including a large array of statistical data, as well as approaches for further generalization of the synthetic indicators in indicators of a higher hierarchy level, a comprehensive assessment of which can be established by the qualimetric method based on linear convolution indicators with different levels of significance of the influence of SEO individual properties on the complex value of the SEO quality.

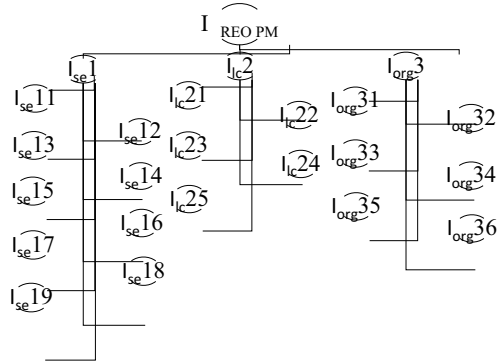
The proposed methodological approach includes the following stages for conducting a digital assessment of REO public management quality:

1) the construction of a hierarchy of REO public management quality indicators, including integrated, complex, synthetic and a priori indicators, as the key and crucial stage of the study related to the REO nature; 2) digitizing a priori indicators and bringing them to a single measurement scale, including bringing into a unified form the values of a priori indicators having digital values in various units of measurement (rubles, percent, units, kilometers, etc.) based on standard values, and also the development of a questionnaire and an expert survey to establish the digital value of indicators that do not have a digital measurement, and if necessary, reduce the number of a priori statistical indicators based on statistical and probabilistic methods of relationship tightness analytics; 3) the formation of models that include integral, complex and synthetic indicators at the hierarchy levels; 4) analysis of the data to develop managerial decisions.

Designing the Hierarchy of REO Public Management Quality Indicators

According to the accepted concept of quality, the main goal of the REO public management is to achieve its comprehensive utility for the population and the state. The goal includes 3 groups of indicators, divided into smaller indicators, in total 20 indicators, which are a posteriori indicators synthesized from many a priori indicators [19]. The hierarchy of indicators is shown in Fig. 2.

Fig. 2 The hierarchy of REO public management quality indicators



Estimation of a Priori Indicators. Due to the fact that most indicators of the REO PM are measured in various scales, and many quality indicators of the REO PM do not have generally accepted numerical measuring, it is possible to convert indicators to dimensionless units or points units to obtain the same dimension of all indicators. The most preferred scale is a 10-point scale. All a priori indicators that have digital values must be converted to normalized form depending on the type of data trends for the selected score scale. For example, for a monotonically increasing dependence (i.e., the greater the value of x , the higher the quality), the value of the corresponding unified variable \tilde{x} is calculated by the formula:

$$\tilde{x} = \frac{x - x_{min}}{x_{max} - x_{min}} * N \tag{8}$$

where x_{min} and x_{max} - accordingly the smallest (worst) and largest (best) values of the initial indicator, $N = 10$, the selected scale of points.

To digitize indicators that do not have measurers, expert surveys are conducted on a questionnaire containing questions regarding quality indicators. In socio - economic research, various scales are used. In this case, a 10-point Likert scale (10 for the highest quality, 1 for the lowest quality) containing gradations is accepted. To obtain data, an expert survey and an assessment of their reliability according to the Alpha Cronbach indicator were carried out.

Designing the Model of the REO Public Management Quality Integrated Assessment. Models are formed in order to calculate $I_{REO PM}$ - an integral indicator of the higher level REO public management quality; I_1, I_2, I_3 - complex indicators of the 1st level in the socio-economic, legal, organizational group. I_{ij} -synthetic (posterior) indicators are determined, where i is the number of the indicator group of the 1st level; j - serial number of synthetic indicators within the group. The definition of complex quality indicators must begin in a sequence from the lowest level of the indicators' hierarchy to one single integral indicator of the upper level. The digital value of the synthetic indicators I_{ij} for subjects (regions), including I_{ijk} a priori indicators, can be determined on the basis of the main components methodology: firstly, all a

priori indicators are reduced to a dimensionless N-point scale; secondly, the value of synthetic indicators is defined as the value of the modified main component of unified a priori indicators. For complex indicators I_1, I_2, I_3 , consisting of synthetic indicators I_{ij} with varying degrees of socio-economic significance, scalar vector convolution can be used taking into account specific weights of indicators. The integral indicator of the upper level is the vector $REO\ PM = \{I_1, I_2, I_3\}$, which characteristics show the level of quality result in the three components of the REO PM. The form of the integral assessment of the REO PM is represented in the formula (9):

$$I_{REO\ PM} = a_1 \cdot I_1 + a_2 \cdot I_2 + a_3 \cdot I_3 \quad (9)$$

It is possible to establish the relative weights of indicators in models in various ways, among which the most common is expert ranking of the indicators' significance and assigning ranks to simple ranking or based on the application of the Saati hierarchy method in pairwise comparison.

Comprehensive and integrated indicators of the regions REO PM are presented in the summary table and an analysis is carried out on the priorities for improving indicators based on their constructed matrix of priorities.

3 Results

The methodology for assessing the quality of REO public management by subjects (regions, districts), built on the methodological principles described above, consists of three parts: part 1 - collecting a priori indicators of REO public management, their normalization and determination of synthetic indicators I_{ij} ; Part 2 - calculation of complex indicators I_i and integral indicator $I_{REO\ PM}$ by subjects based on the determination of the indicators significance and their specific weights; Part 3 - assessment of the REO public management quality indicators in the regions and their analysis. In this study, due to the limited statistical data and the difficulty in organizing the collection of expert data on the indicators of the REO legal and organizational utility, the methodological recommendations on the REO indicators of social and economic utility are carried out, as there is a quite sufficient database of Rosstat statistical indicators, including number of Russian regions. Also, due to the large number of constituent entities of the Russian Federation, statistical data are presented for eight federal districts of the Russian Federation. To collect a priori indicators and calculate synthetic indicators, an array of a priori indicators of REO public management social and economic significance for the Federal Districts was collected and, indicators were unified on a 10-point scale and synthetic indicators were identified. In the qualimetric assessment of the complex REO public management quality the indicator I_1 (indicator for the socio-economic significance) takes nine synthetic indicators, the weights of each group are defined according to expert survey. The specific weights

Table 1 Analysis of the REO public management of the Russian Federation for the analyzed period in a ten-point scale

Period	I ₁₁	I ₁₂	I ₁₃	I ₁₄	I ₁₅	I ₁₆	I ₁₇	I ₁₈	I ₁₉
2016	4.55	5.35	4.54	5.27	3.98	5.99	3.92	5.11	3.93
2017	4.77	6.94	4.28	4.40	4.09	6.13	5.10	4.35	4.36
2018	4.41	3.79	4.42	5.29	4.11	5.97	2.80	4.56	4.56
Total for the period	4.58	5.36	4.41	4.99	4.06	6.03	3.94	4.67	4.28

Table 2 Assessment of REO public management quality indicators by districts in a ten point scale

District	2016	2017	2018	Avg. for the period
Central Federal District	5.39	5.51	5.20	5.36
North-West Federal District	4.46	5.44	4.46	4.79
Southern Federal District	4.93	4.76	4.77	4.82
North Caucasus Federal District	5.58	5.12	4.70	5.14
Volga Federal District	4.27	4.17	3.50	3.98
Ural Federal District	4.20	4.68	3.75	4.21
Siberian Federal District	4.35	4.84	3.67	4.29
Far Eastern Federal District	4.64	6.01	5.05	5.23
Avg. for Russia	4.73	5.07	4.39	4.73

were determined by using the arithmetic mean method. As a result, a comprehensive assessment of the quality indicator I_1 has the form:

$$I_1 = 0,185 \cdot I_{11} + 0,168 \cdot I_{12} + 0,040 \cdot I_{13} + 0,119 \cdot I_{14} + 0,044 \cdot I_{15} + 0,074 \cdot I_{16} + 0,104 \cdot I_{17} + 0,089 \cdot I_{18} + 0,178 \cdot I_{19} \quad (10)$$

Tables 1, 2 are formed for the period and present the result of the calculations carried out using the program Math Lab.

From the analysis of Table 1, we can conclude that the REO public management quality indicators of the Russian Federation are below average and are declining, and the weakest link is I17, which reflects the growth in budget revenues.

The analysis of the Table 2 shows that the indicators of the integrated REO public management quality in the districts as a whole are low and are declining. It can be noted that the Central Federal District and the Far Eastern Federal District reached the highest comprehensive assessment of the socio-economic utility of the REO public management, and the lowest is observed in the Volga and Ural Federal Districts.

To develop measures to improve the REO public management quality, we place the results of the assessments in a matrix that includes ranking according to the importance of indicators and their achieved values, in four areas of analysis. In this study, the following distinction is made between matrix areas: - less significant indicators - these are indicators with a specific weight less than 0.08; - significant indicators are indicators with a specific weight of more than or equal to 0.08; - a

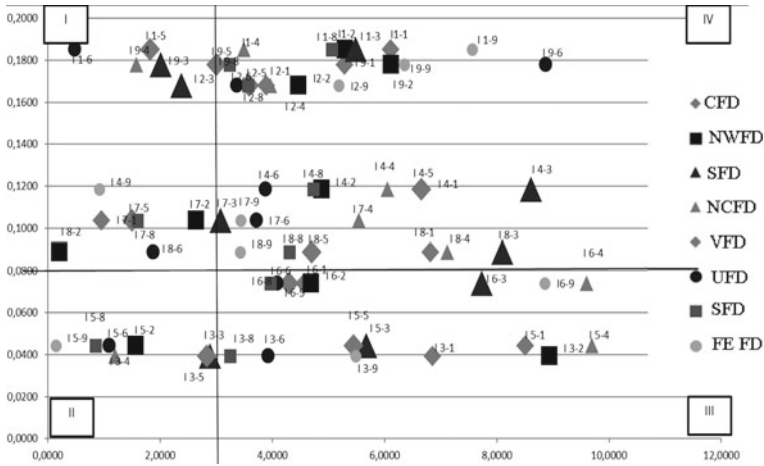


Fig. 3 A comparative analysis of the quality indicators of the REO public management in 8 districts for 2018 (author’s figure) *.(** Explanation for Fig. 3: in Fig. 3, the indicator I_{jm} is introduced, where j is the number of the indicator component I (from 1 to 9); m is the region number (from 1 to 8).*)

low rating is a rating of up to 3 inclusive; - a rating of 3 to 10 is an acceptable level of quality management. The distribution of the REO public management quality indicators for 8 federal districts for 2018 is presented in Fig. 3. Figure 3 shows that 13 problem indicators requiring a deeper analysis were included in the first quadrant. For example, indicator I 1–6 - the utility of the direct REO use in economic turnover and the provision of public services of the Ural Federal District is extremely low. This happens because of the lowest value of the capital productivity ratio in this district and the low dynamics of its growth, as well as because of the highest value of the depreciation rate and the specific weight of completely worn-out funds with low update rates.

4 Discussion

Despite the fact that the real estate industry is becoming more competitive part of an increasingly dynamic environment, where high quality management is the essential part that ensures the satisfaction of all stakeholders, research in this area is extremely low. Search in the Scopus database that includes terms “quality, management, real estate” in the title, abstract or key words gives only 115 documents. Screening of abstracts made it possible to leave only 86 articles relevant to the subject of the real estate management and elements of its management quality, as management efficiency, customer satisfaction, investors and owners added value, evaluation models. Analysis of these articles with the help of VosViewer carried for co-occurrence of

keywords revealed that only 20 papers contain the term “quality” in keywords, along with the terms “management” and “real estate”, also there is one publication taking into account Russian national context, devoted to corporate real estate management during the period of transition that doesn’t correlate with the estimation of public real estate management quality.

The study of publications devoted to the real estate management in Russia, identified that “management effectiveness” in the sphere of real estate is of high popularity, whereas “management quality” is absent. The studies regarding “management effectiveness” are mainly theoretical in nature and do not take into account the stakeholders theory, and mainly appeal to indicators of commercial results. Another group of studies, such as the study of A. Anufrieva and M. Ninth, consider only certain regions of Russia and assess real estate management there, which does not allow us to compare the results obtained, since the assessment methods differ significantly and no interregional matching is possible [20, 21].

5 Conclusion

The proposed methodology and the method for the digital assessment of the REO public management quality on the basis of the multidimensional assessment theoretical principles can be applied to improve the quality of REO public management and allows to monitor the quality of REO public management on the subjects of REO to develop improvement measures.

References

1. Gross M, Żróbek R (2015) Good governance in some public real estate management systems. *Land Use Policy* 49:52–364
2. Klimach A, Dawidowicz A, Żróbek R (2018) The Polish land administration system supporting good governance. *Land Use Policy* 79:547–555
3. Abubakari Z, Richter C, Zevenbergen J (2018) Exploring the “implementation gap” in land registration: how it happens that Ghana’s official registry contains mainly leaseholds. *Land Use Policy* 78:539–554
4. Marona B, Van den Beemt-Tjeerdsmā A (2018) Impact of public management approaches on municipal real estate management in Poland and the Netherlands. *Sustainability* 10(11):4291
5. Mika M (2018) An analysis of possibilities for the establishment of a multipurpose and multidimensional cadastre in Poland. *Land Use Policy* 77:446–453
6. Muczyński A, Dawidowicz A, Żróbek R (2019) The information system for social housing management as a part of the land administration system – a case study of Poland. *Land Use Policy* 86:165–176
7. Constantin D-L, Mitrut C, Grosu RM, Profiroiu M, Iosif AE (2018) Municipal real properties and the challenges of new public management: a spotlight on Romania. *Int Rev Adm Sci* 84(1):122–143
8. Li Y, Shang H (2019) Service quality, perceived value, and citizens’ continuous-use intention regarding e-government: Empirical evidence from China. *Inf Manage* 57(3):103197

9. Kaya I, Kaya O (2019) Foreign aid, institutional quality and government fiscal behavior in emerging economies: an empirical investigation. *Q Rev Econ Finance* 76:59–67
10. Pozega Z, Crnkovic B, Zivkovic A (2014) Effective Management of state property as prerequisites for economic development. *Econ. Eastern Croatia Yesterday, Today, Tomorrow* 3:418–426
11. Local Government Asset Management Guidelines (2005) RICS/ODPM
12. Muñoz SF, Cueto LC (2017) What has happened in Spain? the real estate bubble, corruption and housing development: a view from the local level. *Geoforum* 85:206–213
13. Kaufmann D, Kraay A, Massimo M (2010) The worldwide governance indicators: methodology and analytical issues (September 2010). World bank policy research working Paper No. 5430. <https://ssrn.com/abstract=1682130>. Accessed 20 Mar 2021
14. Deloitte Real Estate Group: Comparing Public Real Estate Management In European Cities (December 2011). <http://www.mondaq.com/uk/x/156662/Market+Commentaries/Comparing+Public+Real+Estate+Management+In+European+Cities>. Accessed 20 Mar 2021
15. Zamanifard H, Alizadeh T, Bosman C (2018) Towards a framework of public space governance. *Cities* pp 155–165
16. Klumbyte E, Apanaviciene R (2014) Real estate strategic management model for Lithuanian municipalities. *Int J Strateg Prop Manag* 18(3):279–291
17. Vermiglio C (2011) Public property management in Italian municipalities: framework, current issues and viable solutions. *Prop Manage* 29(5):423–442
18. Ugolini F, Massetti L, Sanesi G, Pearlmutter D (2015) Knowledge transfer between stakeholders in the field of urban forestry and green infrastructure: results of a European survey. *Land Use* 49:365–381
19. Kamynina NR, Gorbashko EA (2019) Methodology of digital quality assessment of public real estate management of organizations. *Sci Bus Dev Ways* 92:278–288
20. Pivovarova OV (2017) Analysis of existing approaches to assessing the efficiency of state property management: advantages, disadvantages, areas for improvement. *Russ Entrepreneurship* 18(13):2035–2048
21. Anufrieva AA, Devyatova NS (2018) Comprehensive approach to evaluation of region public property management's efficiency. *Public Adm Issues* 1:164–180

Tuning the PID Controller According to the Criterion of the Maximum Phase Margin



Natalia Lysova , Nina Myasnikova , Dmitrii Plotnikov ,
and Anatolii Semenov 

Abstract In this work, the authors provide a concise overview of the applied forms of PID controllers, algorithms for their automatic setting and adaptive control in technical automation systems. The paper proposes a method for setting the PID controller by the criterion of the maximum phase margin for objects with delay. In the proposed method for calculating the controller parameters, the open-loop phase margin is chosen as the objective function, which makes it possible to replace the nonlinear programming problem with a much simpler task of finding the maximum phase-frequency characteristic of an open-loop system in a function of the controller parameters. The calculation of the PID controller settings based on the conditions of the quality criteria adopted in the heat power industry has been carried out. As an example, the calculation of the controller parameters for the object of the electric generator air cooling system was carried out. A comparative analysis of the obtained characteristics allows concluding that the proposed method for calculating the parameters of the PID controller provides a maximum and significantly larger phase margin, which almost eliminates overshoot in the system.

Keywords PID controller · Tuning method · Phase-frequency response · Control object · Parameter · Transfer function · Transient

1 Introduction

Today, proportional-integral-derivative (PID) controllers are widely used in technical systems. The laws of PID regulation and control are constantly being expanded and updated. The main direction of development of the laws of PID control is the minimization of the integrating component.

According to the theory of automatic control, the parameters of the controller are unambiguously related to the characteristics of the controlled object. Since the manufacturer of the automation does not have information about these characteristics, the factory settings of the controller are selected for some abstract object, and

N. Lysova · N. Myasnikova (✉) · D. Plotnikov · A. Semenov (✉)
Penza State University, 40, Krasnaya Street, Penza 440026, Russian Federation

the task of the installer is to select the optimal parameters of the controller. The key issue when using PID controllers was and is the issue of calculating the coefficients and setting. There are many methods, from the simplest to the optimization ones. Initially, the problem of setting controllers was solved with the help of the experience and intuition of the designer. Over time, with the advent of computers and SCADA systems, automatic methods for setting controllers gained popularity, which allows calculating the parameters one-time or on request. Although, this method is not suitable for systems with drifting parameters. In this regard, it is necessary to constantly reconfigure the PID controller depending on the changing parameters of the control object. The solution to this problem is achieved using adaptive control, which, depending on the adaptation algorithm, implies constant or periodic adjustment of the PID controller coefficients. Direct and indirect adaptive control algorithms are distinguished. Direct algorithms adjust the PID controller coefficients based on the analysis of the controlled variable. Indirect algorithms are based on the identification of the control object model and correction based on its PID controller coefficients [1, 2].

2 Methods

PID controllers are widely used in modern automatic control systems, such as the control of thermal systems and positioning systems [3–5]. The use of PID controllers helps to reduce energy losses for setting the system and provide faster access to the required parameters. For the correct operation of the controller, it is necessary to correctly select its coefficients. The accuracy and speed of the system will depend on the correct selection of the coefficients. Quite often, the empirical selection of coefficients does not bring the desired results and takes a lot of time. In this regard, it becomes necessary to use mathematical methods for setting controller [6–10].

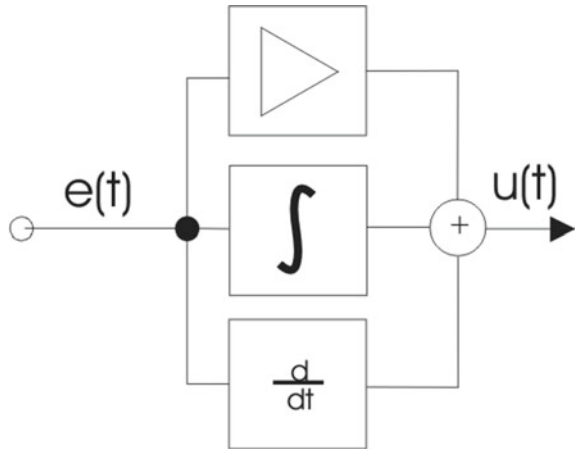
Figure 1 shows a diagram illustrating the principle of operation of the PID controller.

There are a large number of methods for calculating and setting PID controllers, ranging from the simplest empirical methods [11, 12] and ending with optimization methods [13].

The existing methods for the synthesis of PID controllers can be divided into the following groups:

- 1) Intuitive setup. Modifying the PID controller parameters until the control target is achieved.
- 2) Characteristic methods. Setting the PID controller according to the data obtained from the open loop test [14].
- 3) Analytical methods. PID controller parameters are calculated from analytical or algebraic dependencies between the object model and the control target.
- 4) Frequency methods. The frequency characteristics of the control object are used to set the PID controller.

Fig. 1 PID controller circuit



- 5) Optimal synthesis. These methods can be considered as a special kind of optimal control, where the coefficients of the PID controller are found using numerical optimization methods. Each of these methods has advantages and disadvantages. At the same time, other things being equal, preference should be given to optimization setting methods, which are based on the apparatus of mathematical programming, as more constructive methods. With the optimization approach, the calculation of the controller parameters is reduced to solving a nonlinear programming problem with all the resulting difficulties [15, 16].

3 Statement and Solution of the Problem

In the proposed method for calculating the controller parameters, the open-loop phase margin is chosen as the objective function, which makes it possible to replace the nonlinear programming problem with a much simpler task of finding the maximum phase-frequency characteristic of an open-loop system in a function of the controller parameters [17–23].

Let us formulate the initial problem statement as follows.

A linear stationary object of the second order with delay is given with a transfer function

$$W_o(p) = \frac{k_o e^{-p\tau}}{(T_1 p + 1)(T_2 p + 1)} \tag{1}$$

Let’s find the settings for the PID controller with the transfer function for the given object

$$W_p(p) = k_p + \frac{1}{T_i p} + T_d p, \tag{2}$$

providing maximum phase margin $\Delta\phi(k_p, T_i, T_d)$ at maximum cutoff frequency $\omega_c(k_p, T_i, T_d)$.

To solve the problem, we represent the transfer function of the controller in the form

$$W_p(p) = \frac{(T_3 p + 1)(T_4 p + 1)}{T_i p}, \quad (3)$$

where $T_3 T_4 = T_i T_d$, and $T_3 + T_4 = k_p T_i$.

We assume that $T_1 = T_3$, where T_1 – maximum time constant of the controlled object. Then the expression for the phase-frequency characteristic of an open-loop system will be written in the form

$$\phi(\omega) = -\frac{\pi}{2} - \omega\tau - \arctg\omega T_2 + \arctg\omega T_4. \quad (4)$$

The maximum phase-frequency characteristic at the cutoff frequency ω_c is found from the condition

$$\frac{d\phi}{d\omega} = -\tau - \frac{T_2}{1 + (\omega_c T_2)^2} + \frac{T_4}{1 + (\omega_c T_4)^2} = 0. \quad (5)$$

Let us find such a T_4 that when it is substituted into (5), ω_c is maximal. Obviously, this condition is satisfied for

$$\omega_c T_4 = 1. \quad (6)$$

Substituting (6) into (5), we obtain a cubic equation for calculating T_4 .

$$T_4^3 - 2(\tau + T_2)T_4^2 + T_2^2 T_4 - 2\tau T_2^2 = 0 \quad (7)$$

Substituting the value of the cutoff frequency obtained from (6) into the expression for the frequency response of an open-loop system

$$A(\omega) = \frac{k_0 \sqrt{1 + (\omega T_4)^2}}{\omega T_i \sqrt{1 + (\omega T_2)^2}} \quad (8)$$

You can calculate the constant of integration T_i

$$T_i = k_o T_4^2 \sqrt{\frac{2}{T_2^2 + T_4^2}} \quad (9)$$

Knowing the integration constant T_i from the ratio between the time constants obtained in (3), we can calculate the remaining parameters of the controller

$$k_p = \frac{T_3 + T_4}{T_i} \tag{10}$$

$$T_d = \frac{T_3 T_4}{T_i} \tag{11}$$

4 Calculation of the Controller Parameters for the Object of the Electric Generator Air Cooling System

As an example, the controller parameters for the object of the electric generator air cooling system were calculated, the transfer function of which is.

$$W_o(p) = \frac{0.3e^{-10\tau}}{(303p + 1)(102p + 1)}$$

Figure 2 and 3 show the log magnitude, phase-frequency characteristic, and the transient characteristics of the object and the system, obtained by calculating the

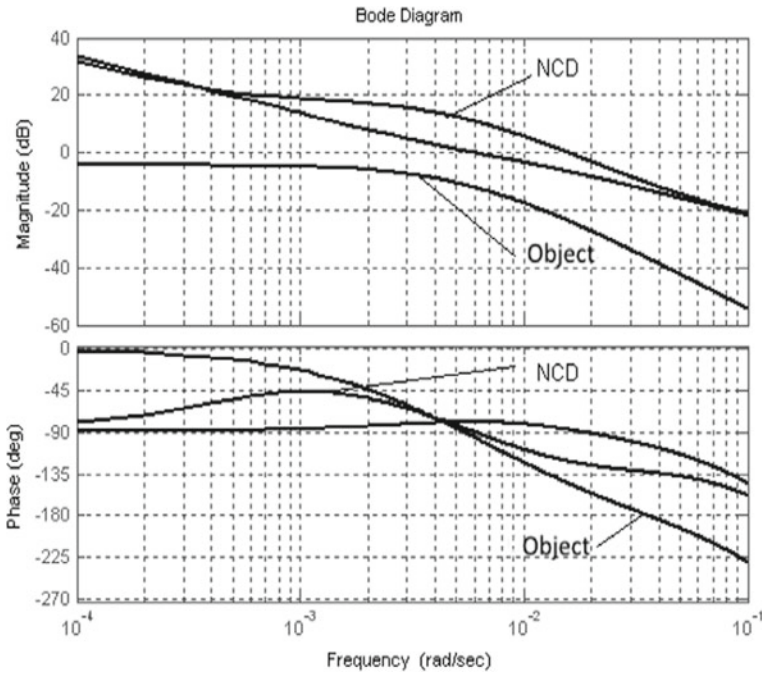


Fig. 2 Log magnitude and PFC of the object and systems at different controller settings

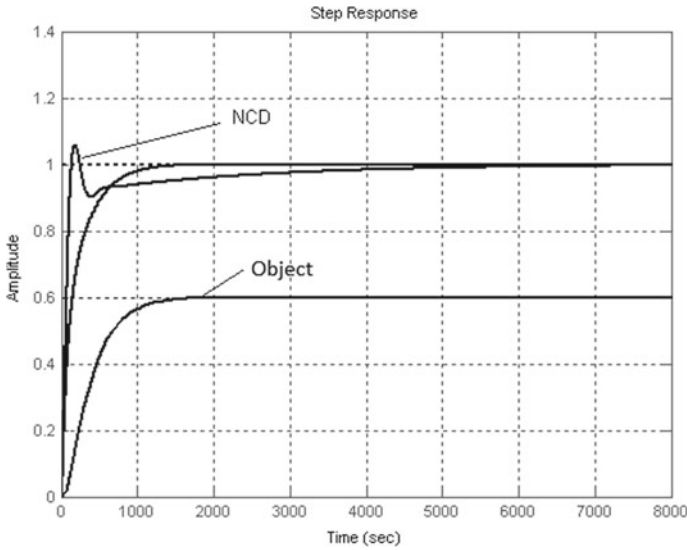


Fig. 3 Transient characteristics of the object and systems at various controller settings

parameters of the controller by the proposed method and using the Matlab NCD application.

To calculate the parameters of the controller in the proposed method for calculating the controller parameters, the open-loop phase margin is chosen as the objective function, which makes it possible to replace the nonlinear programming problem with a much simpler task of finding the maximum phase-frequency characteristic of an open-loop system in a function of the controller parameters.

The possibility of loss of stability is the main disadvantage of systems with feedback. Therefore, providing the necessary margin of stability is the most important step in the development and configuration of a PID controller.

The figure shows that the proposed method for calculating the parameters of the PID controller provides a maximum and significantly larger phase margin.

Logarithmic frequency response and phase response can be used to graphically represent the transfer function of an open-loop system and assess the stability margin. To assess the phase margin, first, using the frequency response, it is necessary to find the frequency ω_1 ("cutoff frequency" or "gain-crossover frequency"), at which $|G(j\omega_1)|=1$, then the corresponding phase margin is found from the phase response. To assess the gain margin, first, using the phase response, the frequency ω_{180} is found, at which the phase shift is 180° , then the gain margin is found from the frequency response. Examples of plots for assessing phase margin and gain for a system are provided.

It is shown that the presented method is more effective when tuning the PID controller for systems with a selected object and adopted parameters. When tuning the PID controller for objects with lagging according to the criterion of the maximum

phase margin, the transient process at the output of the control system is characterized by minimal overshoot and minimal (in comparison with other methods) transient process time.

The results of modeling the control system indicate the positive quality of control in full compliance with the requirements for the systems. From this it can be concluded that developed method allows calculating the settings of the controller, which implements the integral–differential control law in proportion to the given value of the the degree of oscillation, and, therefore, with the required degree of attenuation of the transient process.

5 Conclusions

PID controllers are widely used in modern automatic control systems, such as control of thermal systems and positioning systems. The use of PID controllers helps to reduce energy losses for tuning the system and provide faster approach of the required parameters.

At first glance, tuning a PID controller seems to be a simple operation, because it is necessary to determine the values of only three gain factors: proportional, integral and differential components. But in practice, determining the set of gains that provide the best performance in a closed-loop system is a difficult task. Traditionally, PID controllers are tuned manually or using formalized iterative procedures. Manual methods are time-consuming, and if they are applied to real equipment, this equipment can be damaged. Formalized iterative procedures are not always compatible with unstable objects, high-order objects, as well as objects with a small time constant. When working with a PID controller, it is also necessary to solve design problems, such as time sampling and scaling for fixed-point arithmetic.

For the correct operation of the regulator, it is necessary to correctly select its coefficients. The accuracy and speed of the system will depend on the correct selection of the coefficients. Quite often, the empirical selection of coefficients does not bring the desired results and takes a lot of time. Therefore, the task of developing new methods for tuning the PID controller is urgent. A comparative analysis of the obtained characteristics allows concluding that the proposed method for calculating the parameters of the PID controller provides a maximum and significantly larger phase margin, which almost eliminates overshoot in the system, but in this case the system response decreases.

The obtained parameters for setting the PID controllers ensured stable transient processes, both in terms of control and disturbing influences. ACS with PID controllers set according to the proposed methods provided transient processes in ACS with minimal overshoot and short control time. Thus, the methods proposed in this paper can be used in the production and commissioning of automation tools and automatic control systems.

The results of the experiments have shown the effectiveness and practical significance of the above methods and conducted studies.

Acknowledgements This work is supported by the Russian Foundation for Basic Research under grant 19-38-90186.

References

1. Desborough L, Miller R Increasing customer value of industrial control performance monitoring – honeywell’s experience. Honeywell Hi-Spec Solutions, Thousand Oaks, CA 91320
2. Tan W et al (2006) Comparison of some well-known PID tuning formulas. *Comput Chem Eng* 30:1416–1423
3. Astrom KJ et al (2004) Revisiting the Ziegler-Nichols step response method for PID control. *J Process Control* 4:635–650
4. Yaniv O et al (2004) Design of PID controller satisfying gain margin and sensitivity constraints on a set of plants. *Automatica* 40:111–121
5. O’Dwyer A (2006) *Handbook of PI and PID controller tuning rules*, 2nd edn. Imperial College Press, London
6. Alexandrov AG, Palenov MV (2011) Self-tuning PID-I controller. In: *Preprints of the 18th IFAC World Congress*, 28 August - 2 September 2011, Milano, Italy, pp 3635–3640
7. Astrom KJ, Hagglund T, Hang CC, Ho WK (1993) Automatic tuning and adaptation for PID controllers - a survey. *Control Eng Pract* 1:699–714
8. Astrom KJ, Hagglund T (2006) *Advanced PID control*. Systems, and Automation Society, The Instrumentation, p 460
9. Blevins TL, McMillan GK, et al (2003) *Advanced Control Unleashed*. ISA, North Carolina, Research Triangle Park
10. Hagglund T, Astrom KJ (1991) Industrial adaptive controllers based on frequency response techniques. *Automatica* 27:599–609
11. Hang CC, Astrom KJ, Ho WK (1993) Relay auto-tuning in the presence of static load disturbance. *Automatica* 29(2):563–564
12. Hjalmarsson H, Gevers M, Lequin O (1998) Interactive feedback tuning: theory and applications. *IEEE Control Syst Mag* 18(4):26–41
13. Ho WK, Hang CC, Wojsznis W, Tao QH (1996) Frequency Domain Approach to Self-Tuning PID Control. *Control Eng. Practice* 4(6):807–813
14. McMillan GK (1983) *Tuning and Control Loop Performance*, second edition. ISA, North Carolina, Research Triangle Park
15. Sato T, Kameoka K (2008) Self-Tuning Type-2 PID Control System and its Application. *Proceeding of 17th IFAC World Congress* pp 11287–11292 Seoul Korea
16. Suda N et al (1992) *PID Control*. Asakura Shoten Co., Ltd., Japan
17. Voda A, Landau ID (1995) A method for the auto-calibration of PID controllers. *Automatica* 31(2):41–53
18. Ziegler JG, Nichlos NB (1942) Optimum settings for automatic controllers. *Trans. ASME* 64:759–768
19. Chien KL, Hrones JA, Reswick JB (1952) On automatic control of generalized passive systems // *Trans. ASME*, 74, 175185.
20. Willis MJ (2009) Proportional-integral-derivative PID controls. *Proc. IEEE*, 10, 150–163. [Electron. resource]. <http://www.PAControl.com>.
21. Vrani D, Kocijan J, Strmnik S (2004) Rejection tuning method for PID controllers. [Electron. resource]. <http://asc2004.ee.mu.oz.ru>
22. Hien KL, Hrones JA, Reswick JB (1952) An automatic control of generalized passive systems// *IEEE Intern. conf. robotics and automation*. San Diego: IEEE Press, 175–185
23. Dorf RC (2008) *Modern control system*. Pearson Educat, Boston

Detailing the Impact Structure of the Participants of the Complex Transport Service



Valerii Zubkov 

Abstract In the period of reforms being implemented in the railway industry, the expected volume of carriage in the near term can be achieved through a complex approach, namely through: consolidation of companies and means of transport, formation of new models of transport services, creation and introduction of integrated high-technology information systems. In such a case, the holistic approach to effective management of the production system should enable impact estimability on implementation of quality of transport services by each party of the production process and determine the degree of their responsibility. The article illustrates the main aspects of quality management of customer service as one of the key factors of transportation company efficiency in the segment of freight transportation. The procedure of quality estimation of the transportation service is presented in the Target model of the complex transport service by each of its parties in the different transportation categories. Specification of the impact structure of the parties of the complex transport service on its quality level through calculation of a responsibility ratio has been made.

Keywords Quality of transport services · Detailed structure of impact · Consumers of transport services · Responsibility coefficient · Quality coefficient

1 Introduction

Most transport production processes in the railway industry consist of multiple transport services, in many cases not interconnected and not interacting, which in itself complicates a single technological process and reduces its efficiency. Currently, in the current conditions for the consumer of transport services there is a problem of determining the zones of influence of the participants of transport - providing functions on the quality of service and determining the degree of their influence on the quality criteria. To solve these problems, the author of the article proposed a target model of integrated transport services in the freight market segment. It uses the principles of

V. Zubkov (✉)
JSC FGC, Masha Poryvaeva Street, 34, Moscow 107078, Russia

consolidated, consistent and preferential application of various transport services in a single transport system and in different categories of transportation. The use of this model allows one to achieve optimal planning and quality management of transport services, while providing maximum aggregate profit. This article represents a logical development of the early editions. Thus, in [1] the model of complex transport service is proposed, in [2] the stages of formation of the target model of complex transport service in the field of freight transportation are presented. To improve the production process, in terms of improving the quality of transport services and reducing costs, it is necessary to develop new approaches.

2 Materials and Methods

In this article the method of evaluation of quality of transport service in the target model of the complex transport service by detailing the structure of influence of subjects of the complex transport service on the level of its quality in different categories of transportations [2, 3] is presented. At present, the main quality criteria in the market of transport services in the cargo transportation space are: the safety of the transported cargo and goods (Ksafe), the safety of the transportation of finished products (Kfp), the speed of delivery of goods and goods (Ksp), constancy and mass transportation of products (Ktr), price availability and rationality of transport services (Kprice) [3, 4]. These criteria actually give an idea of the consumers' attitude towards observance and effective improvement of transport services quality by all participants of the transport process. In order to ensure the level of each quality criterion, it is necessary to develop and implement a set of measures aimed at increasing the quality of transport services, which in turn require large financial investments.

In the existing model of transport services in the area of cargo transportation, the level of mandatory quality and its significance according to the requirements of federal laws of the Russian Federation is established in the legal field of responsibility for failure to meet the criteria of quality of services [4, 5].

Figure 1 shows the subjects of services in a descending order of the level and competence of responsibility for compliance with the requirements of the main quality criteria.

It can be seen that the carrier, the owner of infrastructure and the owner of the rolling stock [5] must meet five main quality criteria. Therefore, the quality factor ($K_{qua}^{tr.s}$) is 1. The consignor, consignee and the owner of the track are responsible [6] for the 4 main quality criteria, resulting in a quality factor of 0.8. The rolling stock operator and freight forwarder [6, 7] actually fulfil two main quality criteria, respectively, the quality factor is 0.4. When organizing a single transportation process [7], each transport service subject is responsible for quality criteria in its area of influence. Coefficients of quality of transport services show full compliance with the conditions of transport service, but cannot be part of a single quality compliance (as a result, do not give a total of 1 or 100%).

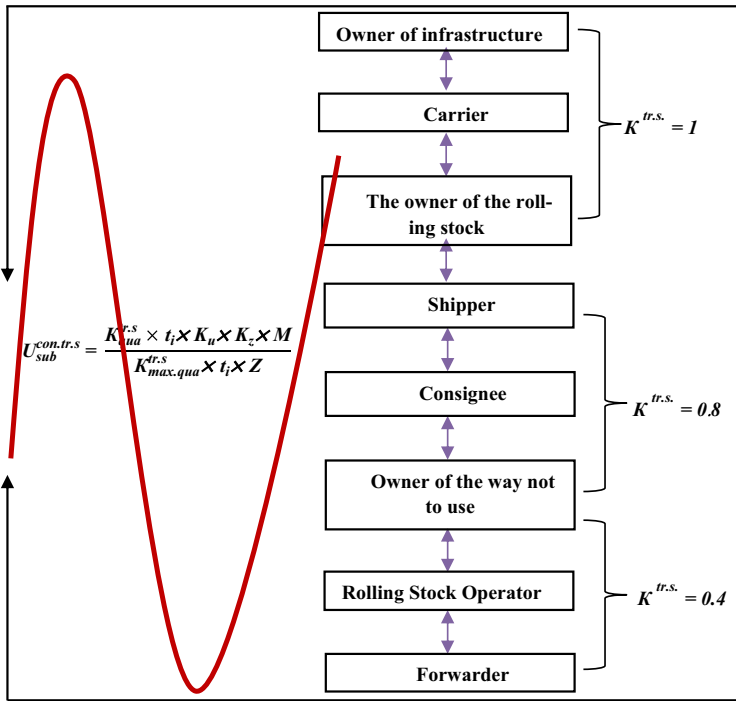


Fig. 1 Spatial structure of the location of transport services subjects in a descending order by the level and competence of responsibility for compliance with the requirements of the main quality criteria

Calculation of the quality factor provides an opportunity to assess the impact on compliance with the level of quality criteria by transport service providers, but does not provide a definition of their responsibility [7, 8]. For this purpose, it is necessary to detail the structure of the impact of the participants of the production transport process on the quality of services provided [8] by calculating the coefficient of maximum quality assurance by all subjects ($K_{max.qua}^{tr.s.}$). The coefficient of maximum quality assurance is defined as a sum of the coefficients of quality of the subjects of transport services participating in a single transport process [9]. The number of transport services subjects participating in a single process of goods - cargo movement may vary depending on the design of the transport services market:

$$K_{max.qua}^{tr.s.} = \sum_{qua\ 1...i} K_{qua\ i}^{tr.s.} = K_{qua\ 1}^{tr.s.} + K_{qua\ i}^{tr.s.} \tag{1}$$

To determine the amount of responsibility of the subjects of transport services, the responsibility coefficient is calculated by dividing the coefficient of quality of the subject of transport services ($K_{qua}^{tr.s.}$) by the coefficient of maximum quality assurance ($K_{max.qua}^{tr.s.}$):

$$K_{sub}^{con.tr.s.} = \frac{K_{qua}^{tr.s.}}{K_{max.qua}^{tr.s.}}, \quad (2)$$

To determine the quality level of transport and logistics services, the coefficient of the quality level of service is calculated by the following formula:

$$U_{sub}^{con.tr.s.} = \frac{K_{qua}^{tr.s.} \times t_i \times K_u \times K_z \times M}{K_{max.qua}^{tr.s.} \times t_i \times Z}, \quad (3)$$

where:

t_i - time for performing i - transport service;

K_u - correlative coefficient of the transport service provider's liability;

K_z - correlation coefficient of the Client's liability for transport services;

M - number of calendar days in the reporting period;

Z - rhythm of transport services provision is determined by the number of calendar days required to fulfill the transport services provision plan by the Provider.

The formula shows that the service quality level factor depends on the time of transport service performance, the correlation coefficients of responsibility of the Contractor and the Customer, the quality factor of the subject of transport services. It follows from this that the increase of responsibility of the subjects for compliance with the plan of transport services is the most important condition for improving the quality of service and reducing the cost of transport services.

3 Results

In the existing model, the coefficient of maximum quality assurance of transport services is 6.2. Provided that there is the impact of all participants of transport services allows providing functions on the quality of provided services in a single transportation process.

Figure 2 shows the dependence of the quality factor of the subjects of transport services on their responsibility factor.

In Fig. 2, you can see that the dependency curve tends to decrease (curve 3) and increase (curve 1). Moreover, the higher the value of the responsibility factor is (curve 1, curve 2), the higher the value of the quality factor of the subject of transport services is, i.e., the more investments are made by the corresponding participants of the process to provide guaranteed transport services.

Thus, in the current model of transport services on the railway transport there are subjects, including those with a minimum share of responsibility for compliance with the main quality criteria, and therefore less effective in the development of transport services quality [10, 11]. The possibility of effective and rational interaction with other modes of transport in a single transport system has been eliminated [11, 12], which ultimately leads to higher prices for finished products and non-competitive consumers of services.

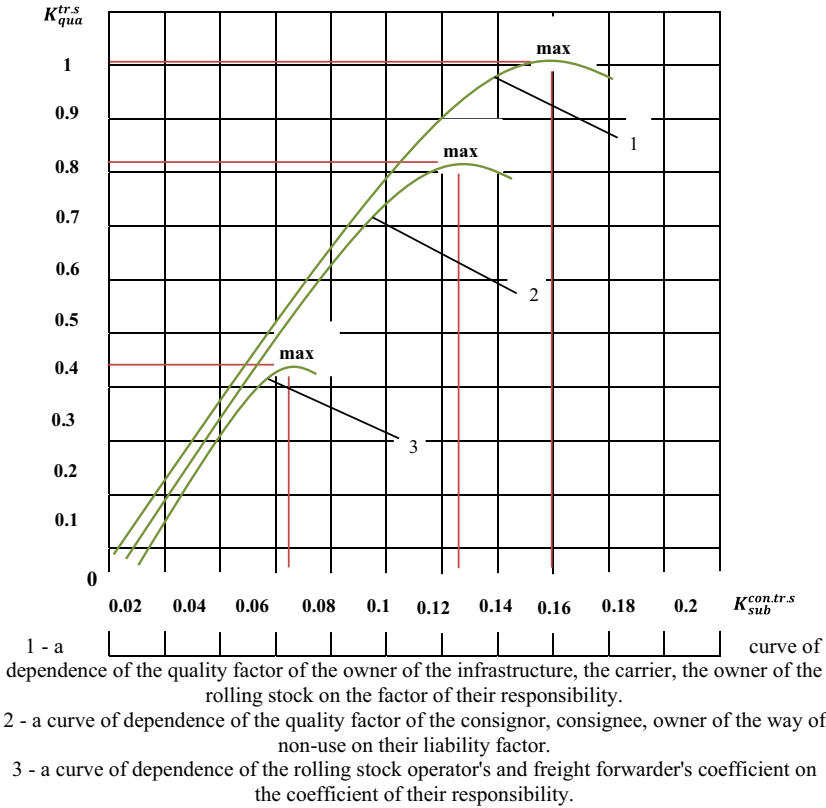


Fig. 2 Dependence of the quality factor of transport service subjects on their responsibility factor

4 Discussion

In conditions of declining growth rate of the country's economy, it is necessary to search for new, alternative ways to improve the quality of the transport process in the market of transport services in various categories of transport using the potential of a unified transport system [12, 13].

The author of the article suggests a new target model of complex transport service, which presents new subjects of transport services and defines the areas of their impact by categories of transportation [13, 14].

Figure 3 presents new subjects of transport services and their impact areas in categories of transportation in the proposed target model of the integrated transport service.

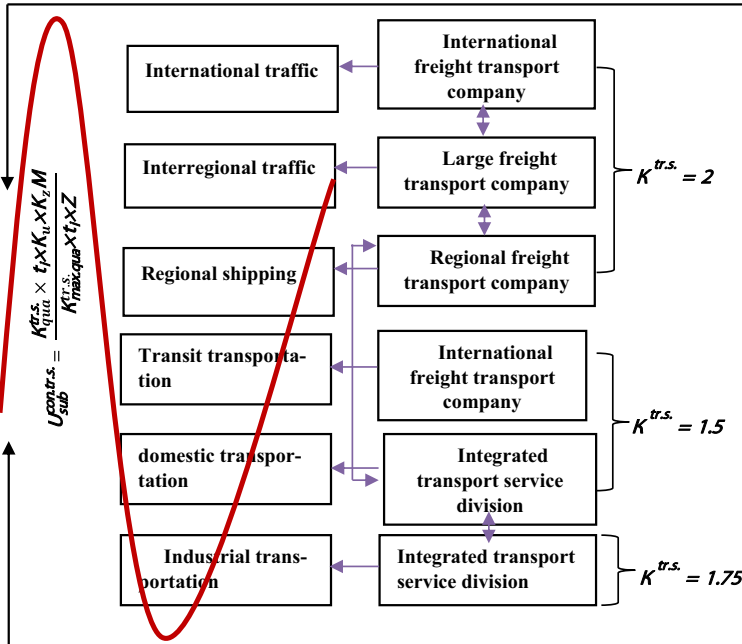


Fig. 3 Spatial structure of new subjects of transport services and areas of their influence in the categories of transportation in the proposed target model of the complex transport service

Figure 3 shows that a regional freight transport company in the category of transportation (regional), a large-scale freight transport company in the category of transportation (interregional) and an international freight transport company in the category of transportation (international) ensure the fulfillment of all eight main criteria of quality of a complex transport service. Consequently, the quality factor ($K_{qua}^{tr.s}$) is 2. Division of the complex transport service in the category of transportations (domestic), the international freight transport company in the category of transportations (transit) ensures the fulfillment of seven main quality criteria. The quality coefficient ($K_{qua}^{tr.s}$) is 1.75. The division of the complex transport service in the category of transportations (industrial) ensures the fulfillment of six main criteria, respectively, the quality coefficient ($K_{qua}^{tr.s}$) is equal to 1.5.

The coefficient of maximum quality assurance is defined as the sum of the coefficients of quality of the subjects of transport services participating in the complex transport service:

$$K_{max.qua}^{tr.s} = \sum K_{qua\ 1...i}^{tr.s} = K_{qua1}^{tr.s} + K_{qua\ i}^{tr.s}, \tag{4}$$

The responsibility factor of the subjects in the model of the complex transport service is calculated as a partial division of the factor of quality of the complex transport service of the subject ($K_{qua}^{tr.s.}$) by the factor of maximum quality assurance of the complex transport service ($K_{max.qua}^{tr.s.}$):

$$K_{sub}^{con.tr.s.} = \frac{K_{qua}^{tr.s.}}{K_{max.qua}^{tr.s.}}, \tag{5}$$

The quality level coefficient of transport and logistics services is calculated by the formula:

$$U_{sub}^{con.tr.s.} = \frac{K_{qua}^{tr.s.} \times ti \times Ku \times Kz \times M}{K_{max.qua}^{tr.s.} \times ti \times Z}, \tag{6}$$

In the proposed model the coefficient of maximum quality assurance of the complex transport service is 11 under the conditions of the impact on the quality of services provided by all participants of the complex transport service and the use of two types of transport in the transport scheme, namely: road and rail. When used in the transport process [14, 15] in more modes of transport, this coefficient increases.

As a result, the liability factor for an international freight transport company in the categories of transportation (international and transit) is calculated as follows:

$$K_{sub}^{con.tr.s.} = \frac{2+1.75}{11} = 0.34.$$

For subdivision of the complex transport service in categories of transportation (internal and industrial) the coefficient of responsibility is calculated as follows:

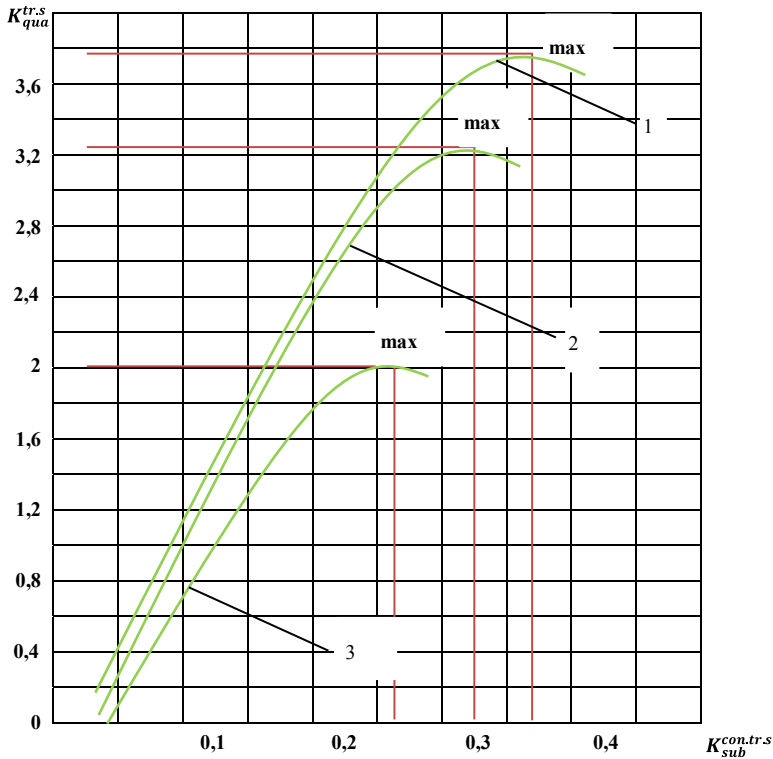
$$K_{sub}^{con.tr.s.} = \frac{1.5+1.75}{11} = 0.3.$$

For a regional freight transport company in the category of transportation (regional) and a large-scale freight transport company in the category of transportation (inter-regional) the calculation of the coefficient of responsibility looks like this:

$$K_{sub}^{con.tr.s.} = \frac{2}{11} = 0.18.$$

Figure 4 shows the dependence of the quality coefficient of the subjects of transport services on the coefficient of their responsibility for the categories of transport in the target model of the complex transport service.

Figure 4 shows that the curve of dependence between $K_{qua}^{tr.s.}$ and $K_{sub}^{con.tr.s.}$ has the desire to fill, and the higher the value of $K_{qua}^{tr.s.}$, this filling occurs earlier (curve 1, 2). In its turn, the coefficient of responsibility of transport service subjects depends on the coefficient of maximum quality assurance.



- 1 - Curve of dependence of the quality factor of an international freight transport company in the categories of transportation (international and transit) on the liability factor.
- 2 - Curve of dependence of the quality coefficient of the division of complex transport service in the categories of transportation (domestic and industrial) on the liability coefficient.
- 3 - Curves of dependence of the quality coefficient of a regional transport company in the category of transportation (regional) and a large-scale freight transport company in the category of transportation (interregional) on the liability coefficient.

Fig. 4 Dependence of the quality factor of transport services subjects on the factor of their responsibility by transport categories in the target model of the complex transport service

As a result, the parameters of conducted calculations show [15] that the processes of rendering transport services in the New Target Model have been formed effectively. The data on responsibility coefficients show that investment in ensuring the main criteria of quality by the subjects of transport services will be maximum. In practice, there may be cases in the process of rendering transport services in which a certain subject could not provide on the proper level those quality criteria that must be met. This leads to incomplete compliance with the quality index of complex transport services. It should be noted that this provision leads to failure to meet the requirements of transport and logistics services, and, therefore, compensation of losses to the

consumer, the subject of the service because of which occurred failure to meet one of the quality indicators.

5 Conclusion

The presented in the article technique of transport service quality estimation in the Task model of the complex transport service allows one to trace and accordingly estimate influence of each subject on quality assurance of services with the help of maximum values of quality coefficients.

On the basis of the detailed structure of influence of participants of the complex transport service on improvement of the quality of service, coefficients of their responsibility for observance of the plan of transport services, calculated for each category of transportations, are defined.

By calculating the coefficients of the quality service, it is possible to assess the value of the contribution to the compliance with the requirements of transport and logistics services not only by the Executor, but also by the Customer of these services.

The presented Task Model of Integrated Transport Services excludes subjects of transport services with a minimum share of responsibility for compliance with the main quality criteria, and therefore less effective in the development of the quality of transport services. In this model we formed an effective and rational mutualization of different types of transport in a single transport system, which as a result reduces the rate of growth of value added of finished products and increases the competitiveness of consumers of integrated transport services.

The responsibility coefficients should be used rationally when determining the size of obstacles to the subjects of transport services, as well as when calculating the cost of transport services and income rate.

References

1. Chen Z, Daito N, Gifford JL (2017) Socioeconomic impacts of transportation public-private partnerships: a dynamic CGE assessment. *Transp Policy* 58:80–87
2. Dementiev A (2018) Contracting out public transport services to vertical partnerships. *Res Transp Econ* 69:126–134
3. Baklanov A, Cárdenas B, Lee T-C et al (2020) Integrated urban services: experience from four cities on different continents. *Urban Clim* 32:100610
4. Weber KM, Heller-Schuh B, Godoe H, Roeste R (2014) ICT-enabled system innovations in public services: experiences from intelligent transport systems. *Telecommun Policy* 38:539–557
5. Jittrapirom P, Marchau V, Van Der Heijden R, Henk Meurs H (2014) Dynamic adaptive policymaking for implementing Mobility-as-a Service (MaaS). *Res Transp Bus Manag* 27:46–55

6. Sun L, Wang S, Liu S, Yao L, Luo W, Shukla A (2018) A complete research on the feasibility and adaptation of shared transportation in mega-cities – a case study in Beijing. *Appl Energy* 230:1014–1033
7. Kavanagh P (2016) A case for negotiated performance-based contracting rather than competitive tendering in government public transport (bus) service procurement. *Res Transp Econ* 59:313–322
8. Gao X, Cao M, Yang T, Basiri A (2020) Transport development, intellectual property rights protection and innovation: the case of the Yangtze River Delta Region, China. *Res Transp Bus Manag* 37:100563
9. Lovelace R, Parkin J, Cohen T (2020) Open access transport models: a leverage point in sustainable transport planning. *Transp Policy* 97:47–54
10. Kiba-Janiak M (2019) EU cities' potentials for formulation and implementation of sustainable urban freight transport strategic plans. *Transp Res Procedia* 39:150–159
11. Blyde J, Molina D (2015) Logistic infrastructure and the international location of fragmented production. *J Int Econ* 95(2):319–332
12. Shahin M, Babar MA, Chauhan MA (2020) Architectural design space for modelling and simulation as a service: a review. *J Syst Softw* 170:110752
13. Rothengatter W (2019) Megaprojects in transportation networks. *Transp Policy* 75:A1–A15
14. Jokinen J-P, Sihvola T, Mladenovic MN (2019) Policy lessons from the flexible transport service pilot Kutsuplus in the Helsinki Capital Region. *Transp Policy* 76:123–133
15. Nowakowska-Grunt J, Strzelczyk M (2019) The current situation and the directions of changes in road freight transport in the European Union. *Transp Res Procedia* 39:350–359

Reproducibility of the Properties of Foamed Ceramics by the Processability Factor Method



Denis Portnyagin  and Elena Loginova 

Abstract The selection of formulations and technological parameters for the production of foamed ceramics is complicated by the multicomponent composition and the variety of technological modes of firing. In order to predict the properties of foamed ceramics and obtain reliable its characteristics, as well as taking into account the peculiarities of the studied production technology, a computational-graphical method is used using the so-called “factor of manufacturability” of foamed ceramics. This coefficient connects the dependences of properties on changes in average density and at the same time takes into account a specific technological scheme of production. Foam ceramics compositions were selected on the basis of previous studies. The main conclusions on the influence of the main components of the compositions on the properties of foamed ceramics are presented. Samples of foam ceramics were made using low-temperature foaming technology and their properties were determined using standard methods. The reproducibility of the values of the properties of foamed ceramics produced by experimental industrial testing with the properties determined using a nomogram was checked. The normative values according to the nomogram are confirmed by verification studies with a batch of prototypes. Thus, the ultimate strength of the foam ceramics was predicted depending on the average density and manufactured according to a specific technological scheme.

Keywords Foam ceramics · Workability factor · Porosity · Raw ceramics · Crock · Low-temperature firing

1 Introduction

Ceramic materials have a combination of a set of demanded consumer and operational properties, such as lightness and low thermal conductivity. The shortage of durable, fireproof, bio- and corrosion-resistant inorganic heat-insulating materials

D. Portnyagin (✉) · E. Loginova
Department of Construction, Khakass Technical Institute - Branch of Siberian Federal University,
Abakan, Russia

can be reduced by producing piece goods in the form of bricks and blocks of highly porous ceramics.

Foam ceramics is an environmentally friendly energy-saving heat-insulating and building material. It is used for external wall insulation and building walls. The main raw materials for the production of foamed ceramics are both primary raw materials—feldspar, clays, etc., and secondary raw materials—ash and slag waste, overburden, ceramic waste, shale, etc. As a result of physical processes and chemical reactions in the production process, incl. firing, many even closed pores are formed, evenly distributed throughout the entire volume of the product. At the same time, such factors as the multicomponent composition of the charge, as well as a high sensitivity to the parameters of the technological scheme, complicate the production of foamed ceramics.

The process of producing foamed ceramics, like foam glass, consists in drying raw materials, cleaning them from dirt, grinding, heating together with foaming agents in rotary kilns. The predominant use in the composition of waste allows a significant reduction in the cost of the product obtained in this way.

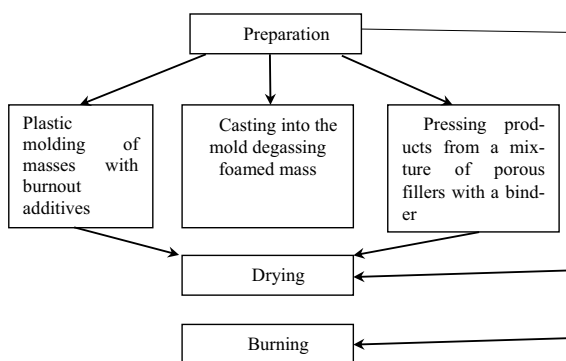
The porous structure of the investigated foam ceramics is created according to the energy-efficient technology of low-temperature foaming of masses during gas evolution [1–3]. At the same time, the technology allows the manufacture of piece products in a one-stage firing mode, [4–11] bypassing the stage of preliminary production of porous granules (Fig. 1).

However, a significant obstacle to the mass production of foamed ceramics is its multicomponent nature and the absence of developed technical compositions that provide stability, structural strength of raw foamed masses and porous ceramics [12–15].

The internal structure and strength characteristics of foamed ceramics are also determined by the parameters of the structure of the original porous matrix.

For the mass production of ceramic foam materials and products, it is necessary to develop a number of technological requirements for the basic properties of ceramic foam [16–20]. To simplify the selection of formulations and technological parameters for the production of foamed ceramics, regression equations of dependences, as well

Fig. 1 Technological scheme for the production of heat-insulating porous ceramics



as nomograms of dependences of the investigated properties on characteristics, have been tested.

2 Methods

The chemical composition of the studied raw materials, including used industrial waste, is shown in Table 1. Based on these data, the compositions of the masses were previously selected [1–3]. The main requirements for clay raw materials to obtain defect-free ceramic foam products are: low melting point and high coagulability. Taking into account these factors, 2 types of clay raw materials were selected for the study, namely: Izykh clay and mudstones.

A standard technological scheme for the production of foam ceramics was used, which includes the following stages: preparation of the raw material mixture; receipt of slip; foaming of a slip; forming, drying and firing the product. The charge was prepared by joint mixing in a mixer of the components, the ratios of which are shown in Table 1.

At the second stage of preparing foam ceramics, a slip is prepared. For this, a mixture of water and liquid glass is prepared separately. The latter is introduced to fix the structure of the slip during drying, to reduce the shrinkage and density of the raw ceramic foam. Subsequently, a pre-prepared mixture of components is added to the slip, mixed for 1–2 min until a homogeneous slip is obtained. The combined sodium hydroxide and water glass helps to accelerate the process of structure formation of the raw material, reducing its shrinkage.

The resulting foam slurry is poured into metal collapsible molds $50 \times 50 \times 50$ mm in size, lined with paper from the inside, which is necessary to protect the raw material after stripping from mechanical damage during further transportation to the furnace.

Table 1 Chemical composition of the studied raw materials

Raw materials	The content of oxides, % wt								
	SiO ₂	Al ₂ O ₃	TiO ₂	Fe ₂ O ₃	CaO	MgO	Na ₂ O	K ₂ O	Loss on ignition
Izykh clay	61.26	16.45	0.31	4.76	4.82	1.41	0.43	0.32	9.18
Argillite	58.12	20.35	0.01	6.01	3.17	1.66	1.20	2.30	8.20
Wollastonite rock	51.70	0.11	–	0.31	46.08	1.23	0.25		0.32
Diopside-containing rock	57.80	0.18	0.03	0.09	23.30	13.40	0.09	0.06	5.05
Sorsky quartz-feldspar sand	62.05	15.94	0.58	4.18	4.72	2.01	4.27	3.85	2.39
High-calcium slag	50.69	8.09	–	8.94	27.51	3.50	0.27	0.20	0.80
High-calcium ash	46.24	6.56	0.84	7.78	29.28	5.28	0.51	0.24	1.44
Cullet	67.40	5.81	–	1.76	7.21	3.38	12.73	2.0	–

Then the samples are sent for drying within 24 h until the residual moisture content of the product is 5–7% at 40–60 °C. The process of drying ceramic foam materials consists of two main redistributions: holding the laid foam clay mass in molds until the required plastic strength is achieved and drying the foam clay raw after stripping. The most important ceramic characteristic that has a direct impact on the quality is a moisture content, sensitivity to the drying of raw materials. The material content of materials characterizes the diffusion coefficient of moisture, which is a function function, and for the falling velocity period also the function of moisture content. The evaporation of water from bodies with a porous structure differs from the evaporation of a liquid from a free surface, because the plane of evaporation is located at a certain depth from the surface. In a porous mass, the depth of the evaporation plane changes as the foam breaks down, which leads to an increase in the heat transfer coefficient. This fact should also be taken into account when predicting the properties of the final product.

In accordance with the technology under study, three control samples were made, its ultimate compressive strength and average density were determined according to standard test methods.

After firing, ceramic samples were visually inspected. In all samples, burnout, underburning, cracks and spalling are not visible. Then the determination of the physical and mechanical properties was carried out.

In accordance with the technology under study, three control samples were made, its compressive strength and average density were determined according to standard test methods.

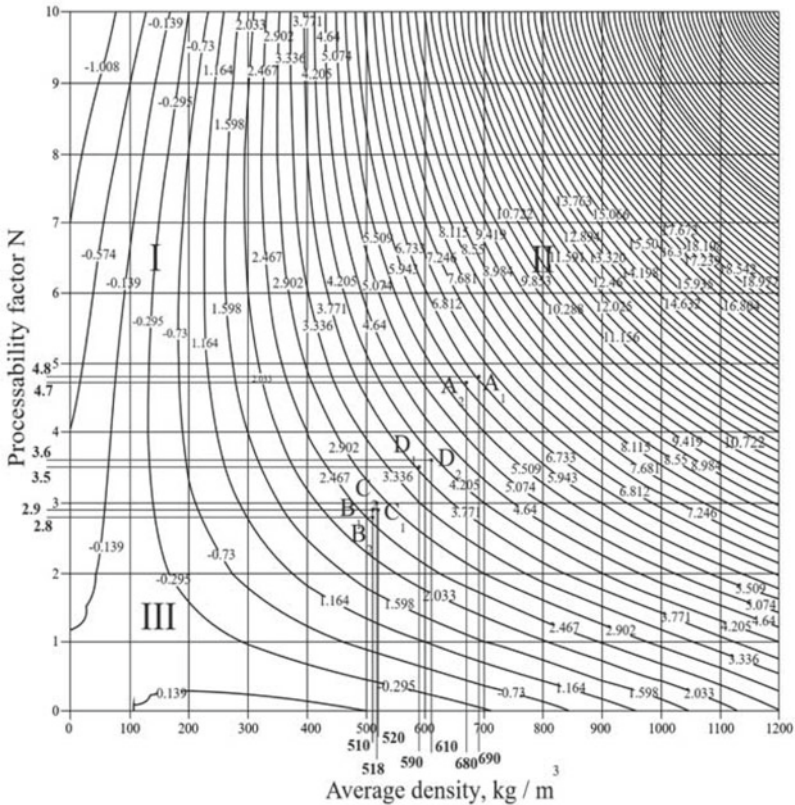
In order to predict the properties of foamed ceramics and obtain reliable its characteristics, as well as taking into account the peculiarities of the studied production technology [13–20], a computational and graphical method is used using the so-called “manufacturability factor” of foamed ceramics [20]. This coefficient is a certain constant for a specific production method and connects the dependences of changes in properties on changes in average density. Based on the analysis of numerous works, the authors [20] constructed the curves of the dependences of the change in the ultimate strength in compression of foamed ceramics for the range of average density values in the range from 100 to 1200 kg/m³.

3 Results

The processes of the technology for producing foam ceramics are very complex, and the analyzed phenomena cannot be described by a simple function of one variable. When describing the process of producing foamed ceramics, the number of these variables can be increased, which increases the forecasting accuracy, but at the same time complicates the forecast. Although the theory of similarity and the theory of dimensions make it possible to reduce the number of parameters, the resulting criterion equations usually contain more than two variables. The display of such functions using graphs is associated with a number of inconveniences, including the possibility

of forecast errors. The use of the presented nomogram allows one to obtain an image of the function of several variables (technological factors), with the help of which it is possible to determine the value of one of the functions (for example, the density of foam ceramics), if the values of all variables are known.

Transferring the results of laboratory tests according to the developed technology for the production of foamed ceramics and analyzing the numerical values of the nomogram (Fig. 2) shows that the properties of foamed ceramics largely depend on the selected mode of the technological scheme. The values of the properties of foamed ceramics with the same average density vary over a wide range. However, using the factor of manufacturability, it is possible to accurately predict the properties of foamed ceramics. Thus, the introduction of the manufacturability factor makes it possible, based on the data of the literature review, for structural, structural-heat-insulating and heat-insulating ceramic foam materials, to predict the basic indicators of the ultimate compressive strength and the density of products by the computational and graphic method.



Using nomograms [20], one can predict the ultimate strength of foamed ceramics made according to a specific technological scheme. To check the reproducibility of the results of experiments with the studied nomogram, three control samples were made using this technology. The ultimate strength of the samples in compression and the average density (Table 2) were determined by the known standard methods.

4 Discussion

The normative values developed by the authors [20] are confirmed by verification studies with a batch of prototypes (Tables 2 and 3). The use of Izykh clay and mudstones is due to their high plasticity (plasticity number 13–20 for mudstones, 19–29 for Izykh clay) and binding properties that determine the process of foaming of the masses and stabilization of their structure. At the same time, it is necessary to take into account the specific effect of stabilizing foaming additives with a simultaneous decrease in the amount of water, drying time and shrinkage, and to correlate these factors with the technological scheme of production.

Diopside-bearing and wollastonite rocks, composed of diopside and wollastonite minerals, respectively, and some calcite, high-calcium slag, consisting of a

Table 2 Properties of heat-insulating ceramic samples

Material property	Composition 1		Composition 2	
	Consignment 1	Consignment 2	Consignment 1	Consignment 2
Density, kg/m ³	690	670	510	510
Compressive strength, MPa	4.8	4.7	2.9	2.8

Table 3 Properties of thermal insulation ceramics in pilot tests

Material property	Composition 1		Composition 2	
	Consignment 1	Consignment 2	Consignment 1	Consignment 2
Firing temperature, °C	1090–1100	1090–1100	950–970	950–970
Shrinkage, %	4.2	4.3	1.6	1.8
Density, kg/m ³	520	518	590	610
Water absorption, % wt	37.3	37.4	35.3	34.9
Porosity, %	72,1	72,2	69,1	69,0
Compressive strength, MPa	2,9	3,0	3,5	3,6
Thermal conductivity coefficient, W/m·K	0,12	0,17	0,20	0,21

glass phase (80–90%) of a calcium-ferroaluminosilicate composition and a crystalline phase (10–20%) of minerals anorthite, diopside, wollastonite, wollastonite and quartz-feldspar sorsk sand containing orthoclase, albite and anorthite are promising as structure- and flux-forming additives for the formation of a strong inter pore wall of the macrostructure of foamed ceramics. The cullet intensifies the sintering process of foam ceramics and contributes to the formation of the phase composition of the wall of the macrostructure of the foam ceramics.

At a temperature of 20–30 °C in clay-containing compositions with the use in their composition for foaming of aluminum powder and 2 N sodium hydroxide solution in an amount of 30% due to its chemical interaction with clay minerals, sodium hydroaluminosilicate is formed. Aluminum powder solves two problems in structure formation: it acts as a gas former, and also binds the alkaline component into insoluble sodium hydroaluminosilicates. Sodium hydroaluminosilicate helps to increase the strength properties of the solid phase of clay rocks, and, consequently, the strength of the foamed masses. In addition, sodium hydroaluminosilicates and calcium hydrosilicates form neoplasms in the form of strong crystalline hydrates. This increases the viscosity of the clay slurry compositions, which guarantees a porous structure of sufficient strength at the stage of low-temperature foaming.

Water glass or gypsum in a composition with sodium hydroxide increases the strength of the foamed ceramics after foaming. This is explained by the inherent astringent properties of water glass and calcium hydrosilicates formed by chemical interaction with clay minerals. Thus, an increase in viscosity and hardening of water-clay-containing compositions occurs more intensively, since water glass and gypsum independently have astringent properties. Gypsum, which is inert to chemical interaction with clay minerals, but at the same time has astringent properties and therefore increases the viscosity of water-clay-containing compositions and their hardening over time, the more intensively the higher its grade.

When using the addition of high-calcium ash, free ash calcium oxide takes an active part in the formation of wollastonite. Kaolinite provides a more intense formation of the mullite-like phase. At the same time, the use of kaolinite in comparison with mudstones determines a higher strength of ceramics from compositions based on it.

Experimental-industrial testing was carried out, as a result of which it was found that foam ceramics can be obtained using energy-efficient technology of low-temperature foaming. The slip was prepared from a mixture of Izykh clay, and variants of compositions from a mixture of mudstones and non-plastic components on water heated to 50–60 °C were considered. Subsequently, an aluminum suspension is added and thoroughly mixed. Pilot testing data correlate with the results of preliminary laboratory tests (Fig. 2).

5 Conclusions

The developed heat-insulating materials provide a 2.42–4.05-fold increase in the heat-transfer resistance of a wall of an assumed thickness while reducing its mass by a 2.3–2.92-fold. At the same time, the use of the nomogram of the manufacturability factor makes it possible to predict the ultimate strength of foam ceramics manufactured according to the investigated technological scheme with sufficient accuracy.

The results of production testing, obtained on two batches of samples made on different batches of raw materials (Table 2 and 3), confirm the results of laboratory research on the development of ceramic building thermal insulation materials.

Solving the issues of reducing the average density of ceramic products while ensuring the required physical and mechanical indicators is one of the promising scientific directions that need to be developed and brought to industrial adaptation. Expansion and improvement of nomograms will significantly speed up this process due to accurate prediction of the properties of foamed ceramics.

References

1. Selivanov YuV, Shchiltsina AD, Loginova EV (2010) Thermal insulation ceramic materials with using binders. *Build Mater* 7:49–51
2. Selivanov YuV, Shiltsina AD, Loginova EV, Selivanov VM (2011) Heat-insulating ceramics based on low-energy-consuming process of foaming masses. *Izv. Univ Constr* 3:12–19
3. Selivanov YuV, Selivanov VM, Loginova EV, Shiltsina AD, Portnyagin DG (2010) The use of porous aggregates in the construction of thermal insulation of floors. *Build Mater* 2:25–26
4. Li L et al (2020) Overall utilization of vanadium–titanium magnetite tailings to prepare lightweight foam ceramics. *Process Saf Environ Prot* 139:305–314
5. Nibedita S, Garai M, Karmakar B (2015) Preparation and characterization of novel foamed porous glass-ceramics. *Mater Charact* 103:90–100
6. Ashish P et al (2013) Processing of porous ceramics by direct foaming: a review. *J Korean Ceram Soc* 50(2):93–102
7. Yang L et al (2019) An eco-friendly and cleaner process for preparing architectural ceramics from coal fly ash: Pre-activation of coal fly ash by a mechanochemical method. *J Clean Prod* 214:419–428
8. Salvini VR et al (2016) Nontoxic processing of reliable macro-porous ceramics. *Int J Appl Ceram Technol* 13(3):522–531
9. Shimamura A et al (2020) Effect of thermal conductivity of ceramic compact on the porous structures of foamed bodies via direct-foaming method. *J Asian Ceram Soc* 8(1):176–182
10. Badanoiu AI et al (2015) Preparation and characterization of foamed geopolymers from waste glass and red mud. *Constr Build Mater* 84:284–293
11. Ohji T, Fukushima M (2012) Macro-porous ceramics: processing and properties. *Int Mater Rev* 57(2):115–131
12. Xingjun C, Lu A, Qu G (2013) Preparation and characterization of foam ceramics from red mud and fly ash using sodium silicate as foaming agent. *Ceram Int* 39(2):1923–1929
13. Maltseva IV (2017) Improving the rheological properties of clay suspensions due to the introduction of electrolytes. *Eng Bull Don* 45(2):45

14. Awoyera PO, Babamide FB (2020) Foamed concrete incorporating mineral admixtures and pulverized ceramics: Effect of phase change and mineralogy on strength characteristics. *Constr Build Mater* 234:117434
15. Babashov VG, Varrik NM, Karaseva TA (2020) Porous ceramics for filtration of metal melts and hot gases (review). In: *Proceedings of VIAM*, vol 8, no 90
16. Nurlybaev RE et al (2017) Production of ceramic foam products based on amorphous microsilica by low-temperature foaming. *BBK* 1(A28):28
17. Apanskaya DE et al (2018) Expanding the raw materials for producing effective ceramic building materials. *Basic Res* 12–2:197–202
18. Gorbunov GI, Pronina TN (2017) Improving the efficiency of ceramic wall materials. *Vestnik MGSU* 3:29–39
19. Heydari MS, Mirkazemi SM, Abbasi S (2014) Influence of Co_3O_4 , Fe_2O_3 and SiC on microstructure and properties of glass foam from waste cathode ray tube display panel (CRT). *Adv. Appl. Ceram.* <https://doi.org/10.1179/1743676114Y.0000000151>
20. Gabidullin MG, Gabidullina AN (2012) Computational-graphical method for the development of basic indicators of the properties of gas-ceramics using the Manufacturability factor. *Izv Kazan State Univ Archit Civ Eng* 4(22):285–295

Optimized Chemical Composition of Concrete Used in Waterproof Objects



Ashot Antonyan 

Abstract Although the issue is studied well, the chemical composition of concrete continues to raise discussion concerning its specific properties. The quantitative variation of each of the components changes the properties of the concrete in different ways. In the transition to the concept of sustainable development of modern civilization, resource-saving technologies take on special significance. In concrete technology this concept is realized by increasing the durability of manufactured structures. One of the important properties of concrete for its durability is water impermeability, therefore this property is subject to constant research. The durability of concrete is usually ensured by creating a natural anti-filtration barrier for water, aggressive fluids by improving the micro and pore structure of concrete. The durability of structures made of concrete can be increased by protecting concrete structures with special waterproofing materials (glued, wetted or penetrating) or by using watertight concrete. The latter method eliminates secondary waterproofing and is more progressive and reliable because, first, it eliminates the need for labor-intensive insulation, Second, it ensures that the construction is securely insulated for the duration of its operation. Therefore, ensuring the high water-tightness of concrete used is a key task in the issue of increasing the durability of structures. This paper contains research data on how changes in concrete's chemical makeup influence its water tightness. Particularly, it describes changes in the composition in cases when there is a stable water/cement ratio, flowability, and sand content in the aggregate mix. Each case implies specific makeup optimization recommendations.

Keywords Concrete · Water resistance · Composition · Cement · Sand · Content · Strength

A. Antonyan (✉)

The National University of Architecture and Construction of Armenia, Teryan Street 105, Index 0009, Yerevan, Armenia

1 Introduction

Concrete composition is mass fraction of all components that makes up a volume unit for a concrete mix. Obviously, changes in the composition affect all properties, including water-tightness [1, 2]. The following paragraphs describe the influence of changes in the content of each component (cement, fine and coarse aggregates) on water-tightness.

There are no questions about water: any increase in the content of water (over $W/C = 0.38$) will increase the number of capillary pores and reduce water-tightness. However, it takes research to assess the influence of other components on water-tightness.

For example, cement concentration can influence the property in two ways:

- When cement content increases and water concentration remains the same, given the water need of the cement paste with unchanged flowability (water/cement \neq const, $OK = \text{const}$);
- When the concentration of cement increases along with the concentration of water with stable water/cement ratio and the cement paste's changing flowability (water/cement = const, $OK \neq \text{const}$).

The influence of the content of the aggregate mix is determined by the mass fraction of sand in the aggregate mix (r). Therefore, a change in the amount of sand makes it necessary to consider the influence of the changing amount of crushed rock.

Cement concentration and water/cement ratio \neq const, $OK = \text{const}$.

The following substances were used during research: crushed basalt rock (5–20 mm) extracted from the Yeghegis deposit (the Republic of Armenia), washed river sand ($FM = 2.6$), Portland cement CEMII/A-P 42.5N (The Ararat Cement Plant).

2 Methods

Basic composition: $CR = 1110 \text{ kg/m}^3$, $S = 740 \text{ kg/m}^3$, $C = 360 \text{ kg/m}^3$, W/C ratio = 0.64 (the composition changed depending on cement content). Concretes with cement content ranging from 200 to 500 kg/m^3 have been researched. In all cases, concrete mix flowability has been 20 to 21 cm.

Concretes were tested for water resistance based on water penetration depth by the “wet spot” method. Also, water penetration rate and water absorption described in papers [3, 4] have been determined. Six cylindrical test specimens were made per cement quantity; three of those have hardened in water, and the other three have hardened under normal conditions (with a humidity of $95 \pm 5\%$).

The cylindrical test specimens were tested at 28 days of age. Those hardening in water were extracted from water on the 21st day and stayed in a laboratory for the rest of the time. Those hardening under normal conditions were extracted from the

Table 1 EN12390-8 water resistance test results

Cement content, kg/m ³		200	240	280	320	360	380	400	450	500
Water penetration depth (mm)	Normal hardening	125	123	95	64	61	62	57	59	61
	Hardening in water	124	122	75	47	24	30	36	37	38

Note: every result is an average value of three specimens

chamber on the 27th day. The water-tightness test was conducted at 0.5 MPa/72 h; after that, the specimens were removed from the testing facility and broken in half to measure water penetration depth. The results are shown in Table 1 and in Fig. 1 (area B-E).

The analysis of the results demonstrates that water-tightness curves show minimal dependence with a cement content of 360 kg/m³. An increase or decrease in cement content results in an increased water penetration depth. Also, water penetration depth increases with a lower Water/Cement ratio and increased cement content. For example an increase in cement content from 360 to 500 kg/m³ results in an increase in water penetration depth from 24 to 38 mm. This happens due to an increase in the volume of cement rock and, consequently, filtration via capillaries and microcracks.

A lower than optimal cement content, with a stated flowability of the mix, has resulted in a much higher Water/Cement ratio and, consequently, an increased capillary porosity. For example, a decrease in cement content from 360 kg/m³ down to 200 kg/m³ has doubled permeability.

As mentioned above, the point of minimal permeability for these concrete types is relevant to a cement content of 360 kg/m³. Evidence shows that minimal permeability comprises a concrete content range of 360 to 410 kg/m³ rather than a single concrete content value. Therefore, it is optimal cement content that minimizes concrete permeability rather than low water/cement ratio, while the latter is required by some construction norms and regulations (SNiPs).

To compare water penetration depth and types of concrete according to water resistance, 150 × 150 mm cylindrical test specimens were made (six specimens per test batch) according to GOST 12,730.5. After demoulding, the main specimens would harden under normal conditions. Also, a composition-specific batch was prepared, where specimens would harden in water. All specimens were tested at 28 days of age.

Test results are shown in Table 2 and Fig. 1 (A-E area).

3 Results and Discussion

As follows from the above, a 200 to 320 kg/m³ increase in cement content raises water-tightness from grade W2 to grade W12.

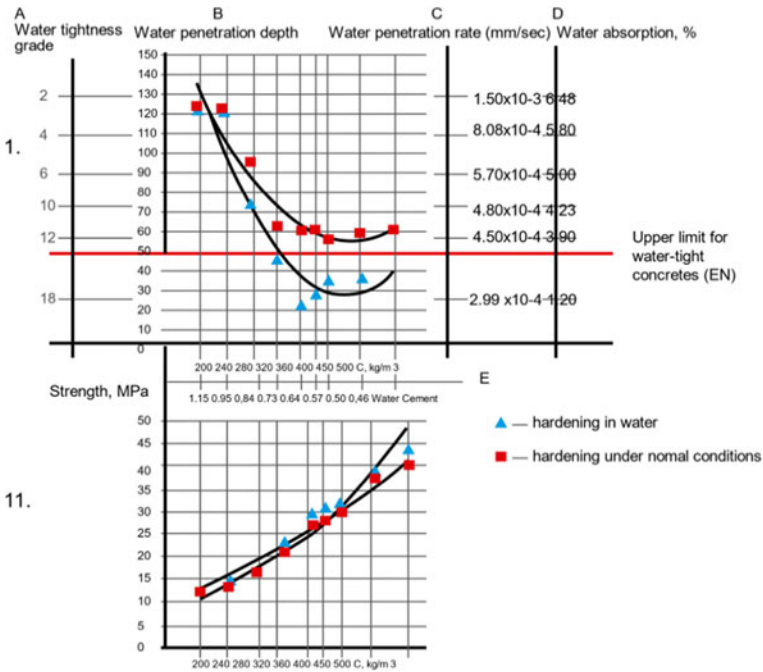


Fig. 1 Dependence of water-tightness on cement content: I-Hydrophysical properties of concrete; A-E Dependence of water-tightness of a specific type of concrete on cement content; B-E Dependence of penetration depth on cement content; C-E Dependence of water penetration rate on cement content measured with a Germann GWT-4000 device; D-E Dependence of water absorption by mass on cement content; II-Dependence of concrete density on cement content

Table 2 Water-resistance test results (GOST 12,730.5)

Cement content, kg/m ³		200	240	280	320	360	380	400	450	500
Water-tightness grade	Normal hardening	W2	W4	W6	W10	W12	W12	W12	W12	W12
	Hardening in water	W2	W4	W10	W14	W16	W18	W18	W18	W18

Concretes with cement content reaching 340 kg/m³ or higher demonstrate interesting results. As follows from Table 3, higher cement content values and, consequently, lower Water/Cement ratios, do not cause water-tightness to increase: all concrete types have demonstrated grade W12, although EN assessment based Table 2 has demonstrated a visible increase in concrete permeability with a higher-than-optimal cement content. The conclusion is that grading concrete according to water-tightness is a rough method, because concretes of a specific grade show different water penetration depth.

All cylindrical test specimens tested according to GOST and EN, had been tested initially on a Germann GWT-4000 device. The test results are shown in Fig. 1 (area C0E).

The results show that a move from grade W2 to grade W4 slows down water penetration rate by a decade (from 1.50×10^{-3} down to 8.08×10^{-4} mm/s). To reduce the penetration rate by another decade, it is necessary to achieve grade W18.

To determine these concretes' water absorption values and comparing these results with those obtained by other methods, $10 \times 10 \times 10$ cubic test specimens were made (3 specimens per batch). The results are shown in Fig. 1 (area D-E).

Based on the results, we can draw the following conclusion: maximal water tightness implies reaching a cement content level optimal for a particular type of composition. Higher than cement content results in higher permeability, although the water/cement ratio decreases.

3.1 *Cement Content with Water/Cement Ratio = Const, OK ≠ Const*

The most recommended step to increase concrete's water-tightness is reducing or limiting the Water/Cement ratio. However, a particular Water/Cement ratio may imply a broad range of cement content variations (along with water volume variations). Therefore, when analyzing the influence of cement content on water-tightness, we were relying on a stable water/cement ratio while increasing or reducing the amount of cement and water in batches.

During the study, we have used the following materials: crushed basalt rock (5–25 mm) extracted from the Cilician deposit, washed river sand ($M_{\text{кр}} = 2.2$), Portland cement CEMII/A-P 42.5N (The Ararat Cement Plant). Concrete types with cement content 300, 320, 360, 420, 450 kg/m³ have been researched. The Water/Cement ratio was the same in all cases (0.65), given that the basic concrete type had a cement content of 360 kg/m³ and a mix flowability of 15 cm. For other types, we increased or reduced water and cement to achieve a Water/Cement ratio of 0.65. The mix's flowability would change respectively.

Also, for concretes with cement content 300 and 320 kg/m³ a Rheobuild 1000 superplasticizer (NSF) was used with doses 1.5% and 0.8% respectively.

The water-tightness test was conducted according to GOST 12,730.5 using the "wet spot" method on 28-day-old cylindrical test specimens hardening under normal conditions. The test results are shown in Fig. 2 and in Table 3.

As follows from the formula $P_{cap} = \frac{W/C-0.38}{W/C+0.32} \cdot 100$ (where P_{cap} is capillary pore volume), the amount of capillary pores, which are the main water transfer channel within the given Water/Cement ratio interval, depends on the latter only; therefore, hypothetically, all concrete types in question should have the same water-tightness value. However, the test results demonstrate the opposite. For example, reduction of

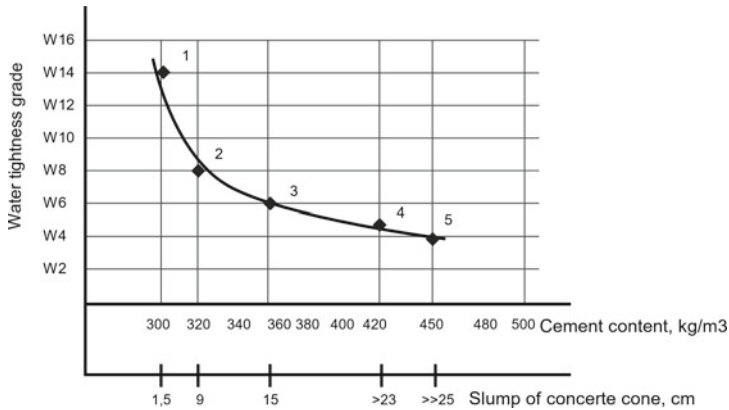


Fig. 2 Influence of cement content on water-tightness with a stable water/cement ratio = 0.65

cement content from 450 kg/m³ down to 300 kg/m³ has raised water-tightness grade from W4 to W14.

This happens due to a lower general amount of cement stone and, most important, a lower probability of shrinkage microcracks, given the fact that the size of capillary pores is unchangeable [5–10].

A maximally possible decrease in cement content with a never changing Water/Cement ratio is only curbed by the flowability limit and, consequently, water content. The conclusion is that, to increase concrete's water-tightness, it is necessary to minimize cement content within a particular Water/Cement ratio [11, 12].

As to cement content for water-tight concretes, it may be noted that:

With fixed flowability, maximal water-tightness of concrete is predetermined by optimal cement content within a range of 360 to 410 kg/m³. If cement content exceeds the optimal level, permeability increases, even though the Water/Cement ratio decreases.

With a fixed water/cement ratio, maximal water-tightness is predetermined by minimal cement content and workability of wet concrete.

3.2 Influence of Sand Content in Aggregate Mixes

It is convenient to analyze the influence of sand content because any change in it influences the content of coarse aggregates.

Table 3 Test results with a stable water/cement ratio

Mix number	Relative composition	Density of concrete, kg/m ³	Strength, MPa		Water-tightness grade
			7 days	28 days	
1	C = 300 kg/m ³ + Rheobuild 1000 1.5%	2386	19	28	W14
2	C = 320 kg/m ³ + Rheobuild 1000 0.8%	2378	21	29	W8
3	C = 360 kg/m ³	2403	20	28	W6
4	C = 420 kg/m ³	2392	22	29	>W4, but <W6
5	C = 450 kg/m ³	2381	19	27	W4

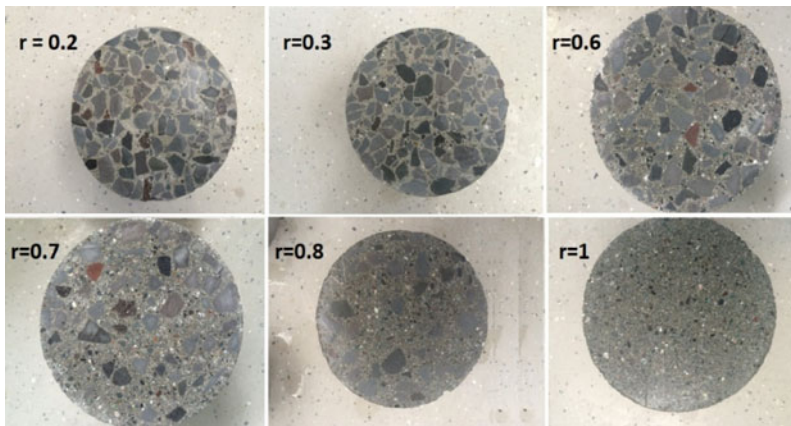


Fig. 3 Butt ends of concrete specimens with different *r* values

Sand content in the aggregate mix is: $r = \frac{S}{S+CBR}$, where S is sand content, and CBR is crushed basalt rock content. In terms of technology, optimal content values are determined by standards applied to concrete. For example, high-performance concrete requires a maximal amount of crushed stone (to provide a strong frame), so *r* values come within a range of 0.35 to 0.40. Cast-in-situ construction implies that high-quality concrete is pumped into its place to prevent stratification, and its *r* value is increased up to 0.5 to 0.6.

In all cases, the *r* value must ensure somewhat excess filling of cavities around crushed rock fragments for better separation of granules and higher flowability of the concrete mix.

We analyzed the influence of the *r* value ranging from 0.2 to 1 on concrete’s water-tightness. Particularly, concretes with an *r* of 0.2, 0.3, 0.4, 0.5, 0.6, 0.7, 0.8 and 1 (Fig. 3).

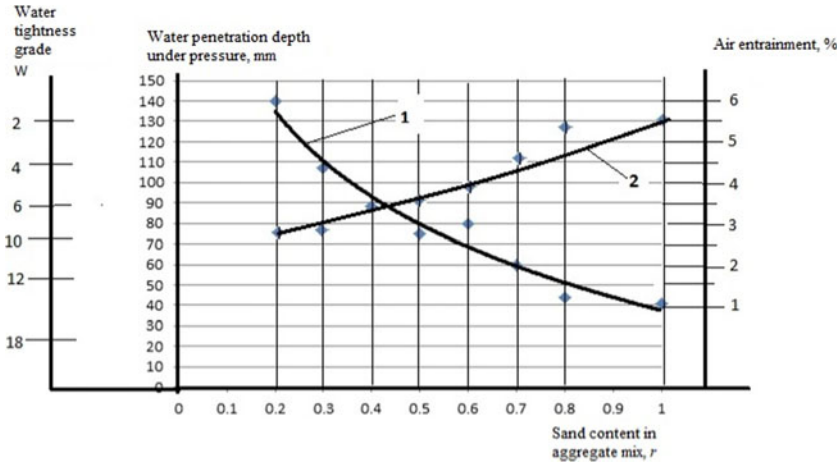


Fig. 4 Influence of sand content on water-tightness and air entrainment; 1: Correlation between water-tightness and the r value; 2: Correlation between air entrainment and the r value

During research, the following materials were used: crushed basalt rock (5–20 mm) extracted from the Yeghegis deposit (the Republic of Armenia), washed river sand ($FM = 2.6$), Portland cement CEMII/A-P 42.5 N (The Ararat Cement Plant).

With the basic composition— $r = 0.4$, $C = 360 \text{ kg/m}^3$, $\text{Water/Cement} = 0.64$ (with a flowability of 21 cm), in further batches the r value was changed by way of gradual replacement of crushed rock with sand. Cement content and the Water/Cement ratio was the same in all samples. The $150 \times 150 \text{ mm}$ cylindrical test specimens (used to determine water-tightness) and the $100 \times 100 \times 100 \text{ mm}$ cubical test specimens (used to determine strength) would harden under normal conditions and were tested on the 28th day after molding. Water-tightness was evaluated based on water penetration depth. The results are shown in Fig. 4, Fig. 5 and Table 4.

The test results demonstrate that increased sand content in the aggregate mix significantly reduces concrete’s permeability. For example, an increase in r from 0.2 to 1 reduces permeability from 140 to 40 mm and therefore raises the grade from W2 up to W12. This can be explained by many factors.

First, an increased r value significantly reduces the total contact zone (concrete mix/coarse aggregate mix, [13–15]), which concentrates portlandite, has defects and is highly porous. Second, an increased sand content result in increased air entrainment. For example, with $r = 0.2$, the volume of entrained air reaches 2.5%, with $r = 1$ air entrainment increases up to 5.5% (Fig. 4). This stabilizes the concrete mix, reduces bleeding and improves concrete’s macrostructure.

High sand content also influences concrete rheology (Fig. 5). With stable water content, flowability decreases from 22 cm (with $r = 0.2$) down to 0 cm (with $r = 1$). Therefore, when choosing an optimal r value for water-tight concretes, it is necessary

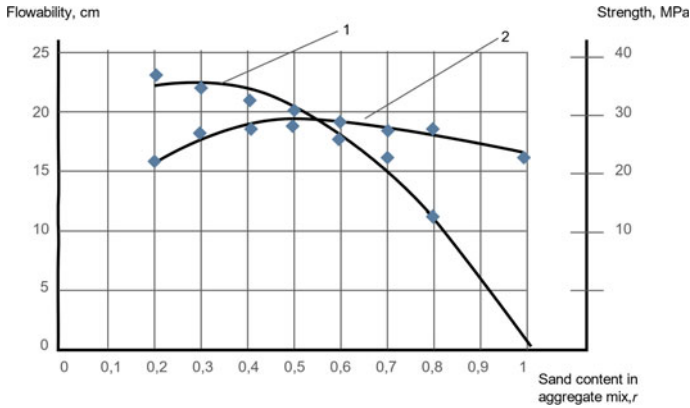


Fig. 5 Influence of sand content on flowability and strength: 1—correlation between flowability and the *r* value; 2—correlation between strength and the *r* value

Table 4 Results of water-tightness tests of concretes with different *r* values

R value	0.2	0.3	0.4	0.5	0.6	0.7	0.8	1
Water penetration depth, mm	140	109	90	75	80	60	45	40
Concrete water-tightness grade	W2	W6	W8	W10	W10	W12	W14	W14

to use a give-and-take approach with a lower permeability and a higher water need, as well as reduced strength due to air entrainment [16–23].

Obviously, an acceptable sand content for aggregate mixes used in water-tight concretes can be expressed as $r = 0.7\text{--}0.8$.

4 Conclusions

1. Concrete’s water-tightness greatly depends on its composition, which differs in the content of cement and aggregate mix. Any increase in water content beyond $\text{water/cement} = 0.38$ reduces water-tightness.
2. With a set flowability ratio, maximal water-tightness is determined by optimal cement content within a range of 360 to 410 kg/m³. Excess cement content results in increased permeability even with lower water/cement ratios.
3. With a given water/cement ratio, maximal water-tightness is predetermined by minimal cement content with consideration of concrete mix placeability.
4. Higher sand content (with lower coarse aggregate content) increases concrete water-tightness, reduces flowability and (slightly) strength due to increased air entrainment.

References

1. Eglinton M (1998) Resistance of concrete to destructive agencies. *Lea's Chem Cem Concr* 1:252 p
2. Ortega-Lopez V, Fuente-Alonso JA, Santamaria A et al (2018) Durability studies on fiber-reinforced EAF slag concrete for pavements. *Constr Build Mater* 163:471–481
3. Antonyan AA (2017) Some specifics of modern concrete water-tightness test methods. *Concr Technol* 9–10:29–33
4. Antonyan AA (2016) Water-tightness of concrete hardening in dry and hot climates. Specifics of the test method. *Concr Reinf Concr* 1:44–45
5. Zhang Y, Zhang M, Ye G (2018) Influence of moisture condition on chloride diffusion in partially saturated ordinary Portland cement mortar. *Mater Struct* 51(2):36
6. Chalee W, Jaturapitakkul C (2009) Effects of W/B ratios and fly ash finenesses on chloride diffusion coefficient of concrete in marine environment. *Mater Struct* 42(4):505–514
7. Kondraivendhan B, Bhattacharjee B (2013) Pore size distribution modification of OPC paste through inclusion of fly ash and sand. *Mag Concr Res* 65(11):673–684
8. Song HW, Kwon SJ (2007) Permeability characteristics of carbonated concrete considering capillary pore structure. *Cem Concr Res* 37(6):909–915
9. Yoo J-H, Lee H-S, Ismail MA (2011) An analytical study on the water penetration and diffusion into concrete under water pressure. *Constr Build Mater* 25(1):99–108
10. Kermani A (1991) Permeability of stressed concrete. *Build Res Inf* 19(6):123–135
11. Wang K, Jansen DC, Shah SP et al (1997) Permeability study of cracked concrete. *Cem Concr Res* 27(3):37–84
12. Warran JE, Root PJ (1963) The behavior of naturally fractured reservoirs. *Soc Petrol Eng* 3:245–255
13. Richards LA (1931) Capillary conduction of liquids through porous mediums. *Physics* 1(5):318–333
14. Zhang YZ, Li XZ, Wei XJ et al (2015) Water penetration in underwater concrete tunnel. *J Chin Ceram Soc* 43(4):368–375
15. Papyianni I, Papachristoforou M, Kesikidou F (2017) The effect of binding system of mortars on chloride ion penetration. In: *Concrete solutions: proceedings of concrete solutions, 6th international conference on concrete repair*, pp 287–292
16. Mehta PK, Monteiro PJM (2014) *Concrete: microstructure, properties, and materials*. 4th edn. McGraw-Hill Education, New York. [http://refhub.elsevier.com/S0008-8846\(19\)30188-7/1655](http://refhub.elsevier.com/S0008-8846(19)30188-7/1655)
17. Chia K, Zhang MH (2002) Water permeability and chloride permeability of high strength light weight aggregate concrete. *Cem Concr Res* 32:639–645. [https://doi.org/10.1016/S0008-8846\(01\)00738-4](https://doi.org/10.1016/S0008-8846(01)00738-4)
18. Zhang SP, Zong L (2014) Evaluation of relationship between water absorption and durability of concrete materials. *Ann Mater Sci Eng* 1–8. <https://doi.org/10.1155/2014/650373>
19. Hughes DC (1985) Pore structure and permeability of hardened cement paste. *Mag Concr Res* 37(133):227–233. <https://doi.org/10.1680/mac.1985.37.133.227>
20. Bilir T (2012) Effects of non-ground slag and bottom ash as fine aggregate on concrete permeability properties. *Constr Build Mater* 26(1):730–734. <https://doi.org/10.1016/j.conbuildmat.2011.06.080>
21. Loosveldt H, Lafhaj Z, Skoczylas F (2002) Experimental study of gas and liquid permeability of a mortar. *Cem Concr Res* 32(9):1357–1363. [https://doi.org/10.1016/S0008-8846\(02\)00793-7](https://doi.org/10.1016/S0008-8846(02)00793-7)
22. Kumar S, Gupta RC, Shrivastava S (2016) Strength, abrasion and permeability studies on cement concrete containing quartz sandstone coarse aggregates. *Constr Build Mater* 125:884–891. <https://doi.org/10.1016/j.conbuildmat.2016.08.106>
23. Talamona D, Tan KH (2012) Properties of recycled aggregate concrete for sustainable urban built environment. *J Sustain Cem-Based Mater* 1(4):202–210. <https://doi.org/10.1080/21650373.2012.754571>

Modelling of Ultrasonic Wave Propagation Through the Border of Two Mediums



Sergey Gerasimov  and Tatiana Igumnova 

Abstract When solving problems of acoustic control, processes are most often analyzed within the framework of geometric acoustics and the theory of propagation of plane elastic waves, while the phenomena associated with the diffraction of acoustic waves by inhomogeneities are not considered. The occurrence of inhomogeneities in the material can be attributed to various factors: the heat treatment, non-metallic inclusions, discontinuities. In practice, the homogeneous objects are rare. With the help of the COSMOS/M software package, it is possible to define the regions of the model with different mechanical characteristics and predict the displacements of nodes in different regions of the model after the acoustic waves refraction. In this paper, an example of a welded joint of a rail is considered, which is a multilayer system with a dispersion of mechanical characteristics along the length of the rail. Using the results of numerical simulation allows finding practical solutions in a short time. These results can be used to substantiate the locations of the recording sensors. The numerical method makes it possible to significantly expand the area of application of acoustic flaw detection methods and increase the resultsreliability.

Keywords Ultrasonic waves · Finite-element method · Wave refraction

1 Introduction

The methods of ultrasonic testing of joints of aluminum-thermite welding of rails are well developed and widely used in practice [1, 2]. In this case, the sensitivity of ultrasonic testing significantly depends on the minimum size of detected defects and on the setting of the sounding schemes that can detect a defect in a certain part of the welded joint.

Numerical modeling allows one to create the objects that include areas with dissimilar mechanical properties. When analyzing the results, it is possible to predict the nature of the movements in the object of control and the speeds of the nodes of the numerical model. With these capabilities, a numerical approach to the analysis

S. Gerasimov (✉) · T. Igumnova
Siberian Transport University (STU), Dusi Kovalchuk Str., 191, 630049 Novosibirsk, Russia

of the objects with a complex structure becomes relevant. The numerical method allows to reduce the cost of preliminary testing of objects.

2 Methods

Model 1 is designed to analyze the refraction of a wave at the interface between media with the significantly different mechanical properties. The model consists of two layers: steel and copper. The top layer is made of copper. It is followed by the interface between the two media and the lower layer made of steel.

Let the plane longitudinal wave fall from the prism of the transducer to the face of the BC Model 1 along the normal [3] (See Fig. 1).

Let the force F depend on time as shown in Fig. 1. During the action of the force, a part of the Model is deformed, and an acoustic wave of tension–compression is excited in the model. For the given pulse duration and geometry of the model, the key ones are: the sampling step in time when calculating the problem and the size of the model element, respectively.

Table 1 summarizes data on the physical properties of the steel and copper layers:

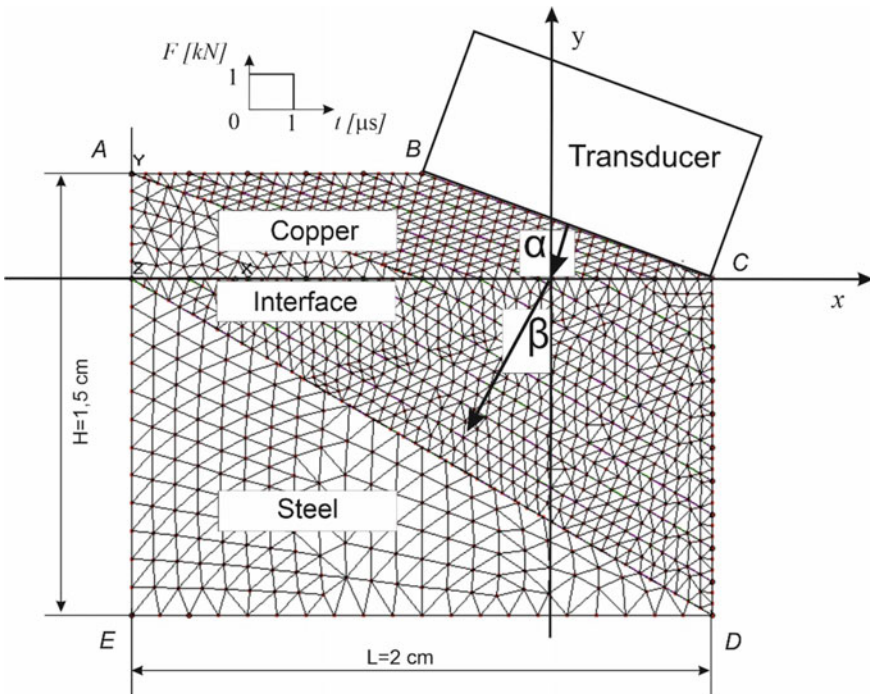


Fig. 1 Geometry of Model 1

Table 1 Physical properties of two layers of Model 1

	Modulus of elasticity, E , MPa	Poisson's ratio, ν	Density, ρ , kg/m ³	Shearing Modulus, G , MPa	Longitudinal wave speed, c_l , m/s
Copper	$1.1 \cdot 10^5$	0.37	$8.9 \cdot 10^3$	$4 \cdot 10^4$	3500
Steel	$2.1 \cdot 10^5$	0.28	$7.9 \cdot 10^3$	$7.9 \cdot 10^4$	5200

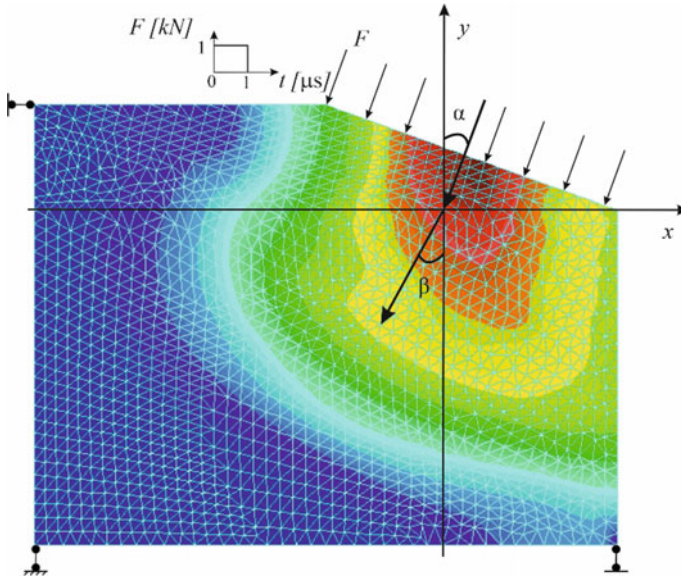


Fig. 2 The picture of displacements U_{res} and wave vectors at $2.5 \mu s$

The wavelength in a real experiment is a few millimeters. When numerically simulating the megahertz range of an ultrasonic wave, the critical element size should be no more than 0.2 mm [4]. Thus, the simulation of real objects of non-destructive testing requires a huge number of finite elements and significant computational resources. Therefore, at the initial stage of work, the plate was modeled with an interface of only two media and overall dimensions of a unit of centimeters.

After obtaining correct results using a simple example, you can proceed to creating more complex Models.

So, the dimensions of Model 1 were: 2 cm in thickness and ≈ 1.5 cm in height. Elements of SHELL6T type were used. Wavelength λ for Model 1 is 5.2 mm. The critical size of the element at the interface between the two media is provided, and is equal to 0.5 mm. A single plate thickness is accepted. The boundary conditions of the Model are shown on the Fig. 2.

The plane front of acoustic vibrations begins to propagate from the transducer in the upper layer of the plate, refracts at the interface between the media and passes into

the lower layer. It is assumed that at the interface between two media with different mechanical properties, wave refraction occurs according to the laws of geometric acoustics, and the plane wave front changes its direction according to Snell's law:

$$\frac{C_{11}}{\sin\alpha} = \frac{C_{12}}{\sin\beta} \quad (1)$$

where α is the angle of input of acoustic vibrations, β is the angle of propagation of the acoustic wave in the second layer after refraction, C_{11} and C_{12} are the velocity of the longitudinal wave in the upper (copper) and lower (steel) layers of the model.

Based on the Snell's formula:

$$\beta = \arcsin \frac{C_{12} \sin \alpha}{C_{11}},$$

$$\beta = \arcsin \frac{5200 \cdot \sin 20^\circ}{3500} \approx 30^\circ. \quad (2)$$

A wave is introduced into the upper layer of Model 1 at an angle of 20° , and, according to solution (2), in the lower layer the wave will propagate at an angle of 30° . The upper and lower layers of the numerical Model are divided into sub-regions (Surfaces), oriented parallel to each other and perpendicular to the expected direction of wave propagation. The grid was chosen in such a way to ensure the clarity of the results. If the mesh is randomly generated, the rotation of the resulting vector of each node will not change.

According to the recommendations [5] for the numerical simulation of wave processes, the calculated integration step, considering the duration of the impulse effect on this model, should be no more than 5·10–8 s.

The resulting displacements of the nodes are analyzed. Figure 2 shows a picture of the contour lines of the resulting displacements U_{res} and the wave vectors for Model 1 at the time equal to 2.5 μ s, when the elastic wave already passes the boundary of the media. The contours of different colors indicate different absolute values for the resulting displacement vectors in the model. The wave vectors are oriented perpendicular to the contours in the figure, and relation (2) is fulfilled for them.

The pulse stops its action when the elastic wave passes half of the upper layer, therefore, the effects associated with the action of the trailing edge of the pulse are excluded. For the correct wave propagation, the trailing edge should not interfere with the leading edge.

Figure 3 shows a picture of the vectors of displacements of the model nodes at the time of 2.5 μ s (a) and the speed of those nodes, as the first time derivative of their displacement at the same moment in time (b), it can be seen from the figure that after passing the transition zone the resulting displacement vectors in the lower layer of Model 1 match the expected direction of propagation. They line up perpendicular to the guidelines. The vectors are oriented at an angle of 30° , which can be seen from the constructed finite element mesh.

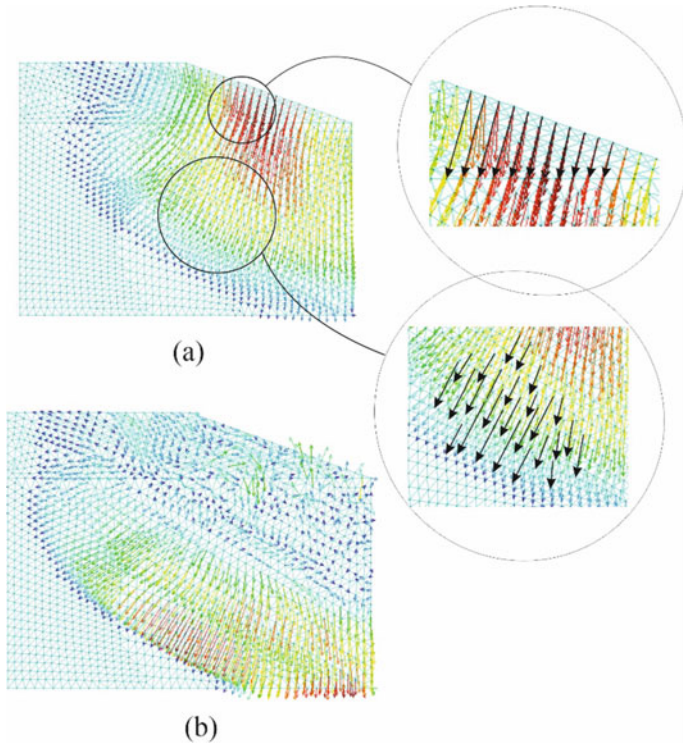


Fig. 3 The picture of the resulting displacement of the nodes of Model 1: (a)—the resulting movement of nodes, (b)—the speed of nodes

A zone commensurate with the wavelength is a buffer zone. In this zone, the vectors of the resulting displacements are multidirectional, which can be seen from Fig. 4.

It is not possible to speak about the same direction of the vectors of the resulting displacements within this zone. Only after passing through it, the wave vectors line up in the oriented front of the plane wave, shown in Fig. 3(a).

The obtained results of the length of the buffer zone can be used to consider the limitations of the numerical method.

One of the informative results of the numerical model is the velocity vectors shown in Fig. 3(b).

3 Results and Discussion

A non-destructive testing of the welded joints is the most important throughout the entire life cycle of products. Let us consider a numerical approach as applied to real

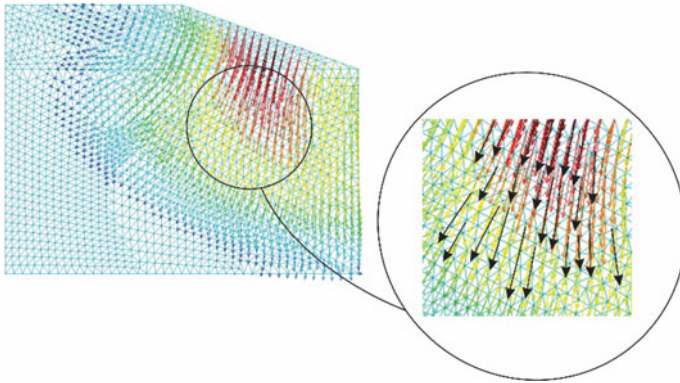
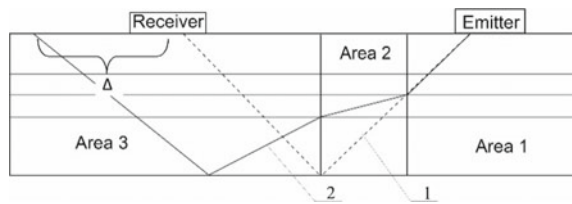


Fig. 4 Model 1. Buffer (transition) zone for a moment of time equal to 2.5 μ s

Fig. 5 Scheme of ultrasonic testing of a rail



models, using the example of the passage of an acoustic wave of a welded rail joint. To control welded joints, focusing emitters and special techniques are used to obtain the maximum useful signal-to-noise ratio on the receiving transducer. The anisotropy of the welded joints can be successfully monitored using the frequency analysis.

The complexity of the welded joints control, in particular of a rail, lies in the heterogeneity of mechanical properties along the length of the rail. The possible defects are: lack of penetration, undercuts, pores, slag inclusions, shells. The results of testing a welded joint are affected by the anisotropy of the metal in the controlled volume and the heterogeneity of the properties of heat-treated steel along the length of the rail [6–8]. This leads to a dispersion of the physical properties of the material. We are talking about the change in the modulus of elasticity of the material along the length of the rail. A numerical approach as applied to objects of railway transport on the example of a rail can be implemented on multilayer models. In this case, the finite element mesh should be optimized taking into account the real dimensions of the objects of non-destructive testing and the size of the buffer zone should be taken into account.

The analysis of the existing methods of ultrasonic testing of a welded rail joint showed that when arranging sensors, the dispersion of the mechanical properties of steel along the joint is not taken into account, therefore, an error Δ appears for the receiver coordinate [9–12]. This is shown schematically in Fig. 5. The dashed lines (1) indicate the path that is adopted for design schemes in ultrasonic testing

methods. Lines (2) show the actual path of the ultrasonic beam, which is refracted at the interfaces. Area 2 has different mechanical characteristics and simulates a welded rail joint.

As a result, an error appears for the coordinates of the sensor installation during control. In this case, the model shown in Fig. 6(a) can be used to analyze the processes occurring during the propagation of an acoustic wave in a welded joint of a rail.

The areas into which it is proposed to split the model are shown in Fig. 6(b). These are areas №. 1, 2, 3 for setting various mechanical properties. The graph of the dependence of the hardness HB of an alumo-thermic joint on the longitudinal coordinate of the rail section, shown in Fig. 6(c), was obtained at the Research Laboratory of the Siberian Transport University [13–15]. Assuming that $HB = f(\sigma_y)$, it is possible to obtain the values of the elastic modulus and shear modulus for each region of the model (where σ_y is the yield strength of M76 rail steel).

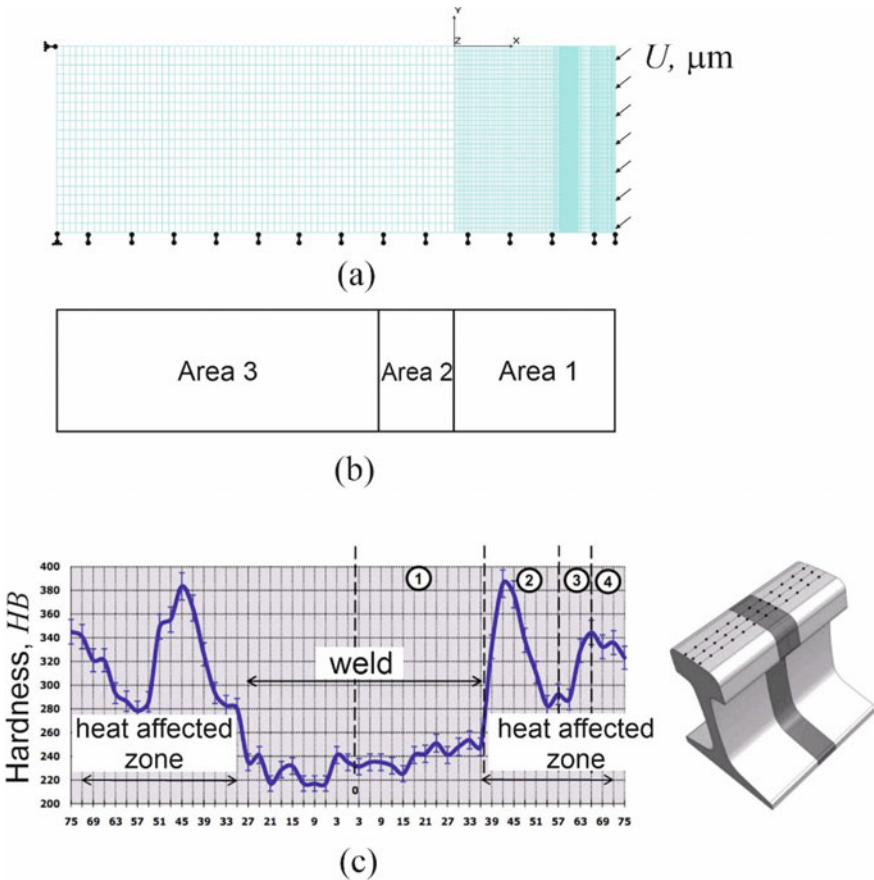


Fig. 6 Numerical model of a welded joint of a rail

4 Conclusions

Results are obtained for a model consisting of two dissimilar media with different mechanical properties. The results of modeling the refractive effect are consistent with the laws of geometric acoustics. After passing a distance commensurate with the wavelength, the vectors are oriented according to the expected direction of propagation. All nodes of the central zone of the acoustic front are displaced in the same direction. It can also be stated that the length of the buffer (transition) zone is of the order of the wavelength.

References

1. Van Pamel A, Sha G, Rokhlin SI, Lowe MJS (2017) Finite-element modelling of elastic wave propagation and scattering within heterogeneous media. *Proc Roy Soc A: Math Phys Eng Sci* 473:20160738. <https://doi.org/10.1098/rspa.2016.0738>
2. Muravev VV, Tapkov KA, Lenkov SV (2019) In-production nondestructive testing of internal stresses in rails using acoustoelasticity method. *Russ J Nondestr Test* 55(1):8–14. <https://doi.org/10.1134/S1061830919010078>
3. Gerasimov SI, Sych TV (2019) Computational and experimental studies of shock waves in thin plates. In: *AIP conference proceedings*, vol 2125, p 030027. <https://doi.org/10.1063/1.5117409>
4. Gerasimov S, Sych T, Kuleshov V (2016) Application of finite elements method for improvement of acoustic emission testing. *J Phys: Conf Ser* 671(1):012017. <https://doi.org/10.1088/1742-6596/671/1/012017>
5. Ryzhova AO, Bekher SA, Popkov AA (2020) Using the method of acoustoelasticity for evaluating elastic mechanical stresses in the material of bearing rings. *Russ J Nondestr Test* 56(11):898–906. <https://doi.org/10.1134/S1061830920110078>
6. Stepanova L, Kurbatov A, Tenitilov (2020) Methods of monitoring longitudinal stresses in rails using acoustoelastic effect. In: *Advances in intelligent systems and computing*, vol 1115, p 778–787. https://doi.org/10.1007/978-3-030-37916-2_76
7. Chen X, Yang Z, Zhang X, He Z (2012) Modeling of wave propagation in one-dimension structures using B-spline wavelet on interval finite element. *Finite Elem Anal Des* 51:1–9. <https://doi.org/10.1016/j.finel.2011.10.007>
8. Ryzhova A, Bekher S, Popkov A (2021) Patterns of acoustic wave propagation in the contact layer of press joints. *Transp Res Proc* 54:455–460. <https://doi.org/10.1016/j.trpro.2021.02.095>
9. Gushchina LV, Muraviev VV, Zlobin DV, Zemskov TI (2019) Development of the experimental equipment for measuring the velocity of ultrasonic waves with high accuracy. *J Phys: Conf Ser* 1327(1):12021. <https://doi.org/10.1088/1742-6596/1327/1/012021>
10. Gerasimov SI, Sych TV (2017) Finite element modelling of acoustic emission sensor. *J Phys: Conf Ser* 881(1):012003. <https://doi.org/10.1088/1742-6596/881/1/012003>
11. Gerasimov SI, Sych TV (2018) Numerical modelling and experimental analysis of acoustic emission. *J Phys: Conf Ser* 1015(3):032039. <https://doi.org/10.1088/1742-6596/1015/3/032039>
12. Zelenyak A-M, Schorer N, Sause MGR (2018) Modeling of ultrasonic wave propagation in composite laminates with realistic discontinuity representation. *Ultrasonics* 83(2):103–113. <https://doi.org/10.1016/j.ultras.2017.06.014>
13. Bekher S, Kolomeets A (2018) Automation of control processes in the non-destructive testing units. In: *MATEC web of conferences*, vol 239, p 01025. <https://doi.org/10.1051/mateconf/201823901025>

14. Murav'ev VV, Volkova LV, Platonov AV, Gushchina LV (2018) Acoustic assessment of the internal stress and mechanical properties of differentially hardened rail. *Steel Transl* 48(10):690–694. <https://doi.org/10.3103/S0967091218100078>
15. Stepanova LN, Kabanov SI, Ramazanov IS, Chernova VV (2019) Acoustic-emission procedure for rejecting defects in multiple-pass girth welds. *Russ J Nondestr Test* 55(12):898–908. <https://doi.org/10.1134/S106183091912012X>

Clustering Methods and Time Parameterization in the Management of Port Cargo Flows



Oleg Chislov , Natalya Magomedova , Alexandra Kravets ,
Danil Bezusov , and Vyacheslav Zadorozhniy 

Abstract Methodological approaches to assessing the prospects for the development of port transport and technological systems in terms of interaction management in the “railway station - port” system are investigated. The issues of updating clustering methods and time parameterization in the management of cargo flows of port transport systems at a new stage of development with the prospect of their application in intelligent control systems for the selection of rational schemes for the transportation process operation are considered. Three types of clusters are proposed that function within the boundaries of the regional port transport and technological system, and include homogeneous objects or objects performing a single transport function: a loading cluster, a single port cluster and a port cluster. To form the analytical model of cargo flow management based on the principles of time parameterization, criteria for the rationality of transport processes have been determined for the minimum demurrage time of the rolling stock in the transport system, the minimum number of transport processes when performing the maximum amount of work, and the maximum speed of transport processes with the values of rational loading of infrastructure facilities of the transport system.

Keywords Multimodal freight transportation · Transport and cargo cluster · Axiomatics of transport processes · Time indicators parameterization · Cargo flows management

O. Chislov · V. Zadorozhniy

Sirius University of Science and Technology, 1 Olympic Avenue, 354340 Sochi, Russia

O. Chislov · N. Magomedova · A. Kravets · D. Bezusov (✉) · V. Zadorozhniy

Rostov State Transport University, Rostovskogo Strelkovogo Polka Narodnogo Opolcheniya Sq. 2, 344038 Rostov-On-Don, Russia

1 Introduction

1.1 Literature Review

In conditions of economic instability, frequent irregularities of cargo flows to port systems and related transportation processes, traditional forecasting and management technologies often do not give tangible results. This is especially evident in transport hubs that provide multimodal transportation, which use rail, road and water transport.

It is known that methods based on the ideas of linear programming, queuing theory, reliability theory, graph theory, probability theory and new promising scientific directions - intelligent control systems, principles of fuzzy logic, neural networks, etc. are widely used in the cargo flows management [1]. Artificial intelligence systems in transport monitor the components of the transportation process, simultaneously solving additional tasks related to the assessment of variable time parameters of the traffic flow in a dynamic situation [2].

Researches within the framework of multimodal transportation systems serve as the basis for further development of theories and methods of cargo flow management in port transport systems [1–14].

For example, in paper [3] the design of a queuing network in the system of organizing rail freight transportation with non-deterministic parameters is considered. In [1] a combined two-stage model of cargo transportation is studied. In [2] a model of decision-making support for the formation of a cargo delivery chain using Pareto-optimal criteria is presented. In [4] questions of the theory of reliability in the organization of stable cargo transportation are investigated.

The articles [5, 6] study issues related to the influence of the volume of freight traffic and capacity of transport links on the development of ports.

The author of the article [7] has proposed a cluster approach to the functioning of seaports under conditions of competition.

The combined use of methods of mathematical programming, game theory and graph theory [8, 9] makes it possible to model the transport network and carry out research to attract additional cargo volumes.

Digitalization of management transport decisions is presented in the form of a cybernetic model [7] that is called “white box” and allows you to take into account the input parameters to choose the optimal transportation scheme.

It can be concluded that the interaction of transport modes is based on the principles of continuity, science, flexibility, accuracy and priority.

1.2 Prospect for Further Research in the Field of Multimodal Freight Transportation Management

To manage transport processes, the following methods are most often used: software-target method; balance method; normative method; economic and mathematical

method; forecasting method; intuitive methods based on intuitive-logical thinking and fuzzy logic. They are used when, due to the significant complexity of the transport object, it is impossible to take into account the joint influence of contradictory factors, or if the object has a too simple structure that does not require labor-intensive calculations.

The analysis of works [1–14] indicates the need for further research on the principles of developing logistics approaches, modeling the freight transport market, forming mathematical models for optimizing multimodal freight transportation in accordance with the current process parameters: technical and technological, organizational and managerial, time, economic, regulatory and even linguistic - to form a new paradigm of digitalization of management.

At the same time, the decision-making procedure comes to the fore that includes the following stages: 1 - goal setting; 2 - formulating the task; 3 - identification of ways and means to achieve the goal; 4 - considering alternative solutions; 5 - setting deadlines for achieving the goal.

Rail transport plays a crucial role in the organization of export–import freight flows and determines the importance of the successful interaction between shippers and port complexes. Road freight transport also has a significant share in the total volume, but only in the segment of individual nomenclature of goods and short-haul deliveries.

The positive aspects of multimodal transport and the possibility of their further increase should be supported by modern scientific, technical and technological solutions taking into account market conditions of operation, various forms of ownership of shippers, freight forwarders, vehicle owners, infrastructure and operator companies.

This work is devoted to the study of the issues of modern actualization of clusterization and time parameterization methods in the management of cargo flows of port transport systems at a new stage of development and the prospect of application in intelligent control systems to determine rational schemes for the implementation of the transportation process.

2 Development of Clustering Methods and Time Parametrization in the Management of Cargo Flows of Port Transport Systems

2.1 Updating Clustering Methods in Multimodal Cargo Flow Management

Cluster development is considered to be one of the ways to strengthen competitive economic advantages. The initial condition for creating a cluster is the territorial proximity of the production and transport enterprises that form the cluster. It is known that to determine the suitability of an object for performing certain transport

and logistics operations the terms “source capacity” or “warehouse capacity turnover ratio” are used in the scientific literature.

The paper proposes to use the author’s term - “coefficient of the cargo mass dynamics”, which reflects the functional and qualitative capabilities of the cargo warehouse: the rate/speed/intensity of cargo transfer from loading sites to transport. To determine the proportions of capacity E and productivity Q indicators in loading clusters, the cargo mass dynamics coefficient k_{dcm} is equal to:

$$k_{dcm} = \frac{E_i}{Q_i}, \quad (1)$$

where E_i is the capacity of the i -th storage, Q_i is the productivity of the transport equipment of the i -th storage.

The formation of production, transport and storage clusters is proposed to be carried out according to the developed algorithm:

Approach: ABC analysis of storages by capacity and productivity indicators.

Result: the ranking of storages into groups A, B (two subgroups), group C is considered separately for each of the indicators.

Approach: Combining storages of group C and larger ones based on the modified Scheffle-Weber gravity method using a fractional-power function:

$$W_{ij}(Q) = \alpha^{(Q)} \frac{\sum_1^i Q_i \sum_1^j Q_j}{l_{ij}^2} \text{ or } W_{ij}(E) = \alpha^{(E)} \frac{\sum_1^i E_i \sum_1^j E_j}{l_{ij}^2}, \quad (2)$$

where W_{ij} is the value of the traffic flow between the objects of transport and technological system, Q_i , Q_j are the productivity of the transport equipment of i -th and j -th storages, l_{ij} is the distance between i -th and j -th storages, E_i , E_j are the capacities of i -th and j -th storages, α is the proportionality coefficient:

$$\alpha^{(Q)} = \frac{Q_{\min}}{Q_{\max}} \text{ or } \alpha^{(E)} = \frac{E_{\min}}{E_{\max}}. \quad (3)$$

Result: reduction of sampling volume by combining storages of group C. As a result, the sampling consists of three groups of storages in each indicator of A, B *, C *, where B *, C * are modified subgroups.

Approach: Comparative analysis of the results of the modified ABC analysis.

Result: the formation of storages groups (loading clusters), taking into account the joint indicators of capacity and productivity (groups AA, AB/BA, BB, BC/CB, CC).

1. Approach: Identification of warehouses with the required proportion of capacity and productivity indicators using the k_{dcm} coefficient according to the formula (1).

Table 1 The result of the ABC-analysis by capacity and productivity of storages

ABC-analysis group		By capacity		
		A	B	C
By productivity	A	AA	AB	AC
	B	BA	BB	BC
	C	CA	CB	CC

Table 2 Modification of the ABC analysis of storages by capacity and productivity

ABC-analysis group		By capacity		
		A	B	C
By productivity	A	α -storage	β -c storage	0
	B	β -storage	γ -storage	δ -storage
	C	0	δ -storage	ω -storage

Result: the intervals of rational values of the k_{dcm} range are determined, at which the proportion of capacity and productivity indicators of warehouses most satisfy time conditions of the organization of multimodal cargo transportation.

2. Approach: Identification of loading clusters that meet the requirements for ensuring traffic volumes. To do this, an ABC analysis is performed on two indicators simultaneously (table 1).

For the study, the concepts of enlarged storage objects are introduced: α , β , γ , δ , ω -storages of the loading regional cluster (Table 2).

Result: By analogy with the theory of hierarchy dominance, the most powerful in terms of capacity and productivity are α and β -storages that are advantageous in choosing the center of the loading cluster; γ and δ -storages have disadvantages (for example, insufficient capacity), as a result of which they are second-rate when choosing; ω -storage is an undesirable choice when determining the center of the cluster; 0 is a variant with an imbalance of indicators.

As a result of merging of small storages of group C with larger ones, the warehouse can move from one group to another according to the scheme in Fig. 1.

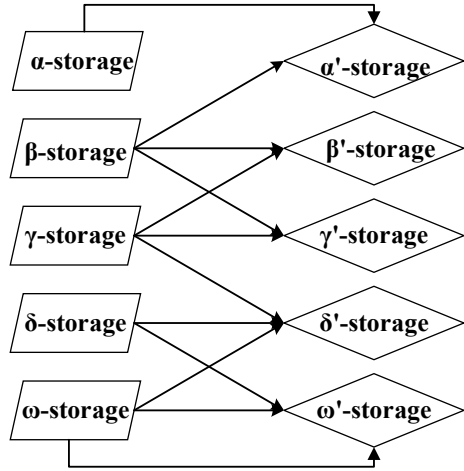
Approach: Joint ranking according to the method of standards of neighboring loading and unloading points in the regional territory according to the indicator of a larger storage capacity and choosing the best one. For example, two classes V1 (AB) and V2 (BA) have two standards [15], which are gravity centers of different class points:

$$X^{\exists 1} = \frac{1}{l_1} \sum_{x^j \in V_1} x^j, X^{\exists 2} = \frac{1}{l_2} \sum_{x^j \in V_2} x^j, \tag{4}$$

where l_1 and l_2 are the number of training sequence objects belonging to V_1 and V_2 .

The decision on the belonging of the object X to a particular class is made by the proximity to the standards.

Fig. 1 Scheme of transition of storage parameters after merging (clustering)



$$X \in V_1, \text{ если } d(X, X^{\beta 1}) < d(X, X^{\beta 2}), \tag{5}$$

$X \in V_2$ – otherwise.

For the purpose of developing the presented approach when organizing multi-modal transportation, it is proposed to distinguish three types of clusters operating within the boundaries of the regional port transport and technological system and including homogeneous objects or objects that perform a single transport function: a loading cluster, a unified port cluster and a port cluster.

Cluster of loading (CL) is a set of production, transport and storage facilities that accumulate and load cargo, the final product of which is a loaded transport unit.

Unified cluster of port (UCP) is a number of ports geographically close to each other (a single sea basin) that perform similar production, transport and storage functions for transshipment of cargo nomenclatures.

Cluster of port (CP) is a set of production, transport and storage facilities of a certain port with the inclusion of rear warehouses, as well as “dry ports”.

When forming these types of clusters, “border” zones can be formed - zones of joint influence of several system objects at the same time, or the so-called “islands” - clusters that tend to a certain port, but are not included in the main structure of the cluster. The presented clustering makes it possible to determine the boundaries of port activities, based on the geographical features of their location and their market cooperation (Fig. 2).

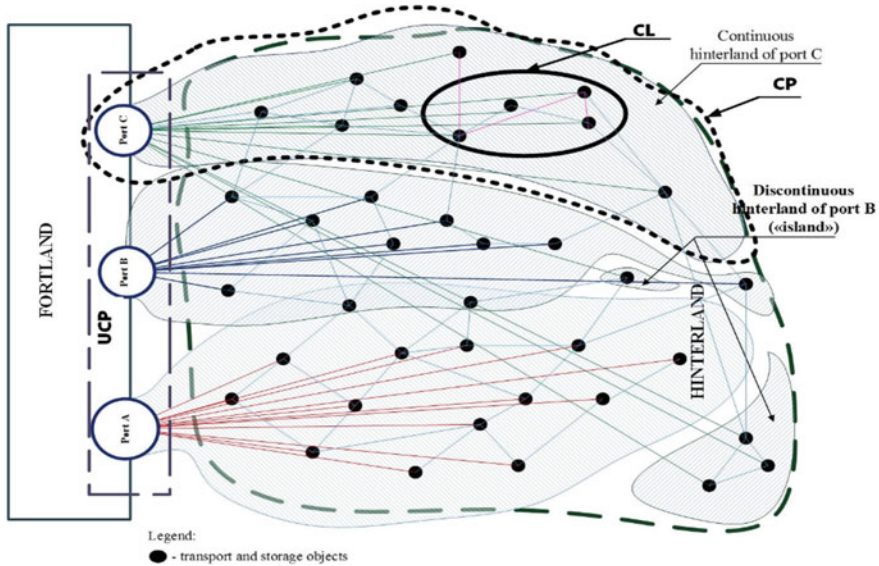


Fig. 2 Clustering of port production, transport and storage facilities

3 Time Parameterization Method in Multimodal Cargo Flow Management

Time parameterization in the management of multimodal cargo flows is considered from the standpoint of the axiomatics of transport services in places (clusters) of cargo concentration and distribution. This approach allows us to determine the logical specification of transport processes and structures of transport objects by means models or structures. The models are designed to analyze the consistency of managerial decisions, assess the consequences of actions taken and diagnose situations [1–14].

The specification of a logical model (prototype) of a transport object is given by formulas $\forall \bar{x}(\varphi(\bar{x}) \rightarrow \psi(\bar{x}))$, where \bar{x} is a vector of variables, $\varphi(\bar{x})$ is a conjunction of relations (predicates), equalities of terms or their negations, $\psi(\bar{x})$ is a conjunction of predicates and terms considered as a definition of a relation or a in a logical model. A special subset of definitions is initial data that use constants to define objects instead of variables.

Figure 3 shows an example of transport processes axiomatic for a port railway station. The model scheme of the transport process is as follows: $GL \leftrightarrow PG \leftrightarrow SU \leftrightarrow PS1 \leftrightarrow PG \leftrightarrow PR \leftrightarrow (GFP)_i$.

Process description: A freight train arrives from the GL running line and is accepted into the PG fleet for handling. The wagons are then broken up in two groups on the SU sorting device. From the sorting device SU, the cars of the first group are rearranged on the tracks of the sorting yard PS1 (then the second half). From the PS1 fleet tracks through the connecting tracks and the PG fleet (operations

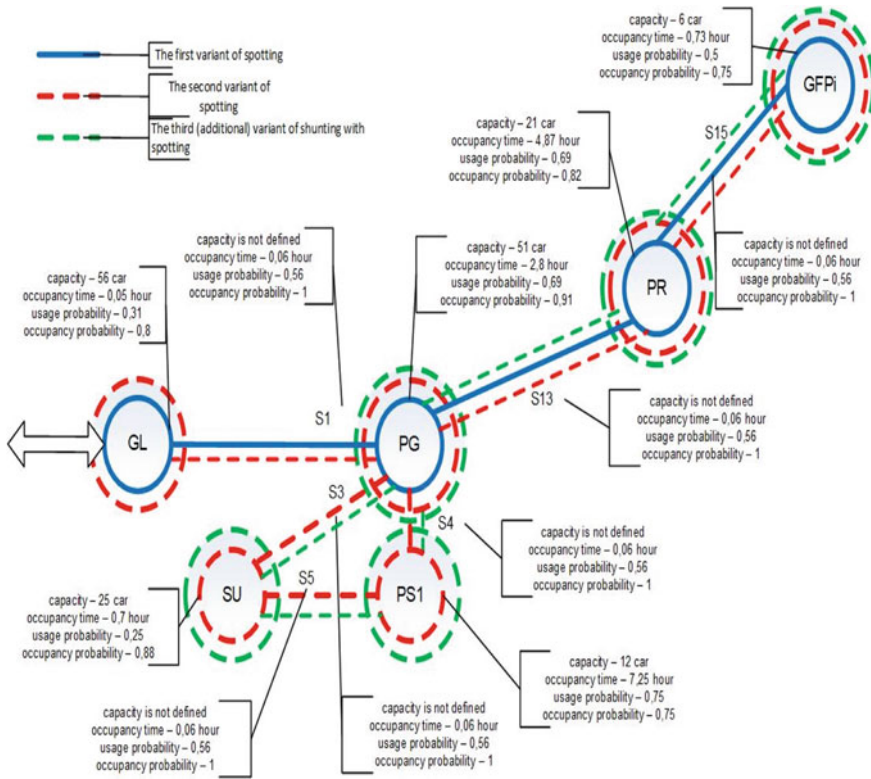


Fig. 3 An example of the axiome of transport processes at a port railway station

are not performed in it), cars are transferred to the tracks of the PR port fleet. The capacity of the port’s cargo berths is known. To start the calculations, it was assumed that cars with a 50% probability can be accepted to the cargo berths of the GFP port, bypassing the PR port fleet. Or, with a 50% probability, they will be accepted to the PR port fleet tracks, and then, in groups, the wagons are accepted to the cargo fronts of the GFP port, where they are located during a given technological time of unloading and loading. Then everything is repeated in reverse order.

Figure 3 shows in blue (solid line) the first option of transport operation - the freight train follows through GL to PG. After processing in PG, the wagons follow to PR, and then to GFP and back. The second option of transport operation (red, dashed line) provides for the disbandment and formation of a freight train on the tracks of the PS1 park.

The probabilities of choosing the axiome options take the following values: $Ver(T_i) = 1,0$ – the entire cargo flow follows to the port without additional technological operations; $0,5 \leq Ver(T_i) < 1,0$ – cargo flow is divided into parts by N_i transport units and goes to the port berths in parts; $0,25 \leq Ver(T_i) < 0,5$ – cargo flow is divided into parts, with each part being sprayed onto several cargo berths

of the port; $0 < Ver(T_i) < 0,25$ – cargo flow is divided into parts, with each part being sprayed onto several consignees of the transport hub, one of which is the port; $Ver(T_i) = 0$ – no transport unit or cargo assignments.

To form an analytical model of cargo flow management based on the principles of time parameterization, the criteria for the rationality of transport processes are defined: 1 – minimum demurrage time of the rolling stock in the transport system; 2 – minimum number of transport processes while performing the maximum volumes of work; 3 – maximum speed of transport processes at values of rational loading of infrastructure facilities of the transport system.

For the solution, the mathematical apparatus of environment *Maple* for analytical computer modeling is used in the framework of the open assignment problem to minimize the total time spent on performing all transport operations. Thus, the following is determined [5]: the number of technological operations for the given operating conditions (T_i); transport service axiomates; the probability of performing the i -th technological operation for the n -th axiomate of transport service.

Initial data of the model: s_k – is the number of technological blocks of the transport object scheme ($k = 1, 2, \dots, v$), z_{ij} – is the technology of the object block operation (axiomate); a_i is the number of vehicles (freight trains, transfers of wagons, cars, ships) arriving in the transport system for the estimated period of time ($i = 1, 2, \dots, n$), b_j is the number of vehicles that can be processed by the port system ($j = 1, 2, \dots, m$) under condition that all cargo fronts are provided to the maximum and the rolling stock demurrage time is minimum.

Let us consider approaches to solving this transport problem in open (I) and closed (II) form.

- (I) all arriving vehicles can be processed in the system without excessive demurrage time and traffic delays. A finite set of interaction options $Z(S)$ of technological blocks of a transport object (railway station, port) s_k is formed, providing a rational option for organizing transport processes z_{ij} : $Z(S) \cup (z_{ij} \forall s_k)$ at a minimum of the vehicle's demurrage time (the vessel, the wagon, the car) t_{ij} . Then the objective function has the form $Z(S) = \min_{i,j,k} \{t_{ij}, z_{ij}, sgn s_k\}$, where $sgn s_k$ takes values (0.1). Thus, the equality

$$\sum_{i=1}^m a_i = \sum_{j=1}^n b_j \text{ is fulfilled.}$$

- (II) if the balance condition is not met, then $\sum_{i=1}^m a_i < \sum_{j=1}^n b_j$ или $\sum_{i=1}^m a_i > \sum_{j=1}^n b_j$.

Inequality means that the total capacities of receiving vehicles with cargo assigned to the port station (port) exceed the processing capacity of all cargo fronts, or vice versa.

Let x_{ij} be the number of vehicles (trains, ships, cars) according to the option of organizing transport processes (with the restriction $x_{ij} \geq 0$) that can be sent from the i -th module of the cluster object (station, port) to some module of the cargo front of the cluster (port berth) in the set A of admissible options for organizing transport processes (x_{ij}) provided:

- a) all vehicles planned for delivery to the port must be organized and executed;
 b) the total number of vehicles transferred to the port should not exceed the amount that can be processed according to the condition $\sum_{j=1}^n x_{ij} = a_i, \sum_{j=1}^m x_{ij} \leq b_j$.

Let us consider the time parameters of transportation t_{ij} - the average travel time of the vehicle (train route, car) between the i -th loading station and some port station (port).

Technological restrictions that reflect the interests of cargo transportation participants in the port system:

- priority of wagons (cars) being spotted for loading and unloading to the cargo front (berth) of the port is determined by the agreed decision of the consignor and the consignee (port);
- interests of consignees (clients) do not affect the sequence of operations in the axiomatics of transport processes;
- priority of transport process axiomatics can be changed by means of economic regulation within the framework of contractual relations, which reflects the economic benefits of the parties involved in the transport of cargo in the port system.

The first objective function of the transport unit demurrage time has the form $T_1 = \max_{i,j} \{t_{ij} \operatorname{sgn} x_{ij}\}$. The values x_{ij} are the number of trains (wagons), cars directed from any cluster module (railway station) to the cargo front module (port berth). T_1 is the time of the last maximum in time axiomatics of the transport process for the entire volume of operation with transport units in the considered transportation management option (x_{ij}), i.e. the total demurrage time of the mobile unit in the transportation management system.

The second objective function of the module occupation time and the number of modules of the transport system according to the variant of the axiomatics of transport processes when performing the maximum volume of operation has the form:

$$T_2 = \sum_{i=1}^m \sum_{j=1}^n \sum_{k=1}^v t_{ij} s_k.$$

The value T_2 is the total occupation time of all modules of the transport system according to the options for implementing the plan for the arrival of wagons at the port berths. The objective function can be considered as an integer mathematical programming problem at $T_2 \rightarrow \min$.

The best option is the one in which the total time of occupation of all modules of the transport system according to the variant of the axiomatics of transport work through which the transport organization option is implemented does not exceed the time of all possible variants of the axiomatics of transport processes through which this work is carried out.

For the time indicators of the transportation process T_1 and T_2 it is obtained that for $\forall (x_{ij} \cup s_k) \in A$, there are inequalities $T_1 = \max_{i,j} \{t_{ij} \operatorname{sgn} x_{ij}\} \leq \max_{i,j} \{t_{ij}\}$ and

Table 3 Variants of the axiomates of the transport work organization in a single-criterion model

Nº of a variant	Probabilities $Ver(x_{ij})$ of transport system modules occupancy for transport process axiomates	T_1 , hour
1	$Ver(x_{11})^1, Ver(x_{1j})^1, Ver(x_{21})^1, Ver(x_{22})^1, \dots, Ver(x_{ij})^1$	T_1^1
2	$Ver(x_{11})^2, Ver(x_{1j})^2, Ver(x_{21})^2, Ver(x_{22})^2, \dots, Ver(x_{ij})^2$	T_1^2
...
k	$Ver(x_{11})^k, Ver(x_{1j})^k, Ver(x_{21})^k, Ver(x_{22})^k, \dots, Ver(x_{ij})^k$	T_1^k

$$T_2 = \sum_{i=1}^m \sum_{j=1}^n \sum_{k=1}^v t_{ij} s_k \leq \max_{i,j} \{t_{ij}\} \sum_{i=1}^m \sum_{j=1}^n x_{ij} \leq \max_{i,j} \{t_{ij}\} \sum_{i=1}^m a_i.$$

The third objective function of transport processes speed with rational loading of transport system modules is

$$\Psi_3 = \max_{i=1, \dots, m} \{ \forall (N_{ij}(s_k) / t_{ij} \operatorname{sgn} x_{ij}) \} (j = 1, 2, \dots, n).$$

Indicators of target functions of transport processes characterize:

- efficiency of transport operation time in the port system (cluster, “station - port”) for the regional level of transportation organization (road polygon), $T_1 \rightarrow \min$;
- efficiency of the usage time of each module of the transport subsystem (station - port) according to the variant of organization of transport work axiomates. Minimization of the indicator T_2 is of interest for the infrastructure owner.
- commercial interest for the clientele and operator’s freight companies on the basis of the fastest delivery of goods - the speed of transportation in the port transport system (“station - port” system). Indicator $\Psi_3 \rightarrow \max$.

Table 3 shows the form of recording of possible variants of transport work based on probabilistic features of transport system modules occupancy for a single-criterion optimization.

In case of two-criteria optimization for T_1 and T_2 , each variant of the transport work organization with a set of axiomates $(x_{ij}) \in A$ corresponds to the utility vector $\{T_1, T_2\}$. The optimal variant is transport work organization with a set of axiomates $(X_{ij}) \in A$ with the utility vector $\{T_1^*, T_2^*\}$ for which there is no other variant of transport work organization with a set of axiomates $(x_{ij}) \in A$, which the utility vector $\{T_1, T_2\}$ coordinates satisfy the conditions

$$\begin{cases} T_1 < T_1^* \\ T_2 \leq T_2^* \end{cases} \vee \begin{cases} T_1 \leq T_1^* \\ T_2 < T_2^* \end{cases}$$

Table 4 shows the form of recording of acceptable options of transport work organization with a set of axiomates for two-criterion optimization.

In case of three-criteria optimization for T_1, T_2 , and Ψ_3 , each variant of the of transport work organization with a set of axiomates $(x_{ij}) \in A$ corresponds to the utility

Table 4 Variants of the axiomates of the transport work organization for a two-criterion model

Nº of a variant	Probabilities $Ver(x_{ij})$ of transport subsystem modules occupancy for transport process axiomates	T_1 , hour	T_2 , hour
1	$Ver(x_{11})^1, Ver(x_{1j})^1, Ver(x_{21})^1, Ver(x_{22})^1, \dots, Ver(x_{ij})^1$	T_1^1	T_2^1
2	$Ver(x_{11})^2, Ver(x_{1j})^2, Ver(x_{21})^2, Ver(x_{22})^2, \dots, Ver(x_{ij})^2$	T_1^2	T_2^2
...
k	$Ver(x_{11})^k, Ver(x_{1j})^k, Ver(x_{21})^k, Ver(x_{22})^k, \dots, Ver(x_{ij})^k$	T_1^k	T_2^k

vector $\{T_1, T_2, \Psi_3\}$. The optimal variant for transport work organization $(X_{ij}) \in A$ with the vector of utilities $\{T_1^*, T_2^*, \Psi_3^*\}$ is the variant for which the coordinates of the vector of utilities satisfy the conditions

$$\left\{ \begin{array}{l} T_1 < T_1^* \\ T_2 \leq T_2^* \\ \Psi_3 \geq \Psi_3^* \end{array} \right\} \vee \left\{ \begin{array}{l} T_1 \leq T_1^* \\ T_2 < T_2^* \\ \Psi_3 \geq \Psi_3^* \end{array} \right\} \vee \left\{ \begin{array}{l} T_1 \leq T_1^* \\ T_2 \leq T_2^* \\ \Psi_3 > \Psi_3^* \end{array} \right\}$$

Thus, a model of transport work organization of a port system (station, port) with a set of axiomates is formed, which is a multi-criteria problem of integer nonlinear programming. The developed method can be used in relation to distribution terminals of port clusters for organizing transport processes in interaction with motor transport.

4 Results

The study presents a comprehensive approach to the organization of multimodal cargo flows using the clustering capabilities of transport and production facilities in order to achieve the highest results for all cluster participants. An algorithm has been developed that allows parameterization of transport processes according to time criteria in certain types of clusters and their elements.

Due to the voluminous computational procedures with the multivariate organization of transport processes, a program for calculating time parameters in the Maple environment has been developed. As a result of the program, the values of the time spent on the implementation of transport processes in the “railway station-port” system are obtained according to the axiomate with different probabilities of its implementation.

To assess the effectiveness of the organization of transport processes in the port system, in addition to the generally accepted indicators of freight turnover, demurrage time, static load, etc., it is necessary to use new modified data on the speed of transport processes, the amount of transport action along the infrastructure, the cargo pressure on the transport infrastructure, the utilization coefficient of infrastructure capacity over the time of transport processes.

It should also be taken into account that when developing concepts for managing cargo flows of port transport systems, it is necessary to solve related problems associated with increasing the safety of the transportation process, developing public-private partnerships, creating a culture of interaction between the parties participating in the cargo transportation, improving human resources, developing software for model building procedures and making decisions in the promotion of cargo (blockchain technology, artificial intelligence, Big Data, Data Mining, etc.).

Acknowledgements The reported study was funded by RFBR, Sirius University of Science and Technology, JSC Russian Railways and Educational Fund «Talent and success», project number 20-38-51014.

References

1. Mogale DG, Cheikhrouhou N, Tiwari MK (2020) Modelling of sustainable food grain supply chain distribution system: a bi-objective approach. *Int J Prod Res* 58(18):521–5544
2. Maiyar LM, Thakkar JJ (2020) Robust optimisation of sustainable food grain transportation with uncertain supply and intentional disruptions. *Int J Prod Res* 58(18):5651–5675
3. Gao Y, Yang L, Li S (2016) Uncertain models on railway transportation planning problem. *Appl Math Model* 40(7–8):4921–4934
4. Tian W, Cao C (2017) A generalized interval fuzzy mixed integer programming model for a multimodal transportation problem under uncertainty. *Eng Optim* 49(3):481–498
5. Sun Y, Liang X, Li X, Zhang C (2019) A fuzzy programming method for modeling demand uncertainty in the capacitated road-rail multimodal routing problem with time windows. *J Symmetry* 11(1):91. <https://doi.org/10.3390/sym11010091>
6. Aulin V, Lyashuk O, Pavlenko O et al (2020) Realization of the logistic approach in the international cargo delivery system. *Commun Sci Lett Univ Zilina* 21(2):3–12
7. Prachi A, Talari G (2018) Multi-choice stochastic transportation problem involving logistic distribution. *Adv Appl Math Sci* 18(1):45–58
8. Wiradanti B, Pettit S, Potter A, Abouarghoub W (2018) Ports, peripherality and concentration – deconcentration factors: a review. *Marit Bus Rev*. <https://doi.org/10.1108/MABR-09-2018-0040>
9. Valls J, Langen P, Garcia-Alonso L et al (2020) Understanding port choice determinants and port hinterlands: findings from an empirical analysis of Spain. *Marit Econ Logist* 22:53–67
10. Chislov ON, Bogachev VA, Zadorozhniy VM et al (2019) Modelling of the rail freight traffic by the method of economic-geographical delimitation in the region of the South-Easter Coast of the Baltic Sea. *Transp Probl* 14(2):77–87
11. Chislov O, Bogachev T, Kravets A, Bogachev V, Zadorozhniy V, Egorova I (2020) Time parameters optimization of the export grain traffic in the port railway transport technology system. In: Sierpiński G (eds) *Smart and green solutions for transport systems (TSTP 2019)*. *Advances in Intelligent Systems and Computing*, vol 1091, pp 126–137
12. Meng F, Zhang Z, Hou X (2019) Machine learning for prediction of sudden cardiac death in heart failure patients with low left ventricular ejection fraction: study protocol for a retrospective multicentre registry in China. *BMJ Open* 9:e023724. <https://doi.org/10.1136/bmjopen-2018-023724>
13. Kolesnikov MV, Lyabakh NN, Mamaev EA, Bakalov MV (2020) Efficient and secure logistics transportation system. In: *VIII International Scientific Conference Transport of Siberia 2020*, vol 918, p 012031. *IOP Conf Ser Mater Sci Eng*. IOP Publishing. <https://doi.org/10.1088/1757-899X/918/1/012031>

14. Rozewsky P, Novikov D, Zaikin O, Bakhtadze N (eds) (2016) Incentive mechanisms for multi-agent organizational systems. New frontiers in information and production systems modeling and analysis – incentive mechanisms, competence management, knowledge-based production. Series “Intelligent Systems Reference Library”, vol 268, pps 35–57. Springer, Berlin
15. Lyabakh N, Saryan A, Dergacheva I et al (2020) Development of the pattern recognition theory for solving the tasks of object classification and yard processes. *Adv Intell Syst Comput* 1226:59–68

High Speed Transport Systems for Urban Agglomerations



Oleg Larin , Alexander Bokov , and Liudmila Ponimatkina 

Abstract In the paper, based on the results of the analysis of the prospects for changing the population in cities, the expediency of organizing high-speed passenger transportation in metropolises is substantiated. Modern transport systems of urban agglomerations do not provide high-speed connection between cities and suburban areas. Therefore, it is proposed to create high-speed rail lines for promising urban agglomerations with a commissioning date after 2030. Nowadays, high-speed rail lines are mainly used for inter-regional connections. Considering the high density of urban areas, it is proposed to use the tube-type high-speed rail lines. The use of “vacuum-free” transport systems with natural atmospheric pressure in an insulated transportation device has been substantiated. To reduce the profile air resistance to the movement of the train, an innovative tube structure has been developed that provides synchronous and balanced air exchange during the movement of the train. The estimated average speed of high-speed rail lines movement along the route network within urban agglomerations will exceed 200 km/h, the length of radial routes can reach 250 km with a length of 50 km and an average passenger travel distance of 100 km.

Keywords Transportation infrastructure · Future urban mobility · Gigapolis · Urban sustainability · High-speed rail · Urban agglomeration · Tube transport

O. Larin (✉)

Russian University of Transport (MIIT), 9b9 Obrazcova Street, Moscow 127994, Russia
e-mail: larin_on@mail.ru

O. Larin · A. Bokov

Plekhanov Russian University of Economics, Stremyanny Lane 36, Moscow 117997, Russia
e-mail: av_bokov@mail.ru

L. Ponimatkina

Financial University Under the Government of the Russian Federation, 49 Leningradsky Prospekt, Moscow 125993, Russia
e-mail: laponimatkina@fa.ru

1 Introduction

Modern urban agglomerations are centers of economic activity and innovation. According to official estimates and forecasts, the urban format of living and doing business will dominate in most countries of the world in the future. According to the UN Department of Economic and Social Affairs [18], over a long period of time, the world's population will continue to grow. By 2030, the total number of the world's inhabitants will increase by about 12% compared to 2018, reaching 8.6 billion inhabitants. At the same time, the largest population growth is expected in cities (+22.4%), while the number of rural residents will decline (−1%) [19 and 21]. The data of the forecast of the UN Department of Economic and Social Affairs for the world population for the period up to 2030 are presented in Table 1.

The highest growth rates of residents will be characteristic of cities with a population of more than 1 million inhabitants (+34% on average), and the highest growth

Table 1 Distribution of residents by settlements, the result of 2018 and the forecast for 2030, (according to [18, 19])

Types of settlements	2018			2030		
	Number of settlements, units	Population, million inhabitants	Share of total population, %	Number of settlements, units	Population, million inhabitants	Share of total population, %
Cities, including:	—	4 220	55.3	—	5 167	60.4
<i>over 10 million inhabitants</i>	33	529	6.9	43	752	8.8
<i>from 5 to 10 million inhabitants</i>	48	325	4.3	66	448	5.2
<i>from 1 to 5 million inhabitants</i>	467	926	12.1	597	1 183	13.8
<i>from 500,000 to 1 million inhabitants</i>	598	415	5.4	710	494	5.8
<i>less than 500,000 million inhabitants</i>	—	2 025	26.5	—	2 291	26.8
Rural settlements	—	3 413	44.7	—	3 384	39.6

rates of urban residents will be observed in the largest agglomerations with a population of more than 10 million inhabitants (+42%). By 2050, the number of urban residents will exceed 5.8 billion people and will account for 69% of the total population. In turn, some of the largest urban agglomerations will move into the category of gigapolises, the population of which, taking into account the adjacent territories, will reach 100 million people [16, 17 and 20].

Urbanization is accompanied by many positive effects, in particular, conditions are provided for improving the quality of education, developing entrepreneurial activity, and creating innovations. According to the World Bank, more than 80% of global GDP is generated in cities. At the same time, cities account for two-thirds of global energy consumption and more than 70% of greenhouse gas emissions, with a significant contribution of transport to these indicators. Therefore, to ensure the sustainable growth of urban ecosystems, it is necessary to introduce innovative transport technologies for the effective implementation of the population’s promising demands for movement, the number and range of which is expected to increase significantly [2, 3, 7 and 12].

The population’s need for movement is determined by the level of development of society, its social structure, the level of development of social production, the prevailing way of life, the nature of settlement, etc. An increase in the transport mobility of the population occurs due to economic, social and demographic factors: the way of life of people, the level of real income of the population, the nature of settlement, the structure of the economy, opportunities for recreation, etc. Transport mobility of the population is the main initial value in the calculations when designing transport systems cities. The indicator of population mobility is defined as the number of movements per person of the total number of participants in movements for the estimated period of time, usually a year. Table 2 shows the dependence of the transport mobility of the population, taking into account all types of transport, on the number of inhabitants of settlements.

Transport mobility, as well as the choice of the mode of transport, largely depends on the travel time. In some cities, the share of travel time in the overall structure of travel time may be negligible. For example, if, to travel by transport, a passenger needs to make significant pedestrian movements associated with the approach to the stopping point and departure from it. In this case, the passenger can completely

Table 2 Dependence of the number of trips per inhabitant on the size of the city

Number of city residents, thousand people	Number of trips per person per year
up to 50	150–200
50–100	250–300
101–300	300–400
101–300	400–500
501–1000	500–650
Over 1000	650–750

abandon transport movement in favor of direct pedestrian movement, of course, if there are direct pedestrian communications between objects of gravity. Therefore, an increase in the speed of transport will provide a reduction in travel time and increase the level of implementation of the potential mobility of the population.

The transport systems of the largest urban agglomerations in the world have significant transportation capabilities, provide a high level of transport accessibility for the population. At the same time, the existing high-speed transportation systems, including those using separate railways of surface and underground type, already now do not provide convenience of movement in terms of the duration of the trip. Therefore, with the growth of urban agglomerations, the need for high-speed movement will increase [1, 4 and 22].

The task of increasing the speed of passenger transportation is relevant for many urban agglomerations in Russia. For example, the most efficient urban transport system in the country has been created and is successfully operating in Moscow. Further expansion of the metro network, the launch of additional diametrical lines and other projects can provide a high level of transport accessibility for residents of the city and adjacent territories. However, even now these high-speed public transport systems do not provide a high speed of transportation in suburban-urban traffic. The average duration of trips over 20 km (by air line) can exceed 60 min, taking into account transfers. An integrated approach to solving this problem should provide for the development of new types of transport and the introduction of innovative high-speed transport systems in the agglomeration, which can significantly reduce the time spent by residents on everyday trips between megapolises and large cities of neighboring regions.

2 Materials and Methods

Please note that the first paragraph of a section or subsection is not indented. The first Nowadays, the highest speed of land communications is provided by high-speed rail systems (HSR), which are capable of transporting passengers at an average speed of over 200 km/h. However, HSR is not currently being used to serve metropolitan areas. The basic concept of HSR creation involves the use of highways to connect the most important economic and political regions of the country [5, 13 and 15]. The most extensive HSR network in the world was created in China [24], the length of which exceeds 36 thousand km. The configuration of the route network of the Chinese HSR is focused on connecting the largest megapolises and regional centers of the Celestial Empire [6].

Modern ground-based HSRs can be used to service urban agglomerations. At the same time, the implementation of such projects with a commissioning date after 2030 may be associated with restrictions, for example, the lack of land plots sufficient in area for laying highways in cities with a high building density. Therefore, it seems expedient to develop high-speed transport systems in which the rolling stock moves inside a tunnel or tube-type transporting device isolated from the external

environment (Tube Transport) [7 and 14]. Such constructions will be “easier” to fit into the architectural and planning solutions of the cities of the future. However, today there is no unambiguous understanding of how to organize the movement of rolling stock within the tube transport system.

It is a known fact that the movement of a train inside an insulated transport pipeline is accompanied by high energy losses for unproductive work to overcome the profile air resistances generated from the front and rear surfaces of the rolling stock. Therefore, various technical solutions are being developed to reduce such losses and, as a result, increase the speed capabilities and energy efficiency of tunnel and tube-type transport systems. The most famous solutions are Evacuated Ultra-High-Speed Tube Transport Systems (EUSTS) with sealed transport lines, from which air, which creates resistance to vehicle movement in an isolated space, is pumped out using compressor units. For the EUSTS to work, it is necessary that the pressure inside the transport pipeline does not exceed 100 Pa.

Nowadays, the American Hyperloop TT and Virgin Hyperloop have made significant progress in the creation of EUSTS. Hyperloop TT was one of the first in the world to develop EUSTS in an industrial format - from research to prototype testing. Hyperloop TT is currently designing a ground-based evacuated ultra-high-speed tube-type system with an outer structure diameter of 4 m. The passenger capsule can accommodate up to 50 passengers, the speed is up to 1.2 thousand km/h. It is planned to use magnetic levitation technology to move the capsule. In 2019, Hyperloop TT published a feasibility study for the Chicago-Cleveland-Pittsburgh ultra-high speed corridor. The journey from Chicago to Pittsburgh (750 km) will be approximately 35 min. Virgin Hyperloop also designs tunnel and tube structures. In 2020, the company reported on a successful test of the movement of a prototype ultra-high-speed vactrain with passengers in a capsule on board at a speed of 172 km/h. To develop the passenger segment of the vacuum transport system, Virgin Hyperloop is creating a research center in West Virginia worth \$500 million. The company's portfolio includes projects to create ultra-high-speed systems around the world. For example, in Saudi Arabia, an EUSTS ride from Riyadh to Jeddah (900 km) will take about one hour.

It is worth noting that EUSTS have a number of disadvantages: they require significant capital expenditures for their construction; it is necessary to ensure the safety of transportation in low pressure conditions; pipeline maintenance costs may exceed the effect of increasing the speed of traffic, etc. Therefore, in our opinion, it is advisable to create “Vacuum-Free” Ultra-High-Speed Tube Transport Systems (VFUSTS) with natural atmospheric pressure inside isolated transport device. To reduce the profile resistance in an environment with air, it is proposed to use an innovative method, which is based on the theoretical principles of creating tube-type transport systems, the results of a comparative analysis of transport pipelines with various degrees of air pumping (deep vacuum and forevacuum). In addition, the well-known methods of redistribution of residual air volumes in the transport pipeline, proposed in the Hyperloop and TransPod systems, were taken into account.

To reduce the force of air resistance to the movement of the train, it is proposed to carry out forced air exchange, which provides for a synchronous and balanced

redistribution of air masses from the front to the rear of the transport pipeline relative to the direction of movement of the rolling stock by means of an external air exchange device, which consists of air ducts, compressor units, valves, and an air accumulator. The process of external air exchange is carried out only during the movement of the train; preliminary evacuation of air is not required for the movement of the vehicle. The parameters of the air exchange system are regulated on the basis of gas-dynamic models, taking into account the speed of the vehicle, its location in the transport pipeline, the design features of the tunnel and rolling stock. The vehicle speed for each section of the high-speed track is normalized depending on the actual performance of the components of the air exchange system. The movement of a train along a transport pipeline with normal atmospheric pressure in the inner cavity provides conditions for the safe transportation of goods and passengers [9–11 and 23].

3 Results

The main unique advantages of the proposed innovative VFUSTS in comparison with similar EUSTS:

- the design solution does not provide for the creation of a vacuum in the transport pipeline to reduce the force of air resistance, as is done in vacuum analogues (for example, Hyperloop TT and Virgin Hyperloop);
- the movement of a vehicle in conditions with normal atmospheric pressure of the air mass in the inner cavity of the transport pipeline excludes man-made risks inherent in vacuum structures;
- the process of air exchange is automatically regulated taking into account the speed of the vehicle and its location in the transport pipeline;
- the vehicle speed for each section of the high-speed track is normalized depending on the actual performance of the components of the air exchange systems;
- no significant investment is required for the construction and operation of transport pipelines, which must withstand high pressure drops;
- the carrying capacity of the transport system increases due to the use of rolling stock with a larger capacity;
- design development allows creating high-speed underground and underwater transport systems.

Table 3 shows the results of a comparison of the functional and cost characteristics of VFUSTS and EUSTS, which show the presence of both advantages and disadvantages in each of the two systems.

The data presented in the table are not intended to cast doubt on the development prospects and the efficiency of using EUSTS, but only indicate the significant advantages of vacuum-free transport systems in comparison with vacuum analogs. At the same time, it is possible to create VFUSTS without an air accumulator, the operation of which requires significant costs. In this case, air exchange between the front and rear parts of the inner cavity of the transport pipeline will be carried out through the

Table 3 Comparison of functional and cost characteristics of VFUSTS and EUSTS (based on expert estimates)

Characteristics	VFUSTS	EUSTS
The amount of necessary investments for the implementation of the project	Basic level of investment for the creation of the main elements of the transport system (transport pipeline, air pumping system, rolling stock)	Higher relative to the basic level The excess is formed due to the high costs of creating special structures of the transport pipeline and rolling stock capable of withstanding significant pressure drops on the inner and outer surfaces of the hull
Speed potential	Basic level - high-speed traffic (over 300 km/h) At the same time, VFUSTS is capable of ensuring the movement of a vehicle at ultra-high speeds (700–1000 km/h). However, it is not advisable to develop such a speed within metropolitan areas	Theoretical estimates show that the speed of the capsule in the tube can reach 1.3 thousand km/h
Safety	Basic level of safety typical for existing transport systems	Safety level is lower (unsafe) relative to the basic level Increased risks of accidents during depressurization of the body of the transport pipeline and rolling stock
Operating costs	Higher relative to the basic level The excess is formed due to the high costs of controlling the operation of the air pumping system	Basic level (expenses for energy resources, for maintaining the elements of the transport system in good condition, etc.)

atmosphere. This design can be used to reduce project implementation costs. At the same time, this option will not allow laying the transport pipeline underground and underwater.

VFUSTS systems can be used to organize the movement of rolling stock on the basis of both the classic wheel-rail technology, and the promising magnetic levitation technology. Moreover, for the latter option, the use of an insulated pipe structure of the transport pipeline is more preferable, since it will eliminate the negative impact on the train movement of external factors, for example, strong gusts of wind and atmospheric precipitation.

Table 4 Forecast of potential traffic volumes

City	Population, thousand people	Distance to Moscow, km	Trips, thousand / day
Rzhev	57	230	3
Tver	770	180	58
Klin	79	103	18
Volokolamsk	18	120	3
Istra	33	66	18
Solnechnogorsk	49	71	24
Dubna	74	130	11
Yaroslavl	601	272	20
Sergeev Posad	99	73	45
Vladimir	352	186	25
Noginsk	103	55	82
Bronnitsy	22	58	16
Ryazan	534	202	32
Kolomna	144	113	27
Tula	496	182	36
Serpukhov	126	105	28
Kaluga	328	195	21
Obninsk	105	114	20
Mozhaisk	30	109	6
Dmitrov	68	65	39
Naro-Fominsk	67	70	33
Zvenigorod	22	65	13
Kubinka	20	76	8
Ruza	13	113	2
Total	4210	123	543

4 Discussion and Conclusions

In the future, innovations in housing and communal services, construction and transport spheres will require a large-scale modernization of the housing background and infrastructure of urban ecosystems. To service the transportation of the population in the agglomerations of the future, high-speed vacuum-free tube-type transport systems may be required. Basic characteristics of the VFUSTS network for urban agglomerations: the average section length is about 50 km; the total length of radial routes is on average up to 250 km. For the metropolitan agglomeration of Russia - the city of Moscow - the following routes can be proposed connecting the metropolis with the adjacent territories and major regional centers:

1. Rzhev - Volokolamsk - Istra - Moscow;
2. Tver - Klin - Solnechnogorsk - Moscow;
3. Dubna - Dmitrov - Moscow;
4. Yaroslavl - Sergeev Posad - Moscow;
5. Vladimir - Noginsk - Moscow;
6. Ryazan - Kolomna Bronnitsy - Moscow;
7. Tula - Serpukhov - Moscow;
8. Kaluga - Obninsk - Naro-Fominsk - Moscow;
9. Mozhaisk - Kubinka - Moscow;
10. Ruza - Zvenigorod - Moscow.

For the proposed route network made a forecast of potential traffic volumes, excluding population growth (Table 4). For the forecast used a Gravity's model, since the potential mobility of the population of neighboring regions in the direction of the Moscow agglomeration is latent [25, 26]. There is a need for travel, but it is not reported due to the long duration.

The results of the analysis show that for the route network of 24 cities, the total number of daily trips will exceed 500 thousand people. The average journey time on the routes will not exceed 60 min. Therefore, the use of HSR for the transportation of passengers will improve transport services for the residents of the megalopolis, increase the connectedness of territories, and provide conditions for strengthening cooperation of regional economies.

References

1. Malmberg A (2009) Agglomeration. In: Kobayashi, A. International encyclopedia of human geography. 2nd edn., pp 61–65. <https://doi.org/10.1016/B978-0-08-102295-5.10025-3>
2. Ceder A (2020) Urban mobility and public transport: future perspectives and review. *Int J Urban Sci*. <https://doi.org/10.1080/12265934.2020.1799846>
3. Barney C (2006) Urbanization in developing countries: current trends, future projections, and key challenges for sustainability. *Technol Sci* 28:63–80
4. Hensher D (2020) Chapter 26 - Estimating the wider economic benefits of the Sydney North West rail link project. In: Hensher D (ed) *Bus transport*, pp 325–347. <https://doi.org/10.1016/B978-0-12-820132-9.00026-1>
5. Cascetta E, Carteni A, Henke I, Pagliara F (2020) Economic growth, transport accessibility and regional equity impacts of high-speed railways in Italy: ten years ex post evaluation and future perspectives. *Transp Res Part A Policy Pract* 139:412–428. <https://doi.org/10.1016/j.tra.2020.07.008>
6. Sun H (2016) Study on the correlation between the hierarchical urban system and high-speed railway network planning in China. *Front Archit Res* 5(3):301–318. <https://doi.org/10.1016/j.foar.2016.04.003>
7. Janzen R (2017) Transpod ultra-high-speed tube transportation: dynamics of vehicles and infrastructure. *Procedia Eng* 199:8–17. <https://doi.org/10.1016/j.proeng.2017.09.142>
8. Soria-Lara J, Ariza-Álvarez A et al (2021) Participatory visioning for building disruptive future scenarios for transport and land use planning. *J Transp Geogr* 90:102907. <https://doi.org/10.1016/j.jtrangeo.2020.102907>

9. Larin O, Bokov A (2019) Decreasing of profile air drag to the train movement inside the tube transport. *Transp Syst Technol* 5(2):47–59. <https://doi.org/10.17816/transsyst20195247-59>
10. Larin O, Bokov A (2019) A method for reducing the profile air drag to the movement of a vehicle inside a transport pipeline of tunnel and pipe-type due to the organization of external air exchange and a device for its implementation. Russian Patent no 2721024
11. Larin O, Bokov A, Goryaev N (2019) Mathematical models of the process of air removal from the airtight transport pipeline during vehicle movement. *Adv Intell Syst Comput* 1115:747–755. <https://doi.org/10.1007/978-3-030-37916-2>
12. Lerch M (2017) International migration and city growth. Population Division Technical Paper 2017/10. United Nations, New York
13. Tian M, Li T, Ye X, Zhao H, Meng X (2021) The impact of high-speed rail on service industry agglomeration in peripheral cities. *Transp Res Part D Transp Environ* 93:102745. <https://doi.org/10.1016/j.trd.2021.102745>
14. Oster D, Kumada M, Zhang Y (2011) Evacuated tube transport technologies (ET3)tm: a maximum value global transportation network for passengers and cargo. *J Mod Transp* 19:42–50. <https://doi.org/10.1007/BF03325739>
15. Jia S, Zhou C, Qin C (2017) No difference in effect of high-speed rail on regional economic growth based on match effect perspective? *Transp Res Part A Policy Pract* 106:144–157. <https://doi.org/10.1016/j.tra.2017.08.011>
16. Custer J (2018) Sustainable Cities: a guide to Urban Planning. Clanrye international
17. World population policies 2019 (2020) ST/ESA/SER.A/442. United Nations Department of Economic and Social Affairs, Population Division, New York
18. The World's Cities in 2018 (2018) – data booklet (ST/ESA/SER.A/417). United Nations, New York
19. World population prospects 2019, Volume I (2019) Comprehensive tables (ST/ESA/SER.A/426). United Nations, New York
20. World Urbanization prospects (2019) The 2018 revision (ST/ESA/SER.A/420). United Nations, New York
21. World Urbanization prospects 2018 (2019) Highlights (ST/ESA/SER.A/421). United Nations, New York
22. Custer J (ed) (2020) Urban transportation. Future perspectives. Clanrye international
23. Vakulenko S, Larin O, Bokov A, Korytova M (2021) Mathematical simulations of air exchange processes in evacuated tube transport. *Transp Res Procedia* 54:84–593
24. Huang Y, Xu W (2021) Spatial and temporal heterogeneity of the impact of high-speed railway on urban economy: empirical study of Chinese cities. *J Transp Geogr* 91:102972. <https://doi.org/10.1016/j.jtrangeo.2021.102972>
25. Converse P (1949) New laws of retail gravitation. *J Mark* 14(3):379–384. <https://doi.org/10.2307/1248191>
26. Edward JT, Howard LG, Morton EO'K (1996) Geography of transportation. Morton O'Kelly

On Some Properties of the Blow-Up Solutions of a Nonlinear Parabolic System Non-divergent Form with Cross-Diffusion



Alisher Matyakubov and Dilmurod Raupov

Abstract In this paper, studies the blow-up properties of solutions of nonlinear parabolic systems of non-divergent equations with a source. In solving the initial boundary value problems for the equations of mathematical physics by the difference method important issue is the choice of the order of approximation with respect to the spatial coordinates and the choice of a function as an initial approximation, as well as the search of an efficient algorithm for solving the systems of difference equations. We construct the scheme of high accuracy for nonlinear system of not in divergence form. Computational experiments confirming the high order accuracy scheme were conducted.

Keywords Blow-up solution · Non-divergent form · Cross-diffusion

1 Introduction

In this paper, we study the qualitative properties of solutions to the following nonlinear system of a non-divergent parabolic equation

$$\frac{\partial u}{\partial t} = v^{\alpha_1} \nabla(u^{m_1-1} \nabla u) + u^{\beta_1}, \quad \frac{\partial v}{\partial t} = u^{\alpha_2} \nabla(v^{m_2-1} \nabla v) + v^{\beta_2}, \quad (1)$$

$$U|_{t=0} = u_0(x) \geq 0, \quad v|_{t=0} = v_0(x) \geq 0, \quad x \in \mathbb{R}^N \quad (2)$$

where $m_1, m_2, \alpha_1, \alpha_2, \beta_1, \beta_2$ are the positive numbers, $N \geq 1$ the size of the space, $\nabla(\cdot) = \text{grad}_x(\cdot)$, the functions $u = u(t, x) \geq 0, v = v(t, x) \geq 0$ are the solutions.

Nonlinear equations and systems of equations in non-divergent form are often used to describe various physical phenomena, such as the diffusion process for biological species, resistive diffusion phenomena in powerless magnetic fields, flow shortening curve, the spread of infectious diseases, and so on, see [3–6, 9, 10].

A. Matyakubov (✉) · D. Raupov
National University of Uzbekistan, Tashkent, Uzbekistan

As shown in the works of many authors [3–10, 18, 19, 20], nonlinear equations are the source of new nonlinear effects, such as the finite velocity of perturbation propagation, spatial localization, blow up, etc. These properties for a divergent cross-system were investigated in [7, 8, 21–24].

The term cross-diffusion refers to the movement flow of one species of individuals substances due to the presence of a gradient of other individuals of substances. The value of the cross-diffusion coefficient can be positive, negative or equal to zero. A positive cross-diffusion coefficient indicates that the movement of individuals occurs in the direction of a low concentration of other individuals; a negative one indicates that the movement occurs in the direction of a high concentration of other species of substances. In nature, cross-diffusion systems are quite common and play a significant role, especially in biophysical and biomedical systems.

This system describes the processes of heat diffusion and gorenje in two-component continuous media with nonlinear thermal conductivity and volumetric energy release. The functions u and v can be interpreted as the temperatures of the components of a certain combustible mixture interacting with each other. We will be particularly interested in the conditions for the emergence of unbounded solutions, as well as the condition for their localization in the Cauchy problem.

In [6] investigated some properties of solutions of the Cauchy problem for a nonlinear parabolic equation of non-divergence form with variable density

$$|x|^n \frac{\partial u}{\partial t} = u^m \operatorname{div} (|\nabla u|^{p-2} \nabla u), \quad p > 1, 0 \geq m < \frac{(p-2)(N+n) + p+n}{p-N}$$

and found a self-similar solution of Barenblatt-Zel'dovich-Kompaneets, proved asymptotic self-similar solutions in the case of fast and slow diffusion, and the numerical results confirming the properties of finite speed of heat propagation and spatial localization of solutions of the Cauchy problem.

In [12, 13], the existence and uniqueness of the classical solution of the Cauchy problem is investigated

$$\begin{aligned} u_t &= u^{\alpha_1} (u_{xx} + av), \quad v_t = v^{\alpha_2} (v_{xx} + bu), \quad x \in \Omega, \quad t > 0, \\ u &\equiv v|_{\partial\Omega} \equiv 0, \quad t > 0, \quad u(x, 0) \equiv u_0(x), \quad v(x, 0) \equiv v_0(x), \quad x \in \Omega. \end{aligned} \tag{3}$$

The local existence of positive classical solutions is proved: for $\min\{a, b\} \leq \lambda_1$ there are positive classical solutions, for $\min\{a, b\} > \lambda_1$ here are no positive classical solutions.

In [14], a degenerate parabolic system with a nonlinear localized source is considered

$$u_t = u^\alpha (\Delta u + u^p(x, t)v^q(x_0, t)), \quad v_t = v^\beta (\Delta v + v^m(x, t)u^n(x_0, t)),$$

it is proved that the system has a unique positive classical solution, estimated the rate of exacerbation and blow-up solutions by changing the Souplet method. Studying the establishment of the blow-up solution and the rate of exacerbation with

respect to the radial variable of the blow-up solution when the region has the form of a ball.

In [15], nonlinear degenerate parabolic systems $u_t = v^{\gamma_1}(u_{xx} + au)$, $v_t = u^{\gamma_2}(v_{xx} + bv)$ with Dirichlet boundary conditions are studied. The regularization method and the upper-lower solution technique are used to show the local existence of a solution for a nonlinear degenerate parabolic system. The existence of a global solution is discussed, and the blow-up property of the solution is established.

In [16], positive solutions of degenerate quasilinear parabolic systems in not in divergent form

$$u_{it} = f_i(u_{i+1})(\Delta u_i + a_i u_i), x \in \Omega, t > 0, i = 1, 2, \dots, n - 1,$$

$$u_{nt} = f_n(u_1)(\Delta u_n + a_n u_n), x \in \Omega, t > 0$$

with a homogeneous Dirichlet boundary condition and a positive initial condition are investigated. The local existence and uniqueness of the classical solution are proved. It is shown when $\min\{a_1, \dots, a_n\} \leq \lambda_1$ (where λ_1 is the first eigenvalue $-\Delta$ in Ω with a homogeneous Dirichlet boundary condition), then there exists a global positive classical solution, and all positive classical solutions do not have the blow-up property.

In [17], self-similar solutions of a degenerate parabolic equation in non-divergent form are investigated

$$\frac{\partial u}{\partial t} = u^m \operatorname{div}(|\nabla u|^{p-2} \nabla u), m \geq 1, p > 1$$

Self-similar solutions in the form of $u(t, x) = (t + 1)^{-\alpha} f((t + 1)^\beta |x|^2)$. The asymptotic of a non-divergent parabolic equation

$$u'_t = u^m \operatorname{div}(|\nabla u|^{p-2} \nabla u) + \lambda u^q, m \geq 1, p > 1, q > 0, \lambda > 0$$

with Dirichlet boundary conditions is discussed in [5], where three cases are studied depending on the values of numerical parameters, the stability of stationary states is proved, and the asymptotic stability of the solution with a periodic source is discussed.

2 Preliminaries

In this work we investigated the qualitative properties of the solution of problem (1) based on self-similar analysis and its numerical solutions using the methods of

modern computer technologies, the study of linearization methods to the convergence of the iterative process with further visualization. We introduce the following definitions

Definition 1 Solutions that satisfy the condition $\max_{x \in \Omega} u(t, x) \rightarrow +\infty, \max_{x \in \Omega} v(t, x) \rightarrow +\infty$, by $t \rightarrow T_0^-$ they are called modes with aggravation (or unlimited), where Ω —restricted area in R^N , T_0 —the lifetime of the solution.

Definition 2 A function $u_+(t, x), v_+(t, x)$ ($u_-(t, x), v_-(t, x)$), is called an upper (lower) solution of problem (1), (2) if the conditions in Q are satisfied $L(u_+(t, x)) \leq 0, L(v_+(t, x)) \leq 0$ ($L(u_-(t, x)) \geq 0, L(v_-(t, x)) \geq 0$), and $u_0(x) \leq u_+(0, x), v_0(x) \leq v_+(0, x)$ ($u_0(x) \geq u_-(0, x), v_0(x) \geq v_-(0, x)$).

3 Approximate Self-similarity for the Nonlinear System of Equations

We have established the existence and uniqueness off with compact carriers, which imply that the self-similar solution is narrowed. Based on this, we also established the convergent velocity of these solutions at the carrier boundary.

To construct a self-similar system (1), a nonlinear splitting algorithm is proposed, for which the solution of system (1) is sought in the form

$$u(t, x) = (T - t)^{q_1} w(\tau(t), r(t), x)^{q_2} (\tau(t), r(t)|x|)) \tag{4}$$

$$q_1 = -\frac{1}{\beta_1 - 1}, \quad q_2 = -\frac{1}{\beta_2 - 1}$$

$$\tau(t) = \begin{cases} \int (T - t)^{\frac{m_1-1}{1-\beta_1} + \frac{\alpha_1}{1-\beta_2}} dt, & \frac{m_1-1}{1-\beta_1} + \frac{\alpha_1}{1-\beta_2} + 1 \neq 0 \\ Ln(T - t), & \frac{m_1-1}{1-\beta_1} + \frac{\alpha_1}{1-\beta_2} + 1 = 0 \end{cases} \tag{5}$$

In the future, the system (1) is investigated when the condition is met

$$\frac{m_1 - 1}{1 - \beta_1} + \frac{\alpha_1}{1 - \beta_2} = \frac{m_2 - 1}{1 - \beta_2} + \frac{\alpha_2}{1 - \beta_1}, \quad \frac{m_1 - 1}{1 - \beta_1} + \frac{\alpha_1}{1 - \beta_2} + 1 > 0$$

Then, relatively (w, φ) we obtain a system of equations

$$\begin{aligned} \frac{\partial w}{\partial \tau} &= \varphi^{\alpha_1} \nabla (w^{m_1-1} \nabla w) - b_1 \tau^{-1} (w^{\beta_1} + w) = 0, \\ \frac{\partial \varphi}{\partial \tau} &= w^{\alpha_2} \nabla (\varphi^{m_2-1} \nabla \varphi) - b_2 \tau^{-1} (\varphi^{\beta_1} + \varphi) = 0, \end{aligned} \tag{6}$$

where $b_i = \frac{q_i}{q_i(m_i-1)+q_{3-i}\alpha_i}$, $i = 1, 2$
 And then by entering (4) the transformation

$$w(\tau, x) = f(\xi), \quad \varphi(\tau, x) = \phi(\xi), \quad \xi = \frac{\|x\|}{(T-t)^{\frac{1}{2}}} \tag{7}$$

we obtain a self-similar system of equations

$$\begin{aligned} \varphi^{\alpha_1} \xi^{1-N} \frac{d}{d\xi} \left(\xi^{N-1} f^{m_1-1} \frac{df}{d\xi} \right) + \frac{\xi}{2} \frac{df}{d\xi} - b_1(f^{\beta_1} + f) &= 0, \\ f^{\alpha_2} \xi^{1-N} \frac{d}{d\xi} \left(\xi^{N-1} \phi^{m_2-1} \frac{d\phi}{d\xi} \right) + \frac{\xi}{2} \frac{d\phi}{d\xi} - b_2(\phi^{\beta_1} + \phi) &= 0, \end{aligned} \tag{8}$$

Below we will study the asymptotic of solutions of self-similar equations for system (8).

To do this, we transform the original system to a relatively easy-to-study form. To obtain such an auxiliary system of equations, we apply the following transformations to Eqs. (8)

$$f(x) = \bar{f}(\xi)y_1(\eta), \quad \phi(x) = \bar{\phi}(\xi)y_2(\eta) \tag{9}$$

3.1 The Case of Fast Diffusion

We will consider non-negative solutions of the system of Eqs. (6) satisfying the following conditions:

$$f'(0) = 0, \phi'(0) = 0, f(\infty) = 0, \phi(\infty) = 0 \tag{10}$$

$$\bar{f}(\xi) = (a + \xi^2)^{p_1}, \bar{\phi}(\xi) = (a + \xi^2)^{p_2}, \quad a > 0, \eta = \ln(a + \xi^2),$$

$p_i = \frac{m_{3-i}-\alpha_i-1}{(m_1-1)(m_2-1)-\alpha_1\alpha_2}$, $y_1(\eta), y_2(\eta)$ – the desired functions.

Then the system (6) is reduced to the form

$$y_{3-i}^{\alpha_i} \frac{d}{d\eta} (Ly_i) + a_{i1}(\eta)y_{3-i}^{\alpha_i}Ly_i + a_{i2} \left(a_{i0}y_i + \frac{dy_i}{d\eta} \right) + a_{i3}(\eta)y_i + a_{i4}(\eta)y_i^{\beta_i} = 0, \quad (i = 1, 2) \tag{11}$$

in which

$$a_{i0}(\eta) = p_i, \quad a_{i1}(\eta) = \frac{Ne^\eta}{2(e^\eta - a)} - 1 + p_i m_i, \quad a_{i2}(\eta) = \frac{1}{4}, \quad a_{i3}(\eta) = -\frac{b_i e^\eta}{4(e^\eta - a)},$$

$$a_{i4}(\eta) = -\frac{b_i e^{s_i \eta}}{4(e^\eta - a)}, \quad Ly_i = y_i^{m_i-1} \left(p_i y_i + \frac{dy_i}{d\eta} \right), \quad s_i = p_i(\beta_i - 1) + 1, \quad (i = 1, 2)$$

3.2 The Case of Slow Diffusion

We will consider non-negative solutions of the system of Eqs. (6) satisfying the following conditions:

$$f'(0) = 0, \phi'(0) = 0, f(\infty) = \infty, \phi(\infty) = \infty \tag{12}$$

$$\bar{f}(\xi) = (a - \xi^2)^{p_1}, \bar{\phi}(\xi) = (a - \xi^2)^{p_2}, \quad a > 0, \quad \eta = -\ln(a - \xi^2),$$

$$p_i = \frac{m_{3-i} - \alpha_i - 1}{(m_1 - 1)(m_2 - 1) - \alpha_1 \alpha_2}, \quad y_1(\eta), \quad y_2(\eta) \text{ - the desired functions.}$$

Then the system (6) is reduced to the form

$$y_{3-i}^{\alpha_i} \frac{d}{d\eta} (Ly_i) + a_{i1}(\eta) y_{3-i}^{\alpha_i} Ly_i + a_{i2} \left(\frac{dy_i}{d\eta} + a_{i0} y_i \right) + a_{i3}(\eta) y_i + a_{i4}(\eta) y_i^{\beta_i} = 0, \quad (i = 1, 2) \tag{13}$$

in which

$$a_{i0}(\eta) = p_i, \quad a_{i1}(\eta) = \frac{Ne^\eta}{2(e^\eta - a)} - 1 + p_i m_i, \quad a_{i2}(\eta) = \frac{1}{4}, \quad a_{i3}(\eta) = -\frac{b_i e^\eta}{4(e^\eta - a)}$$

$$a_{i4}(\eta) = -\frac{b_i e^{-s_i \eta}}{4(e^\eta - a)}, \quad Ly_i = y_i^{m_i-1} \left(\frac{dy_i}{d\eta} - p_i y_i \right), \quad s_i = p_i(\beta_i - 1) + 1, \quad (i = 1, 2)$$

4 Main Results

Let's introduce the notation

$$b_{i1}(\eta) = \left(\frac{N}{2} - 1 + p_i m_i \right) p_i, \quad b_{i2}(\eta) = \frac{p_i - b_i}{4}, \quad c_{i1}(\eta) = (p_i m_i - 1) p_i,$$

$$c_{i2}(\eta) = -\frac{p_i}{4}, \quad c_{i3}(\eta) = \frac{-b_i}{4a}, \quad (i = 1, 2)$$

The following theorems are proved:

Theorem 1 Let in the case of rapid diffusion $\beta_i > 1$, $p_i < 0 (i = 1, 2)$ and $\frac{m_1-1}{1-\beta_1} + \frac{\alpha_1}{1-\beta_2} + 1 > 0$. Then the solution of the system of Eq. (1) has the asymptotic in this case, the solution of the system of Eq. (1) has asymptotic at $\xi \rightarrow \infty$.

$$u(t, x) = A(T - t)^{q_1} (a + \xi^2)^{p_1} y_1(\eta), \quad v(t, x) = B(T - t)^{q_2} (a + \xi^2)^{p_2} y_2(\eta), \quad (14)$$

where $y_i(\eta) = y_i^0 + o(1)$, $0 < y_i^0 < +\infty$, $(i = 1, 2)$ and y_i^0 , $(i = 1, 2)$ are respectively the roots z_i , $(i = 1, 2)$ of a system of nonlinear algebraic equations

$$b_{i1} z_i^{m_i-1} z_{3-i}^{\alpha_i} + b_{i2} = 0, \quad (i = 1, 2)$$

Proof Assuming in the system (9)

$$v_i(\eta) = y_i^{m_i-1} \left(\frac{dy_i}{d\eta} - a_{i0} y_i \right), \quad (i = 1, 2) \quad (15)$$

we get the identities

$$v'_i = -a_{i1}(\eta)v_i(\eta) - a_{i2}(\eta)y_{3-i}^{\alpha_i}y_i^{1-m_i}v_i(\eta) - a_{i3}(\eta)y_i^{\beta_i}y_{3-i}^{-\alpha_i} - a_{i4}(\eta)y_iy_{3-i}^{-\alpha_i} = 0, \quad (i = 1, 2) \quad (16)$$

Consider now the function

$$g_i(\lambda_i, \eta) = -a_{i1}(\eta)\lambda_i - a_{i2}(\eta)y_{3-i}^{-\alpha_i}y_i^{1-m_i}\lambda_i - a_{i3}(\eta)y_i^{\beta_i}y_{3-i}^{-\alpha_i} - a_{i4}(\eta)y_iy_{3-i}^{-\alpha_i}, \quad (i = 1, 2)$$

where $\lambda_i \in R$, $(i = 1, 2)$

Let $\frac{m_1-1}{1-\beta_1} + \frac{\alpha_1}{1-\beta_2} + 1 > 0$. Then the function stores the sign on a certain interval $[\eta_1, +\infty) \subset [\eta_0, +\infty)$ for each fixed value λ_i $(i = 1, 2)$ other than the values satisfying the system

$$-a_{i1}^0\lambda_i - a_{i2}^0(y_i^0)^{1-m_i}(y_{3-i}^0)^{-\alpha_i}\lambda_i - a_{i3}^0(y_i^0)^{\beta_i}(y_{3-i}^0)^{-\alpha_i} - a_{i4}^0y_i^0(y_{3-i}^0)^{-\alpha_i} = 0, \quad (i = 1, 2)$$

Hence the view

$$\begin{aligned} \lim_{\eta \rightarrow +\infty} a_{i1}(\eta) &= \frac{N}{2} - 1 + m_1 p_1; & \lim_{\eta \rightarrow +\infty} a_{i2}(\eta) &= \frac{1}{4}; \\ \lim_{\eta \rightarrow +\infty} a_{i3}(\eta) &= 0; & \lim_{\eta \rightarrow +\infty} a_{i4}(\eta) &= \frac{-b_i q_i}{4}; \end{aligned} \quad (i = 1, 2) \text{ of } \beta_i > 1; \quad p_i < 0$$

follows that the function $g_i(\lambda_i, \eta)$, $(i = 1, 2)$ saves the sign on the gap $[\eta_1, +\infty) \subset [\eta_0, +\infty)$, where $\lambda_i \neq 0$, $(i = 1, 2)$.

By assumption the function $v_i(\eta)$, $(i = 1, 2)$ according to (15) and has a limit at $\eta \rightarrow +\infty$. Then $y'_i(\eta)$, $(i = 1, 2)$ has a limit when $\eta \rightarrow +\infty$, and, equal to zero.

Then $v_i(\eta) = y_i^{m_i-1} \left(\frac{dy_i}{d\eta} + a_{i0}y_i \right) = a_{i0}(y_i^0)^{m_i} + o(1)$, ($i = 1, 2$) at $\eta \rightarrow +\infty$ and by virtue of (16) the derivative of the function $v_i(\eta)$, ($i = 1, 2$) has a limit when $\eta \rightarrow +\infty$, which is obviously equal to zero. Therefore, it is necessary that

$$\lim_{\eta \rightarrow +\infty} \left(a_{i1}(\eta)v_i(\eta) + a_{i2}(\eta)y_{3-i}^{-\alpha_i}y_i^{1-m_i}v_i(\eta) + a_{i3}(\eta)y_i^{\beta_i}y_{3-i}^{-\alpha_i} + a_{i4}(\eta)y_iy_{3-i}^{-\alpha_i} \right) = 0, \quad i = 1, 2.$$

From here, it is easy to see that system (11) had solutions $(y_1(\eta), y_2(\eta))$ with a finite limit equal to zero when it is necessary that the conditions of Theorem 1 are met.

Therefore, by virtue of the introduced transformations (4), (7), (9) solution of the system of Eqs. (1) for $\xi \rightarrow +\infty$ has the asymptotics (14).

Theorem 2 Let $\frac{m_1-1}{1-\beta_1} + \frac{\alpha_1}{1-\beta_2} + 1 > 0$. In order for the system (9) to have solutions.

$$(y_1(\eta), y_2(\eta)) \text{ species } y_i(\eta) = y_i^0 + o(1), \quad \eta \rightarrow \infty, \quad (i = 1, 2) \quad (17)$$

where $0 < y_i^0 < +\infty$, ($i = 1, 2$) one of the following conditions must be met:

1. $p_i = \frac{1}{1-\beta_i}$, y_i^0 , ($i = 1, 2$) - are respectively the solutions of z_i , ($i = 1, 2$) systems of nonlinear algebraic equations

$$c_{i1}z_i^{m_i-1}z_{3-i}^{\alpha_i} + c_{i2} + c_{i3}z_i^{\beta_i-1} = 0, \quad (i = 1, 2)$$

2. $p_i \left(\frac{1}{1-\beta_i}, p_i m_i \right) 1$, y_i^0 , ($i = 1, 2$) - are respectively the solutions of z_i , ($i = 1, 2$) systems of nonlinear algebraic equations

$$c_{i1}z_i^{m_i-1}z_{3-i}^{\alpha_i} + c_{i2} = 0, \quad (i = 1, 2)$$

3. $p_1 = \frac{1}{1-\beta_1}$, $p_2 \left(\frac{1}{1-\beta_2}, p_2 m_2 \right) 1$, y_i^0 , ($i = 1, 2$) - are respectively the solutions of z_i , ($i = 1, 2$) systems of nonlinear algebraic equations

$$\begin{cases} c_{11}z_1^{m_1-1}z_2^{\alpha_1} + c_{12} + c_{13}z_1^{\beta_1-1} = 0 \\ c_{21}z_2^{m_2-1}z_1^{\alpha_2} + c_{22} = 0 \end{cases}$$

4. $p_1 \left(\frac{1}{1-\beta_1}, p_2 = \frac{1}{1-\beta_2}, p_1 m_1 \right) 1$, y_i^0 , ($i = 1, 2$) - are respectively the solutions of z_i , ($i = 1, 2$) systems of nonlinear algebraic equations

$$\begin{cases} c_{11}z_1^{m_1-1}z_2^{\alpha_1} + c_{12} = 0 \\ c_{21}z_2^{m_2-1}z_1^{\alpha_2} + c_{22} + c_{23}z_2^{\beta_2-1} = 0 \end{cases}$$

Corollary The generalized solution of the system of Eq. (1) has asymptotic at $|x| \rightarrow a^{\frac{1}{2}}\tau^{-\frac{1}{2}}$,

$$u(t, x) = z_1(T - t)^{q_1} \left(a - |x|\tau^{-\frac{1}{2}} \right)^{p_1} (1 + o(1)), \quad u(t, x) = z_2(T - t)^{q_2} \left(a - |x|\tau^{-\frac{1}{2}} \right)^{p_2} (1 + o(1)),$$

where $z_1, z_2, p_1, p_2, q_1, q_2$ - the constants defined above.

5 Computational Experiment

Iterative methods are known to require a suitable initial approximation that provides fast convergence to the exact solution. In this case, the above obtained asymptotic formulas are chosen as suitable initial approximations.

In the numerical solution of nonlinear problems, it is very important to choose a suitable initial approximation that preserves nonlinear properties. In this regard, a computational experiment was conducted on the basis of the above-mentioned qualitative properties of solutions [1]. For this purpose, system Eq. (1) was approximated with the second order of accuracy in spatial coordinates and with the first order in time. For numerical simulation, an iterative process is constructed, in the internal steps of the iteration; the values of the nodes are calculated by the run method. It is known that iterative methods require a good initial approximation that quickly converges to the desired solution and preserves the qualitative properties of the studied nonlinear processes, which is the main difficulty of numerical analysis of the problem under consideration. This difficulty, depending on the value of the numerical parameters included in the equation, can be overcome by a successful choice of initial approximations. Below we present numerical schemes for the one-dimensional case and some results of numerical experiments.

The creation of data visualization systems is one of the most developed and important areas of work for the analysis of the results of numerical modeling of physical processes. Currently, there are many tools designed for graphical representation of the results of calculations of mathematical physics problems. One of them is a package of application programs for solving problems of technical and mathematical calculations and a programming language of the same name - MATLAB, which is designed to work with grid mathematical models [2].

Programs for the numerical solution of non-divergent nonlinear systems in an inhomogeneous environment are developed in MATLAB. The programs are compact. The user sets the necessary numeric parameters.

At the end of the working file, the calculation results are automatically displayed in the form of matrices and a graph. In the same place, by running the animation command, you can follow the evolution of the process over time.

We present some results of numerical experiments.

5.1 The Case of Slow Diffusion $p_i > 0, (i = 1, 2)$

The initial approximation is taken as [10, 11]:

$$u_0(x) = \bar{u}(0)f_A(\xi), v_0(x) = \bar{v}(0)\varphi_A(\xi), \text{ where } f_A(\xi) = A(a - \xi^2)_+^{p_1}, \varphi_A(\xi) = B(a - \xi^2)_+^{p_2},$$

$$\bar{u}(0) = T^{-\frac{1}{\beta_1-1}}, \bar{v}(0) = T^{-\frac{1}{\beta_2-1}}, \xi = \phi(x)[\tau(0)]^{-\frac{1}{2}}, \phi(x) = |x|,$$

$$\tau(0) = \frac{1}{\frac{\alpha_1}{1-\beta_2} + \frac{m_1-1}{1-\beta_1} + 1} T^{\frac{\alpha_1}{1-\beta_2} + \frac{m_1-1}{1-\beta_1} + 1}, p_i = \frac{m_{3-i} - \alpha_i - 1}{(m_1 - 1)(m_2 - 1) - \alpha_1\alpha_2}, i = 1, 2.$$

5.2 The Case of Fast Diffusion $p_i < 0, (i = 1, 2)$

The initial approximation is taken as [10, 11]:

$$u_0(x) = \bar{u}(0)f_A(\xi), v_0(x) = \bar{v}(0)\varphi_A(\xi),$$

where $f_A(\xi) = A(a + \xi^2)_+^{p_1}, \varphi_A(\xi) = B(a + \xi^2)_+^{p_2},$

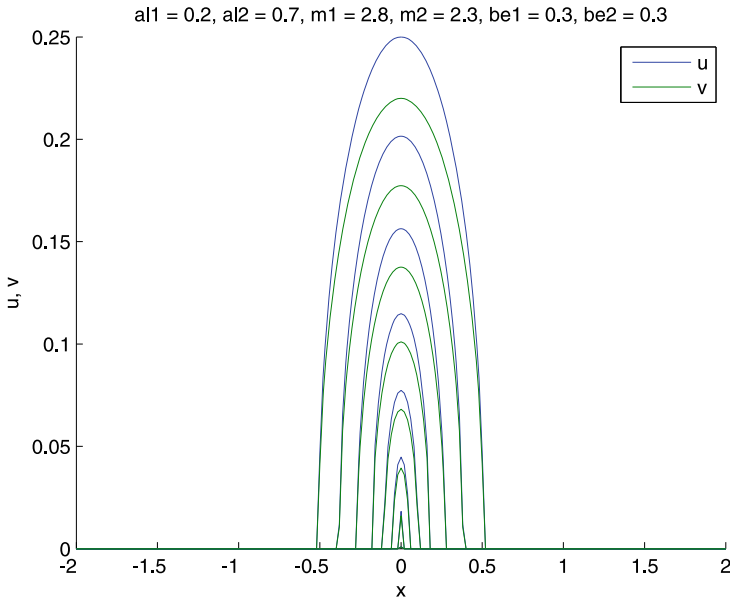


Fig. 1 Numerical solution of the problem (1)–(3) for $\alpha_1 = 0.2, \alpha_2 = 0.7, m_1 = 2.8, m_2 = 2.3, \beta_1 = 0.3, \beta_2 = 0.3$

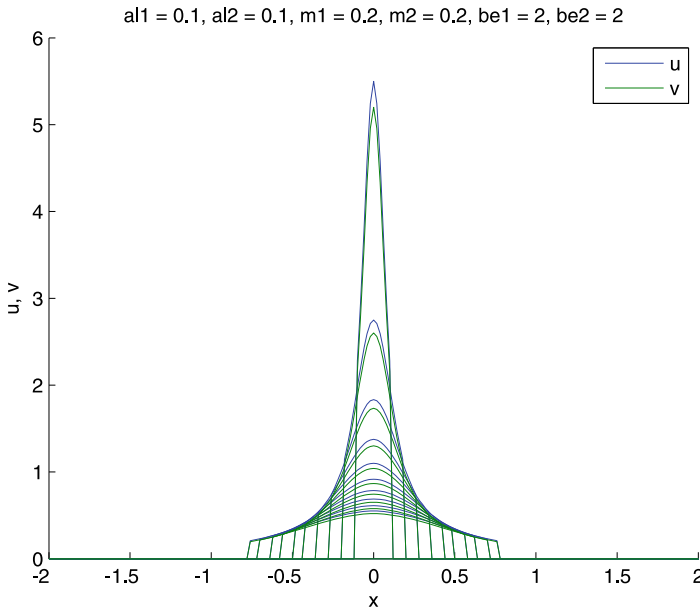


Fig. 2 Numerical solution of the problem (1)–(3) by $\alpha_1 = 0.1, \alpha_2 = 0.1, m_1 = 1.2, m_2 = 0.2, \beta_1 = 2, \beta_2 = 2$

$$\bar{u}(0) = T^{-\frac{1}{\beta_1-1}}, \bar{v}(0) = T^{-\frac{1}{\beta_2-1}}, \xi = \phi(x)[\tau(0)]^{-\frac{1}{2}}, \phi(x) = |x|,$$

$$\tau(0) = \frac{1}{\frac{\alpha_1}{1-\beta_2} + \frac{m_1-1}{1-\beta_1} + 1} T^{\frac{\alpha_1}{1-\beta_2} + \frac{m_1-1}{1-\beta_1} + 1}, p_i = \frac{m_{3-i} - \alpha_i - 1}{(m_1-1)(m_2-1) - \alpha_1\alpha_2}, i = 1, 2.$$

6 Conclusions

Note that the main difficulty in the numerical study of problem (1)–(2) arises from the non-uniqueness of the solution. Therefore, the question arises of choosing a good initial approximation that preserves the properties of nonlinearity. Depending on the value of the parameters of the equation system, this difficulty is overcome by a successful choice of initial approximations, which are taken as the above-established asymptotic formulas. Based on the above qualitative studies, numerical calculations were performed. Computational experiments have shown fast convergence of the iterative process due to the successful choice of the initial approximation.

Figure 1 shows the results of the numerical solution of the problem (1)–(2) for $\frac{\alpha_1}{1-\beta_2} + \frac{m_1-1}{1-\beta_1} = \frac{\alpha_2}{1-\beta_1} + \frac{m_2-1}{1-\beta_2}$ when $m_{3-i} > \alpha_i + 1$, corresponding to the case of slow diffusion.

Figure 2 shows the results of the numerical solution of the problem (1)–(2) by $\frac{\alpha_1}{1-\beta_2} + \frac{m_1-1}{1-\beta_1} = \frac{\alpha_2}{1-\beta_1} + \frac{m_2-1}{1-\beta_2}$, when $p_i > 0$, corresponding to the case of rapid diffusion.

The results make it possible to obtain the following estimate for the free boundary, $|x(t)| \leq \left[\frac{a}{b}\right]^{\frac{1}{2}} (T-t)^{\frac{b}{2}}$, where $b = \frac{\alpha_1}{1-\beta_2} + \frac{m_1-1}{1-\beta_1} + 1$.

References

1. Samarskiy AA (2005) Introduction to numerical methods. Textbook, 3rd ed. Lan, MSU, SPb, p 288
2. Woodford C, Phillips C (2020) Numerical methods with worked examples: Matlab Edition. SpringerLink, Bücher, Springer Netherlands, pp 1–16
3. Aripov M, Sadullaeva SA (2015) Qualitative properties of solutions of a doubly nonlinear reaction-diffusion system with a source. *J Appl Math Phys* 3(9):1090–1099
4. Zhou W, Yao Z (2010) Cauchy problem for a degenerate parabolic equation with non-divergence form. *Acta Math Sci* 30B(5):1679–1686
5. Jin C, Yin J (2013) Self-similar solutions for a class of non-divergence form equations. *Nonlinear Differ Equ Appl Nodda* 20(3):873–893
6. Aripov M, Raimbekov J (2019) The critical curves of a doubly nonlinear parabolic equation in non-divergent form with a source and nonlinear boundary flux. *J Siberian Fed Univ Math Phys* 12(1):112–124
7. Sadullaeva SA (2016) Numerical investigation of solutions to a reaction-diffusion system with variable density. *J Siberian Fed Univ Math Phys* 9(1):90–101
8. Aripov M, Rakhmonov Z (2016) On the behavior of the solution of a nonlinear multidimensional polytrophic filtration problem with a variable coefficient and nonlocal boundary condition. *Contemp Anal Appl Math* 4(1):23–32
9. Aripov M, Matyakubov AS (2016) To the qualitative properties of solution of system equations not in divergence form. *Int J Innov Sci Eng Technol* 3(8):533–537
10. Aripov M, Matyakubov AS, Imomnazarov BK (2020) The Cauchy problem for a nonlinear degenerate parabolic system in non-divergence form. *Math Notes NEFU* 27(3):27–38
11. Matyakubov AS (2017) Finite speed of the perturbation distribution and asymptotic behavior of the solutions of a parabolic system not in divergence form. *Univ J Comput Math* 5(3):57–67
12. Wang M (2020) Some degenerate and quasilinear parabolic systems not in divergence form. *J Math Anal Appl* 274:424–436
13. Wang MX, Xie CH (2004) A degenerate strongly coupled quasilinear parabolic system not in divergence form. *Z Angew Math Phys* 55:741–755
14. Wang M, Wei Y (2008) Blow-up properties for a degenerate parabolic system with nonlinear localized sources. *J Math Anal Appl* 343:621–635
15. Duan Z, Zhou L (2000) Global and blow-up solutions for nonlinear degenerate parabolic systems with crosswise-diffusion. *J Math Anal Appl* 244:263–278
16. Lu H (2009) Global existence and blow-up analysis for some degenerate and quasilinear parabolic systems. *Electron J Qual Theory Differ Equ* 49:1–14
17. Deng W, Li Y, Xie Ch (2003) Global existence and nonexistence for a class of degenerate parabolic systems. *Nonlinear Anal Theory Methods Appl* 55(3):233–244
18. Aripov M, Matyakubov AS (2017) To the qualitative properties of solution of system equations not in divergence form of polytrophic filtration in variable density. *Nanosyst Phys Chem Math* 8(3):317–322
19. Aripov M, Matyakubov AS (2017) To the properties of the solutions of a cross-diffusion parabolic system not in divergence form. *Univ J Comput Math* 5(1):1–7
20. Aripov M, Matyakubov AS (2017) Self-similar solutions of a cross-diffusion parabolic system with variable density: explicit estimates and asymptotic behaviour. *Nanosyst Phys Chem Mathe* 8(1):5–12

21. Rakhmonov ZR, Tillaev AI (2018) On the behavior of the solution of a nonlinear poly-tropic filtration problem with a source and multiple nonlinearities. *Nanosyst Phys Chem Math* 9(3):323–329
22. Rakhmonov ZR, Urunbayev JE (2019) On a problem of cross-diffusion with nonlocal boundary conditions. *J Siberian Fed Univ Math Phys* 5:614–620
23. Rakhmonov ZR, Khaydarov A, Urunbaev JE (2020) Global existence and nonexistence of solutions to a cross diffusion system with nonlocal boundary conditions. *Math Stat* 8(4):404–409
24. Parovik R, Rakhmonov Z, Zunnunov R (2020) Modeling of fracture concentration by Sel'kov fractional dynamic system. *E3S Web Conf* 196:02018

Block Matrix for Three-Factor Analysis of Machinery Failures



Irina Buslaeva  and Lena Yakovleva 

Abstract The methodological foundations of the study of a correlation between vehicle failures and operational and natural-climatic factors characteristic of the cryolithozone have been developed. For the three-factor analysis of the failures, it is proposed to use the block matrix, which determines the failures per car at various combinations of a mean daily air temperature, a diurnal temperature variation and a vehicle mileage. Based on the analysis of variance (ANOVA) of the block matrix data, relationships between the failure rate of the KAMAZ truck and the factors of the vehicle mileage, mean daily temperature and diurnal temperature variation were established. With increasing the mileage, the influence of the climatic factors on truck operability rises. A negative impact of the air temperatures below $-30\text{ }^{\circ}\text{C}$ on the operability of the KAMAZ vehicles with the high mileage is already observed starting from the mileage of 48,000 km. Significance of the factor of the diurnal temperature variation for the failure number per truck is shown for temperature intervals from -30 to $-8\text{ }^{\circ}\text{C}$ and above $10\text{ }^{\circ}\text{C}$. This study aims to improving quality of failure prediction and provides useful information to practitioners.

Keywords Machinery · Natural and climatic factors of the cryolithozone · Truck · Failures · Mileage

1 Introduction

The natural-climatic and operational conditions of the cryolithozone impose increased requirements on the technical base efficiency for the maintenance, repair and storage of the cars. Enterprises and individuals incur significant costs due to the insufficient knowledge of vehicle operability prediction problems. The purpose of this research is to investigate the relationship of the machinery failures with the operation duration, air temperature and diurnal temperature variation.

I. Buslaeva (✉) · L. Yakovleva
The Yakut Scientific Centre of the Siberian Branch of the Russian Academy of Sciences,
Petrovskogo Street 2, 677980 Yakutsk, Russia

The cryolithozone climate is marked by the extreme air temperatures (below $-60\text{ }^{\circ}\text{C}$ in winter and above $30\text{ }^{\circ}\text{C}$ in summer), sharp diurnal temperature variations ($25\text{--}30^{\circ}$) in spring and autumn, long cold period, short daylight hours and fogs in winter. In such climatic conditions, machinery reliability is reduced [1]. At low temperatures, brittle damage probability of metal and elastomeric elements of the machinery rises [2], viscosity of lubricants and technical liquids grows [3], this leads to an increase in loads on the elements, components and units [4]. Also, the vehicle operability is influenced by the usage intensity and operating conditions, which in Yakutia change significantly during the calendar year. The uneven intensity of the motor transport operation over the year is associated with the seasonal changes in the road network. In the off-season and sometimes in summer, some roads in the cryolithozone become practically unpassable for the vehicles. This leads to the fact that freight delivery by the vehicle occurs mainly after building the ice roads. In addition, during the ice formation and melting of ice on the rivers there are no crossings. The ice crossings, pontoon bridges and ferry services operate throughout other seasons. Variability of the road conditions is associated with the seasonal changes in the state of the local roads in the cryolithozone. Deterioration of the road quality causes the increase in the dynamic loads on the parts and units of the vehicles [5].

Thus, when operating vehicle in the permafrost zone, fluctuations in the failure number are observed, due to the negative influence of the climatic and road factors that change over time. Therefore, in the different periods of the year, certain elements of the trucks are most often damaged. Their identification will allow planning nomenclature of the spare parts, repair and maintenance of the machinery in the Far North.

2 Materials and Methods

This paper examines the failure data sample of the heavy-duty KAMAZ vehicles, which were used for the transportation of the freights of a diamond mining company in Yakutia. The KAMAZ truck with a weight carrying capacity of 10 to 40 tons has been produced in Russia from 1976 to the present. These trucks have been successfully operated in the northern regions of the Russian Federation, where they have proven themselves to be reliable vehicles at low climatic temperatures and in the difficult road conditions of the cryolithozone. To study their operability, the database “KAMAZ” with statistical information about the failures of 50 trucks of this brand for four full years of the operation was created in the MS Access. This database management system made it possible to group the failure data by the systems, units and elements, distribute them over the time and other intervals. Over the four years period of the KAMAZ truck operation 13,913 failures were registered.

The company began to operate the trucks at the same time, but they were operated unevenly: for 50 trucks the maximum mileage was recorded in the range of up to 150 thousand km, for 33 – from 150 to 225 thousand km, and only for 16 – over 225 thousand km. This is probably due to the fact that each machine has its own

characteristics, which are manifested in the process of manufacturing and assembly, which can affect the change dynamics in the vehicle operability during its function. Therefore, to check sample homogeneity, the analysis of the failures of 50 trucks over four years in the software package STATISTICA was made [6]. The sample of the failures has the following characteristics: the average value of the failures per truck is 278, the standard deviation is 71.4. The value of the coefficient of variation is 25.6%. It is less than 33%, which makes it possible to consider this failure sample to be homogeneous [7]. The failures of the KAMAZ vehicles has a normal distribution law, which was confirmed by the Shapiro–Wilk W -test.

To assess the influence of the cryolithozone climate factors, the database “KAMAZ” has been supplemented with the information on the climate data for the corresponding period. The sequence, duration and frequency of these factors, as well as their combinations, change randomly. This study of the failure data and associated natural and climatic factors was carried out using the mathematical statistics methods.

3 Results and Discussions

Based on the results of the previous researches [1, 2], it was determined that the increase in the failure number of the vehicle elements in the cryolithozone is influenced by the mileage and air temperature. The study of the failure distributions of the most vulnerable elements of KAMAZ trucks by months showed that the damage number of some elements increases significantly in March–April and August. This suggests that these elements are affected by the diurnal temperature amplitudes, since the maximum ones are usually observed in these months. According to the climate data for the four years under consideration, graphs of the mean monthly air temperatures and the monthly average values of the diurnal temperature variations have been plotted (see Fig. 1). It can be seen that January and December are the coldest months of the year and are characterized by the minimal diurnal temperature variations. The highest variations are noted for March (15.3°), April (14°), July (14.1°) and August (13.7°). These months correspond to the local maximum of the failures of some elements of the KAMAZ vehicle.

Based on the foregoing, the vehicle mileage, mean air temperature per day and diurnal temperature variation have been selected as external factors affecting the truck operability. MS Access allows you to distribute the failures over the intervals of different parameters present in the database record of each failure [8]. All the change ranges of the selected parameters are divided into four intervals so as to ensure uniformity. The mileage intervals are selected so that approximate equality of the total mileage of all the trucks for each interval is fulfilled. The following mileage intervals have been defined: less than 48,000 km; from 48,000 to 96,000 km; from 96,000 to 150,000 km; and over 150,000 km. Division of the ranges of the mean daily air temperatures and diurnal variations in the town of Lensk was carried out in such a way as to obtain the approximately equal number of the days with such

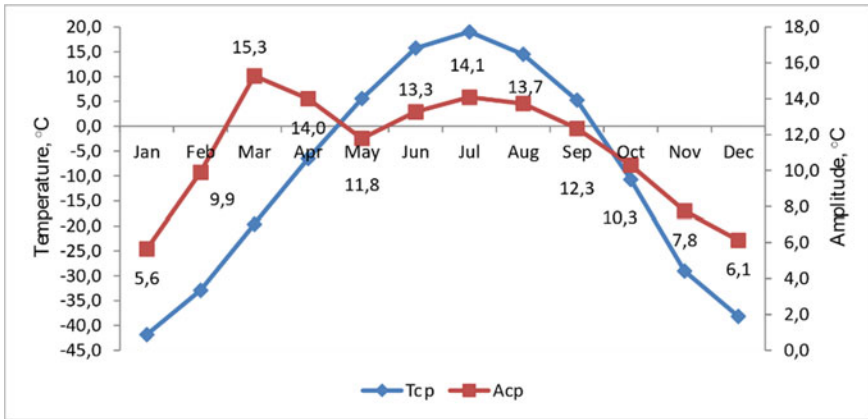


Fig. 1 Average monthly air temperatures and monthly average values of the diurnal temperature variations

parameters in each interval. For the mean daily temperatures the following intervals have been selected: below $-30\text{ }^{\circ}\text{C}$; from -30 to $-8\text{ }^{\circ}\text{C}$; from -8 to $10\text{ }^{\circ}\text{C}$ and above $10\text{ }^{\circ}\text{C}$. The range of the diurnal temperature variations was divided into the intervals: less than 7.25° ; from 7.25° to 11.2° ; from 11.2° to 14.9° and more than 14.9° .

In order to investigate a combined effect of these three factors, we proposed to represent the failure distribution over the intervals of their change in the form of the block matrix. In this matrix, the mileage defines the “block” rows of the main matrix and the diurnal temperature variation determines the “block” columns. The cells of the main matrix contain 2-by-2 submatrices, each cell of which corresponds to the certain interval of the mean daily air temperatures according to Table 1.

According to calculating the distribution of KAMAZ failures over the intervals of three external factors, the block matrix has been constructed (Table 2).

For each temperature interval, the average failure values for the entire matrix have been calculated: 244.8 at the air temperatures below $-30\text{ }^{\circ}\text{C}$; 242.7 in the interval from -30 to $-8\text{ }^{\circ}\text{C}$; 187.4 in the interval from -8 to $10\text{ }^{\circ}\text{C}$ and 194.6 for the temperatures above $10\text{ }^{\circ}\text{C}$. The matrix cells with the values of the failure number exceeding the obtained average values have been highlighted in different colors. In Yakutia, the stable cold weather in winter is formed under the influence of the Siberian anticyclone, so at very low air temperatures, small values of their daily amplitudes are observed (see Fig. 1). As a result, the large number of the failures at the temperatures below $-30\text{ }^{\circ}\text{C}$ (highlighted in yellow) is noted for the diurnal

Table 1 Layout of cells of submatrix corresponding to intervals of mean daily temperatures

$t \leq -30\text{ }^{\circ}\text{C}$	$-30\text{ }^{\circ}\text{C} < t \leq -8\text{ }^{\circ}\text{C}$
$-8^{\circ} < t \leq 10\text{ }^{\circ}\text{C}$	$t > 10\text{ }^{\circ}\text{C}$

Table 2 Block matrix of failure number of KAMAZ trucks

Mileage, km	Diurnal temperature variation							
	$A \leq 7.25^\circ$		$7.25^\circ < A \leq 11.2^\circ$		$11.2^\circ < A \leq 14.9^\circ$		$A > 14.9^\circ$	
$L \leq 48.000$	324	69	277	203	68	229	23	260
	114	30	93	65	206	156	91	261
$48.000 < L \leq 96.000$	665	154	282	274	62	290	36	296
	116	21	256	71	195	136	146	252
$96.000 < L \leq 150.000$	871	190	217	279	111	234	17	193
	143	30	284	211	244	326	134	344
$L > 150.000$	610	258	235	312	92	352	27	290
	136	26	357	344	234	362	250	479

temperature variations less than 7.25 °C for all the mileage intervals. The green-highlighted values of the failure number in the temperature interval from -30 to -8° C are marked for all the intervals of the diurnal temperature variations. But for the trucks with the low mileage, they are not observed at the low temperature variations. The failure numbers marked in the matrix in blue and gray are visible at the diurnal temperature variations exceeding 7.25 °C, as the air temperatures above -8 °C are characterized by the large diurnal variations.

The block matrix of the number of the malfunctioning vehicles has been constructed similarly. This made it possible to form the block matrix of the failure number per truck in each interval of the mileages, air temperatures and diurnal variations (Table 3). It should be noted qualitative differences between the block matrix of the failures per truck and the matrix of the absolute failures (Table 2).

Table 3 Block matrix of failures per vehicle

Mileage, km	Diurnal temperature variation							
	$A \leq 7.25^\circ$		$7.25^\circ < A \leq 11.^\circ$		$11.2^\circ < A \leq 14.^\circ$		$A > 14.9^\circ$	
$L \leq 48.000$	8.3	4.3	6.9	6.6	4.5	5.5	4.6	6.7
	5.0	3.3	3.6	4.6	5.7	4.9	3.5	6.1
$48.000 < L \leq 96.000$	13.3	4.7	6.3	6.4	3.3	7.3	4.5	6.7
	4.5	5.3	6.1	5.1	5.9	5.2	5.2	7.4
$96.000 < L \leq 150.000$	18.1	5.4	6.0	6.5	4.3	6.9	3.4	4.8
	5.7	3.8	7.3	6.4	7.4	8.0	4.8	8.6
$L > 150.000$	18.5	8.9	8.4	10.8	5.1	12.1	2.7	9.4
	6.2	3.7	12.3	12.7	9.8	12.5	9.6	16.5

The average values of the failure number per vehicle for each temperature interval are 7.4 at the air temperatures below $-30\text{ }^{\circ}\text{C}$; 7.1 in the interval from -30 to $-8\text{ }^{\circ}\text{C}$; 6.4 in the interval from -8 to $10\text{ }^{\circ}\text{C}$ and 7.3 at the temperatures above $10\text{ }^{\circ}\text{C}$. The cells of the matrix with the number of failures exceeding these average values are highlighted in different colors. At low air temperatures (below $-30\text{ }^{\circ}\text{C}$), the large failure numbers are highlighted in yellow, there are significantly more of them in the first column of the main matrix (at the diurnal variations up to $7.25\text{ }^{\circ}\text{C}$), and their growth is noticeable as the mileage increases. This indicates the negative impact of the low climatic temperatures on the KAMAZ vehicle operability with the large mileage already starting with the mileage of 48,000 km.

At low ambient temperatures (from -30 to $-8\text{ }^{\circ}\text{C}$), the average number of the failures exceeding the average value for the temperature interval (the corresponding cells are highlighted in green) is noted in all the intervals of the diurnal temperature variations, mainly for the trucks with the mileage of more than 150,000 km.

At moderate (from -8 to $10\text{ }^{\circ}\text{C}$) and warm (above $10\text{ }^{\circ}\text{C}$) air temperatures, the average failure number rises with the mileage increase of the trucks in all the diurnal temperature variations intervals. The failure numbers per vehicle that exceed the average values (the cells are highlighted in blue and gray, respectively) are noted mainly for the mileage over 96,000 km and diurnal variations greater than 7.25° . This may indicate the negative impact of the operation duration of the trucks on their operability in the cryolithozone conditions.

To quantify the influence of the factors of the diurnal variations and mileage on the failure number per KAMAZ truck and to identify the most significant of them, the variance analysis of variance in MS Excel was performed. The characteristics of the mean daily air temperatures intervals for the four years under consideration are presented in Table 4.

In Yakutia at the air temperature below $-30\text{ }^{\circ}\text{C}$ there is a smoothed daily course of the temperature with the small diurnal variations. The average diurnal temperature variation is almost two times less than for the other temperature intervals. To check independence of the factors of the ambient temperature and diurnal temperature variation, the correlation analysis of the climate data for four years was done [9]. It showed the moderate positive correlation on the Chaddock's scale (0.52). However, when performing the correlation analysis for each interval of the mean daily temperatures, the same moderate correlation was established only for the interval with the

Table 4 Characteristics of intervals of mean daily air temperatures

Interval of temperatures	Number of days with temperatures of interval	Average temperature in interval	Average diurnal temperature variation in interval
$t \leq -30\text{ }^{\circ}\text{C}$	349	- 39.45	6.48
$- 30\text{ }^{\circ}\text{C} < t \leq -8\text{ }^{\circ}\text{C}$	362	- 19.72	12.34
$- 8\text{ }^{\circ}\text{C} < t \leq 10\text{ }^{\circ}\text{C}$	365	2.19	11.56
$t > 10\text{ }^{\circ}\text{C}$	385	16.70	14.00

Table 5 Matrix of failure number per truck at temperatures above 10 °C

Mileage, km	Diurnal temperature variation			
	$A_t \leq 7.25^\circ$	$7.25^\circ < A_t \leq 11.2^\circ$	$11.2^\circ < A_t \leq 14.9^\circ$	$A_t > 14.9^\circ$
$L \leq 48.000$	3.3	4.6	4.9	6.1
$48.000 < L \leq 96.000$	5.3	5.1	5.2	7.4
$96.000 < L \leq 150.000$	3.8	6.4	8.0	8.6
$L > 150.000$	3.7	12.7	12.5	16.5

temperatures below -30°C (the correlation coefficient equals to 0.52). While for the other intervals, the correlation coefficients are 0.217, 0.081, 0.299, respectively, that is less than the value of 0.3, defined as the lower bound of the low correlation. Therefore, the analysis of variance can be considered correct only for these three intervals of the air temperatures, especially since the block matrix of the failures per KAMAZ vehicle (Table 3) for the temperatures below -30°C does not show the influence of the diurnal temperature variation on the failure number.

For the air temperatures above 10°C , there is a tendency to the failure increase over the intervals of the changes in the diurnal temperature variation for almost all the truck mileage intervals. To determine the relationship between the diurnal temperature variations and the KAMAZ vehicle failures, the matrix of the failures per truck for the interval of positive air temperatures above 10°C has been constructed (Table 5) on the basis of the block matrix (Table 3).

For the data in Table 5, the two-way analysis of variance was made using the MS Excel tool “ANOVA: Two-Factor Without Replication” [10]. For the diurnal variation factor, the Fisher’s F-statistic, equals to 4.41, is greater than the critical value of the criterion $F_{cr} = 3.86$ with the p-level of $0.035 (< 0.05)$. For the mileage factor, the statistics $F = 6.98$ exceeds $F_{cr} = 3.86$ with the p-level of $0.01 (< 0.05)$. It can be concluded that both factors significantly affect the failures of KAMAZ trucks at the ambient temperatures above 10°C .

In the block matrix (Table 3) the increase in the failure number per KAMAZ truck by the columns for the temperatures from -8°C to 10°C is not traced. But when the air temperature fluctuates around 0°C , ice appears on the roads and glaze ice is often observed. As a result, the road conditions deteriorate and, when driving, the dynamic loads on the entire car increase. To assess the influence of the factors of the diurnal temperature variation and mileage on the truck operability for this interval of the air temperature changes, the failure matrix (Table 6) was compiled according to the data in Table 3.

The analysis of variance for the air temperature interval from -8°C to 10°C not confirmed the influence significance of the diurnal temperature variations. However, the vehicle mileage impact on the failure variability was statistically proven at the p-level of 0.003: the value of Fischer’s statistic $F = 10.05$ is greater than the critical value $F_{cr} = 3.86$.

According to the block matrix (Table 3) the influence of the diurnal temperature variations and mileage for the air temperature intervals from -30 to -8°C has been

Table 6 Matrix of failure distribution per truck at temperatures above 10 °C

Mileage, km	Diurnal temperature variation			
	$A_t \leq 7.25^\circ$	$7.25^\circ < A_t \leq 11.2^\circ$	$11.2^\circ < A_t \leq 14.9^\circ$	$A_t > 14.9^\circ$
$L \leq 48.000$	5.0	3.6	5.7	3.5
$48.000 < L \leq 96.000$	4.5	6.1	5.9	5.2
$96.000 < L \leq 150.000$	5.7	7.3	7.4	4.8
$L > 150.000$	6.2	12.3	9.8	9.6

Table 7 Matrix of failure distribution per truck at temperatures from -30 to -8 °C

Mileage, km	Diurnal temperature variation			
	$A_t \leq 7.25^\circ$	$7.25^\circ < A_t \leq 11.2^\circ$	$11.2^\circ < A_t \leq 14.9^\circ$	$A_t > 14.9^\circ$
$L \leq 48.000$	4.3	6.5	5.5	6.7
$48.000 < L \leq 96.000$	4.7	6.4	7.3	6.7
$96.000 < L \leq 150.000$	5.4	6.5	6.9	4.8
$L > 150.000$	8.9	10.8	12.1	9.4

traced with the small deviations. The failure data depending on the mileages and diurnal temperature variations for this temperature interval are presented in Table 7. The two-way analysis of variance without repetitions showed that both factors are significant in the considered interval of the air temperatures. For the car mileage factor the value of Fischer's statistic is 26.64, which is greater than the value $F_{cr} = 3.86$ with the p-level almost equal to zero. For the factor of the diurnal temperature variations $F = 4.79 > F_{cr} = 3.86$ with the p-level of 0.029.

Thus, it is statistically established that the mileage factor has the influence on the number of the failures per KAMAZ truck in all the considered mileage intervals, but the influence of the diurnal air temperature variations is confirmed only in two intervals of the mean daily temperatures: from -30 °C to -8 °C and above 10 °C. The obtained results can be explained as follows. When analyzing the failures of the considered KAMAZ vehicles, it was revealed that the most vulnerable elements are the electrical wiring and oil seals, respectively (9.6 and 6.6% of all the failures). Moreover, they are often damaged in all the ambient temperatures intervals, but much more at the low temperatures. With large diurnal temperature variations observed in the late winter and early spring in Yakutia, there is a loss of seal tightness of the vehicle equipment, associated with the difference in the values of the coefficient of linear thermal expansion for steel and rubber. At that time, quite low climatic temperatures are still observed, at which the elasticity and strength of the rubber parts of the vehicles (oil seals, seals, gaskets) is reduced [11]. Leakage of technical fluids or lubricants is possible, which causes to deterioration in the operating conditions of the interacting parts of the equipment. Also in electrical wiring, the different values of the thermal expansion coefficients of steel and thermoplastic polymers with fluctuations in the daily air temperatures lead to the different changes in linear dimensions of

the metal wires and their insulation, causing additional mechanical stresses between them. When the air temperature decreases, the elasticity of the polymers is reduced and the insulation breaks down in places with the mechanical stresses [12]. This induces to the frequent failures of the electrical wiring. Besides under the considered conditions, condensation and freezing of the condensate occur in the thin tubes of the air dryer of the brake system and in the brake tubes, evoking the brake valve failures.

In the warm season, the strength of the rubber elements of the vehicles decreases at large diurnal temperature variations. The temperature variations and high air humidity typical for that time lead to the oxidation of electrical contacts. However, it is possible that the increase of the truck failure rate is caused by an action of other factors. For example, in Yakutia there are many failures of the vehicle in the wettest month of August when the temperature is above 10 °C. In these time the road quality deteriorates significantly, which can affect the truck failure dynamics. The problem of the influence of the diurnal air temperature variations on the vehicle operability requires further research.

4 Conclusion

The study results of the failure distributions of the KAMAZ trucks operated in the extreme conditions of the cryolithozone showed that the operability of their elements depends on the operational and natural-climatic factors. That is, there are the truck elements which respond with failures to these variable operating factors and their combinations. It is proposed to analyze the influence of the factors under consideration using the block matrix, which defines the failure number per car at the various combinations of the mean daily air temperature, diurnal temperature variation and mileage. To do this, the change ranges of these factors are divided into the certain number of the intervals to ensure the uniformity. In this article, four intervals have been selected for each factor. It is convenient to allocate the failure sample by the intervals of the different parameters in the MS Access.

When detecting trends in the block matrix, the influence significance of the factors on the vehicle operability is established using the two-dimensional analysis of variance of the matrices made up of the block matrix. As a result of the variance analysis of the failures of the heavy-duty KAMAZ trucks in MS Excel, the significance of the mileage influence for all the change intervals in the air temperatures has been confirmed. In addition, the significance of the diurnal temperature variation factor for the temperature intervals from -30 to -8 °C and above 10 °C has been shown. The correlation between the mean air temperatures and the diurnal temperature variations for these intervals has been estimated to be negligible.

The mileage influence on the number of the failures per KAMAZ truck has been statistically confirmed. This indicates an accelerated wear of the vehicles in the cryolithozone conditions. The negative effect of the operation duration of these cars on their operability is most pronounced at the air temperatures below -30 °C for trucks with the large mileage, starting with the mileage of 48,000 km.

Thus, using the example of the failure distribution of KAMAZ trucks by three variable factors, it has been established that the presentation of the data in the form of the block matrix makes it possible to determine those external factors, the influence of which has not been identified in other ways. In particular, the relationship between the large diurnal temperature variations and the failures of KAMAZ trucks was found only for two temperature intervals: from -30 to -8 °C and above 10 °C. However, the further research of the machinery operability in the cryolithozone is required.

References

1. Zudov GY, Buslaeva II, Lebedev MP, Levin AI (2018) KAMAZ performance in conditions of permafrost region. Proc ISTU 10(22):166–177. <https://doi.org/10.21285/1814-3520-2018-10-166-177> (in Russian)
2. Zudov GY, Buslaeva II, Levin AI (2019) New approach to assessment of influence of climatic temperatures on working capacity of KAMAZ trucks in the North. In: Lepov VV, Rousakis T (eds) 1st International conference on integrity and lifetime in extreme environment 2019. Procedia structural integrity, vol 20. Elsevier, Amsterdam, pp 300–305. <https://doi.org/10.1016/j.prostr.2019.12.155>
3. Bukhina MF, Kurlyand SK (2007) Low-Temperature behavior of elastomers. VSP, Leiden-Boston
4. Korneev SV, Buravkin RV, Anoprienko AA, Ivannikov AA (2015) Modern approaches to technical operation of equipment and the equipment in the conditions of low temperatures. J Siberian Fed Univ Eng Technol 4:414–418
5. Grigoriev RS, Larionov VP, Urzhumcev YuS (1987) Methods of improving the operability of machinery in the Northern version. Nauka, Novosibirsk (in Russian)
6. Borovikov VP (2001) STATISTICA program for students and engineers. Komp'yuterPress, Moscow (in Russian)
7. Fisher RA (1992) Statistical methods for research workers. In: Kotz S, Johnson NL (eds) Breakthroughs in statistics. Springer series in statistics (perspectives in statistics). Springer, New York. https://doi.org/10.1007/978-1-4612-4380-9_6
8. MacDonald M (2010) The missing manual. O'Reilly Media, Inc., Sebastopol. Accessed 2010
9. Kobzar AI (2012) Applied mathematical statistics: for engineers and researchers. Fizmatlit, Moscow. (in Russian)
10. Brandt S (2014) Data analysis: statistical and computational methods for scientists and engineers, 4th edn. Springer, Heidelberg
11. Shilov IB, Fomin SV, Durnev EA, Khlebov GA, Kirovski D (2014) Study of the influence of low temperatures on rubbers. Kauchuk i rezina [Caoutchouc and rubber] 5:40–41 (in Russian)
12. Khripchenko MS, Nartov PA, Yudin RV (2018) Features of the instruments electrical equipment transport vehicles at low temperatures. In: Priadkin I (ed) ARKTIKA innovatsionnye tekhnologii kadry turizm [ARCTIC: innovative technologies, personnel, tourism]. Voronezh State University of forestry and technologies named after G.F. Morozov, Voronezh, pp 394–397. (in Russian)

Research on Load-Bearing Constructions Behavior During Pit Excavation Under «Slurry Wall» Protection



Vasilii Komolov , Artem Belikov , and Peter Demenkov 

Abstract The article presents an analysis of the work of load-bearing structures of deep pits, the influence of changes in the parameters of the elements and the scheme of the pit on the deformation of the soil. The results of numerical simulation of the construction of a semi-buried structure under the protection of a “Slurry wall” in the three-dimensional problem statement in the Plaxis 3D software package are presented. In the work, the regularities of changes in the stress-strain state were revealed depending on the parameters of the wall, transverse and angular struts. The paper presents graphs of longitudinal forces and maximum bending moments in the struts of the pit, mulds of displacement and subsidence of the earth’s surface, graphs of vertical movements of the bottom of the pit. As a result of the study, it was found that an increase in the thickness of the “slurry wall” of more than 800 mm with an increase in the depth of more than 1 m does not have a positive effect in the framework of the considered construction conditions. In the course of the work, the most rigid scheme of the pit design was determined, which allows to obtain less deformations of the surface of the enclosing soil. This scheme has the most rational operation of structural elements.

Keywords Geomechanical forecast · Semi-buried structures · Construction in dense urban development · Underground construction · Construction of parking lots · Stress–strain state of the ground · Pit · Slurry wall · Subsidence · Clay soils · Watered soils · Finite element method

1 Introduction

The reduction of the area free from development, the development of transport infrastructure and engineering systems in large cities requires the active use of underground space, which leads to the need to use deep pits and build semi-buried structures in

V. Komolov (✉) · A. Belikov · P. Demenkov
Saint-Petersburg Mining University, 2, 21st Line, 199106 St. Petersburg, Russia

© The Author(s), under exclusive license to Springer Nature Switzerland AG 2022
A. Mottaeva (ed.), *Technological Advancements in Construction*, Lecture Notes in Civil Engineering 180, https://doi.org/10.1007/978-3-030-83917-8_29

313

the conditions of dense development of the historical center of the city. The development of the underground space of cities is carried out both in an open and closed way [1–3].

Intensive development of the underground space of cities has a negative impact on nearby buildings and structures. To reduce the negative impact of the construction of semi-buried structures on the structures of neighboring buildings, the most effective and economical enclosing structure is considered to be a “slurry wall”. This design allows you to minimize the impact on the surrounding buildings [4–6].

Geomechanical assessment and numerical simulation of the construction of a semi-buried structure under the protection of a “slurry wall” in the three-dimensional formulation of the problem were performed in the Plaxis 3D software package. The three-dimensional model allows you to get an idea of the overall picture of the stress–strain state of the soil on the construction site and to calculate taking into account all stages of construction of a semi-buried structure. Numerical analysis helps to make an accurate forecast of the development of soil sediments by using advanced soil models. These models take into account the nonlinear work of the soil under the action of the load [7–9].

Depending on the physical and mechanical properties of the soil and the depth of the pit, there are three main options for constructing a deep pit [10].

Cantilever sealing is usually used in pits with a depth of no more than 5 m, in cohesive soils. The spacer system is widely used in practice. Compared to the ground anchor system, it is easy to use and requires less economic and technological costs. In this paper, we consider the type of construction of a pit using a system of struts [11–13].

The aim of the research is to analyze the work of load-bearing structures of deep pits of semi-buried structures. Determine the result of changing the parameters of the elements and the scheme of the pit on the deformation of the soil in specific construction conditions. Determine the most optimal design scheme for the construction of a pit in the construction of semi-buried structures in conditions of dense urban development.

2 Model Description

The width of the pit –20 m, length –40 m, depth –19 m. To prevent horizontal displacements of the pit walls, a “slurry wall” made of B40 concrete is used. To increase its rigidity, a spacer system is used, installed in increments of 5 m in depth. The soil is developed in five stages. The ground water level was lowered by 1 m below the bottom of the pit at all stages (Fig. 1, 2). A steel pipe with a diameter of 500 mm and a thickness of 10 mm is used as struts. I-beam No. 55 was adopted as the distribution belt. Transverse struts are installed in increments of 5 m, angular—at an angle of 45° (Fig. 3). Such parameters of the location of structural elements are most common among developers, in the absence of transverse struts for the end part

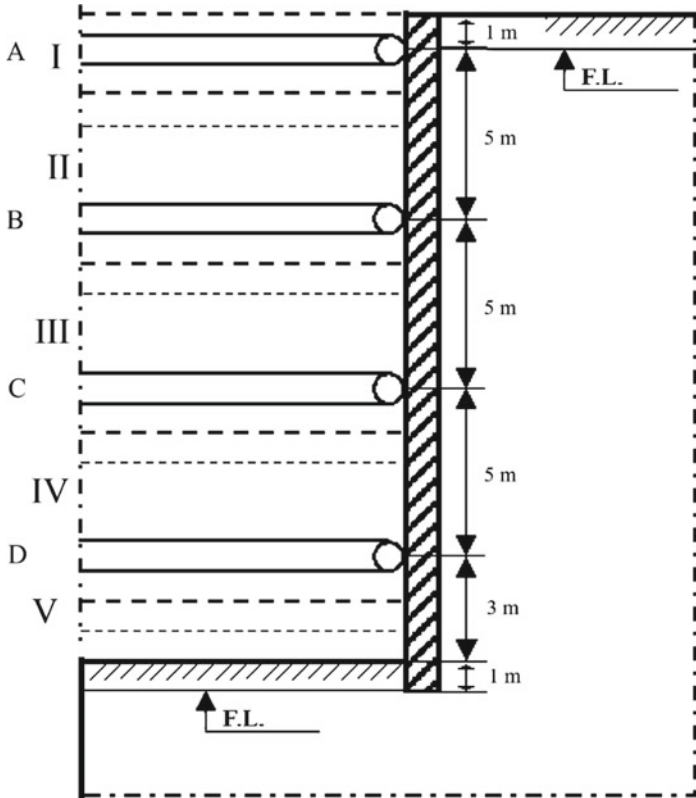
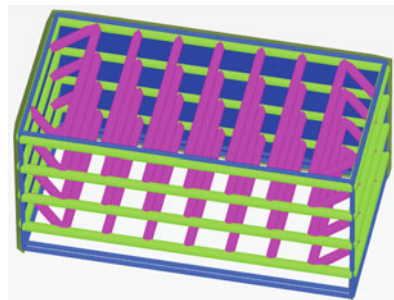


Fig. 1 Cross-section of the pit with an indication of the modeling stages. A - D - tiers of space systems; I - V - stages of excavation development

Fig. 2. 3D model of the pit spacer system



of the pit. This allows you to have technological openings for the entire width of the pit.

For modeling, the soils most typical for St. Petersburg were used, the physical and mechanical properties of which are presented in Table 1. In the calculations, a

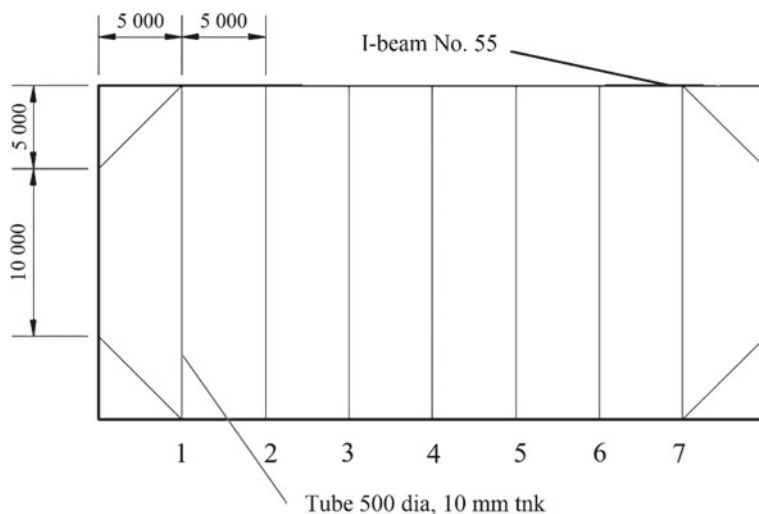


Fig. 3 Structural scheme of the tier: 1–7 – the number of the strut in the tier

Table 1 Physical and mechanical properties of the soil

γ_{unsat} , kN/m ³	γ_{sat} , kN/m ³	e_0	E_{so} , mPa	E_{oed} , mPa	E_{ur} , mPa	m	c' , °	φ' , °
18.5	21	0.70	14	14	56	0.9	23	21

hardening soil model was used, taking into account the change in properties at small deformations [14–16].

Numerical experiments were performed in a three-dimensional setting using the Plaxis 3D software package [17–20].

3 Calculation Results

At the first stage of modeling, the optimal thickness of the «slurry wall» structure was determined. For this purpose, models with a wall thickness of 500 to 1000 mm were built. Models with a wall thickness of less than 500 mm did not have convergence points during the solution process, which indicates insufficient structural rigidity. As the wall thickness increases, the compressive longitudinal forces acting in the transverse struts on all tiers increase. The maximum bending moments on tier B decrease, on tier C there is an extremum with a wall thickness of 800 mm (Fig. 4), while on tier B there is no such extremum. Therefore, under these conditions, it is most rational to use a «slurry wall» with a thickness of 800 mm. Further models will be considered with this wall thickness.

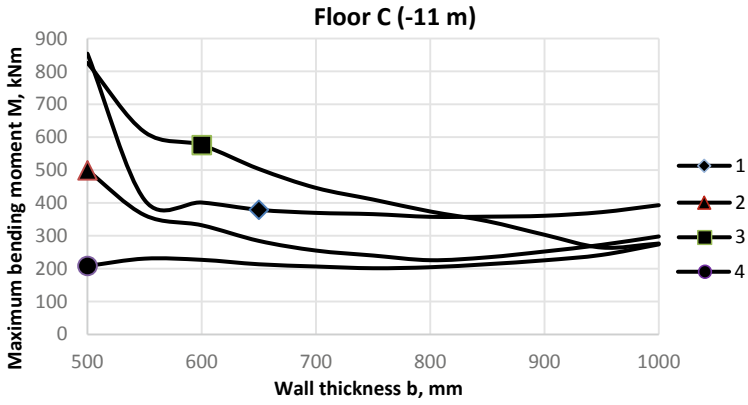


Fig. 4 Graphs of moments in the transverse struts of tier C: 1–4-strut numbers

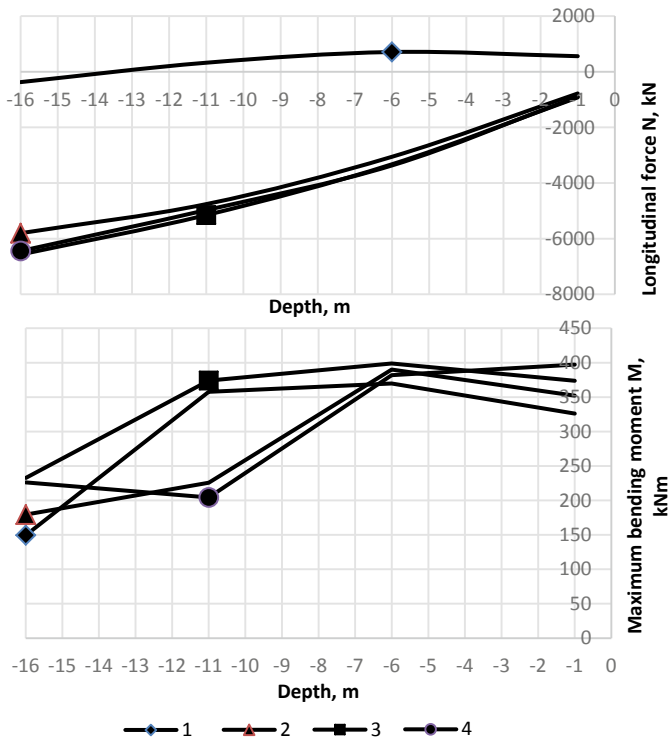


Fig. 5 Graphs of forces and moments in transverse struts: 1–4-strut numbers

Figure 5 shows graphs of forces and moments in the struts, depending on the depth of the tier. In the extreme transverse struts on tiers A, B, and C, there is a tensile

longitudinal force, while in the rest there is a compressive force, and it increases with increasing depth from 780 to 6400 kN. The maximum torque, with the exception of the extreme row, decreases with increasing depth from 370 to 230 kNm.

In view of the presence of tensile forces in the extreme struts, they can be excluded from the design scheme (Fig. 6). A variant of the design scheme without extreme struts is called-scheme I.

Comparing the results of calculations according to two schemes (basic scheme and scheme I), it is seen that in the transverse struts the compressive forces increased slightly, and the moments decreased (Fig. 7). In the angular struts, the compressive force did not change, but the moment decreased (Fig. 8). This can be seen on all tiers. Thus, the new layout of the struts is more preferable.

The disadvantage of scheme I is that the central part of the end wall has the least rigidity along the width of the pit. This leads to the maximum subsidence of the earth's surface in this area (Fig. 9). Therefore, the option of adding a second row of corner struts was proposed.

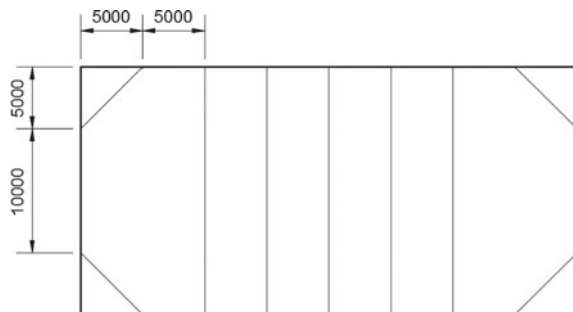
Let's consider two schemes of the device of struts of the pit. In scheme II, the second row of corner struts is installed at a distance of 2.5 m from the first row of corner struts. In scheme III-the second row of corner struts is installed at a distance of 5 m from the first row of corner struts (Fig. 10).

When considering the forces in the transverse struts, it is concluded that in scheme II the minimum moments are calculated, and in scheme III – the overestimated values of the moments and compressive force. In the first row of corner struts in scheme II, the least effort occurs (Fig. 11).

In the second row of angular struts, the compressive force is greater in scheme II, and the moments in scheme III. To select the circuit with the lowest stresses, it is necessary to take into account the combined effect of the compressive force and the bending moment.

To solve this problem, we introduce the average coefficient of proportionality k between the moment of resistance and the area of the ring (1). It is proportional to the outer diameter of the pipe and inversely proportional to the wall thickness. For pipes with a diameter of 0.5 m, this coefficient will be equal to 0.1185. Substituting it into the equation for determining the stress (2), we can see that numerically the moment increases the stress in the roll by 8.44 times, which is more than the compressive

Fig. 6 Structural scheme of the tier without extreme transverse struts (scheme I)



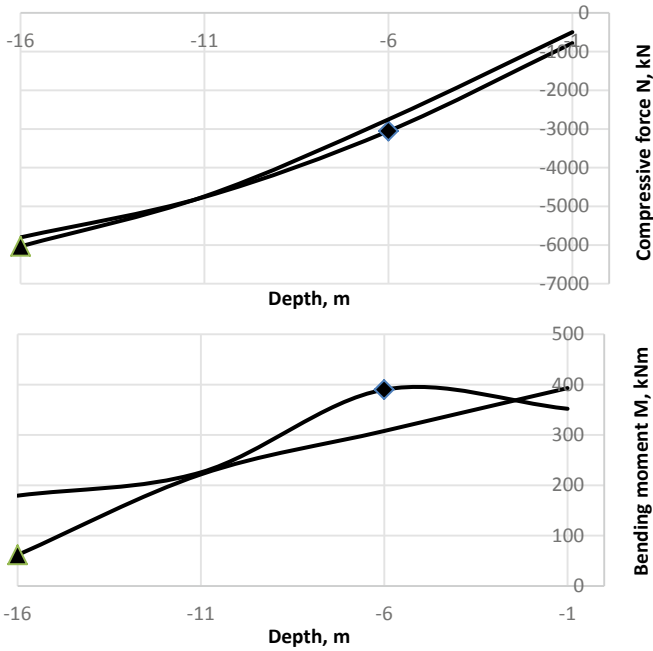


Fig. 7 Graphs of forces in the second transverse strut: \blacktriangle - using the extreme transverse struts; \blacklozenge - without the use of extreme transverse struts

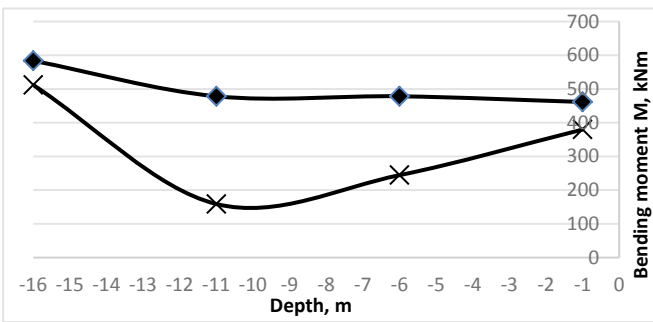


Fig. 8 Graph of the bending moment change in the angular spacers as a function of the depth change: \blacklozenge - basic scheme, X - scheme I

force (3). Therefore, for the arrangement of the angular struts according to scheme II, the stresses in the second row will be less than in scheme III.

$$W_x = k \cdot F, \tag{1}$$

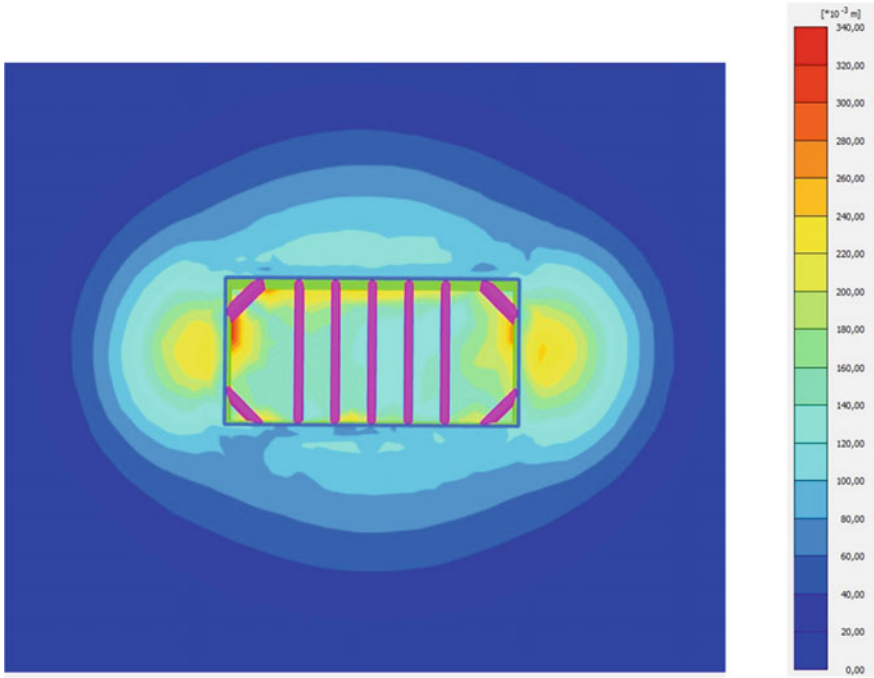


Fig. 9 Mulds of subsidence of the earth’s surface

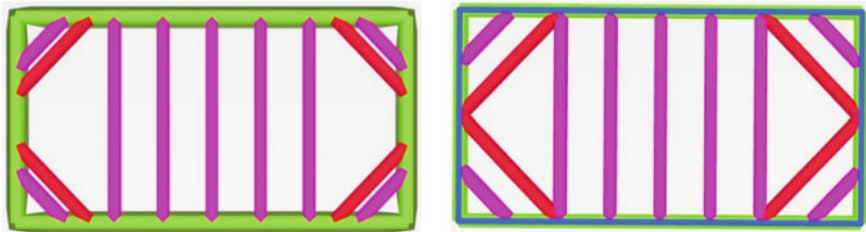


Fig. 10 Structural schemes with additional corner spacers: on the left - scheme II; on the right - scheme III

where W_x – a moment of resistance of the ring, cm^3 ; k – a average coefficient of proportionality, cm ; F – ring area, cm^2

$$\frac{N}{F} + \frac{M}{W_x} = \sigma, \tag{2}$$

where N – compressive force N ; M – maximum bending moment, $\text{N}\cdot\text{m}$; σ – stress, Pa .

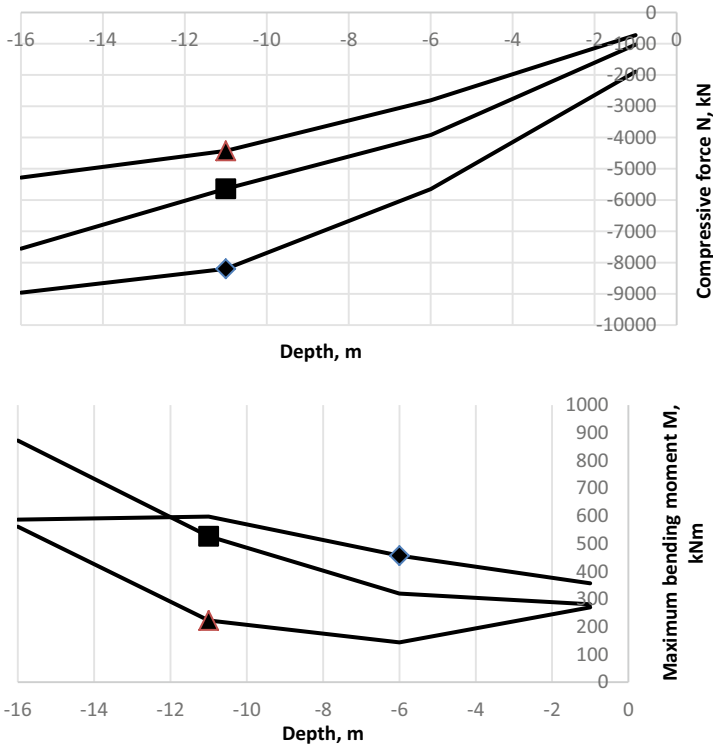


Fig. 11 Graphs of changes in forces and bending moment in the first row of angular struts:
 ◆ scheme I, ▲ scheme II, ■ scheme III

$$\frac{N}{F} + \frac{M}{0,1185 \cdot F} = \frac{N + 8,44 \cdot M}{F} = R, \tag{3}$$

Cross-sectional area of corner struts:

$$F = \frac{N + 8,44 \cdot M}{R}, \tag{4}$$

where R – steel resistance.

Next, an estimate of the depth of the pit wall in the ground is made. Initially, the wall was modeled with a depth of 1 m. Comparing the stress–strain state of the struts when the wall is deepened by 3 and 5 m, of the positive effects, we can only notice a decrease in the moments in the first row of the angular struts, in other cases we observe an increase in the compressive force. At the same time, the displacement of the surface of the soil both is containing the pit and its bottom increases (Fig. 12, 13).

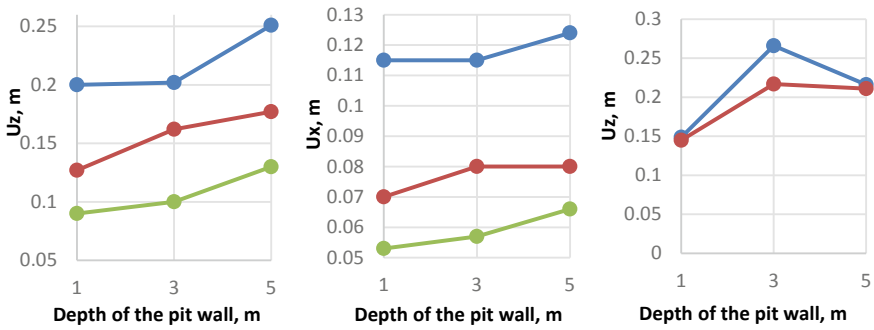


Fig. 12 Displacements of the ground surface: a) maximum subsidence, b) maximum horizontal displacement, c) vertical displacement of the pit bottom. The blue color indicates scheme I, red – scheme II, green – scheme 3

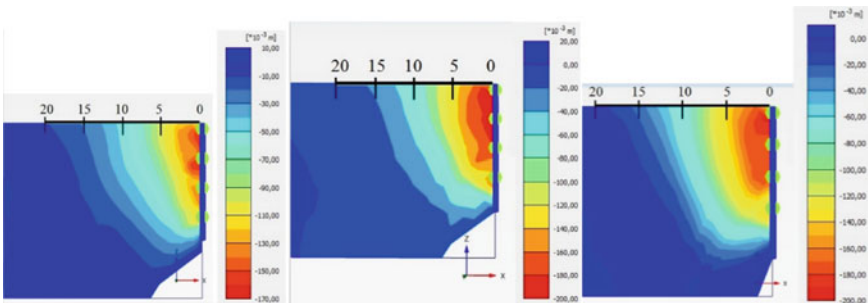


Fig. 13 Vertical movements of the soil: on the left – a wall depression of 1 m; in the center – a depression of 3 m; on the right – a depression of 5 m

4 Conclusion

Based on the results of numerical modeling of the construction of semi-buried structures under the protection of the “Slurry wall” structure in the volumetric formulation, it was possible to determine the most optimal structural scheme of the supporting structure of the pit. With this scheme, it was found that an increase in the thickness of the wall in the ground of more than 800 mm with an increase in the depth of more than 1 m does not have a positive effect in the framework of the considered construction conditions. In the course of the work, the most rigid scheme of the pit design was determined, which allows to obtain less deformations of the surface of the enclosing soil. Thus, in clay watered soils, the pit III scheme has the greatest structural rigidity and causes the least subsidence of the earth’s surface. But scheme II provides the most efficient operation of the structural elements. This scheme will be the most optimal for conducting the construction of semi-buried structures in conditions of dense urban development.

Acknowledgements The reported study was funded by RFBR, project number 20-35-90111\20.

References

1. Demenkov PA, Belyakov NA, Ochkurov VI (2017) Forecast of a safe zone of influence of the construction of semi-buried underground structures on the environment. *Bulletin of the Tula State university. Earth Sci* 4:311–324
2. Goldobina LA, Demenkov PA, Trushko OV (2019) Ensuring the safety of construction and installation works in the construction of buildings and structures. *Notes Min Inst* 239:583–595. <https://www.elibrary.ru/item.asp?id=41213348>
3. Demenkov PA, Goldobina LA, Trushko OV (2018) The method of forecasting the deformation of the earth's surface during the construction of pits in the conditions of dense urban development using the "Wall in the ground" method. *Notes Min Inst SPb* 233:480–486
4. Gospodarikov AP, Zatsepin MA (2017) *J Min Inst* 226:405
5. Protosenya AG, Karasev MA, Belyakov NA (2016) *J Min Sci* 54(1):53
6. Trushko OV, Demenkov PA (2018) *ARPN J Eng Appl Sci* 23(13)
7. Trushko OV, Kutuyavin DV (2018) Construction of a pit in conditions of strong deformable soils during the construction of a multi-storey business center, taking into account the stability of nearby buildings and structures. *Bulletin of Eurasian science*, no 1
8. Simankina T, Romanovich M (2016) *Procedia Eng* 165:1587
9. Simankina T, Romanovich M, Tsvetkov O (2016) Wavelet analysis function of changing average work amounts in monolithic construction. In: Murgul V (ed) *MATEC web of conferences*, p 01054
10. Long S, Zhou W, Fu J, and Zhang L (2018) Deformation monitoring, simulation, and prediction of subway deep excavations. *Electron J Geotech Eng* 23(04):768–710
11. Khaibullina KS, Sagirova IR, Sandyga MS (2020) Substanciação e seleção de um inibidor para evitar a formação de depósitos de asfalto-resina-parafina. *Periódico Tchê Química* 17(34). ISSN 2179-0302
12. Maksarov VV, Keksins AI, Filipenko IA (2020) Improvement of magnetic-abrasive finishing of nonuniform products made of high-speed steel in digital conditions. *Key Eng Mater* 836:71–78
13. Nguen TT, Karasev MA, Vilner MA (2020) Study of the stress-strain state in the sub-rectangular tunnel. In: Duc Long P, Dung N (eds) *Geotechnics for sustainable infrastructure development. Lecture Notes in Civil Engineering*, vol 62. Springer, Singapore, pp 383–388. https://doi.org/10.1007/978-981-15-2184-3_49
14. Mustafin MG, Valkov VA, Kazantsev AI (2017) Monitoring of deformation processes in buildings and structures in metropolises. *Procedia Eng* 189:729–736
15. Kolybin IV (2008) Emergency situations during the construction of the pits in an urban environment. *Dev Cities Geotech Eng* 12:90–124
16. Luccio M (2002) The concrete and the clay: monitoring large structure deformation. *GPS World* 13(8):16
17. Alonso EE, Gens A, Alcoverro J, Ortuño L (2007) Unexpected behavior of a large excavation in saturated sands. In: *Proceedings of the 14-th European conference on SMGE*, vol 2. Madrid, pp 495–502
18. Brandl H (2007) The collapse of a deep excavation pit in urban surroundings. In: *Proceedings of the 14-th European conference on SMGE*, vol 2. Madrid, pp 545–552
19. Law KH, Zubaidah I, Hashim R (2016) 3D finite element analysis of a deep excavation considering the effect of anisotropic wall stiffness. In: *19th Southeast Asian geotechnical conference & 2nd AGSSEA conference (19SEAGC & 2AGSSEA)*, Kuala Lumpur, 31 May – 3 June 2016
20. Brinkgreve RBJ (2018) *PLAXIS 3D 2017. Material Models Manual*. Netherlands, p 212

Assessment of Stress-Deformed State of Armocement Two-Layer Elements



Salis Bayramukov , Zuriat Dolaeva , and Tolya Khezhev 

Abstract One of the main causes of death of people and damage from the fires is the collapse of building constructions. Efficiently increases in limit of fire resistance of building constructions drawing heat-protective coverings is. As expanded aggregates for such coverings, bellied vermiculite and perlite are used. Along with the main function of fire protection, they can improve acoustic, decorative, heatphysical characteristics of designs that increases efficiency of their application.

Keywords Armocement · Stress–deformed · Stress–strain state · Damage

1 Introduction

The intense state of strain of two-layer armotsementny elements is considered. The analysis of teamwork of fireproof and constructional concrete layers in two-layer designs made. Impact assessment of vermiculitobetony layer on durability, rigidity and crack resistance of the bent elements made. Samples of two-layer designs with careful selection of structure of both layers experimentally investigated. The contact zone of coupling of armotsementny and vermiculitobetony layers analyzed.

The nonlinear nature of charts of dependence of moment of flexion on relative deformation of the stretched edge revealed that demonstrates that in work of sample not only elastic properties of concrete and mesh reinforcement, but also plastic properties of materials are considered. The nonlinear nature of schedules indicating gradual development of cracks owing to which the stretched concrete layers with

S. Bayramukov (✉) · Z. Dolaeva (✉)
North-Caucasian State Academy, 36b, Stavropolskaya Street, Cherkessk 369000, Russia

S. Bayramukov
Nevinnomyssk State Humanitary and Technical Institute, 17, Bulvar Mira Street,
357108 Nevinnomyssk, Russia

T. Khezhev (✉)
Kabardino-Balkarian State University named after H.M. Berbekov, 173b, Chernyshevsky Street,
360004 Nalchik, Russia

cracks one by one are switched off from work that leads to step-by-step decrease in rigidity of section of sample is established [1, 2].

For the solution of nonlinear problem of calculation of standard cross-sections, the deformation model using numerical method of the analysis of the considered task offered.

The analysis of comparison of results of numerical and experimental methods of researches has shown that the vermiculite-concrete layer increases rigidity and crack resistance of armotsementny designs. The offered numerical method of calculation provides acceptable coincidence to pilot researches on armotsementny samples.

2 Materials and Methods

To assess the stress–strain state of two-layer reinforced-cement elements, as well as to analyze the joint operation of the fire-retardant and structural concrete layers, 4 series of samples (Fig. 1) with dimensions of 100×400 mm were tested for bending, differing in the manufacturing method, the thickness of the vermiculite-concrete layer, the number and location steel woven mesh. The bending test also evaluated the effect of the vermiculite-concrete layer on the strength, stiffness and crack resistance of bending elements [3].

The production of plates with a size of 2000×500 mm carried out on a laboratory installation by the method of vibration profiling. The molding of the vermiculite-concrete layer carried out from the bottom or from the top of the reinforced-cement layer. The mixing zone between the layers was 2–3 mm. Samples measuring 400×100 mm for pure bending tests cut from the slab [1, 4].

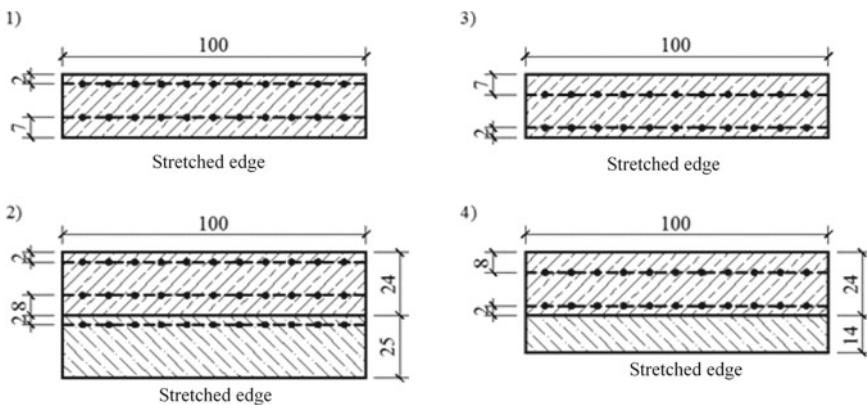


Fig. 1 Reinforcement schemes for single-layer (1, 3) and two-layer specimens with a vermiculite-concrete layer (2, 4)

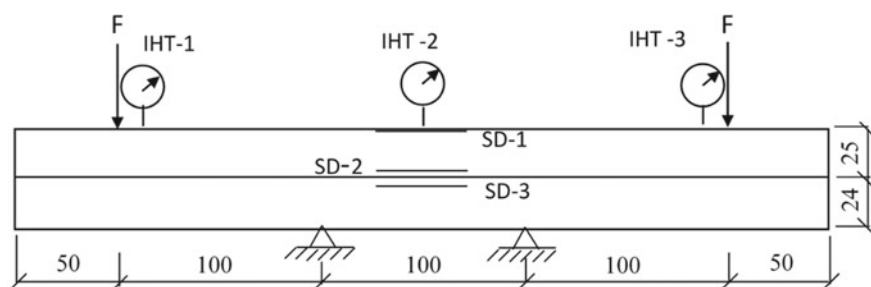


Fig. 2 Scheme tests series No.2 samples with pure bend IHT - Indicator of hour type; SD – The sensor for measurement of deformations

For the reinforced, cement layer, sand with a fineness modulus of 2.37 and a maximum grain size of 5.0 mm used. Fine-grained concrete mixture used with the composition C: S = 1: 2.5 with W/C = 0.4 ($R_{cg} = 55$ MPa, $R_{izg} = 6.5$ MPa).

To reinforce the samples, we used a woven mesh No. 8 with a wire diameter of 0.7 mm in accordance with GOST 3826–82.

For the vermiculite-concrete layer, we used expanded vermiculite of the Kovdor deposit with a maximum grain size of 5.0 mm, composition C: vermiculite = 1: 3 (by volume), W/C = 1.25 ($\rho = 640$ kg/m³, $R_{comp} = 2.3$ MPa, $R_{man} = 1.3$ MPa).

The loading of samples was of a short-term nature and carried out through a special device with piece weights. To monitor deformations, displacements and the process of cracking, the following were used: strain gauges (TD) with a base of 50 mm; movement indicators (IP) of the watch type; microscope MPB - 2 with $24 \times$ magnification, graduation 0.05 mm [2, 5].

Samples tested for flexion at one month of age. The test carried out according to the scheme of pure bending in the flat position with the location of the vermiculite-concrete layer in the stretched zone; the span between the supports was 300 mm (Fig. 2). Three samples tested in each series.

3 Results

During the testing of the samples with the help of a microscope, cracks in single-layer armoured samples could not be detected, however, the tensatons recorded relative deformations in the preceding destruction, equal to 35–10–5.

In testing the two-layer samples, the first cracks in the vermiculite concrete layer with a width of 0.01–0.02 mm at bending moments of 5–6 kn·cm, which roughly correspond to the destructive for single-layer samples. The maximum width of the cracks at the time leading up to the destruction was 0.03 to 0.05 mm. The number of cracks varied from 4 to 7. Some cracks sprouted up to 1015 mm in vermiculite concrete by the time before the destruction. No cracks found in the stretched face of the armoured layer in the two-layer samples.

At loads ($M = 5 - 6$ kNs) corresponding to destructive for single-layer samples, deformations, measured in two-layer samples in the transition zone of the armcement layer to vermicolitoconcrete, 10–15·10–5. This indicates that the vermicolitoconcrete layer significantly increases the rigidity of single-layer armcement samples. In the time preceding the destruction, the bending moment was 9.5 and 8.7 kn·cm, respectively, for the two-layer samples [6].

Higher relative deformations of second-series samples compared to the fourth series are due to the presence of an additional woven mesh in the vermicolitoconcrete layer that applied for technological purposes.

4 Discussion

It should note that during the tests of two-layer armcement samples, there was no violation of the clutch layers, detachments of vermicolito concrete layer from the armcemental.

Thus, until the cracks formed with a width of 0.05–0.1 mm in single-layer armcement samples, the additional fire retardant layer significantly increases their crack resistance [7].

The test results of samples from all four series shown in Fig. 3.

The non-linear nature of the curves from the relative deformation of the stretched face indicates that that in the work of the sample should take into account not only the elastic properties of concrete and reinforcement mesh, but also the plastic properties of materials. In addition, the non-linear nature of the graphs indicates the gradual development of cracks, because of which stretched layers of concrete with cracks one by one turned off from work, this results in a phased reduction in the rigidity of the sample section [2, 8].

To analyze the tense-deformed state of cross-sectional single-layer and two-layer samples, we used the so-called “deformation model” of the section at pure bending. This method based on the use of deformation diagrams describing the non-linear work of concrete and fittings, and some law of distribution of relative deformations by the area of cross-section elements: here the hypothesis of flat sections used. As diagrams of deformation of materials, the dependence of “tension - relative deformations” of the curved species was used, based on the method of N.I. Karpenko [4]. Unlike the method of marginal effort, the “deformation model” allows to perform the analysis of the section not only in the limit, but also in pre-determined and exorbitant states. However, the use of a “deformation model” requires a numerical method of solving the non-linear problem of calculating normal segments.

The following method proposed to solve the non-linear problem of calculating normal sections.

The section is broken down in height to n the final elements of a small area (Fig. 4). At the same time, the hypothesis of flat section follows:

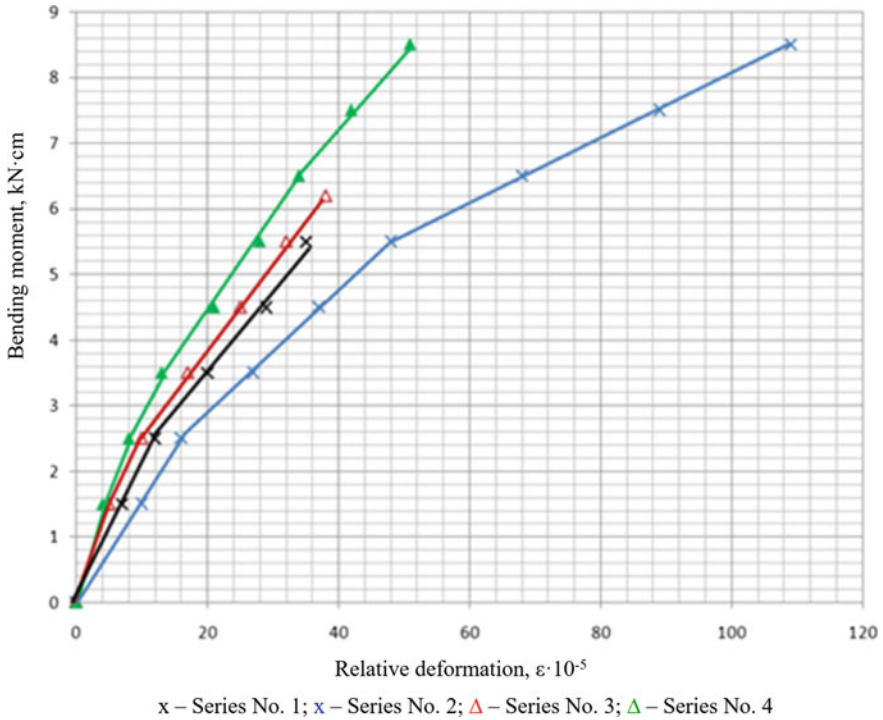


Fig. 3 Deformations of the stretched edge (averages for zone of pure bending) is model

$$\begin{cases} \varepsilon_i = \varepsilon_{bt} \cdot \left(\frac{i}{n}\right) - \varepsilon_b \cdot \left(\frac{n-i}{n}\right); \\ \varepsilon_b = \frac{Y_c}{h-Y_c} \cdot \varepsilon_{bt}; \\ \varepsilon_{sj} = \frac{Y_{sj}-Y_c}{h-Y_c} \cdot \varepsilon_{bt}. \end{cases} \quad (1)$$

where ε_b , ε_{bt} , ε_i , ε_{si} - accordingly, the relative deformation of the compressed, stretched, i-fiber concrete and i-rebar mesh; Y_{si} - distance from the center of gravity of the reinforcement grid to the compressed face of the element;

Y_s - the distance from the compressed face of the element to the neutral cross-section axis [1, 9, 10].

Let us express from (1) the relative deformation of the i-fiber section through the deformation of the stretched face according to the formula

$$\varepsilon_i = \frac{Y_c - Y_i}{h - Y_c} \cdot \varepsilon_{bt} = \frac{Y_c - \left(\frac{i \cdot h}{n}\right)}{h - Y_c} \cdot \varepsilon_{bt}, \quad i = 0, 1, 2, \dots, n. \quad (2)$$

Using the analytical dependence of the split module of the deformation of concrete E on the relative deformation of the ε it is possible to determine the tension that occurs in the i-th final element of the section according to the formula

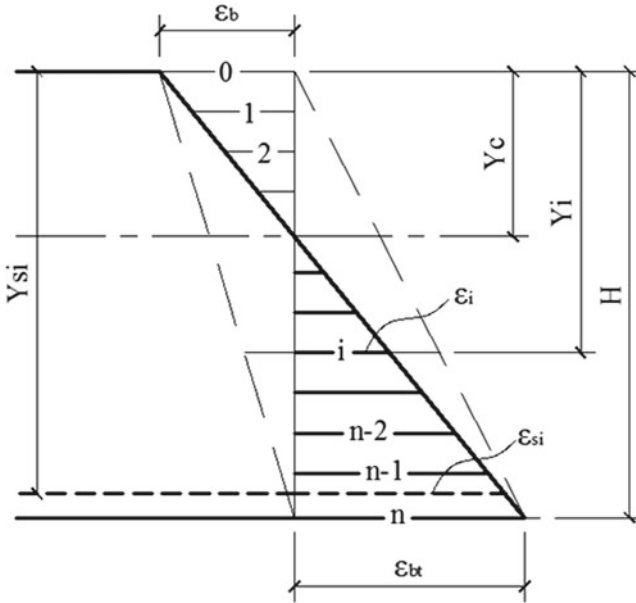


Fig. 4 Scheme to the definition of deformations in the normal part

$$\sigma_i = \frac{\sigma_{i-1} + \sigma_i}{2} = \frac{\varepsilon_{i-1} \cdot f(\varepsilon_{i-1}) + \varepsilon_i \cdot f(\varepsilon_i)}{2}, \quad i = 1, 2, \dots, n. \tag{3}$$

$$\sigma_{sj} = E \cdot \varepsilon_{sj}, \quad j = 1, 2, \dots, k. \tag{4}$$

The distance from the stretched face to the neutral axis of the section determined by the formula

$$Y_c = \frac{\sum_{i=1}^n S_{red,i} + \sum_{j=1}^k S'_{red,j}}{\sum_{i=1}^n A_{red,i} + \sum_{j=1}^k A'_{red,j}}; \tag{5}$$

where

$$S_{red,i} = A_{red,i} \cdot \left(Y_l - \frac{h}{2 \cdot n} \right) = A_{red,i} \cdot \left(\frac{2 \cdot i - 1}{2 \cdot n} \right) \cdot h; \tag{6}$$

$$S'_{red,j} = A_{red,i} \cdot Y_{sj}; \tag{7}$$

$$A_{red,i} = b \cdot \frac{h}{n} \cdot \left(\frac{f(\varepsilon_{i-1}) + f(\varepsilon_i)}{2 \cdot f(\varepsilon_0)} \right); \tag{8}$$

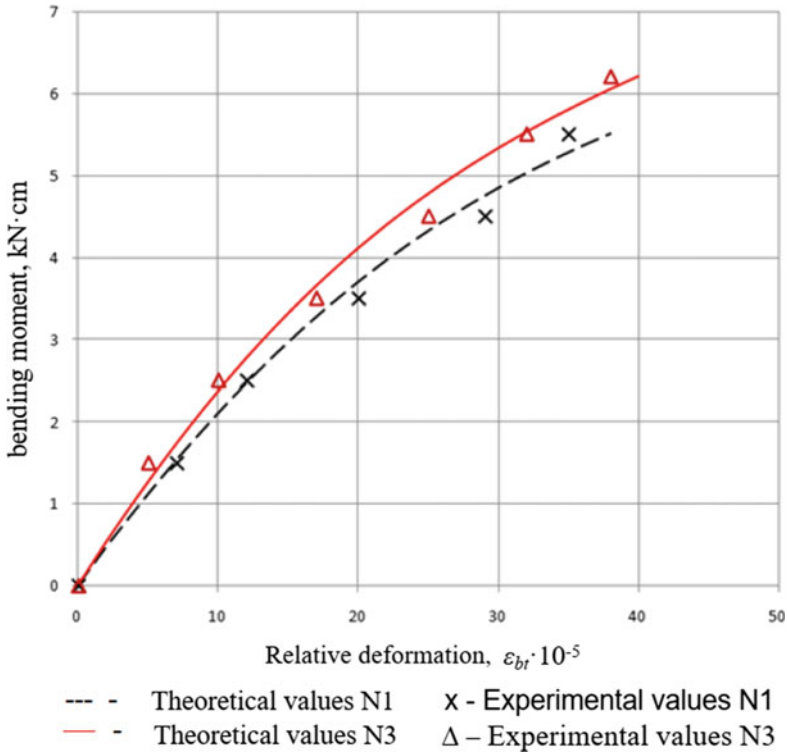


Fig. 5 The dependence of the curving moment on the deformation of the stretched face of the ermoement element

$$A'_{red,j} = A_{red,i} \cdot \frac{E_s}{f(\epsilon_i)}; \tag{9}$$

$S_{red,i}$ and $A_{red,i}$ – respectively, the static moment and the area of the i -part of the compressed section fiber brought to the concrete, $S'_{red,j}$ и $A'_{red,j}$ – accordingly, the static moment and the area of the j -woven steel mesh brought to the concrete of the compressed section fiber [1, 11].

From the equilibrium of the normal section of the element at a pure bend follows

$$M = \sum_{i=1}^n \left(\frac{\sigma_{i-1} + \sigma_i}{2} \right) \cdot \frac{b \cdot h}{n} \cdot \left(Y_i - \frac{h}{2 \cdot n} - Y_c \right)^2 + \sum_{j=1}^k \sigma_{sj} \cdot A_s \cdot (Y_{sj} - Y_c)^2. \tag{10}$$

The rigidity of the section determined by the formula

$$D = \frac{M}{\chi} = \frac{M \cdot h}{\epsilon_{bt} + \epsilon_b}. \tag{11}$$

Thus, by setting the relative strain of the ε_{bt} and driving the values $i = 1, 2, \dots, n$, $j = 1, 2, \dots, k$ formulas (7–11), in each final element you can determine the relative deformation and tension, also determine the position of the neutral axis, bending moment and stiffness at any level of tension in the section under consideration [12].

A graphic illustration of the results of the method and its comparison with experimental data shown in the Fig. 5.

5 Conclusions

Thus, natural and numerical methods of researches have shown that the vermikulitobetonny layer increases rigidity and crack resistance of armotsementny designs. The offered numerical method of calculation provides acceptable coincidence to pilot researches on armotsementny samples.

The existing ways of production of two-layer concrete and concrete products provide formation of heat-insulation layer on heavy constructive layer. Made by these ways, generally products of the small sizes and simple geometrical outline. For the majority of the armotsementny designs formed in mounting position it is necessary to priformovyvat fireproof layer from below.

For production of two-layer armotsementny designs with providing clear boundary and design thickness of layers it is offered to maintain previously svezheotformovanny vermikulitobetonny layer within 40–60 min. before formation of armotsementny layer. Necessary plastic durability of vermikulitobetonny layer for high-quality consolidation on it armotsementny layer is 0.015–0.025 MPas.

Teamwork of concrete layers in the two-layer armotsementny elements made on the developed technology provided up to the destruction moment. The Vermikulitobetonny layer and woven grid in vermikulitobetonny layer increase rigidity and crack resistance of the bent armotsementny elements.

By the developed numerical calculation method, it revealed that drawing fireproof layer from vermikulitobeton 15 mm thick allows increasing bearing capacity of thin-walled design in comparison with single-layer the same thickness by 25% in the conditions of 1 h of influence of temperatures of the standard fire.

References

1. Abrams MS, Gustaferro AH (1972) Fire endurance of prestressed concrete nits coated with sprayapplied insulation. *J Prestr Concr Inst* 1:82–103
2. Paschen H (1974) Measurement for appropriate fire resistance duration. *Concr Plant+Prefabr Part Technol* 40(5):334–342
3. Thermax fire protection plate (1977) Company isovolta. Information osterreichische isolierstoffwerke aktiengesellschaft
4. Karpenko NI (1996) General models of reinforced concrete mechanics. Stroyizdat, Moscow

5. Karpov VV, Korobeinnikov AV, Malyshev VF, Frolkis VA (1998) Mathematical processing of the experiment and its planning: Learning. manual. ASV, St. Petersburg, S.-Peterb. State architecture.-builds. Un-t
6. Milovanov AF (1986) Fire resistance of reinforced concrete structures. Stroyizdat, Moscow
7. Bry VB, Golikova GI (1976) Logical grounds of planning of the experiment. Metallurgy
8. Panarin SN, Hezhev TA (1982) Armocement designs of increased fire resistance. A visual aid. LDNTP, St. Petersburg
9. Panarin SN, Hezhev TA. (1982) Explosive structures of increased fire resistance. A visual aid. LDNTP, St. Petersburg
10. Romanenkov IG, Siegern-Korn VN (1984) Fire resistance of construction structures from effective materials. Stroyizdat, Moscow
11. Hezhev TA (1980) Raising the fire resistance limit of thin-walled rm momentary structures by applying vermiculito concrete insulation. Study of thin-walled spatial structures and technology of their manufacture: Sat. Tr. LenzNIIEP, St. Petersburg
12. Yakovlev AI (1980) Basic principles of calculating the limits of fire resistance of construction structures. Fire Res Build Struct 8:3–14 Sat. Tr. VNIPO

Estimation Residual Resource of Unreinforced Stone Structures by Changing the Parameters Masonry



Dmitry Korolkov , Galina Bolodyan , and Marina Gravit 

Abstract In this article, the authors describe a method for calculating the limiting service life of unreinforced masonry structures by changing the geometric parameters of the section. Formulas for calculating the limiting service life of unreinforced stone structures for a number of design cases are derived. The advantages and disadvantages of this method are indicated. A number of assumptions are described for calculating the ultimate service life. It describes how to calculate the residual resource after determining the service life limit. The authors proposed to calculate the rate of change of geometric parameters using regression equations.

Keywords Stone structures · Residual resource · Central compressed elements · Center stretched elements · Bending elements · Shear · Crushing

1 Introduction

Currently, there are no methods for assessing the residual life of stone structures based on the data of instrumental survey. As a rule, the residual life is determined by indirect methods based on an estimate of the amount of physical wear and tear [1–9]. Since most of the stone buildings were built quite a long time ago, there is an urgent need to assess the remaining service life. This article will consider the cases of calculating the residual resource or the limiting service life for the first group of limiting states.

D. Korolkov (✉)

Saint Petersburg State University of Architecture and Civil Engineering, 4 2nd Krasnoarmeyskaya Street, St. Petersburg 190005, Russian Federation

G. Bolodyan

Federation for Civil Defense, Emergencies and Elimination of Consequences of Natural Disasters, All-Russian Research Institute for Fire Protection of Ministry of Russian, 12 VNIPO Microdistrict, Balashikha, Moscow 143903, Russian Federation

M. Gravit

Peter the Great St. Petersburg Polytechnic University, 29 Politechnicheskaya Street, St. Petersburg 195251, Russian Federation

2 Methods

During the operation of stone structures, the dimensions of the cross-section of structural elements change. In the limit, the value of these dimensions will be minimal. Such a change in time in the dimensions of the cross-section of the elements occurs at a certain speed. From here it follows that other geometric characteristics of the section also change. This fact can be used to determine the residual resource of the elements of stone structures. To do this, subtract the actual service life from the maximum permissible service life. The maximum service life will be determined by the formula:

$$T_{ult} = \frac{P_{factual} - P_{min}}{v} \quad (1)$$

$P_{factual}$ – parameter value, at the moment of technical condition monitoring;

P_{min} – minimum parameter value;

v – rate of change of the parameter value over time.

The design resistance of the masonry to compression should be multiplied by the coefficients of the operating conditions γ_c , equal to:

- a) 0.8 – for pillars and piers with a cross-sectional area of 0.3 m² or less;
- b) 0.6 – for elements of circular cross-section made of ordinary (non-calcined) bricks, not reinforced with mesh reinforcement;
- c) 1.1 – for blocks and stones made of heavy concrete and natural stone ($\gamma \geq 1800 \text{ kg/m}^3$);
0.9 – for masonry of blocks and stones made of silicate concrete of strength classes higher than B25;
0.8 – for masonry made of blocks and stones made of large-porous concrete and autoclaved aerated concrete;
0.7 – for masonry from blocks and stones from non-autoclaved aerated concrete;
- d) 1.15 – for masonry after a long period of mortar hardening (more than a year);
- e) 0.85 – for masonry made of silicate bricks on a mortar with potash additives;
- f) for winter masonry, performed by the freezing method, by the coefficients of working conditions γ_{c1} according to Table 1.

The design compressive resistance of natural stone masonry should be taken with the coefficients:

0.8 – for masonry made of semi-finished stones (protrusions up to 10 mm);

0.7 – for masonry of coarse stones (projections up to 20 mm).

The design resistance to compression of masonry made of adobe bricks and ground stones should be taken with the coefficients:

0.7 – for laying external walls in areas with a dry climate;

0.5 – the same in other zones;

0.8 – for laying internal walls.

Table 1 Coefficients of working conditions for winter masonry

Type of stressed state of winter masonry	Coefficients of working conditions	
	Masonry γ_{c1}	Mesh reinforcement γ_{cs1}
Compression of hardened (after thawing) brickwork	1.0	–
Compression of hardened (after thawing) rubble masonry from bed stone	0.8	–
Stretching, bending, shearing of hardened masonry of all types along mortar joints	0.5	–
Compression of masonry with mesh reinforcement, erected by the method of freezing in the thawing stage	–	0.5
The same, hardened (after thawing)	–	0.7
The same, erected on mortars with anti-frost additives when hardening in frost and the strength of the solution is not less than 1.5 MPa (15 kgf/cm ²) at the time of thawing	–	1.0

Later in this article, in the formulas for determining the maximum service life, the rate of change of the cross-sectional parameters will be written in the form of the symbol v , since the law itself can be represented by various dependencies and its choice depends on the specific case.

Formula (1) is a general case, and it can take on a different form depending on which cross-sectional parameter we have adopted.

In this article, in the future, we will consider various cases of determining the maximum service life only for elements of unreinforced masonry.

Cases will be considered when calculating only the first group of limiting states.

3 Results and Discussion

3.1 Calculation of Centrally Compressed Members

The formula will look like this:

$$T_{ult} = \frac{\left[\left(1 - \eta \cdot \frac{N_g}{N} \right) \cdot \varphi \cdot A \right]_{fact} - \frac{N}{R}}{v} \tag{2}$$

- φ – buckling coefficient;
- N – calculated longitudinal force;

N_g – calculated longitudinal force from continuous loads;
 η – coefficient;
 R – calculated resistance to compression of the masonry;
 A – sectional area of the element.

For $h \geq 30$ cm or $i \geq 8.7$ cm, the mg factor should be taken equal to one.

3.2 Calculation of Eccentrically Compressed Members

The formula will look like this

$$T_{ult} = \frac{\left[\left(1 - \eta \cdot \frac{N_g}{N} \left(1 + \frac{1,2 \cdot e_{0g}}{h} \right) \right) \cdot \frac{\varphi + \varphi_c}{2} \cdot \varphi \cdot A \cdot \left(1 - \frac{2 \cdot e_0}{h} \right) \cdot \omega \right]_{fact} - \frac{N}{R}}{\nu} \quad (3)$$

e_{0g} – eccentricity from long-term loads;
 h – height of the section in the plane of the bending moment;
 e_0 – eccentricity of the calculated force N relative to the center of gravity of the section;
 φ – coefficient of longitudinal bending for the entire section in the plane of action of the bending moment;
 φ_c – coefficient of buckling for the compressed part of the section, determined by the actual height of the element H in the plane of the bending moment;
 ω – coefficient.

3.3 Oblique Eccentric Compression

The calculation of the ultimate service life for oblique eccentric compression is carried out according to formula (3) with a rectangular stress diagram in both directions. The area of the compressed part of the section A_c is conventionally taken in the form of a rectangle, the center of gravity of which coincides with the point of application of the force and the two sides are limited by the contour of the section of the element (see Fig. 1), while $h_c = 2ch$; $b_c = 2cb$ and $A_c = 4c_h c_b$, where c_h and c_b are the distances from the point of application of force N to the nearest boundaries of the section.

In cases of a complex section in order to simplify the calculation, it is allowed to take a rectangular part of the section without taking into account the sections that complicate its shape (see Fig. 2).

Fig. 1 Design model of a rectangular section with oblique eccentric compression

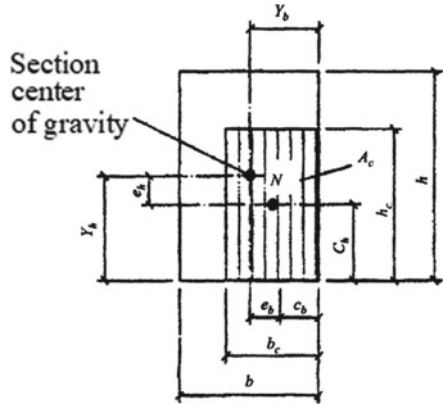
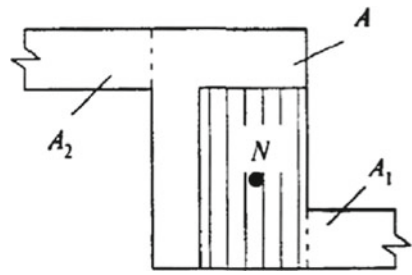


Fig. 2 Design diagram of a complex section with oblique eccentric compression; areas A_1 and A_2 are not taken into account in the calculation



The quantities ω , φ_1 and m_g are determined twice:

- a) with a section height h or a radius of gyration i_h and an eccentricity e_h in the direction h ;
- b) with a section height b or a radius of gyration i_b and an eccentricity e_b in the direction b .

The lesser of the two values calculated by formula (3) at two values of ω , φ_1 and m_g is taken as the final value of the limiting service life.

3.4 Crushing (Local Compression)

For brick and vibrobrick masonry, as well as masonry made of solid stones or blocks made of heavy and lightweight concrete:

$$T_{ult} = \frac{\left[\psi \cdot (1,5 - 0,5 \cdot \psi) \cdot \sqrt[3]{\frac{A}{A_c}} \cdot A_c \right]_{fact} - \frac{N_c}{R}}{\nu} \quad (4)$$

For masonry of hollow concrete or solid stones and blocks of large-pore and cellular concrete; large-format ceramic stones:

$$T_{ult} = \frac{\left[\psi \cdot \sqrt[3]{\frac{A}{A_c}} \cdot A_c \right]_{fact} - \frac{N_c}{R}}{\nu} \tag{5}$$

N_c – longitudinal compressive force from local load;
 Ψ – coefficient of completeness of the pressure diagram from local load.

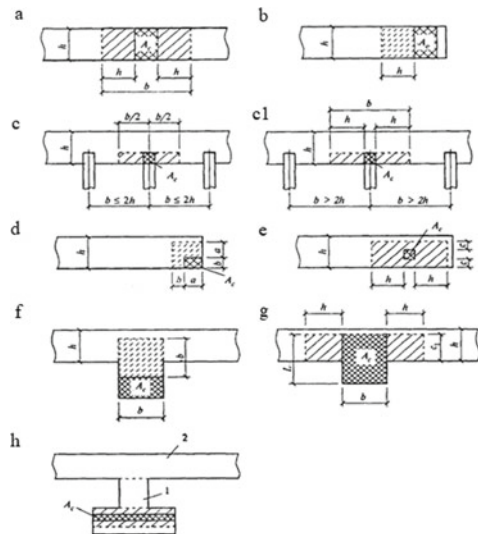
With a uniform pressure distribution $\Psi = 1$, with a triangular pressure diagram $\Psi = 0.5$.

A_c – crumple area to which the load is transferred.

The calculated cross-sectional area A is determined according to the following rules:

- a) with a collapse area that includes the entire wall thickness, the calculated collapse area includes sections with a length not exceeding the wall thickness on each side of the local load boundary (see Fig. 3a);
- b) when the area of the collapse is located at the edge of the wall along its entire thickness, the calculated area is equal to the area of the collapse, and when calculating the sum of local and main loads, the calculated area indicated in Fig. 3b by the dotted line is also taken;
- c) when the ends of the girders and beams rest on the wall, the calculated area of the collapse includes the cross-sectional area of the wall with a width equal to the embedment depth of the support section of the girder or beam and no longer

Fig. 3 Determination of the calculated cross-sectional areas under collapse (local compression); a - h - various cases of local compression



- than the distance between the axes of two adjacent spans between the beams (Fig. 3c); if the distance between the beams exceeds double the wall thickness, the length of the calculated cross-sectional area is determined as the sum of the beam width b_c and double the wall thickness h (Fig. 3c1);
- d) in case of collapse under the edge load applied to the corner section of the wall, the calculated area is equal to the area of the collapse, and when calculating the sum of local and main loads, the calculated area is taken, limited by a dotted line in Fig. 3d;
 - e) with a crumple area located on a part of the length and width of the section, the calculated area is taken in accordance with Fig. 3e. If the crumple area is located near the edge of the section, then when calculating the sum of local and main loads, the calculated sectional area is taken, not less than that determined according to Fig. 3d, when the same load is applied to the corner section of the wall;
 - f) when the area of the collapse is located within the pilaster, the calculated area is equal to the area of the collapse, and when calculating the sum of local and main loads, the calculated area is taken, bounded in Fig. 3f by a dotted line;
 - g) with a collapse area located within the pilaster and part of the wall or wall, an increase in the calculated area compared to the collapse area should be taken into account only for the load, the resultant of which is applied within the shelf (wall) or within the rib (pilaster) with an eccentricity $e_0 > 1/6 L$ towards the wall (where L is the length of the collapse area, e_0 is the eccentricity with respect to the axis of the collapse area). In these cases, in addition to the crushing area, part of the sectional area of a shelf with a width C equal to the depth of embedding of the support plate into the wall masonry and a length in each side of the edge of the plate not exceeding the wall thickness (Fig. 3g) is included in the calculated sectional area;
 - h) if the section has a complex shape, it is not allowed to take into account when determining the calculated cross-sectional area the sections, the connection of which with the loaded section is insufficient for pressure redistribution (Sects. 1 and 2 in Fig. 3h).

In all the cases shown in Fig. 3, the area of collapse A_c is included in the calculated cross-sectional area A .

3.5 Bending Elements

For bent unreinforced elements:

$$T_{ult} = \frac{[W]_{fact} - \frac{M}{R_{tb}}}{v} \tag{6}$$

M – calculated bending moment;

W – moment of resistance of the section of the masonry during its elastic work;
 R_{tb} – design tensile resistance of the masonry in bending along the tied section.

For bending unreinforced elements, the shear force:

$$T_{ult} = \frac{[b \cdot z]_{fact} - \frac{Q}{R_{tw}}}{v} \quad (7)$$

R_{tw} – design resistance of the masonry to the main tensile stresses in bending;

b – section width;

z – shoulder of the internal pair of forces.

3.6 Centrally Stretched Elements

For elements of unreinforced stone structures:

$$T_{ult} = \frac{[A_n]_{fact} - \frac{M}{R_t}}{v} \quad (8)$$

N – calculated axial tensile force;

R_t – design tensile resistance of the masonry for the tied section;

A_n – calculated net cross-sectional area.

3.7 Shear

$$T_{ult} = \frac{Q - [(R_{sq} + 0,8 \cdot n \cdot \mu \sigma_0) \cdot A]_{fact}}{v} \quad (9)$$

R_{sq} – design shear resistance;

μ – coefficient of friction along the seam of the masonry, taken for masonry made of bricks and stones of regular shape, equal to 0.7;

σ_0 – average compressive stress at the smallest design load, determined with a load safety factor of 0.9;

n – coefficient taken equal to 1.0 for solid brick and stone masonry and equal to 0.5 for hollow brick and stones with vertical voids, as well as for torn rubble stone masonry;

A – calculated cross-sectional area.

Since the calculation of the limiting service life of stone structures is carried out at once according to several formulas, then the minimum of those obtained is taken as the final result.

4 Conclusions

In the process of analysis of methods for calculating the maximum service life of building structures, it was found that existing methods do not allow to reliably Now let's talk about some points of calculating the maximum service life.

The first thing that should be addressed is the presence in a number of formulas of such a value as the calculated length of the element. When calculating the limiting service life, we proceed from the assumption that this value remains unchanged throughout the entire service life, i.e., firstly, the fastening scheme of the element does not change and, secondly, the change in the actual free length of the element is negligible. This means that the change in length occurs only due to the influence of the external environment.

The second thing you should pay attention to is that the calculation does not imply a change in geometric parameters as a result of artificial strengthening or weakening of the element cross-section.

Third, you should pay attention to the fact that the calculation assumes that the action of transverse and longitudinal forces, bending moments remains unchanged during the entire service life.

The advantage of this method of calculation can be considered that we obtain objective values of the value of the maximum service life and, accordingly, the residual resource, since the initial data are obtained during the instrumental examination.

The disadvantage of this approach can be considered its complexity or the impossibility of implementation in some cases in practice.

This method can be implemented directly when it is possible to directly measure the change in geometric parameters.

When considering the rate of change of geometric parameters, the question arises about the lack of data for the past period of operation. Since the rate of change in geometric parameters is not the same at different time intervals, in the absence of observation data, the estimate of the rate of change in geometric parameters will be incorrect and, accordingly, we will receive an incorrect value for the maximum service life.

To solve this problem, it is important to record the current values of geometric dimensions when organizing regular technical inspections. In this case, having a number of data, you can apply regression analysis and build equations for the dependence of changes in geometric parameters [10–24].

To solve this problem, the authors propose to use regression equations. The most commonly used multivariate regression equations are:

1. Multiple Linear Regression:

$$y = \alpha_0 + \alpha_1 \cdot x_1 + \dots + \alpha_n \cdot x_n + \varepsilon \tag{10}$$

2. Polynomial Regression:

$$y = \alpha_0 + \alpha_{n,i} \cdot x_i^n + \alpha_{n-1,i} \cdot x_i^{n-1} + \dots + \alpha_{1,i} \cdot x_i + \dots + \varepsilon \quad (11)$$

3. Power regression:

$$y = \alpha_0 \cdot x_1^{\alpha_1} \cdot \dots \cdot x_n^{\alpha_n} + \varepsilon \quad (12)$$

4. Significant regression:

$$y = \alpha_0 \cdot \alpha_1^{x_1} \cdot \dots \cdot \alpha_n^{x_n} + \varepsilon \quad (13)$$

5. Exponential regression:

$$y = e^{(\alpha_0 + \alpha_1 \cdot x_1 + \dots + \alpha_n \cdot x_n)} + \varepsilon \quad (14)$$

6. Logarithmic regression:

$$y = \alpha_0 + \alpha_1 \cdot \ln x_1 + \dots + \alpha_n \cdot \ln x_n + \varepsilon \quad (15)$$

$$y = \alpha_0 + \alpha_1 \cdot \lg x_1 + \dots + \alpha_n \cdot \lg x_n + \varepsilon \quad (16)$$

7. Semilogarithmic regression:

$$y = \alpha_0 + \alpha_1 \cdot \log x_1 + \dots + \alpha_n \cdot \log x_n + \varepsilon \quad (17)$$

In conclusion, I would like to note that despite the fact that the proposed method was considered for stone structures, it can be applied to other types of structures (reinforced concrete, metal, stone and composite).

References

1. Erokhhina OO (2019) Analysis of publications about the methods of static friction definition for bulk material. IOP Conf Ser Mater Sci Eng 560:012014. <https://doi.org/10.1088/1757-899x/560/1/012014>
2. Braila NV, Khazieva KL, Staritsyna AA (2017) Results of technical inspection monitoring of the operation object. Mag Civ Eng 74(6):70–77. <https://doi.org/10.18720/MCE.74.7>
3. Soldatenko VS, Smagin VA, Gusenitsa YN, Gera VI, Soldatenko TN (2017) The method of calculation for the period of checking utility systems. Mag Civ Eng 70(2):72–83. <https://doi.org/10.18720/MCE.70.7>
4. Volkov M, Kibkalo A, Vodolagina A, Murgul V (2016) Existing models residual life assessment of structures and their comparative analysis. Procedia Eng 165:1801–1805. <https://doi.org/10.1016/j.proeng.2016.11.925>

5. Gravit M, Antonov S, Nedviga E, Shkorko M, Kozlova K (2016) Strength test of high-precision tunnel lining blocks. *Procedia Eng* 165:1658–1666. <https://doi.org/10.1016/j.proeng.2016.11.907>
6. Gravit M, Nedviga E, Vinogradova N, Teplova Z (2017) Fire resistance of prefabricated monolithic slab. In: International Science Conference SPbWOSCE-2016 «SMART City». MATEC Web of Conferences 106. <https://doi.org/10.1051/mateconf/201710602025>
7. Gravit M, Dmitriev I, Ishkov A (2017) Quality control of fireproof coatings for reinforced concrete structures. *IOP Conf Ser Earth Environ Sci* 90:012226. In: EMMFT 2017. <https://doi.org/10.1088/1755-1315/90/1/012226>
8. Chernykh A, Korolkov D, Nizhegorodtsev D, Kazakevich T, Mamedov S (2020) Estimating the residual operating life of wooden structures in high humidity conditions. *Archit Eng* 5(1):10–19. <https://doi.org/10.23968/2500-0055-2020-5-1-10-19>
9. Korolkov D, Chernykh A, Gravit M (2020) Method for determining the residual resource of building structures by the terms of their operation. In: Anatolijs B, Nikolai V, Vitalii S (eds) *Proceedings of EECE 2019. Lecture Notes in Civil Engineering*, vol 70, pp 389–402. Springer
10. Aven T (2011) Interpretations of alternative uncertainty representations in a reliability and risk analysis context. *Reliab Eng Syst Saf* 96(3):353–360. <https://doi.org/10.1016/j.res.2010.11.004>
11. Aven T, Zio E (2011) Some considerations on the treatment of uncertainties in risk assessment for practical decision making. *Reliab Eng Syst Saf* 96:64–74. <https://doi.org/10.1016/j.res.2010.06.001>
12. Payan C, Abraham O, Garnier V (2018) Ultrasonic methods. In: *Non-destructive testing and evaluation of civil engineering structures*. Elsevier Inc. <https://doi.org/10.1016/B978-1-78548-229-8.50002-9>
13. Vu QA, Garnier V, Chaix JF, Payan C, Lott M, Eiras JN (2016) Concrete cover characterisation using dynamic acousto-elastic testing and Rayleigh waves. *Const Build Mat* 114:87–97. <https://doi.org/10.1016/j.conbuildmat.2016.03.116>
14. Hassan AMT, Jones SW (2012) Non-destructive testing of ultra high performance fibre reinforced concrete (UHPRC): a feasibility study for using ultrasonic and resonant frequency testing techniques. *Const Build Mat* 35:361–367. <https://doi.org/10.1016/j.conbuildmat.2012.04.047>
15. Garnier V, Piwakowski B, Abraham O, Villain G, Payan C, Chaix JF (2013) Acoustic techniques for concrete evaluation: improvements, comparisons and consistency. *Const Build Mat* 43:598–613. <https://doi.org/10.1016/j.conbuildmat.2013.01.035>
16. Planès T, Larose E (2013) A review of ultrasonic Coda Wave Interferometry in concrete. *Cem Concr Res* 53:248–255. <https://doi.org/10.1016/j.cemconres.2013.07.009>
17. Schabowicz K (2014) Ultrasonic tomography - the latest nondestructive technique for testing concrete members - description, test methodology, application example. *Arch Civ Mech Eng* 14:295–303. <https://doi.org/10.1016/j.acme.2013.10.006>
18. Moradi-Marani F, Rivard P, Lamarche CP, Kodjo SA (2014) Evaluating the damage in reinforced concrete slabs under bending test with the energy of ultrasonic waves. *Const Build Mat* 73:663–673. <https://doi.org/10.1016/j.conbuildmat.2014.09.050>
19. Xu Y, Jin R (2018) Measurement of reinforcement corrosion in concrete adopting ultrasonic tests and artificial neural network. *Const Build Mat* 177:125–133. <https://doi.org/10.1016/j.conbuildmat.2018.05.124>
20. Wolf J, Pirskawetz S, Zang A (2015) Detection of crack propagation in concrete with embedded ultrasonic sensors. *Eng Frac Mech* 146:161–171. <https://doi.org/10.1016/j.engfracmech.2015.07.058>
21. Choi H, Popovics JS (2015) NDE application of ultrasonic tomography to a full-scale concrete structure. *IEEE Trans Ultrason Ferroelectr Freq Control* 62:1076–1085. <https://doi.org/10.1109/TUFFC.2014.006962>
22. Tsioulou O, Lampropoulos A, Paschalis S (2017) Combined Non-Destructive Testing (NDT) method for the evaluation of the mechanical characteristics of Ultra High Performance Fibre Reinforced Concrete (UHPRC). *Const Build Mat* 131:66–77. <https://doi.org/10.1016/j.conbuildmat.2016.11.068>

23. Karaiskos G, Deraemaeker A, Aggelis DG, Van Hemelrijck D (2015) Monitoring of concrete structures using the ultrasonic pulse velocity method. *Smart Mat Str* 24:113001. <https://doi.org/10.1088/0964-1726/24/11/113001>
24. Karaiskos G, Tsangouri E, Aggelis DG, Van Tittelboom K, De Belie N, Van Hemelrijck D (2016) Performance monitoring of large-scale autonomously healed concrete beams under four-point bending through multiple non-destructive testing methods. *Smart Mat Str* 25:055003. <https://doi.org/10.1088/0964-1726/25/5/055003>

Importance of Solar in Aeration of High-Rise Buildings in Cities of Southern Countries with Hot Climatic Condition



Adham Giyasov 

Abstract The analysis of the natural ventilation of the space-planning solution of urban buildings is carried out, which in the planning structure is dominated by repeated mainly linear, lowercase and open planning schemes of buildings that form urban canyons, taking into account the condition of insolation. The mechanism of the origin of local winds in urban areas, canyons of development, adjacent territories and wall layers of buildings of urban structures, formed due to the active insolation of building elements of southern cities, is revealed. The role of insolation in aeration of urban development with low-wind climatic conditions is revealed.

Keywords City · Building · Aeration · Climate · Insolation · Heat · Energy activity · Comfort · Wind

1 Introduction

One of the essential conditions for normal human life is to provide a comfortable environment for the surrounding air, both indoors and on the territory of urban development.

Urban development is characterized by considerable complexity, due to a variety of space-planning and compositional solutions, which cannot be ignored when researching and studying the factors of micro-and environmental climate inside the building and in the premises of buildings.

In the process of studying the aerodynamic and thermodynamic characteristics in the insolation of urban areas and the morphology of buildings with different architectural and planning and spatial solutions of buildings, the presence of many different physical processes of a local nature that determine the microclimatic and ecological regime was found.

On the territory of cities, the centers of heat and coolness, which are different in terms of thermophysical characteristics, size, mobility, and scale of distribution,

A. Giyasov (✉)

Moscow State University of Civil Engineering National Research, Yaroslavskoe sh.,
26, Moscow 129337, Russian Federation

predominate, creating islands of heat and islands of coolness, the combination of which is the basis of the mechanism for the formation of natural ventilation of the territory of urban complexes.

Urban development, depending on the spatial planning and compositional solution, is a very diverse and complex structure. Modeling of heat and wind processes in such building structures is a multi-factorial and very complex task. However, the analysis of space-planning solution to existing and projected urban development shows that in the planning structure which prevails is repeated many times mainly linear characteristic, large and open layout scheme of buildings forming urban canyons with oppositely located between the buildings and creates an architectural appearance of the road network, streets, areas between houses, etc., which allow to solve tasks of forecasting and evaluation of heat wind and thermal processes, which are the basis for the formation factors of micro-, bio- and the ecological environment of human habitation.

The speed of atmospheric wind in the city is affected by buildings with different floors, its density and landscaping. This position is confirmed by Serebrovskiy F. L. [1], which on the basis of theoretical and experimental studies shows that at the level of 2 m, the wind speed among 5-storey buildings does not exceed on average 60–70% of the speed of the main stream in the open. With the increase in the number of storeys of buildings and the greening of the surrounding area with large-scale green spaces, the wind regime of the building area and premises of buildings is aggravated even more significantly.

According to the research of the laboratory of microclimate of the Central Research Institute for Urban Planning significant change, both in strength and direction of the wind flow is subject to in the territory of the buildings themselves. For example, directly behind a building that stands in the path of the air flow, the wind speed is 5–10% of the speed in the open [2].

However, the analysis of the projects of detailed planning of buildings and general plans of cities, as well as the spatial planning solution of urban structures shows that in the development of cities there are repeatedly repeated characteristic urban areas formed by open, lowercase and linear planning schemes of development, which form city streets, open inter-house spaces due to parallel and opposite buildings located among themselves.

The wind speed in the city is also affected by vegetation. Semashko K. I. [3] indicates that the green dress of trees reduces the wind speed in the summer by 20–30%, after the fall of leaves, the wind will increase by 20–40% on average. In General, in various points of the city, there is a decrease in wind speed by 30–60%. It is also established that in green areas the wind speed is reduced to 100%.

In the field of weakened circulation, local winds arise, which are movements of thermal convection, which are particularly important in cities and regions with low wind and calm climate conditions. They are formed as a result of thermal perturbation caused by inhomogeneity of heating of the energy-active active surface of urban development and the air adjacent to it.

Atmospheric wind can change the direction of movement of both descending and ascending air currents formed in the Islands of heat and cool Islands, as well as create

conditions for their mixing. At the same time, local winds of thermal origin can affect the direction of the atmospheric wind, depending on the strength of their field.

If on windy days the wind speed among buildings decreases, then on warm calm days in the cities of southern countries, on the contrary, favorable conditions are created for the occurrence of weak local air currents. The speed of these flows according to the observations of Sheleikhovsky G.V. [4], on average 2 m/s, according to Kratzer P. A. [5]—up to 3.3 m/s. These air currents are closely related to the contrasting thermal and temperature conditions formed in the built-up area during insolation. According to our observations, with the contrast of the heat island and the cool island in 6 °C, the speed of local winds reaches up to 3.4 m/s.

In southern countries, an important criterion for comfort, along with the intensity of solar radiation, is the speed of air movement in urban areas, which should be within 0.5–3.0 m/s [6–8]. At the same time, according to the recommendations of the Kiev research Institute of General and communal hygiene, the air mobility in the room should be 0.1–0.15 m/s [9].

Aeration environment is one of the natural factors that significantly affect the physiological and hygienic conditions of housing and residential development. Wind is a factor that determines the thermal state of a person.

At a high temperature of +45° C and low wind speed on the territory of cities and low air mobility in the premises of buildings, the thermoregulatory apparatus of a person comes to extreme tension.

In urban areas, countries located near the equator on both sides of the Northern and southern latitudes within the range of 0 to 45° geographical latitude, the duration of the summer overheating period is from 4 to 7 months. In such extreme climate conditions, the human thermoregulatory apparatus in indoor and urban areas, under the dominant insolation condition (960-1000 W/m²), high temperature up to 38–45 °C in the shade, low wind speed (1–3 m/s) and arid climate conditions, is in extreme stress [10–14].

Studies have found that in arid climate conditions in still air, unpleasant sensations occur in humans at a temperature of +31 °C, and when the air moves at a speed of about 1 m/s - at a temperature of at least + 35 °C. The comfort zone expands by 8–10 °C if the stationary air moves into motion [15, 16].

When the wind speed changes from 0.01 m/s to 0.6 m/s, the human heat transfer by convection increases twice, and when it increases from 1 m/s to 4 m/s, it increases by 75% [17].

According to Kratzer P. A., if you increase the wind speed from 0 to 3.5 m/s, then the heat perception on the EET scale at a stable air temperature (+30 °C) and low relative humidity (20%) from +23 °C to +19.9 °C, i.e., the assessment of such climatic conditions goes from “hot” to “comfortable” [18].

Hygienic characteristics of the human condition in a hot climate reveal that the most severe conditions are the combination of heat with no wind. Along with this, the possibility of mitigating the effect of heat is indicated, even a weak air movement of about 1 m/s expanding the comfort zone by 8–10 °C at the effective temperature.

Thus, the cooling effect of local winds in an urban area can be expressed in the following values (Table 1).

Table 1 The cooling effect of wind

Wind speed		Cooling effect (°C)
(m/s)	(km/h)	
0.1	0.36	0
0.25	0.9	0.5
1.5	5.4	4
3	10.8	6
5	18	7

Table 2 Summer temperature and wind indicators of cities of foreign countries

City (<i>country</i>)	Maximum air temperature in July, °C	Wind for July	
		Speed, m/s	Direction
Tirana (<i>Albania</i>)	42	1.2	NW, calm
Bucharest (<i>Romania</i>)	41.1	2	E, calm
Manama (<i>Bahrain</i>)	45	2.8	N, calm
Nicosia (<i>Cyprus</i>)	44.4	1.8	NW, calm
Aden (<i>Yemen</i>)	41.1	2.8	NE, calm
Muscat (<i>Oman</i>)	46.6	1.8	NW, calm
Rawalpindi (<i>India</i>)	47	0.9	SE, calm
El-Dzhazair (<i>Algeria</i>)	41.7	1.6	NE, calm
Rio de Janeiro (<i>Brazil</i>)	36.4	2.8	SSE, calm

On the basis of the above analysis, the role of wind in the formation of microclimate and bioclimate factors of the urban area and building premises is determined. For low-wind and calm cities in the southern region, the wind regime of development should be considered together with the insolation regime, since the mechanism of interaction of insolation with the active surface of urban development is the determining factor of natural aeration.

Due to the significant number of calm days in the southern region [17], the systematization of architectural and construction means for organizing convective flows and the development of a natural aeration technique based on the process associated with the heat-wind regime plays an important role in the issue of natural ventilation of urban development and building premises (Tables 2, 3).

2 Methods

In order to identify the role of insolation in the formation of local winds of thermal origin, methods of theoretical research, large-scale instrumental field surveys of climate and microclimate factors using meteorological and thermophysical devices,

Table 3 Repetition of the bar during the summer period according to the data of weather stations in the cities of Central Asia, Kazakhstan and Transcaucasia

Republics, cities	Average of cases calm in July, %	Average number of cases from May 15 to September 15, %
<i>Tajikistan</i>		
Dushanbe	69	43
Gissar	80	75
<i>Uzbekistan</i>		
Samarkand	41	38
Kokand	62	57
<i>Kazakhstan</i>		
Almaata	25	22
Leninogorsk	37	37
<i>Georgia</i>		
Batumi	47	42
Tsqaltubo	64	59

as well as visual observation by smoke bombs on the territory of existing high-rise buildings and individual buildings in the structure of the city territory were adopted.

3 Results

The results of summer field instrumental surveys (July, 2019, Dushanbe), temperature and thermal regimes of urban structures of the southern city showed that at an average air temperature of $+37\text{ }^{\circ}\text{C}$, the wall oriented to the southern sector heats up to $+55\text{ }^{\circ}\text{C}$ at an insolation value of 470 W/m^2 , to the West—up to $+72\text{ }^{\circ}\text{C}$ at an insolation value of 740 W/m^2 , to the North—up to $+32\text{ }^{\circ}\text{C}$ when the insolation value is 120 W/m^2 , the concrete coating is about $+63\text{ }^{\circ}\text{C}$ when the insolation value is 920 W/m^2 . during this period, a relative decrease in air temperature by $4\text{--}6\text{ }^{\circ}\text{C}$ and the underlying surface by $20\text{--}25\text{ }^{\circ}\text{C}$ is observed in the territory planted with large-sized deciduous tree plantations and shaded areas (Fig. 1, 2).

In the most heated areas and territories, warm and, consequently, lighter air rises up by convection, a certain pressure difference is formed, so that the surrounding cool air rushes to places with more rarefied air, local air exchange or air circulation occurs.

Local winds of thermal origin are formed when the speed of the prevailing wind does not exceed 2 m/s .

A clear qualitative picture of the nature of convection air exchange was also obtained by using smoke bombs to smoke the residential area. Such phenomena

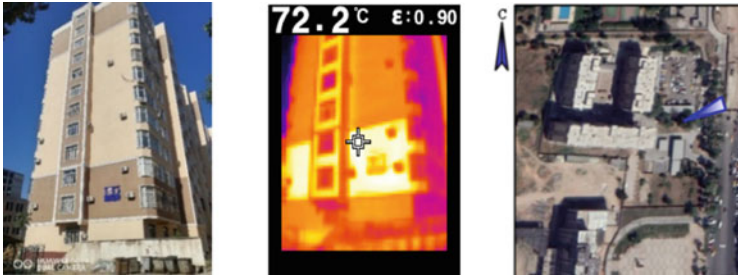
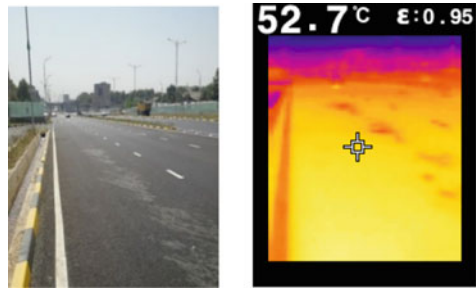


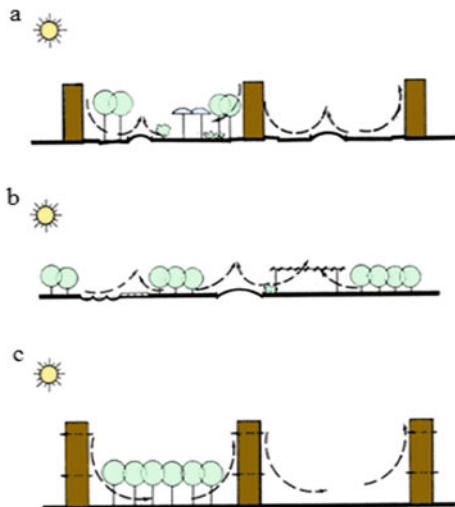
Fig. 1 Thermal imaging survey of the walls of the south-oriented building

Fig. 2 Thermal imaging survey of the city road with asphalt surface



occur between the insulated and shadow walls of opposing buildings, or between the insulated area and a dense green area located nearby (Fig. 3).

Fig. 3 Local wind patterns
a—in well-equipped and poorly equipped inter-city space, b—in urban territory, c—in inter-city space and premises



Analysis of literature sources, as well as our meteorological and thermophysical studies show that the kinematics of air flows is difficult for urban development under the dominant insolation conditions, which is variable depending on the time of day.

In order to determine the main regularities of the formation of air flow in the territory of urban development, allowing to establish theoretical prerequisites and develop practical recommendations for accounting and regulation of local wind in urban planning and construction design, experimental studies were conducted in a typical neighborhood during the hot summer period, in which calm weather conditions prevail. The mechanism of formation and development of local winds between contrasting Islands of heat and coolness a fragment of the building structure was studied by simulating the heating of vertical walls and horizontal areas, using the theory of modeling heat and wind processes.

The quality of the project was evaluated as a model of a fragment of a residential neighborhood consisting of 37 buildings with different heating walls, roofs and house plots. In these tests, wind speeds and directions were measured in the ground layer and in vertical sections up to 4 heights of different-height buildings (Figs. 4, 5 and 6).

Based on the study of variants of the physical model of urban residential development in a climate chamber, while creating calm conditions and thermal conditions of the active layer of urban structures by simulating the heating of the surfaces of walls, roofs and adjacent territories under insolation, based on the theory of modeling, a method for calculating natural aeration based on the following provisions is developed:

- calculation of the qualitative and quantitative characteristics of the insolation regime by searching for and identifying zones with the maximum duration of insolation (Fig. 4);
- forecasting of local wind speed and direction (Fig. 5);
- identification of convective flow zones by constructing a vector field wind map (Fig. 6);
- identification of zones of convective flows by constructing an aerodynamic wind map of the vector field (Fig. 6).

It is known that the air temperature in the city is higher than outside the city. In this case, the air movement occurs from the periphery to the center at a speed of 2 m/s or more. In addition to urban winds, microwinds of development are formed within the building due to the thermal and temperature contrast, which contribute to or in some cases resist the development of urban winds. In the formation and development of the microwinds of development, multi-insulated residential buildings are the main material structure of transformation, because vertical insulated and shadow facades of buildings and adjacent areas create temperature-contrast environment conditions that promote the movement of air mass even within the micro-scale.

The reason for the organization of local winds of development from differently insulated territories and walls of facades of buildings is the thermodynamic processes formed when exposed to the sun, artificial energy-active architectural and building structures created during the design process.

Fig. 4 Solar map of residential building with indication of isoline. June 22

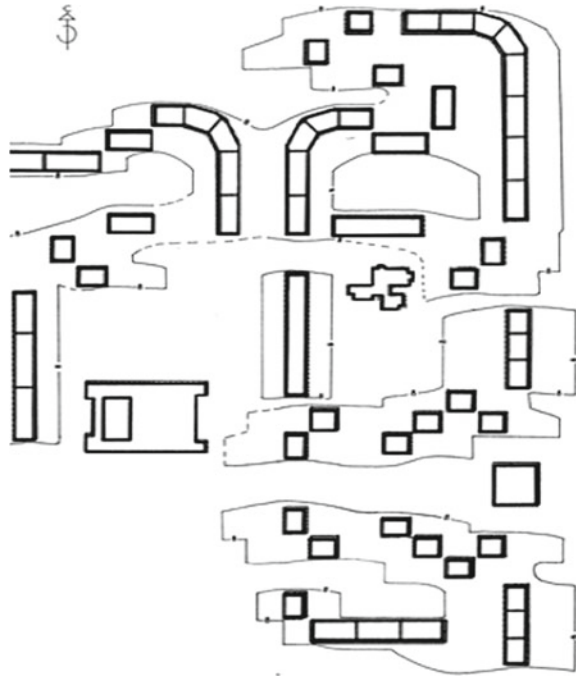


Fig. 5 Vector field of residential development wind. Day, 16 h

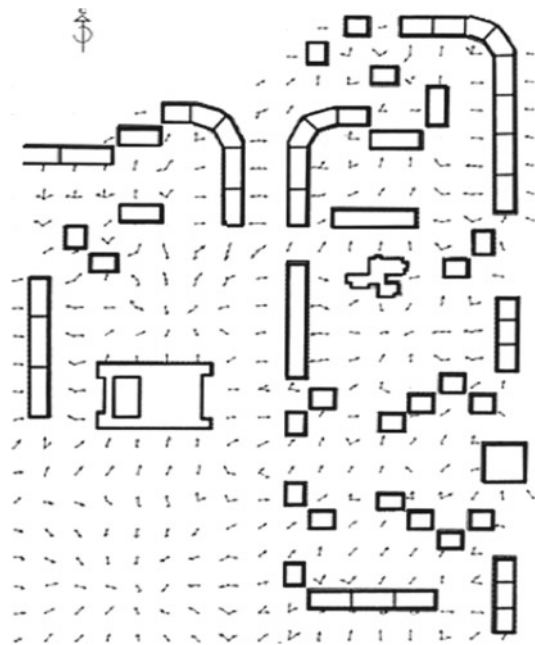




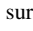
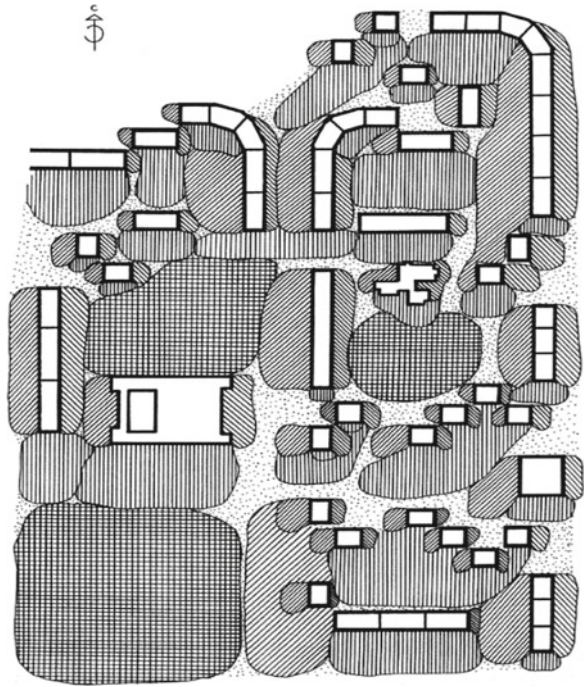


Fig. 6 Aeration map field of microwind residential building. Day, 16 h

 —movement of air flow towards the eastern facade,
 —movement of air flow towards the western facade,
 —movement of air flow towards the southern facade,
 —vertical convective flow from the underlying surface,
 —stagnant zone.



Microvetors have a relatively small length and largely depend on the insolation conditions and the heat capacity of building structures.

The speed of a microwinds at any point in *i* space is expressed as the following dependence

$$\vec{U}_i = \vec{U}_a k_a + \vec{v}_c k_c \tag{1}$$

where \vec{U}_a and \vec{v}_c are the vector of advective and convective wind speed; k_a and k_c are the coefficients of air flow transformation due to the horizontal and vertical micro-roughness of the building.

For the considered design situation of building, the following zones are determined based on the obtained air flow velocities, which correspond to the spatial coefficients of the aeration zones:

- stagnant (uncomfortable) zone - a zone of calm, in the territory where the speed of the micrometer reaches up to 0.5 m/s, which in combination with a high temperature of up to 45 °C creates thermal discomfort in the air in which the thermal state of a person reaches an excessively high level, and this condition contributes to the settling and accumulation of harmful substances, dust, etc.;
- the zone of air mass flow to the insulated energy-active western, eastern and southern walls of the facades. At the same time, in the inter-house spaces of the

canyons of the development, air circulation occurs with the flow of air from the side of the shadow to the side of the insulated facade at a speed of 1–3 m/s.

The analysis of the zoning of the development area allowed us to determine the following important coefficients:

- relative coefficient of discomfort (lull)

$$K_{\partial} = F_s / F_t \quad (2)$$

- relative comfort factor

$$K_c = F_c / F_t \quad (3)$$

where F_c and F_t —are the total area of stagnant and comfortable zones; F_t —the total area of the development area under consideration. aeration conditions.

4 Discussion

The proximity of two sections of the energy active surface of the city with different heating conditions under insolation causes the formation of local winds of thermal origin above them, which contribute to the natural ventilation of the territory. Thus, after analyzing the results of complex studies performed in relation to the formation of local winds of thermal origin in the boundary layer of urban developments, the following definition should be given. Local winds that form in cities are air currents of a small length from a few meters to ten kilometers, generated by the characteristics of the active surface of the building and the condition of their insolation. These features, caused by the inhomogeneity of heating of various sections of the underlying surface, create perturbations of the temperature field and the wind field. The resulting horizontal gradient temperatures (a green garden or square, an irradiated facade—a shadow facade, lakes—a built-up area, etc.) are the cause of local circulations. Thermal disturbances can be either periodic or continuous. The horizontal extent of local winds depends on the thermal contrast and the degree of energy activity of the active layer of urban structures and the temperature difference of neighboring heat Islands and cool Islands organized by architectural and construction means.

It is noted that arranging the combinations of heat Islands and the Islands of coolness, which is formed by architectural and construction funds (planning solutions of buildings, orientation of buildings, landscaping, gardening and irrigation) urban area, at the preliminary stage, you can pre-predict and laying the Foundation for the natural ventilation of the organization of local winds are of thermal origin, taking into account the mode of exposure of the built areas is able to plan urban area.

5 Conclusions

Local winds of thermal origin are periodic, develop in cities with hot, low-wind or calm climate conditions and weaken in the presence of atmospheric wind.

In the absence of a General circulation wind field, independent local air currents are formed on the territory of urban development due to thermal differences. Thermal disturbances contribute to the airing of the surface microclimatic layer, i.e. an increase in its power.

Moving on to the assessment of the development of local micro-breezes, we note that they are determined by the horizontal gradient of air temperature, which for convenience can be expressed in terms of the temperature difference between the energy-active surface and the green zone. At the same time, it can be argued that the conditions for the development of microbreeze circulation are more favorable the greater this temperature contrast.

Urban local winds are very common local meteorological processes that are formed by thermal contrast at the active surface of the building. They create conditions for natural aeration, transport and dispersion of pollutants in the surface atmosphere.

We determine that it is possible to identify and quantify the General conditions for the occurrence and development of many local winds in urban areas by correctly selecting mesoclimate-forming and microclimate-forming factors that favor the development of local winds.

Thus, the method of qualitative and quantitative assessment of the aeration regime of high-rise buildings in cities of southern geographical latitude with a low-wind climate condition was determined, which allows zoning of urban areas with natural ventilation and air stagnation, which are important in the formation of microclimatic, bioclimatic and environmental conditions of the environment.

6 Recommendations

When considering the mechanism of formation of local winds, a well-developed local circulation in cities should have the following characteristics:

The presence of a sufficiently large temperature contrast between the two neighboring heat Islands and the cool island, as well as the air layers above them.

Frequent presence of temperature inversion in the transition layer with a weakening of wind speed.

Baric field, with small horizontal pressure gradients at daytime wind speeds in the lower layer no more than 3 m/s.

References

1. Serebrovsky FL (1985) Aeration of settlements, Stroyizdat, p 170
2. Recommendations on consideration of natural and climatic factors in the planning and improvement of cities and group systems of settlements (1980) CNIP of urban planning, p 138
3. Semashko KI (1978) Methods of determining wind mode of complex configuration construction. Improving the urban environment. Coll Sci Works 64–70
4. Sheleikhovsky GV (1948) Microclimate of southern cities. Prod. Academician honey of the USSR, p 236
5. Krattser PA (1958) Climate of the city, (translation from German). Publishing House of Foreign Literature, p 253
6. Giyasov A (2006) Residential development in the conditions of hot steele climate. Hous Constr Ladya 1:12–14
7. Hang J, Sandberg M, Li Y (2009) Effect of urban morphology on wind condition in idealized city models. Atmos Environ 4:869–878
8. Fernandez ML, Rubio R, Gonzalez SM (2013) Architectural envelopes that interact with their environment. In: Proceedings of new concepts in smart cities: fostering public and private alliances (SmartMILE), pp 144–158
9. Miyagkov MS, Gubernskiy UD, Konova LI, Lyckevich VK (2007) City, architecture, man and climate. Architecture-S 344
10. Giyasov A, Barotov YuG (2018) The thermal state of man in the development of cities with a hot climate condition. Polytech Messenger Eng Res Ser 4:151–156
11. Stadnik VV, Elistratov VV (2014) Renewable energy resources, Proceedings of the Main Geophysical Observatory A.I. Voeikova, 574, 179–223.
12. Ma JY, Luo Y, Liang H, Li SK (2011) Variation trend of direct and diffuse radiation in china over recent 50 years. Wuli Xuebao. 60(6):069601
13. Morozov MN, Strizhak PA (2016) Investigation of the influence of insolation heat input in order to improve the heat supply control system of the building. Ind Power Eng 2:52–57
14. Strebkov DS (2018) Prospects for the creation of a global solar energy system. Tech Oppon 1:14–23
15. Ghiaus C, Allard F, Santamouris M, Georgakis CF (2006) Nicol Urban environment influence on natural ventilation potential. Build Environ 4:395–406
16. Esenov A (1968) Development of residential neighborhoods in the cities of Central Asia. Hous Constr 6:2–6
17. Goromosov MS (1963) Microclimate of dwellings and its hygienic regulation. Medgiz, p 134
18. Giyasov AI, Barotov YuG (2018) Bioclimatic assessment of the territory of cities in the arid zone and its impact on the human condition. Sci Innov 2:223–230

Effectiveness of the Use of Instrumental Measuring Tools for Cadastral Surveying



Anna Osennyaya , Dmitry Gura , Sergey Samarin ,
and Daria Bespyatchuk 

Abstract This paper analyzes the application of geodetic equipment (electronic tacheometers and GPS) used in cadastral and land surveying work. The paper presents an analysis of the most common brands of tacheometers in Russia. The accuracy of these instruments was analyzed, and the use of tachometers was compared with the use of GNSS receivers. As a result of the study carried out in this scientific work, it was concluded that there is a need for legislative and methodological modernization of the requirements for cadastral surveys, first of all, in the preparation of technical plans.

Keywords Cadastral works · Land survey plan · Technical plan · Tacheometer · GNSS receiver · SDGs

1 Introduction

Preparation of cadastral documentation is the most important stage of cadastral surveying. As practical experience shows, most often a cadastral engineer is faced with the preparation of boundary and technical plans, the quality of which determines the state cadastral registration of real estate objects and the subsequent state registration of rights to them [1].

In most cases, the preparation of technical and boundary plans requires field geodetic survey. It is geodetic measurements that allow the cadastral engineer to obtain the coordinates of the characteristic points of the boundaries of land plots or the contours of capital construction objects (buildings, structures, parking lots, premises), from which such important characteristics as length, width and area are derived. It is the coordinates and the main characteristics arising from them that make it possible to individually identify the property, which is the main task of cadastral registration. Further, the coordinates and the above characteristics are entered into the Unified State Register of Immovable Property (hereinafter—USRIP), which, in

A. Osennyaya · D. Gura (✉) · S. Samarin · D. Bespyatchuk
Kuban State Technological University, Moskovskaya 2, 350072 Krasnodar, Russian Federation
e-mail: gurada@kubstu.ru

Fig. 1 Tacheometer from Leica Geosystems



turn, is the only legitimate source of information about all real estate objects located on the territory of the Russian Federation. Information taken from the USRIP is used in many related fields of activity, for example, when determining the cadastral value of real estate objects or in urban planning activities when issuing building permits. And if, for example, the USRIP indicates the wrong area of a real estate object, then this will inevitably lead to an incorrect calculation of the cadastral value, which, in turn, can lead to an unfair distribution of the tax burden on taxpayers and, of course, will negatively affect the economic situation in the country [1–3].

Therefore, the cadastral engineer must dutifully determine the coordinates, area and other characteristics of the real estate object. At the same time, it cannot be denied that the type of geodetic equipment used during cadastral work also affects the accuracy of calculating numerical data about a particular property. Field work can be carried out with various measuring instruments, the main of which are electronic tacheometers and GNSS receivers.

A tacheometer is a geodetic device that measures distances, vertical and horizontal angles. The tacheometer is used to determine coordinates, for topographic surveys, for location survey, etc. A photograph of the tacheometer is shown in Fig. 1.

2 Materials and Methods

This analysis was carried out according to the following components:

- Analysis of the use of tacheometers by the largest companies selling them in Russia;

- Analysis of the accuracy of tacheometers with the requirements for the accuracy of cadastral surveying;
- Comparative analysis of the quantitative prevalence of tacheometers with GNSS receivers.

The materials for this study were more than 50 scientific publications and about 400 boundary and technical plans for over the past 5 years.

3 Analysis of the Use of Tacheometers in Cadastral Surveying

Nowadays, tacheometers of the following manufacturers are most often used in Russia:

- Leica Geosystems;
- Sokkia;
- Topcon;
- Trimble.

Leica Geosystems is one of the giants in the market for the sale of geodetic equipment not only in Russia, but also in the world. The company was founded in Switzerland in 1921. The devices of this company have found wide application in carrying out engineering and geodetic surveys, monitoring the deformation of buildings and structures, and, of course, in carrying out cadastral surveys. In addition, Leica Geosystems representatives actively cooperate with Russian higher educational institutions, actively supplying them with tacheometers, Leica Geosystems laser scanners and GPS receivers. This, in turn, also increases the popularity of this brand among participants in the educational process.

Sokkia was founded in Japan at the beginning of the twentieth century. Nowadays, Sokkia is one of the main representatives in the market of geodetic equipment along with Leica Geosystems, especially in Russia. The main advantage of Sokkia over competitors is that this company is focused on the production of high-precision and technological devices. At the same time, in 2008, Sokkia and Topcon merged into one company, Topcon Sokkia. Despite the fact that Sokkia was acquired by Topcon, the equipment of this brand continues to enter the market and is quite popular.

Despite the fact that the American company Trimble Navigation is quite young compared to other giants in the market for the sale of geodetic equipment (it was founded in 1978). The company has found its place and clients in Russia and in the world. The main difference between Trimble Navigation and its competitors is that this company is more focused on the production of satellite surveying equipment than tacheometers. But at the same time, this brand produces very good quality tacheometers.

Like Sokkia, the Topcon brand was created in Japan in 1932. Today, this company (Topcon Sokkia) is a global holding in the market for the sale of geodetic equipment.

In addition to engineering and geodetic and cadastral surveys, Topcon total stations are widely used in the oil and gas industry, one can even say that this brand is a monopoly in this industry, especially in Russia.

Of course, each of these companies is a fairly large supplier of total stations in Russia. But at the same time, it cannot be said that each brand has the same market share in the sale of geodetic equipment. Infographics of the distribution of the use of tacheometers of these brands in the preparation of boundary plans is shown in Fig. 2 [1–6].

The diagram shows that Leica Geosystems tacheometers have become more widespread in the preparation of boundary plans.

In turn, the infographics of the operation of the tacheometers of the above companies in the preparation of technical plans is shown in Fig. 3.

Based on what is indicated in Fig. 3, it follows that the most widespread in the preparation of technical plans were the tacheometers by Leica Geosystems and

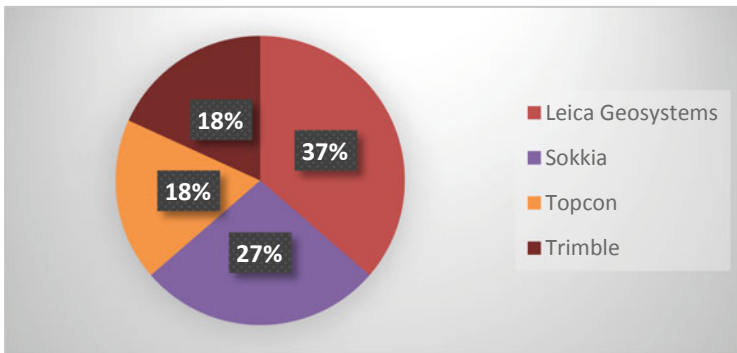


Fig. 2 Infographics of tacheometer application distribution by manufacturers

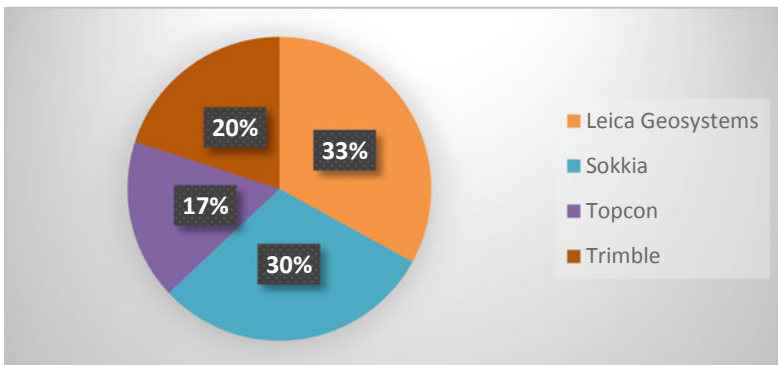


Fig. 3 Infographics of the distribution of the use of tacheometers in the preparation of technical plans by manufacturers of geodetic equipment

Sokkia. These diagrams (Figs. 2 and 3) were made on the basis of detailed study of 400 landmarks and technical plans for over the past 5 years. Each document identified the tools that were used to carry out the cadastral and land management work and the manufacturer of the used surveying equipment.

The above data allow concluding that none of the firms is a monopolist in the market of geodetic equipment, which, in turn, is a rather positive trend, since each of the firms has to “fight” for its client base. This does not allow these brands to diminish the quality of the produced equipment.

For a complete analysis of the use of geodetic equipment used in the preparation of boundary and technical plans, it is necessary to analyze their passport accuracy, because the more accurate the device, the less likely it is to incorrectly determine the quantitative characteristics of the real estate object. This part of the analysis was carried out among the geodetic equipment by Leica Geosystems, Sokkia, Topcon, and Trimble.

Since the strictest requirements for the accuracy of determining coordinates are imposed on the lands of settlements, the accuracy of the used tacheometers is compared with the requirements for this category of land. According to the Order of Federal Service for State Registration, Cadastre and Cartography of 23.10.2020 N P/0393 “On approval of the requirements for accuracy and methods for determining the coordinates of characteristic points of the boundaries of a land plot, requirements for accuracy and methods for determining the coordinates of characteristic points of the contour of a building, structure or an object of construction in progress on a land plot, as well as requirements for determining the area of a building, structure, room, parking lot”, the minimum accuracy with which the distance must be determined is $m_p = 10 \text{ cm}$ [7–9]. The root mean square error (hereinafter—RMS) with which it is allowed to determine the coordinates of the characteristic points of the land plot is calculated by the formula:

$$m_{x;y} = \frac{m_p}{\sqrt{2}} \quad (1)$$

According to calculations using (1), we find that the accuracy of determining the coordinates of the points of the boundaries of land plots of settlements should be at least 7 cm. It should also be noted that the accuracy of determining the coordinates can be calculated using the following formula:

$$m_p = \sqrt{m_{\text{mes}}^2 + m_{\text{in}}^2} \quad (2)$$

m_{mes} —RMS of the definition of a point relative to the state geodetic network;

m_{in} —RMS of the definition of the point relative to the point from which its survey was carried out;

Since in (2) $m_{\text{mes}} = m_{\text{in}}$, then the RMS of the point definition with respect to the state geodetic network is determined as follows:

$$m_{\text{mes}} = \frac{m_p}{\sqrt{2}} \quad (3)$$

Substituting $m_p = 10$ cm in (3), we find that the RMS of the point definition relative to the state geodetic network is 7 cm.

In this case, for tacheometers, m_{meas} are calculated by the formula:

$$m_{\text{mes}} = \sqrt{m_{\text{et}}^2 + m_{\text{ps}}^2} \quad (4)$$

where,

m_{et} —RMS of the point, which depends on the accuracy of determining the coordinates of the laid traverse.

m_{ps} —RMS of the point, which depends on the method of determining the coordinates.

Since $m_{\text{et}} = m_{\text{ps}}$, then m_{ps} is determined by the formula:

$$m_{\text{ps}} = \frac{m_{\text{mes}}}{\sqrt{2}} \quad (5)$$

When carrying out calculations in (5), we find that the RMS of a point, which depends on the method of determining the coordinates, is 5 cm. It is also possible to calculate m_{ps} using the following formula

$$m_{\text{ps}} = \sqrt{m_d^2 + \left(\frac{d}{\rho''}\right)^2 * m_\beta^2} \quad (6)$$

where,

ρ'' —206,265", (const.);

d —100,000 mm (const.);

m_β —RMS of the angle calculation.

At the same time, m_d from (6) can be represented as:

$$m_d = \frac{m_{\text{ps}}}{\sqrt{2}} \quad (7)$$

Since for the subsequent analysis of the accuracy of the tacheometers used for performing cadastral survey, it is necessary to find out the RMS of the angle calculation m_β based on (6), and when substituting (7) into (6), we obtain the following formula:

$$m_\beta = \frac{m_{\text{ps}} * \rho''}{\sqrt{2} * d} = \frac{5 * 206265}{\sqrt{2} * 100000} = 5'' \quad (8)$$

Based on the above calculation cycle, it is possible to find that the RMS of the angle calculation is 5". Since the requirements for the accuracy of determining distances

and coordinates are too low, especially for tacheometers, therefore, the comparison of the used tacheometers and the required standard deviation is carried out only in terms of the accuracy of determining the angles.

The general infographics of the passport accuracy of the geodetic equipment used in the preparation of boundary plans is shown in Fig. 4.

Based on the information presented in Fig. 4, it follows that most often tacheometers with a passport accuracy of 5'' are used to prepare boundary plans.

The infographics for technical plans are shown in Fig. 5.

Based on Fig. 5, it can be said that when preparing technical plans, tacheometers with a passport angular accuracy of 5'' are mainly used. And at the same time, it should be noted that the average passport angular accuracy with which tacheometers are used in the preparation of boundary and technical plans is quite optimal. But if you have to use a tacheometer with an accuracy of less than 5'', then you need to lay more stations on the theodolite traverse. The image of the laid traverse is shown in Fig. 6.

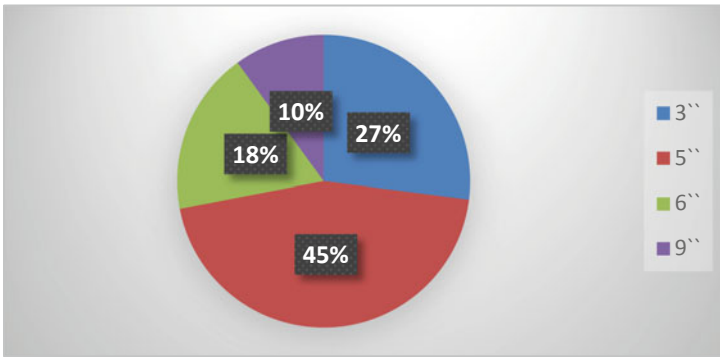


Fig. 4 Infographics of the passport accuracy of tacheometers in the preparation of boundary plans

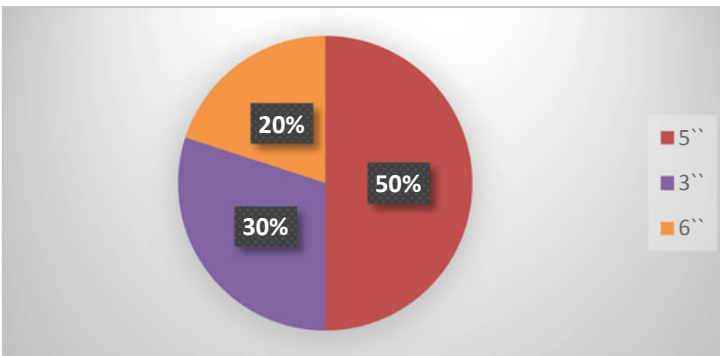


Fig. 5 Infographics of the passport accuracy of tacheometers in the preparation of technical plans

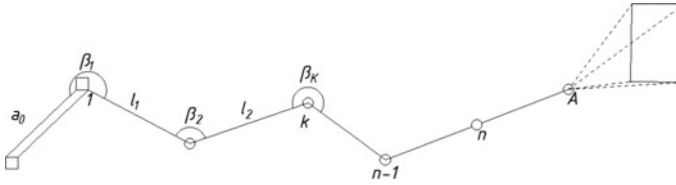


Fig. 6 Image of the laid traverse

Fig. 7 GNSS receiver



For a complete analysis of the use of tacheometers, it is necessary to make a comparison with another popular geodetic device—a GNSS receiver. A satellite receiver is a radio receiver for determining the geographic coordinates of an object. And of course, after determining the coordinates, it is possible to calculate the area, length and width of the object. An image of the GNSS receiver is shown in Fig. 7.

As for the comparison of the quantitative characteristics of the prevalence of the use of GNSS receivers and tacheometers, the diagram of the use of GNSS receivers and tacheometers in the preparation of boundary and technical plans is shown in Fig. 8 [7–10].

Based on the information shown in Fig. 8, it should be noted that on the territory of Russia, GNSS receivers are more common than tacheometers.

4 Results and Discussion

An analysis of the use of tacheometers by manufacturer and by accuracy, carried out in the third section of the paper, shows that there are no negative trends in these points. Comparing the frequency of use of tacheometers and GNSS receivers, it can be concluded that tacheometers are less widespread, especially when preparing

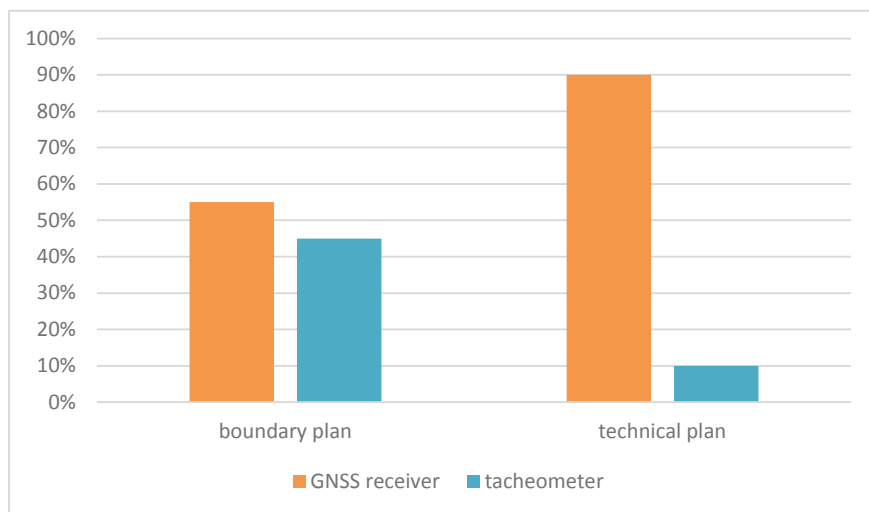


Fig. 8 Comparative diagram of the use of tacheometers and GNSS receivers in the preparation of boundary and technical plans

technical plans. This is primarily due to the fact that receivers are easier to operate and cheaper than tacheometers. It should also be emphasized that when carrying out cadastral survey using GNSS receivers, the maximum duration of measurements is 10 h. When working with tacheometers, the total time of field work can reach up to 20 h. It should be noted that for the ease of use, cadastral engineers have to pay with the accuracy of determining the coordinates, because of this, in turn, the quality of the work performed decreases. Since there are quite strict standards for the accuracy of determining the coordinates of a land plot, GNSS receivers are not so widespread in the preparation of boundary plans as in the preparation of technical plans. When preparing technical plans, GNSS receivers have become widespread because there are no permissible errors anywhere in the current legislation in determining the coordinates of buildings, structures, capital construction facilities, parking lots and premises. Presumably, the reason is that there is no big difference where exactly the object will be located, because it is located inside the same land plot, which means that the owner should not have questions about the quality of determining the location of the property. Obviously, this is not the correct policy, especially since currently, mainly high-rise buildings are being built in Russia, and the receiver signal may not be initialized within the corner of the object and even at a considerable distance from it, especially if it is a very tall building. This factor contributes to an even greater decrease in the accuracy of determining the coordinates of the object [10–15].

5 Conclusions

As a result, it should be noted that at the moment, there are big problems in the preparation of technical plans for real estate objects on the territory of Russia, because in 9 out of 10 cases GNSS receivers are used for cadastral work in relation to buildings, structures, capital construction facilities, parking lots, and premises. This, in turn, leads to the fact that the USRIP may contain incorrect information about these objects, which is fraught with negative consequences. This problem can be solved either by establishing permissible errors in determining the coordinates of objects for which a technical plan is being prepared, or by prohibiting the use of GNSS receivers in relation to high-altitude objects, i.e. it is necessary to improve legislation on this issue. The above measures will improve the quality of cadastral surveying in Russia and reduce the likelihood of incorrect information about real estate objects in the USRIP.

References

1. Alfaro P, Sánchez-Alzola A, Martín-Rojas I, García-Tortosa FJ et al (2021) Geodetic fault slip rates on active faults in the Baza sub-Basin (SE Spain): insights for seismic hazard assessment. *J Geodyn* 144:101815. <https://doi.org/10.1016/j.jog.2021.101815>
2. Liu Q, Zhang Sh (2021) An improved sea level retrieval method using the differential evolution of GNSS SNR data. *Adv Space Res* 67(3):975–984. <https://doi.org/10.1016/j.asr.2020.10.050>
3. Jincheng L, Tauheed UKh, Zhengang N, Qiang Y, Zhongke F (2021) Calibration and precise orientation determination of a gun barrel for agriculture and forestry work using a high-precision total station. *Measurement* 173:108494. <https://doi.org/10.1016/j.measurement.2020.108494>
4. Jianguo Z, Henglin X, Weiwei J, Wenfeng B, Guanlan L (2020) Automatic subway tunnel displacement monitoring using robotic total station. *Measurement* 151:107251. <https://doi.org/10.1016/j.measurement.2019.107251>
5. Klausner F, Pauschinger D (2021) Entrepreneurs of the air: sprayer drones as mediators of volumetric agriculture. *J Rural Stud* 84:1–9
6. Osennaya A, Khakhuk B, Sokolova Y, Husht N (2019) Town-planning value of territory as the basis of the evaluation of zoning when conducting cadastral valuation of real estate. In: *E3S web of conferences*, vol 110, P 02121
7. Gura D, Markovskii I, Khushht N, Rak I, Pshidatok S (2021) A complex for monitoring transport infrastructure facilities based on video surveillance cameras and laser scanners. *Transp Res Proc* 54:775–782
8. Shkorkina I, Chubyr N, Gudza V, Urtenov M (2020) Analysis of the theoretical current-voltage characteristic of non-stationary transport in the cross-section of the desalination channel. In: *E3S web of conferences*, vol 224 P 02015
9. Shevchenko GG, Bryn MJ, Afonin DA, Gura DA (2020) Experimental researches in defining deformations by free station method and results processing by search method. *Lect Notes Civ Eng* 50:163–175
10. Gura DA, Pavlyukova AP, Solodunov AA (2020) Updating the algorithm for processing laser scanning data using linear objects as an example. In: *IOP conference series: materials science and engineering*, vol 913, no 4, P 042041
11. Atroshchenko VA, D'yachenko RA, Kichkar IYu (2020) Results of modeling relay control of motors of a vibrating screen drive system in the phase plane. *Chem Petrol Eng* 56(3-4): P 223–229

12. Zámečníková M, Neuner H (2018) Methods for quantification of systematic distance deviations under incidence angle with scanning total stations. *ISPRS J Photogr Remote Sens* 144:268–284. <https://doi.org/10.1016/j.isprsjprs.2018.07.008>
13. Shevchenko G et al (2019) The evaluation of the contractor's risk in implementing the investment projects in construction by using the verbal analysis methods. *Sustainability* 11(9):2660. <https://doi.org/10.3390/su11092660>
14. Bannikov A, Gordeev V (2020) The accuracy improvement of angular measurements by the means of systematic errors models incorporating. In: International multidisciplinary scientific geoconference surveying geology and mining ecology management, SGEM, 2020-August (2.2)
15. Madjid A, Saeed A, Alireza A-S (2019) Geodetic calibration network for total stations and GNSS receivers in sub-kilometer distances with sub-millimeter precision. *Measurement* 141:258–266. <https://doi.org/10.1016/j.measurement.2019.04.044>

Tensoresistor-Based Microfluidics and Telemetric Strain-Gauge Lens-Less Detectors as Specialized Labs-on-a-Chip for Soil Mechanics and Foundation Monitoring



Feodor Orekhov  and Oleg Gradov 

Abstract A current trend in the development of the applied measuring techniques is the design of integrated analytical systems on a chip, in particular, labs on a chip based on various physical principles of the substance analysis. Recently, the term “lab-on-a-chip” implied analytical microsystems, requiring macro-scopic readers for the data obtained, which strongly limited the possibilities of their introduction into the field studies and routine analytical measurements. However, a progress in the design of telemetric labs on a chip, including those capable of broadcasting the analytical signal to the receivers with positional sensitivity provided by the use of the labeled counting chambers, made it possible to use such devices beyond the scientific laboratories: in the field practice or in monitoring of the natural systems and artificial structures. This can be applied not only to the chemical and biological field measurements, but also to the mechanics, in particular, to geomechanics or soil mechanics. This work briefly considers the results obtained in the Russian laboratory of the second author during the period up to 2011–2013, which have not been published earlier due to the know-how restrictions.

Keywords Tensoresistor · Strain gauge · Civil engineering · Soil mechanics · Lens-less microscopy · Soft matter microfluidics · Foundation monitoring · Telemetry

1 Introduction

Microfluidic devices and lab-on-a-chip-like systems and topologies are known to be very useful for micromechanical measurements. They can be applied for solving of different problems in physico-chemical mechanics, such as monitoring of the effect of interfacial tension on the droplet formation [1]/interfacial tensiometry [2, 3] and estimation of different surface tensions on a wettability gradient surface [4]; pressure drop measurement [5, 6]; integrated temperature and pressure sensing [5, 7]; monitoring/analysis of microhydrodynamic microcurvilinear flow effects in some

F. Orekhov (✉) · O. Gradov
N.N. Semenov Institute of Chemical Physics, Kosygina str. 4, Moscow 119991, Russia

processes on the chips [8], including biological ones [9]; real time force or pulse sensing and regulation, including biomimetic, biosynthetic and bio-artificial ones [10–12], etc. Biological or biomedical applications of mechanical measurements are also very “wide-field” on the cellular/tissue formation level [13–17]. Such measurements are usually based on the elastic microfluidics, including elastomeric one (which can be applied not only for biomicrofluidic aims [18, 19]). Contemporary studies in this field are complex and multi-disciplinary. For example, in some works, microfluidic micro-pipette aspiration microdevice is used for the study of the single-cell mechanics inspired by the principle of the Wheatstone bridge [20].

Similar principles can be implemented not only at the cellular level biomechanical measurements, but also in different micromechanical and mesomechanical studies. It is well known, that Wheatstone bridge is widely used in mechanical/tensometric measurements using strain gauges/tensoresistors, including elastomeric/foil-based ones (including those used in situ in polymerization and extrusion processes). The above examples can be found in the “multiplexed” old literature on tensoresistors [21–32]. This fact is the prerequisite for realization of microfluidic-based/lab-on-a-chip-based tensoresistor measurement systems and structures, usable in wet conditions (soils, foundations or buried archaeological/architectural building fragments), such as standard open microfluidics, or for integration of the standard tensoresistors with microfluidic/optofluidic data acquisition/control schemes. We have previously proposed to use mesofluidic labs-on-a-chip for biogeochemical monitoring of non-standard greenhouse soils and grounds [33] based on telemetric broadcasting of position-sensitive signals from lensless microscopes. Similar methods can be applied for studying of the different mechanical processes (including evaluation of the disjoining pressure and the start of registration of the phractographic processes in real time, as well as freezing and thawing accompanied by expansion and contraction on a chip, as in cryoscopic osmometers). In this case, the functions of microfluidic channels can be performed by the boundary topology of the foil tensoresistor. In this work, we illustrate the possibility of lensless-telemetric monitoring of the tensoresistor state - up to its physical destruction.

2 Materials and Methods

A setup used in this study consisted of a deformable tensoresistor fixed on the filter surface of the lens-less CMOS array. Visualization results were transmitted to the computer via the universal serial bus after processing at the PCB (printed circuit board) level. On the basis of the densitometry maps (bitmap), three-dimensional reconstructions were built using 3D Field Pro software. Annotations to the latter, including the experimental conditions, were introduced into the output file metadata. In some cases, depending on the network configuration, digital data transmission over a radio frequency channel was used. In the early versions of the experiment (until 2012), analog data transmission through the receiver until the stage of the video signal digitization was also applied.

3 Results

The main results obtained are shown in the illustrations. The original planar 2D micrograph obtained from the lensless microscope is shown in Fig. 1-a. Its isophote/isoopaque map is given in Fig. 1-b. Shadow relief based on Lommel-Seeliger photometric model application is provided on the Fig. 2-a. A corresponding 3D map of the optical beam transmission is given in Fig. 2-b, while the corresponding 3D absorption map (by optical density) is given in Fig. 2-c.

In the case of accounting for the small contaminants and the medium to which the strain gauge is adhered, we need to estimate their absorption (up to the NIR region) in order to characterize the inhomogeneity of the experimental medium, which acts almost like a “filled composite”. This inhomogeneity is shown in Fig. 3-a (in pseudocolors) and Fig. 3-b (in pixelized monochromatic shadow reliefs).

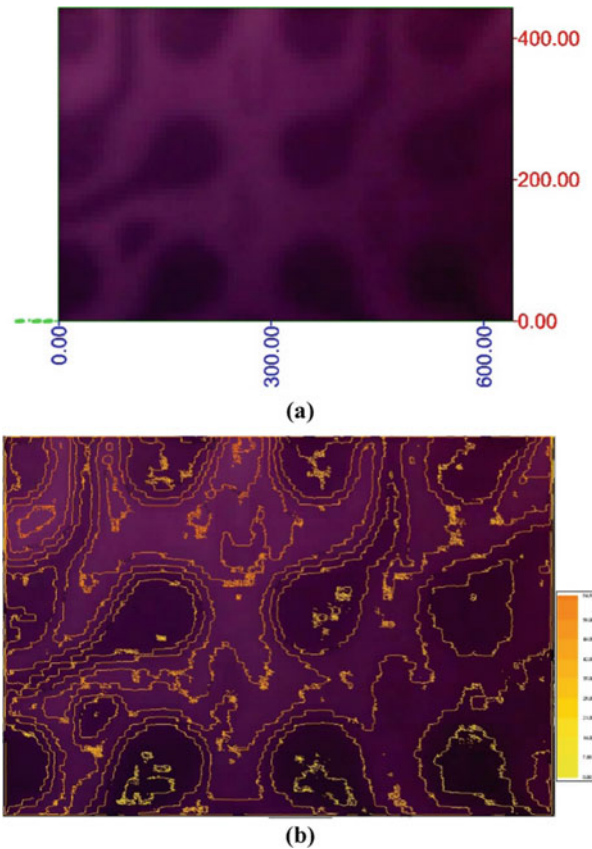


Fig. 1 a. Lens-less micrograph of a tensorresistor layer. b. Isoline representation of photo/densitometric map of the bitmap (a)

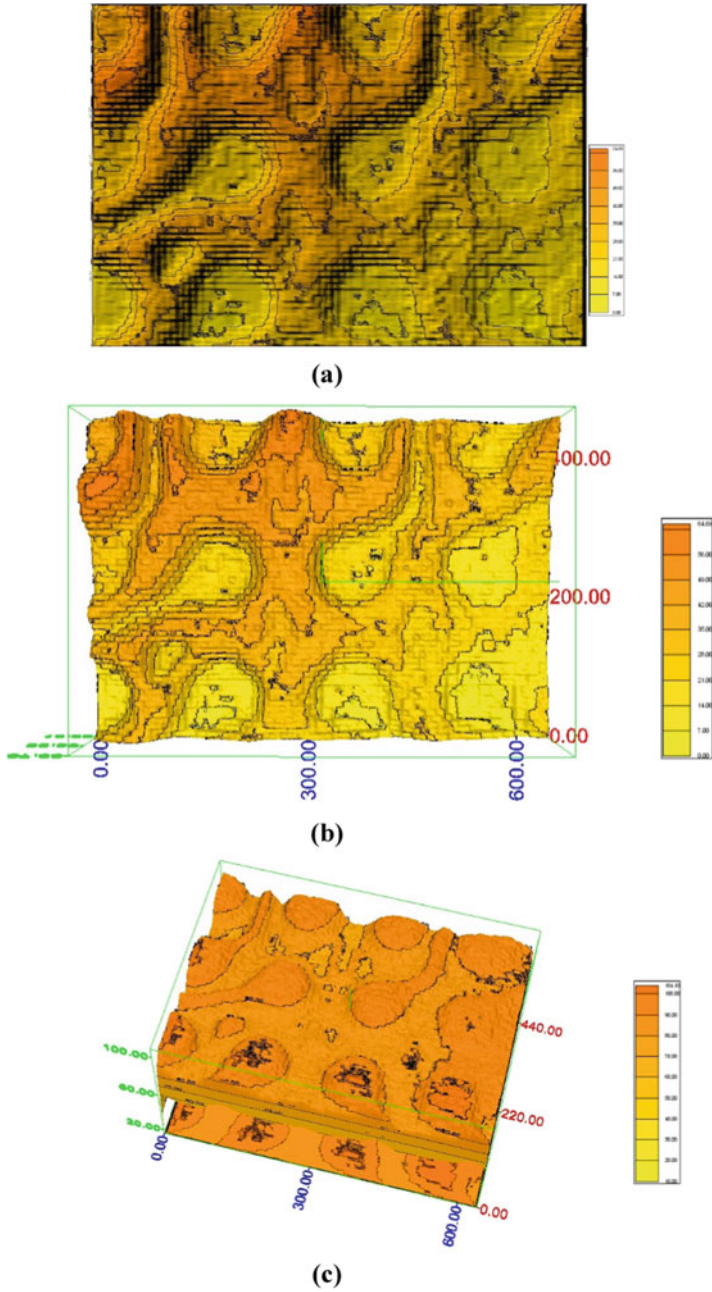


Fig. 2 a. Shadow relief of the foil tensoresistor (Lommel-Seeliger model; 135°). b. 3D map of the transmission levels of the optical beam for the microstructure. c. 3D map of the absorption levels (by optical density) of the tensoresistor microstructure

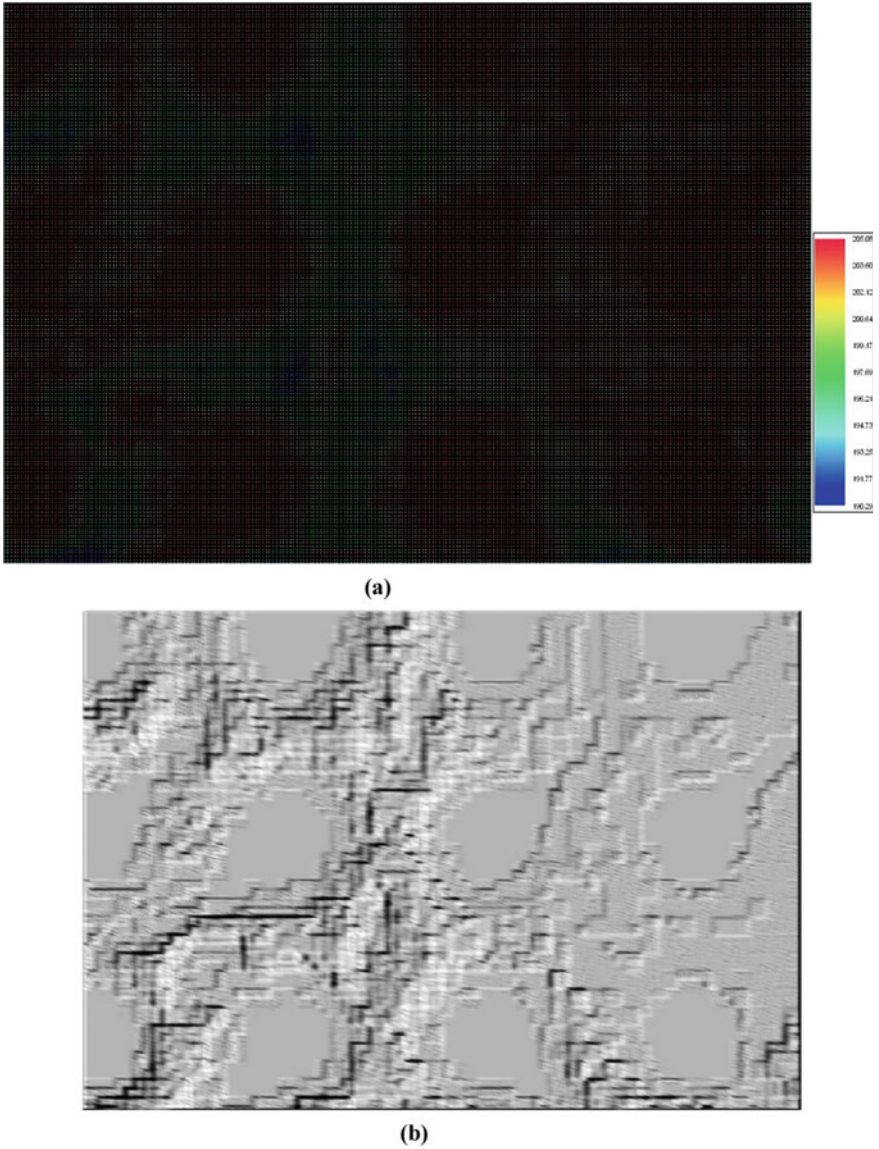


Fig. 3 **a.** “Thermal map”, which can be used for visualization of the microinclusions and inhomogeneities of the natural medium (e.g., soil) or experimental media (e.g., adhesive or glues). **b.** Distortion of isophotes due to the presence of the medium and its granularity around the foil channels

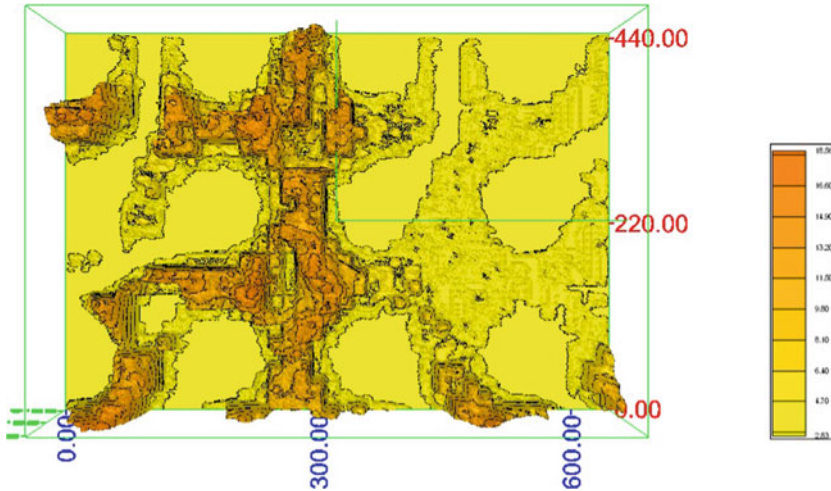


Fig. 4 Changes in the contours of the medium which is in contact with the tensoresistor channels after its fine deformation

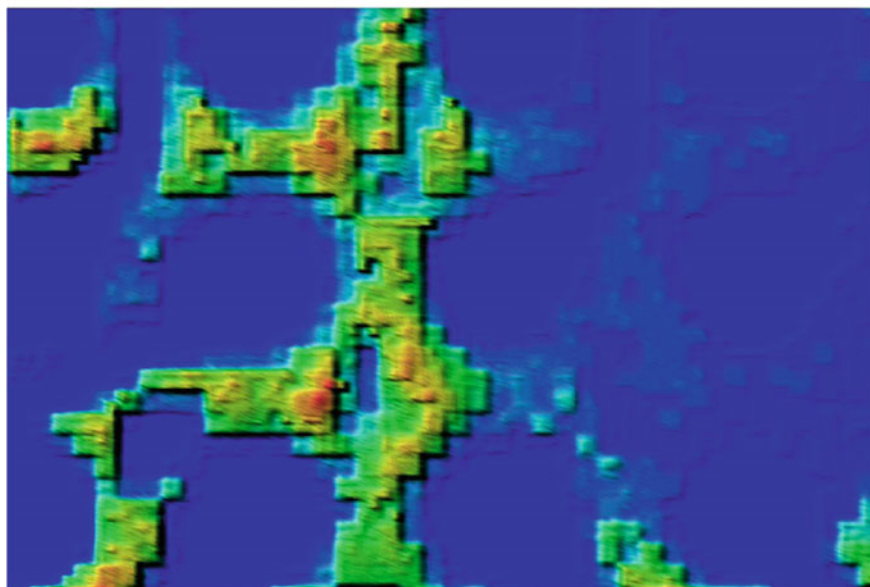
Any mechanical distortions can be estimated from the distortions of the contours of the boundary between the geometry/topology of the foil structures of tensoresistor and the medium located inside them (either experimental or native). This point is illustrated in 3D in Fig. 4. However, it can be seen that in some cases photometric information is not completely reliable, since with a low contrast/gradient or low intensity of the photometric signal in the area of accumulation of a large number of particles or a high concentration of the substance, the device applies binning - integrating the signal from several pixels. In some cases, it can be a source of metrological artifacts, but such failures can be detected, as it is shown in Fig. 5, and, therefore, this source of artifacts can be successfully eliminated.

4 Discussion

The operation of tensoresistors is based on the well-known strain effect when the materials change their electrical resistance upon deformation. The resistance of either a conductor or a semiconductor depends on its length. In the case of a mechanical action on a conductor, a change in its resistance is caused by a change in its length, cross-sectional area or resistivity. The ratio of the change in the active resistance of tensoresistors to the relative deformation that caused the above change is called sensitivity, calculated using the Poisson coefficient. Therefore, being able to evaluate the changes in the length/geometry of the conductor on a foil tensoresistor using a lensless contact microscope, one can analyze the sensor deformations and the resistance changes in correlation. To measure the mechanical stress of the material,



(a)



(b)

Fig. 5 a. Determination of the geometric boundaries of the pixel binning in the case of insufficient microphotometric/microdensitometric information: a) isophote map. **b.** Determination of the geometric boundaries of the pixel binning in the case of insufficient microphotometric/microdensitometric information: a); b) its representation of the isophote map (a) in pseudocolors



Fig. 6 An example of a visual optical mechanical displacement sensor for the construction tasks, known since the nineteenth century. Application of lensless microscopes with tensoresistive contact elements makes it possible to increase the sensitivity of optical detection by 3–4 orders of magnitude. Open source of the image: Wikimedia

a tensoresistor is glued along the axis of action of this stress. Its surface can be simultaneously examined by a CCD sensor or CMOS array which is in contact with it.

The possibility of morphometric assessment of epy deformation from the projections of the tensoresistor to the CCD sensor or CMOS array at different time points allows us to speak about the replacement of the old optical types of mechanical sensors well-known since the nineteenth century (for example, such as shown in Fig. 6) by the proposed tensoresistor-based lens-less analyzers. Due to the micron/submicron pixel sizes used in contact measurements, the measurement sensitivity and accuracy is expected to be improved up to the level required for the integrated strain array for cytological and mechanomicrobiological measurements [34]. In some cases, the geometry of the tensoresistor channels itself can contribute to the signal, being a diffraction grating or a ptychographic transducer [35–40] with a variable scale of the structure regularity.

Acknowledgements The authors are grateful to Gradova M.A. for the assistance in translation and proof-reading of the text.

References

1. Peng L, Yang M, Guo S-S, Liu W, Zhao X-Z (2011) The effect of interfacial tension on droplet formation in flow-focusing microfluidic device. *Biomed Microdevice* 13(3):559–564

2. Cabral JT, Hudson SD (2006) Microfluidic approach for rapid multicomponent interfacial tensiometry. *Lab Chip* 6(3):427–436
3. Tsai SS, Wexler JS, Wan J, Stone HA (2013) Microfluidic ultralow interfacial tensiometry with magnetic particles. *Lab Chip* 13(1):119–125
4. Yeh S-I, Fang W-F, Sheen H-J, Yang J-T (2013) Droplets coalescence and mixing with identical and distinct surface tension on a wettability gradient surface. *Microfluid Nanofluid* 14(5):785–795
5. Ko HS, Gau C (2011) Local heat transfer process and pressure drop in a micro-channel integrated with arrays of temperature and pressure sensors. *Microfluid Nanofluid* 10(3):563–577
6. Riaud A, Tostado CP, Wang K, Luo G (2013) A facile pressure drop measurement system and its applications to gas–liquid microflows. *Microfluid Nanofluid* 15(5):715–724
7. Ko HS, Gau C (2011) Microscale thermal fluid transport process in a microchannel integrated with arrays of temperature and pressure sensors. *Microfluid Nanofluid* 10(4):793–807
8. Cheng C-M, Kim YT, Yang J-M, Leuba SH, LeDuc PR (2009) Dynamics of individual polymers using microfluidic based microcurvilinear flow. *Lab Chip* 9(16):2339–2347
9. Liang P-S, Yoon J-Y (2013) Optofluidic lab-on-a-chip monitoring of subsurface bacterial transport. *Biol Eng Trans* 6(1):17–28
10. Chang DS, Langelier SM, Zeitoun RI, Burns MA (2010) A Venturi microregulator array module for distributed pressure control. *Microfluid Nanofluid* 9(4–5):671–680
11. Doll JC et al (2009) SU-8 force sensing pillar arrays for biological measurements. *Lab Chip* 9(10):1449–1454
12. Lucarotti C, Oddo CM, Vitiello N, Carrozza MC (2013) Synthetic and bio-artificial tactile sensing. *Rev Sens* 13(2):1435–1466
13. Moraes C, Wyss K, Brisson E, Keith BA, Sun Y, Simmons CA (2010) An undergraduate lab (on-a-chip): probing single cell mechanics on a microfluidic platform. *Cell Mol Bioeng* 3(3):319–330
14. Guido I, Xiong C, Jaeger MS, Duschl C (2012) Microfluidic system for cell mechanics analysis through dielectrophoresis. *Microelectron Eng* 97:379–382
15. Dahl JB, Lin JM-G, Muller SJ, Kumar S (2015) Microfluidic strategies for understanding the mechanics of cells and cell-mimetic systems. *Annu Rev Chem Biomol Eng* 6:293–317
16. DeCortin ME, Brass LF, Diamond SL (2020) Core and shell platelets of a thrombus: a new microfluidic assay to study mechanics and biochemistry. *Res Pract Thromb Haemost* 4(7):1158–1166
17. Pinon L, Pineau J, Montel L, Mesdjian O, Pierobon P, Fattaccioli J (2020) Oil-in-water emulsion droplets and microfluidic tools to study B cells polarization and mechanics of immunological synapse. *Biophys J* 118(3):321a
18. Zhang B, Dong Q, Korman CE, Li Z, Zaghoul ME (2013) Flexible packaging of solid-state integrated circuit chips with elastomeric microfluidics. *Sci Rep* 3:1098
19. Vyawahare S, Sitaula S, Martin S, Adalian D, Scherer A (2008) Electronic control of elastomeric microfluidic circuits with shape memory actuators. *Lab Chip* 8(9):1530–1535
20. Li YJ et al (2019) A microfluidic micropipette aspiration device to study single-cell mechanics inspired by the principle of Wheatstone bridge. *Micromachines* 10(2):131
21. Borshchevskii SP, Chubrik SS (1976) Method of designing diaphragm-type tensoresistor pressure transducers. *Meas Tech* 19(7):991–994
22. Daichik ML, Lakin YG, Polyakov AL, Fetisov BV (1978) Using strain gauges in a reactor experiment. *Strength Mater* 10(5):611–614
23. Kozlov IA, Leshchenko VM, Petrov AA, Potapova VF, Tatarchuk NI (1978) Methods to protect tensoresistors used in phenol formaldehyde resin medium during polymerization. *Strength Mater* 10(6):736–738
24. Ignatov AV, Lukashik VF, Volchek AV, Fal'ko II, Shelomanova AA, Kuznetsova AF, An-tipova NB, Makova AI (1979) Tensoresistors for measurement devices. *Meas Tech* 22(11):1367–1370
25. Beklemishchev AI, Blokin-Mechtaln YK, Vlasenko VM, Alekseenko VA (1980) Apparatus for the measurement of signals from tensoresistive pressure transducers. *Meas Tech* 23(3):230–233

26. Galzman EG, Vulikhman LM, Semenyuk VF (1985) Reversible force sensor with spirally wound tensoresistors. *Meas Tech* 28(7):644–645
27. Khatuntsev EA (1986) Characteristics of tensoresistors. *Meas Tech* 29(7):643–645
28. Nekhendzi EY (1987) Point and interval evaluation of the errors of tensoresistors and of the results of strain measurements. *Meas Tech* 30(8):787–791
29. Dubov BS, P'yanzin GI, Kopytin NM, Samsonova VN, (1989) Metrological investigation of tensoresistor dynamometers. *Measur Tech* 32(1):57–60
30. Barmushkin AA, Troshin VP, Il'in YM (1991) Influence of stress concentrators on the stressed-strained state of a tubular elastic element in a tensoresistor force sensor. *Meas Tech* 34(1):45–47
31. Antonets EV, Bragin GE, Fadeeva TS (1992) Minimizing the temperature effect on the characteristics of a tensoresistive pressure gauge. *Meas Tech* 35(1):83–88
32. Patokin EV (1993) Testing foil tensoresistors in the vicinity of elastoplastic deformations. *Meas Tech* 36(4):393–397
33. Gradov OV (2012) Monitoring of nonstandard greenhouse soils. *Greenhouse Land* 5:43–46
34. Simmons CS et al (2011) Integrated strain array for cellular mechanobiology studies. *J Micromech Microeng* 21:054016–054025
35. Guo K, Dong S, Nanda P, Zheng G (2015) Optimization of sampling pattern and the design of Fourier ptychographic illuminator. *Opt Express* 23:6171–6180
36. Ou X, Horstmeyer R, Yang C, Zheng G (2013) Quantitative phase imaging via Fourier ptychographic microscopy. *Opt Lett* 38:4845–4848
37. Tian L, Liu Z, Yeh LH, Chen M, Zhong J, Waller L (2015) Computational illumination for high-speed in vitro Fourier ptychographic microscopy. *Optica* 2:904–911
38. Bian L, Suo J, Zheng G, Guo K, Chen F, Dai Q (2015) Fourier ptychographic reconstruction using Wirtinger flow optimization. *Opt Express* 23:4856–4866
39. Godden TM, Suman R, Humphry MJ, Rodenburg JM, Maiden AM (2014) Ptychographic microscope for three-dimensional imaging. *Opt Express* 22:12513–12523
40. Bian Z, Dong S, Zheng G (2013) Adaptive system correction for robust Fourier ptychographic imaging. *Opt Express* 21:32400–32410

An Approach to Assessing Construction Enterprise Intellectual Capital in the Digital Age



Oksana Pirogova , Vladimir Plotnikov , and Agakhanum Yusufova 

Abstract In the context of the development of the digital economy, the intellectual assets of enterprises play a significant role in the formation of value. The paper analyses the main problems of identification, assessment, and management of the intellectual capital of a construction enterprise. The features of intellectual capital are considered, and it is shown that it is formed from intangible unidentified assets, which are characterized by a low level of consolidation, a high level of investment risk and, as a consequence, a high required rate of return, as well as non-marketability, closed transactions with such assets, which complicates the market valuation of such assets. Based on the analysis of assessment methods, it is substantiated that scoring methods are applicable only for solving problems of identification and assessment of relative dynamics. Management of intellectual capital requires a comparison of the costs and benefits of investments in intangible assets of an enterprise, which in turn requires the use of valuation of intellectual capital and its elements. The currently proposed residual profit models do not consider the financial aspects of investing in intellectual capital. A high proportion of intellectual capital can lead to an increase in the weighted average capital cost rate and a decrease in the residual profit. The paper proposes a modification of the model, which considers the financial characteristics of the activities of enterprises with a high level of intellectual capital.

Keywords Construction enterprise · Intellectual capital · Digital transformation · Digital economy

O. Pirogova

Peter the Great St. Petersburg Polytechnic University, 29 Polytechnicheskaya str.,
195251 St. Petersburg, Russia

V. Plotnikov (✉)

St. Petersburg State University of Economics, 21 Sadovaya str., 191023 St. Petersburg, Russia

Southwest State University, 94 50 let Oktiabria str., 305040 Kursk, Russia

A. Yusufova

Dagestan State Technical University, 70 Imam Shamil av., 367026 Makhachkala, Russia

1 Introduction

Currently, digital transformation is one of the main modern trends in all areas of activity. The acceleration of digital change is also seen in the economy. The term “digital economy” does not have an unambiguous and generally accepted interpretation. Various researchers, private and government agencies classify different types of economic activities in this sector. The digital sector of the economy includes independent “digital” types of economic activity. Their economic activity is considered in official statistics and analysed by researchers as “digital”, so they include the production of computers and other similar equipment, telecommunications services, software, etc. These are the types of economic activities for which digital technologies are the main ones, i.e., without digitalization, these types of economic activities cannot be carried out. Their progress is directly related to innovations in the field of digitalization [1].

In addition, the types of economic activities are distinguished where the use of digital technologies is complementary. For example: the use of digital navigation, control, and other systems in cars [2]; the use of digital equipment for diagnostics in medicine [3], etc. Digital technologies play an important role in construction. Construction is a traditional industry. This industry uses, as a rule, traditional technologies. The analysis showed that digital advances are gaining importance here, too [4, 5].

An analysis of empirical data (on the example of China) showed that the economic performance of construction enterprises is largely determined by their intellectual capital [6]. These businesses must increase their investment in intellectual capital. The success of investments in the intellectual capital of construction enterprises is associated with the exchange of knowledge and innovative activity. Therefore, these problems should be solved by the management of construction companies jointly.

In modern conditions, construction is becoming a science-intensive type of economic activity [7]. This leads to an increase in the strategic importance of knowledge for construction contractors and requires the accumulation of intangible assets in the form of intellectual capital. Research into the relationship between intellectual capital and productivity in contracting construction enterprises has highlighted the importance of research and operations innovation in the industry. These innovations prioritize the development of the intellectual capital of construction enterprises.

The correlation between intellectual capital and construction business productivity is supported by empirical evidence from Taiwan [8]. Construction managers are encouraged to pay more attention to the accumulation of intellectual assets. The construction industry has traditionally been perceived as capital and labour intensive. Simulations have shown that this industry has a high intellectual capitalization. In terms of the development of intellectual capital, construction enterprises are comparable to high-tech industries.

The formation and development of intellectual capital requires effective knowledge management [9]. In the area under consideration, this management is cross-cutting. It integrates such types of economic activity as architecture, design, construction. To be effective, businesses in this sector are encouraged to use three types of knowledge management models (knowledge sharing; knowledge fostering; organizational and social value creation). In doing so, one should consider: the capabilities of individuals, groups and organizations in the sector; ICT evolution and adoption models; philosophy of construction management. The competitiveness of a business with this approach depends on social networks, social capital, intellectual capital, and technological assets.

In the types of economic activities under consideration, the main value for consumers is created during the implementation of traditional technological processes (production, marketing, logistics, etc.) and in this case, the use of digital technologies radically improves the organization of these processes, gives them new properties. Thus, the use of digital technologies in the economic activity of economic entities changes the quality of their human and intellectual capital, because of which the cost of such enterprises increases [10]. As a result, the efficiency of enterprises' activities begins to depend largely on the level of development of their intellectual capital.

The concept of intellectual capital arose due to the need to explain the effects of generating benefit and increasing the total value of an enterprise through mechanisms and levers that lie outside the traditional financial plane. It turned out that within the framework of the value concept it is impossible to give a full explanation of these phenomena. This led to the emergence of the concept of "intellectual capital"—a new construct, or economic category, which was entrusted with the mission of explaining why some companies are more successful and their value grows faster than others [11].

The purpose of this study is to develop a modification of the method for assessing the intellectual capital of companies CIV, proposed by Stewart, based on the residual profit method. The authors suggest using this method for construction enterprises.

2 Materials and Methods

The study of intellectual capital is a new direction in enterprise management. The problem of its assessment is related to the fact that there is no unified methodology for assessing and measuring intellectual capital, and the current reporting does not allow for real assessment of intellectual assets. Research into the phenomenon of intellectual capital has shown that it has a complex internal structure and consists of the following elements: human, organizational, and relational capital. These components of intellectual capital are interconnected by deep internal connections and the allocation of individual components, as well as assessing the impact of some components of intellectual capital on other components is currently significant difficulties.

In the works [12] it is shown that changes in the elements of intellectual capital, such as human capital, can lead to changes in other components.

According to Lev [13], the emergence of the term “intellectual capital” is one of the most important economic events of the late XX and early XXI century. This attitude is due to the observed significant gap between the carrying and market value of corporate securities.

The generally accepted approach is that intellectual capital represents a portion of assets that are difficult to identify. For some of the intellectual capital, there are currently methods of identification, accounting, and depreciation, i.e., they become full-fledged assets in the traditional sense of this economic term. However, the other part, which is often more significant, is non-identifiable, i.e., there are no generally accepted legal methods for identifying the valuation, accounting, and depreciation of these assets. The ratio between different types of assets, as well as the ratio of the company’s assets to capital is shown in Fig. 1 [14].

A distinctive feature of intellectual capital is two features: the difficulty of retention, as well as non-marketability. Intellectual assets are difficult to retain under the influence of competitors, the market is saturated with analogous goods, employees and managers can move to another company, taking with them human capital, part of which was formed at the enterprise. Legally, apart from the rights to patents, trademarks and know-how, there are practically no legal ways of securing elements of intellectual capital.

That is, the owner of intellectual assets has incomplete ownership rights to these assets. This increases the risks of investing in intangible assets and, as a result,

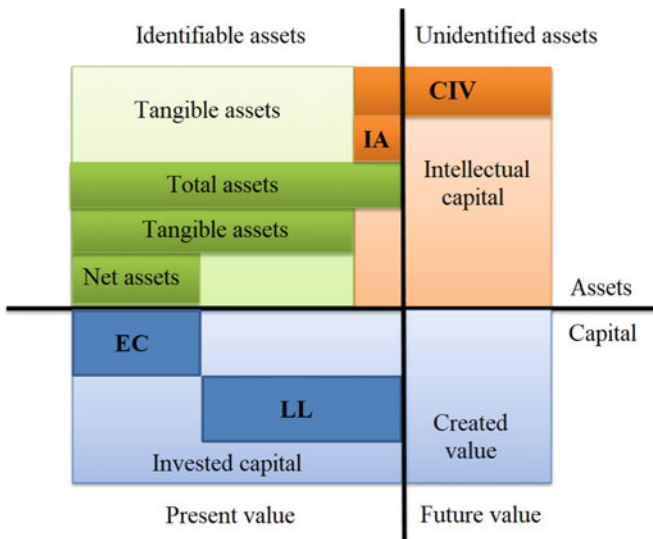


Fig. 1 The ratio between different types of assets to capital of company

should increase the required rate of return on investment in intellectual capital. Non-marketability of intellectual assets lies in the low level of their tradability in financial and other markets, which increases information asymmetry. The reasons for this situation are the growth of innovation and commoditization, i.e., lowering barriers to enterprise access to markets, technologies and assets associated with the development of digitalization and networkization.

According to many scientists [15], intellectual capital includes intangible assets, which are divided into two categories—identifiable and non-identifiable. In addition, unidentifiable assets make a significant contribution to the company's success [16]. The development of methods for assessing intellectual capital initially included two main areas—methods based on the scoring of various unidentifiable aspects of activities and methods based on cost estimates. The main methods and indicators for calculating the intellectual capital of enterprises are presented in Table 1.

The presented assessment methods do not allow to fully consider the influence of financial decisions and financial policy of the enterprise. Thus, the problem of assessing intangible assets, as comparing the flow of investments and the benefits that they bear to the company in the future, is still the main problem in assessing intellectual capital.

3 Results and Discussion

One of the recognized methods for giving a valuation of intellectual capital is the CIV method (Calculated Intangible Value) [17, 18]. This scheme was developed by Thomas Stewart in 1995. This indicator was developed to help investors and company management assess the value of knowledge-intensive companies and to increase interest in intellectual capital as such. This calculation method assumes that investments in physical assets can bring only the industry average income, and everything that the company receives more than it is due to the competent use of its intangible assets.

An increase in the CIV indicator over time indicates the company's ability to generate income in the future and vice versa, a decrease in the indicator indicates that investments in intangible assets or structural changes in the company do not pay off [19]. Among the advantages of this method, researchers note the simplicity of calculations and the availability of data, which can be obtained directly from the annual reports of public companies on official websites. In addition, the indicator is suitable for both intra-industry and inter-industry comparisons.

- First, within the framework of this method, intangible assets are not disaggregated, not separated, for example, the physical and financial assets of the company.
- Secondly, the method is based on the return on assets indicator, which may be overestimated, underestimated or negative for some companies.
- Third, the key idea of the method is that only companies with a profitability higher than the industry average have intellectual capital, but in some, especially

Table 1 Basic methods and indicators for assessing intellectual capital

Method name	Calculation method	Main indicators
Return on Assets methods—ROA, Methods for measuring intangible assets	The difference between the market value of the company before taxes for a certain period and the tangible assets of the company. The resulting indicator is compared with the industry	EVA, CVA, ROA, CIV Knowledge Capital Earning Calculated Intangible Value
Market Capitalization Methods—MCM	The difference between the market capitalization of a company and the equity of its shareholders	Market to Book Value IAMV FiMIAM
Tobin's Q-index	Dividing the market value of the company (or capitalization) by the book value of the business structure (or the cost of replacing physical assets)	Tobin's Invisible Balance
Direct Intellectual Capital methods—DIC	Individual components of intellectual capital are determined, and then the total assessment of the enterprise's intellectual capital is calculated	Citation-weighted patents HRCA HR Statement The Value Explorer TVC Intellectual Asset Valuation AFTF
Scorecard Methods—SC	Define the different components of intellectual capital that will be represented in scorecards or charts	IC—Index Business IQ National IC Holistic Accounts IC Rating Value Chain Score Board
Scandia Method	Allows you to evaluate intellectual capital in terms of "value creation", i.e. evaluate information about any "hidden values" that may not have been discovered. The index system is used	MAGIC IC-dVAL Balanced Score Card Intangible Assets Monitor Danish Guidelines Meritum Guidelines Knowledge Audit Cycle Value Creation Index
VAIC Method—MVAIC	Allows you to assess the contribution of the enlarged elements of intellectual capital to the creation of added value	VAIC (MVAIC)

knowledge-intensive, industries, even medium-sized companies have intellectual capital, so estimates can be significantly biased.

In accordance with Stewart's concept, the CIV indicator is the discounted part of the company's excess profit, which is defined as the difference between the excess

profit and the average market excess profit generated by the company’s tangible assets:

$$CIV = \sum_{i=1}^{\infty} \frac{(EBIT_i - TangibleAssets_i \times ROA_{ind(i)}) \times (1 - t)}{(1 + WACC)^i} = \sum_{i=1}^{\infty} \frac{REOI_i}{WACC}$$

On an infinite investment interval, if the return on intangible assets does not change, previous expression is transformed to the form:

$$CIV = \sum_{i=1}^{\infty} \frac{REOI_i}{WACC} = \frac{REOI_i}{WACC}$$

The formula only works if $ROA_{comp} > ROA_{ind}$, the profitability of the enterprise is higher than the industry average. Another variant of the technique:

$$CIV = \sum_{i=1}^n \frac{NOPLAT - TangibleAssets \times ROA_{ind} \times (1 - t)}{(1 + WACC)^i} = \sum_{i=1}^{\infty} \frac{REOI_i}{WACC} = \frac{REOI_i}{WACC}$$

Thus, the value of CIV is the sum of the future residual operating income generated by the intangible assets of the company over an infinite period, discounted at the weighted average cost of capital of the enterprise.

It should be noted that in calculating excess returns, Stewart assumes that the cost of capital invested in assets is in line with the market average. At the same time, studies show that an increase in the share of intellectual capital leads to an increase in the level of risk and the required return. Thus, it should be noted that in addition to the above drawbacks of the CIV model, one of the significant drawbacks in assessing the amount of intellectual capital is the failure to consider the difference between the weighted average costs of the company’s capital from the industry average.

In, a modification of the method is proposed, in which the authors propose several assumptions, and propose to divide the value of the company value estimated using the residual profit model into two aspects—the value created by tangible assets and the value created by intangible assets. At the same time, the value created by intangible assets is proposed to be determined based on the expression:

$$V_A^{REOL} = NA_T^{BV} + \frac{REOI}{WACC} = \left[NA_T^{BV} + \frac{REOI_T}{WACC} \right] + \left[\frac{REOI_I}{WACC} \right] = V_T + V_I,$$

where $REOI_T$ —part of the residual profit generated by the tangible assets of the enterprise, and $REOI_I$ —part of the residual profit generated by the intangible assets of the enterprise, which are intellectual capital.

This approach also ignores the difference between the cost of capital of an enterprise and the industry average cost of capital. To overcome this disadvantage, it is proposed to calculate the cost of intellectual capital because there are differences in the spread between the return on assets and the weighted average rate of capital costs calculated for the enterprise and the industry average.

The residual profit that is generated by the total assets of the enterprise will be calculated using the expression:

$$REOI_i = NOPLAT_i - TotalAssets \times WACC_i.$$

The residual profit that is generated by the tangible assets of the company based on the industry average indicators of profitability and cost of capital can be calculated using the expression:

$$REOI_{Ti} = TotalAssets_i \times ROA_{ind} - TangleAssets_i \times WACC_{ind}.$$

The definitively intangible identifiable assets can be defined as the difference between the two residual profits $REOI_i$ and $REOI_{Ti}$, discounted at the company's weighted average capital rate and in terms of:

$$CIV = \frac{NOPLAT - TtA \times ROA_{ind} + TgA \times WACC_{ind} - TtA \times WACC}{WACC}.$$

This formula considers the influence of the following factors on the formation of the value of intellectual capital: profitability of the company's assets; average industry Return on assets (ROA); the cost of capital of the enterprise; average industry value of the enterprise.

4 Conclusion

The study of intellectual capital continues to be a relevant direction in enterprise management. The problem of its assessment is related to the fact that there is no unified methodology for assessing and measuring intellectual capital, and the current reporting does not allow for real assessment of intellectual assets. In addition, for enterprises of different industries, the assessment of intellectual capital has specific features. Construction enterprises have great features. Existing methods do not allow for this specificity to be sufficiently considered.

One of the recognized methods for valuing intellectual capital is the CIV method developed by Thomas Stewart, which is based on the calculation of excess returns, and the cost of capital invested in assets is in line with the market average. To date, a modification of this method has been proposed. The authors propose to divide the value of the company, estimated using the residual profit model into two aspects—the value created by tangible assets and the value created by intangible assets, but this approach also does not consider the difference between the cost of the enterprise's capital and the industry average cost of capital.

To overcome this shortcoming, the paper proposes a method for calculating the cost of intellectual capital, because there are differences in the spread between the

return on assets and the weighted average rate of capital costs calculated for the enterprise and the average industry indicators. The proposed methodology will allow considering the influence of the following factors: profitability of the company's assets, the average industry return on assets, the cost of capital of the enterprise, the average industry cost of the enterprise's capital. According to the authors, the proposed method can be applied to the assessment of assets of construction enterprises.

Acknowledgements The study was supported by a Grant from the President of the Russian Federation for state support of leading scientific schools of the Russian Federation NSh-2702.2020.6 «Conceptual foundations of a new paradigm of economic development in an era of technological and social transformation».

References

1. Mićiak M (2019) The efficiency of investment in human capital in IT enterprises. *Transp Res Procedia* 40:1134–1140. <https://doi.org/10.1016/j.trpro.2019.07.158>
2. Klaas BS, Klimchak M, Semadeni M, Holmes JJ (2010) The adoption of human capital services by small and medium enterprises: a diffusion of innovation perspective. *J Bus Ventur* 25:349–360. <https://doi.org/10.1016/j.jbusvent.2008.12.002>
3. Castillo AE, Pacheco GV, Hernández-Fernández L, Manotas EN, Silva J (2019) Factorial analysis in the Intellectual capital's dimensions on micro, small, and medium-sized export enterprises. *Procedia Comput Sci* 160:567–572. <https://doi.org/10.1016/j.procs.2019.11.046L>
4. Kankhva V, Andryunina Y, Belyaeva S, Sonin Y (2021) Construction in the digital economy: prospects and areas of transformation. In: *E3S web of conferences*, vol 244, p 05008
5. Panenkov A, Lukmanova I, Kuzovleva I, Bredikhin V (2021) Methodology of the theory of change management in the implementation of digital transformation of construction: problems and prospects. In: *E3S web of conferences*, vol 244, p 05005
6. Li Y, Song Y, Wang J, Li C (2019) Intellectual capital, knowledge sharing, and innovation performance: evidence from the Chinese Construction Industry. *Sustain (Switzerland)* 11(9):2713
7. Duodu B, Rowlinson S (2021) Intellectual capital, innovation, and performance in construction contracting firms. *J Manag Eng* 37(1):04020097
8. Lin D-J, Yu W-D, Wu C-M, Cheng T-M (2018) Correlation between intellectual capital and business performance of construction industry—an empirical study in Taiwan. *Int J Constr Manag* 18(3):232–246
9. Rezgui Y, Hopfe CJ, Vorakulpipat C (2010) Generations of knowledge management in the architecture, engineering and construction industry: an evolutionary perspective. *Adv Eng Inform* 24(2):219–228
10. Prys M, Krysińska J, Janaszkiwicz P, Winiecki P, Różewski P (2018) System analysis of human capital for information system development. *Procedia Comput Sci* 126:1197–1205. <https://doi.org/10.1016/j.procs.2018.08.060>
11. Gomes P, Kuehn Z (2017) Human capital and the size distribution of firms. *Rev Econ Dyn* 26:164–179. <https://doi.org/10.1016/j.red.2017.03.004>
12. Holland SB (2017) Firm investment in human health capital. *J Corp Finan* 46:374–390. <https://doi.org/10.1016/j.jcorpfin.2017.08.003>
13. Jacobs B (2007) Real options and human capital investment. *Labour Econ* 14:913–925. <https://doi.org/10.1016/j.labeco.2007.06.008>

14. Sevilir M (2010) Human capital investment, new firm creation and venture capital. *J Finan Intermediation* 19:483–508. <https://doi.org/10.1016/j.jfi.2009.08.002>
15. Christiansen C, Joensen J, Nielsen H (2007) The risk-return trade-off in human capital investment. *Labour Econ* 14:971–986. <https://doi.org/10.1016/j.labeco.2007.06.001>
16. Almeida R, Carneiro P (2009) The return to firm investments in human capital. *Labour Econ* 16:97–106. <https://doi.org/10.1016/j.labeco.2008.06.002V>
17. Plotnikov V, Pirogova O, Vertakova Y (2019) Model for assessing the human capital of an enterprise. In: *IOP conference series: earth and environmental science*, vol 272, p 032225. <https://doi.org/10.1088/1755-1315/272/3/032225>
18. Pirogova O, Gorin E, Plotnikov V (2019) The algorithms for the environmental finance based on adjusted present value models. In: *E3S web of conferences*, vol 91, p 08021 <https://doi.org/10.1051/e3sconf/20199108021>
19. Plotnikov V, Pirogova O (2018) Key competencies as an enterprise value management tool. In: *IBIMA 2018*, pp 1716–1721

Automatic Defect Recognition in Glass Rod Production Using Machine Vision and Deep Learning



Yury Matveev  and Mohammed Alaqabi 

Abstract The paper deals with the issues of automatic assessment of the quality of glass rods in the production process. Traditionally, quality control at glass enterprises is carried out visually by a process control operator. The high speed of modern technological processes leads to errors in quality assessment. To improve the quality of glass rods, an automatic control system based on machine vision methods is required. Such a system should automatically recognize defects in digital images that continuously come during the production process. The main task of image processing in the quality control system is the automatic search and recognition of defects. The proposed solution to this problem includes two stages. At the first stage, a set of features (descriptors) is formed, which are necessary for the classification of defects. The paper describes the presentation of features based on the use of statistical methods of segmentation of textured images. For the formation of descriptors, the information contained in the histograms of the first and second orders was used. A grayscale difference matrix was also used. The procedure for validating and classifying defects was carried out using a deep learning neural network. The description of the network and the algorithm for its training are given. In order to assess the effectiveness of the automatic defect recognition system, tests were carried out. The results of these tests showed that the use of a neural network and the proposed representation of features provides good discrimination for the analysis and classification of glass rod defects.

Keywords Quality control · Machine vision · Neural networks

1 Introduction

Glass rods are glass tubes from which various medical containers, such as ampoules, syringes, vials, etc., are subsequently made. During the manufacturing process, glass may contain various foreign inclusions called defects. The presence of defects in glass rods affects the quality of the final product. This causes serious economic damage to

Y. Matveev (✉) · M. Alaqabi
Tver State Technical University, Lenin av., 25, 170024 Tver, Russia

the pharmaceutical industry [1]. Increasing the level of quality control of glass rods will reduce economic losses and increase production efficiency.

Nowadays, quality control is carried out visually by a process control operator, who is examining each rod. The quality control system can be improved through its automation based on machine vision methods [2–4]. The concept of such an automated system developed by the authors is described in [5]. It includes various software and hardware components related to the acquisition and processing of images and process control. The main task of image processing is the automatic search and recognition of defects in the continuous production process.

The most common defects in the production of glass rods are stones, knots, striae, bubbles, scratches.

Stones are crystalline inclusions formed as a result of crystallization of glass melt.

Knot is also a crystalline inclusion of glass droplets of a different chemical composition into the glass melt. Stria, like knot, contains inclusions of foreign glass, which are enclosed in the glass melt. Unlike knot, it represents not separate inclusions, but separate stripes or threads (threadlike striae are very thin striae).

Bubbles are gaseous inclusions in glass in the form of rounded or slightly elongated cavities. Depending on the size, micro bubbles (with a diameter of less than 0.1 mm), small bubbles (with a diameter of 0.2 to 0.5 mm), and large bubbles (with a diameter of more than 0.5 mm) are distinguished. A capillary bubble is a capillary whose length is ten or more times the diameter.

The procedure for searching for defects and their location in the automated system of continuous quality control of glass rods includes the following steps (Fig. 1).

The video data stream coming from the video cameras is divided into separate frames. Each is assigned a timestamp. The first operation performed on the resulting image is to clear the image of noise and light glare. Random noise was eliminated using a second-order finite impulse response filter that implements a moving average. To remove the noise caused by reflections from the glass surface, an algorithm was developed using a reference system of ideal images. The principle of operation of this system is based on modeling the image background. First, a perfect picture of the glass surface is taken.

Then the noise on this surface is determined. As long as the measurement medium does not change, the noise is considered to be the same on the entire surface of the glass. Thus, subtracting the background from the image allows for further analysis of the pipe surface, which has been cleared of noise. After removing the noise, the image characteristics are analyzed.

The next operation is the identification of the rectangle of interest (ROI), i.e. the part of the image to be analyzed. It is used to account for the vibration of the control object (tube) during the movement on the rollers of the drawing machine. Since the conveyor and the tube moving along it vibrate, its boundaries in the resulting image will constantly move to the right or left of the direction of movement, and this affects the definition of the zone in which the defect search should take place.

To identify the control area of the object in the image, it is necessary to continuously automatically determine the position of the internal boundaries of the tube in

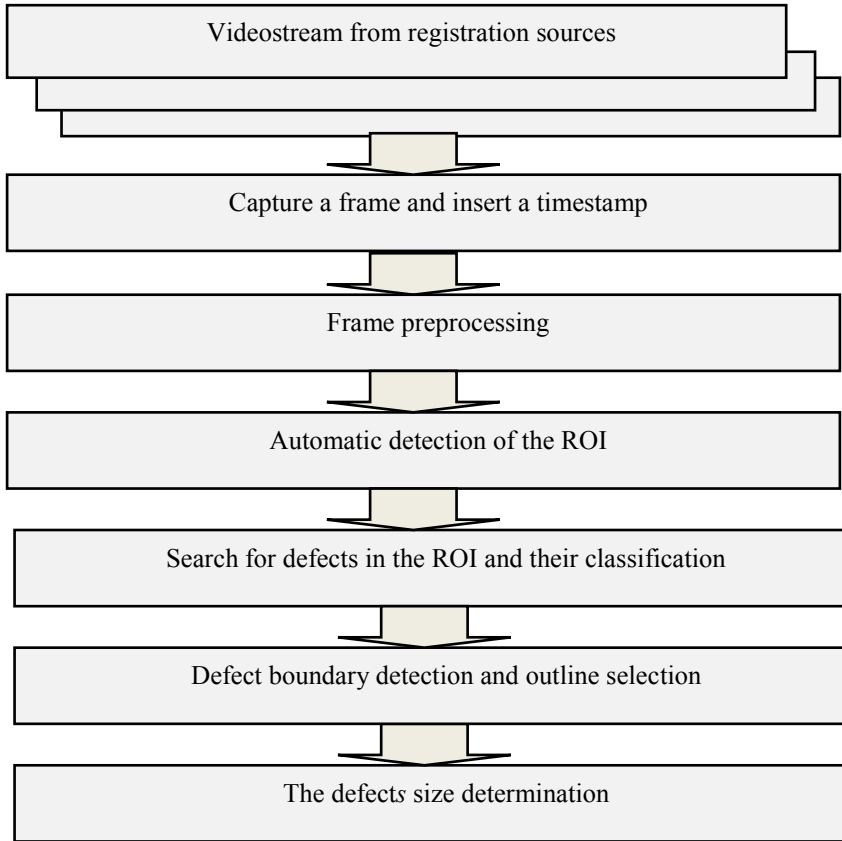


Fig. 1 Video preprocessing unit

the image. For this purpose, an algorithm was developed to find the internal boundaries of the tube in the image during its movement. The algorithm is based on the analysis of changes in the image brightness gradation along the rows of the brightness matrix until the right outer border of the tube in the image and the right inner border of the tube in the image are found. Difference between external borders

$$\Delta_{ext} = R_{ext} - L_{ext}$$

allows you to control the deviation of the tube thickness from the standard value.

The difference between external and internal borders

$$\Delta_{Rh} = R_{ext} - R_{int}$$

and

$$\Delta_{Lh} = L_{ext} - L_{int}$$

allows you to control the deviation of the wall thickness of the tube from the standard value.

Value

$$\Delta_{int} = R_{int} - L_{int}$$

defines the width of the control area in the orthogonal direction. The values of the parameters Δ_{ext} , Δ_{Rh} , Δ_{Lh} and Δ_{int} are used in the formation of control actions in the process of quality control of glass rods.

In order to make the image clearer, threshold segmentation was applied. To do this, a histogram of the gray-level image was constructed, and the state of each pixel was taken into account when calculating the probability. Optimal image segmentation was performed using an adaptive threshold value. This value was determined by the probability of brightness of the corresponding pixel in the image.

Further processing of the resulting digital image was to search for defects in the visual inspection area. A specially developed image recognition method based on the use of deep trust neural networks was used.

To determine the size of the defect, a Canny edge detector was used. Double dilation was applied to the results of processing the image boundaries by the detector in order to fill in the gaps in the contours. After applying the boundary detector, the outer edges of the contours in the images are identified and stored in a linked list that stores only the endpoints of the segment. As a result, a rectangle is formed, which is stored as the four points of its vertices. This information is used later to locate defects on the tube and form commands for the cutting machine for rejection.

Deep learning neural networks are successfully used for image recognition. This paper discusses the proposed approach to improving the efficiency of quality control using a machine vision system and a deep belief network (DBN) [6–9].

2 Methods of Forming Descriptors

DBN consists of several layers of stochastic, hidden variables and performs deep hierarchical transformation of the input data space. The bottom layer of the DBN forms a single layer perceptron that controls the interaction with the top layer. The state of neurons in the lower layer is determined by a set of classification features (descriptors). It is necessary to solve a number of problems when designing a neural

network for the recognition of glass defects. First of all, it is necessary to create a set of classification features that will adequately describe the defects. Next, you need to determine the size of the training sample. The number of training examples should be such as to ensure the necessary classification accuracy. On the other hand, it is necessary to avoid overfitting the neural network. To form a set of descriptors, statistical methods of segmentation of textured images were used [10–13]. The image is considered as a function $I(x, y)$ of two spatial variables $x = 0.1, \dots, N - 1$ and $y = 0.1, \dots, M - 1$. The function $I(x, y)$ can take discrete values $i = 0.1, \dots, L - 1$, where L is the total number of image intensity levels. A short and simple summary of the statistical information contained in an image is a histogram of intensity levels. The histogram contains first-order statistical information about the image (or its fragment).

The histogram of the intensity level is determined by the following expression:

$$h(i) = \sum_{x=0}^{N-1} \sum_{y=0}^{M-1} \delta(I(x, y), i)$$

where $\delta(j, i)$ —Kronecker delta function

$$\delta(j, i) = \begin{cases} 1 & \text{if } j = i \\ 0 & \text{if } j \neq i \end{cases}$$

A sample estimate of the probability density for intensity levels is determined from the expression

$$p(i) = h(i)/NM, \quad i = 0.1, \dots, L - 1.$$

To quantitatively describe the statistical properties of the first-order image, the following were used:

initial moment of the first order

$$m_i = \sum_{i=0}^{L-1} i p(i), \tag{1}$$

and the central moment of the second order

$$\sigma_i^2 = \sum_{i=0}^{L-1} (i - m_i)^2 \tag{2}$$

Also, indicators derived from these values were used, such as: the coefficient of asymmetry

$$As = \sigma^{-3} \sum_{i=0}^{L-1} (i - m_i)^3 p(i); \quad (3)$$

Excess

$$Ex = \sigma^{-4} \sum_{i=0}^{L-1} (i - m_i)^4 p(i) - 3; \quad (4)$$

Shannon information entropy

$$H = - \sum_{i=0}^{L-1} p(i) \log_2 p(i) \quad (5)$$

More detailed information about texture properties is provided by indicators based on second-order statistics. The second order histogram is defined as a matrix $h_{d,\phi}(i, j)$, which is called the occurrence matrix. Here i and j are the brightness of neighboring points located at a distance d from each other in the direction ϕ . An estimate of the probability distribution law for neighboring pixels is obtained by dividing the values of the occurrence matrix elements by the total number of neighboring pixels $K(d, \phi)$

$$p_{d,\phi}(i, j) = h_{d,\phi}(i, j) / K(d, \phi).$$

Using the matrix $p_{d,\phi}(i, j)$, we calculate the estimates for the marginal distributions $p_x(i)$ and $p_y(i)$, the mean values m_i, m_j , and the standard deviations σ_i and σ_j . Using the results of these calculations, we calculate indicators that characterize the texture properties of the image. These include

Correlation

$$\rho = \frac{\sum_{i=0}^K \sum_{j=0}^K (i - m_i)(j - m_j)p(i, j)}{\sigma_i \sigma_j}; \quad (6)$$

inertia (contrast)

$$In = \sum_{i=0}^{K-1} \sum_{j=0}^{K-1} (i - j)^2 p(i, j); \quad (7)$$

absolute value of deviations:

$$Abs = \sum_{i=0}^{K-1} \sum_{j=0}^{K-1} |i - j| p(i, j); \quad (8)$$

second angular momentum (energy)

$$M_2 = \sum_{i=0}^{K-1} \sum_{j=0}^{K-1} (p(i, j))^2; \quad (9)$$

inverse difference

$$v = \sum_{i=0}^{K-1} \sum_{j=0}^{K-1} \frac{p(i, j)}{1 + (i - j)^2}; \quad (10)$$

Shannon's entropy

$$H_2 = - \sum_{i=0}^{K-1} \sum_{j=0}^{K-1} p(i, j) \log_2 p(i, j) \quad (11)$$

To form a set of descriptors, the grayscale difference matrix was also used [Cai Z., Vasconcelos N., 2018]. The grayscale difference matrix is a column vector containing L elements. Its records are calculated based on measuring the difference between the pixel intensity level and the average intensity calculated from a square sliding window centered on the pixel. The intensity level of the image $f(x, y)$ at the point (x, y) is i , $i = 0.1, \dots, L - 1$. The average intensity of the window centered at the point (x, y) is

$$f_i = \frac{1}{W - 1} \sum_{m=-K}^L \sum_{n=-K}^L f(x + m, y + n),$$

where K determines the size of the window, and $W = (2K + 1)^2$. The grayscale difference matrix value is defined as

$$s(i) = \sum_{x=0}^{M-1} \sum_{y=0}^{N-1} |i - f_i|$$

for all pixels having an intensity level i . Otherwise, $s(i) = 0$.

Based on the analysis of the grayscale difference matrix, five different features were obtained to quantitatively describe the cognitive properties of the texture. There are: heterogeneity of the structure of the bitmap, determined by the size of the texture primitives:

$$C_1 = (\varepsilon + \sum_{i=0}^{L-1} p_i s(i))^{-1}, \quad (12)$$

where ε —a small number that prevents the coarseness coefficient from becoming infinite, and p_i is the designed probability of the appearance of the intensity level i ,

$p_i = N_i/n$. N_i denotes the number of pixels having a level i , and $n = (N - K)(M - K)$.

Contrast (value depending on the difference in intensity between adjacent pixels):

$$C_2 = \left(\frac{1}{N_i(N_i - 1)} \sum_{i=0}^{L-1} \sum_{j=0}^{L-1} p_i p_j (i - j)^2 \right) \left(\frac{1}{n} \sum_{i=0}^L s(i) \right), \tag{13}$$

spatial frequency rate of intensity change:

$$C_3 = \left(\sum_{i=0}^{l-1} p_i s(i) \right) / \sum_{i=0}^{L-1} \sum_{j=0}^{L-1} |i p_i - j p_j|, \tag{14}$$

texture complexity:

$$C_4 = (p_i s(i) + p_j s(j)) \sum_{i=0}^{L-1} \sum_{j=0}^{L-1} |i - j| / n(p_i + p_j). \tag{15}$$

3 Recognition of Glass Rod Defects Using Deep Belief Neural Networks

Statistical indicators (1)–(15) are the texture characteristics of the image (descriptors) and form a set of input variables $X_0 = (X_1, X_2, \dots, X_{15})$. The correspondence between the statistical indicators (1)–(15) and the input variables X_0 is shown in Table 1.

To search for defects, a deep belief network (DBN) was used [14, 15], which consists of several layers. Each layer of the DBN is considered as a Restricted Boltzmann Machine (RBM) containing two layers of interconnected neurons—input and hidden ones. A layered procedure was used for training. First, the weights of the first layer are determined using the Restricted Boltzmann Machine Learning Mechanism (RBM). The values of the descriptors X^0 are fed to the input of the first layer of the DBN. The output of the first layer of the DBN forms a set of values of the unobservable variables of the first layer Y^1 . These values are the input for the second layer. After training it, a set of values of unobservable variables of the second layer Y^2 is formed, this is the input for the third layer. Thus, training of all layers of the DBN

Table 1 Correspondence between statistical indicators and input variables of the neural network

Indicators	m_i	σ^2	As	Ex	H	ρ	In	Abs	M_2	v	H_2	C_1	C_2	C_3	C_4
Inputs	X_1	X_2	X_3	X_4	X_5	X_6	X_7	X_8	X_9	X_{10}	X_{11}	X_{12}	X_{13}	X_{14}	X_{15}

takes place. After pre-training, the values of the hidden variables in each layer can be obtained by a single bottom-up pass that starts with the observed data vector in the lower layer and uses the generated weights in the opposite direction. The DBN training algorithm contains the following steps:

1. Initial data are sequentially entered—the values of the set of descriptors X^0 and the corresponding values of the defect signs.
2. A layer-by-layer training of the Restricted Boltzmann Machine (RBM) is performed using the contrast divergence algorithm [16]. After all layers of the DBN have been trained, the pre-setting process is terminated.
3. The DBN is fine-tuned using the supervised backpropagation algorithm, and the synoptic connections of the network are determined.
4. The trained network is tested using control sets until the error stops decreasing or begins to increase over several epochs.

The main advantage of deep learning methods over conventional methods is that they allow the formation of more reliable integrated features that are a combination of both observable variables and latent factors. This allows increasing the accuracy of defect recognition, especially with an increase in the amount of training data.

4 Results

The tests of the machine vision system were carried out in the glass rod production workshop. All rods tested by the machine vision system were analyzed by experts (operators). 962 rods of various sizes were tested. The first group had a diameter of 12 mm, and the second—16 mm. The number of samples in the first group—437. The number of samples in the second group—525.

The neural network was previously trained. A training dataset was prepared for this purpose. It contained 320 tagged BMP images with a resolution of 1536×1536 . To improve the quality, preliminary processing of images was carried out: smoothing, noise removal, etc. To adjust the weights of the neural network, a supervised learning scheme was used. As an initial approximation, we used the weights obtained using a random number generator. The network weights were modified according to the formula:

$$w_{ij}(t + 1) = w_{ij}(t) + v \cdot \delta \cdot x_i \quad (16)$$

where t and $t + 1$ are the numbers of the current and next iterations, respectively; v —is the learning rate coefficient, i —is the input number; j —is the number of the neuron in the layer.

The value of δ is calculated as the difference between the ideal and the obtained output values:

$$\delta = Y_I - Y$$

Training pairs (X^0, Y_I) are sequentially fed to the network input. The network calculates its output Y . If $\delta = 0$, then the next training pair is fed to the network input, until the network stops making errors. Otherwise, the weights are modified in accordance with the expression (16). Obviously, if $Y_I > Y$ the weights will be increased and thus reduce the error. Otherwise, they will be reduced, and Y will also decrease, approaching Y_I .

The actual training is conducted iteratively, by minimizing the objective function $E(w)$ defined only on the training subset.

$$E(w) = \sum_{l=1}^p E(y_l(w), d_l)$$

where p is the number of training pairs (X^0, Y_I) . At each iteration all possible input vectors are presented in random order in turn. Minimizing the $E(w)$ function ensures that the network outputs are sufficiently consistent with the expected values from the training samples. Unfortunately, it is not possible to determine in advance the number of iterations that will need to be performed, and in some cases, to guarantee complete success.

The training procedure must ensure the minimum error in recognizing the test dataset, that did not participate in training. The generalization error $E_G(w)$ depends on the level of the learning error $E_L(w)$ and the confidence interval ε . It's defined by the relation:

$$E_G(w) = E_L(w) + \varepsilon\left(\frac{p}{\eta}, E_L\right)$$

The value of ε functionally depends on the level of training error $E_L(w)$ and on the ratio of the number of training samples p to the actual value of the parameter η , called Vapnik–Chervonenkis dimension (VC). The VC measure reflects the level of complexity of a neural network and is closely related to the number of weights it contains. The value of ε decreases as the ratio of the number of training samples to the level of network complexity increases. The greater the number of different weights, the greater the network complexity and, accordingly, the value of the VC measure. The upper and lower bounds of this measure can be determined using the inequality:

$$2\left[\frac{K}{2}\right]N \leq VC \leq 2N_w(1 + \lg N_n) \quad (17)$$

where $[\]$ is the integer part of the number, N is the dimension of the input vector, K is the number of hidden layer neurons, N_w is the total number of network weights, and N_n is the total number of network neurons. Expression (17) was used when creating the structure of a neural network. It was used to determine the network parameters: the number of neurons, the number of weight functions and hidden layers. The neural network was trained on training images for 1500 epochs with a learning rate of 0.001

Table 2 Test results of the machine vision system

Size (mm)	N	W_1	W_2	W_3	W_4	W_5	W_6	P_1	P_2
12	437	345	92	350	87	15	12	0.043	0.134
16	525	452	73	420	105	10	12	0.022	0.16
Total	962	797	165	770	192	25	24	0.033	0.145

Table 3 Confusion matrix

	Q_1	Q_2	n_i
Q_1	m_1^1	m_2^1	$n_1 = m_1^1 + m_2^1$
Q_2	m_1^2	m_2^2	$n_2 = m_1^2 + m_2^2$

in epochs 0–99, 0.0001 in epochs 100–250 and 0.00001, and so on. As a metric of the quality of prediction, we used the MAE indicator in the form of the average sum of absolute errors with a set of threshold values.

After training the network, it was tested on a control sample. Table 2 shows the test results.

The following conventions are used here. W_1 —glass rods accepted by the machine vision system; W_2 —glass rods rejected by the machine vision system; W_3 —glass rods recognized by qualified operators in accordance with quality requirements; W_4 —glass rods recognized as unsuitable by operators and not meeting quality requirements; W_5 —glass rods rejected by the system, but meeting the quality requirements; W_6 —glass rods accepted by the system, but not meeting the quality requirements. The classification was carried out in accordance with the accepted designations using the following.

Based on the classification results, the probability of making errors of the first and second kind was determined. For this purpose, the confusion matrix of the following form (Table 3) was used.

This table is based on the results of the classification made by the machine vision system, shown in Table 2. A total of $n = n_1 + n_2$ samples were tested. Among of them are:

- n_1 —samples that do not contain a defect (class Q_1);
- n_2 —samples containing a defect (class Q_2).

The statistical estimate of the probability of making a type I error is determined from the expression

$$\tilde{p}(Q_j|Q_i) = \frac{m_i^j}{n_i}, \tag{18}$$

where $i = 1, 2, j = 1, 2$, and m_i^j —the number of samples from the Q_i class assigned to the Q_j class.

Table 4 Confusion matrix for 12 mm specimens

	Q_1	Q_2	n_j
Q_1	333	12	$n_1 = 333 + 12 = 345$
Q_2	15	77	$n_2 = 77 + 12 = 89$

The statistical estimate of the probability of making a type II error is determined from the expression

$$\tilde{p}(Q_i|Q_j) = \frac{m_j^i}{n_j}. \tag{19}$$

For a group of glass rods with a size of 12 mm, the classification results are presented in Table 4.

The values of the parameters given in Table 4 were determined as follows:

$$m_1^1 = W_1 - W_6; m_1^2 = W_5; m_2^1 = W_6; m_2^2 = W_2 - W_5. \tag{20}$$

According to expression (16), the statistical estimate of the probability of a type I error for a group of glass rods 12 mm is

$$\tilde{p}(Q_1|Q_2) = \frac{m_1^2}{n_1} = \frac{15}{348} = 0.043.$$

According to expression (17), the statistical estimate of the probability of a type II error for a group of glass rods 12 mm is

$$\tilde{p}(Q_2|Q_1) = \frac{m_2^1}{n_2} = \frac{12}{89} = 0.135.$$

For a group of glass rods with a size of 16 mm, the classification results are presented in Table 5.

The values of the parameters given in Table 5 were determined in accordance with (18).

According to expression (16), the statistical estimate of the probability of a type I error for a group of glass rods 16 mm is

$$\tilde{p}(Q_1|Q_2) = \frac{m_1^2}{n_1} = \frac{10}{450} = 0.022$$

Table 5 Confusion matrix for 16 mm specimens

	Q_1	Q_2	n_j
Q_1	440	10	$n_1 = 440 + 10 = 450$
Q_2	10	63	$n_2 = 63 + 10 = 73$

According to expression (17), the statistical estimate of the probability of a type II error for a group of glass rods 16 mm is

$$\tilde{p}(Q_2|Q_1) = \frac{m_2^1}{n_2} = \frac{12}{63} = 0.19.$$

Based on the test results, the developed machine vision system has proven its effectiveness in identifying defects and impurities. In particular, the level of misclassification in the control system was in the range of $0.022 \div 0.19$, under conditions of work with extreme quality requirements in test mode.

5 Conclusions

This paper presented new methods of glass rod quality control based on the use of machine vision, neural networks and deep learning methods. The proposed method for representing descriptors can be used for very broad categories of image processing tasks. Experimental results have shown the superiority of deep learning methods over conventional methods. They allow the formation of more reliable integrated features, which are a combination of both observable variables and hidden factors. This allows increasing the accuracy of defect recognition and the speed of image processing, especially with an increase in the volume of training data. The results obtained indicate the advantage of the automatic defect recognition system in comparison with the traditional method.

References

1. Reynolds G (2011) Glass delamination and breakage, new answers for a growing problem. *BioProcess Int* 9(11):52–57
2. Foglia P, Prete C, Zanda M (2015) An inspection system for pharmaceutical glass tubes. *WSEAS Trans Syst Control* 14:123–128
3. Peng X, Chen Y, Yu W (2008) An online defects inspection method for float glass fabrication based on machine vision. *Int J Adv Manuf Technol* 39:1180–1189
4. Hof RD (2018) Is artificial intelligence finally coming into its own? *MIT Technology Review*. Accessed 10 July 2018
5. Matveev YuN, Alaqabi MM (2021) System of continuous monitoring and quality management of glass rod production. *Softw Prod Syst* 1:180–188. <https://doi.org/10.15827/0236-235X.133.180-188>
6. Hinton G (2009) Deep belief networks. *Scholarpedia* 4(5):5947. <https://doi.org/10.4249/scholarpedia.5947>
7. Mosavi A, Varkonyi-Koczy AR (2017) Integration of machine learning and optimization for robot learning. In: Jabłoński R, Szewczyk R (eds) *Recent global research and education: technological challenges*. Springer, Cham, pp 349–355. https://doi.org/10.1007/978-3-319-46490-9_47

8. Kumar A (2008) Computer-vision-based fabric defect detection: a survey. *IEEE Trans Ind Electron* 55(1):348–363
9. Cai Z, Vasconcelos N (2018) Cascade R-CNN: delving into high quality object detection. In: *IEEE/CVF conference on computer vision and pattern recognition (CVPR)*. <https://doi.org/10.1109/CVPR.2018.00644>
10. Li D et al (2014) Defect inspection and extraction of the mobile phone cover glass based on the principal components analysis. *Int J Adv Manuf Technol* 73(9–12):1605–1614. <https://doi.org/10.1007/s00170-014-5871-y>
11. Oktay AB, Gurses A (2019) Automatic detection, localization and segmentation of nanoparticles with deep learning in microscopy images. <https://doi.org/10.1016/j.micron>
12. Park C, Ding Y (2019) Automating material image analysis for material discovery. *MRS Commun* 9:2
13. Gonzalez R, Woods R (2018) *Digital image processing*. 2006-1072
14. Chollet F (2017) *Deep Learning with Python*. 350 ISBN 9781617294433
15. Zhou B, Khosla A, Lapedriza A, Oliva A, Torralba A (2015) Object detectors emerge in deep scene CNNs. In: *ICLR 2015* [arXiv:1412.6856](https://arxiv.org/abs/1412.6856)
16. Xu K, et al (2015) Show, attend and tell: Neural image caption generation with visual attention. In: *ICML 2015* [arXiv:1502.03044](https://arxiv.org/abs/1502.03044)

Automation of Cargo Correspondences in Railway-Water Communication



Nina Sirina  and Valerii Zubkov 

Abstract The organization of local work is analyzed when carrying out correspondences of goods in railway-water communication. Studies have shown a significant increase in the volume of construction (inert) cargo sent to river ports. In the context of the lag in the development of transport infrastructure from the growth in the volume of shipped products, the throughput capacity of railway directions to river ports, the processing capacity of railway stations, decreases, as a consequence, due to the presence of barrier restrictions on the infrastructure of railway transport, long-term abandoned freight trains that should be sent to river ports are formed. To exclude a decrease in the throughput and processing capabilities of the transport infrastructure, a method has been developed and implemented to automate technological processes for forecasting and planning the volume of cargo correspondence, determining the optimal options for cargo correspondence. The software product “Electronic service of complex transport services” has been developed, the methodology for the formation of this software product is used to manage the traffic of construction (inert) cargo. Effective organization of interaction between railway and water transport in the implementation of mixed traffic is possible by using integrating information and intelligent software products that function in a unified transport and information environment and provide automated determination of the optimal options for cargo correspondence and their processing at cargo transshipment facilities.

Keywords Complex transport services · Railway and water communication · Construction cargo · Port station · System · Quality criteria · Organization of local work

N. Sirina

Ural State University of Railway Transport (USURT), ul. Kolmogorova, 66,
620034 Yekaterinburg, Russia

V. Zubkov (✉)

JSC “FGK”, 34 Masha Poryvaeva str., 107078 Moscow, Russia

1 Introduction

In the context of the lag in the development of transport infrastructure from the growth in the volume of cargo correspondence, the most important task is to determine the vector of rational development of technological processes for the timely and reliable satisfaction of consumer demand.

The performance of the transport system is balanced by the way in which local operational work is coordinated. Local operational work is a set of supporting measures, including loading and unloading technological operations on the main transport infrastructure and non-main transport routes [1].

Research shows that in recent years, the number of products shipped and sent (construction cargo) to river ports has been increased. At the same time, in proportion to the fact that railway transport does not provide timely processing of cargo correspondences, there is a long idle of freight trains.

Figure 1 shows a diagram of the correspondence growth of construction (inert) cargo and the number of long-term abandoned freight trains.

Stable coordination and good management of local operational work are achievable with a rational and coordinated interaction of adjacent modes of traffic in the transportation process. For reliable and mutually consistent cooperation of types of transport systems, it is required to develop intelligent software products that will simplify the activities of a person (system user) and timely and on a contractual basis to process the increasing growth of cargo correspondence in mixed railway and water communication [1, 2].

At present, in the space of interaction between types of transport, the railway complex is often the first link in the supply chain, and in case of poor-quality services (due to the lack of high-quality forecast, planned volumes of upcoming

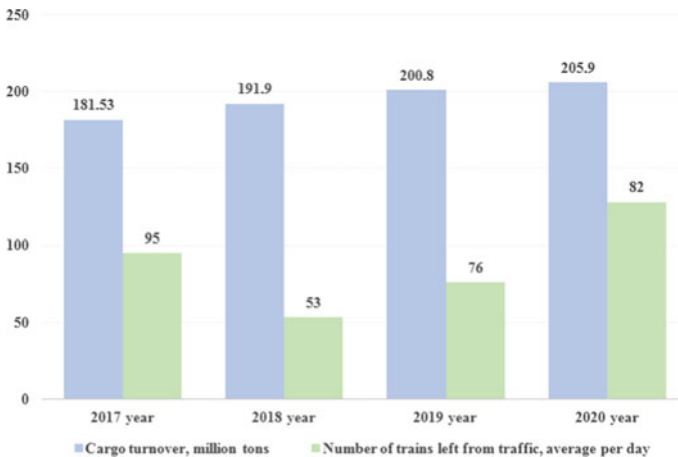


Fig. 1 Diagram of the correspondence growth of construction (inert) cargo and the number of long-term abandoned freight trains

cargo transportation, uncoordinated actions of transportation participants, representatives of different types of transport), regardless for whatever reason this happened, the preconditions are created for the formation of a negative image of work in the organization of internal cargo transportation.

The main disadvantages that are inherent in the interaction of rail and water transport:

- incompleteness (inadequacy) of forecasting, planning the volume of cargo correspondence;
- difference (disproportionality) in the volume of cargo correspondence and the throughput, processing capacities;
- lack of a unified transport and information environment, information infrastructure for coordinating and managing the transport and production process when planning and organizing the delivery of goods from the station of their origin to the station of repayment of cargo transportation or the place of transshipment in a river port;
- imperfection of the regulatory, technical and legal environment, which determines the coordinated cooperation of the subjects of railway and water communication.

The task of eliminating these disadvantages is urgent and priority. The authors see the solution to this problem in the automation of cargo correspondence in railway-water communication.

The main disadvantages identified in the interaction of rail and water transport are shown in Fig. 2.

2 Material and Methods

Under existing conditions, the priority for the supply of trains is determined according to one criterion, namely, according to the possible volume of the processing capacity of the unloading fronts of the tracks of the non-public use of the river port. They do not take into account such criteria as the presence and availability of unloading fronts by the type of cargo, the approach to the port of river vessels and the possible volume of their loading, the volume of ship parties, reserve processing capacities of cargo fronts, etc. The reason for this is the partial automation of the process of long-term and short-term planning of the freight train approach with a predominance of reference and information functions of systems over corrective and control ones.

The main vector of the transformation (development) of cargo correspondence in mixed communication is mutually beneficial coordinated planning of this cargo transportation type and their volumes, including the formation of a unified (all-encompassing) coordination technology based on the principles of identifying problematic tasks (issues) and the optimal choice of making coordination decisions, based on advanced methods and ways of designing information-intelligent software products [3, 4].

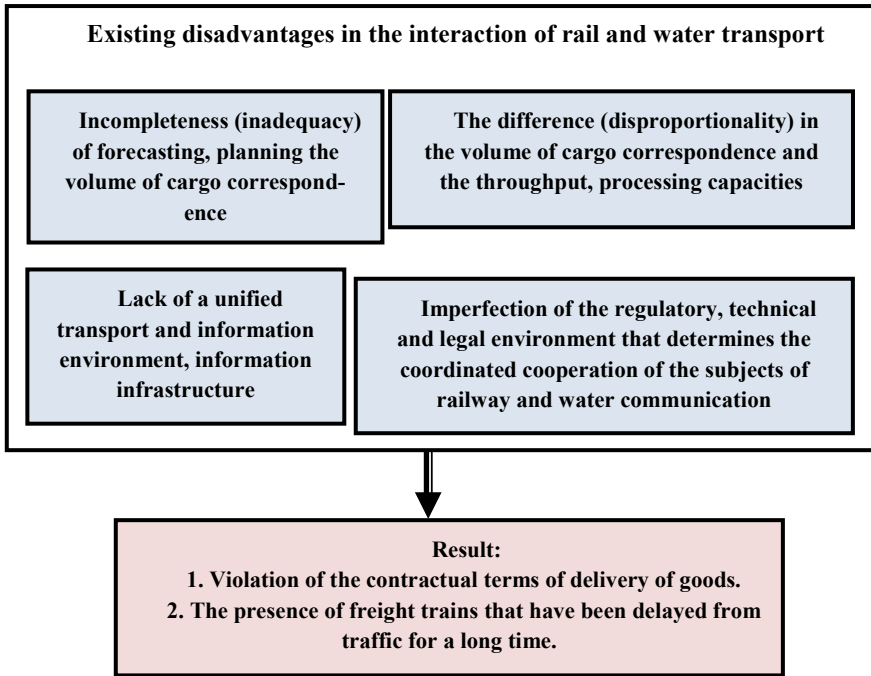


Fig. 2 Main disadvantages in the organization of mixed rail-water communication

The creation of a unified information space in the mixed rail-water communication and the introduction of automation of the forecast calculation process and the freight train approach plan will ensure the identification of factors and additional resources necessary for the high-quality organization of local work, and the formation of a corrective, rational and most effective solution for real conditions. The decision is an algorithm of actions of the subjects of this communication and must be agreed upon by all participants in the transportation in the form of a plan for the upcoming shipment for a specified period.

For the intellectualization of the information and technological process of mutually beneficial forecasting and planning of the volume of cargo correspondence in mixed rail and water communication, the authors have designed and put into operation an information and intellectual product “Electronic service of complex transport services.”

Figure 3 shows a diagram of the transit and transformation of information as it passes from integrators, subjects and users of the system.

The function of transit and transforming information has the form:

$$p_{ij} = \{P1_{ij}; P2_{ij}; P3_{ij}; P4_{ij}; P5_{ij}\}, \tag{1}$$

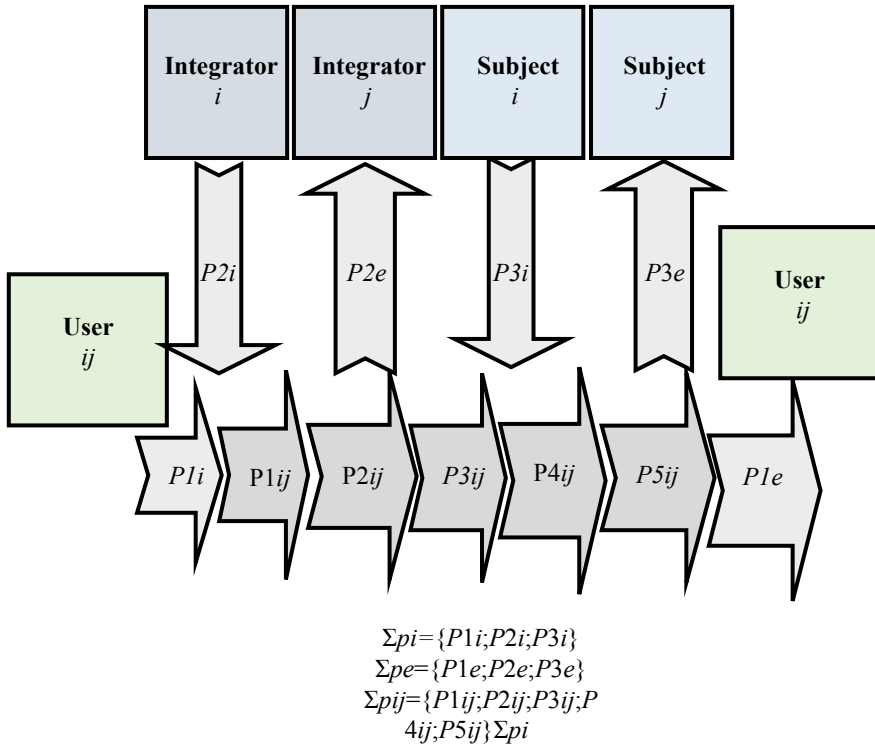


Fig. 3 Scheme of the transit and transformation of information when passing from the subjects (users) of the system: $P1i$, $P2i$, $P3i$ —input information stream; $P1e$, $P2e$, $P3e$ —output information stream; $P1ij$ —identified information stream; $P2ij$ —converted information stream; $P3ij$ —coded information stream; $P4ij$ —considered information stream; $P5ij$ —analyzed information stream

The system “Electronic service of complex transport services” operates in a unified transport and information environment when organizing mixed communication using rail and water transport. The users of the system are consignors, consignees, carrier companies, vehicle owners. Processing and exchange of electronic data takes place according to the approved protocol of the system [5]. The system is an integrating information and intellectual product and provides:

- automated calculation of the optimal options for cargo correspondence at the shortest (rational) distance;
- mutually agreed determination of the amount of cargo correspondence for a certain period of time;
- automated calculation of the tariff for cargo correspondence by rail and water transport;
- construction of analytical electronic reporting forms for railway and water transport;
- automated calculation of throughput and processing capacities on railway lines;

- automated generation of electronic claim documents in case of non-fulfillment of contractual obligations for the transportation of goods.

The system provides the possibility of prompt registration through the WEB-interface of incoming requests for the cargo transportation, informing customers about the progress of their requests. The result of the information exchange of data between the carrier companies and the counterparty is commercial offers for the cargo transportation.

Figure 4 shows the organizational and functional diagram of the information and intellectual product “Electronic service of complex transport services”.

Increasing the efficiency of interaction between the consignor and carriers is achieved by solving the following tasks: ensuring the transparency of the cargo transportation in rail and water communication; ensuring the minimum time and money costs for consignors in the implementation of transportations in the mixed rail-water communication; improving the provision quality of a range of transport and logistics services; implementation of the technology for online ordering of the main service and additional services for the cargo transportation; simplification of the procedure for documenting the planned transportation by the user [6, 7].

Requirements for the information and intellectual system “Electronic service of complex transport services” as a whole. The system structure includes the following objects:

1. System server (WEB server, application server).
2. Database server.
3. Personal computers of system users.

The system server is intended for installing software that implements the functionality of an information and intellectual product.

The database server is intended for installing software that implements the functionality of the database management system, placing and storing the system data.

Personal computers of users are intended for providing a user interface for accessing the system.

Server components of the system (WEB-server, application server, database server) provide the ability to scale in the event of an increase in load when additional users are connected and/or when the functionality of the system is expanded [7].

The system components are based on industrial software. The software is documented in detail and provides a set of subsystems necessary and sufficient for the implementation of the main functions, allocated according to the functional and technological principle. The software provides a user interface in Russian. Software has the property of extensibility of functionality [8].

The system “Electronic service of complex transport services” provides the possibility of prompt registration of incoming applications for the cargo transportation, informing customers about the progress of their requests. It provides the possibility of simultaneous operation (simultaneous login) of 100–500 users with the

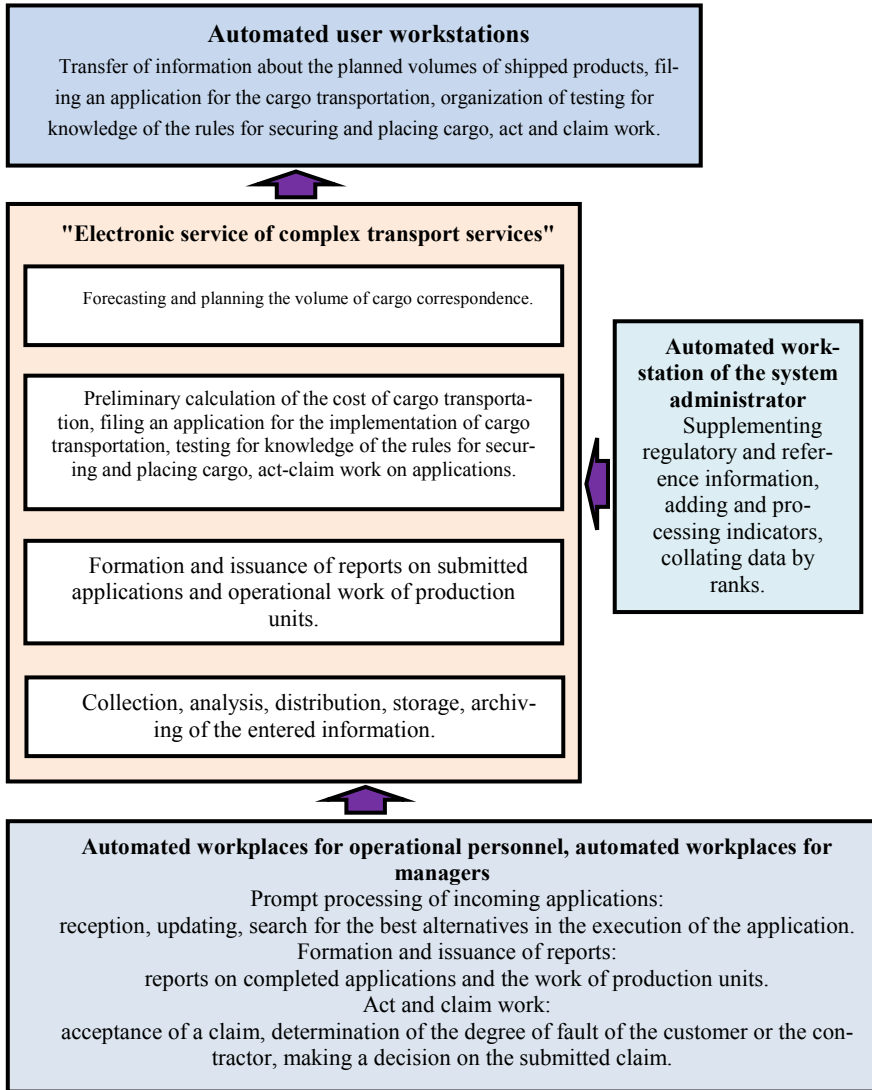


Fig. 4 Organizational and functional diagram of the system

following characteristics of the system: the response time of the system when navigating through the screen forms of the system is no more than 10 s. The system has the ability to scale by modifying the software and hardware complex [9].

For full functioning, the system is provided with an adequate number of qualified personnel. The personnel directly involved in the work is divided into 2 groups. The first group includes personnel who interact with the system in the performance of their direct duties, in particular:

- prompt response to requests from customers for the cargo transportation;
- registration of the primary set of related documents for the upcoming cargo transportation;
- work with registered claims regarding improper or partially proper fulfillment of obligations for the main type of activity;
- viewing reports and obtaining information on registered and executed documents.

The number of this group of personnel is determined based on the needs and staffing of the functional customer.

The second group includes personnel who directly service and administer the system:

- technical personnel serving automated workstations. Considering that standard software (personal computer, operating system, WEB-browser) is required at workplaces for the system to function, maintenance is performed by a highly qualified staff of specialists;
- administrators who ensure the operability of the automated system. These specialists have special knowledge in the field of database management systems, WEB-applications and technical support.

The system remains operational and ensures the restoration of its functions in the event of the following emergency situations:

- power failure;
- malfunction of the system software;
- malfunction of the complex of system technical means.

Interaction with the components of the automated system is carried out through a standard graphical interface displayed on standard automated workstations of the functional customer and using standard WEB-browsers. All demanded functionality is available from any workplace that has a connection to a technological data transmission network or a global information and telecommunications network, under the condition of user authorization [10].

3 Results

Selection of the optimal coordination solution. The main algorithm in the software product is an algorithm for the automated calculation of the predominant value of planning the cargo correspondence to the object of its transshipment from railway transport to water transport [11].

A fragment of determining the optimal coordination solution for the cargo transportation to the object of its transshipment is shown in Fig. 5.

Figure 5 shows an automated process for determining the priority parameters of cargo correspondence that affect the efficiency and quality of customer service. On the basis of these parameters, the conditions and factors affecting the implementation

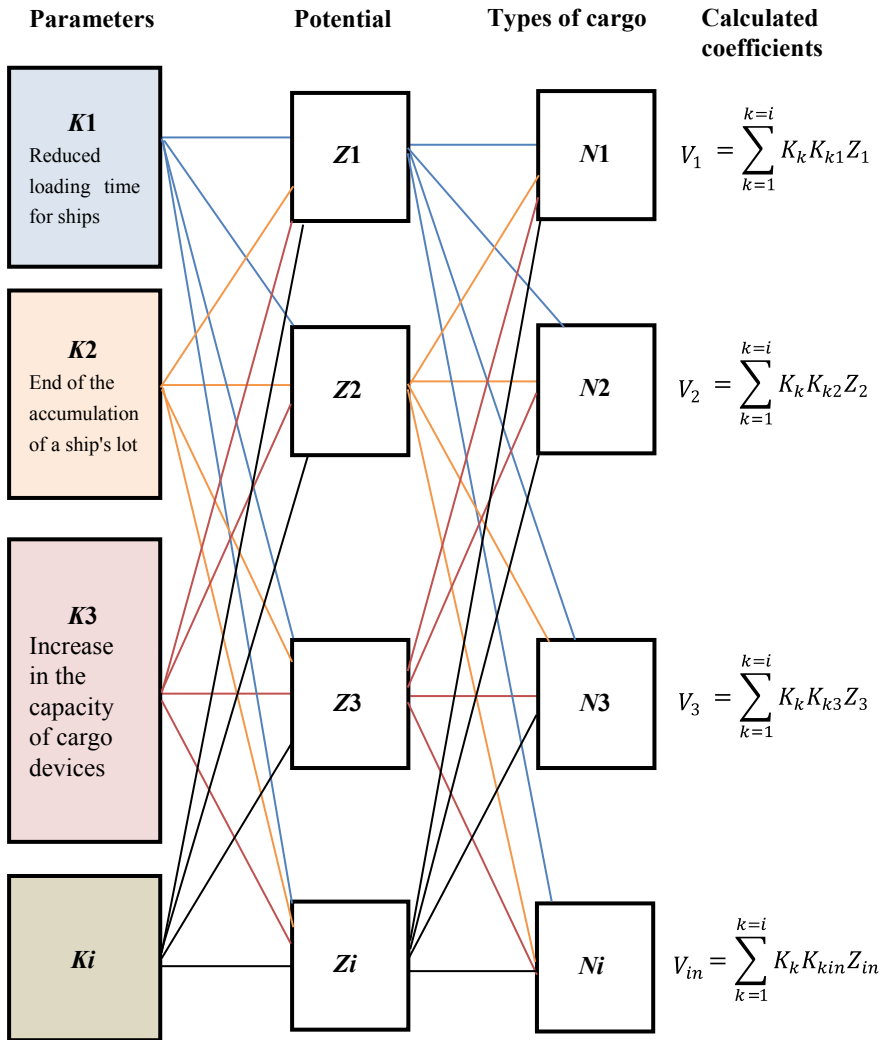


Fig. 5 Fragment of determining the optimal coordination solution for the cargo transportation to the object of its transshipment

of plans for the loading and transportation of construction (inert) cargo are estimated [12].

The predominant value of loading and transportation of goods is formed due to the results of the calculations of the coefficients of the prevailing value of V_{in} for a specific consignment of ship cargo, a specific group of cars and a specific route dispatch [13]. The set of results is equivalent to the number of quality parameters K_i , the amount of resources Z_i , the type of product (goods) N_i . All these values are entered into the software product (the matrix of comparative options) [14]. At the end

of the comparative analysis of the parameter values, the system sets an identification code for the coefficient of the prevailing values of V_{in} , which is the dominant option in the information calculation of the operational plan:

$$V_{in}(N_i) = \sum_{k=1}^{k=i} [K_k K_{k1} Z_1; K_k K_{k2} Z_2; \dots K_k K_{in} Z_{in}], \quad (2)$$

where: K_k, K_{in}, Z_{in} —coefficients of types of goods (calculated), their value ≤ 1 .

Further, in the software product, the best version of the operational local work plan is determined, while the maximum value of the V_{in} coefficient is the optimal coordination work plan:

$$V_{op}(N_i) = \max V_{in}(N_i), \quad (3)$$

To exclude long-term abandoned freight trains on the infrastructure of main transport, the software product defines the technological process of cargo correspondence using railway and water transport by the method of direct cargo transshipment (rolling stock—river ship), while not accumulating excess rolling stock on the approaches to cargo transshipment facilities [15]. This became possible due to the expansion of the forecasting horizon, planning and coordination of actions in the operation of the river port and the railway.

This technology represents the most effective way of organizing local work, which ensures coordination along the entire transport and logistics chain: consignor—railway rolling stock—carriage dispatch, route—river port—ship party—ship—consignee. The implementation of this technology is possible under the following conditions:

1. Coordination of traffic volumes in railway and water communication at the stage of planning the volumes of loading.
2. Introduction and implementation of contact schedules for the supply of railway rolling stock and river ships, which will make it possible to bring the approach of freight trains as close as possible to the time of arrival of ships.
3. Formation of carriages by categories and fractions of construction cargo, which makes it possible to exclude additional sorting operations at the port station and non-public tracks.
4. Transition to servicing the port by one operator of the railway rolling stock on the principle of “one port—one operator”, which will eliminate the downtime of freight trains on the approaches to the station due to the exclusion of additional operations to re-form groups of cars in accordance with the property sign after the end of operations for unloading cars. The implementation of this solution is possible by implementing methods for forming a model of an integrated transport service.

Figure 6 shows the conditions under which it is possible to implement the technology by the direct option method (Fig. 6).

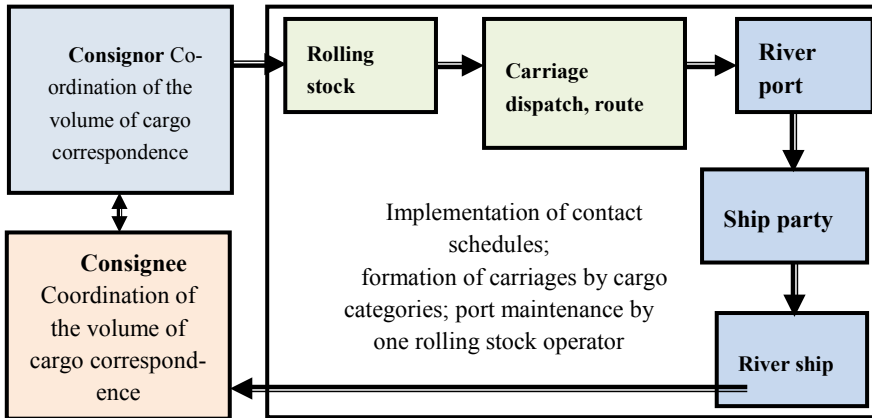


Fig. 6 The structure of the conditions under which the technology of the direct variant method is implemented

As a result of the fulfillment of the listed conditions, the highest level of routing of cargo transportation is achieved.

The compatibility and adaptation of information systems of users and integrators of domestic cargo transportation I_w is assessed taking into account the period for which joint technological operations of the participants of the railway-water communication P_{rw} and the ratio of the number of implemented transport services N_{ts} to the total normative (under a transport service agreement) number of joint technological operations N_{to} are organized, and is determined by the following formula:

$$I_w = P_{rw} \frac{N_{ts}}{N_{to}}, \tag{4}$$

4 Conclusions

Effective organization of interaction between railway and water transport in the implementation of mixed traffic is possible by using integrating information and intelligent software products that function in a unified transport and information environment and provide automated determination of the optimal options for cargo correspondence and its processing at cargo transshipment facilities.

The high-quality functioning of two types of transport, railway and inland waterways, when organizing local work in a unified technological process is expressed in the presence of adaptive and self-supporting information technology links that arise when organizing joint cargo transportation. In the process of organizing local work, each type of transport accounts for the share of transport services in their total number to ensure and achieve the proper quality level of transportation.

The methods of constructing the information and intellectual product “Electronic service of complex transport services” are currently used in the management of transport services when organizing car flows of inert cargo and when determining the forecast of their supply. The system is built on a modular principle, which in the long term allows to expand its functionality and capabilities, which in general will have a positive effect on the level of cargo transportation in mixed rail-water communication.

References

1. Kavanagh P (2016) A case for negotiated performance-based contracting rather than competitive tendering in government public transport (bus) service procurement. *Res Transp Econ* 59:313–322. <https://doi.org/10.1016/j.retrec.2016.06.006>
2. Lovelace R, Parkin J, Cohen T (2020) Open access transport models: a leverage point in sustainable transport planning. *Transp Policy* 97:47–54. <https://doi.org/10.1016/j.tranpol.2020.06.015>
3. Popova O, Gorev A, Shavyraa Ch (2018) Principles of modern route systems planning for urban passenger transport. *Transp Res Procedia*. 36:603–609. <https://doi.org/10.1016/j.trpro.2018.12.146>
4. Canitez F, Alpkokin P, Andrew J (2019) Black. Agency costs in public transport systems: net-cost contracting between the transport authority and private operators - impact on passengers. *Cities* 86:154–166. <https://doi.org/10.1016/j.cities.2018.09.010>
5. Walter J, Abendroth B (2020) On the role of informational privacy in connected vehicles: a privacy-aware acceptance modelling approach for connected vehicular services. *Telematics Inform* 49:101361. <https://doi.org/10.1016/j.tele.2020.101361>
6. Rohloff M (2011) Advances in business process management implementation based on a maturity assessment and best practice exchange. *Inf Syst E-Bus Manag* 9:383–403. <https://doi.org/10.1007/s10257-010-0137-1>
7. Saccani N, Perona M (2007) Shaping buyer–supplier relationships in manufacturing contexts: design and test of a contingency model. *J Purch Supply Manag* 13:26–41. <https://doi.org/10.1016/j.pursup.2007.03.003>
8. Chen Y (2016) Industrial information integration—a literature review 2006–2015. *J Ind Integr* 2:30–64. <https://doi.org/10.1016/j.jii.2016.04.004>
9. Gerhard S, Lukas S (2012) Use of ITS technologies for multimodal transport operations – River Information Services (RIS) transport logistics services. *Procedia Soc Behav Sci* 48:622–630. <https://doi.org/10.1016/j.sbspro.2012.06.1040>
10. Chen Z, Daito N, Gifford JL (2017) Socioeconomic impacts of transportation public-private partnerships: a dynamic CGE assessment. *Transp Policy* 58:80–87. <http://www.sciencedirect.com/science/article/pii/S0967070X16303134>. Accessed 21 Mar 2021
11. Lindsey R (2012) Road pricing and investment. *Econ Transp* 1:49–63. <https://doi.org/10.1016/j.ecotra.2012.07.001>
12. Li Q, Chiu DM, Xu M, Wu J (2014) An economic analysis of routing conflict and its resolution. *Perform Eval* 71:25–43. <https://doi.org/10.1016/j.peva.2103.09.004>
13. Matteis T, Liedtke G, Wisetjindawat W (2016) A framework for incorporating market interactions in an agent based model for freight transport. *Transp Res Procedia* 12:925–937. <https://doi.org/10.1016/j.trpro.2016.02.044>
14. Cooke P (2011) Transition regions: regional–national eco-innovation systems and strategies. *Prog Plan* 76(3):105–146. <https://doi.org/10.1016/j.progress.2011.08.002>
15. Pimentel C, Alvelos F (2018) Integrated urban freight logistics combining passenger and freight flows – mathematical model proposal. *Transp Res Procedia* 30:80–89. <https://doi.org/10.1016/j.trpro.2018.09.010>

Solving Differential Equations by Means of Mathematical Simulation in Simulink App of Matlab Software Package



Maria Semenova , Anastasia Vasileva , Galina Lukina ,
and Ulyana Popova 

Abstract This work considers the use of the simulation to solve differential equations in MatLab/Simulink and its results. The MatLab software package is designed to provide analytical and numerical solutions for various mathematical problems and simulate complex technical objects and systems. The Simulink app is one of the tools within the MatLab package. It has major structured, object-oriented, and visual programming capabilities. The system can solve linear algebra problems, integral and differential equations, and perform Laplace and Fourier transformations. We reviewed both the simplest equations (a first-order differential equation) and more complex linear and non-linear differential equations of the first and second orders. The results of structured modeling (S-model) in Simulink were compared to program code results (M-file) in MatLab. For the first-order linear differential equation, we have a complete correlation of modeling results. When solving the second-order non-linear differential equation, we observed small result deviations due to the method selected and the integration step. When discussing the results, we used the example of the practical application of the MatLab/Simulink environment to calculate the parameters of an electric circuit, namely to obtain the relationship between the current and the modeling time in the series-oscillatory circuit with a harmonic alternating voltage source. It is reduced to solving a nonhomogeneous linear differential equation with constant second-order coefficients describing the forced current change in the oscillatory circuit following the second Kirchhoff's law. In the conclusion, we note the versatility of the MatLab/Simulink modeling environment for the solution of differential equations including those with quotient derivatives.

Keywords Differential equation · Matlab · Simulink · Block library · Simulation method · Integrator · Feedback · Accuracy

M. Semenova (✉) · A. Vasileva · G. Lukina · U. Popova
Polytechnic Institute (Branch) in Mirny, Ammosov North-Eastern Federal University,
678170 Mirny, Russia

1 Introduction

Almost all problems of contemporary science can be reduced to solving differential or integral equations [1–3]. Differential equations are widely used in various branches of mathematics and related sciences like mechanics, physics, engineering, chemistry, biology, economics, etc. [4–10]. This is due to the fact that such equations can be used to solve many problems in the world around us if they are related to some parameters and their numerical changes due to changes in time, coordinates, and other parameters [11].

Problems in various fields are often reduced to solving differential equations or their systems [12]. Solving any problem in physics starts with the specific problem statement [13, 14]. Specific problem statement stands for the selection of the region of the universe, to which the problem belongs as well as a set of laws that can be used in problem-solving. Then, a differential equation is selected for each of the laws. This is the mathematical problem statement [15].

Due to the ongoing development of technology, solving any problem requires taking into account increasingly subtle effects. The mathematical problem statement will complicate as well. As the problem becomes more complicated, obtaining an analytical solution does the same, thus leading to the requirement to use the numerical methods for solving differential equations [16]. A number of numerical methods were developed to solve differential equations, including the new ones [12, 17–19]. Yet it would be a mistake to assume that solving any differential equation of a system of those using numerical methods is a simple task. There is no developed numerical method that would allow solving an arbitrary differential equation. It is crucial to have a clear understanding which numerical method is more efficient in solving this differential equation.

The purpose of this paper is to demonstrate the possibilities of assessing the results of computer simulation for differential equations in simulation modeling of dynamic systems in the Simulink app, MatLab software package. Simulink is one of the most powerful components of the MatLab package. It is designed for computer simulation and analysis of systems whose behavior depends on time [20, 21].

The achievement of the purpose set requires the fulfillment of the following objectives: a brief description of theory on the mathematical simulation in MatLab; description of methods and techniques used in the development of mathematical and simulation models to solve differential equations; the development of models for ordinary differential equations; the development of models for linear and non-linear differential equations of the first and second order; result assessment.

2 Overview of Theory

Today, there are many software products for mathematical simulation available. Many of them are well-known and popular, while some are relatively new. There

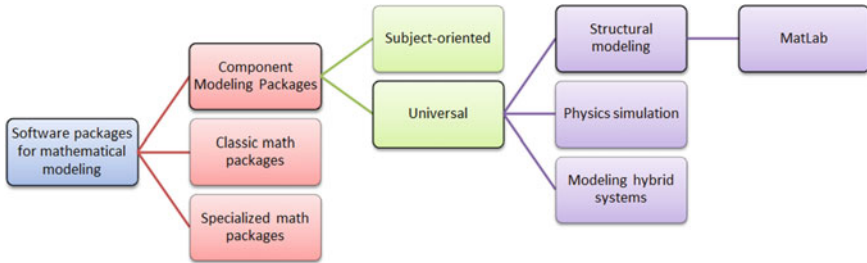


Fig. 1 The classification of mathematical simulation software packages

are programs that can be used to model any systems and those that are tailored for a specific field. The capacities of many programs overlap, and they also rely on similar approaches in solving similar problems. Classify the existing software packages that can be used for mathematical simulation [22]. To do that, we will rely on the following key parameters: software package purpose and capacities; its libraries and applications; modeling principles; integration methods; result visualization tools.

Using these parameters, the classification of mathematical simulation software packages will take a form of being presented in Fig. 1.

So-called “classic” mathematical packages like Mathematica, Maple, and Mathcad are well-suited for the calculations used in sciences when the model is set in an analytical form. These require a relatively small program that mostly consists of macro statements [23]. Component simulation packages are most frequently tooled for numerical experiments. Currently, they dominate technical object design. Based on the representation principles for the original model, component modeling packages can be divided into the following two key groups: structured modeling packages; physical modeling packages. Some authors designate a third group that comprises the packages designed for hybrid system simulation [24]. These packages allow for a visual description of models with complex switching logic.


MatLab software package is a versatile one as it is not tailored for specific application sectors of mathematical simulation. This package is designed to provide analytical and numerical solutions for various mathematical problems and study dynamic systems, including discrete, continuous, and hybrid models. Its key feature is fine-tuned and elaborate programming tools and methods. The MatLab is widely used by engineers, unlike other similar programs. This system comprises the Maple computerized algebra core and the Simulink extension package, as well as dozens of other extensions. Currently, the Simulink mathematical simulation system is one of the most popular tools for numerical computations in various areas of knowledge [25].

Simulink is a block library for multidomain simulation and model design. It supports system design, simulation, automated code generation, and ongoing control including the testing of built-in systems. The Simulink is a graphics editor, custom block library, and solvers for dynamic system modeling and simulation. It is integrated with MatLab and allows including its algorithms in models and exporting simulation results for further analysis.

Key features of Simulink include the following: a graphics editor to construct and manage hierarchic block diagrams; preset block libraries for continuous and discrete-time system modeling; simulation engine with fixed and variable steps; data display area to review simulation results; project and data visualization tools for model file management; model analysis tools to specify its architecture and increase the simulation speed; a functional unit to import MatLab algorithms in models; the Legacy Code Tool application to import C and C++ code in models.

3 Materials and Methods

We solved differential equations via simulations in the MatLab software package. To describe the simulation methods, review the initial stages of working in the MatLab software package and the Simulink app, as well as the simulation procedures for the simplest equation type, i.e. the first-order differential equation that looks as follows: $\frac{dy}{dx} = f(x)$.

To launch the Simulink app, it is necessary to first launch the MatLab package. The home screen of the MatLab package is shown in Fig. 2 (a). It also shows a hint that appears on the screen when you hover the mouse cursor over the Simulink icon in the toolbar. To make a model in Simulink (Fig. 2 (b)), it is necessary to create a new model file through File/New/Model or the  button in the toolbar. The newly created window is shown in Fig. 2 (c). Then you need to locate the blocks in the model window. To do this, you need to open the relevant section of the library, select the required block, and drag it into the window you created. After setting all the

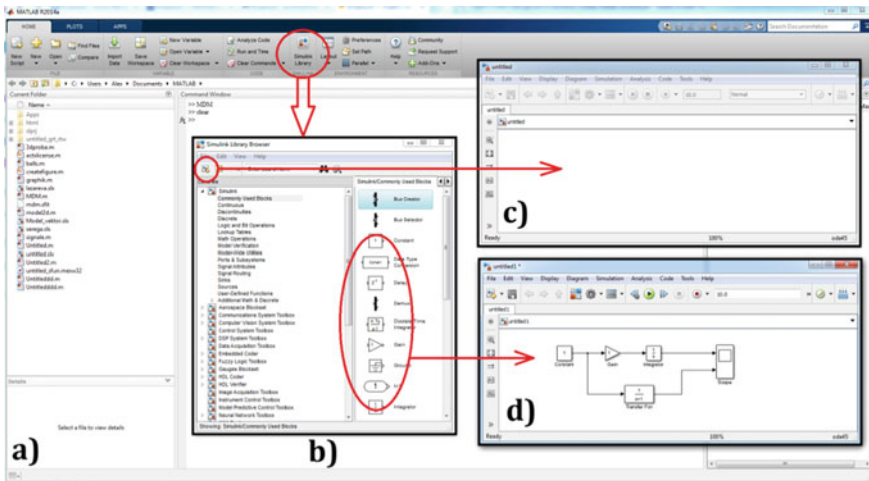



Fig. 2 Model creation procedures in MatLab/Simulink

blocks from the relevant libraries in the model, you need to connect its elements. The model with block connections is shown in Fig. 2 (d).

Before the simulation, it is necessary to preset calculation parameters. Calculation parameters can be set using the control panel in the Simulation/Parameters menu . The calculation time is set by specifying the start time and the stop time values. When selecting the calculation parameters, it is necessary to specify the simulation type and solver for the new state of the system. When simulating continuous systems with variable steps, it is necessary to specify calculation accuracy: relative tolerance and absolute tolerance.

To solve systems of the ordinary first order differential equations, Simulink features the following built-in functions (solvers): ode23, ode45, ode113, ode15s, ode23s, ode23t, and ode23tb. They correspond to various numeric solution methods for differential equations: Runge–Kutta, Adams–Bashforth–Moulton, Rosenbrock, the trapezium method, variable order methods, etc. [26–28].

Review the simulation for the simplest type of differential equation: the one looking like $\frac{dy}{dx} = f(x)$ with discrete variables and the respective integral equation $y = \int f(x)dx + y(0)$. To satisfy the initial condition $y(x_0) = y_0$, the particular solution will look like $y = \int_{x_0}^x f(x)dx + y(0)$. In this particular case, if the equation is $\frac{dy}{dx} = a$, the particular solution that satisfies the initial condition $y(x_0) = y_0$ takes the form $y = a(x - x_0) + y_0$. It is an equation of a straight line passing through a point (x_0, y_0) in plane R^2 . The Simulink model (S-model) for equation $\frac{dy}{dx} = f(x)$ is shown in Fig. 3 (a). Figure 3 (b) shows the simulation result.

Two internal blocks make a key part of the model. Signal $f(x)$ characterizing heterogeneity of the equation is received at the input of the integration block. At the integrator output (Fig. 3 (b)), we received the following equation solution: $y(x)$.

Further on, we describe the simulation procedures and results for more complex differential equations of the first order, as well as linear and non-linear differential equations of the second order.

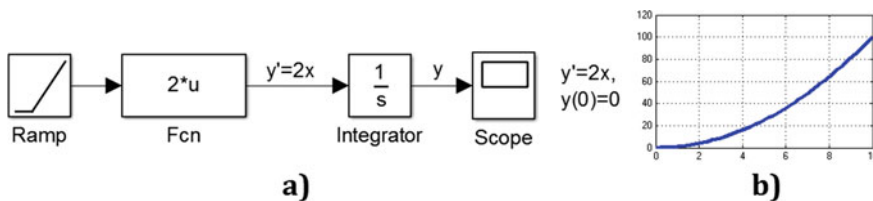


Fig. 3 The structure chart (a) and the graphic results (b) for the ordinary differential equation solution

4 Research Results

Review the first-order linear differential equation $\frac{dy}{dx} = p(x)y + f(x)$. The solution will look like $y' = p(x)y + f(x)$ where $p(x) = \frac{2x}{(1+x^2)}$, $f(x) = 1 + x^2$, $y(0) = 0$. The S-model for the problem is shown in Fig. 4.

The key design element of the linear equation model is the integration block that receives the equation solution as feedback on the input. In the Product block, signal $y(x)$ is multiplied by $p(x)$ and the result is transferred to the Sum block for adding to $f(x)$.

Give a more detailed description of the blocks used in the model: Ramp (Sources library) sets the continuous linear signal; Sum (Math Operations library) is the adder (select the required actions in the parameters: addition or subtraction); Product (Math Operations library) multiplies the input signals; Integrator (Continuous library) integrates the input signal; Scope (Sinks library) builds graphs for the signal and the derivative signal depending on the time; Graph (Sinks library) returns the phase signal of the derivative, i.e., the dependency of the function value on the derivative function in the same points. We select Configuration Parameters in the editor’s Simulation menu. In the resulting window, we select Solver and enter the following parameters: Start Time: 0; Stop Time: 10.0; Type: Variable-step; Solver: ode45 (Dormand-Prince).

Having launched the model, we receive simulation results as function charts for $y(t)$ and $y'(t)$ depending on the time (Fig. 5 (a)), as well as the phase function trajectory (Fig. 5 (b)). To test the result, we use the program code for the same problem in MatLab and apply the dsolve-function. It is obvious that in both cases the graphs will be the same (Fig. 5 (c)).

Review the following first-order logistic differential equation: $y'(t) = -3y(t - 1)(1 - y(t))$. Below we provide the structure chart of the model and the solution result (Fig. 6).

Here we used the Transport Delay block that delays the input signal for the specified time. In the block parameter adjustment window, we specify the signal delay time (Time Delay—1), the initial output signal value (Initial input—1), storage space that contains the delayed signal (Buffer size—in bytes—1024).

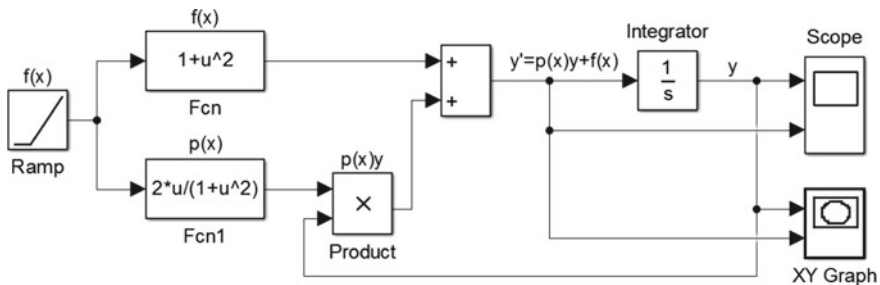


Fig. 4 The structure chart for the solution of the first-order linear differential equation in Simulink

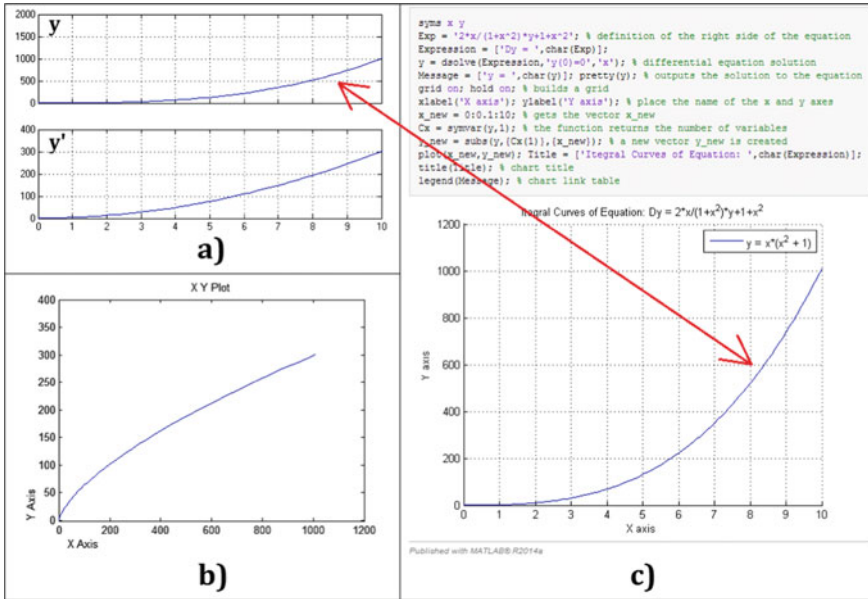


Fig. 5 Simulation results: a) function charts for $y(t)$ and $y'(t)$ depending on the time; b) phase trajectory of the function; c) program code in MatLab

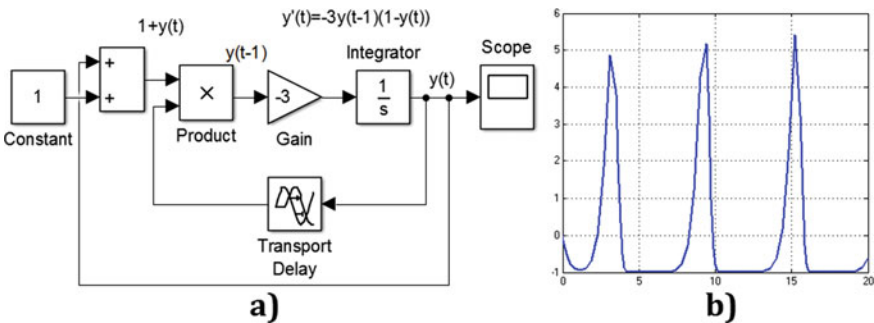


Fig. 6 Structure chart (a) and solution result (b) for the logistic differential equation

Further on we describe the procedures and assess the results of the simulation for second-order linear differential equations. The simplest type of free oscillations is set using equation $\frac{d^2y}{dx^2} = f(x)$. The equation model consists of two integrator blocks that integrate the input signal twice. Forced oscillations in the system are set using equation $\frac{d^2y}{dx^2} = p(x)y + f(x)$. The S-model for this equation is based on two integral blocks with feedback over time (Fig. 7 (a)). If the forced oscillation equation is given as $\frac{d^2y}{dx^2} = p(x)\frac{dy}{dx} + f(x)$, we have the following S model (Fig. 7 (b)).

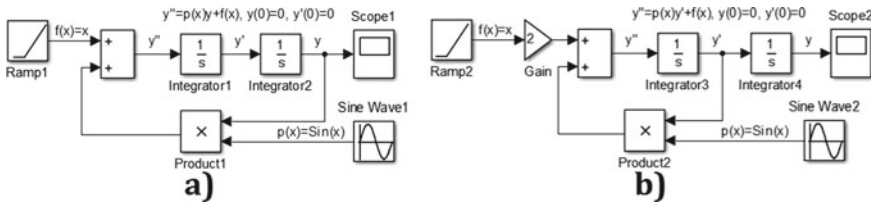


Fig. 7 Structure charts for forced oscillation differential equation models

A key characteristics of the model shown in Fig. 7 (a) is the feedback of two integrators where the signal from the second integrator is transmitted to the input of the first integrator. The model shown in Fig. 7 (b) already has a first-order derivative of the function.

Review the simulation of a free and forced oscillation problem for a mathematical pendulum. In the general case, the forced oscillation equation looks like $\frac{d^2 y}{dx^2} = p(x) \frac{dy}{dx} + q(x)y + f(x)$. If the oscillation system is impacted by the external momentum and the force of viscous friction, the differential equation describing the oscillations of the pendulum will be expressed as follows:

$$\frac{d^2 \varphi}{dt^2} + 2\beta \frac{d\varphi}{dt} + \omega_0^2 \theta_0 \sin \omega t, \tag{1}$$

where φ is the angle of pendulum deflection from the equilibrium position, t is the time, β is the damping coefficient, ω_0 is the natural frequency of the undamped pendulum oscillations, and ω and θ_0 are the frequency and the torque angular amplitude that affects the pendulum respectively.

Due to the non-linear nature of differential Eq. (1), analyzing it stipulates some mathematical difficulties. Thus, it is feasible to apply the Runge–Kutta numerical method for solving this equation. If we consider the phase trajectory of damping ($\omega = 0$) and forced ($\omega = 1$) oscillations with $\omega_0 = 3.13, \theta = 12^\circ, \beta = 0.4, \omega = 1, \varphi(0) = 40^\circ$ and $\varphi'(0) = 0$, we can study the pendulum oscillations. The structure chart for the model is shown in Fig. 8 (a) and the solution results are presented in Fig. 8 (b).

For reference, we provide the solution to this problem in MatLab. Having denoted $x(1) = \varphi(t), x(2) = \varphi'(t)$, we get the vector function of the right side of the equation system $[x(2), -2\beta x(2) - \omega_0^2 \sin(x(1)) + \omega_0^2 \theta_0 \sin(\omega t)]$. Make a file function where we specify the vector of the system right side and a script file for the program code. The program code with the simulation results is shown in Fig. 9.

Consider now a second-order non-linear differential equation $y'' = \frac{y'}{x} + \frac{(y')^2}{y} + 4y \cos x$ with boundary conditions $y(1) = 1$ and $y'(1) = 1$. The model structure chart will look as shown in Fig. 10 (a). In the Math Function block (Math Operations library), we get the squared value of signal $y'(x)$. We divide the signal obtained in the Divide block by the value of signal $y(x)$ and send the result to the Sum block. In the Divide1 block, we divide the derivative signal of the function by the value of x

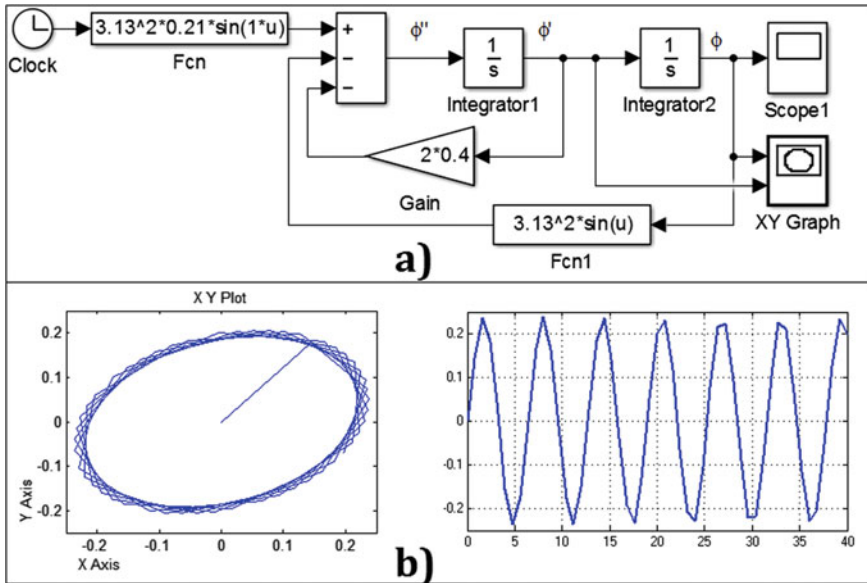


Fig. 8 Structure chart (a) and solution result (b) for the mathematical pendulum differential equation

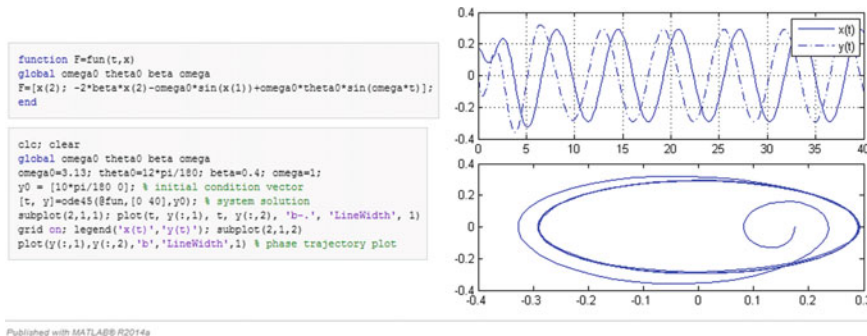


Fig. 9 The program code for the solution of mathematical pendulum differential equation in MatLab

and send the result to the Sum block. From the continuous linear Ramp signal in the Fcn block, we get signal $4\cos(x)$, multiply it by signal $y(x)$ in the Product block, and send the result to the Sum block. As a result, we get the required differential equation at the input of the first integrator block.

Launch the model and present the solution results. Figure 10 (b) shows the phase trajectory of the function and Figure (c) shows the function charts for $y(x)$ and $y'(x)$ depending on the time.

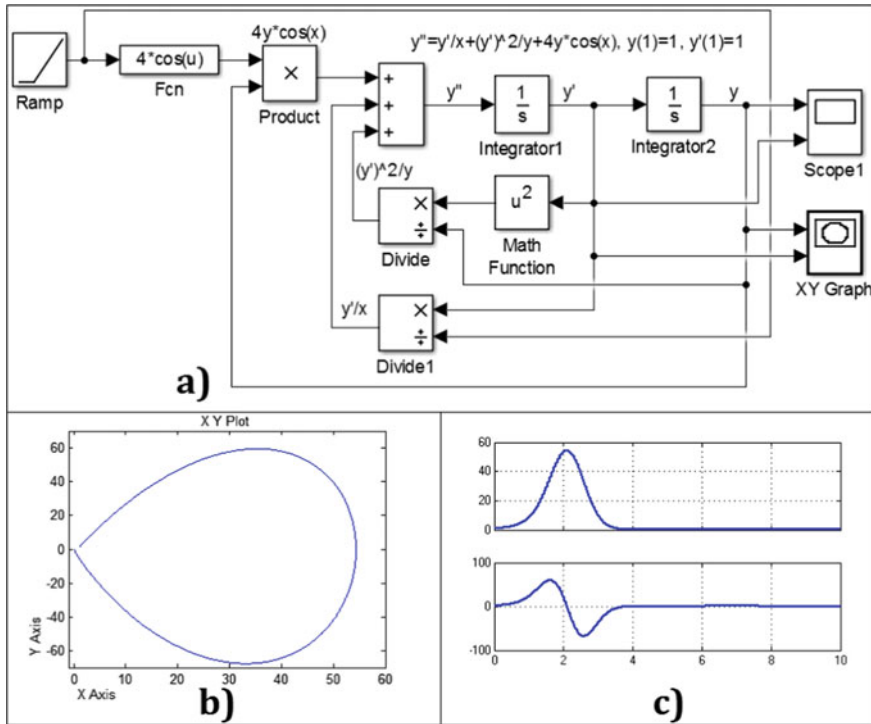


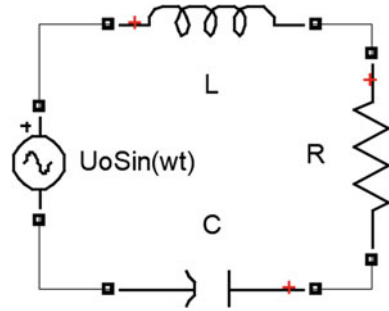
Fig. 10 The solution of the non-linear differential equation: the model structure (a) and simulation results (b, c)

5 Discussion

As mentioned above, the selection of the solving method for differential equations impacts the accuracy of modeling results. In this research work, we used one-step explicit Runge–Kutta methods of the 2-nd, 3-rd, 4-th, and 5-th orders. Modeling time and step also have a significant impact on the result accuracy. In Solver options, there are two integration step parameters: Max step size and Min step size. In both cases, it is set to auto by default. In this case, the value of the Max step size is (Stop time – Start time)/50. This value is often too big, the modeling result has nothing to do with the real process. This can explain small discrepancies between the modeling results obtained via Simulink (Fig. 8 (b)) and the MatLab programming tools (Fig. 9). Even though the parameters used in these two options were identical.

To confirm the significance of the correct solution of differential equations, see the practical application of the simulation method in MatLab/Simulink in one of the fields where the use of differential equations is the most efficient. The electric circuit field is one of these fields. An electric circuit is a finite graph comprising nodes and circuit elements between them. The simplest electric circuit elements include resistances,

Fig. 11 Series-oscillating circuit



inductivities, and capacitances. Each of these elements is a dipole connected to circuit nodes [29].

Calculating an electric circuit means determining the values of the currents at every moment and at every circuit element or determining the potential at each of the circuit nodes and every moment, which is essentially the same. To do this, a system of differential equations describing the circuit is created [30]. This system is built using the Kirchhoff laws. The oscillating circuit (LRC circuit) is the simplest example of an electric circuit. Review the oscillating circuit placed in series with a harmonic alternating voltage source (Fig. 11).

Following the second Kirchhoff law, we have:

$$U_0 \sin(\omega t) = U_R + U_L + U_C = RI + L \frac{dI}{dt} + \frac{1}{C} \int_0^t I dt. \tag{2}$$

After the time-based differentiation of this expression, we obtain a heterogeneous linear differential equation with constant second-order coefficients that describe the forced current changes in the oscillating circuit:

$$\frac{d^2 I}{dt^2} + 2\beta \frac{dI}{dt} + \omega_0^2 I = A \cos \omega t, \tag{3}$$

where $\omega_0 = \sqrt{\frac{1}{LC}}$ is the natural frequency of the oscillating circuit, $\beta = \frac{R}{2L}$ is the damping coefficient, $A = \frac{\omega U_0}{L}$.

As the initial conditions for $t_0 = 0$, we select: $I(t_0) = 0; I'(t_0) = 1$.

Visualize the model for differential Eq. (3) as a structure chart in Simulink using the Integrator block. If the initial block value is the second time derivative of some parameter, we get the first derivative (taking into account the initial conditions) at the output. The mathematical expression of this operation is as follows:

$$I'(t) = I'(t_0) + \int_{t_0}^t I''(\tau) d\tau, \tag{4}$$

where $I''(t)$ is the input signal, $I'(t)$ is the output signal, t_0 is the start time, t is the modeling end time. From this equation, we can see that it is necessary to set initial integration conditions $I'(t_0) = 1$ for the Integrator block in the parameters (Initial condition).

Further on, the use of the integration block for the first derivative helps obtain the current value:

$$I(t) = I(t_0) + \int_{t_0}^t I'(\tau)d\tau. \tag{5}$$

In this case, zero initial integration conditions $I(t_0) = 0$.

Rewrite oscillating circuit Eq. (3) as follows:

$$I'' = -2\beta I' - \omega_0^2 I + A \cos \omega t. \tag{6}$$

Figure 12 (a) shows the Simulink chart for Eq. (6). The behavior of this system may vary depending on the circuit parameters and the source frequency. For the following electrical circuit parameters $C = 10^{-7}/(2\pi)$ F, $L = 10^{-3}/(2\pi)$ H, $R = 100/(2\pi)$ Ohm, and $U_0 = 100$ V, we get particular equations with the following parameters: $\omega_0 = 2\pi \cdot 10^5$ rad/s, $2\beta = 10^5 \Omega/H$, $A = (2\pi)^2 \cdot 10^{11}$ A/s² and $\omega = 2\pi \cdot 10^6$ rad/s. The relationship between the current and the time is shown in Fig. 12 (b) (see the enlarged section of this graph in the top right corner).

Similar results may be obtained via the study of the series-oscillating circuit shown in Fig. 11 using MatLab/Simulink/SimPowerSystems, as described in works dedicated to more complex models [31–34].

Thus, the MatLab/Simulink environment allows for the simulation of multiparameter linear and non-linear, dynamic, event-driven hybrid model systems with continuous or discrete time. The MatLab package provides the users with a wide

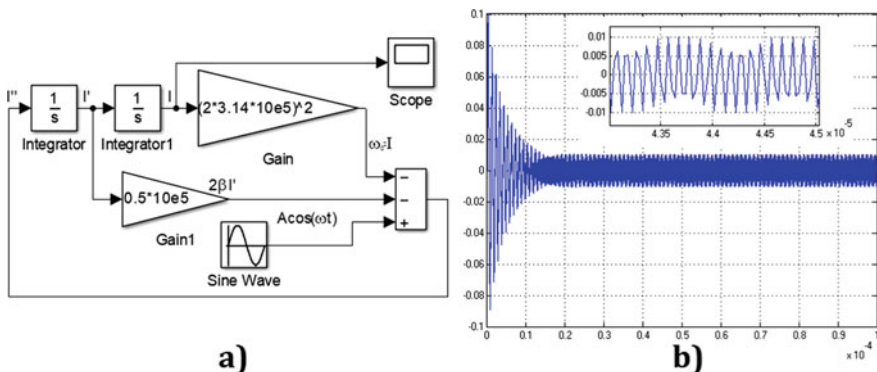


Fig. 12 The structure chart in Simulink (a) and the establishment of forced current oscillations in the oscillating circuit (b)

range of data analysis functions that cover almost all branches of engineering. It is very convenient to use and has diverse functions.

6 Conclusion

This paper presents the key data on MatLab/Simulink and the functions designed to solve ordinary differential equations and their systems. We reviewed the character- and number-driven solutions for these problems. We described the blocks from different Simulink libraries. We provided a description of the procedures and results of simulating linear and non-linear differential equations of the first and the second order. This, however, is not the complete list of MatLab capacities.

List some of MatLab extra solving capacities for differential equations that were not reviewed in this work:

- it allows for character-driven solutions of differential equations if particular derivatives [35];
- to solve boundary-value problems of ordinary differential equations, it features the `bvp4c` method and some auxiliary functions [36];
- for the numerical solution of differential equations with particular derivatives, the PDE Toolbox extension package functions can be used [37];
- there are extension packages (function sets and UIs) designed for the study of mathematical models that can be reduced to solving systems of differential equations that emerge in various branches of physics and engineering [38–41];
- it is possible to create signature functions that would implement any numerical solving methods for differential equations [42].

References

1. Kartashov EM (2020) Analytical approaches to the analysis of unsteady heat conduction for partially bounded regions. *High Temp* 58(3):377–438
2. Iqbal MS (2019) Boundary value problems for non-linear first order systems of partial differential equations in higher dimensions especially in three dimensions. *Adv Appl Clifford Algebras* 29(5):98
3. Aboltins A, Kalis H, Kangro I (2019) Cam with special splines for solving of diffusion-convection problems with discontinuous coefficients for layered materials exposed to fire. *Eng Rural Dev* 18:1147–1154
4. Kumar N, Singh S (2021) A novel physics-based preconditioner for nodal integral method using JFNK for 2D Burgers equation. *Progress Nucl Energy* 134:103668
5. Ghosh A, Maitra S (2021) The first integral method and some nonlinear models. *Comput Appl Math* 40(3):79
6. Gosse L (2021) Diffusive limit of a two-dimensional well-balanced scheme for the free Klein-Kramers equation. *Multiscale Model Simul* 19(1):568–587
7. Djikaev YS, Ruckenstein E (2020) Effect of chemical aging of aqueous organic aerosols on the rate of their steady-state nucleation. *Phys Chem Chem Phys* 22(31):17612–17619

8. Wang W, Ralescu DA (2021, in press) Option pricing formulas based on uncertain fractional differential equation. *Fuzzy Optim Decis Making*. <https://doi.org/10.1007/s10700-021-09354-z>
9. Guardasoni C, Rodrigo MR, Sanfelic SA (2020) Mellin transform approach to barrier option pricing. *IMA J Manag Math* 31(1):49–67
10. Bressloff PC (2021) Construction of stochastic hybrid path integrals using operator methods. *J Phys A Math Theor* 54(18):abf38f
11. Brenna M, Lazaroiu GC, Roscia M, Saadatmandi S (2020) Dynamic model for the EV's charging infrastructure planning through finite element method. *IEEE Access* 8:102399–102408
12. Baumann H, Hanschke T (2021) Computation of solutions to linear difference and differential equations with a prescribed asymptotic behavior. *Adv Differ Equ* 2021(1):173
13. Doerr B, Zheng W (2020) Working principles of binary differential evolution. *Theor Comput Sci* 801:110–142
14. Babicheva RI, Semenov AS, Soboleva EG, Kudreyko AA, Zhou K, Dmitriev SV (2021) Discrete breathers in a triangular β -Fermi-Pasta-Ulam-Tsingou lattice. *Phys Rev E* 103(5):052202
15. Eickhoff F, Anders FB (2020) Strongly correlated multi-impurity models: the crossover from a single-impurity problem to lattice models. *Phys Rev B* 102(20):205132
16. Sylvain TTA, Patrice EA, Marie EEJ, Pierre OA, Huber B-BG (2021) Analytical solution of the steady-state atmospheric fractional diffusion equation in a finite domain. *Pramana – J Phys* 95(1):1
17. Jafari H, Mahmoudi M, Noori Skandari MH (2021) A new numerical method to solve pantograph delay differential equations with convergence analysis. *Adv Differ Equ* 2021(1):129
18. Nuugulu SM, Gideon F, Patidar KC (2021) A robust numerical solution to a time-fractional Black-Scholes equation. *Adv Differ Equ* 2021(1):123
19. Ali I, Haq S, Nisar KS, Baleanu D (2021) An efficient numerical scheme based on Lucas polynomials for the study of multidimensional Burgers-type equations. *Adv Differ Equ* 2021(1):43
20. Pourhassan MR, Raissi S, Apornak A (2021, in press) Modeling multi-state system reliability analysis in a power station under fatal and nonfatal shocks: a simulation approach. *Int J Qual Reliab Manag*. <https://doi.org/10.1108/IJQRM-07-2020-0244>
21. Wu Y, Morgan EF (2020) Effect of fabric on the accuracy of computed tomography-based finite element analyses of the vertebra. *Biomech Model Mechanobiol* 19(2):505–517
22. Bebikhov YV, Semenov AS, Semenova MN, Yakushev IA (2019) Analysis of methods of modeling technical systems in MATLAB. *Model Optim Inf Technol* 7(3):12
23. Bebikhov YV, Semenov AS, Semenova MN, Yakushev IA (2019) Application of mathematical modeling for solving linear algebraic and ordinary differential equations. *Mod Sci Actual Prob Theory Pract Ser Nat Tech Sci* 4:29–36
24. Semenov AS, Yakushev IA, Egorov AN (2017) Mathematical modeling of technical systems in the MATLAB. *Mod High Tech* 8:56–64
25. Semenov A, Semenova M, Bebikhov Y, Yakushev I (2021) Mathematical modeling of physical processes in metals and ordered alloys. *Smart Innov Syst Technol* 247:40
26. Bertram C, Faßbender H (2021) A quadrature framework for solving Lyapunov and Sylvester equations. *Linear Algebra Appl* 622:66–103
27. Hidayat MIP (2021) Meshless finite difference method with B-splines for numerical solution of coupled advection-diffusion-reaction problems. *Int J Thermal Sci* 165:106933
28. Egger H, Schmidt K, Shashkov V (2021) Multistep and Runge–Kutta convolution quadrature methods for coupled dynamical systems. *J Comput Appl Math* 387:112618
29. Bebikhov YV, Semenov AS, Yakushev IA, Kugusheva NN, Pavlova SN, Glazun MA (2019) The application of mathematical simulation for solution of linear algebraic and ordinary differential equations in electrical engineering. In: *IOP conference series: materials science and engineering*, vol 643, no 1, p 012067

30. Semenov AS, Khubieva VM, Kharitonov YS (2018) Mathematical modeling of static and dynamic modes DC motors in software package MATLAB. In: 2018 international Russian automation conference (RusAutoCon), 8501666
31. Thakallapelli A, Kamalasadana S (2020) Measurement-based wide-area damping of inter-area oscillations based on MIMO identification. *IET Gener Transm Distrib* 14(13):2464–2475
32. Semenov A, Yakushev I, Kharitonov Y, Shevchuk V, Gracheva E, Ilyashenko S (2020) Calculation of load diagrams and static characteristics of multimotor electric drive systems using the methods of equivalent forces and reduced moments. *Int J Technol* 11(8):1537–1546
33. Zagolilo SA, Semenov AS, Semenova MN (2020) Computer modeling of a multimotor electric drive system in the MatLab suite. In: Proceedings - 2020 international Russian automation conference (RusAutoCon), 9208078
34. Faraji A, Hesami Naghshbandy A (2019) A combined approach for power system stabilizer design using continuous wavelet transform and SQP algorithm. *Int Trans Electr Energy Syst* 29(3):e2768
35. Ghanbari B, Kuo C-K (2021) Abundant wave solutions to two novel KP-like equations using an effective integration method. *Physica Scripta* 96(4):045203
36. Maklakov VN (2021) A method for increasing the order of approximation to an arbitrary natural number by the numerical integration of boundary value problems for inhomogeneous linear ordinary differential equations of various degrees with variable coefficients by the matrix method. *Vestnik Samarskogo Gosudarstvennogo Tekhnicheskogo Universiteta, Seriya Fiziko-Matematicheskie Nauki* 24(4):718–751
37. Ding L, Ma W-X, Chen Q, Huang Y (2021) Lump solutions of a nonlinear PDE containing a third-order derivative of time. *Appl Math Lett* 112:106809
38. Krylova KA, Lobzenko IP, Semenov AS, Kudreyko AA, Dmitriev SV (2020) Spherically localized discrete breathers in bcc metals V and Nb. *Comput Mater Sci* 180:109695
39. Krylova KA, Korznikova EA, Semenov AS, Bachurin DV, Dmitriev SV (2020) Linking tracks in mica crystals with phase transitions in a bistable lattice. *Eur Phys J B* 93(2):23
40. Poletaev GM, Zorya IV, Rakitin RY, Semenov AS, Starostenkov MD (2020) Influence of carbon and oxygen impurities on migration velocity of grain-boundary triple junctions in FCC metals. *Russ Phys J* 62(10):1840–1845
41. Poletaev GM, Novoselova DV, Rakitin RY, Semenov AS (2020) Modeling the formation of free volume at grain boundaries and triple junctions during nickel crystallization. *Lett Mater* 10(3):299–302
42. Shloof AM, Senu N, Ahmadian A, Salahshour S (2021) An efficient operation matrix method for solving fractal–fractional differential equations with generalized Caputo-type fractional–fractal derivative. *Math Comput Simul* 188:415–435

Information and Intelligent Models in the Management of Transport and Logistics Systems



Valerii Zubkov and Nina Sirina

Abstract The analysis of the development of technologies in the railway industry, the application of transport processes, the use of its resources, shows a positive correlation with the development and improvement of information technologies. This is explained by the constantly increasing knowledge-intensive nature of the transport system, the acceleration of scientific and technological progress in the field of industrial, information and digital technologies, the creation of electronic methods for obtaining, processing, accounting, storing and using information data. The paper considers the intellectualization of transport and logistics system management by creating information-intelligent models for collecting, processing, analyzing, ranking, accumulating, storing the necessary information and providing a favorable environment for searching, viewing, visualizing data, comparing possible solutions to problematic issues and choosing the best one based on accumulated knowledge, experience and available resource opportunities. The paper presents a conceptual model of transport and logistics system management, as well as a methodology for forming ontologies. This technique is necessary to reflect the problem areas of the implementation of transport and production processes (sub-processes). The methodology of ontology formation was used in the creation of information and intelligent models of transport and logistics system management.

Keywords Intellectualization of management · Transport and logistics system · Transport and production process · Transport and information space · Information model

V. Zubkov (✉)
Joint-Stock Company “Federal Cargo Company”, JSC “FGK”, 34 Masha Poryvaeva Street,
Moscow 107078, Russia

N. Sirina
Ural State University of Railway Transport (USURT), Ul. Kolmogorova, 66, 620034
Yekaterinburg, Russia

1 Introduction

The uniqueness of the present time is the increased attention to the acquisition of knowledge from the information space from the implementation and application of transport and production processes (sub-processes) and the creation of technologies for its use with the help of information systems, models that have received the definition as artificial cognitive systems.

The analysis of the development of technologies in the railway industry, the application of transport processes, the use of its resources, shows a positive correlation with the development and improvement of information technologies. This is explained by the constantly increasing knowledge-intensive nature of the transport system, the acceleration of scientific and technological progress in the field of industrial, information and digital technologies, the creation of electronic methods for obtaining, processing, accounting, storing and using information data.

The implementation of the concept of industrial development in the transport system, on the one hand, leads to an increase in the possibility of converting consumers of railway services, increasing their productivity, and on the other hand, complicates the process of quality management of transport companies (systems).

In the field of intellectualization of transport and logistics system management, as well as automated processing of production and technical information coming from global and corporate networks, the task of analyzing and further accumulating its qualification (professional) layer of knowledge remains unsolved. Also, on the basis of this knowledge, determining the best option for management actions necessary for solving problematic issues, searching for interested partners in their solution, evaluating the effectiveness of decisions made and choosing strategic directions of production activities [1].

Ontologies in information systems create opportunities for in-depth search for the necessary information, but the search itself requires a long time and the presence of such an active ontology that would correspond to a specific transport and production process (sub-process), despite the fact that the creation of an ontology at the present time is a time-consuming and complex engineering task.

The user (the head of the transport and logistics system or its structural enterprise), without getting the necessary result, is interested in automating this process. Such a process, which, with minimal detail and minimal time, will allow to manage the information search, the acquired and accumulated knowledge about a particular object or process, as well as ensure the choice of the best option for managerial action, in the context of the available resource capabilities and in accordance with the qualification (professional) interest [2, 3].

This work is presented in the context of the development of the information theory of the conciliatory management structures of transport and logistics systems. The practical component of the theory refers to the guidelines for increasing the quality of organization and management of large-scale transport systems. Efficiency is achieved by improving and optimizing the management activities of the company, by creating sophisticated information technology products. The main issue that arises

in the course of solving the problem of management optimization is the question of determining the criterion of complexity of planning and accounting the time of the company’s managers. The complexity criterion is necessary for the creation and formalization of the normative and target functions of the manager, the criteria for his effectiveness in delegating and delineating job responsibilities. The criteria for the complexity of planning and accounting, respectively, management, directly depend on the scale of the transport system, the number of its structural enterprises, its versatility and performance indicators.

Figure 1 shows the factors that determine the complexity indicator criterion and its parameters.

The criterion of the complexity indicator of the organization and management depends on the following factors:

- the complexity of the tasks to be solved;
- features of the effects of external and internal conditions;

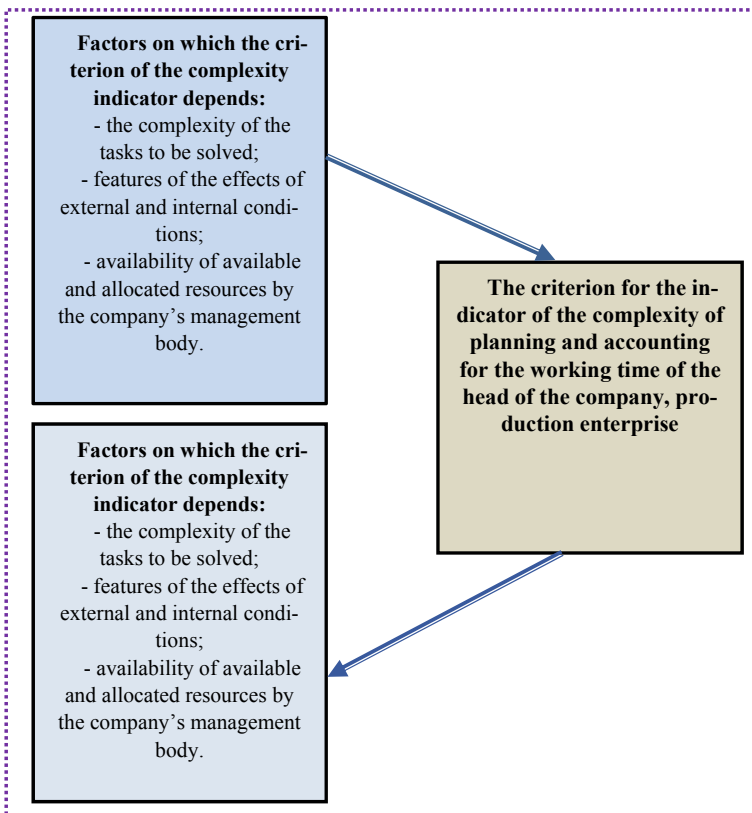


Fig. 1 The structure of the factors that determine the criterion of the complexity indicator and its defining parameters

- availability of available and allocated resources by the company's management body.

The complexity criterion can be a pointer to parameters such as:

- possible risks of reduced manageability (the more multi-agent management system, the more difficult it is to manage);
- self-adaptation to changing influences (less complex system, more flexible);
- production costs (more complex and multi-agent system, more expensive);
- transparency of the system's production processes (complex system, less transparent, less manageable).

Multi-criteria and multi-complexity of management are related to the effectiveness of the organization and management as a whole (it is more difficult to manage qualitatively). The predicted and weighted value of the complexity assessment in the field of strategic management provides the possibility of excluding greater complexity in solving the tasks assigned to the manager. [4] It allows to maintain the principle of equal complexity of all structural divisions of the transport system and to observe fair incentives when performing tasks of appropriate complexity. As a result, such measures should have a rational impact on the quality functioning of the transport and logistics company.

One of the solutions to this problem is to create an information model for collecting, processing, analyzing, ranking, accumulating, storing the necessary information and providing a favorable environment for searching, viewing, visualizing data, comparing possible solutions to problem issues and choosing the best one based on accumulated knowledge, experience and available resource opportunities.

Figure 2 schematically shows the structure of possible indicators used to determine the estimated value of the complexity of transport and logistics system enterprises.

As shown in Fig. 2, the value of the complexity of transport and logistics system enterprises depends on the volume of cargo transportation (D), the content of transport and production infrastructure (DPI), the content of traction rolling stock (T), marketing (M), the volume of sales of transport services (C), corporate and technological management (Y). The presented diagram shows the intersection of many possible criteria for the complexity of management. In the multi-agent model of the transport and logistics system, it is very difficult for managers, both structural divisions and companies, when considering complex management tasks and solving emerging problematic issues, to qualitatively and effectively plan personal time resources of working time, take into account, analyze and give a correct assessment of the timeliness of their actions.

2 Materials and Methods

To create an information-intellectual model of transport and logistics system management, it is necessary to develop a methodology for the formation of ontologies. This

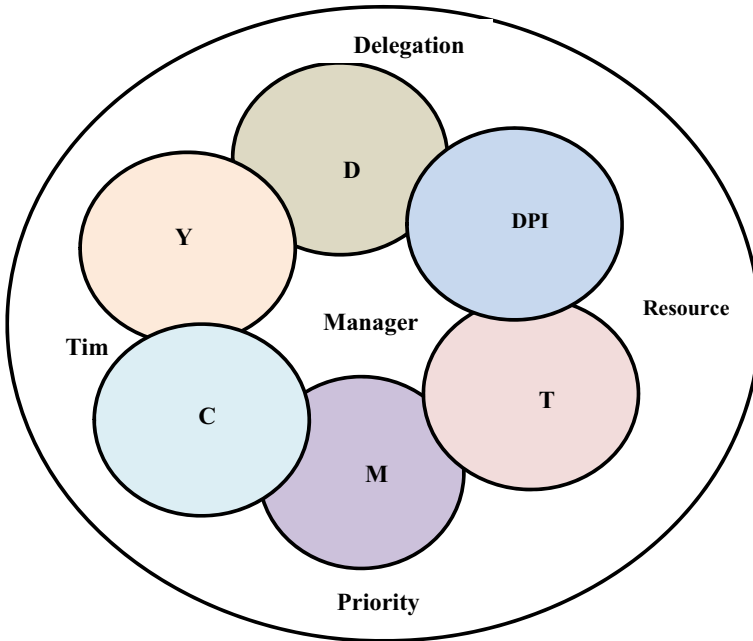


Fig. 2 The structure of indicators used to determine the complexity of enterprises

methodology is necessary to reflect the problem areas of the implementation of transport and production processes (sub-processes). Such ontologies are necessary for interested subjects of the transport system to coordinate its interactions when solving problematic issues and taking (applying) managerial actions. In particular, the methodology should provide a cognitive link between the reflection of the problem area of the implementation of processes (sub-processes) and the formal reflection of the transport and production processes (sub-processes) themselves. Processes (sub-processes) are reflected in such a way that it is possible to form a prototype of a system that is a multi-agent system that has the ability to model processes (sub-processes) and further manage them [5, 6].

To form a methodology for building the system, a conceptual model of transport and logistics system management is developed, based on the accumulated knowledge and available resource capabilities, shown in Fig. 3.

Figure 3 shows that the lower levels of the conceptual model are the levels of description of the problem areas of the implementation of transport and production processes. The main product of these levels is the description of knowledge about the problem areas of implementation. This description should take place in a universal form that will correspond to the necessary model of the ontology.

The infrastructure level of the conceptual model is represented by an agent platform, which ensures the interaction of interested model agents in solving management tasks [7].

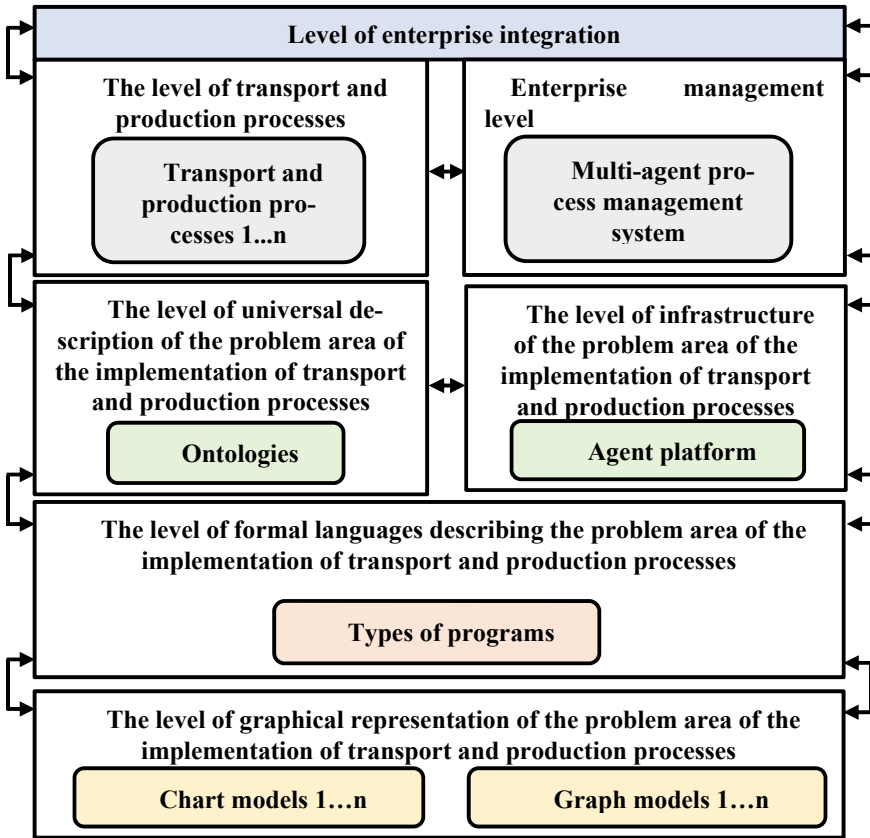


Fig. 3 A conceptual model of transport and logistics system management based on accumulated knowledge and available resource opportunities

Ontologies together with the agent platform create conditions for the formation of the next level of the conceptual model, namely, the level of self-support of transport and production processes and the level of management of production enterprises.

Transport and production processes are formalized using the created ontologies, while the resource opportunities and stakeholders that are planned to be used in the implementation of the processes are determined directly in the ontologies.

This approach, when describing transport and production processes based on the created ontologies, creates conditions for additional control over the production environment of the enterprise (changing the scope of implementation of processes through the influence of internal or external factors leads to changes or adjustments in the processes themselves) [8].

The introduction of ontologies, their further formalization, which is determined on the basis of the acquired knowledge, ensures the formation and implementation of the top level of the conceptual model, this is the level of integration. The main

product of this level is the integration of production enterprises into integrated information systems for managing transport and production processes [9]. Ontologies at this level define a protocol for the implementation of the integration process of interacting information systems and form common rules and norms of interaction between interested agents (subjects).

Integration is implemented on the basis of information self-support of transport and production processes of enterprises.

Thus, the conceptual model defines the relations between the problem areas of process implementation and the transport and production processes themselves.

In this case, each ontology (K_n), can be expressed as a tuple:

$$K_n = \{K_n^w, K_n^c, K_n^p, K_n^s\}, \quad (1)$$

where: K_n^w - the set of values of the n-th ontology;

K_n^c - the set of relations between the positions (representations) of the n-th ontology;

K_n^p - the set of processes of the values of the n-th ontology;

K_n^s - the set of sub-processes of the values of the n-th ontology.

The set of values of the n-th ontology looks like this:

$$K_n^w = \{w_{nj} | j = \overline{1, J^w}\}, \quad (2)$$

where: J^w - number of values of the n-th ontology, $K_n^w \neq \emptyset$.

From the entire set of values, we distinguish the following two fundamental subsets:

$$K_n^{wp} \subseteq K_n^{wR} \subseteq K_n^w, \quad (3)$$

where: K_n^{wp} - the set of values of executors of processes (sub-processes) of production enterprises in the n-th ontology;

K_n^{wR} - the set of values of the resource opportunities of the n-th ontology.

The executors of the processes (sub-processes) and resource opportunities are determined for each problem area of the implementation of transport and production processes.

The set of relations between the positions (representations) of the n-th ontology, expressed by the form:

$$K_n^c = \{c_{nj} | j = \overline{1, J^c}\}, \quad (4)$$

where: J^c - the number of relations between the values of the n-th ontology, $J^c = |K_n^c|$.

$$c_{nj} = (c_j^f C_j), \quad (5)$$

where: c_j^f – the set of properties of the j -th relation.

C_j – the tuple of the j -th links of the n -th ontology.

The relations between the values of the ontology provide a description of the norms and rules that determine the interaction of objects (subjects) in the organization and management of transport and production processes.

The set of processes of the values of the n -th ontology is represented as:

$$K_n^p = \{p_{nj} | j = \overline{1, J^p}\}, \quad (6)$$

where: p_{nj} – the set of processes of the j -th value of the n -th ontology, $J^p = |K_n^p|$. In this case, K_n^p , may have no values, then:

$$p_{nj} = \{p_{njA} | A = \overline{1, A_j^p}\}, \quad (7)$$

where: p_{njA} – A -th the process of the j -th value of the n -th ontology;

A_j^p – the number of processes of the j -th value of the n -th ontology, p_{nj} can be \emptyset .

The set of sub-processes of the values of the n -th ontology looks like this:

$$K_n^s = \{s_{nj} | j = \overline{1, J^s}\}, \quad (8)$$

where: s_{nj} – the set of sub-processes of the j -th value of the n -th ontology, $J^s = |K_n^s|$. In this case, K_n^s , when defining values, it may not have them, then:

$$s_{nj} = \{s_{nja} | a = \overline{1, a_j^s}\}, \quad (9)$$

where: s_{nja} – a -th sub-process of the j -th value of the n -th ontology;

a_j^s – number of sub-processes of j -th value of the n -th ontology, s_{nj} can be \emptyset .

It follows that before starting the description of transport and production processes, it is necessary to formalize the areas of implementation of these processes, including the formalization of problem areas of implementation. For this purpose, it is necessary to define and describe the values of the ontology, in particular the objects (norms, rules, standards) used in information flows that link transport and production sub-processes, processes and their executors. When defining and describing the executors of processes (sub-processes), it is necessary to describe their resource opportunities in the ontology, which will or will not be able to provide the implementation of the function of the process (sub-process) itself [10].

3 Results

The proposed methodology for the formation of ontologies was used in the creation of information models for the management of the transport and logistics system, such as:

- “Automated workplace Problematic issues”;
- “Automated system for planning and accounting the working time of the manager”.

The information model “Automated workplace Problematic issues”, designed to intellectualize the management of the transport and logistics system when choosing the most effective and rational option for the management solution of problematic issues. Virtualization of workplaces, affects the improvement of the quality of management of large-scale transport and logistics companies. The construction of the program is based, among other things, on the method of analyzing hierarchies. The estimated value of solutions to problem issues using the proposed methodology for the formation of ontologies and the method of analyzing hierarchies is based on objective and subjective incoming information [11].

Problems in determining the most correct choice are relevant in all types of activities of manufacturing enterprises. Managers who manage transport and production processes solve them, at the tactical and strategic levels. The chosen optimal solution should be characterized as the best possible one. It is impossible to take into account all the factors that influence this choice without intellectualizing this process, while it is much more difficult to do this when choosing strategic decisions that affect both enterprises and the system as a whole in the long term [12].

The developed program is designed to systematize, manage, control and take into account priority areas of activity when solving problematic issues. The breadth of the spectrum of emerging problematic issues arising from production activities, a large number of structural divisions that form priority areas in their activities, dictate and form the need to ensure systematization, ranking, distribution and appointment of curators who ensure the solution of “problematic issues”.

The developed information model provides storage, ranking and monitoring in an automated database of all priority areas of activity of structural divisions and the company as a whole. Accumulates knowledge about the problem areas of the implementation of transport and production processes, as well as provides an optimal choice of management solutions from their possible options and provides this information to the heads of production verticals, authorized commissions, with a subsequent assessment of their opportunities, including resource and control of the process of their implementation [13].

The escalation of the level of consideration of priority areas in this information model is shown in Fig. 4.

In a multi-level and multi-agent transport and logistics system, it is difficult for the heads of structural divisions, heads of management bodies at various levels of the system, when considering problematic issues, multi-complex management tasks, to

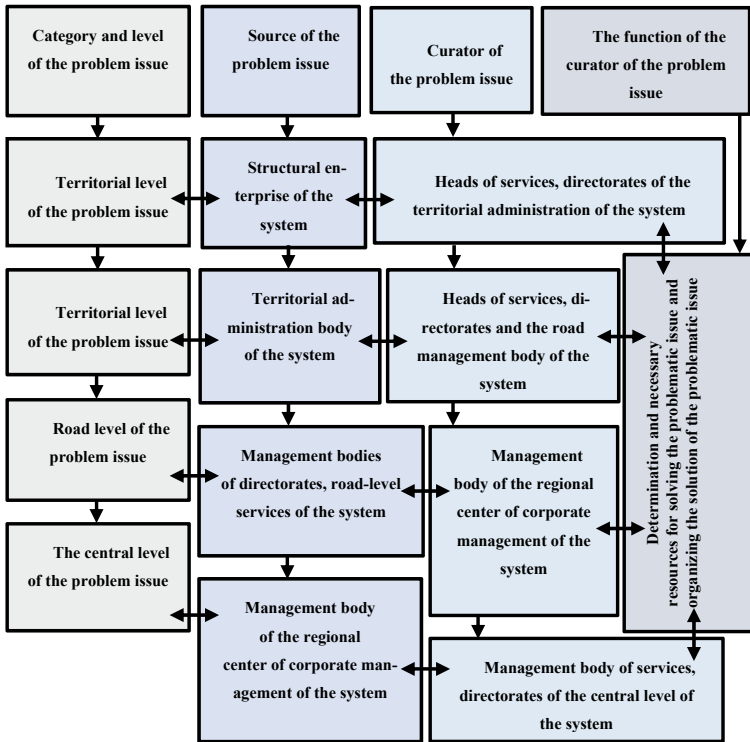


Fig. 4 The scheme of escalation of the level of consideration of priority areas in the model “Automated workplace Problematic issues”

qualitatively and rationally predict and plan the resources of working time, analyze, take into account and timely evaluate their actions. To eliminate these risks in the work of managers, an information model “Automated system for planning and accounting for the working time of the manager” was developed.

The developed information model is designed for the rational use, accounting, systematization and control of the working time of the manager. It allows to systematize and efficiently distribute the performance of production tasks in time periods. Record activities that require their repetition in order to obtain a positive result from the implementation of transport and production processes [14]. Identify temporary reserves of managers of structural enterprises and management bodies of the system at all stages of production processes. Provides storage and notification of interested subjects of transport services about all organizational and administrative documents accompanying the solution of problematic production issues. Storage in an automated database of information about planned and actually completed activities that contribute to the assessment of the effectiveness of both decision-making and the use of their working time [15].

Figure 5 shows the scheme of the information and intellectual cognitive system “Automated system of planning and accounting of the working time of the manager”.

The combination of quantitative and qualitative monitoring, accounting and analysis of the manager’s working time does not limit the evaluative actions only to a set of template criteria, but at the same time makes it possible to formalize the parameters unstructured among themselves.

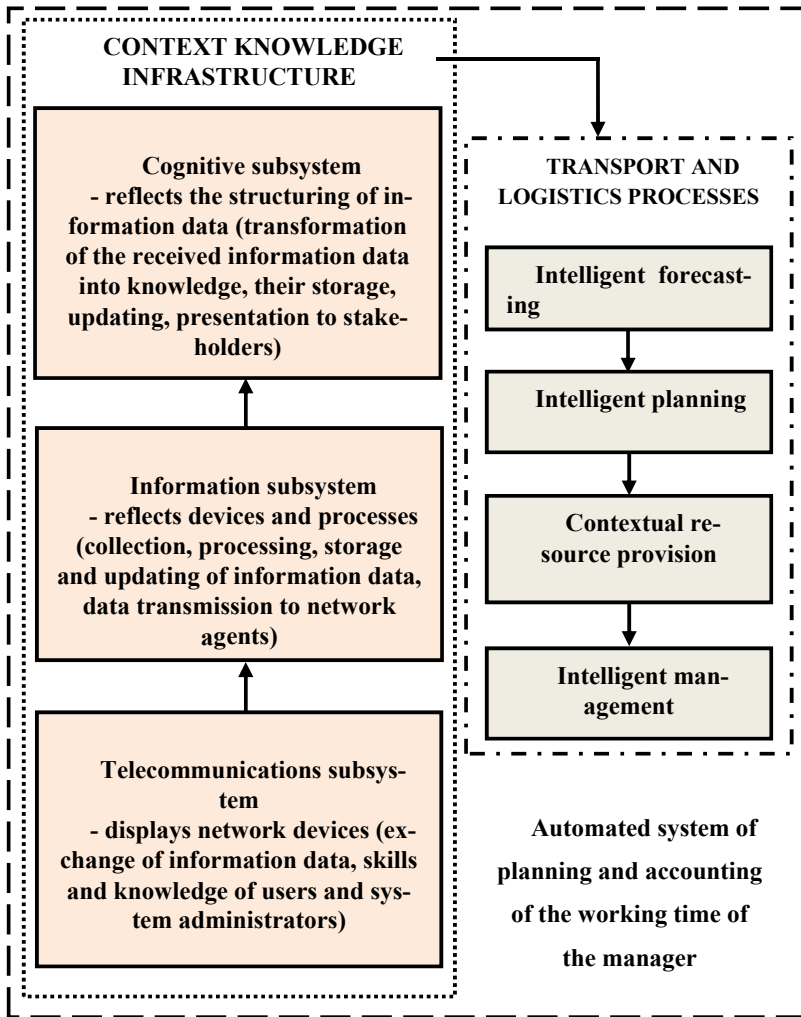


Fig. 5 The scheme of the information and intellectual cognitive system “Automated system of planning and accounting of the working time of the manager”

The presented information models function in a single transport and information space and are integrated into a complex of information systems for managing transport and production processes.

4 Conclusion

Intellectualization of transport and logistics system management, by creating information models for collecting, processing, analyzing, ranking, accumulating, storing the necessary information and providing a favorable environment for searching, viewing, visualizing data, comparing possible solutions to problem issues and choosing the best one based on accumulated knowledge, experience and available resource opportunities, is an alternative way to improve the quality of organization and management of a multi-level and multi-agent system, as well as rational use, accounting, systematization and control of the manager's working time.

The conceptual model of transport and logistics system management, defines and establishes links between the problem areas of process implementation and the transport and production processes themselves.

The methodology of ontology formation reflects the problem areas of the implementation of transport and production processes (sub-processes).

Based on the developed methodology for the formation of ontologies, information models for the management of the transport and logistics system "Automated workplace Problematic issues" and "Automated system for planning and accounting for the working time of the manager" were created. These information products have passed state registration.

References

1. Treber S, Breig R, Kentner M, Hafner B, Lanza G (2019) Information exchange in global production networks: increasing transparency by simulation, statistical experiments and selection of digitalization activities. *Procedia CIRP* 84:225–230. <https://doi.org/10.1016/j.procir.2019.04.214>
2. Leviakangas P (2016) Digitalisation of Finland's transport sector. *Technol Soc* 47:1–15. <https://doi.org/10.1016/j.techsoc.2016.07.001>
3. Wang H, Yang H (2019) Methodological ridesourcing systems: a framework and review. *Transp Res Part B* 129:122–155. <https://doi.org/10.1016/j.trb.2019.07.009>
4. Kavanagh P (2016) A case for negotiated performance-based contracting rather than competitive tendering in government public transport (bus) service procurement. *Res Transp Econ* 59:313–322. <https://doi.org/10.1016/j.retrec.2016.06.006>
5. Blyde J, Molina D (2015) Logistic infrastructure and the international location of fragmented production. *J Int Econ* 95(2):319–332. <https://doi.org/10.1016/j.jinteco.2014.11.010>
6. Lovelace R, Parkin J, Cohen T (2020) Open access transport models: a leverage point in sustainable transport planning. *Transp Policy* 97:47–54. <https://doi.org/10.1016/j.tranpol.2020.06.015>

7. Li Y, Wu F (2012) The transformation of regional governance in China: The rescaling of statehood. *Prog Plan* 78:55–99. <https://doi.org/10.1016/j.progress.2012.03.001>
8. Canitez F, Alpkokin P, Andrew Black J (2019) Agency costs in public transport systems: net-cost contracting between the transport authority and private operators - impact on passengers. *Cities* 86:154–166. <https://doi.org/10.1016/j.cities.2018.09.010>
9. Walter J, Abendroth B (2020) On the role of informational privacy in connected vehicles: A privacy-aware acceptance modelling approach for connected vehicular services. *Telematics Inform* 49:101361. <https://doi.org/10.1016/j.tele.2020.101361>
10. Rothengatter W (2019) Megaprojects in transportation networks. *Transp Policy* 75:A1–A15. <https://doi.org/10.1016/j.tranpol.2018.08.002>
11. Chen Y (2016) Industrial information integration—A literature review 2006–2015. *J Ind Integr* 2:30–64. <https://doi.org/10.1016/j.jii.2016.04.004>
12. Popova O, Gorev A, Shavyraa Ch (2018) Principles of modern route systems planning for urban passenger transport. *Trans Res Procedia* 36:603–609. <https://doi.org/10.1016/j.trpro.2018.12.146>
13. Cooke P (2011) Transition regions: Regional–national eco-innovation systems and strategies. *Prog Plan* 76(3):105–146. <https://doi.org/10.1016/j.progress.2011.08.002>
14. Saccani N, Perona M (2007) Shaping buyer–supplier relationships in manufacturing contexts: Design and test of a contingency model. *J Purch Supply Manag* 13:26–41. <https://doi.org/10.1016/j.pursup.2007.03.003>
15. Matteis T, Liedtke G, Wisetjindawat W (2016) A framework for incorporating market interactions in an agent based model for freight transport. *Transp Res Procedia* 12:925–937. <https://doi.org/10.1016/j.trpro.2016.02.044>

A Review of the Earthquake Caused Damage on Reinforced Concrete and Masonry Buildings in Turkey



Başak Zengin 

Abstract Earthquake damaged buildings give valuable information about attenuation of earthquake, directivity of earthquake waves, magnitude of seismic shaking and causes of damage distribution. It also shows effects of earthquake on buildings in detail. In this way taking precautions on designing of new structures and on soil structure interaction can be achieved. Besides, increasing seismic safety of existing buildings against earthquake can be provided in this way. In this study, the earthquake damages on reinforced concrete and masonry building are investigated. Taking destructive earthquakes that recently occurred in Turkey, acceleration records are compared with the spectrums of Turkish seismic code regulations. Addition to this, causes of earthquake damages and earthquake-building relation are given.

Keywords Earthquake damage · Reinforced concrete buildings · Masonry buildings · Turkish Sesimic Code

1 Introduction

Turkey is one of the most earthquake –prone areas in the world. According to Turkish Tectonic ap (Fig. 1) 92% of Turkey takes place in earthquake region and, almost all citizens live in this area. Turkey has official earthquake code since 1940, and it is renewed at regular intervals in view of both the developments in earthquake engineering and in line with social needs. 2019 Building Earthquake Code of Turkey has improved the previous version published in 2007 by expanding its coverage. The most important improvements are the site-specific earthquake hazard definition as well as earthquake design of tall buildings, seismic isolation and piled foundations. Non-linear analysis methods are used as mandatory for performance evaluation in some special cases. In addition, a design supervision system has been formed for non-standard practice and special applications that require expertise [1, 2].

B. Zengin (✉)

Construction Technology-Elbistan Vocational School, Kahramanmaraş Istiklal University, 46060 Kahramanmaraş, Turkey
e-mail: basak.zengin@istiklal.edu.tr

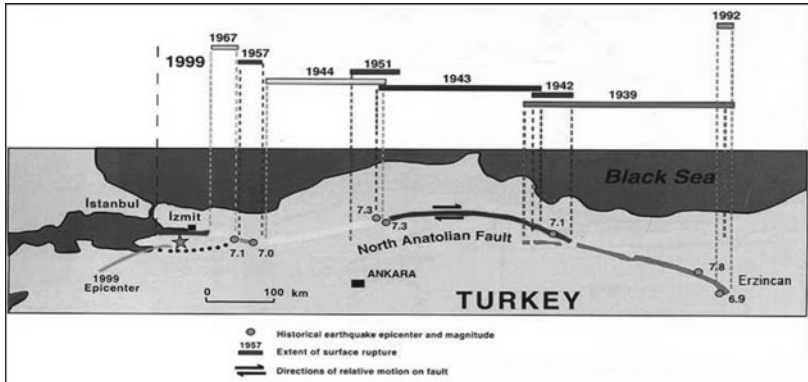


Fig. 1 North Anatolian fault and destructive Earthquakes happened in North Anatolian faults [13]

In August 17th 1999 Kocaeli Earthquake and November 12th 1999 Earthquakes, 3,605 buildings were collapsed and 32,637 buildings were damaged in İstanbul. On the other hand, 63,368 residential buildings and 10,369 office buildings were collapsed and 211,746 buildings were damaged, while 2,000 people were killed and 45,000 people were suffered in total at districts of 200 km away from the epicenter of 1999 Kocaeli and 1999 Düzce Earthquakes, except İstanbul [3–7]. In addition to this, when the earthquakes other than 1999 earthquakes which were happened in Turkey is examined, damages occurred was higher than the expectations which reveals that structure quality is low. 34,567.

Damages occurred due to earthquake gives valuable information for designing seismically safe buildings and help to understand seismic behaviour of buildings. Also, wide range of information such as soil-structure interaction, material behaviour under seismic loads and earthquake-structure interaction is obtained after earthquakes. When damaged or destroyed buildings after devastating earthquakes occurred in Turkey is investigated, damage similarities were found as well as the quality of the building and structural defects the similarities [8–12].

In this study, damage type of reinforced concrete and masonry buildings occurred in recent destructive earthquakes in Turkey is examined. Furthermore, additional information caused damages such as distance of buildings from epicenter, local site conditions effects is given.

In this research, 1992 Erzinçan, 1999 Kocaeli, 1999 Düzce, 2003 Bingöl and 2010 Van Earthquakes are examined. Acceleration response spectra are compared with the Turkish Seismic Code regulations as well as the damages occurred in these earthquakes.

North Anatolian Fault which has about 2000 km length starts from Karlıova at the east Anatolian extends to west of Greece between. There have been 6 destructive earthquakes between 1939–1967 after 1939 Erzinçan Earthquake which results to transfer seismic load step by step to İstanbul and caused to 1999 Kocaeli Earthquake and 1999 Düzce Earthquake [13].

Table 1 The seismicity of regions considered

	1992 Erzincan Earthquake	1999 Kocaeli Earthquake	1999 Düzce Earthquake	2003 Bingöl Earthquake	2011 Van (Tabanlı) Earthquake	2011 Van (Edremit) Earthquake
History	13.03. 1992	17.08.1999	12.11.9	01.05.2003	23.10.2011	9.11.2011
Magnitude	Ms = 6.8	Ms = 7.4	Ms = 7.2	Ms = 6.4	Ms = 7.2	ML = 5.6
Fault	Nort Anatolian Fault (NAF)	Nort Anatolian Fault (NAF)	Nort Anatolian Fault (NAF)	Nort Anatolian Fault (NAF)	Nort Anatolian Fault (NAF)	Nort Anatolian Fault (NAF)
Hypocenter Location	39.72°N, 39.63°E	40.639°N, 29.830°E	40.82°N, 31.20°E	39.01°N, 40.46°E	38.76°N, 43.36°E	38.43°N, 43.23°E
EW direction	0.45 g	0.33 g	0.84 g	0.53 g	0.20 g	0.27
Duration (seconds)	32	31.88	9.8	4.7	19	8.4

On the other hand, Bingöl province where the city is located at the intersection point of Nort Anatolian Fault and East Anatolian Fault, and Van province close to Bingöl is also seismically active regions. Recently earthquakes occurred in Bingöl and Van, building damages and loss of life happened extensively. The seismicity ($M > 5.5$) of regions considered in this study and damage information in the earthquakes is given in Table 1 [14].

2 Characteristics of the Earthquakes

In this study, five destructive earthquakes are examined. Brief information about the earthquakes is given. Furthermore, acceleration response spectra of the earthquakes are compared with the Turkish Seismic Code requirements. The acceleration-time History of EW component Comparison of response spectrum of EW acceleration component of Some Earthquakes with Turkish Seismic Code requirements (Table 2).

The comparison of all the acceleration response spectrums according to Turkish Seismic code requirements are given in Fig. 2.

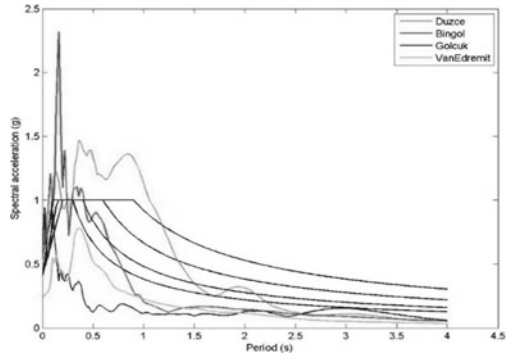
3 Damages Caused by Earthquakes

It is pointed out by Kocak 2010 [7] that almost all buildings have same type of structural defects earthquake damaged buildings in Turkey are examined. As it can be seen easily on Table 1, even if the earthquake magnitudes lower than magnitude 6, damage is also high. Hence, unfortunately It is usual to see damages in earthquakes. One of the important ways of lowering magnitude of damages is determining the causes

Table 2 Comparison of the acceleration response spectryums of the earthquakes with the Turkish seismic code’s response spectrum for different local site conditons

	The acceleration-time History of EW component	Comparison of response spectrum of EW acceleration component of Some Earthquakes with Turkish Sesimic Code requirements.
1992 Erzincan Earthquake		
1999 Kocaeli Earthquake		
1999 Düzce Earthquake		
2003 Bingöl Earthquake		
2011 Van (Tabanlı) Earthquake		
2011 Van (Edremit) Earthquake		

Fig. 2 Comparison of the acceleration response spectryums of the earthquakes with the Turkish seismic code's respone spectrum for different local site conditons



of damages in detail and implementation of a simple and cost-effective retrofiting techniques according to findings. This will help to minimize the loss of life and property. Damages occurred in the earthquakes considered in this study are summarized below.

The general reasons that cause damage to structures due to the earthquakes are material defects, reinforcement defects, incomplete or faulty workmanship, the incompatibility of local ground conditions, wrong designs. When the damaged structures are investigated, main causes of the damages are as follows:

- (1) Having insufficinet bearing capacity due to local site conditions and damages due to liquefaction are widely seen in almost all earthquake zones. Increase in ratio of damaged structures at liquefaction susceptible areas are more than the damages ocured at other zones. Damages of infrastructures are also occurred as well as damages of structures at liquefied zones.
- (2) Total and partial collapse are usual in structures which have unsuitable architectural design and load carrying system against earthquake resistant design principle. Short columns due to slide window space on infill walls, irregular load carrying system, and those which makes extreme torsional displacement, non-ortogonal architectural designs are the most common situations.
- (3) Damages due to soft and weak storey which has irregularity in stiffness between two adjacent floor are the main reasons of damages. Extensive damages had seen on lots of buildings at the base floor, which are designed as a shopping store, due to lack of infill walls while upper floors have infill walls.
- (4) Relative displacement increase and different material usage in adjacent storeys, existance of cold joints caused damages at middle floors. Also irregularities likewise faulty workmanship increase damages.
- (5) Although it is an obligation in seismic code that adjacent buildings must have dilatation, most of the adjacent buildings have no dilatation. This causes pounding effect that leads to damage. Especially different storey heights between adjacent buildings increase damages.

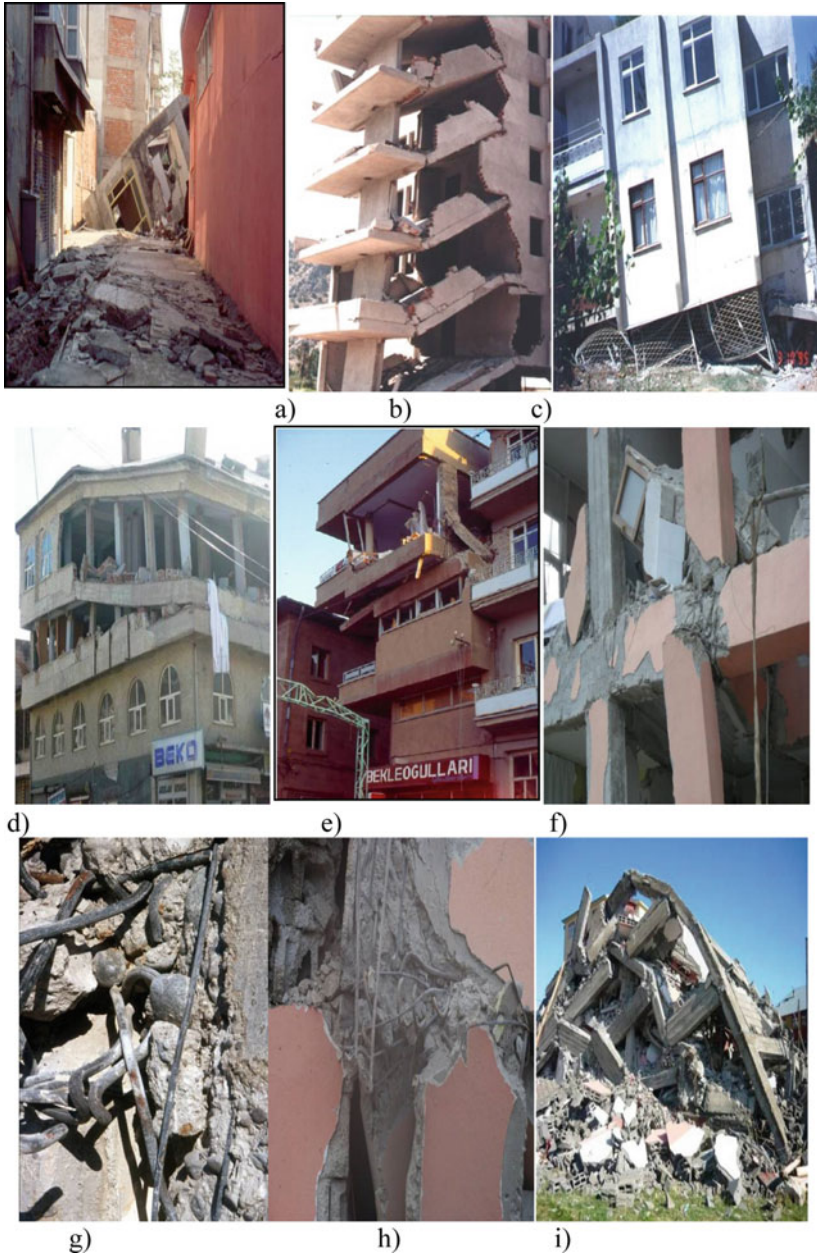


Fig. 3 Earthquake caused damages a) Damages of structures at soils of low bearing capacity b) Damages at structures with faulty load carrying system and architectural design c) Damages due to soft and weak storey d) Middle floor damages e) Damages at adjacent buildings f) Damages at load carrying system members f) Damages at joints g) Damages due to insufficient material h) Damages due to material defect and faulty application i) Totally collapsed buildings j) Damages of infill and outer walls k) Damages of Building Installations l) Damages on masonry structures m) Damages on lifelines (bridges n) Damages on lifelines (electricity transmitting line o) Damages on lifelines (water supply system)

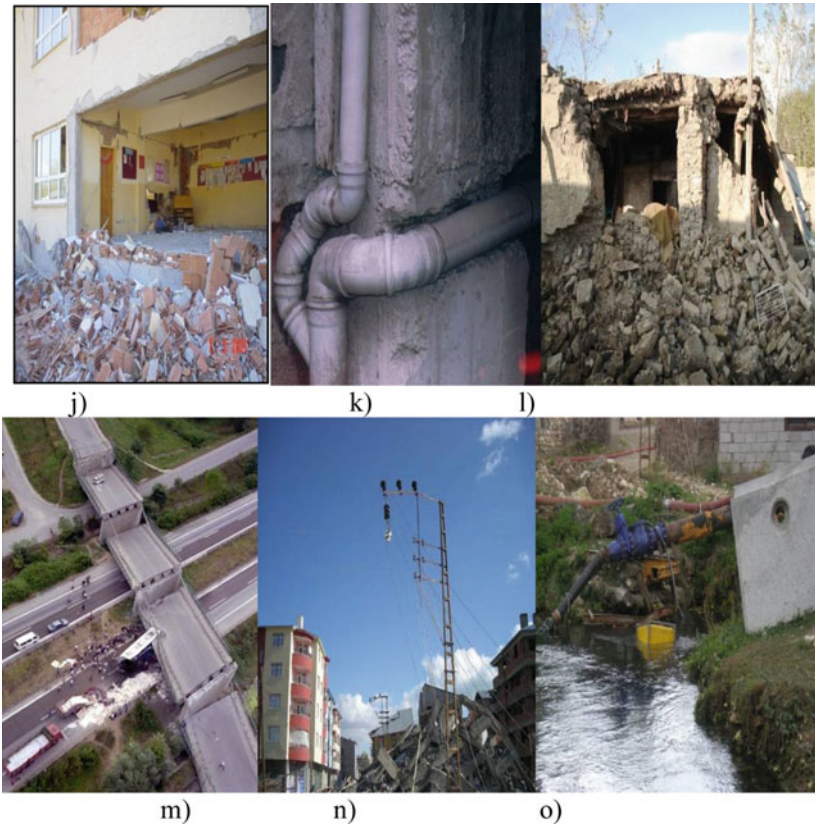


Fig. 3 (continued)

- (6) The main causes of damages at load carrying system members are widely seen on damaged structures due to weaker columns than beams, insufficient horizontal stiffness. It is generally caused by, buckling of reinforcement bars, having plastic hinges at joints.
- (7) It is common that damages of buildings occurred due to insufficient reinforcement at joints where columns and beams connect.
- (8) It is widely seen at investigated areas that local soils such as sands obtained from rivers and seas are used as aggregate to produce concrete. Using without any treatment, having granular materials with diameters up to 15 cm, having high air void ratio in concrete, decomposition of concrete, having low ratio of cement is commonly observed.
- (9) the effect of reinforcement defects is the main causes of the damages. Especially, frequency of transverse bar usage and replacement is scarcely low. Most of the replacements are achieved up to the range of 50 cm to 80 cm. There is no stirrup at sufficient rates at joints. Also, stirrups are used at joint up

to the column height. Therefore, it causes the joints to become plastic hinge which leads to loss of function of concrete. In addition, misplacing of reinforcements at overlapping zone that causes discontinuity, faulty replacement of transverse bars, faulty connection of stirrups on the vertical bars, breaking of stirrups at vertical bars show that workmanship is not properly done.

- (10) Lots of building totally collapsed after earthquakes due to insufficient strength and stiffness, inappropriate material usage, improper construction of building against local site condition, insufficient quality control. However, buildings constructed according to seismic code scarcely have little damages while buildings not constructed according to seismic code are heavily damaged or totally collapsed.
- (11) Because masonry walls are non-ductile materials, it is known as firstly damaged materials during earthquake shaking. If the masonry walls are constructed properly, contribution on initial stiffness of building is also known. So, properly constructed infill walls help to damp seismic energy while improperly constructed infill walls have adverse effects.
- (12) Most of the buildings is heavily damaged at the locations where the electricity, plumbing installation is done. Especially, infill walls and beams are damaged during installation of electricity which leads to loss of function
- (13) In masonry buildings, lack of quality in mortar used in masonry buildings cause separation of walls at joints, window and door openings. Furthermore, lack of concrete or wooden beams in walls increases damages.
- (14) As well as the building damages, other damages occurred on lifelines. Roads, minarets, infrastructure, electricity and telephone transmitting line columns are also heavily damaged. Damages on sewerage and freshwater networks causes public disease.

4 Conclusion

It is interesting in a country where devastating earthquakes are so intense that building quality so low but living life with this reality. Looking magnitude of examined earthquake damage should not be so high. But damage and loss of life are so high. Due to being columns are weaker than beams, structures are not able to damp earthquake energy by inelastic behavior, structures having heavy weight, many of the joints became hinge, structures have material defects and faulty workmanship. Masonry structures are lack of horizontal load capacity or lack of joints, having no reinforced beams which caused not to resist horizontal loads. In addition, lifeline damages really effect daily life after an earthquake and sometimes caused public disease.

Therefore from 1975 to 1997 Turkish Seismic Code have had revision. The seismic code has almost regenerated. Similarly, in Turkish Seismic Zoning Map has regenerated and most of cities are classified as first-degree seismic zone. After the Kocaeli Earthquake in 1999 the number of loss of life and damaged buildings were too much which starts debate about examination and evaluation of existing structures.

As a result of these debates evaluation of existing structure and urban renewal law entered into force. By the law, many methods including demolition of structures that damaged in earthquake are created to improve quality of inadequate building stock as described above. It is going to be made earthquake-resistant. This process will take long time period but there is no another option about reducing loss of life and structure damage in earthquake.

In terms of the relationship between the type of damage and the cause of damage, it can be said that many causes of damage have varying effects at different levels. Although the degree of impact of a cause of damage cannot be exactly defined based on observational data, it is seen that types and levels of damage reach more destructive proportions as the number of causes for the damage increases.

References

1. Sucuoglu H (2019) New improvements in the 2019 building earthquake code of Turkey. Turkish J Earthq Res 1(1):63–75 <https://www.afad.gov.tr>. Accessed 25 May 2021
2. TR ministry of public works and settlement, general directorate of disaster affairs, the report of august 17th 1999 Izmit Earthquake Ankara
3. Koçak A (2003) The district of Küçükçekmece following august 17th 1999 gölcük earthquake, technical congress of Küçükçekmece and it's periphery, pp 42–55 Istanbul
4. Sucuoglu H (2000) The engineering report belonging to the Marmara and Düzce Earthquakes, Ankara
5. Elnashai AS (2000) Analysis of the damage potential of the kocaeli (Turkey) earthquake of august 17th 1999. Eng Struct 22:746–754
6. Koçak A (2010) A study with a purpose to determine structural defects and faults: the seismic risks of the existing buildings in various districts of Istanbul/Turkey. Sci Res Essays 5(5):468–483
7. Koçak A (2000) Structural system design for the reinforced concrete buildings and present building stock, symposium on earthquake in Avcılar and its effects, Avcılar Municipality, Istanbul, Turkey
8. Tankut T, Ersoy U, Koçyiğit A, Wasti T, Ural D (1995) October 1st 1995 dinar earthquake, Tübitak, research group of construction technology, Ankara, Turkey
9. Arslan MH, Korkmaz HH (2007) What is to be learned from damage and failure of reinforced structures during recent earthquake in Turkey. Eng Fail Anal 14:1–22
10. Sahin M, Tari, E (2000) The August 17th 1999 and November 12th 1999 eastern Marmara earthquakes and the Turkish reality, Turkish Engineers and Architects Association
11. Ersoy U (1993) Lessons to be learned from Erzincan 1992 earthquake, 2nd national earthquake engineering conference, pp 395–404, Istanbul
12. Okutucu FS (1993) The damages of the march 13th 1992 erzincan earthquake on buildings due to faulty design, construction and control. In: 2nd national earthquake engineering conference, pp. 464–469, Istanbul
13. Barka A, Eyidogan H (1993) The erzincan earthquake of march 13th 1992 in eastern turkey terra nova 5(2) 190–194
14. KOERI preliminary report on 2003 bingol earthquake (2021) Kandilli observatory and earthquake research institute. Bogazici University, Istanbul

Identification of Defective Supports by Visual and Instrument Aids in the Operating Environment of a Railway Power Supply Division



Valeriy Li , Lyudmila Demina , and Sergey Vlasenko 

Abstract The findings of the destructive tests, visual inspections, and instrument diagnostics completed at the operating landfill of Russia's Far Eastern Railway were reviewed to assess the current state of the support facilities. The support strength test schematic alongside the railway track, the analytical model, and the bending moment curve have been developed. Instrument diagnostics, visual inspection, and destructive tests revealed different parameters, so their final judgments on how the supports should be used further differed as well. It should be highlighted that instrumental diagnostics may not be universally reliable or acceptable: the measurements made by the instrument are not corroborated by destructive testing of the supports.

Keywords Reinforcement · Concrete · Railway · Diagnostics · Measurement

1 Introduction

The accumulation of damage in the catenary supports during operation reduces their strength and increases their stress–strain characteristics, affecting the carrying capacity of the supports and eventually leading to their breakdown [1]. The risk of damage grows as they grow in size.

Domestic and international scientists have contributed significantly to the development of diagnostic systems for support facilities, gaining valuable experience in the development and improvement of non-destructive testing methods for reinforced concrete structures, as well as methods for assessing the condition and monitoring of reinforced concrete supports of the catenary system [2].

Diagnostics is primarily used to assess the technical condition of the remaining service life, according to world experience in the operation of reinforced concrete structures [3]. The domestic approach, on the other hand, assumes an extension of service life after the structure has passed the limit set by the manufacturer [4].

V. Li · L. Demina · S. Vlasenko (✉)

Far Eastern State Transport University, Seryshev Street 47, Khabarovsk 680021, Russia

According to the type of defect and the size of the damage, centrifuged racks are categorized as critically defective and defective, with the classification and maximum allowable dimensions given in [5].

2 Materials and Methods

The survey of reinforced concrete supports of the catenary system of electrified railways was carried out on the Okeanskaya – Vladivostok section of the Far Eastern Railway which operates under challenging climatic conditions [6]. This stretch is 105 km long in total. A defect report was created based on the findings of the visual inspection, including the kind of defect, its size, and orientation. A total of 966 supports were inspected, with 241 units determined to be defective, accounting for 25% of the total, and 69 units being severely defective, accounting for 7% of the total. It should be noted that a recommendation for additional monitoring is made for some defective supports, with the requirement for repair and restoration work as well as direct monitoring of the development of cracks for 5 years.

For the diagnostic of reinforced concrete buildings, a rather broad instrument range has been developed by now [7]. On AC railways, instrument diagnostics is carried out using instruments such as:

- UK-1401 determines the strength of concrete by the speed of ultrasound in concrete;
- PK-2 is used to assess the electrical corrosion condition of the catenary supports on the DC and AC sections. It allows assessing the magnitude of electrical corrosion on the metal reinforcement of reinforced concrete catenary supports by measuring the resistance of the supports and the rail-to-ground potential;
- ISO-1M monitors the earthing circuit of reinforced concrete catenary supports by measuring resistance values; the diagnostics are carried out in the same way as by the PK-2 instrument;
- UGK-1 measures the inclination angle of catenary supports [4].

A magnifying glass, a caliper, a non-metallic tape measure, binoculars, dipsticks, and an ultrasonic thickness gauge is used for linear measurements.

The task of sonic flaw detection is to find faults in products by emitting and receiving ultrasonic waves [8].

The UK-1401 (or UK-14PM, made in Moldova) is the most often used instrument in practice for ultrasonic testing of concrete shells. It determines the speed and duration of ultrasonic spread through concrete.

The UK-14PM instrument was used to measure the results of visually diagnosed defective and critically defective supports on the Okeanskaya–Vtoraya Rechka section.

Before the measurement, the time of ultrasound propagation in the supports with no defects was measured for a qualitative assessment of ultrasonic flaw detection. The instrument measured 5 C-type supports stored in the Power Supply Division

(ECh) warehouse, 5 SKU-type supports standing at the EChK-20 test site, and 5 ZhBK and SZhBK-type supports standing on the Okeanskaya –Sedanka stretch to fix this issue.

The sensors were applied in the longitudinal and transverse directions relative to the axis of the support. Chalked squares with sides of 125 mm (a sounding base of the instrument) at a height of 1; 1.5 and 2 m from the railhead were applied on the four sides of the support. The sounder was placed against the surface of the support by applying a small amount of pressure of about 4–5 kgf. The instrument was applied repeatedly to the same point so as to get consistent readings.

The findings of the measurements were as follows:

1. The ultrasonic propagation time in the concrete of all types of supports did not exceed 30 μ s;
2. The instrument would occasionally record very low or very high readings described as random and discarded at the measurement stage;
3. The measurements were occasionally distorted when a longitudinal reinforcement entered the sounding region. The reinforcement had little effect on the ultrasonic propagation time for the supports made of concrete grade 400 or higher, with a protective layer thickness of 23 mm. The correctness of this conclusion was proved experimentally: we measured several critically defective supports (support No. P23 of the Sedanka station, opening width 18 mm, reinforcement opening; support No. 148 of the Okeanskaya –Sedanka stretch, opening width 20 mm, reinforcement opening). The sensors of the sounding device were installed alongside the reinforcement, next to the reinforcement and across it at least 30 mm away from the cracks. At an ultrasonic speed of 4000 m/s in concrete, the distance between the sounding line and the rods was 2.8 cm, and at 4500 m/s it was 2 cm.

These suggestions can be considered as recommendations for the instrument and visual inspection [9].

The average value in the longitudinal and transverse directions is calculated from the ultrasonic propagation time measurements acquired in concrete. In this respect, the passage time of the ultrasound in the concrete is subtracted from every single measurement, which is 10 μ s assuming the instrument is properly configured [10]. The concrete strength indicators P1, P2 are derived based on the resulting data, and the bearing capacity of the supports is evaluated (Table 1).

Destructive testing of the supports was carried out in field conditions at the Far Eastern Railway by employees of the Power Supply Systems Department of the Far Eastern State Transport University (FESTU) and the Vladivostok Power Supply Division to work out the methods of using the UK-14PM ultrasonic device to assess the condition of the concrete part of the catenary supports. The tests were conducted on unloaded supports that were not dug out of the earth (Fig. 1).

A rope was attached to the upper part of the tested support using a wedge clamp KS-035 and a clamp via a dynamometer and a winch, the second end of the rope was also attached to the lower part of another support using a clamp. A dynamometer measured the force generated by the winch. The bending moment at the point of

Table 1 Some results of transverse and longitudinal ultrasonic propagation time measurements on the Okeanskaya-Vitoraya Rechka section

No	Type	Classification	Time, μ s		P1	P2	Reference force for support, f_f m (%)
			Across the reinforcement	Alongside the reinforcement			
Okeanskaya–Sedanka							
148	ZhBK - 8	Critically defective	48.6	27.1	47.75	1.75	Replacement
			47.6	27.4			
			47.7	27.3			
			47.1	27.1			
165	SK – 136.6 - 2	Critically defective	37.5	29.0	37.6	1.29	4.58 (76%)
			37.5	29.1			
			37.7	29.2			
			37.6	29.4			
Sedanka							
9	SZhBK – 4.5	Critically defective	29.3	26.8	29.48	1.1	4.5 (100%)
			29.4	26.9			
			29.6	27.6			
			29.6	27.6			

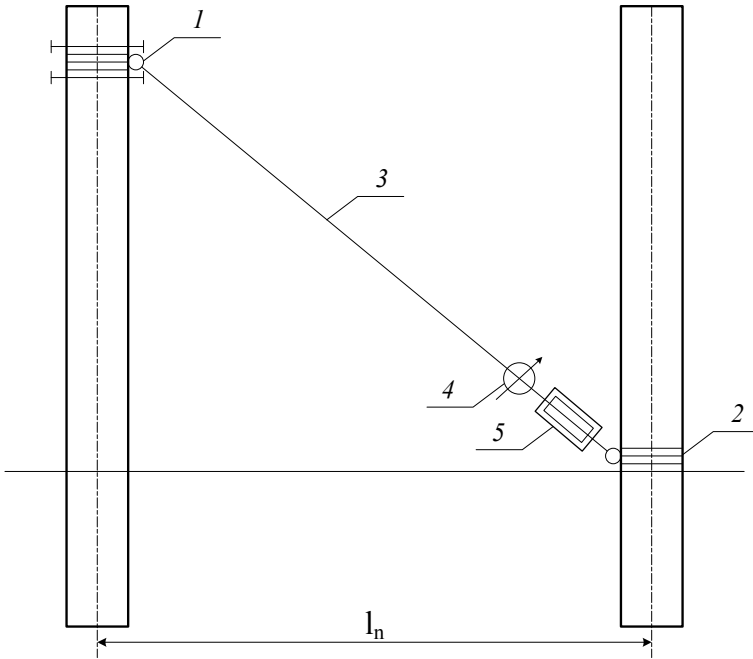


Fig. 1 Schematic of the support strength test alongside the railway track: 1, 2 are the steel clamps, 3 is the cable, 4 is the dynamometer, 5 is the coupling or winch, l_n is the span length

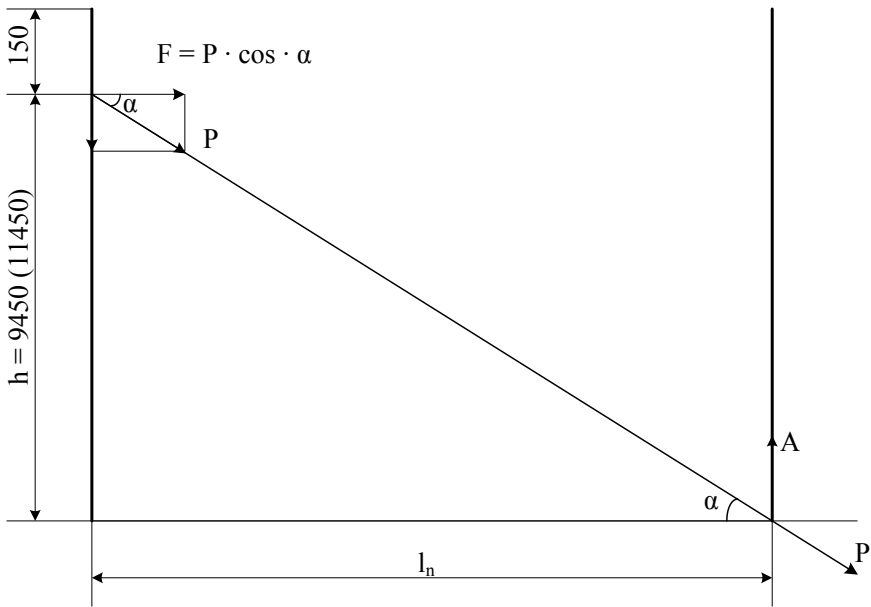


Fig. 2 Analytical model for the field strength tests of the support

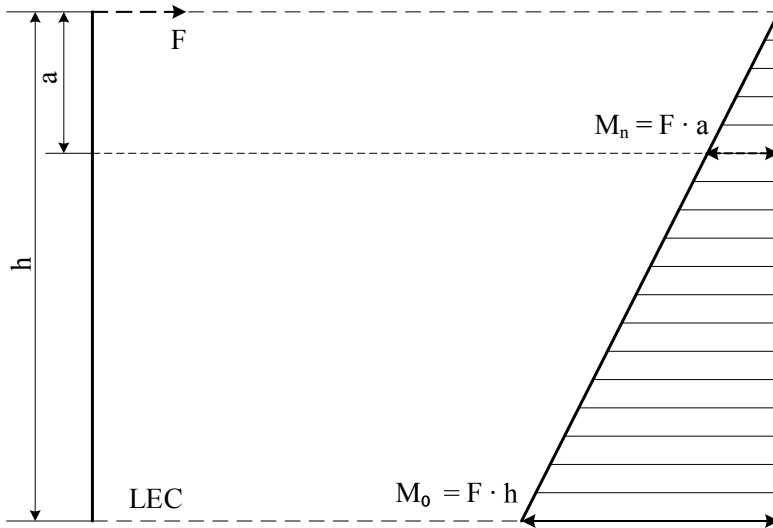


Fig. 3 The curve of bending moments

interest was calculated and compared to the standard value based on the obtained value [11].

The upper clamp was attached at least 100 mm above the top of the support. Securing bolts fitted in holes 1 and 2 fixed the clamp against possible movement on the support (Fig. 1). For the lower part, there was a calculation of the adhesion of the steel clamp to the concrete to see if it would slip on the support.

The analytical model of field tests of the support and the curve of the bending moments are shown in Fig. 2 and 3, respectively, where h and a are the rack size, mm; P is the force applied to the support, daN; F is the horizontal force acting on the support, kN; A is the axial force evenly distributed between the clamp hub halves, kN; M_n is the moment of force at a distance a from the point of application of force, kN·m; M_o is the torque at the base of support, kN·m; LEC is the conditional edge of the foundation; l_n is the span lengths

The results of calculations for a support with a bearing capacity of $M_0 = 110$ kN·m and $l_n = 50$ m are shown in Table 2.

Table 2 Design loads acting on the support

Rack size, mm			α , degrees	F, kN	P, kN	M_n , kN·m
L	h	a				
15,600	11,450	1450	12.9	9.6	9.6	13.9
13,600	9450	1450	10.7	11.6	11.8	16.8
10,800	9450	1450	10,7	11.6	11.8	16.8

The rope is selected with a minimum breaking force equal to $H = 60.04$ kN. According to the diameters of the support in the places where the rope and winch are attached to them, the type of clamps is selected:

- upper clamp 129–76;
- lower clamp 130–76 (type II) or bracket mounting clamp 131–76 (type III).

The lower clamp is checked for slipping on the support according to the schematic in Fig. 4. The results of the calculations are presented in Table 3.

According to the calculations, the clamp will not slip because the total pressure force is easily created by the bolts that tighten the clamp.

Two supports Nos. 65 and 71 of the catenary system on the Ugolnaya – Okeanskaya stretch were selected for the destructive tests: supports No. 71 SZhBK-8 and No. 65 SZhBK-4,5. The year of installation is 1962.

According to the results of visual inspection (Table 4), these supports are recognized as critically defective.

It should be noted that before the destructive testing, the supports in question (under load) were measured using a UK-14PM instrument. Moreover, for ease of

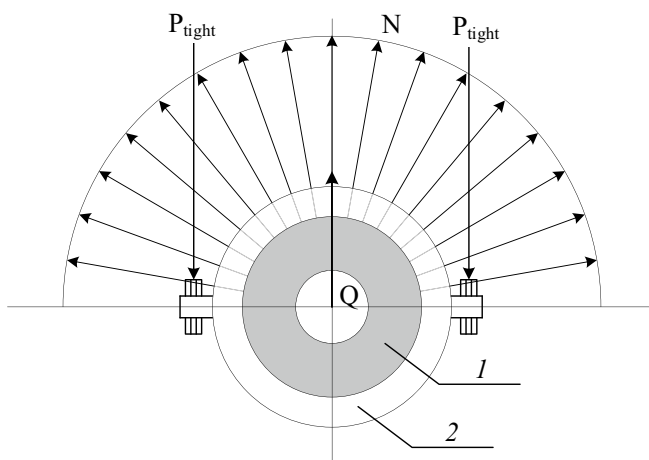


Fig. 4 Clamp pressure distribution diagram: 1 is the reinforced concrete support, 2 is the steel clamp, N is the total pressure force to the support surface from the clamp hub halves, kN; P_{tight} is the tightening force of the screws, kN; Q is the resultant of the pressure force from each hub half

Table 3 Results of calculations for checking the lower clamp for sliding on the support

Rack size, mm	A, kN	N, kN	Q, kN	P, MPa	P_{tight} , kN
15,600	2.63	6.59	4.19	0.15	1.05
13,600	1.82	4.55	2.9	0.11	0.72
10,800	1.82	4.55	2.9	0.11	0.72

Table 4 Results of visual inspection of reinforced concrete supports

No	Defect index	Quantity	Width, mm; % puncture	Length, m	Orientation around the world
71	5c; 7c; 8c	2; 2; 1	4; 3; 4; 3; 5	4; 4.5	South; east; west
65	7c; 5c; 1c	2; 3; 1	5; 4; 3; 5; 4, 5, 15%	4; 4; 4 (from LEF)	South; west

observation of the surface condition of the support at the time of destruction, chalk squares were drawn on the rack on four sides. The measurement results using the instrument are shown in Table 5.

Based on the data obtained, it was concluded that support No. 65 has exceeded its service life and should be replaced as the P2 value is greater than 1.4. Support No. 71 has reduced its load-bearing capacity since the P2 value is greater than the permissible (1.1) but less than the limit (1.4) value.

Although visual inspection showed that support No. 71 was found to be critically defective and was replaced with a new support, instrumental diagnostics before the destructive testing indicated that the support could still be in service.

Event history.

Support No. 71: a pattern of transverse cracks appeared and the process of opening longitudinal cracks began at 500 daN; an increased opening of longitudinal cracks and there are transverse cracks at a height of 0.8 m from the LEC at 750 daN; a sharp push towards the load and chaotic dynamometer readings at 900 daN.

The fracture occurred at 1150 daN 0.8 m from the FRA on a clean cut. No cracking was observed in the remaining part. Corrosion traces were found on the three rods in the cracked areas. The rest of the reinforcement showed no corrosion traces. On the north side, the distance from the outer edge of the support to the reinforcement has been reduced (a factory defect).

The reference force for support No. 71 with a standard moment of 8 tf·m is known to be 2680 daN. As the support collapsed at 1150 daN, the load-bearing capacity has consequently decreased by 57% over the years of service.

Support No. 65 was characterized by a similar fracture process, which started at 300 daN.

The break occurred at 665 daN at the same level as the LEC. This means that it has lost 56% of its load-bearing capacity over the years since it was in service (the reference force for support No. 65 with a standard moment of 4.5 tf·m is 1510 daN).

The results of the destructive tests revealed that the supports can still be in service: the residual bearing capacities of supports Nos. 65 and 71 are 44% and 43% respectively.

The results of the measurements and tests performed indicate that instrumental diagnostics may not always be reliable and acceptable: the measurements performed by the UK-14PM instrument are not corroborated by destructive testing of the supports [12].

Table 5 The measurement results using the UK-14PM instrument before the beginning of destructive tests

Ultrasound propagation time in concrete, μ s									
Across the reinforcement	Alongside the reinforcement	P2	Across the reinforcement	Alongside the reinforcement	P2	Across the reinforcement	Alongside the reinforcement	P2	Across the reinforcement
West			East			North			
South									
Support No. 71									
32.9	27.3	1.2	32.3	27.4	1.18	34.1	27.9	1.23	28.3
32.0	27.6		32.0	27.7		34.5	28.0		28.5
32.7	27.1		32.5	27.5		34.5	27.8		28.2
32.9	27.2		32.9	27.5		34.3	26.1		28.5
32.68	27.3		32.43	27.53		34.35	27.95		28.38
Support No. 65									
41.5	29.0	1.44	45.6	35.4	1.29	43.3	31.8	1.32	40.9
41.2	28.8		44.4	34.9		43.6	32.5		40.9
41.5	28.3		45.1	34.9		43.3	33.2		40.5
40.9	28.4		45.4	34.8		42.9	33.4		40.8
41.28	28.63		45.13	35		43.28	32.73		40.78
									38.6
									39.2
									39.0
									38.2
									38.75
1.05									

The visual inspection of the 19 critically defective supports showed that only 7 of the supports truly need to be replaced, according to the results of the instrumental diagnostics.

Visual inspections provide more plausible information on the condition of the supports, as the presence of cracks, their size, orientation alongside the support body, etc. are assessed. It should be pointed out, however, that these types of inspections take more time.

The visual method, in our opinion, does not provide a qualitative assessment of the actual condition, but it does serve as a beginning point for further research. Instrumental diagnostics necessitates more precise and dependable tools, therefore a comprehensive method to assessing the condition of catenary supports is required.

3 Results and Discussion

Four concrete samples with an area of at least 10 cm² were selected from each support immediately following the destructive testing. The samples were forwarded to the FESTU “Building Materials” laboratory for independent examination.

The non-uniform structure of the samples suggested that delamination of the concrete mix happened during the manufacturing of the supports, based on the interpretation of the test report for the concrete samples of the catenary supports.

The outer layer of concrete was 10–20 mm thick and had a dense, cohesive structure with cement-sand mortar filling all the spaces between the coarse aggregate grains. Some samples had micro-cracks on the outer surface, either from the use of the supports or from the sampling process.

The lack of cement-sand mortar to fill the voids between the grains of crushed stone (gravel), which was the result of the cement paste pressed against the outer surface of the supports and flowing out of the rotating mould, gave the 5–50 mm thick inner layer of concrete a coarse porous structure. In most samples the coarse aggregate grains were easily separated from the solid, being bound together only in some places by thin interlayers of cement stone. The inner zone also had larger defects in the form of caverns up to 20 mm in size; these mostly occurred at the points where the concrete contacted the reinforcement.

On top of that, there was a breach of the specifications regarding the thickness of the concrete protection layer of the supports. The presence of micro-cracks in it can contribute to the rapid corrosion of the reinforcing steel.

The compressive strength of the concrete (R_{compr}) of the submitted samples was determined by an indirect splitting method using conversion factors. The density (ρ), mass (W_m), and volumetric (W_o) water absorption, characterizing the open porosity of the concrete, were determined by water absorption and hydrostatic weighing. The test results are shown in Table 6.

The analysis of the test results showed that the compressive strength of concrete samples varies widely: $R_{\text{compr}} = 359 \pm 47 \text{ kgf/cm}^2$ (support No. 65) and $R_{\text{compr}} = 228 \pm 101 \text{ kgf/cm}^2$ (support No. 71). This is a manifestation of the non-uniformity

Table 6 Physical and mechanical characteristics of concrete sample tests

No sample	Strength, kgf/cm ²		Density ρ , kg /m ³	Water absorption, %	
	Splitting, R_{split}	Compressive, R_{compr}		W_m	W_o
65.1	67.1	402.6	2512	3.20	8.00
65.2	59.2	355.2	2514	3.26	8.15
65.3	64.0	384.0	2525	3.08	7.70
65.4	49.1	294.6	2446	3.74	9.35
71.1	23.2	139.2	2533	3.42	8.66
71.2	34.5	207.0	2481	4.26	10.57
71.3	56.3	337.8	2535	3.46	8.77

of the concrete structure of the supports. Higher strength values are typical with samples having a thin interior layer of porous concrete. If this layer becomes thicker, and in particular if there are micro-cracks in the outer layer of concrete, the strength of the concrete will be much reduced.

Density and water absorption proved to be less variable characteristics of concrete as they were determined on small samples obtained by splitting the original samples mainly consisting of an outer, more uniform concrete layer. Sample No. 65.4 stands out because it has the greatest inner zone and so is the least dense. In general, the density of concrete varies within relatively narrow limits, as well as the volume water absorption: $p = 2500 \pm 36 \text{ kg/m}^3$, $W_o = 8.3 \pm 0.7\%$ (support No. 65) and $\rho = 2516 \pm 31 \text{ kg/m}^3$, $W_o = 9.3 \pm 1.0\%$ (support No. 71).

The study of the concrete samples of catenary supports revealed a non-uniform structure due to the delamination of the concrete mix during the production of the supports. The result is the presence of micro-cracks in the outer layer and a large variation in the strength values of the concrete.

At the same time, a small proportion of the samples of the outer layer of the supports are characterized by a fairly uniform structure with high density and rather low water absorption.

Thus, the test results obtained do not allow these reinforced concrete supports to be considered as solid uniform products [13]. They should be represented as tube-shaped structures, in which a core of low-quality, large-porous concrete with cavities up to 20 mm with reinforcement located inside is surrounded by a 10–20 mm dense concrete wall shell split into separate sections by micro-cracks [14].

Each support is very distinctive in terms of the manufacturing technology, design expense, and operating conditions, so data from trustworthy research, measurements, and diagnostics of the catenary supports is required to assess their residual service life [15].

4 Conclusions

1. The dependences of mechanical stress, deflection of supports by height under the condition of additional factors reflecting characteristic points on supports more prone to cracking are determined.
2. Existing instruments for studying reinforced concrete catenary supports need to be improved.
3. Based on the results of visual and instrumental diagnostics of supports on the studied section of the Far East Railway and according to the destructive tests performed, the need to increase the reliability of research results for assessing the bearing capacity of reinforced concrete supports of the catenary system has been proved.

References

1. Uteuliyev B (2017) Residual life assessment of overhead transmission lines 110 kV and above and determination of their reconstruction terms. E3S Web of Conferences 25, 04005 <https://doi.org/10.1051/e3sconf/20172504005>
2. Li VN, Demina LS, Vlasenko SA, Tryapkin EY (2020) Assessment of the impact of the electromagnetic field of the catenary system on crack formation in reinforced concrete supports. IOP Conference Series: Materials Science and Engineering 918, 012118 <https://doi.org/10.1088/1757-899X/918/1/012118>
3. Ignatenko IV, Vlasenko SA (2021) Current issues to diagnose electric connections of the traction energy system. IOP Conference Series: Earth and Environmental Science 666, 032012 <https://doi.org/10.1088/1755-1315/666/3/032012>
4. Galkin A, Kovalev A, Okunev A (2020) Assessing remained service time of contact-line support under the constant load. Adv Intell Syst Comput 1115:693–702. https://doi.org/10.1007/978-3-030-37916-2_68
5. Li V, Demina L, Vlasenko S (2020) Assessment of the concrete part of the contact system supports in the field. E3S Web of Conferences 164, 03028 <https://doi.org/10.1051/e3sconf/202016403028>
6. Sakharov II, Paramonov VN, Kudryavtsev SA (2020) The account of frost heave and thawing processes when designing road embankments in cold regions. Lect Notes Civil Eng 49 https://doi.org/10.1007/978-981-15-0450-1_3
7. Frankowskib PK, Sikora R, Chadya T (2016) Identification of rebars in a reinforced mesh using eddy current method. AIP Conf Proc 1706:090008. <https://doi.org/10.1063/1.4940545>
8. Schlicke D, Hofer K, Nguyen VT (2020) Adjustable restraining frames for systematic investigation of cracking risk and crack formation in reinforced concrete under restrained conditions. Adv Tech Test Cem-Based Mater. https://doi.org/10.1007/978-3-030-39738-8_7
9. Tsunemoto M, Shimizu M, Kondo Y, Kudo T, Ueda H, Ijima T (2017) Replacement criteria for concrete catenary poles. Q. Rep. RTRI. 58:270–276. https://doi.org/10.2219/rtrqr.58.4_270
10. Rozli M, Safiuddin C, Harun M, Ahmad J, Amin N, Dora A (2019) The behaviour of Prestressed Concrete Sleeper (pcs) sitting on railway track. IOP conference series materials science and engineering 615, 012123 <https://doi.org/10.1088/1757-899X/615/1/012123>
11. Maierhofer C, Reinhardt H, Dobmann G (2010) Non-destructive evaluation of reinforced concrete structures. Vol. 2: Non-destructive testing methods. Woodhead Publishing. <https://doi.org/10.1533/9781845699536>

12. Romanenko EY, Trubitsin MA (2018) Combined way of diagnostics of reinforced concrete conical structures. *Mater Sci Forum* 931:346–351 <https://doi.org/10.4028/www.scientific.net/msf.931.346>
13. Li G, Liu Q, Zhao S, Qiao W, Ren X (2020) Automatic crack recognition for concrete bridges by fully convolutional neural network and Naive Bayes data fusion based on visual detection system. *Meas Sci Technol* <https://doi.org/10.1088/1361-6501/ab79c8>
14. Downey A, D'Alessandro A, Ubertini F, Laflamme S (2018) Automated crack detection in conductive smart-concrete structures using a resistor mesh model. *Meas Sci Technol* 29(3):035107. <https://doi.org/10.1088/1361-6501/aa9fb8>
15. Kobylitsky AN, Ignatenko IV, Vlasenko SA, Tryapkin EY, Rebrov IA (2020) Digital information exchange technologies at electric power facilities of the railway transport and its cost-benefit. *IOP IOP conference series materials science and engineering* 918, 012185 <https://doi.org/10.1088/1757-899X/918/1/012185>

Concrete Hydraulic Curing Under Different Moisture Conditions



Ashot Antonyan 

Abstract The temperature and humidity conditions are extremely important for the normal reaction of cement hydration and concrete structure formation. Due to the fact that the influence of temperature in the literature has been considered in some detail and that it has less significance on changes in water tightness and concrete strength, the contribution of moisture conditions on the formation of concrete properties is considered in the article. The research was carried out both in the laboratory and on the building site.

Keywords Watertightness · Concrete · Strength · Normal conditions · Air-dry conditions

1 Introduction

Portland cement belongs to the hydration group of binders. The structure formation is due to the interaction of minerals in portland cement with water and their subsequent binding into insoluble crystalline hydrates. For most of the currently used concrete, the amount of mixing water in excess is sufficient for complete hydration of cement (if mixing water ratio more than 0.38), provided that part of it will not evaporate. In practice, however, as the concrete curing process is usually prolonged, evaporation from the concrete surface will occur when ambient moisture falls below 80%. Therefore, concrete should be cured in conditions that prevent the evaporation of water from the concrete body [1–3].

Normal and water-curing conditions are commonly used for concrete specimens. For precast structures and products heat and water curing are used (mainly reinforced concrete pipes and tunnel segments). In the case of cast-in-place concrete, curing compounds are used that prevent the evaporation of water. All these conditions have in common the fact that they aim to retain the concrete's own water in its body (with the exception of autoclave curing, where water is pressed through) [4].

A. Antonyan (✉)

The National University of Architecture and Construction of Armenia, Teryan Street 105, 0009 Yerevan, Armenia

2 Normal Conditions

Normal conditions for concrete are considered: $95 \pm 5\%$ humidity and $20 \pm 20^\circ\text{C}$ ambient temperature. Often normal conditions are created in special storage chambers for samples with the possibility of controlling the temperature and humidity of the environment. Since the air in the normal curing chamber is saturated with water vapor, there is no evaporation from the samples. Curing under normal conditions is regulated in a number of standards: GOST 10180, BS 1881-111, AASHTO T23.

3 Hydraulic Setting

Hydraulic setting of concrete is stipulated in the European standard EN 12390. The water temperature must be $20 \pm 20^\circ\text{C}$.

Once the concrete specimen has been stripped and placed in the water, the water protects the specimen from moisture loss. During the initial period, it is not possible to add water into the specimen, as the capillaries of the concrete are occupied by the concrete's "own" water. The water action of the pores then fills them during curing, due to cement setting and the creation of a vacuum in the contracting pores, in contrast to normal conditions where the contracting pores are filled with air. As for the capillary pores, the latter are filled with water from outside in an amount equal to the volume of water displaced into the contractile pores. The opinion of some experts about complete water saturation of concrete samples curing in water is erroneous, since the ambient water can penetrate into the sample only at higher pressure, as well as in the presence of free volume [5–10].

To study influence of humidity conditions on water impermeability, concretes with cement content $200\text{--}500\text{ kg/m}^3$, curing under normal conditions ($T = 20 \pm 2^\circ\text{C}$, $\phi = 95 + 5\%$), in water ($T = 20 \pm 2^\circ\text{C}$, $\phi = 100\%$) and in air at $T = 20 + 5^\circ\text{C}$, $\phi = 30\text{--}40\%$, where T —temperature, ϕ —humidity of environment were tested.

The following materials were used in this study: 5–20 mm basalt crushed stone from Yeghegi (Armenia), washed river sand (Plastic big bag = 2.6) and CEMII/A-P 42.5N Portland cement (Ararat factory). The basic composition of concrete: $\text{CS} = 1110\text{ kg/m}^3$, $\text{S} = 740\text{ kg/m}^3$, $\text{C} = 360\text{ kg/m}^3$, $\text{W} = 0.64$ (according to variation of cement consumption, the composition of concrete was changed correspondingly), where CS—Crushed stone, S—sand, C—cement, W—water. In all cases mobility of concrete mixtures was 20–21 cm.

4 Methods

For each cement consumption 9 cylinder specimens were made, 3 of which were cured in water, 3 under normal conditions and 3 in air. After curing for 28 days under appropriate conditions, the concretes were tested for water penetration depth. The water tightness grade, water penetration rate on the Germann GWT-4000 and water absorption of the concrete were also determined. The test results are shown in Tables 1, 2, 3, 4, 5 and in Fig. 1.

Table 1 Results of EN12390-8 water tightness tests on cylinder specimens

Cement consumption, kg/m ³		200	240	280	320	360	380	400	450	500
Water penetration depth, mm	Normal curing	125	123	95	64	61	62	57	59	61
	Hydraulic curing	124	122	75	47	24	30	36	37	38
	Air curing	>150	>150	>150	141	102	104	109	103	113

Notes - Each result is an average of 3 samples

- Result >150 means that signs of filtration were observed on the top end of the samples until 72 h had elapsed.

Table 2 Increased permeability of concrete (several times) compared to hydraulic curing (according to Table 1)

Cement consumption, kg/m ³	200	240	280	320	360	380	400	450	500
Hydraulic curing	1	1	1	1	1	1	1	1	1
Normal curing	1.01	1.01	1.27	1.36	2.54	2.07	1.58	1.59	1.61
Air curing	>1.21	>1.23	>2	3	4.25	3.47	3.03	2.78	2.97

Table 3 Results of water tightness tests for cylinder specimens according to GOST 12730.5

Cement consumption, kg/m ³		200	240	280	320	360	380	400	450	500
Water resistance grade	Normal curing	W2	W4	W6	W10	W12	W12	W12	W12	W12
	Hydraulic curing	W2	W4	W10	W14	W16	W18	W18	W18	W18
	Air curing	<W2	<W2	<W2	W2	W6	W6	W6	W6	W6

Note - The series consists of 6 samples

Table 4 Results of Germann GWT-4000 water infiltration rate tests

Cement consumption, kg/m ³		200	240	280	320	360	380	400	450	500
Water infiltration rate, mm/s	Normal curing	1.04×10^{-3}	9.54×10^{-4}	6.40×10^{-4}	4.60×10^{-4}	4.60×10^{-4}	4.56×10^{-4}	4.50×10^{-4}	4.64×10^{-4}	4.65×10^{-4}
	Hydraulic curing	1.01×10^{-3}	9.26×10^{-4}	4.92×10^{-4}	3.94×10^{-4}	2.99×10^{-4}	3.08×10^{-4}	3.12×10^{-4}	3.35×10^{-4}	3.45×10^{-4}
	Air curing	9.44×10^{-3}	9.01×10^{-3}	9.08×10^{-3}	2.26×10^{-3}	7.04×10^{-4}	7.12×10^{-4}	7.95×10^{-4}	7.20×10^{-4}	8.08×10^{-4}

Note - Each result is an average of 3 samples

Table 5 Test results for water absorption of concrete by mass

Cement consumption, kg/m ³		200	240	280	320	360	380	400	450	500
Water absorption by mass, %	Normal curing	5.91	5.85	5.10	3.98	3.92	3.95	3.90	3.94	3.95
	Hydraulic curing	5.84	5.74	4.35	2.94	1.05	1.10	1.32	1.45	1.36
	Air curing	8.05	8.12	7.56	6.54	5.10	5.08	5.78	5.60	5.80

Note - Each result is an average of 3 samples

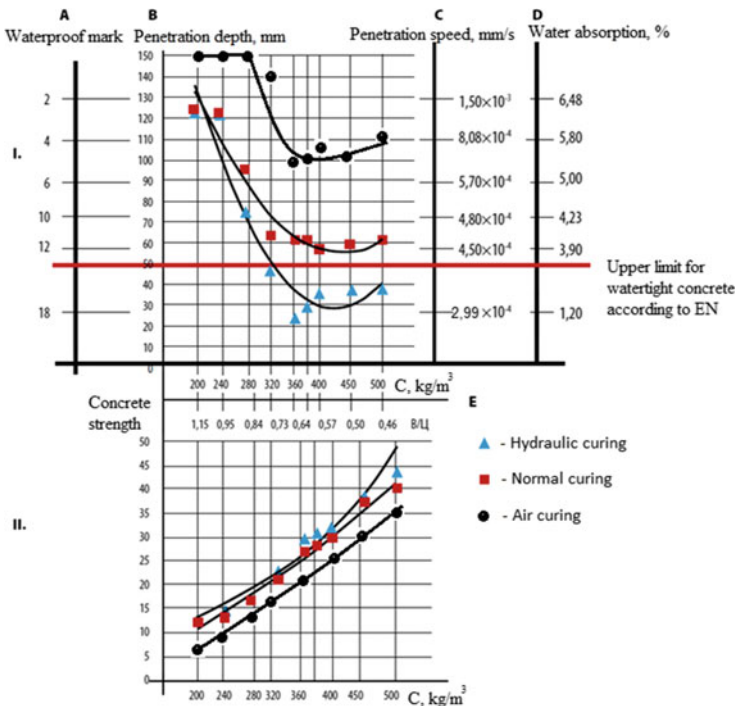


Fig. 1 Change of hydrophysical and mechanical properties of concrete depending on curing conditions. I-Hydrophysical properties of concrete A-E change in concrete waterproof mark, B-E change in water penetration depth, C-E change in Germann water penetration speed, D-E change in concrete water absorption II- change in concrete strength

5 Results and Discussion

It follows from the above results that the curing conditions of concrete have a strong influence on its water tightness. Thus, if we compare the water hardening and curing under normal conditions, it follows that at a cement content of 200–240 kg/m³ no difference in permeability of concrete is observed. It is obvious that at high V/C relations the capillary sizes are so large that even the water hardening, which pre-determines a more optimal regime for structure formation, is not able to reduce the average capillary radius.

The difference between these curing conditions can already be observed from a cement content of 280 kg/m³. With the appropriate V/C ratio the capillary size decreases and the advantage of aqueous curing becomes evident. With increasing cement content the difference between aqueous and normal hardening increases proportionally. Thus, taking aqueous curing as the basic method, depending on the cement content, the permeability of concrete in normal hardening increases by a factor of 1.27–2.54 and that in air curing by a factor of 3–4.25 (Table 2). As for water impermeability grades it follows that water hardening increases them by 2–3 steps in comparison with normal hardening and by 4–6 steps in comparison with air hardening.

Similar results are observed when testing the water permeation rate and the water absorption of concrete on a mass basis. Thus, the water penetration rate during air curing increases by one order of magnitude in almost all cases compared to water curing and normal curing.

Considering the results of the strength change depending on the curing conditions it follows that the difference between aqueous and normal curing over the whole cement content interval does not exceed 2 MPa (Fig. 1). Consequently, the effect of moisture conditions on the mechanical properties, in contrast to hydrophysical conditions, is minimal. Also a lower loss of strength compared to the water tightness is observed for air-cured concretes.

The water hardening of the samples, however, creates some uncertainty for the evaluation of concretes of real structures. For example, according to the guidelines of the German Reinforced Concrete Committee, concrete is considered water impermeable if the depth of water penetration under pressure (according to EN 12390-8) does not exceed 50 mm. An examination of the data in Table 1 shows that starting from a cement content of 320 kg/m³, the same concrete, depending on the curing conditions, is considered to be waterproof in one case (water curing) and not waterproof in the other case (normal conditions). As will be shown below, under actual construction site conditions, the moisture conditions are at best close to normal (when properly maintained). This applies in particular in dry, hot climates. The hydro-physical properties of water-curing concrete are therefore not precisely correct.

The above results were obtained by testing concrete specimens curing under laboratory conditions. To investigate the change of properties under real site conditions, the following tests were carried out.

From a production mix of concrete (composition: CS = 1000 kg/m³, S = 920 kg/m³, C = 300 kg/m³, SP-3 kg/m³, W = 210 l/m³) were made the samples-cylinders 150 × 150 mm for determination of water resistance and samples-cubes 150 × 150 × 150 mm for determination of strength of concrete from calculation:

- The 3 cylindrical and cubic samples were left in moulds outdoors for 28 days after manufacture, in a dry, hot climate (average daily temperature $T = 30 \pm 2$ °C, humidity $\phi = 30\%$).
- 3 cylindrical and cubic samples were cured under laboratory conditions in water ($T = 20 \pm 1$ °C, $\phi = 100\%$).
- 3 cylindrical and cubic specimens were cured under laboratory conditions under normal conditions ($T = 20 \pm 1$ °C, $\phi = 100\%$).
- 3 cylindrical and cubic specimens were cured in water under construction site conditions ($T = 30 \pm 2$ °C, $\phi = 100\%$). This curing method is used in American concrete quality control practice.

In this study the following materials were used: crushed stone basalt 5–20 mm of Yeghegi deposit, washed river sand (Plastic big bag = 2.6), Portland cement CEMII/A-P 42.5N (Aratarat factory), superplasticizer Rheobuild 561 (based on naphthalene-sulfoformaldehyde). A 600 mm cubic specimen was produced in parallel, the purpose of which was to increase the size (and volume) of the specimen while leaving the surface modulus at the same level. The day after concrete pouring this block was unpacked and cured for 28 days in the open air after which 3 cores 15 and 10 cm in diameter and 30 cm in length were selected from the block in the direction of concreting for testing for water resistance and durability respectively. The cores were then sawn into 15 cm height specimens to test the properties of the top layer, which was directly exposed to the sun, and the inner layer. The watertightness tests for concrete were carried out according to EN 12390-8 and on the Germann GWT-4000 (Fig. 2) [11]. The test results are shown in Table 6.

The results show that outdoor curing of cylindrical and cubic specimens strongly affects the water resistance of concrete, reducing it by more than 3 times compared to water-curing specimens. The loss in strength in this case compared to water-curing specimens is 13% and 7% under normal conditions. For cores taken from a large



Fig. 2 a) General scheme of the Germann GWT-4000, b) Concrete water penetration rate test. 1-concrete sample, 2-installation GWT-4000, 3-clamps.

Table 6 Test results for hydrophysical and mechanical properties of concrete

Type of samples	Concrete curing conditions	Depth of water penetration under pressure, cm (EN12380-9)	Speed of penetration, mm/s	Water resistance grade	Strength, MPa
Cylindrical and cubic samples	In the water T = 20 ± 3 °C (temperature) φ = 100% (humidity)	39	3.00 × 10 ⁻⁴	W16	27.0
	In the water (at the construction site) T = 30 + 2 °C φ = 100%	42	4.05 × 10 ⁻⁴	W16	26.0
	Normal T = 20 ± 2 °C φ = 95 + 5%	73	4.11 × 10 ⁻⁴	W12	25.1
	In outdoor moulds T = 30 + 2 °C φ = 30%	128	2.07 × 10 ⁻³	W4	23.4
Cores drilled from a 600 × 600 mm cube curing outdoors	Top layer 15 cm T = 30 + 2 °C φ = 30%	78	6.03 × 10 ⁻⁴	W10	21.2
	Bottom layer 15 cm T = 30 + 2 °C φ = 30%	52	4.98 × 10 ⁻⁴	W12	24.9

cubic block, the results for the upper layer of concrete (15 cm) are 200% higher than water-curing specimens and 6% higher than normal curing specimens. For the bottom layer of the block drilled to a depth of 30 cm the permeability of the concrete is 33% greater than that of the samples cured in water and 29% less than that of the samples cured under normal conditions.

When comparing the permeability results between samples and a large block, a large difference is observed, even though the surface modulus is at the same level. It is obvious that the permeability of concrete is not influenced more by the surface modulus, but by the volume of the specimen or structure being manufactured.

As can be seen from the results, the curing environment of concrete specimens has a strong influence on the water tightness of concrete. GOST 18105-2010 “Concretes. Rules of control and estimation of strength” provides curing of test specimens directly in the conditions of construction site in the conditions similar to the conditions of hardening of structures [12–15]. This method is also widely used in American



Fig. 3 Water hardening of concrete specimens under construction site conditions

practice of concrete quality control [16]. Only in contrast to GOST 18105 where the specimens are simply protected from moisture loss, in American practice the specimens are cured in a tank of water (Fig. 3).

On the basis of the results given above, these methods can only be applied for the determination of strength, as they give fairly reliable information. With regard to the water tightness of concrete, this method is not acceptable: specimens that are cured under site conditions (partially protected against moisture loss) have a permeability almost twice as high as real structures, and specimens that are cured in water (under site conditions) show underestimated permeability results [17–20].

Reliable results for the water tightness of concrete are only obtained if the specimens are cured under normal moisture conditions (humidity greater than 95%). In addition, the difference between water-curing and normal-curing results depends on the amount of cement, and the higher the cement content of the concrete, the greater will be the difference from the real permeability value (Fig. 1).

6 Conclusions

- Humid storage conditions have a strong effect on the water resistance of concrete.
- The water-curing concretes have the highest relative density. The permeability of the latter is 1.27–2.54 times lower than that of normal concretes and 3–4.5 times lower than that of air-cured concretes.
- The difference between the strength of concrete curing in water and under normal conditions is negligible.
- Air-dry conditions have a strong effect on the permeability of concrete, increasing it by more than 50% compared to normal-cured concrete.
- The permeability of concrete is strongly dependent on the volume of concrete laid. As the volume increases, the negative effect of the hot climate decreases.
- For checking the permeability of concrete in dry, hot climates, only normal moisture curing of specimens is acceptable.

References

1. Rinker ME (2013) Determination of Acceptance Permeability Characteristics for Performance-Related Specifications for Portland Cement Concrete. Report Submitted to Florida Department of Transportation, University of Florida
2. Cantero B, Saez de Bosque IF (2019) Water transport mechanisms in concrete bearing mixed recycled aggregates Cements and concrete composites. <https://doi.org/10.1016/j.cemconcomp.2019.103486>
3. Nataadmadja AD, Runtuwene JAP (2018) Analysis of concrete permeability with additional waterproofing admixture. In: IOP conference on series earth environment science, vol 195, p 012002
4. Wang H, Sun X, Wang J, Monteiro PJM (2016) Permeability of concrete with recycled concrete aggregate and pozzolanic materials under stress. *Materials* 9(4):252. <https://doi.org/10.3390/ma9040252>
5. Sandhu AR, Lakhari MT, Jhatial AA, Karira H, Jamali QB (2019) Effect of river Indus sand and recycled concrete aggregates as fine and coarse replacement on properties of concrete. *Eng Technol Appl Sci Res* 9(1):3832–3835. <https://doi.org/10.48084/etasr.2558>
6. Eglinton M (1998) Resistance of concrete to destructive agencies. *Lea's Chemistry of Cement and Concrete*
7. Ortega-López V, Fuente-Alonso JA, Santamaría A, San-José JT, Aragón Á (2018) Durability studies on fiber-reinforced EAF slag concrete for pavements *Construct. Build Mater* 163:471–481
8. Simonov MZ, Khudaverdyan VM (1958) Hydro-technical concrete on lithoidal pumice. *Academy of Sciences Publishing House, Yerevan*, p 296
9. Antonyan AA (2018) Lithoidal pumice-material for waterproof concrete. *Concr Technol* 3–4:18–23
10. Antonyan AA (2019) Change of water resistance of high-functional concrete under dry hot climate conditions. *Concr Technol* 7–8:4–8. <http://germann.org/products-by-application/water-penetrability-2/gwt>. Accessed 21 Mar 2021
11. Antonyan A (2020) Water resistance of lightweight concrete on porous aggregates of volcanic origin. *Int J Adv Sci Technol* 29(9s):6454–6464
12. Antonyan AA (2017) On some features of modern methods of determining the water resistance of concrete. *Concr Technol* 9–10:29–33
13. Cark AI, Sumer M (1996) The effect of curing temperature on compressive strength and water permeability of concrete. Presented at concrete technology for developing countries, forth international conference, East Mediterranean University, Gazimagusa, North Cyprus
14. Demirboğa R, Örüng İ, Gül R (2001) Effects of expanded perlite aggregate and mineral admixtures on the compressive strength of low density concretes. *Cem Concr Res* 31(11):1627–1632
15. Michael A (2009) *Caldarone high-strength concrete. A practical guide*. Taylor & Francis, Canada, p 252
16. Standard B (1992) *Specification for aggregates from natural sources for concrete*. BSI, London
17. Adnan SH, Lee YL, Rahman IA, Mohd H, Wimala M (2008) Water permeability of recycled aggregate concrete. Presented at the technology and innovation for sustainable development conference, Khon Kaen, Thailand
18. Shin KJ, Bae W, Choi S-W, Son MW, Lee KM (2017) Parameters influencing water permeability coefficient of cracked concrete specimens. *Constr Build Mater* 151:907–915
19. Yi S-T, Hyun T-Y, Kim J-K (2011) Effects of hydraulic pressure and crack width on water permeability of penetration crack-induced concrete. *Constr Build Mater* 25(5):2576–2583
20. Rani BD, Rao BK (2019) Service life prediction of high-performance concrete with respect to chloride ion penetration by incorporated with fly ash and silica fume. In: *International conference on advances in civil engineering (ICACE-2019)*

Parametric Model of Cement Soil



Nikolai Seregin 

Abstract The article discusses the conditions for the construction of pile foundations. The interconnection between the structures of pile foundations and soil properties is analyzed. Special attention is paid to the properties of loess subsidence soils. A comparison is made between bored and bored ones. The task of developing a parametric model of a cementitious soil is formulated. A parametric model of the cement soil has been developed. The results of applying of the parametric model of cement-soil for solving practical construction problems are considered. The economic efficiency of the installation of mixing piles in comparison with bored piles has been illustrated.

Keywords Pile foundations · Bored piles · Loess soils · Subsidence soils · Cement soils · Parametric model · Soil strength

1 Introduction

For new construction usually allocate territories that were not previously built up due to the complexity of geotechnical conditions. In this regard, piles are used in the design of building foundations. Need to improve the production technology. Pile foundations erected on soils with insufficient bearing capacity and in permafrost conditions are widespread. The use of pile foundations is facilitated by the introduction of industrial construction methods and the equipping of construction organizations with mobile equipment for the production of pile works [1–3].

With significant thicknesses of subsiding soils, bored piles are most effective, because when drilling a well, the soil near the pile space is compacted and the bearing capacity of the pile increases [6, 7]. The main disadvantage of bored piles is the need for concreting them in the field and heating the concrete mixture in winter. There is also quality control of the construction of bored piles.

N. Seregin (✉)

National Research Moscow State University of Civil Engineering (NRU MGSU), 26, Yaroslavskoe shosse, Moscow 129337, Russia

e-mail: SereginNG@mgsu.ru

Among the bored piles, a special place is occupied by piles made by the drilling-mixing method. For this method use drilling rigs and drilling machines. All types of weak and unstable soils can be fixed using the mixing method. The drilling-mixing method is the most promising in foundation construction due to the use of local soils directly at the construction site, low cost and complete mechanization of work with the prospect of fixing loess subsidence soils [8, 9].

Favorable physical and chemical properties of loess soils, a small content of clay particles, an alkaline reaction of the environment and a small amount of readily soluble salts caused the use of loess soils for the construction of cement soil foundations. The most suitable for strengthening with cement are soils based on light loam and sandy loam, which have high strength and frost resistance due to the presence of calcium carbonates in them [10, 11]. From which it follows that the cementitious soils used for the construction of foundations must have high strength and frost-resistant characteristics.

When developing land under construction sites that were not previously built up due to the complexity of engineering and geological conditions due to heterogeneity of soils. Design organizations are increasingly using piles in the construction of foundations of buildings and structures.

Recently, various designs and piling technologies have been used. Factory-made piles were widely used: screw, driven, and other designs.

There are various technologies for making piles directly at the construction site. Consider one of these technologies in Fig. 1.

The manufacturing process of the pile foundation at the construction site, shown in Fig. 1, consists of five stages. At the first stage, the drilling rig forms a well in the ground under the future pile. At the second stage, a pipe of the corresponding diameter, which serves as the formwork, is immersed in the well obtained at the first stage of the technological process. At the third stage, a steel reinforcing cage is placed in the pipe. At the fourth stage, the steel reinforcement cage is poured with concrete mixture. The concrete mixture is sealed with a vibrator. Without waiting

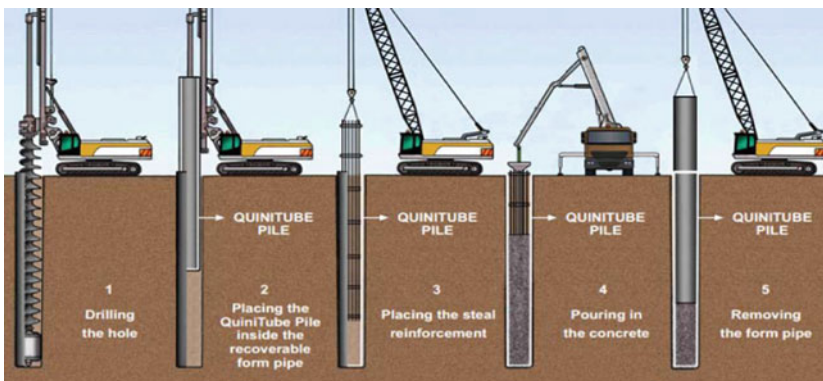


Fig. 1 Manufacturing technology of the pile foundation at the construction site

for the curing of the concrete mixture, not the fifth stage, a pipe is removed from the raw concrete solution. After curing the concrete mixture, the resulting pile is ready for the further construction of the foundation.

The advantages of the considered technology for manufacturing a pile foundation include:

- the ability to build the foundation of a building under construction or structures near existing buildings, as this technology belongs to the category of unstressed;
- the foundation obtained by this technology has a large bearing capacity;
- there is the possibility of building the foundation for this technology in any soil conditions.

The disadvantages of the considered technology for manufacturing the pile foundation are the need for heating the concrete mixture in winter, so concreting occurs in the field, and the complexity of controlling the quality of well formation.

However, during the construction of buildings and structures, especially on heterogeneous soils in difficult engineering and geological conditions, pile foundations account for approximately 25% of the total volume of constructed foundations. Therefore, research to improve the technology of their construction today is very relevant. Especially technologies that, while ensuring the strength and reliability of pile foundations, reduce the complexity and cost of manufacture.

One of the most promising methods of constructing pile foundations is the mixing method [1]. The drilling mixing method of constructing pile foundations allows fixing all types of structurally unstable and weak soils regardless of their moisture and the location of the groundwater horizon. The mixing method is quite economical, thanks to:

- the use of local soil piles as part of the material;
- low cost of the process;
- a high level of mechanization of work;
- the prospect of fixing soils under the object under construction, such as filler soils of any moisture and activity, clay flowing and fluid-plastic soils, as well as loose water-saturated sands.

This method is characterized by environmental cleanliness and the possibility of application, both for the construction of foundations of new buildings and structures, and for the reconstruction of existing ones.

Many years of experience in strengthening soil confirms the need to improve methods for improving the properties of cement-soil pile foundations [1]. One of them is the method of mechanical activation of soils, which allows to reduce cement consumption and increase the strength of cement-pile pile foundations.

A drilling mixing method for constructing pile foundations with mechanical activation of soils can be implemented by using drilling mixing machines, drilling rigs, as well as hollow drill rods providing for the forced supply of the drilling composition (Fig. 2).

Control flow tanks with flow meters

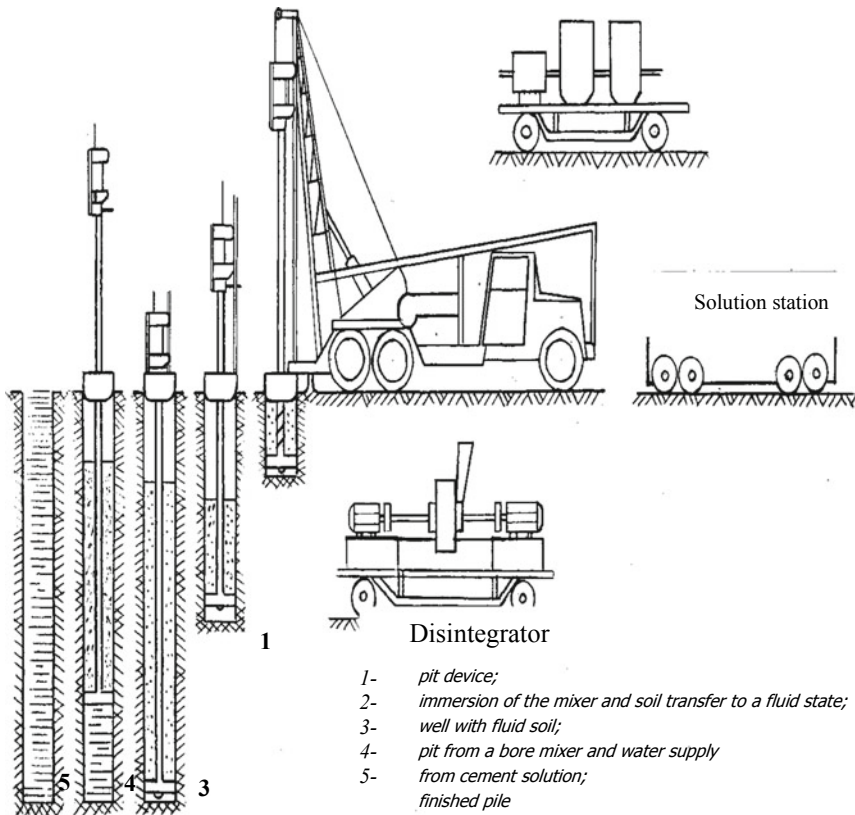


Fig. 2 The technological scheme for the manufacture of cement piles by the mixing method using mechanical activation

The technological scheme for the manufacture of cement piles by the mixing method using mechanical activation of the soil consists of the following operations (Fig. 2):

- 1) pit device;
- 2) immersion of the mixer and transfer of soil to a malleable state;
- 3) Filling the well with a soil of viscous consistency;
- 4) Deepening of the mixer and the supply of water-cement mortar.

The pit device is drilled by a receiving well with a diameter of 0.1 m greater than the diameter of the piles being constructed and a depth of 0.5–2 m, depending on the length of the future pile and the physical and mechanical properties of the soil. The receiving well is designed to receive the excess cement-soil mixture that arose when water and cement were pumped into the ground. The soil extracted from the well is used to prepare a mechanically activated cement-soil mixture. Depending on the

physical and mechanical properties of the soil and the amount of binder introduced, determine the depth of the well.

The immersion of the mixer and the transfer of soil into a malleable state is performed by drilling the soil with a paddle mixer and water supply to transfer the crushed soil into a malleable state.

A well is filled with a soil of a viscous consistency by supplying water when the mixer is immersed in the soil. In this case, two processes occur simultaneously: cutting the soil and its moistening to a malleable state.

The boring mixer is deepened and the water-cement-cement mortar is supplied by removing the boring mixer with the simultaneous supply of the water-cement mixture in the required volume for the estimated amount of cement to enter the ground mass.

The construction of a pile foundation in fluid mixtures, compared with plastic ones, reduces the immersion and removal times of the mixer by three times by increasing the speed to 130 rpm and reduces the cutting force of the soil by two to three times. And also, the development of the soil with a mixer with the supply of a given volume of water to the well to transfer the soil to a malleable state allows you to get the soil of the required degree of grinding.

The main advantages of the drilling mixing method for constructing pile foundations with mechanical activation of soils are the use of local soil extracted directly from the well as the material of the piles, and the possibility of installing piles near existing foundations and other underground structures without damaging them.

2 Materials and Methods

The macrostructure of the cement soil is formed in two stages. At the first stage, the soil is mixed. At the second stage, fine grinding is preliminarily carried out, and then the soil is compacted. The process of enveloping the soil with mixing proceeds with a decrease in surface energy. And external energy is spent on overcoming internal friction and on mixing the soil.

The adhesion between the binder and the soil is formed in the adhesive-active centers of the surface in the presence of wetting due to the forces of dispersion or chemical interaction. The larger the specific surface area of the soil, the more adhesive-active centers and the higher the strength of the soil, provided that the specific content of the binder is preserved per unit surface.

At high rates of chip formation, which take place in cement soils, amorphous structures are formed, which have low plasticity, but high heterogeneity in strength.

The strength of the material of soil solids R , depending on the porosity, is expressed by the dependence:

$$R = f\left(\prod^{-n}\right), \quad (1)$$

where:

Π —the porosity of the solid material;

n —an index that ranges from 3 to 6.

The mathematical description of the dependence of material strength R on the size of soil units is as follows:

$$R = R_0 d^{-1/m}, \quad (2)$$

where:

R_0 —strength of hardened soils from units smaller than 1 mm;

d —unit diameter in mm;

$1/m$ —an index characterizing the homogeneity of the hardened soil.

From formula (2) we can see that the smaller the absolute value of $1/m$, the greater the strength of the hardened soil. That is, the strength of a given type of material is less dependent on the size of the units, and to a greater extent depends on its homogeneity. This conclusion suggests itself from the fact that formula (2) does not reflect the essence of the process of forming the structure of these materials. Therefore, we will consider the strength of materials based on soils, taking into account the patterns of the formation of structures in the process of its hardening.

Units with a dimension less than 1 mm have the largest area in the structure of soils, and in the range of grain sizes from 0 to 300 mm, granulometry does not affect the work of mixing. The area of the resulting surface with the thickness of the bonding layer h is found by the formula:

$$S_{sp} = \pi h(d - h), \quad (3)$$

where:

d —unit diameter.

If we assume that soil units have a spherical shape with a diameter d , then the soil surface area will be in cm^2/g :

$$S_{sp} = N\pi d^2, \quad (4)$$

where:

N —number of units in one gram of soil.

Number of units in one gram of soil N is defined by formula:

$$N = -6/\pi d^3 \rho_{gr}, \quad (5)$$

where:

ρ_{gr} —average density of the soil structure.

Considering formulas (4) and (5) get the formula for calculating diameter of units:

$$d = 6/S_{sp}\rho_{gr}. \quad (6)$$

And formulas (5) and (6) make it possible to calculate the formula for the number of units in one gram of soil N:

$$N = S_{sp}^3 \rho_{gr}^2 / 36\pi. \tag{7}$$

Assume that the thickness of the layer gluing the soil grains is equal to the thickness of the binder layer evenly distributed over the surface of the soil units of the mix. Then the formula for calculating the thickness of the adhesive layer h will be:

$$h = 1/100 \rho_b S_{sp} \tag{8}$$

where:

ρ_b —density of the binding material in g/cm^2 .

In the case of hexagonal packing, each soil unit has six points of contact with other units.

Then the value of the entire area of contact between the units in one gram of soil will be:

$$S_c = 6N\pi h(d - h), \tag{9}$$

$$S_c = \rho_{gr}^2 S_{sp} / 600 \rho_b (6/\rho_{gr} - 1/100 \rho_b) \tag{10}$$

In the average density of the soil structure ρ_{gr} is equated to 1,8 gr/cm^3 , and density of the binding material ρ_b is 3,1 gr/cm then the value of the entire contact area of the units in one gram of soil S_c will be:

$$S_c = 0,00174 S_{sp} - (3,3 - 0,0032 S_{sp}) \tag{11}$$

or in general:

$$S_c = b_1 S_{sp} - (b_2 - b_3 S_{sp}), \tag{12}$$

where:

b_1, b_2 and b_3 —indexes equal to 0.00174, 3.3 and 0.0032.

Since b_2 is almost 1 000 times larger than b_1 , hen the surface area of the bonding layer can be considered proportional to the specific surface area:

$$S_c = B S_{sp}. \tag{13}$$

The total strength of the soils strengthened with this binder depends on the area of the binder layer that glues the soil units together. Then, dividing S_{sp} by the actual strength of the soil material R, the following mathematical expression:

$$L_R = S_{sp}/R \tag{14}$$

where:

L_R —structural criterion of soil material strength.

The structural criterion of the strength of the soil material L_R depends on the specific surface area of the soil unit S_{sp} and on a number of technological factors TF . Such as the quality of mixing K_p , the quality of compaction P and the conditions for the hardening of the cement soil t_c .

Based on this, the structural criterion for the strength of the soil material L_R will be:

$$L_R = f(T_F)/R, \quad (15)$$

where:

$TF = f(K_p, P, t_c)$.

The technological factor of the quality of mixing of the cement-soil K_p manifests itself at the beginning of the technological process, the quality of compaction P and the conditions for the hardening of the cement-soil t_c manifest themselves at the end of the technological process. This allows us to write the structural criterion of the strength of the soil material L_R as follows:

$$L_R = (C_R S_{sp} + M)/d \quad (16)$$

where:

C_R —coefficient of variation characterizing the homogeneity of the strength of the resulting cement soil material;

M —a value characterizing the degree of aggregation of the adhesive layer of the material after compaction and subsequent curing of the cement-soil mixture.

A joint consideration of mathematical expressions (15) and (16) allows one to obtain the desired value of the strength of the material of solid bodies of soil R :

$$R = S_{sp} \cdot d / (C_R S_{sp} + M). \quad (17)$$

The mathematical expression (17) is a parametric model of a cement soil, the analysis and application of which will be considered in the next section of this scientific work.

3 Results and Conclusions

Analyzing the parametric model of the cement soil (17), it can be concluded that the main role in the formation of the quality of the cement soil belongs to the dispersion of the soil filler S_{sp} . And the coefficient of variation C_R , which characterizes the homogeneity of the strength of the resulting material of the cement soil, and the value of M , which characterizes the degree of aggregation of the adhesive layer of the material after compaction and subsequent hardening of the mix of cement soil, have a certain dependence on the dispersion of the soil filler S_{sp} .

An increase in the dispersion of the soil to be strengthened at the beginning contributes to an increase in the strength of the cement soil material, and after a certain level of dispersion, the quality of the material deteriorates.

This happens for the following reasons:

- insufficiency for the increasing surface, the introduced amount of binder;
- increased by several times the difficulty of uniform distribution of the mineral binding material in the volume of the ground filler.

In the process of work, the required level of soil dispersion was investigated to obtain material grade 60. To perform analytical studies, the parametric model of cement soil (17) was transformed with respect to the specific surface of the material per unit volume S . And, omitting intermediate transformations, the mathematical dependence took the following form:

$$S = M/(d/R - C_R). \tag{18}$$

Number of contacts per unit area χ in cm^{-2} depends on unit diameter d in cm :

$$\chi = 2.67/d^2. \tag{19}$$

In theory, soil units are generally spherical. Therefore, the value of M , which characterizes the degree of aggregation of the adhesive layer of the material after compaction and subsequent curing of the cement-soil mix, is equal to:

$$M = 6/d^2. \tag{20}$$

Replacing in formula (20) the diameter of the aggregate d in cm by the number of contacts per unit area χ in cm^{-2} from formula (19), the following dependence was obtained:

$$M = \sqrt{(36\chi/2, 67)}. \tag{21}$$

Based on the average value of the number of contacts per unit area χ , equal to $120\,000\ \text{cm}^{-2}$, the value M was obtained, which characterizes the degree of aggregation of the adhesive layer of the material after compaction and subsequent hardening of the cement soil, equal to $1\,270\ \text{cm}^{-1}$.

For further calculations using formula (18), the experimental values of the remaining quantities are taken. As a result of the substitution of the calculated and experimental values of the quantities, the value of the specific surface area of the material per unit volume S was obtained, equal to $3\,772.277\ \text{cm}^{-1}$.

To convert the specific surface area of the material per unit volume S (cm^{-1}) into the specific surface area of the soil unit S_{sp} (cm^2/gr), it had to be divided by the density of the material equal to $1.85\text{gr}/\text{cm}^3$. As a result, the specific surface area of the soil filler is $S_{sp} = 2\,039.069\ \text{cm}^2/\text{gr}$.

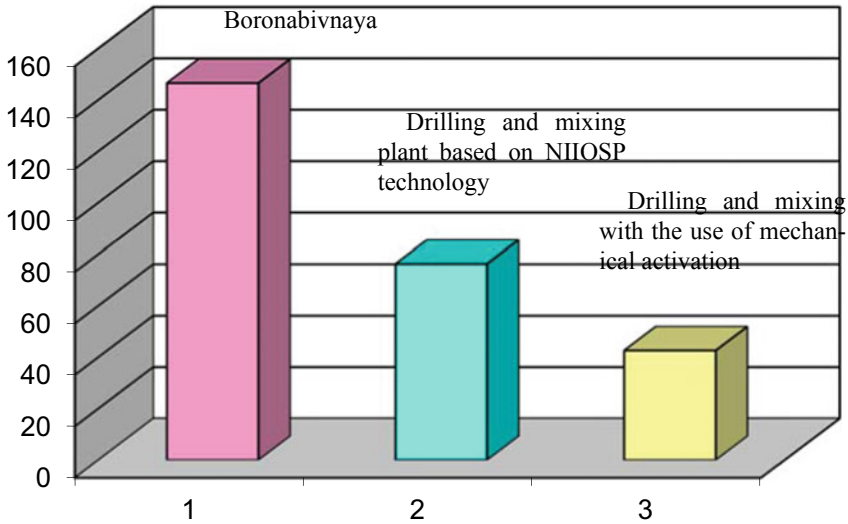


Fig. 3 Economic efficiency of the device of drilling piles in comparison with bored piles

As a result, it can be concluded that to obtain grade 60 material, the dispersion of the soil filler is required within the range $S_{sp} = 2000 \text{ cm}^2/\text{gr}$. And this is possible only with preliminary crushing of the soil to the specified dimensions of the units d .

For this purpose, taking into account the significant volume of work on crushing the soil, it is necessary to use high-performance disintegrators.

A comparative economic analysis of the effectiveness of the use of mixing piles based on cement soils, regardless of their manufacturing technology, shows that they are more than two times cheaper than bored piles (Fig. 3).

References

1. Sakai T, Nakano M (2015) Interpretation of the mechanical behavior of embankments having various compaction properties based on the soil skeleton structure. *Soils Found* 55:1069–1085
2. Kumor LA, Kumor MK (2016) Changes in mechanical parameters of soil, considering the effect of additional compaction of embankment. *Transp Res Proc* 14:787–796
3. Ang JB, Fredriksson PG (2018) Trade, global policy, and the environment: new evidence and issues. *J Comp Econ* 46:616–633
4. Garmanov G, Urazaeva N (2015) The paper presents design and calculation of cost effectiveness of various types of foundations on the example of the city of Vologda. *Proc Eng* 117:465–475
5. Aguiar dos Santos R, Rogério Esquivel E (2018) Saturated anisotropic hydraulic conductivity of a compacted lateritic soil. *J Rock Mech Geotech Eng* 10:986–991
6. Lu Z, Xian S, Yao H, Fang R, She J (2019) Influence of freeze-thaw cycles in the presence of a supplementary water supply on mechanical properties of compacted soil. *Cold Reg Sci Technol* 157:4252
7. Kante N, Kryshchuk M, Lavendels J (2017) Charged particle location modeling based experiment plan acquisition method. *Proc Comput Sci* 104:592–597

8. Baraffe HD, Cosson M, Bect J, Delille G, Francois B (2018) A novel non-intrusive method using design of experiments and smooth approximation to speed up multi-period load-flows in distribution network planning. *Electr Power Syst Res* 154:444–451
9. Hong Y, Wang Y, Wu J, Jiao L, Chang X (2018) Developing a mathematical modeling method for determining the potential rates of microbial ammonia oxidation and nitrite oxidation in environmental samples. *Int Biodeterior Biodegr* 133:116–123
10. Jayanudin J, Fahrurrozi M, Wirawan SK, Rochmadi R (2019) Mathematical modeling of the red ginger oleoresin release from chitosan-based microcapsules using emulsion crosslinking method. *Eng Sci Technol* 22(2):458–467
11. Stephenson CL, Harris CA (2016) An assessment of dietary exposure to glyphosate using refined deterministic and probabilistic methods. *Food Chem Toxicol* 95:28–41

Construction of Diagnostic Algorithms for Complex Systems



Dmitry Orlov , Aleksandr Michailov , Vladimir Makhov ,
and Igor Kazan 

Abstract The issues of constructing diagnostic algorithms for complex systems by the method of double wavelet transform of the received vibroacoustic signals are considered. By selecting the wavelet types for the first and second continuous wavelet transform, stable parameters of the curves of the coefficients of the second continuous wavelet transform are achieved for each type of defects, which makes it possible to use them to identify system defects. An increase in the accuracy of determining defects is achieved by using the filtering properties of the wavelet and choosing a significant set of wavelet transform scales. For a preliminary assessment of the system and defects, it is proposed to use the entropy of the decomposition nodes of the received signal. An increase in detectability of defects by four times is achieved, the possibility of integrating the proposed algorithms into an artificial neural network is shown.

Keywords Continuous wavelet transform · Discrete wavelet transform · Double continuous wavelet transform · Curves of coefficients of continuous wavelet transform

1 Introduction

In complex technical systems, multiple processes take place, differing in the features of mechanics and target functioning. Any physical defects in the components and mechanisms of such systems cause deviations in its operation and, as a consequence, distortion of the vibroacoustic signals received from it. To diagnose such systems, sensors of various physical nature and methods of receiving signals from them are used.

D. Orlov · I. Kazan
Saint-Petersburg Mining University,
21-ya Liniya Vasil'yevskogo Ostrova 2, St. Petersburg 199106, Russia

A. Michailov (✉) · V. Makhov
Mozhaisky Military Space Academy, Krasnogo Kursanta str. 21, St. Petersburg 197110, Russia

These systems primarily include road transport. Diagnostics of the technical condition of transport is currently an urgent task that affects the safety of people and issues of predicting the need for maintenance or repair. Currently, there are many methods and tools for technical diagnostics [1]. Any diagnostics is based on obtaining sufficient and reliable information received in the process of processing signals from diagnostic equipment. Diagnostics is always a laborious process that requires special equipment and highly qualified personnel. Vibroacoustic control methods can be considered the least laborious and more technologically advanced [2].

Taking into account the multiplicity of types of diagnosed systems and possible defects, timely and high-quality diagnostics requires mathematical methods and algorithms for obtaining information, which ensure the search for defects in a wide spectrum of the signal and the influence of interfering factors on it.

2 Methods and Tools for Diagnostics of Complex Systems

The simplest diagnostic methods are those that use the parameters of the time signal taken by the sensors from various parts of the system being diagnosed. The main parameter used in the analysis is the root mean square value (RMS) of vibration velocity (vibration acceleration) [3], which is calculated by the following formula:

$$X_{av}(t, T) = \sqrt{\frac{1}{T} \int_t^{t+T} X(t)^2 dt}. \quad (1)$$

The RMS method detects system defects at the very last stages of their development, when the vibration level rises. Recently, attempts have been made to use the functions of moments of the fourth order—kurtosis, or the Kurtosis factor (FC) as a diagnostic feature [4].

Spectral analysis based on the Fourier transform (FT) [5] is one of the methods for processing vibration signals. FT is based on the representation of a periodic signal as a sum of harmonic components, which allows to determine the frequency composition of the measured signal. The most common types of diagnostics based on spectral analysis are: broadband spectrum, direct spectrum, envelope spectrum. Spectral methods have low sensitivity and resolution to minor system defects.

In contrast to spectral analysis, the joint time–frequency analysis (JTFA) offers great opportunities [6]. The JTFA algorithms implemented in this toolbox fall into two categories—linear and quadratic. The specifics of JTFA algorithms are described in the works of Qian and Chen [7] and Cohen [8].

Continuous and discrete wavelet transform (CWT, DWT) [9] is a new method of mathematical processing of vibration signals, which has recently received practical application in diagnostics. The wavelet transform is three-dimensional. It shows

how the magnitude of the amplitude value of each harmonic in the signal changes over time. Sometimes the analysis of such three-dimensional connections allows to obtain qualitatively new diagnostic conclusions [2]. The wavelet transform of a one-dimensional signal is its representation in the form of a generalized series or Fourier integral over a system of some basic functions.

The result of the wavelet decomposition of the signal $S(t)$ is a two-dimensional function (orthogonal basis), depending on the specific values of the shift time b and its scale a , which carry information about the frequency and time:

$$W_S(a, b) = \langle S(t)\psi_{a,b}(t) \rangle \frac{1}{\sqrt{a}} \int_{-\infty}^{\infty} S(t) \cdot \psi\left(\frac{t-b}{a}\right) dt \tag{2}$$

where $\psi(t)$ is generating or parent function (wavelet); a is a scale parameter related to frequency; b is parameter of the wavelet shift along the time axis; $W_S(a, b)$ is the coefficient corresponding to the given scale and the shift of the parent wavelet along the time and amplitude scales.

Well-known functions can be used as the generating function $\psi(t)$: Mexican Hat, Meyer, Morlet, Daubechies (db02...db14), Hear, biorN_M, coif K, sym L and others that meet certain requirements [9].

Cepstral analysis is the same data compression as the spectrum itself in relation to time realization [10]. According to the original definition, the signal power spectrum is defined as the direct Fourier transform of the power spectrum $S_{xx}(\omega)$.

The theory of fractals is one of the promising areas of mathematical processing of vibration signals. A fractal is a structure consisting of parts, which are in a sense similar to the whole [11].

Methods for analyzing the direct spectrum and the envelope spectrum can be implemented using the theory of artificial neural networks (ANN) [12]. The use of the mathematical apparatus of neural networks provides an increase in the accuracy of the diagnostic process by applying existing knowledge about the operation of similar units. Bayesian classifier [13] generates a wide class of classification algorithms based on the principle of maximum posterior probability and making it possible to recognize defects.

The analysis shows that wavelet analysis methods have sufficient sensitivity, which provide obtaining the stable diagnostic results.

3 Mathematical Model

It is assumed that the system gives a signal of complex shape $s(t)$ generated by periodic processes. The defect gives distortions in the periodic signal $F(t)$. The task is to detect the defect and identify it. As previously assumed, the most effective tool is wavelet analysis based on continuous wavelet transform (CWT). The algorithm for obtaining the dominant information component is shown in Fig. 1.

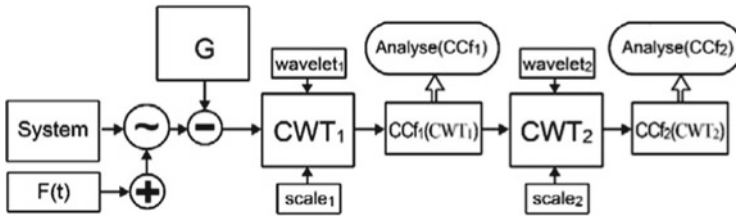


Fig. 1 Signal processing algorithm based on wavelet transform

For effective use of CWT, it is advisable to maximally isolate the signal component $F(t)$ by simulating a periodic signal of the system being diagnosed.

The coordinates of the signal slew rate character are determined by the position of the maxima and minima of the curves of the CWT coefficients (CCf) obtained by various mathematical methods:

$$\{T_k\} = \{t_{\max D(x)}^k\} \leftarrow \left\{ \frac{dS_k}{dt} = 0 \right\}_k \tag{3}$$

The accuracy of determining the coordinates of the extrema CCf and the amplitude of the discrete function depends on the method used, the nature of its behavior, and the level of discretization.

The CCf CWT shape reflects the rate of signal change (analogue of wavelet differentiation [14]). The filtering properties of the wavelet allow to exclude vibration and noise artifacts. Significantly more informational content of determining the coordinates and features of the waveform can be provided by the analysis of the scalogram CWT2 from CCf of the first CWT1 function of the signal $S(t)$ with the new selected wavelet ψ_2 [15]:

$$W_{CCf}^2(a, b) = \langle CCf(t)\psi_{a,b}^2(t) \rangle \frac{1}{\sqrt{a}} \int_{-\infty}^{\infty} CCf(t) \cdot \psi_2\left(\frac{t-b}{a}\right) dt \tag{4}$$

4 Investigation of System Defects

As an example, we use the signal from the intake manifold vacuum sensor received in the scrolling mode by the starter. If the engine is in good working order, the intake manifold vacuum oscillogram has a shape close to a sinusoid. The oscillogram acquires a sawtooth shape if the belt or chain is installed incorrectly. The vacuum os-cillogram (Fig. 2) in the intake manifold indicates that the intake valves are so car-bonated that carbon deposits on the valve disc prevent efficient filling of the cylin-ders with the air–fuel mixture.

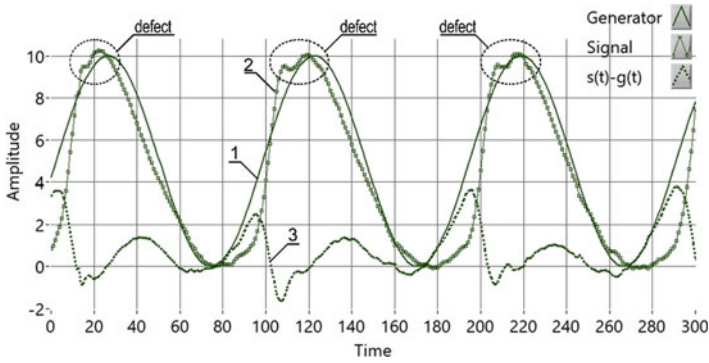


Fig. 2 Signal (1), parametric generator (2), difference between signal and generator (3)

The difference signal (3) carries information about the deviation of the signal (2) from the sinusoidal one (1), highlighting the defects in the engine operation (curve $s(t) - g(t)$).

The difference signal CWT algorithm (Fig. 1) is implemented in the development environment for virtual instruments from National Instruments (NI)—NI LabView [16], with additional signal processing modules [17]. A three-dimensional CWT scalogram of the difference signal is shown in Fig. 3. The analysis of the CWT scalogram shows that the defects of the valve operation are displayed in the area of small scales of the wavelet transform. Therefore, in the curves of the coefficients it is advisable to use this particular region of scales. The curves of the CWT coefficients are formed taking into account the particular area of defects as follows:

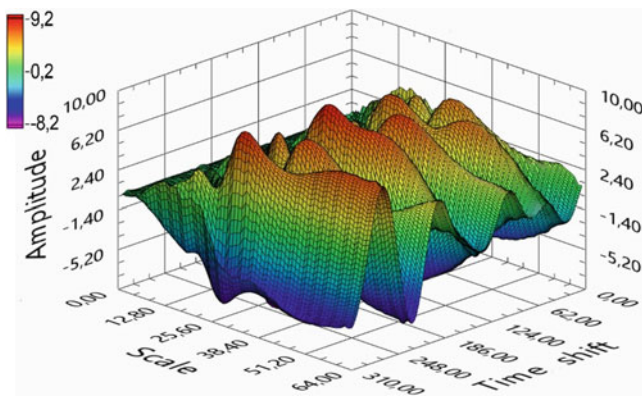


Fig. 3. 3-D scalogram of the first wavelet transform of the signal under study

$$CCf_{def}(t) = \int_0^{a_{def}} CCf(a, t) \cdot da \tag{5}$$

which are the basis for obtaining the scalogram of the second CWT:

$$W_{CCf}(a, b) = \frac{1}{\sqrt{a}} \int_{-\infty}^{\infty} CCf_{def}(t) \cdot \psi_2\left(\frac{t-b}{a}\right) dt$$

Next, on the basis of the second wavelet transform, we form new curves of the coefficients - the second CWT with a given number of scales (N):

$$CCf_{def}^2(t) = \sum_{i=1}^N W_{CCf}(a_i, t) \tag{6}$$

having their own coordinates and amplitudes of maxima, which are a new informational sign of the presence and nature of defects.

The curves of the coefficients of the first and second CWT ($\psi_1 = db14, \psi_2 = bior3_1$) of the signal under study are shown in Fig. 4. It can be seen that the curves of the coefficients of the second CWT₂ (4) have a smoother character, a greater number of maxima and minima. Coordinates (X^i_{max}, X^i_{min}) and amplitudes of maxima and minima (A^i_{max}, A^i_{min}) are informative parameters of the curves of coefficients.

The values and positions and amplitudes of the maxima of the first and second CWT are presented in Table 1.

It can be seen from the table that with an appropriate choice of wavelet types, we obtain the stability of the parameters (position and amplitudes) of the curves of the coefficients of the second CWT to certain types of defects at different moments of time.

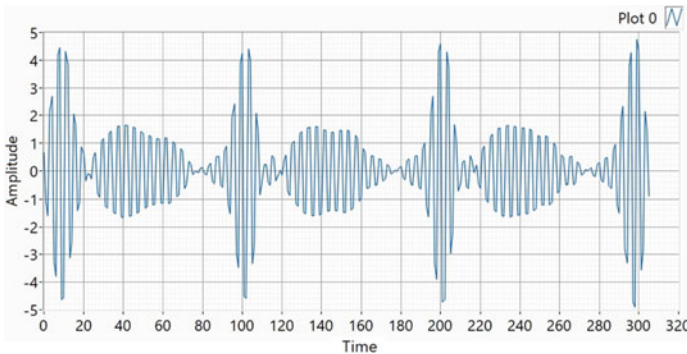


Fig. 4 Curves of coefficients of the first and second CWT signal

Table 1 Maxima of curves of CWT coefficients

Parameter	Value										
First wavelet transform											
Position	---	14.2	29.0	109.3	123.3	139.8	209.0	223.0	237.8		
Amplitude	---	1.87	1.10	1.12	1.04	0.92	1.28	1.18	0.34		
Second wavelet transform											
Position		2.7	10.0	18.0	26.0	34.2	105.6	112.4	119.8	128.0	136.7
	205.3	212.0	219.2	227.3	235.2						
Amplitude		1.71	2.40	2.45	2.14	1.28	0.93	1.54	2.70	2.30	0.91
	1.11	1.78	1.84	1.38	0.83						

The signal decomposition method can be used to automate defect control. The principle of decomposition is that the signal under study is fed to the filters for decomposition of low and high frequencies of the discrete wavelet transform (DWT), after which, using the decimation operation $\downarrow 2$ (reducing the number of frequency components by half), it is possible to obtain the approximation coefficients at the output of the low-pass filter and detailing coefficients at the output of the high-pass filter. Further, this algorithm can be continued according to the scheme, giving the coefficients of approximation of the next level ($j + 1$):

$$\begin{aligned}
 cA_j &\rightarrow \text{Lo_D} \rightarrow \downarrow 2 \rightarrow cA_{j+1} \\
 &\rightarrow \text{Hi_D} \rightarrow \downarrow 2 \rightarrow cD_{j+1}
 \end{aligned}$$

As a result of these operations, we obtain a signal decomposition tree (Fig. 5). By combining the data of the decomposition nodes, we obtain a signal with a certain information component.

The decomposition scheme allows to isolate a signal that simulates the system under study and a signal that characterizes system defects. In this case, the choice of the type of wavelet makes it possible to model the system in the best way, to separate the signal of the defects of interest from it. The significance of each node is determined by its entropy and the choice of the wavelet type, which is also determined by the wavelet type (Table 2). It should be borne in mind that, due to the frequency

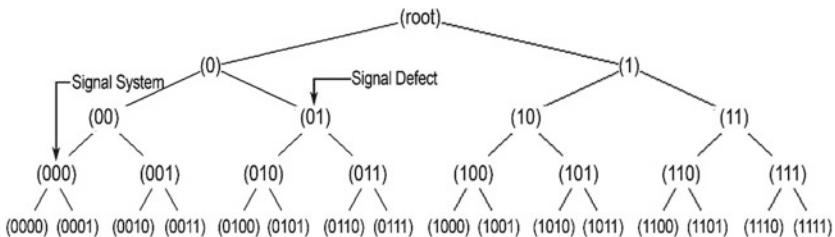


Fig. 5 Signal decomposition tree

Table 2. Entropy of DWT signal decomposition nodes.

Parameter	Value of entropy of nodes (k0)-(k1) – (k00)-(k01)-(k10)-(k11), k=0, 1								
wavelet db14									
Level (0)	5.1·10 ⁴		6.5·10 ⁴	3.5·10 ⁰					8.9·10 ⁴
	8.6·10 ⁰	1.3·10 ⁰	2.9·10 ⁰						
Level (1)	1.4·10 ⁵	9.7·10 ²	4.8·10 ⁰	4.4·10 ⁰	9.5·10 ⁻¹	9.6·10 ⁻¹	2.8·10 ⁰	2.4·10 ⁰	
	1.8·10 ⁰		1.1·10 ⁰	1.5·10 ⁰				4.9·10 ⁻¹	
	1.2·10 ⁰	1.1·10 ⁰	1.2·10 ⁰						
	3.4·10 ⁻¹	3.9·10 ⁻¹	6.7·10 ⁻¹	1.0·10 ⁰	6.5·10 ⁻¹	1.0·10 ⁰	6.4·10 ⁻¹	1.3·10 ⁰	
wavelet bior 3_1									
Level (0)	5.1·10 ⁴		6.5·10 ⁴	5.8·10 ²					6.3·10 ⁴
	3.4·10 ³	5.0·10 ²	3.9·10 ²						
Level (1)	6.7·10 ⁴	1.6·10 ⁴	2.4·10 ³	1.6·10 ³	3.9·10 ²	2.2·10 ²	2.6·10 ¹	1.5·10 ³	
	2.4·10 ¹		5.3·10 ¹	5.5·10 ⁰				5.4·10 ¹	
	3.7·10 ¹	4.6·10 ⁰	2.6·10 ¹						
	4.7·10 ¹	2.2·10 ¹	3.0·10 ⁰	2.1·10 ⁰	3.1·10 ⁰	2.0·10 ¹	1.4·10 ⁰	4.3·10 ¹	

range, level 0 describes the system itself to a greater extent, and level 1 describes its defects. To avoid the effect of frequency aliasing, the sampling rate of the sample of the received signal should be no more than 10 times the Nyquist frequency of the system signal. Tracking the change in entropy makes it possible to monitor the system and the behavior of defects, which is of interest in dynamic systems with variable parameters.

By the level of entropy in the decomposition tree nodes, one can preliminarily estimate the presence of a particular defect in the system. To identify specific defects, one can then build an ANN that will adapt to the characteristics of the system and the impact of external uncontrollable factors.

The presence and size of a defect is determined by the position and magnitude of the signal amplitudes of the decomposition nodes (Fig. 6). The obtained signal

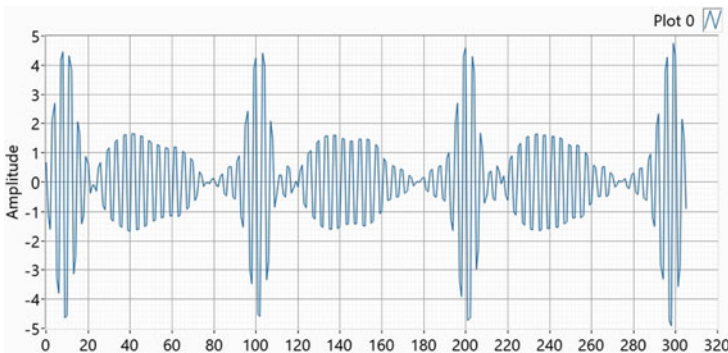


Fig. 6 Signal decomposition in node 01

parameters should be compared with experimental data within the ANN, making the diagnostic system intelligent and automated. The main difficulty of such a diagnostic system is the choice of the wavelet and the determination of the stability range of the diagnostic results.

5 Conclusions

Studies have shown that the construction of stable algorithms for diagnosing complex systems must be based on the analysis of the difference vibroacoustic signal and the function of the modeling system, for example, a parametric generator using continuous wavelet transform methods.

The system model and the system defect signal can be obtained from the vibroacoustic signal by the method of its decomposition with discrete wavelet transform.

The use of a double continuous wavelet transform due to a more than two-fold increase in the number of extrema of the curves of coefficients makes it possible to increase the detectability of defects in complex systems by more than four times under the conditions of stochastic processes occurring in the system, and is an identification feature that can be used in artificial neural networks.

References

1. Ol't Yu, Maksarov VV, Makhov VE (2020) Intelligence systems for quality assessment of threaded surfaces and flaw monitoring based on digital light field recording. *Russ J Nondestruct Test* 56:915–926
2. Matyushkova OYu, Tatter VYu (2013) Modern methods of vibroacoustic diagnostics. *Omsk Sci Bull* 3(123):294–299
3. Bratash OV, Kalinov AP (2006) Analysis of methods for vibration diagnostics of asynchronous motors. *Bulletin of the Kremenchutsk State Polytechnic University*, April 2006
4. Tatter VYu, Shchedrin VI, Sidorov EN, Buyalsky KL, Tatter AYu (2010) The Kurtosis factor as a diagnostic sign of bearing malfunctions. *Control Diagnost* 3:28–34
5. Sneddon LN (1951) *Fourier transforms*. McGraw-Hill, New York, p 542
6. Grochenig K (2001) *Foundations of time-frequency analysis*. Birkhauser, p 360
7. Qian SD (1996) *Chen joint time-frequency analysis*. Prentice-Hall, Englewood Cliffs
8. Chen D (1995) *Time-frequency analysis*. Prentice-Hall, Englewood Cliffs
9. Daubechies I (1992) Ten lectures on wavelets. In: *CBMS-NSF conference series in applied mathematics*. SIAM Ed
10. Kostyukov VN, Naumenko AP (2011) *Fundamentals of vibroacoustic diagnostics and monitoring of machines*, p 360
11. Feder E (2014) *Fractals: trans. From English*. 2nd edn., p 256
12. Kabaldin YuG, Shatagin DA, Kolchin PV, Kuzmishina AM, Anosov MS (2018) *Artificial intelligence and cyber-physical mechanical processing systems in digital production*, p 329
13. Hastie T, Tibshirani R, Friedman J (2001) *The elements of statistical learning*
14. Patrikeev IA, Stepanov RA, Frick PG (2005) Wavelet regularization of the operation of differentiating signals with noise. *Comp Progr Methods* 6(1):35–42

15. Makhov VE, Potapov AI, Shirobokov VV, Emelyanov AV (2021) Investigation of the accuracy of measuring the parameters of remote objects observed by the optical-electronic system with a light field recorder. *Sci Tech J Inf Technol Mech Opt* 21(3):342–351 (in Russian)
16. Travis J, Kring J (2006) *LabVIEW for everyone: graphical programming made easy and fun*, 3rd edn, p 1032
17. Fedorov VP (2010) Digital processing of sound and vibration signals in LabVIEW. In: *Reference functions of the NI sound and vibration LabVIEW system*, p 1296

Determination of the Convergence of the Behavior of a Full-Scale Model of a Tower Crane with a Real Object



Lev Khakhulin , Etibar Balaev , and Vladimir Eliseev 

Abstract The article shows the analysis of the behavior of a full-scale model of a tower crane carried out in the SolidWorks software package and the SolidWorks Simulations calculation module; the convergence of the results obtained in the analysis of the model showed convergence with the full-scale model with a possible error of 2–3%. At the same time, the behavior of a full-scale model of a tower crane, both in terms of kinematics and behavior when lifting a load, completely imitates the behavior of a real tower crane, which allows us to consider the full-scale model fully imitating a real object (physical model) and allows you to use it to understand the behavior of a tower crane in various operating conditions. The article also shows the dependences of the effect of the load on stability and entering the resonance of the full-scale model, obtained during the analysis in the calculation module SolidWorks Simulations.

Keywords Tower crane · Tipping · Stability · Vibration amplitude · 3D model · Solidworks · Solidworks simulation

1 Introduction

The tower crane is an integral equipment used in construction, allowing for loading operations in the construction of buildings as well as in factories and ports. At the same time, the most common construction tower cranes, the main tasks of which are:

- lifting heavy loads to a certain height;
- movement of goods within the construction site;
- loading and unloading vehicles.

Formation of an understanding of the principles of tower cranes, both their movement, and in terms of the behavior of the structure when lifting and transporting cargo, as well as during unloading is an important task in the design. Today, the

L. Khakhulin · E. Balaev (✉) · V. Eliseev
Kuban State Technological University, 2 Moskovskaya St., 350072 Krasnodar, Russia

SolidWorks software package and the SolidWorks Simulations module are increasingly used as a design and calculation tool. However, to form an understanding of the real behavior of tower crane structures when lifting and unloading loads, the model is not always sufficiently informative, especially when studying the behavior of cranes, taking into account the peculiarities of the environmental conditions. Thus, the use in the development of design features of tower cranes for designers should not be limited to the use of the SolidWorks software package with the SolidWorks Simulations calculation module. So when designing, it is also possible to use the creation of a physical model (full-scale model), which also allows you to analyze the behavior of tower cranes with a full imitation of the conditions in which the equipment is planned to operate. However, a full-scale model of a tower crane should include all the design features of the real object to which it is attached, in particular, the location and configuration features: lifting mechanisms, boom, control cabin, cargo trolley, undercarriage, frame, ballast, tower, slewing support, counterweight and a cantilever counterweight, which will allow to reproduce the full operating conditions with obtaining additional information on the possible behavior of tower cranes and to clarify the values of the safety factors.

To determine the possible use of a full-scale model of tower cranes as a source of additional information, studies were carried out on a full-scale model of a tower crane for stability and entering into resonance, when conducting a study of a 3D model of a tower crane in the SolidWorks software, with a stability analysis in the SolidWorks Simulations application, which in its the queue showed a high convergence of the results for this type of calculation with a real object, with a discrepancy of the results of 2–3% [1–4].

Thus, the analysis of a full-scale model and a 3D model of a tower crane in the SolidWorks software in the SolidWorks Simulations application will make it possible to draw a conclusion about the possible use of full-scale models in studying the behavior of tower cranes during operation and obtaining additional data.

2 Materials and Equipment

For the study, a full-scale model of a tower crane used in the construction of facilities in the Krasnodar Territory was selected (Fig. 1).

According to all the features of a full-scale model of a tower crane, a 3D model was developed in the SolidWorks software package Fig. 2 with calculations for stability and vibrations in the SolidWorks Simulations module. Measurements of the geometric dimensions of a full-scale model of a tower crane for comparison with the obtained values of displacements of points with a similar type of loading and the values of the counterweight and load masses were determined using the ACCURA coordinate measuring machine.

In the 3D model, as in the full-scale model of a tower crane, riveted and brazed connections are used as fastening elements. At the same time, the geometric features

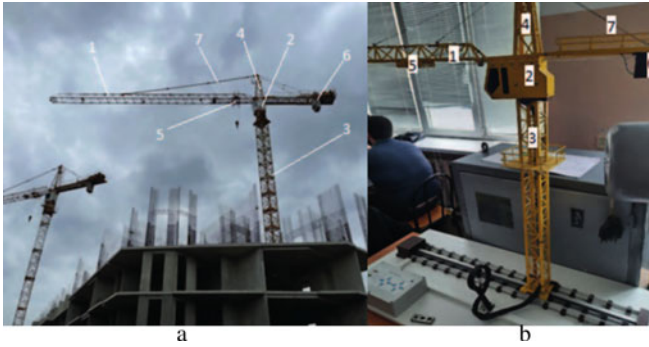


Fig. 1 Tower crane: a—real object; b—full-scale model. Legend: 1—arrow; 2 control cabin; 3—tower; 4—head; 5—cargo trolley; 6—counterweight; 7—thrust

Fig. 2 3D model of a tower crane

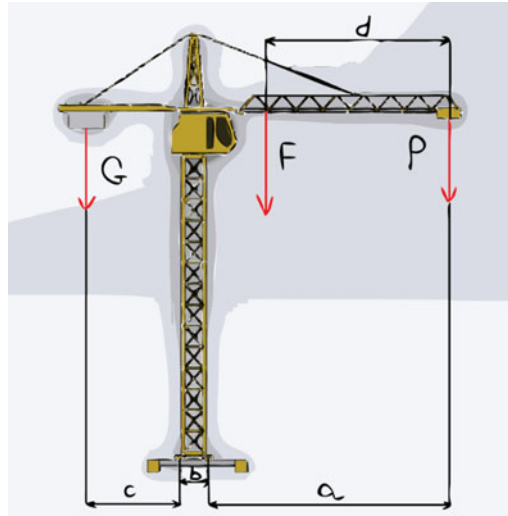


of the rollers on the undercarriage and the rails on the site make it possible to further reduce the likelihood of a full-scale crane tipping over when it lifts loads.

The maximum weight and counterweight were calculated using the MathCad Prime 4.0 software package for the scheme shown in Fig. 3 using the following calculation formulas [5–7]:

$$G = \frac{F(a + b - d)}{c}$$

Fig. 3 Diagram of the force application of a 3D model of a tower crane. where a is the shoulder of the force P ; b is the distance between the supports; c -arm of force G ; d -shoulder strength; P is the force of gravity of the load; G is the gravity of the counterweight; F is the weight of the crane



$$P = \frac{F \times b(a + b + c - d)}{a \times c}$$

$$G = \frac{66,478(0,602 + 0,072 - 0,622)}{0,232}$$

$$P = \frac{66,478 \times 0,072(0,602 + 0,072 + 0,232 - 0,622)}{0,602 \times 0,232}$$

The calculation showed that the maximum mass of the load is $P = 9.732H$, and the counterweight is $G = 15.186H$.

3 Analysis of Simulation Results and Experimental Data

The calculations performed to determine the maximum mass of the load and counterweight allowed us to determine that for this full-scale model the maximum weight of the load is $P = 9.732 N$, and the counterweight is $G = 15.186 N$, which correspond to the extreme position of the counterweight and the load trolley with a hook, by means of which lifting and transportation takes place cargo.

Using the data obtained, the stability of a 3D model of a tower crane was calculated using the SolidWorks Simulations calculation module, where the dependence of the effect of the weight of the load and the counterweight at the extreme points on the stability of the tower crane and entering into resonance was determined, the condition of which was that the crane should not lose balance in its various positions and applied loads [8–12].

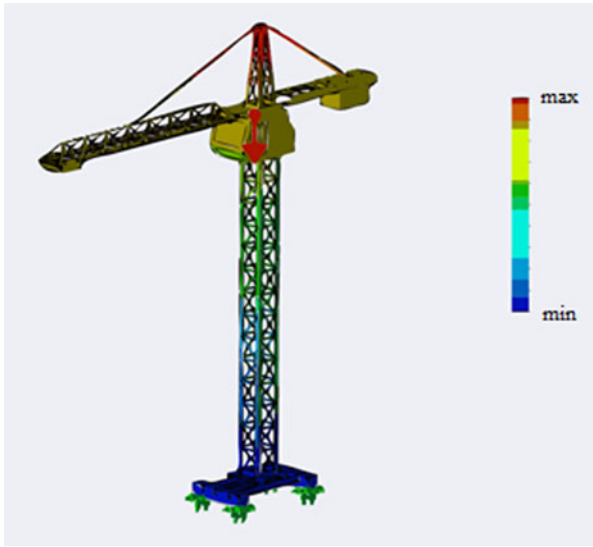


Fig. 4 Plot of displacements of various points of a 3D model of a full-scale model of a tower crane for stability analysis in the SolidWorks Simulations module

For example, Fig. 4 shows the result of the calculation in the SolidWorks Simulations module to determine the stability of a full-scale model of a tower crane at the extreme position of a cargo trolley with a hook with the maximum load weight and counterweight of the maximum weight attached to the hook.

The result of the calculation is shown in the form of a color gradient plot of the movement of various points of the full-scale model of a tower crane, where the red color corresponds to the maximum movement. So, according to the data obtained on the diagram, the maximum displacement falls on the rod with the boom and the head of the tower, while with a similar loading of a full-scale sample, similar data were obtained with a discrepancy of 2%. At the same time, the obtained data show that under these loads and displacements, there is no loss of stability of the full-scale model of a tower crane.

An important calculation is also to determine the possibility of entering into resonance when the frequencies of the forced vibrations that arise as a result of the action of the dynamic load, which occurs when the load is lifted and unloaded, coincide with the natural vibrations. It should be noted that when the frequencies of the forced and natural (resonance) oscillations coincide, the oscillation amplitude and frequency increase, which is one of the types of dynamic alternating loads leading to the destruction of the tower crane structure. Therefore, one of the important calculations is frequency analysis, which should show damped oscillations and the absence of resonance, which will allow the conclusion about the suitability of the tower crane [10–15].



Fig. 5 Image of the base of a real tower crane (a) and its full-scale model (b)

Unlike a real tower crane, the special arrangement of the base of the full-scale model allows it not to tip over on its side. The structure, which consists of three rails, makes the base of a full-scale tower crane more resistant to roll. Thus, the determination of the possible force leading to overturning is possible by the applied force to the center rail.

Figure 5 shows the base of a real tower crane and its full-scale model.

So Fig. 6 shows the result of calculating the frequency vibrations of a 3D model for a full-scale model of a tower crane, carried out in SolidWorks Simulation during unloading.

So, according to the data obtained from the diagram, the maximum amplitude of displacement falls on the boom and on the counterweight, while during unloading, the oscillations that arise are damped and do not coincide in frequencies, which was also shown by the results obtained from a full-scale model of a tower crane. At the same time, the frequencies of forced vibrations do not coincide with the frequencies of natural vibrations of a full-scale model of a tower crane, due to which the structure does not enter into resonance and does not fail. When determining the maximum amplitude on a full-scale model of a tower crane in the event of forced vibrations of the boom and counterweight when unloading the load of the maximum lifting mass for this full-scale model, it also showed a high convergence of the results with the results obtained in the calculation module SolidWorks Simulations, with a discrepancy of 3%.

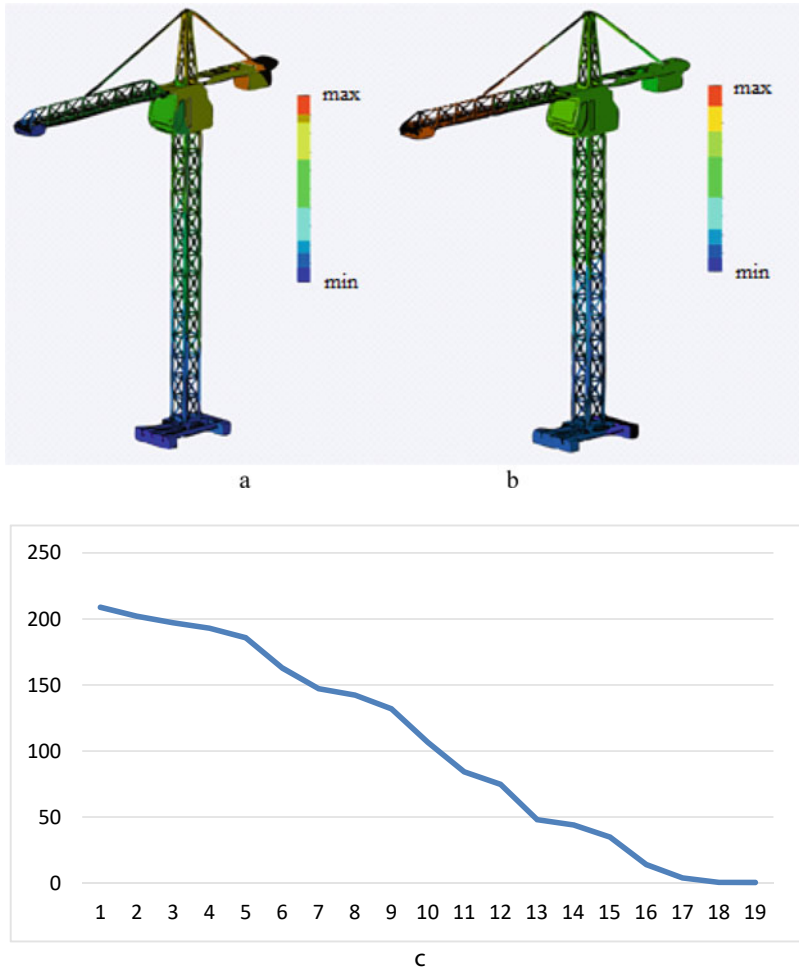


Fig. 6 Diagram of the amplitude of displacements obtained as a result of calculating the frequency oscillations in the SolidWorks Simulations module: a—for the counterweight; b—for the boom; c—frequency dependence on the number of vibrations

4 Conclusion

The obtained values of calculations using the SolidWorks software package with the SolidWorks Simulations calculation module and their comparison with a full-scale model of a tower crane used in the construction of residential multi-storey buildings in the Krasnodar Territory showed the convergence of the results with a general discrepancy of the values of 2–3%. Thus, we can conclude about the convergence of a full-scale model of a tower crane and a real object (tower crane) in behavior not only from the point of view of the kinematics of movement, but also the behavior

of the structure during loading and unloading. In turn, this allows us to study and form an understanding of the real behavior of tower crane structures when lifting and unloading loads, taking into account the peculiarities of working conditions and the environment, namely the possible impact of wind gusts of different speed, possible daily fluctuations of the earth, and others.

References

1. Alyamovsky AA, Sobachkin AA, Odintsov, EV (2005) SolidWorks, Computer modeling in engineering, Saint-Petersburg, Petersburg, p 800
2. Scriabin VA (2020) Strength analysis of metal structures during the repair of cranes using the SOLIDWORKS software product. science and technology scientific journal repair. Sci Technol Sci J Repair Recov Mod 3:24–29
3. Sagirov YuG (2013) Strength analysis of metal structures of cranes using SOLIDWORKS. Bull Priazovskiy State Tech Univ 26, 194–203
4. Zamriy AA (2010) Design and calculation by the finite element method in the APM Structure 3D M. Publishing House APM, p 375
5. Isametova ME, Zhanuzakov MM (2018) Computer-aided design of a tower crane. Bull Kazakh Acad Transp Commun Named After M Tynyshpaeva 1(104):76–82
6. Issekenova DM, Kolotvin AV, Soloviev KN (2016) Modeling and calculation of a truss metal structure of a tower crane in APM WINMACHINE for optimization of elements. Sci J “Fundam Found Mech” 1:124–126
7. Loveikin VS, Romasevich YuF, Stekhno AV (2018) Mathematical modeling of the movement of the tower crane cargo departure mechanism. Sci J “Actual Direct Sci Res 21st Cent: Theory Pract” 6(42):224–225
8. Ariskin MV, Garkin IN (2016) Analysis of the causes of the fall of a tower crane based on the construction of a model in SCAD 11.5. Sci J “Fundam Res” 10–2:243–247
9. Babkin MS, Prokopenko VS, Olyanina IV (2018) Modeling of oscillatory processes in the structures of tower cranes. Pridneprov Sci Bull 8(1):97–100
10. Panasenko NN, Sinelshchikov AV (2017) Linear-spectral method of the theory of seismic resistance of lifting structures. Part 2, computational analysis of seismic resistance of lifting cranes by the linear spectral method. J “Hoist Transp Bus” 6(91):2–6
11. Sharmanov VV, Mamaev AE, Simankina TL, Braila NV, Romanovich MA, Osipenkova IG (2020) Express monitoring of technical condition of tower crane on the basis of integral-differential approach. Bull Civ Eng 2(79):123–131
12. Glukhikh MA, Vakhrušev SI (2017) Investigation of constructive possibilities for increasing the stability of tower cranes to overturning. Sci J "Mod Technol Constr Theory Pract" 2:174–181
13. Efimenko AV, Shcherbak OV (2019) Investigation of the stability of a tower crane on full-scale and computer models. Publishing House “Belgorod State Technological University named after V.G. Shukhov, pp 252–259
14. Kudryavtsev EM, Gavrilenko AV, Gavrilenko OD (2020) Algorithm for modeling influence lines in the boom rods of a tower crane with a jib boom. Priority Areas Innov Ind 117–119
15. Scriabin VA (2020) Strength analysis of steel structures during the repair of cranes using the SOLID WORKS software product. Sci J “Repair Recov Mod” 3:24–29

Modeling of Parameters of Laser Surfacing Zones and Determination of Tribotechnical Properties of Coatings Obtained by Laser Additive Technologies



Vladimir Biryukov 

Abstract The paper presents the results of metallographic and tribotechnical studies of coatings of a multicomponent charge containing a powder based on iron and nickel in a ratio of 3:1 and a powder of ultrafine titanium carbide. The slip coatings were melted with a defocused and oscillating laser beam along the normal to the velocity vector of its movement on steel 45 and 65Mn. The influence of the laser beam power, processing speed, and diameter on the geometric parameters of the deposited coatings is determined using regression equations. The cross-sectional area of the deposited coating with an oscillating beam is higher than that of the surfaced coating with an unfocused beam. Sliding friction tests were carried out using a lubricant at normal atmospheric pressure and temperature according to the scheme plane (deposited sample)—the end of the rotating sleeve (steel 100Cr6). Abrasive wear was performed according to the planar-annular disk surface scheme. Quartz sand was fed into the friction zone using a dispenser. The regularities of the change in the coefficients of friction from the sliding speed are established, showing a decrease in the coefficients of friction with an increase in the microhardness of the coatings. With increasing pressure, the friction coefficients decrease, but at a certain critical pressure, they increase. The wear and tear resistance increases with the increase in the microhardness of the coatings. The abrasive resistance of the coatings is higher than the hardened steel 65Mn.

Keywords Laser surfacing · Microhardness · Coefficient of friction · Wear rate · Abrasive wear

1 Introduction

Improving the wear resistance of surfaced coatings is an urgent task of modern machine-building production. Steels are considered one of the most promising materials for laser surfacing due to their low cost and high mechanical properties [1,

The original version of this chapter was revised: The name of the author has been corrected. The correction to this chapter is available at https://doi.org/10.1007/978-3-030-83917-8_51

V. Biryukov (✉)

Mechanical Engineering Research Institute of the Russian Academy of Sciences (IMASH RAN),
4 Maly Kharitonyevsky Pereulok, 101000 Moscow, Russia

© The Author(s), under exclusive license to Springer Nature Switzerland AG 2022, 511
corrected publication 2022

A. Mottaeva (ed.), Technological Advancements in Construction, Lecture Notes in Civil
Engineering 180, https://doi.org/10.1007/978-3-030-83917-8_46

2]. Among them, steel 410 is the most attractive because of its good weldability and ductility [3–5]. However, laser surfacing of 410 steel is currently limited, since its low carbon content can lead to relatively low hardness and wear resistance. To increase the wear resistance of the deposited coatings as reinforcing particles [5], the effect of chromium carbide Cr₃C₂ (0–10 wt.%) was studied. In addition, single-layer composites of 18% WC/410 were deposited by direct laser deposition and the efficiency of thermal development and dissolution of WC particles of various sizes was studied [6]. Titanium carbide TiC is widely used as a strengthening phase in the composition of powder charge based on Ni [7–9], Ti [10], Co [11] and high-entropy powder alloys [12, 13] used in laser additive manufacturing. To date, there are several reports of composite coatings based on iron reinforced TiC obtained using laser technology [14–18]. The deposited ceramic-reinforced coatings based on metal matrices exhibit enhanced properties, including wear resistance at high operating temperatures [19–21]. However, the above studies do not consider the use of serial powders based on iron and nickel in the composition of the charge with ultrafine powders of titanium carbides.

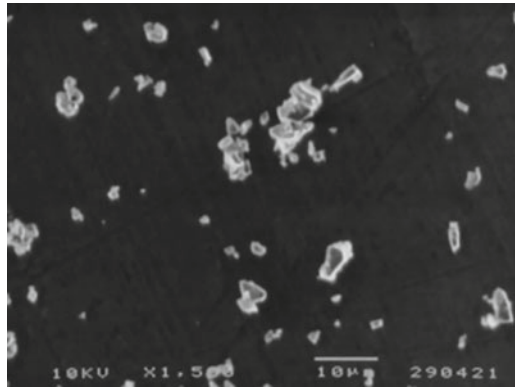
The purpose of the work is to determine the parameters of laser surfacing zones and tribotechnical characteristics of multicomponent coatings based on iron and nickel when introducing ultrafine titanium carbide powder into the charge.

2 Materials and Methods

In experimental studies, the IMASH RAN laser system was used. The samples were made of 45 (495–536HV), 65Mn (580–629HV) steels with dimensions of 15 × 20 × 70 mm. For the production of the charge, commercially available powders based on iron (Fe-Cr-B-Si) and nickel (Ni-Cr-B-Si) were selected in a ratio of 3:1, respectively, with a particle size of 40–100 μm. The powder of ultrafine titanium carbide (TiC) was obtained by crushing. Its particles have an irregular angular or elongated shape (Fig. 1) with a size of 0.5–7 μm. The composition of the powder charge was introduced 5 and 10 wt.% TiC. The powders were mixed in a mechanical device until a uniform distribution of the components of the composite material was obtained. Slip coatings were applied with a thickness of 0.69–0.81 mm. An aqueous solution of hydroxyethylcellulose was used as the binding material. Metallographic studies of the deposited coatings were performed using a PMT-3 microhardness meter, a metallographic microscope, and an AM427 digital microscope. The structure and chemical composition of the deposited layers were studied using a TESCAN VEGA 3 SBH scanning electron microscope with an energy-dispersion analysis system using the modes of reflected and secondary electrons. Typical shapes of TiC particles were observed using JEOL JSM-T330A scanning electron microscope both in standard and YMD (Y-Modulated Detection) modes.

The radiation power $P = 700\text{--}1000$ W, the processing speed $V = 7\text{--}10$ mm/s and the laser beam diameter $d = 2.5\text{--}3.5$ mm were selected as variable parameters. The transverse oscillation of the beam with a frequency $f = 229$ Hz was considered as an

Fig. 1 Typical shape of TiC particles



additional factor. To construct mathematical models, we used data from the full factor experiment (FFE). The height H and width B of the deposited rollers were considered as the responses of the system. Table 1 shows the levels of the experimental factors.

Since FFE 2³ was performed, the number of experiments was 8 for each series.

The regression equation has the form:

$$y = b_0 + b_1x_1 + b_2x_2 + b_3x_3 + b_{12}x_1x_2 + b_{13}x_1x_3 + b_{23}x_2x_3 + b_{123}x_1x_2x_3 \quad (1)$$

where y—is the system response, xi—factor levels, b—coefficients of the regression equation. B

To determine the tribotechnical characteristics of the deposited samples, a test was performed at normal temperature according to the plane (deposited sample)—ring scheme (steel 100Cr6, HRC60-62). The sliding speed and the pressure on the sample varied stepwise in the range of 0.25–3.5 m/s and 1–6 MPa, respectively. M14G2 oil was used as a lubricant. Tests for abrasive wear were carried out according to the disk-plane scheme. The cylindrical surface of the rotating rubber disk was pressed against a flat sample with a 17 N load deposited on it. Quartz sand with a particle size of 140–560 μm was used as an abrasive. The test duration was 10 min.

Table 1 Levels of experimental factors

Factor z_i	Upper level of factor z_i^+	Lower level of factor z_i^-	Center of the plan z_i^0	Variation Interval λ_i	Dependence of the encoded variable on the natural
P (W)	1000	700	850	150	$x_i = \frac{P_i - 850}{150}$
V (mm/s)	9	7	8	1	$x_i = V_i - 8$
d (mm)	3,5	2,5	3,0	1	$x_i = \frac{d_i - 3}{0,5}$

3 Results

Laser surfacing of the samples was performed with a defocused beam and with transverse oscillations of the beam along the normal to the laser processing velocity vector. The microhardness of the deposited coatings was (Fe-Cr-B-Si, Ni-Cr-B-Si), (Fe-Cr-B-Si, Ni-Cr-B-Si + 5 wt % TiC), (Fe-Cr-B-Si, Ni-Cr-B-Si + 10 wt % TiC)—792–920, 870–998, 970–1280 HV. Figure 2(a, b) shows the micro-sections of the deposited tracks with an ultrafine titanium carbide content of 5 wt. % with dimensions of 0.77×2.04 mm, and 0.79×4.26 mm, obtained by a defocused beam and a beam oscillating at a frequency of 229 Hz, respectively.

The penetration zone of the substrate during processing with a defocused beam and a scanning beam was 174 and 56 μm , respectively, which shows a high adhesion strength of the coating to the substrate material. The coating structure consisted of disordered blocks with sizes of 2–6 μm . The cross-sectional area of a single roller when processed with an oscillating beam is 2.12 times larger than when surfaced with an unfocused beam.

The equation for calculating the height of the roller without scanning, H has the form:

$$H = 0.695 + 0.035x_1 - 0.0725x_1x_2 + 0.0075x_1x_2 + 0.0125x_1x_2 - 0.01x_1x_2 + 0.01x_1x_2x_3 \quad (2)$$

The height of the roller when surfacing with transverse beam vibrations, H_s :

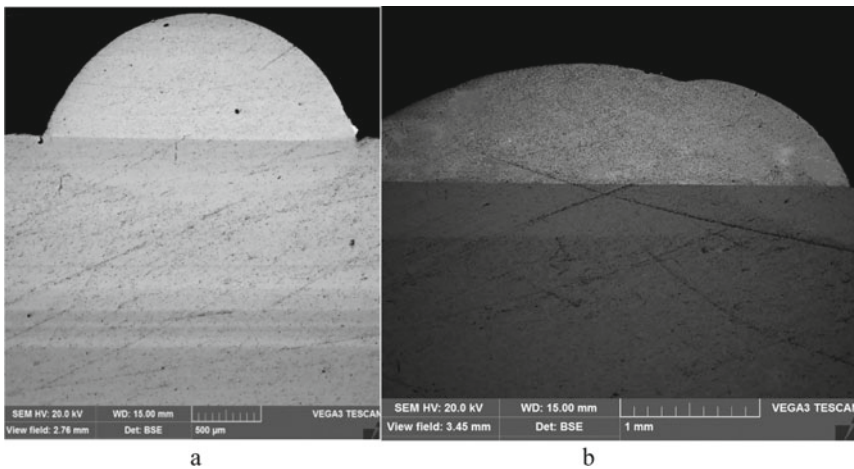


Fig. 2 General view of the deposited coatings on steel 45 with an ultrafine titanium carbide content of 5 wt. %: a-surfacing with a defocused beam; b-surfacing with an oscillating beam

$$Hs = 0.70125 + 0.03125x_1 - 0.04625x_2 + 0.00875x_3 + 0.01875x_1x_3 + 0.01625x_2x_3 + 0.00125x_1x_2x_3 \quad (3)$$

The width of the deposited roller without scanning the beam, B

$$B = 1,87375 + 0,11625x_1 - 0,09375x_2 + 0,06125x_3 - 0,02125x_1x_2 + 0,00375x_2x_3 - 0,00875x_1x_2x_3 \quad (4)$$

The width of the deposited rollers with transverse vibrations of the beam, Bs

$$Bs = 4.34625 + 0.43375x_1 - 0.26875x_2 + 0.11625x_3 - 0.26625x_1x_2 - 0.03875x_2x_3 + 0.02375x_1x_2x_3 \quad (5)$$

The regression Eqs. (2–5) were used for calculations that were compared with the experimental results and they differ from the actual values of the depth and width of the quenching zones by no more than 2.91%.

For dependencies of type H (P, V), B (P, V), comparative surfaces are constructed using the MSEExcel program (Fig. 3) with a spot diameter of 2.5 mm.

The radiation power has a predominant influence on the geometric parameters of the deposited rollers. As the power increases, the width and height of the surfaced tracks increase. As the processing speed increases, the depth and width of the rollers decreases. As the diameter of the laser beam increases, the height and width of the rollers increases.

Figure 4 shows the spectral analysis zones at the boundary with the base and in the central zone of the deposited material containing 5% of ultrafine titanium carbide in the charge. The results of the element analysis are shown in Table 2.

From the analysis of the elemental composition, it follows that there is an almost uniform distribution of Fe, Cr Ni and TiC over the cross-section of the surfacing.

The change in the friction coefficients of steel 45 in the quenched state and the deposited coatings is shown in Fig. 5 Low coefficient of friction in the friction units affects the reduction of fuel and lubricants consumption. The higher the hardness of the coating, the higher the setting pressure of the friction surfaces. With an increase in the load from 1.21 to 3.9 MPa on hardened steel samples, the friction coefficient decreases from 0.11 and 0.09. The friction coefficient for a multicomponent coating varies between 0.038 and 0.049. The minimum coefficient of friction of 0.019–0.026 was obtained on samples with 10 wt additives. % of ultrafine TiC powder. With an increase in the sliding speed (Fig. 4,b) from 0.25 to 1.3 m/s, when tested at a constant pressure on the sample of 2.0 MPa, the coefficient of friction for steel 45 decreases from 0.11 to 0.093. When the speed increases from 1.3 m/s to 1.6 m/s, it increases slightly. For surfaced coatings, the coefficient of friction decreases in the range of sliding speeds of 0.2–0.6 m/s, and with a further increase in the speed of 0.6–1.6 m/s, the coefficient of friction gradually increases.

Figure 6 shows the regularities of the change in the setting load from the sliding speed. Hardened steel samples 45 have a much lower jamming pressure compared to

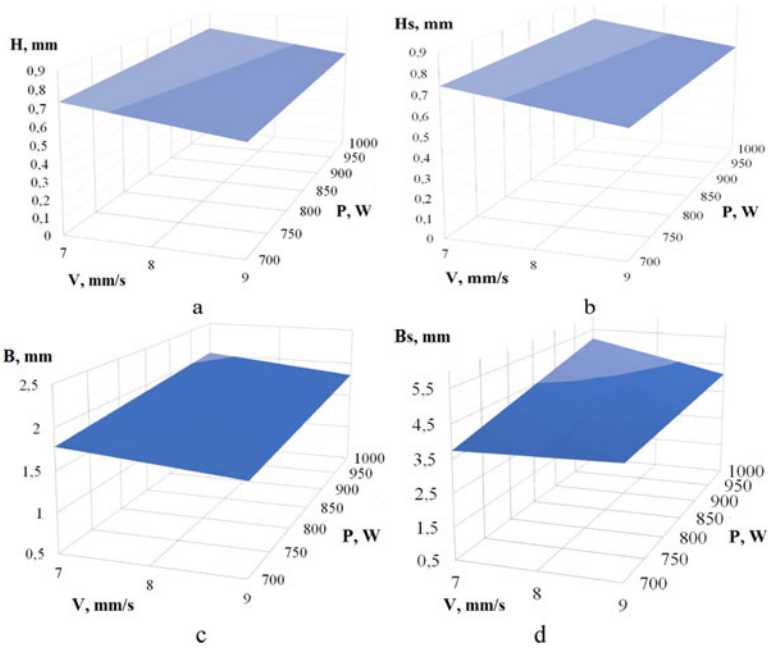


Fig. 3 The dependence of the height (a, b) and width (c, d) of the deposited rollers on the speed and power of processing with a beam diameter of 2.5 mm: a and b—with a defocused beam, b and d—with an oscillating beam

Fig. 4 Zones for determining the elemental composition of the roller with 5% TiC

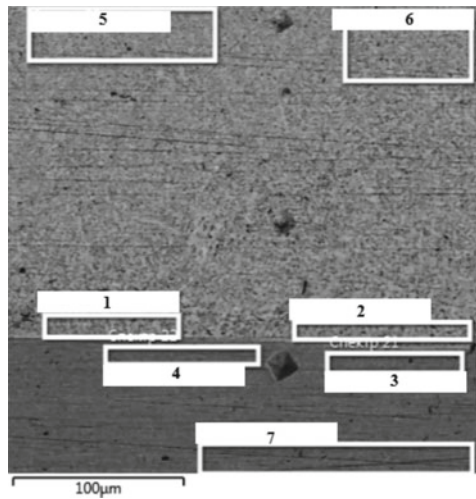


Table 2 Results of the analysis of the elemental composition, weight.%

Spectrum	C	Si	Ti	Cr	Mn	Fe	Ni
1	2.66	2.17	3.15	15.38		66.47	10.17
2	3.67	2.82	2.96	14.45		65.02	11.08
3	2.93	0.17		0.18	0.58	95.86	0.28
4	3.65	0.22		0.23	0.67	95.02	0.21
5	2.05	2.93	3.93	16.31		64.14	10.64
6	3.35	2.19	3.07	17.03		66.19	12.53
7	3.61	0.19		0.21	0.58	95.17	0.24

the deposited coatings and with the addition of ultrafine titanium carbide powder. At a pressure of 5.5 MPa, setting occurred at a speed 1.58–2.9 times lower for hardened steel 45, compared to the deposited multicomponent coatings and with additives of 10 wt. % TiC, respectively.

Figure 7 shows the results of tests on the wear rate of hardened steel samples 45 and deposited coatings. The wear resistance, the inverse of the wear intensity, increases for a multi-component coating by 1.42 times compared to hardened steel 45 and by 2.41 and 3.2 times compared to the addition of 5 and 10 wt.% of the ultrafine TiC powder, respectively.

Tests for abrasive wear during friction with loose abrasive grain of samples of hardened steel 65Mn and with coatings deposited on it (Fe-Cr-B-Si, Ni-Cr-B-Si), (Fe-Cr-B-Si, Ni-Cr-B-Si) + 5 TiC wt.%, (Fe-Cr-B-Si, Ni-Cr-B-Si) + 10 TiC wt.% showed that the weight loss of the samples was $0,064 \cdot 10^{-4}$, $0,046 \cdot 10^{-4}$, $0,033 \cdot 10^{-4}$ and $0.029 \cdot 10^{-4}$ kg, respectively.

The results of the work show that increasing the wear resistance of tillage tools and friction units of agricultural machines is possible with the use of laser additive technologies.

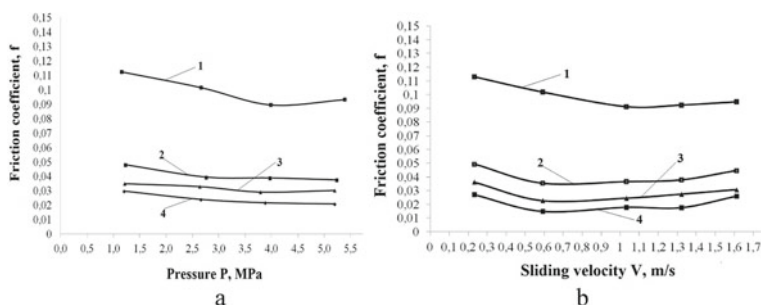
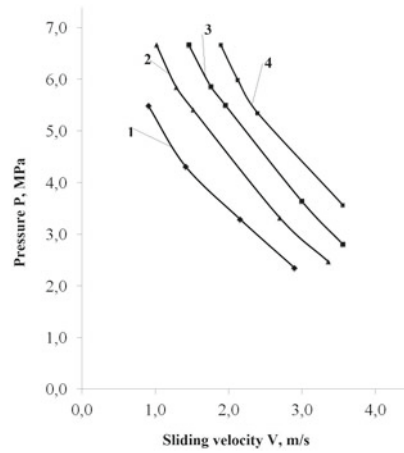


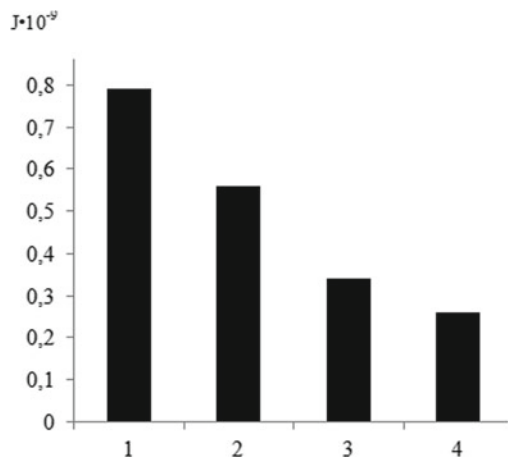
Fig. 5 Dependence of the friction coefficients on the pressure (a) and sliding speed (b): 1—Steel 45, 2—(Fe-Cr-In-Si, Ni-Cr-B-Si) 3- (Fe-Cr-In-Si, Ni-Cr-B-Si) + 5 TiC mass%, 4—(Fe-Cr-In-Si, Ni-Cr-B-Si) + 10 TiC mass.%

Fig. 6 Dependence of the jamming load on the sliding speed: 1—Steel 45, 2—(Fe-Cr-In-Si, Ni-Cr-B-Si) 3—(Fe-Cr-In-Si, Ni-Cr-B-Si) + 5 TiC mass%, 4—(Fe-Cr-In-Si, Ni-Cr-B-Si) + 10 TiC mass.%



Laser surfacing with the introduction of a strengthening phase of titanium carbide into the charge can be used in the restoration of worn friction surfaces of crankshafts, shaft necks for rolling bearings and other machine parts. The use of laser surfacing of tools for tillage will increase their service life several times and reduce the downtime of equipment. Surfacing of the coatings on the working surfaces of the tools will lead to their self-sharpening during operation. The addition of nickel-based powder will increase the corrosion resistance of the coatings.

Fig. 7 Wear rates of samples: 1—Steel 45, 2—(Fe-Cr-B-Si, Ni-Cr-B-Si) 3—(Fe-Cr-B-Si, Ni-Cr-B-Si) + 5 TiC mass%, 4—(Fe-Cr-B-Si, Ni-Cr-B-Si) + 10 TiC mass.%



4 Conclusion

The paper presents the main metallographic and tribotechnical results of research aimed at increasing the service life of parts and friction units and simulates the parameters of deposited composite coatings made of powders based on iron Fe-Cr-B-Si and nickel Ni-Cr-B-Si with the addition of the reinforcing ultrafine phase of titanium carbide TiC.

Metallographically, good adhesion is established between the coating and the substrate.

The performance of the laser surfacing process with transverse beam vibrations is higher than when processing with a defocused beam. The wear resistance of coatings without titanium carbide is 1.4 times higher compared to hardened steel 45 and 2.4 and 3 times higher compared to the addition of 5 and 10 wt.% TiC, respectively.

At a sliding speed of 2.5 m/s, the jamming pressure of deposited coatings with nano-carbides is 1.8–2.5 times higher than that of hardened steel 45.

Coatings with ultrafine carbides had lower coefficients of friction compared to the charge without TiC and the base material. The abrasive wear resistance of the TiC coating is significantly higher than that of 65Mn hardened steel.

To implement the research results into production, it is necessary to conduct field tests of machines and aggregates.

References

1. Hu WF, Zhu HM, Hu JP, Li BC, Qiu CJ (2020) Influence of vanadium microalloying on microstructure and property of laser-cladded martensitic stainless steel coating. *Materials* 13:826
2. Li BC, Zhu HM, Qiu CJ, Zhang DK (2020) Development of high strength and ductile martensitic stainless steel coatings with Nb addition fabricated by laser cladding. *J Alloys Compd* 832:154985
3. Maburi E, Sujianto Anwar MS, Romijarso TB, Adjiantoro B, Adnyana DN (2019) Comparison of strength, microstructure and corrosion resistance of stainless steels type 410 and type 410–3Mo in tempered condition. *Mater Today: Proc* 13:121–126
4. Kirtiratan G, Das CR, Joardar J, Albert SK, Ramji M, Panigrahi BB (2020) Toughening of AISI 410 stainless steel through quenching and partitioning and effect of prolonged aging on microstructure and mechanical properties. *Metall Mater Trans* 51:3377–3383
5. Fenech M, Mallia B, Grech M, Betts JC (2013) Post-deposition heat treatment of co-deposited Cr3C2 and AISI 410 stainless steel using the coaxial laser deposition technique. *J Mater Sci* 48:2224–2235
6. Fenech M, Mallia B, Grech M, Betts JC (2012) The in-flight temperature variation and dissolution of WC powder particles producing an Fe-Cr-W-C system by direct laser deposition. *Surf Coat Technol* 207:211–217
7. He X, Song RG, Kong DJ (2019) Effects of TiC on the microstructure and properties of TiC/TiAl composite coating prepared by laser cladding. *Opt Laser Technol* 112:339–348
8. Gopinath M, Debapriya KP, Ashish KN (2018) In-process detection of microstructural changes in laser cladding of in-situ Inconel 718/TiC metal matrix composite coating. *J Alloys Compd* 740:545–558

9. Mullick S, Nath AK (2020) Development of process maps based on molten pool thermal history during laser cladding of Inconel 718 TiC metal matrix composite coatings. *Surf Coat Technol* 399:126100
10. Hamed MJ, Torkamany MJ, Sabbaghzadeh J (2011) Effect of pulsed laser parameters on in-situ TiC synthesis in laser surface treatment. *Opt Laser Eng* 49:557–563
11. Weng F, Yu HJ, Liu JL, Chen CZ, Dai JJ, Zhao ZH (2017) Microstructure and wear property of the Ti5Si3/TiC reinforced Co-based coatings fabricated by laser cladding on Ti-6Al-4V. *Opt Laser Technol* 92:156–162
12. Guo YJ, Li CG, Zeng M, Wang JQ, Deng PR, Wang Y (2020) In-situ TiC reinforced CoCr-CuFeNiSi0.2 high-entropy alloy coatings designed for enhanced wear performance by laser cladding. *Mater Chem Phys* 242:122522
13. Cai Y, Ao S, Manladan SM (2019) Evolution mechanisms of TiC ceramic particles in FeCoCrNiAl high-entropy alloy laser cladding layers. *Mater Res Express* 6:1065d2
14. Al Mangour B, Grzesiak D, Jenn MY (2016) Selective laser melting of TiC reinforced 316L stainless steel matrix nanocomposites: influence of starting TiC particle size and volume content. *Mater Des* 104:141–151
15. AlMangour B, Grzesiak D, Jenn MY (2018) Densification behavior, microstructural evolution, and mechanical properties of TiC/316L stainless steel nanocomposites fabricated by selective laser melting. *Mater Des* 138:119–128
16. Wu CL, Zhang S, Zhang CH, Zhang JB, Liu Y (2018) Formation mechanism and phase evolution of in situ synthesizing TiC-reinforced 316L stainless steel matrix composites by laser melting deposition. *Mater Lett* 217:304–307
17. Liu YF, Tang MK, Hu Q, Zhang YJ, Zhang L (2020) Densification behavior, microstructural evolution, and mechanical properties of TiC/AISI420 stainless steel composites fabricated by selective laser melting. *Mater Des* 187:108381
18. Zhang ZH, Wang X, Zhang QQ, Liang YH, Ren LQ, Li XJ (2019) Fabrication of Fe-based composite coatings reinforced by TiC particles and its microstructure and wear resistance of 40Cr gear steel by low energy pulsed laser cladding. *Opt Laser Technol* 119:105622
19. Niu F, Wu D, Ma G, Wang J, Guo M, Zhang B (2015) Nanosized microstructure of Al₂O₃-ZrO₂ (Y₂O₃) eutectics fabricated by laser engineered net shaping. *Scr Mater* 95:39–41
20. Hu Y, Ning F, Cong W, Li Y, Wang X, Wang H (2018) Ultrasonic vibration-assisted laser engineering net shaping of ZrO₂-Al₂O₃ bulk parts: effects on crack suppression, microstructure, and mechanical properties. *Ceram Int* 44:2752–2760
21. Hu Y, Cong W, Wang X, Li Y, Ning F, Wang H (2018) Laser deposition-additive manufacturing of TiB-Ti composites with novel three-dimensional quasi-continuous network microstructure: effects on strengthening and toughening. *Compos Part B Eng* 133:91–100

Determination of Tribotechnical Characteristics of Modified Aluminum Alloys



Vladimir Biryukov , Anton Princ , Oleg Gradov ,
and Tatiana Bazlova

Abstract The paper presents the results of metallographic studies, spectroscopy and tribological tests of aluminum–silicon alloy samples with various modifiers: industrial silumin AK21M2.5H2.5, AK21M2. 5H2.5 modified P + Ce, AK21M2. 5H2. 5 + 0.08% P + 0.6% Ce (Tape), AK21M2.5H2.5 + 0.08% P (Tape), AK21 M2. 5H2.5 + 0.08% P + 0.6% Ce (Foil). The tests were carried out according to two schemes: “plane (test sample) – ring” and “flat sample along the forming surface of the rubber disc”. The dependences of the change in the coefficients of friction on the load and the speed of movement, the dependence of the specific load of the jamming of the friction pairs on the speed and intensity of wear of the samples at a constant sliding speed of 0.59 m/s, and the pressure in the friction pair of 1.1 MPa are obtained. According to the test results, in the samples of the initial material AK21M2,5H2,5 and modified P + Ce, the setting moment in the friction pair with steel occurred at a speed 1.5–2 times lower than in the other samples at equal pressure. In terms of wear intensity, these alloys have a wear resistance 1.5 times lower than other materials under study. According to the results of abrasive wear, the sample of the starting material AK21M2. 5H2.5 had a wear significantly higher than the other alloys. Metallographic studies, spectroscopy results, integrated spatial and frequency characteristics, and test results provide a clear understanding of how the size and geometric shape of silicon particles in an alloy affects the hardness and wear resistance of the materials under study.

Keywords Coefficient of friction · Spectroscopy · Abrasive wear · Morphology · Wear intensity

V. Biryukov (✉) · A. Princ
Mechanical Engineering Research Institute of the Russian Academy of Sciences (IMASH RAN),
4 Maly Kharitonyevsky Pereulok, 101000 Moscow, Russia

O. Gradov
N.N. Semenov Institute of Chemical Physics, Kosygina 4, 119334 Moscow, Russia

T. Bazlova
National University of Science and Technology “MISIS”, Leninsky Prospekt 4,
119049 Moscow, Russia

1 Introduction

The development of light aluminum-based alloys is a cost-effective way to reduce fuel consumption and combat environmental pollution in the automotive industry [1]. Aluminum–silicon (Al–Si) alloys have a low shrinkage compared to the base metal (aluminum) and minimizes casting defects [2]. They are widely used for the production of automotive and aerospace components [3, 4], such as cylinders, blocks and liners, connecting rods, pistons, compressor housings, engine cylinder blocks [5, 6], because they have a low density and coefficient of thermal expansion, high strength, abrasion and corrosion resistance, and good machinability [7–9]. However, they have an unfavorable morphology of the constituent phases, such as large primary Si crystals with very sharp angles, needle-like crystals of eutectic Si and iron-containing phases, which are the centers of crack formation [10–12]. The introduction of modifiers such as B, Sr, Ti, Na, and P is well known and used to improve the properties of aluminum–silicon alloys [2, 7, 9, 13]. Al–3Ti–1B and Al–5Ti–1B alloys are popular and commercial [14, 15]. The addition of the Al–5Ti–1B ligature has a problem with the formation of intermetallides, since Ti reacts with Si and forms the compound $(Ti_{1-x}Si_x)Al_3$ and reduces the modification effects as the nucleation site (TiB_2 and Al_3Ti) decreases [15, 16]. The addition of antimony to the alloys leads to the formation of a toxic gas [17] and reduces the packing density and the atomic coordination number in the melt [18]. Rare-earth materials such as Ce (cerium), Y (yttrium), and La (lanthanum) are also effective modifiers of the Al–Si alloy [19], but their addition increases the cost of production. The introduction of Mn [20, 21] can effectively improve the mechanical properties of Al-based alloys without compromising its chemical resistance. In [22], Mo was added to the Al–Si–Mg alloy in order to reduce the harmful effect of the double oxide film defect.

One of the main disadvantages of the Al–Si alloy is the needle shape of the eutectic Si, which acts as a stress concentration point for fracture and makes the alloys brittle. In addition, large primary Si crystals reduce mechanical properties. Many studies have been conducted to solve the above problems. They all focused on two approaches, namely physical and chemical. In the first case, by using ultrasonic [23], electromagnetic [24] or a combination of them [25]. As for the chemical pathway, it was based on the inclusion of such chemical elements as Sr [26] and Sb [27], which can give a less angular shape to Si, as well as reduce the grain size, which is no less important for improving the mechanical properties of the Al–Si alloy [28].

It is shown in [29] that the quality of the modification of the structure of hypereutectic piston silumins is greatly influenced by the dispersion of the structure of the applied modifiers.

The objectives of this work are to reduce the coefficients of friction, increase the setting load depending on the sliding speed and wear resistance of the hypereutectic aluminum–silicon alloy, depending on the parameters of its structure, which are changed by using modifiers with different composition and structure.

2 Materials and Methods of Research

For testing, aluminum–silicon alloys with various additives are accepted: AlSi21 Mg2.5 Ni2.5 (Source material), AlSi21 Mg2.5 Ni2.5 Modif. P + Ce, AlSi21 + 0.08% P + 0.6% Ce (Tape), AlSi21 Mg2.5 Ni2.5 + 0.08% P (Tape), AlSi2121 + 0.08% P + 0.6% Ce (Foil). The dimensions of each sample had parameters of $20 \times 70 \times 15$ mm.

A C45 steel bushing was used as a counter-counter. Tests for friction and wear were performed according to the scheme “plane (test sample)—ring” Fig. 1. The sliding velocity and the pressure on the sample varied discretely in the range of 0.23–3.45 m/s and 1.0–9.0 MPa, respectively. Metallographic studies of the samples were performed on a PMT-3 microhardness meter at a load of 0.49 N, a metallographic microscope, and an AM226 digital microscope. The results of tribological tests were determined as the arithmetic mean of the three samples. ZIG 9X 5 W-40 engine oil was used as a lubricant.

Wear tests with the supply of free abrasive to the friction zone were performed according to the scheme “flat sample on the forming surface of the rubber disc”. Quartz sand with particle sizes from 0.2 to 0.6 mm was fed into the friction zone. The tests were performed at normal atmospheric pressure and temperature. The test load was 15 N, the duration of one test was 10 min. After each test, the samples were cleaned of abrasive particles. As with the wear rate tests, three samples of each material were taken. The weight loss of the samples was determined on a VIBRA HT-220CE analytical balance. The wear value was determined as the arithmetic average of the three samples.

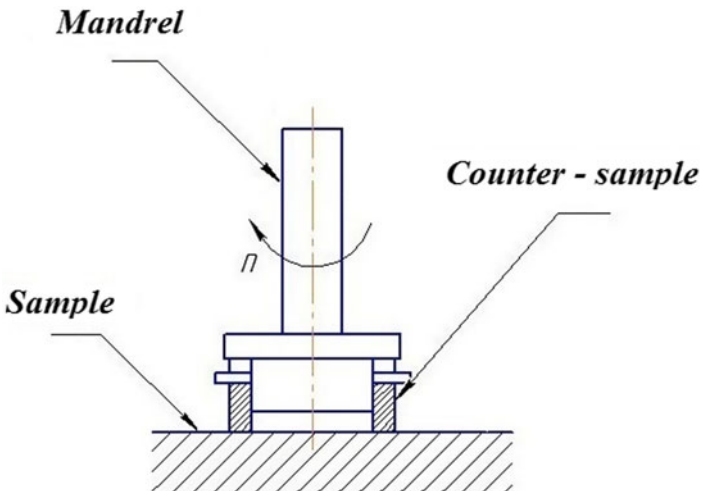


Fig. 1 Friction scheme “plane (test sample)—ring”

The coefficient of thermal expansion was determined by dilatometric analysis on a quenching and deformation dilatometer DIL 805 A/D in the temperature range of 25–400 °C. The average coefficient of linear expansion for a given temperature range was calculated by the formula:

$$\alpha = \frac{\Delta l}{\Delta T} \cdot \frac{1}{l_0}, \quad (1)$$

Where Δl is the change in the length of the sample; ΔT is the change in the temperature of the sample; l_0 is the initial length of the sample.

3 Results

Figure 2 shows the microstructures of the samples of the initial AK21M2, 5H2, 5 alloy (a), and with the modifiers AK21 + 0.08% P + 0.6% Ce (Tape) (b), AK21M2, 5H2, 5 + 0.08% P (Tape) (c), AK21 + 0.08% P + 0.6% Ce (Foil) (d). The primary silicon crystals had an inhomogeneous angular shape with the maximum dimensions in the initial alloy structure. The introduction of modifiers led to a significant reduction in the size of silicon crystals.

Hardness for each sample: AlSi21 Mg2.5 Ni2.5, AlSi21 Mg2.5 Ni2.5 Modif. P + Ce, AlSi21 + 0.08% P + 0.6% Ce (Tape), AlSi21 Mg2.5 Ni2.5 + 0.08% P (Tape) and AlSi21 + 0.08% P + 0.6% Ce (Foil) is 140HV, 119HV, 103HV, 175HV and 88HV, respectively.

Figure 3(a, b) shows the results in the form of the dependence of the coefficient of friction on the normal pressure and speed.

With an increase in the load from 2.0 to 7.5 MPa, the coefficient of friction decreased from 0.10 to 0.052. The minimum coefficient of friction of 0.08–0.52 was shown by the material AlSi21 + 0.08% P + 0.6% Ce (Tape). In contrast, the maximum coefficient of friction was AlSi21 Mg2.5 Ni2.5 for the starting material. With an increase in the sliding speed from 0.29 to 2.5 m/s, the change in the coefficient of friction was unstable, but a predominant decrease was observed. With a further increase in the speed to 3.45 m/s, the coefficient of friction increased for almost all the materials studied. Samples of materials AlSi21 Mg2.5 Ni2.5 + 0.08% P (Tape) and AlSi21 + 0.08% P + 0.6% Ce (Tape) had a significantly smaller and more stable change in the coefficient of friction over the entire range of increasing travel speed. The initial material AlSi21 Mg2.5 Ni2.5 had the highest coefficient of friction in comparison with the rest of the samples, but in the speed range from 0.29 to 2.0 m/s, there is a constant decrease in the coefficient of friction, and then a gradual increase to almost the initial values as at the speed of movement of 0.29 m/s.

Figure 4 shows the patterns of changes in the jamming load from the sliding speed. The starting material AlSi21 Mg2.5 Ni2.5 is significantly inferior to other materials with various inclusions. For this material, at a pressure of 3.9 MPa, jamming occurs at a speed 1.5–2.5 times lower than that of the other samples under study. The best

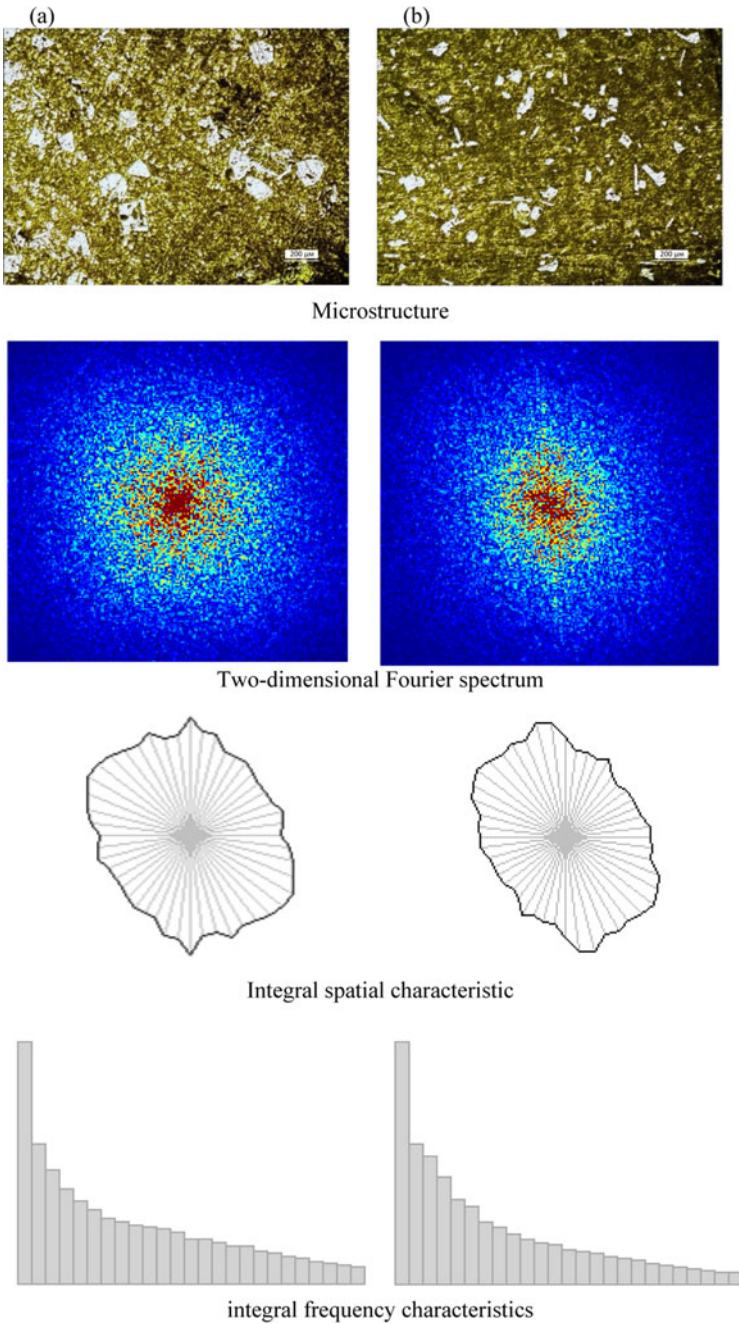


Fig. 2 Microstructure of samples: a)—AlSi21 Mg2.5 Ni2.5; b)—AlSi21 + 0.08% P + 0.6% Ce (Tape); c)—AlSi21 Mg2.5 Ni2.5 + 0.08% P (Tape); d)—AlSi21 + 0.08% P + 0.6% Ce (Foil)

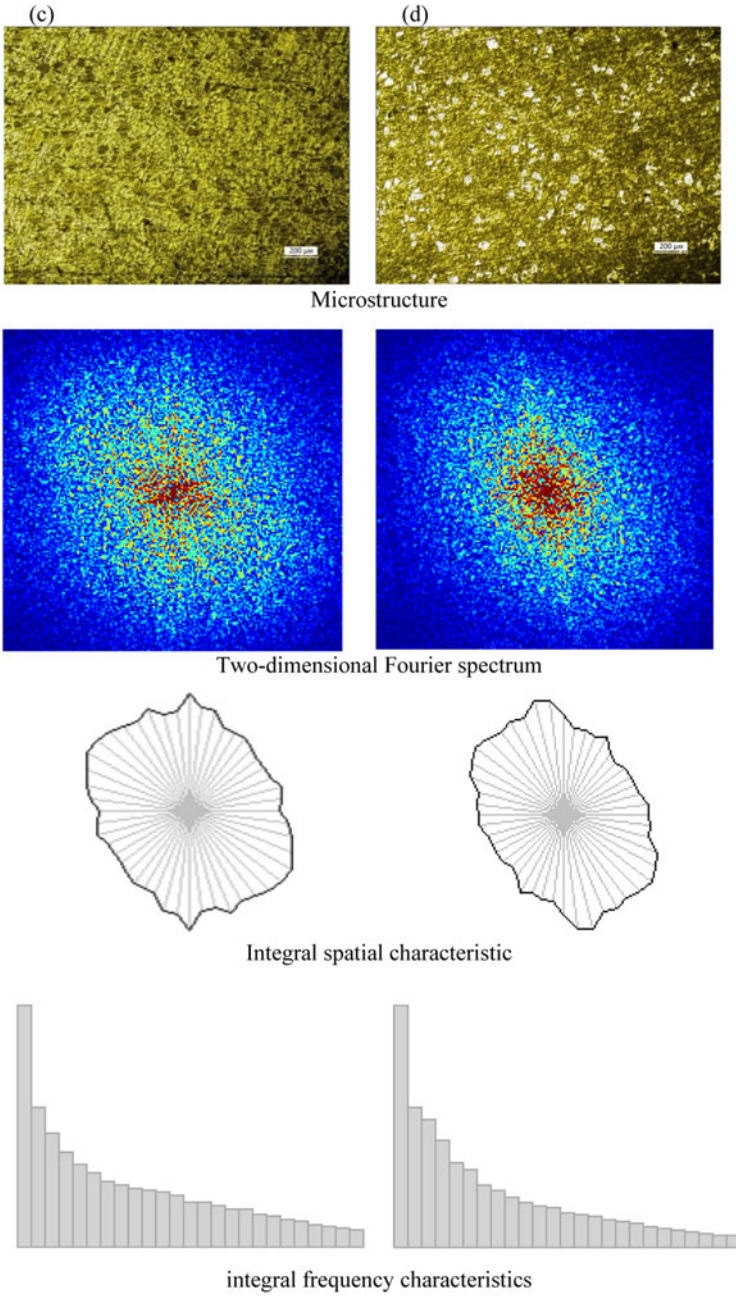


Fig. 2 (continued)

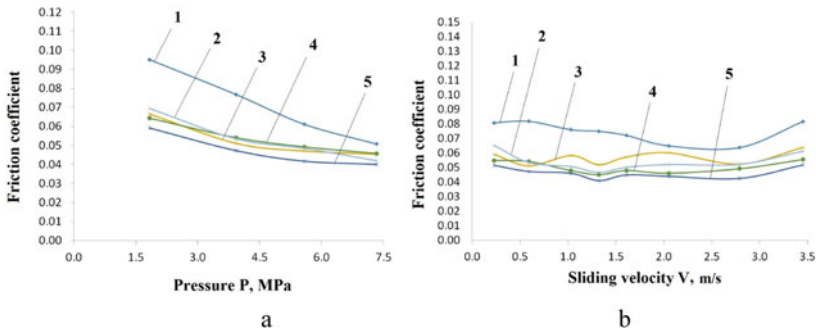


Fig. 3 The dependence of the friction coefficients on the pressure (a) and Sliding velocity (b): 1—AlSi21 Mg2.5 Ni2.5; 2—AlSi21 + 0.08% P + 0.6% Ce (Foil); 3—AlSi21 Mg2.5 Ni2.5 Modif. P + Ce; 4—AlSi21 Mg2.5 Ni2.5 + 0.08% P (Tape); 5—AlSi21 + 0.08% P + 0.6% Ce (Tape)

result was shown by samples of materials AlSi21 + 0.08% P + 0.6% Ce (Foil) and AlSi21 + 0.08% P + 0.6% Ce (Tape), which had a jam in a friction pair with steel at a speed of 2.05 m/s at a pressure of 9.0 MPa. A satisfactory result was shown by the material AlSi21 Mg2.5 Ni2.5 + 0.08% P (Tape), in which the setting moment occurred at a speed of 1.61 m/s at a pressure of 9.0 MPa.

The results obtained are in good agreement with the data on the size of primary silicon particles and the value of the temperature coefficient of linear expansion (TCLE) of the studied samples in the temperature range of 25–200 °C, presented in Table 1.

On the example of the AK21 alloy, we can trace the relationship between the sliding speed, at which the sample seizes, and the TCLE. The lower the value of the coefficient, the higher the speed of rotation, the jamming or jamming of the sample occurs, which occurs mainly due to the increase in the size of the test sample due to strong heating during friction.

Figure 5 shows the wear rates of the samples in a friction pair with 40X steel. The wear resistance, the inverse of the wear intensity, was significantly higher in the samples of material AlSi21Mg2.5Ni2.5 + 0.08% P + 0.6% Sec (Tape) and AlSi21Mg2.5Ni2.5 + 0.08% P (Tape). The wear rate of the counter-tile was lower when tested in a friction pair with AlSi21Mg2.5Ni2.5 + 0.08% P + 0.6% Su (Tape) in comparison with all the materials studied. The worst result was shown in a pair of friction with steel samples of the starting material AlSi21Mg2.5Ni2.5 and AlSi21Mg2.5Ni2.5 modified P + Su. This is probably due to the presence in the industrial alloy of a large number of intermetallic phase particles in addition to primary silicon crystals.

Table 2 shows the mass losses of samples during wear tests with the supply of free abrasive to the friction zone:

All the tests carried out on the friction and wear of aluminum–silicon alloys give a clear picture of the fact that the size of the particles in the structure plays an important

Fig. 4 Dependence of the jamming load on the sliding speed:
 1—AlSi21Mg2.5Ni2.5;
 2—AlSi21 Mg2,5 Ni2,5 Modif. P + Ce;
 3—AlSi21 Mg 2.5 Ni2.55 + 0.08% P (Tape);
 4—AlSi21 + 0.08% P + 0.6% Ce (Tape);
 5—AlSi21 + 0.08% P + 0.6% Ce (Foil)

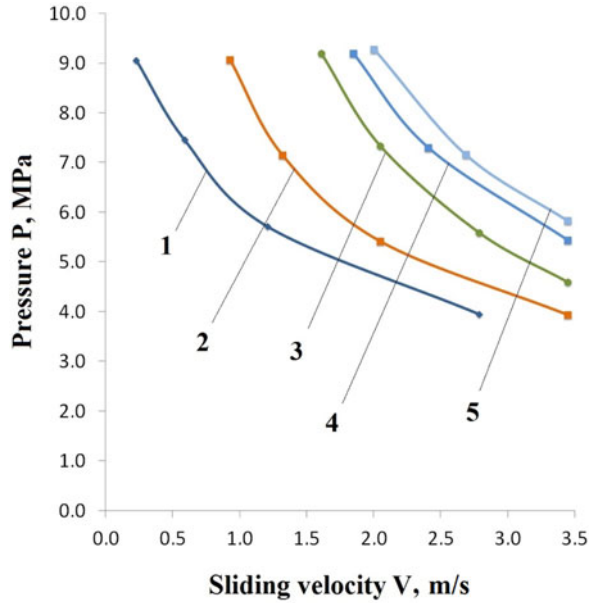


Table 1 The speed of rotation (sliding speed) at which jamming occurs (scuffing) at a constant pressure on the sample of 5.7 MPa

Chemical composition of samples	TKLE (25–200 °C), × 10 ⁻⁶ 1/K	Primary silicon crystal size, μm	Speed of rotation (sliding speed), n, min ⁻¹ (m/s)
AlSi21Mg2.5Ni2.5 (Source material)	19.4	90	900 (1.32)
AlSi21Mg2.5Ni2.5 + 0,08% P (Tape)	18.9	24	1900 (2.79)
AlSi21Mg2.5Ni2.5 Модиф. P + Ce	20.5	20	1400 (2.05)
AlSi21Mg2.5Ni2.5 + 0,08% P + 0,6% Ce (Tape)	19.9	20	2350 (3.45)
AlSi21Mg2.5Ni2.5 + 0,08% P + 0,6% Ce (Foil)	20.2	–	2350 (3.45)

role. Namely, the larger the primary silicon crystals in hypereutectic silumins, the worse the mechanical properties.

The material of the AlSi21Mg2.5Ni2.5 alloy showed the highest coefficient of friction, low resistance to setting depending on the load and speed of movement, and weak wear resistance compared to the rest of the studied samples, which had smaller Si particles in their structure.

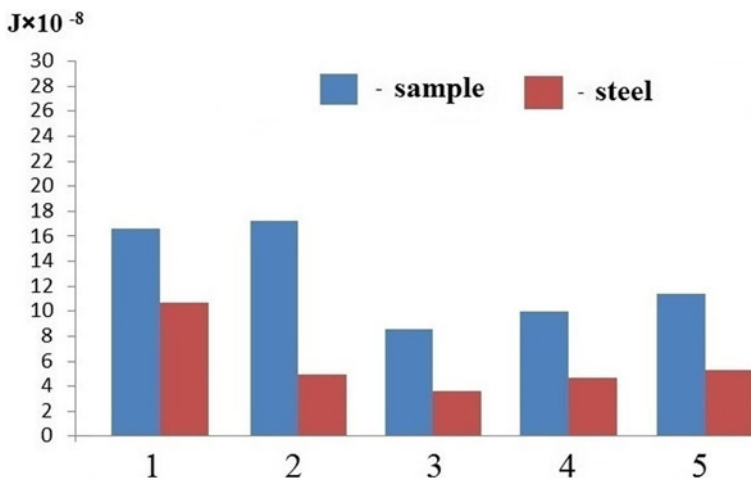


Fig. 5 The wear rate of samples and counter-samples-steel: 1—AlSi21 Mg2,5 Ni2,5; 2—AlSi21 Mg2,5 Ni2,5 Modif. P + Ce; 3—AlSi21 + 0.08% P + 0.6% Ce (Tape); 4—AlSi21 Mg2,5 Ni2,5 + 0.08% P (Tape); 5—AlSi21 + 0.08% P + 0.6% Ce (Foil)

Table 2 Mass loss of samples by composition after abrasive wear tests

Composition	Mass loss, g
AlSi21 Mg2.5 Ni2.5	0.1388
AlSi21 Mg2.5 Ni2.5 Modif. P + Ce	0.1159
AlSi21 + 0.08% P + 0.6% Ce (Tape)	0.1045
AlSi21 Mg2.5 Ni2.5 + 0.08% P (Tape)	0.0847
AlSi21 0.08% P + 0.6% Ce (Foil)	

AlSi21Mg2.5Ni2.5 modified P + alloy Ce had a similar dependence of the change in the coefficient of friction on pressure and velocity with the rest of the studied alloys with different modifiers in the structure. However, it showed low resistance to scuffing, as well as a high wear rate in a pair of friction with steel.

The introduction of various modifiers into the Al-Si melt can further solve many problems related to the size and morphology of primary and eutectic silicon crystals.

4 Conclusions

The regularities of the change in the coefficients of friction from the speed of movement and specific load are obtained, where the samples of the material AlSi21 + 0.08% P + 0.6% Ce (Tape) had the lowest coefficient of friction, both with an increase in pressure and constant speed, and with a uniform increase in the speed of movement and constant pressure.

The dependence of the setting load of the friction pair on the sliding speed showed that in the initial material AlSi21 Mg2.5 Ni2.5 at a pressure of 3.8 MPa, the jamming occurs at a speed 1.5–2.5 times lower than in the rest of the studied samples.

Tests for wear intensity and abrasive wear showed that the greatest wear was in the samples of the starting material AlSi21 Mg2.5 Ni2.5 and AlSi21 Mg2.5 Ni2.5 Modif. P + Ce;

Based on the obtained results on friction and wear, the study of the microstructure of alloys, spectroscopy, as well as the integral spatial and frequency characteristics, it is clear that the introduction of modifiers leads to a decrease in the size of the silicon grain, which contributes to a decrease in the friction coefficients, the wear rate and an increase in the resistance of the alloys to the scuffing.

References

1. Biswas P, Mondal MK, Mandal D (2019) Effect of Mg2Si concentration on the dry sliding wear behavior of Al–Mg2Si composite. *J Tribol* 141(8)
2. Barbosa CR, et al (2019) Tailoring of processing parameters, dendritic microstructure, Si/intermetallic particles and microhardness in as-cast and heat-treated samples of Al7Si0.3Mg alloy. *Metals Mater Int* 26(3):370–383
3. Souza FA, et al (2019) Unsteady-state Horizontal solidification of an Al–Si–Cu–Fe alloy: relationship between thermal parameters and microstructure with mechanical properties/fracture feature. *Met Mater Int* 25:18–33
4. Heo JY, Gwon JH, Park JK, Lee KA (2018) Effects of heat treatment on the microstructures and high temperature mechanical properties of hypereutectic Al–14Si–Cu–Mg alloy manufactured by liquid phase sintering process. *Met Mater Int* 24:586–596
5. Kumar P, Wani MF (2017) Effect of load on the tribological properties of hypereutectic Al–Si alloy under boundary lubrication conditions. *Mater Res Express* 4(11):116519
6. Jia P, Zhang J, Hu X, Teng X, Zuo M, Gao Z, Yang C, Zhao D (2018) Grain refining effects of the melt thermal-rate treatment and Al–Ti–B–Y refiner in as-cast Al–9Si–0.5Mg alloy. *Mater Res Express* 5:066520
7. Li C, Pan Y, Lu T, Jing L, Pi J (2019) Effects of Ti and La additions on the microstructures and mechanical properties of B-refined and Sr-modified Al–11Si alloys. *Met Mater Int* 24(5):1133–1142
8. Lee SW, Kim MS (2016) High temperature deformation behavior of spray-formed and subsequently extruded Al–25Si based alloy. *Met Mater Int* 22:579–584
9. Kim H, Kim MS (2018) High temperature tensile properties of hypereutectic Al–25Si based alloy. *Met Mater Int* 24(1):136–141
10. Kori SA, Murty BS, Chakraborty M (2000) Development of an efficient grain refiner for Al–7% Si alloy. *Mater Sci Eng A* 280(1):58–61
11. Nan K, Pierre C, Chaoyue C, Yan W, Hanlin L, Christian C (2016) Microstructure and wear behavior of in situ hypereutectic Al–high Si alloys produced by selective laser melting. *Mater Des* 99:120–126
12. Li Q, Xia T, Lan Y, Zhao W, Fan L, Li P (2013) Effect of rare earth cerium addition on the microstructure and tensile properties of hypereutectic Al–20% Si alloy. *J Alloy Compd* 562:25–32
13. Biswas P, Prasadu KD, Mondal MK (2018) Effect of Bi addition on microstructure and mechanical properties of hypereutectic Al–17.6Si alloy. *Metals Mater Int* 6:116509
14. Fakhraei O, Emamy M, Farhangy H (2013) The effect of Al–5Ti–1B grain refiner on the structure and tensile properties of Al–20%Mg alloy. *Mater Sci Eng A* 560:148–153

15. Chen Y, Pan Y, Lu T, Tao S, Wu J (2014) Effects of combinative addition of lanthanum and boron on grain refinement of Al–Si casting alloys. *Mater Des* 64:423–426
16. Birol Y (2012) Effect of silicon content in grain refining hypoeutectic Al–Si foundry alloys with boron and titanium additions. *Mater Sci Technol* 28:385–389
17. Gruzleski J, Closset BM (1990) The treatment of liquid aluminum-silicon alloys. *American Foundrymen's Society*, p 34
18. Srirangam P, Kramer MJ, Shanar S (2011) Effect of strontium on liquid structure of Al–Si hypoeutectic alloys using high-energy X-ray diffraction. *Acta Mater* 59(2):503–513
19. Mahmod MG, Elgallad EM, Ibrahim MF, Samuel FH (2018) Effect of rare earth metals on porosity formation in A 356 alloy. *Int J Metalcast* 12:251–265
20. Li L, Zhao Z, Zuo Y, Zhu Q, Cui J (2013) Effect of a high magnetic field on the morphological and crystallographic features of primary Al₆Mn phase formed during solidification process. *J Mater Res* 28:1567–1573
21. Shabestari SG (2004) The effect of iron and manganese on the formation of intermetallic compounds in aluminium–silicon alloys. *Mater Sci Eng A* 383:28298
22. Qi C, Griffith WD (2021) Modification of double oxide film defects with the addition of Mo to an Al–Si–Mg alloy. *Metall and Mater Trans B* 52:502–516
23. Zhao JW, Wu SS (2010) An investigation on primary Si refinement by Sr and Sb additions in a hypereutectic Al–Si alloy *Trans Nonferrous Metals Society of China* 754–757
24. Lu D, Jiang Y, Guan G, Zhou R, Li Z, Zhou R (2007) Hypereutectic Al–Si alloy with completely nodular eutectic silicon. *Microstruct Process Int J Mater Sci Appl* 189:13–18
25. Haghayeghi R, de Paula LC, Zoqui EJ (2017) Comparison of Si refinement efficiency of electromagnetic stirring and ultrasonic treatment for a hypereutectic Al–Si alloy. *J Mater Eng Perform* 26:1900–1907
26. Yilmaz F, Atasoy OA, Elliott R, Cryst J (1992) Growth structures in aluminium-silicon alloys II. The influence of strontium. *J Cryst Growth* 118:377–384
27. Prasada Rao AK, Das K, Murty BS, Chakraborty M (2008) On the modification and segregation behavior of Sb in Al–7Si alloy during solidification. *Mater Lett* 62:2013–2016
28. Lu SZ, Hellawell A (1995) Growth mechanisms of silicon in Al–Si alloys. *J Cryst Growth* 73:316–328
29. Nguyen KKh, Belov VD, Bazlova TA (2020) Preparation and application of nanostructured phosphorus-containing modifying ligatures for hypereutectic silumins. *Metallorobotka* 1:46–53

Obtaining a Coating with Increased Adhesive and Cohesive Strength for High-Speed Flame Spraying for a Pair of Materials Coating-Substrate Metal–Metal



Etibar Balaev  and Vladimir Eliseev 

Abstract The article shows methods for increasing the adhesion and cohesion of the coating-substrate for various combinations of metal–metal for the technology of high-speed flame spraying using local heating to a temperature of $0.8-1T_{\text{melt}}$ of the melting temperature of the substrate surface immediately before spraying particles of powder materials. The residual stresses were determined by the Sachs and Davidenkov methods, as well as the zone of the jump of residual stresses with a change in sign (tensile/compressive), which was mixed into the depth of the part and did not coincide with the substrate-coating interface. Photos of the substrate-coating interface are shown, which is characterized by the absence of a clear interface line. The parameters of coating deposition on a part made of steel alloys are given on the example of steel 45 and for non-ferrous metals on the example of aluminum alloy according to the proposed technology of preliminary local heating of the substrate surface to a temperature of $0.8-1T$ from the melting point of the material on which the coating is applied. The results of tests of samples made of steel alloys on the example of steel 45 and of non-ferrous materials on the example of an aluminum alloy with a coating obtained using the proposed sputtering technology with preliminary local heating of the substrate surface during the formation of the coating by high-speed gas-flame sputtering are also presented.

Keywords Adhesion · High-speed flame spraying · Substrate surface preparation · Residual stresses · Cohesion · Sachs and Davidenkov methods

1 Introduction

Increasingly, in modern mechanical engineering, methods of metallization by spraying are used, which make it possible to obtain various kinds of coatings on the surface of a part, which make it possible to change the physical and mechanical properties of the surface of the part and, as a result, the operational characteristics of the surface and the part as a whole. In this case, a multi-layer coating with

E. Balaev (✉) · V. Eliseev
Kuban State Technological University, 2 Moskovskaya St., Krasnodar 350072, Russia

different layer thicknesses can be obtained. Thus, the structure of the composite type part is obtained, which is a laminated composite. This allows for improved performance, since the layered architecture allows you to combine different physical and mechanical properties characteristic of different materials in one part. This approach to solving the problem of improving the performance of parts has long been known and confirmed as an effective method. In this case, one of the requirements for obtaining a coating is the thickness of the layer, which has an inverse relationship with adhesion, i.e. the greater the thickness of the resulting coating, the lower the adhesive strength, which is one of the factors limiting the spread of this method of increasing the operational characteristics of the part to various areas of mechanical engineering. It is also necessary to understand that those technologies for obtaining coatings with high adhesion strength (magnetron spraying, etc.) usually make it possible to obtain thin films, and technologies of thermal spraying (high-speed gas-flame, cold gas-dynamic, etc.) do not allow obtaining coatings with high adhesion, which is currently the main reason for limiting the scope of applicability of this metallization technology in modern mechanical engineering [1–3].

It was noted that when using the technology of high-speed gas-flame spraying, a clear interface is observed between the substrate and the coating, which indicates the absence of the formation of a single alloy by the sprayed particles of metal powder material with the substrate surface. The reason for this is the incomplete melting of the sprayed particle and the insufficient effect of this particle on the substrate surface to heat the part surface to a temperature close to or equal to the melting temperature, it should be noted that factors affecting both particle heating and heating of the substrate surface material are the transformation of the kinetic energy of the particle into thermal as a result of collision of the particle with the surface of the substrate and directly heating itself from the direct action of the burning gas on the sprayed particle and the surface of the substrate and the transfer of thermal energy by means of heat exchange from the particle to the surface of the substrate. As a rule, this combination of effects is insufficient to ensure fusion of the material of the substrate surface, thus the adhesive strength is provided due to the mechanical part, namely, due to the mechanical adhesion of the coating particle to the substrate surface and due to the chemical component, which is provided mainly due to mutual thermal diffusion of atoms coatings and substrates, which leads to the emergence of requirements for the application of adhesive layers of the coating to use metals with unlimited solubility in the base material and other sprayed materials.

To improve the quality of composite surface layers, both in terms of adhesion strength and in terms of operational and functional properties, it is promising to use various processing methods at different stages of spraying. Thus, the simultaneous combined use of non-consumable electrode welding technologies and the technology of transferring nanoparticles by a high-temperature gas flow and their deposition on a substrate allows increasing the physical and mechanical properties of the composite coating by increasing its adhesion strength and reducing porosity. This is due to the fact that the electric arc heats the surface of parts made of non-ferrous metals to a temperature of $0.9-1T_{\text{melting}}$ and the sprayed powder material, heated also to a temperature equal to $0.9-1T_{\text{melting}}$, collides with a

surface that is not solid, but liquid state phase, which ensures fusion of the material of the steel part with the applied powder material, which significantly increases the adhesive strength. In this case, further transfer of nanoparticles by a high-temperature gas flow and their deposition onto the formed coating layer occurs under a similar effect of an electric arc on the surface of the coated steel part, as a result of which the sprayed layer and the sprayed powder form a homogeneous structure, thereby ensuring a significant decrease in the porosity of the composite coating and increasing the cohesive strength.

2 Materials and Equipment

To obtain the coating, an upgraded GLC-720 high-speed gas-flame spraying unit was used with non-consumable tungsten electrodes installed on the burner, making it possible to obtain an electric arc arising between two tungsten electrodes passing along the surface of the part immediately preceding the deposition of the coating on the surface of the part and heating the surface of the part to a temperature of 0, 9-1Tm (Fig. 1).

The determination of adhesion strength was carried out on an Instron 8801 testing machine. The determination of residual stresses was carried out by the Sachs methods on cylindrical samples with a coating by drilling on a 1E61M screw-cutting lathe, followed by measurement of the dimensions on an ACCURA coordinate measuring machine (Fig. 2), designed to measure the geometric dimensions of parts complex shapes, deviations in the shape and location of surfaces. After the coverage was achieved, further removal of the layer of material on the cylindrical sample from the hole was carried out using a solution of HCl (2 ml) + HF (1 ml) + HNO₃ (1 ml) + H₂SO₄ (1 ml) with tracking changes in the axial and circumferential deformations at the outer radius [4].

Determination of residual stresses (circumferential, radial and axial) was carried out in the MathCad Prime 4.0 software package using the following calculation formulas [4]:

$$\sigma_r(r) = \frac{E}{1 - \mu^2} \cdot \frac{R_2^2 - r^2}{2r^2} [\varepsilon_{\theta 2}(r) + \mu \varepsilon_{z 2}(r)];$$

$$\sigma_z(r) = \frac{E}{1 - \mu^2} \left[\frac{R_2^2 - r^2}{2r^2} \left(\frac{d\varepsilon_{z 2}}{dr}(r) + \mu \frac{d\varepsilon_{\theta 2}}{dr}(r) \right) - \varepsilon_{z 2}(r) - \mu \varepsilon_{\theta 2}(r) \right];$$

$$\sigma_{\theta}(r) = \frac{E}{1 - \mu^2} \left[\frac{R_2^2 - r^2}{2r^2} \left(\frac{d\varepsilon_{\theta 2}}{dr}(r) + \mu \frac{d\varepsilon_{z 2}}{dr}(r) \right) - \frac{R_2^2 + r^2}{2r^2} (\varepsilon_{\theta 2}(r) + \mu \varepsilon_{z 2}(r)) \right]$$

Investigation of the microstructure, as well as determination of the reflow zone along the coating-substrate interface, was carried out on a JSM-7500F scanning microscope.

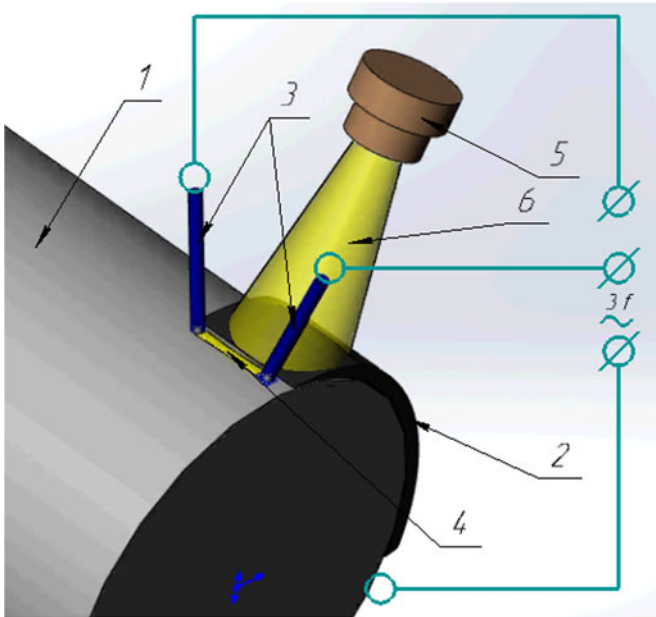


Fig. 1 Schematic diagram of obtaining a coating using the proposed technology with increased adhesive and cohesive strength: 1 - cylindrical specimen St45; 2 - the resulting TiNi coating; 3 - tungsten electrodes; 4 - three-phase combined electric arc between the electrodes and the part and between the electrodes at the same time; 5 - gun for high-speed gas flame spraying; 6 - jet of high-speed gas-flame spraying with particles of sprayed material TiNi



Fig. 2 ACCURA coordinate measuring machine

3 Analysis of Simulation Results and Experimental Data

To conduct research with the subsequent analysis of the effectiveness of the proposed technology, tests were carried out on special cylindrical samples, some of which were made of steel alloy (for example, St45), and the other part from non-ferrous metal alloys (for example, aluminum) with a diameter of 10 mm, on which the method high-speed flame spraying high-speed flame spraying in a protective argon atmosphere TiNi coating 0.8 mm thick. Then this sample was subjected to adhesion tests, which was determined by the shear method. Residual stresses were determined by the Sachs and Davidenkov methods, which are the determination of residual deformations by measuring the geometric dimensions of the sample as a result of sequential layer-by-layer removal of a part of the material with simultaneous tracking of changes in geometric dimensions that are directly related to residual stresses. The use of ferrous and non-ferrous alloys as samples made it possible to determine the possibility of using this technology for a different class of metals and their alloys.

Obtaining a coating on steel samples according to the proposed method was carried out according to the following technological sequence:

- preparation of samples before coating, representing technological methods for degreasing the surface with alcohol, followed by etching in a 5% hydrochloric acid solution, which together removes oil and grease stains from the surface of the product, as well as an oxide film, which guarantees the density of contact of the sprayed metal powder particles with the surface of the substrate, and also provides the chemical component of adhesion;
- after that, the surface of the part was coated by high-speed flame spraying in a protective argon atmosphere, together with the immediately preceding treatment of the part surface using an electric arc arising between two tungsten electrodes and passing over the part surface at a direct current of direct polarity with a force of 30–40 A, with a voltage of 11–15 V at a speed of movement of a high-speed spray gun of a spraying device with a distance between the arc and the gas jet with the sprayed powder material of 2–4 mm.

The process of obtaining a coating on aluminum samples according to the proposed method was obtained in the following sequence:

- preparation of samples before coating, representing technological methods for degreasing the surface with alcohol, followed by etching in a 5% hydrochloric acid solution, which together removes oil and grease stains from the surface of the product, as well as an oxide film, which guarantees the density of contact of the sprayed metal powder particles with the surface of the substrate, and also provides the chemical component of adhesion;
- after which the surface of the part was coated by high-speed flame spraying in a protective argon atmosphere together with the immediately preceding treatment of the part surface using an electric arc arising between two tungsten electrodes and passing over the part surface at an alternating current of 35–45 A, voltage 12–16 V at the speed of movement of the high-speed atomizer of the installation

for spraying at a distance between the arc and the gas jet with the sprayed powder material of 2–4 mm [5].

The use of technology for the transfer of nanoparticles by a high-temperature gas flow and their deposition on a substrate together with the immediately preceding treatment of the part surface using non-consumable electrode welding technologies, namely an electric arc arising between two tungsten electrodes passing over the surface of the part at an alternating current of 35–45 A, voltage 12–16 V at a speed of movement of a high-speed spray gun for a spraying device with a distance between the arc and a gas jet with a sprayed powder material of 2–4 mm, they can improve the physical and mechanical properties of the composite coating by increasing its adhesion strength and reducing porosity. This is due to the fact that the electric arc heats the surface of a part made of non-ferrous metals to a temperature of 0.9–1T_m, which is the melting point, and the sprayed powder material, heated also to a temperature of 0.9–1T_m, the melting temperature, collides with a surface that has no solid, and liquid phase of the state, which ensures fusion of the material of the part with the applied powder material, which significantly increases the adhesive strength. At the same time, when applying the second and subsequent layers, the transfer of nanoparticles by a high-temperature gas flow and their deposition onto the already formed coating layer occurs under a similar effect of an electric arc on the surface of the coated part, as a result of which the sprayed layer and the sprayed powder form a homogeneous structure, thereby providing, a significant reduction in the porosity of the composite coating and an increase in cohesive strength.

At the same time, the alternation of alternating current of direct and reverse polarity, due to reverse polarity, ensures the destruction of oxide films formed on the surface of non-ferrous metal parts and cleaning the surface of the part, and due to direct polarity, the surface of the part melts, with the formation of a narrow deep bath with molten metal on the surface of the part directly in front of the high-temperature gas flow with nanoparticles.

In this case, as a result of a short-term effect of an electric arc on the surface of a part, the surface of parts made of non-ferrous metals is heated, and then it is slowly cooled, due to a high-temperature gas flow with a sprayed powder material, which avoids the occurrence of significant residual stresses and possible formation of cavities and cracks, both in the surface layer of a non-ferrous metal part along the coating-substrate interface, and throughout the entire thickness of the coating.

The coating obtained in this way has high cohesive strength and low porosity, as well as high adhesion strength between the coating and the part made of non-ferrous metals and between the coating layers, in the case of a multilayer coating, which increases the physicomechanical and, as a consequence, performance characteristics of the coated part. The proposed technological modes make it possible to avoid distortion of the part during the transfer of nanoparticles by a high-temperature gas flow and their deposition on the surface of the part, the wall thickness of which does not exceed 3 mm.

Table 1 Parameters of spraying a coating on a part made of non-ferrous materials using the example of an aluminum alloy using the proposed technology

Example No.	Current strength, A	Voltage, V	Distance between arc and high-temperature gas flow with sprayed powder material, mm
1	35	12	2
2	40	14	3
3	45	16	4

Table 2 Test results of samples from non-ferrous materials on the example of an aluminum alloy with a coating obtained by the proposed technology

Example No.	Relative porosity, %	Adhesion strength, MPa	Residual stresses, MPa	
			Coating	Details
1	1.3	120–127	47	–50
2	0.9	130–135	38	–46
3	0.7	135–145	46	–53

The processing parameters of coated samples according to the proposed technology for non-ferrous metal parts using the example of an aluminum alloy are presented in Table 1.

The test results of the sample made using the proposed technology are presented in Table 2.

A feature of the difference in obtaining a coating according to the proposed technology for parts made of steel is reflected in the technological modes of welding with a non-consumable electrode passing over the surface of the part at a direct current of direct polarity with a force of 30–60 A, voltage of 11–15 V arc and gas jet with sprayed powder material 2–4 mm [6].

Direct current of direct polarity ensures that the current is constantly maintained at the same level, which ensures uniform melting of the surface of the steel part in depth and width, with the formation of a narrow deep pool of molten metal on the surface of the steel part immediately before the high-temperature gas flow with nanoparticles.

In this case, as a result of short-term exposure to an electric arc, the surface of the steel part is heated, and then it is slowly cooled due to the high-temperature gas flow with the sprayed powder material, which makes it possible to avoid the occurrence of significant residual stresses and the possible formation of cavities and cracks, as in the surface layer of a steel parts along the coating-substrate interface, and throughout the entire thickness of the coating.

The coating obtained in this way has high cohesive strength and low porosity, as well as high adhesion strength between the coating and the steel part and between the layers of the coating, in the case of a multilayer coating, which increases the physic mechanical and, as a consequence, operational characteristics of the coated steel part. The proposed technological modes also allow avoiding warping of the

Table 3 Parameters of spraying a coating on a part of steel alloys using the example of Steel 45 using the proposed technology

Example No.	Current strength, A	Voltage, V	Distance between arc and high-temperature gas flow with sprayed powder material
1	30	11	2
2	45	13	3
3	60	15	4

Table 4 Test results of samples from non-ferrous materials on the example of an aluminum alloy with a coating obtained by the proposed technology

Example No.	Relative porosity, %	Adhesion strength, MPa	Residual stresses, MPa	
			Coating	Details
1	1.3	100–115	37	–40
2	0.9	120–125	48	–56
3	0.7	120–130	55	–65

steel part during the transfer of nanoparticles by a high-temperature gas flow and their deposition on the surface of the steel part, the wall thickness of which does not exceed 3 mm.

The processing parameters of coated specimens according to the proposed technology for parts made of steel alloys using the example of Steel 45 are presented in Table 3.

The test results of the sample made using the proposed technology are presented in Table 4.

Figure 3 below shows the substrate-coating interface.

It can be seen from Fig. 1 that the coating obtained by high-speed gas-flame spraying has a clear coating-substrate interface, in contrast to the coating obtained by the proposed method, and as a result of calculations of residual stresses, it was found that, in contrast to the existing technologies for increasing the adhesion of the coating-substrate, the proposed technological methods allow avoiding significant residual stresses, which makes it possible to use it for thin-walled products, as well as the zone of abrupt change in residual stresses with a change in sign (tensile/compressive), mixed into the depth of the part and did not coincide with the substrate-coating interface.

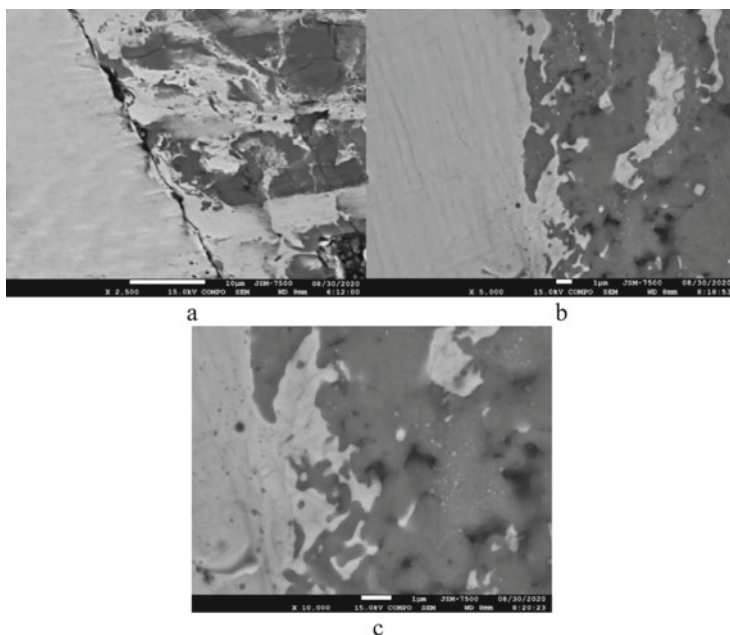


Fig. 3 Microstructure of the substrate (CT45) - coating (TiNi) interface: a - obtained as a result of high-speed flame spraying $\times 2500$; b - $\times 5000$ and c - $\times 10,000$ obtained after spraying using the proposed technology

4 Conclusion

The proposed method for increasing the strength of a coated part provides an increase in the physical and mechanical properties of the part by increasing the adhesion strength between the coating and the substrate, increasing the cohesive strength of the coating, reducing the magnitude of residual stresses, as well as reducing the porosity of the coating, and can also be applied to increase adhesion between the coating layers in the case of obtaining a layered composite coating. In this case, the resulting residual stresses in the coating can be used as compensating for the resulting stresses as a result of thermoelastic phase transformation of a material with a shape memory effect [7], and the zone of their abrupt change with a sign change (tensile/compressive) is mixed into the depth of the part and does not coincide with substrate-coating interface. Thus, the proposed technology will expand the field of application of metallization by thermal spraying methods and can be applied to its various types 5.

Acknowledgements This work was supported by a grant from the President of the Russian Federation (contract No. SP-399.2019.1)

References

1. Baldaev LKh, Borisov VN, Vakhalin VA et al (2007) Thermal spraying. Market DS
2. Kadyrmetov AM (2011) Technological capabilities and problematic issues of plasma deposition and hardening of coatings with modulation of electrical parameters. Sci J “Vestnik VSTU 8:79–82
3. Bagatov VP, Parshev SN, YuPN (2007) The formation of structure and properties of surface coastline products of Electromechanical processing. Fundam Prob Mod Mater Sci 4:36–40
4. Birger IA (1963) Residual stresses. OOO “Publishing house of mechanical engineering”
5. Balaev EYu, Eliseev VN, Patent No. 2710246, IPC C23C 4/134 (2016.01), C23C 4/02 (2006.01), B82Y 40/00, January 2011
6. Likhachev A (1998) Materials with shape memory effect: Ref. Edition. Ed. VA Likhachev. T. 4. - SPb: Publishing house of NIIH SPbGU
7. Lyasnikov VN, Lyasnikova AV, Protasova NV, Pivovarov AV, Antonov IN (2012) Gas-plasma formation of composite coatings based on hydroxyapatite and titanium powders of composite materials structures. 2:30–34
8. Lyasnikova AV, Protasova NV, Dudareva OA (2012) Improving the quality of plasmon dust coatings for medical equipment. 4:4–7

Study of the Compressive Strength of Concrete with Polypropylene Microfiber



Sergey Antonov , Marina Gravit , Evgeny Meshalkin , Ivan Dmitriev , and Alexey Shchukin 

Abstract In this article, the authors conducted experiments to compare the strength of concrete without additives, at which explosive fracture is possible, with concrete containing polypropylene microfiber. The composition of the concrete mixture with polypropylene microfiber and compensating additives can correspond to the same design class for compressive strength as a regular concrete (at least 30 MPa). Analysis and comparison of the studied samples showed that coefficients of working in high temperature conditions of concretes with polypropylene microfiber and compensating additives exceeded the coefficients recommended by requirements for regular concrete. These tests prove that polypropylene microfiber can be used to prevent brittle failure without reducing the strength of the product.

Keywords Polypropylene microfiber · Concrete structure · Structural strength · Axial compression · Concrete mixture · Residual strength

1 Introduction

The possibility of increasing the porosity of concrete to prevent the process of explosive fracture by adding polypropylene microfiber to the matrix was proposed and justified by such Russian scientists as Roitman V.M., Golovanov V.I., Meshalkin E.A. The use of polypropylene microfiber was called theoretically a very effective way to ensure the serviceability of concrete structure in fire conditions, including ensuring its fire safety [1–8].

The fiber, without increasing the fire resistance of the structure itself, allows the concrete to “work out” in a fire the way the designer has intended: the thickness

S. Antonov

Academy of the State Fire Service of Emercom of Russia, Boris Galushkin str., 4, Moscow, Russia

M. Gravit · I. Dmitriev · A. Shchukin (✉)

Peter the Great St. Petersburg Polytechnic University, 29 Politechnicheskaya St., 195251 St. Petersburg, Russia

E. Meshalkin

LLC “Gefest Group”, Malenkovskaya str., 3, Moscow, Russia

of the protective layer remains constant, during the heating process, because of the fiber additives micro pores are formed to create a pathway for water to evaporate from the concrete. Since the protective layer of concrete remains intact for a certain period, the reinforcement frame is not exposed to excessive heating and structure can operate within its design fire-resistance limit [9–13].

The main disadvantages of using polypropylene microfiber are related to the strength and thermal characteristics of concrete [14–21]. The analysis of the experimental data given in the works of V.I. Golovanov and the thesis of N.S. Novikov shows that there is a decrease in axial compressive strength for concrete with polypropylene microfiber compared to the initial composition.

The goal of this article is to investigate the compressive strength of concrete with polypropylene microfiber as a factor used in fire resistance calculations.

The following tasks were set in order to achieve the goal:

1. Check compliance with the design requirements for compression of the concrete mixture with polypropylene microfiber and compensating additives on the basis of experimental data (test No 1);
2. Determine the residual compressive strength on the basis of experimental data (test No 2);
3. Analysis and comparison of the obtained results.

2 Methods

The “Concrete mix BST” was investigated according to Russian State Standard GOST 7473–2010 “Concrete mixtures. Technical conditions”. Structural concrete with design strength at least 30 MPa, cone slump 16–20 cm. Application of fire protection fiber type “PROZASK IGS” (polypropylene monofilament fibrillated microfiber, in bundles, treated, roughened, multiple of elongated, diameter less than 20 μm),

Concrete mix composition:

- Cement CEM I 42.5B. Guaranteed grade 42.5 means the amount of load that one 1 cm^2 of cement stone can withstand after curing. The normal density of the cement dough is 26.0%,
- Sand was used with a particle size modulus of 2.25 and a true density of 2.52 g/cm^3 ;
- Gravel crushed stone. Bulk density - 1.57 g/cm^3 . True density of 2.52 g/cm^3 . Mark of crushability 800. Frost-resistance grade F200. Fraction of 5–10 mm;
- Superplasticizing additive for concrete “Reodin 305” was used pH = 9,8, density 1,12 kg/dm^3 according to Russian State Standard TU 20.59.59-003-26,025,492-2018 «Additives with antifreeze effect for the production of concrete and mortars in the winter period series “Optima”»;
- In the composition of concrete was introduced fireproof microfiber “PROZASK IGS” from polypropylene TU 2272-004-87,550,640, fiber diameter 17–18 mm, fiber length 6 mm, density of 0.91 g/cm^3 .

Test No 1. Concrete cubs made from a concrete mixture with predetermined characteristics (including polypropylene microfiber and compensating additives) are tested to check compliance with the design requirements for compression,

Test No 2. Determination of residual compressive strength values of concrete with PROZASK IGS fiber after exposure to temperatures of 200 °C and 500 °C according to the methodology according to Russian State Standard GOST 20910-2019 “Heat-resistant concretes. Technical conditions”, including the determination of the compressive strength of control specimens at design age.

Equipment:

- VLG-3000/0,1MG4.01 laboratory hydrostatic electronic scales 5-3000 g measurement range, incremental 0.1 g, accuracy class high II;
- Normal curing chamber CST, maintained conditions: temperature (20 ± 2) °C, relative humidity $(95 \pm 5)\%$;
- Compression testing machine MS-2000, measuring range 0–2000 kN, error $\pm 1\%$
- Muffle electric furnace EKPS-10, adjustable temperature range 200–1300 °C;

The test methodology consisted in the preparation of a series of concrete samples and testing the compressive strength at design age and residual strength after heating. The tests were performed in accordance with Russian State Standard GOST 20910-2019 “Heat-resistant concretes. Technical conditions”.

The compressive strength of the concrete was determined after heating to the maximum permissible application temperature to calculate residual strength. Heating of the samples was performed according to the procedure for determining the values of residual compressive strength of concrete according to Russian State Standard GOST 20910-2019 “Heat-resistant concretes. Technical conditions” and Russian State Standard GOST 10180-2012 “Concretes. Methods of determination of strength by control samples” (Fig. 1).

Heating was subjected to samples of concrete after normal-moist hardening. It was carried out in an electric chamber furnace at a speed of 150 °C/h, with a holding time at the desired temperature of 4 h and cooling together with the oven to room temperature.

Concrete specimens of the control series were tested for compressive strength, having been previously brought to dry state by 7 days of ageing in a desiccator at 50 °C.

3 Results and Discussion

3.1 Test No 1

The results of control tests performed by the manufacturer of concrete mixture “BST concrete mix” are shown in Table 1.

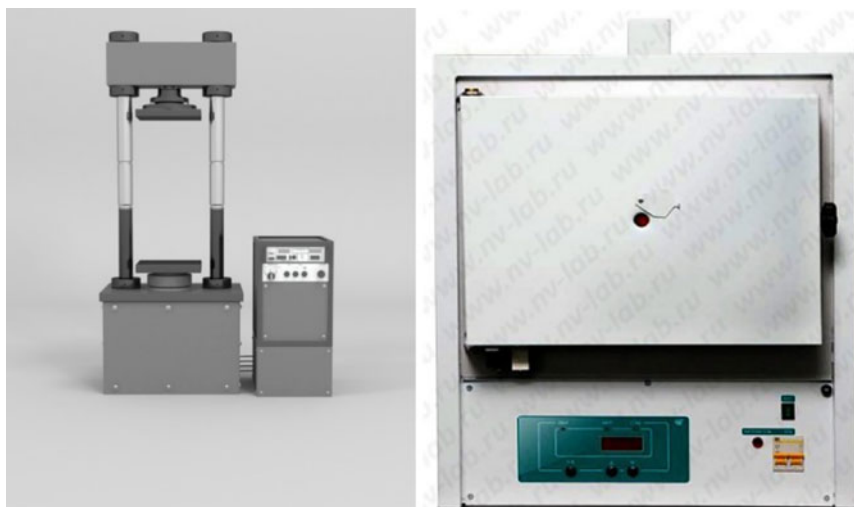


Fig. 1 MS-2000 press (left), Source: https://ekb.pulscen.ru/prod-ucts/press_ms_2000_ooo_rst_sim_160838510, EKPS-10 muffle electric furnace, adjustable temperature range 200–1300 °C (right), Source: https://www.nv-lab.ru/cata-log_info.php?ID=2793&Full=1

Table 1 Strength for cubes of concrete B25

№	Date of manufacture	Test Date	Sample dimensions, mm	Sample density, g/l	Average density of the sample, g/cm ³	Compressive strength, MPa	
						Sample	Average (with coef. 0.95)
1	2.05.2020	04.05.20	100 × 100 × 100	2358	2,358	19,7	18,3
	2.05.2020	04.05.20	100 × 100 × 100	2354	2,354	18,9	
	2.05.2020	04.05.20	100 × 100 × 100	2352	2,352	19,3	
2	2.05.2020	08.05.20	100 × 100 × 100	2362	2,362	25,9	24,4
	2.05.2020	08.05.20	100 × 100 × 100	2355	2,355	25,7	
	2.05.2020	08.05.20	100 × 100 × 100	2353	2,353	25,5	
3	2.05.2020	30.05.20	100 × 100 × 100	2357	2,357	34,5	32,7
	2.05.2020	30.05.20	100 × 100 × 100	2360	2,360	34,6	
	2.05.2020	30.05.20	100 × 100 × 100	2359	2,359	34,5	

- On the 3rd day after the samples were made, the average density of the samples was 2.354 g/cm³, and the compressive strength was at least 18.3 MPa,
- On the 7th day after the samples were made, the average density of the samples was 2.357 g/cm³, and the compressive strength was at least 24.4 MPa
- On 28th day after the samples were made, the average density of the samples was 2.359 g/cm³ and the compressive strength was at least 32.7 MPa.

It is concluded that this composition of the concrete mixture meets the requirements for compressive strength—not less than 30 MPa.

Practically similar results were obtained during the control tests of the concrete samples with polypropylene microfiber and compensating additives. The tests were carried out at the Research, Design and Technological Institute “VNIIZHLEZOBETON”, the results of which are presented in the test report № 03/11.2.1/6/2021-1 NII PKTI “Vniyizhelezobeton” (Table 2).

According to the results of test no. 1, it was concluded that in accordance with Russian State Standard GOST 7473-2010 “Concrete mixes. Technical Conditions” and Russian State Standard GOST 26633-2015 “Concretes heavy and fine-grained. Technical Conditions” the composition of the concrete mix (with polypropylene microfibre and compensating additives) corresponds to the design class of concrete for compressive strength of at least 30 MPa and thus solves the problem of compensating the axial compressive strength of concrete.

3.2 Test No 2

The tests were carried out at the Research, Design and Technological Institute “VNIIZHLEZOBETON”, the results of which are presented in the test report № 03/11.2.1/6/2021-2 NII PKTI “Vniyizhelezobeton”. As a result of the tests were obtained (Table 3).

After thermal exposure at up to 200 °C and 500 °C cracks, chips, peeling on the samples were absent. Residual strength of concrete after conditioning at 200 °C was 105%, after conditioning at 500 °C was 82%.

When calculating fire resistance and refractoriness by means of a deformation model and computer programs, the change of concrete conditions coefficient γ_{bt} over the whole temperature range of the concrete thickness due to sectional heating has to be taken into account. In this case the calculation is carried out using the actual geometric cross-section of the concrete. The values of the coefficients of working conditions in compression γ_{bt} of concretes are determined experimentally, by testing samples-cubes at short-term exposure to temperatures. For heavy concretes on silicate and carbonate aggregates as well as for structural expanded clay aggregate concrete the coefficients of working conditions in compression γ_{bt} are given in Table 3 depending on the temperature of concrete heating.

The figure obtained the tests (82%) is actually the coefficient of concrete working conditions γ_{bt} at +500 °C. It can be used in the calculation of fire protection and

Table 2 Strength for concrete cubes with polypropylene microfiber and compensating additives

Test object, labeling	Heat treatment	Sample weight, gr		Weight loss, %	Density, kg/m ³	Breaking load, kN	Cross-sectional area, cm ²	Compressive strength, MPa	Average value, MPa
		Before	After						
Concrete, sample 1	+50 °C (7 days)	2189	2138	2.33	2153	344	101.6	32.2	32.9
Concrete, sample 2	+50 °C (7 days)	2186	2133	2.42	2154	350	101.2	32.9	
Concrete, sample 3	+50 °C (7 days)	2206	2153	2.40	2199	348	100.1	33.0	

Table 3 Concrete Compressive Strength for Concrete with Microfiber Addition

No	Test object, labeling	Heat treatment conditions	Sample weight, gr		Weight loss, %	Density, kg/m ³	Breaking load, kN	Cross-sectional area, cm ²	Compressive strength, MPa	Average value, MPa	Residual strength, %
			Before	After							
1	Concrete, sample 1	+50 °C (7 days)	2189	2138	2.33	2153	344	101.6	32.2	32,9	—
2	Concrete, sample 2	+50 °C (7 days)	2186	2133	2.42	2154	350	101.2	32.9		
3	Concrete, sample 3	+50 °C (7 days)	2206	2153	2.40	2199	348	100.1	33.0		
4	Concrete, sample 4	+200 °C (4 h)	2154	2051	4.78	2143	365	100.5	34.5	34,6	105
5	Concrete, sample 5	+200 °C (4 h)	2155	2049	4.92	2140	367	100.3	34.8		
6	Concrete, sample 6	+500 °C (4 h)	2170	2031	6.41	2144	275	100.2	26.1	26,9	82
7	Concrete, sample 7	+500 °C (4 h)	2174	2041	6.12	2150	287	101.0	27.0		
8	Concrete, sample 8	+500 °C (4 h)	2171	2034	6.31	2154	292	100.9	27.5		

Table 4 Working conditions factor for concrete

Type of concrete	Value of coefficients γ_{bt} for concrete at temperature, °C		
	+20	+200	+500
Heavy, silicate aggregate concrete	1.0	0.98	0.80
	1.0	0.95	0.70

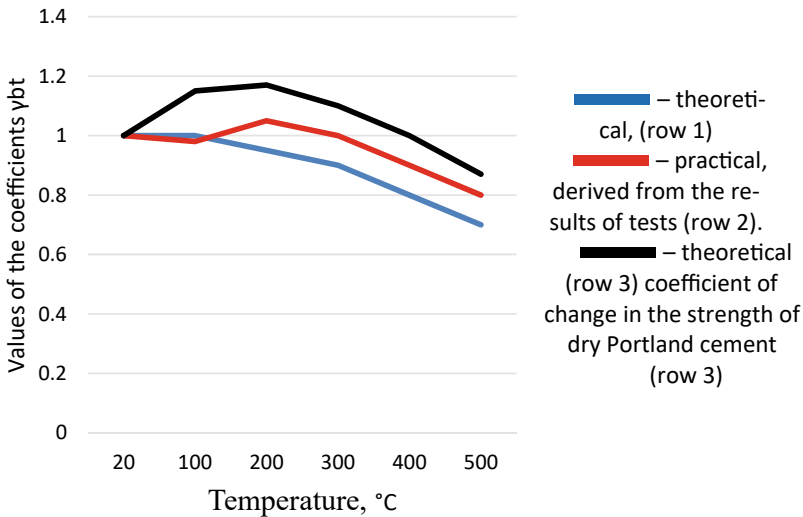


Fig. 2 Coefficients of compressive concrete working conditions

exceeds the calculated figure γ_{bt} at +500 °C (Table 4), which indicates that the application of calculation methods for designing fire protection measures in case of using fiber reinforced concrete with polypropylene microfiber.

The values of γ_{bt} above the line are given for concrete in the heated state and are used in the calculation of fire resistance and below the line for the concrete after heating in the cooled down state. Figure 2 compares the coefficients of compressive working conditions γ_{bt} , two theoretical and one obtained during the tests (row 2). The figure shows the coefficients of compressive concrete working conditions:

4 Conclusions

Analysis and comparison of the studied indicators (Fig. 2) showed that obtained coefficients of working conditions of concretes with polypropylene microfiber and compensating additives even exceeded the coefficients recommended by Russian State Standard SP 468.1325800.2019 “Concrete and reinforced concrete structures. Rules for ensuring fire resistance and fire safety”. It should also be noted that

this normative document does not present in its tables any data reflecting such a phenomenon as an increase in the compressive work factor of concretes occurring at temperatures around 200 °C.

Initially, when the Portland cement stone heats up to 100–150 °C, the strength may decrease slightly. The subsequent increase in strength can be seen as a result of a process similar to the autoclave hardening of concrete. Given that the group of autoclave hardening binders (at saturated steam pressure and temperature of 170–200 °C) include mixtures of fine sand with Portland cement (which can also harden under normal conditions), we can assume that they give a higher increase in strength in autoclave curing mode. When heated to 200 °C, there is a chemical bonding of calcium hydroxide with silica silica of quartz sand. As a result of this compound is formed an additional amount of calcium hydrosilicates, which leads to some increase in the strength of concrete.

When heating the same concrete above 200 °C, there are oppositely directed deformations of the binder and expanding aggregate, which begins to reduce the strength of concrete. It was also noted that when testing the compressive strength of control specimens there is no detachment of broken parts of the concrete (not shooting off), which is not characteristic of traditional heavy concrete.

References

1. Alan E (2006) Compressive strength of concrete with polypropylene fibre additions. <https://doi.org/10.1108/02630800610666673>
2. Dahesh AZ, Othman FM, Abdullah-Hamead AA (2010) Use of polypropylene microfibers to improve mass concrete by controlling the cracksealing mechanism. <https://doi.org/10.1088/1757-899X/871/1/012010>
3. Mashrei MA, Ali AS., Alaa MM (2018) Effects of polypropylene fibers on compressive and flexural strength of concrete material International Journal of Civil Engineering and Technology (IJCIET). <http://www.iaeme.com/ijciet/issues.asp?JType=IJCIET&VType=9&IType=11>. Accessed 21 March 2021
4. Pu Y et al (2018) Preparation of polypropylene micro and nanofibers by electrostatic-assisted melt blown and their application. *Polymers* 10(9):959. <https://doi.org/10.3390/polym10090959>
5. Smirnova OM, Shubin AA, Potseshkovskaya IV (2017) Strength and deformability properties of polyolefin macrofibers reinforced concrete. *Int J Appl Eng Res* 12: 9397–9404. Research India Publications ISSN 0973-4562
6. Gravit M, Golub E (2018) Increase of fire resistance of reinforced concrete structures with polypropylene microfiber MATEC. *Web Conf.* 245:03005. <https://doi.org/10.1051/mateconf/201824503005>
7. Manica G, Bolina F, Tutikian BF (2019) Analysis of the resistance to fire of solid concrete boards with polypropylene microfibers and long curing time. *Revista de la construcción* 18(3): 595–602. <https://doi.org/10.7764/RDLC.18.3.595>
8. Dudin MO, Vatin NI, Barabanshchikov YuG (2015) Modeling a set of concrete strength in the program ELCUT at warming of monolithic structures by wire. *Mag Civ Eng* 54(2):33–45. <https://doi.org/10.5862/MCE.54.4>
9. Vatin NI, Nemova DV, Rymkevich PP, Gorshkov AS (2012) Influence of building envelope thermal protection on heat loss value in the building. *Mag Civ Eng* 34(8):4–14. <https://doi.org/10.5862/MCE.34.1>

10. Farediwala MA (2015) Improving the mechanical properties of conventional concrete by using fiber. *Int J Adv Eng Res Stud*
11. Zhang P, Li QF (2013) Effect of polypropylene fiber on durability of concrete composite containing fly ash and silica fume. *Compos Part B Eng* 45(1): 1587–1594
12. Khan S, Khan RA, Khan AR, Islam M, Nayal S (2015) Mechanical properties of polypropylene fibre reinforced concrete for M 25 & M 30 mixes: a comparative study. *Int J Sci Eng Appl Sci (IJSEAS)*
13. Singh AK, Jain A, Singh D (2013) Evaluation of mechanical properties for polypropylene and steel fibre reinforced concrete. *Int. J Eng Res Technol (IJERT)* 2(4): 1507–1517
14. Selvi MT, Thandavamoorthy, TS (2013) Studies on the properties of steel and polypropylene fibre reinforced concrete without any admixture. *Int J Eng Innov Technol (IJEIT)* 3(1)
15. Mandava N, Murali K, Reddy SM, Reddy MN (2018) Investigation of reinforced concrete beams by incorporating polypropylene fibre reinforced polymer composites. *Int J Civ Eng Technol (IJCIET)*
16. Murahari K, Rao RM (2013) Effects of Polypropylene fibres on the strength properties of fly ash-based concrete. *Int J Eng Sci Invent* 2(5):13–19
17. Bagherzadeh R, Pakravan H, Sadeghi A-H, Latifi M, Merati AA (2012) An investigation on adding polypropylene fibers to reinforce lightweight cement composites. *J Eng Fibers Fabr* 7(4):13–19
18. Hsie M, Tu C, Song PS (2008) Mechanical properties of polypropylene hybrid fibre reinforced concrete. *Mater Sci Eng* 494:153
19. Gorshkov AS, Vatin NI (2013) Properties of the wall structures made of autoclaved cellular concrete products on the polyurethane foam adhesive. *Mag Civ Eng* 40(5): 5–19. (rus). <https://doi.org/10.5862/MCE.40.1>
20. Sychova AM, Svatovskaya LB, Starchukov DS, Soloviova VY, Gravit MV (2018) *Mag Civ Eng* 80(4): 3–14
21. Nedviga E, Beresneva N, Gravit M, Blagodatskaya A (2018) *Adv Intell Syst* 692: 739–749

Methodology for Assessing the Response Parameters of Multi-storey Buildings with Non-linear Dynamic Vibration Dampers in Case of Seismic Impacts



Galina Bogdanova and Andrey Benin

Abstract This paper proposes a methodology for estimating the parameters of a multi-storey building with non-linear dynamic vibration dampers under seismic action. A calculation-theoretical efficiency analysis of the dynamic vibration damper (DVD) in buildings was performed to identify the optimal combinations of the main parameters of the dynamic vibration damper under the impacts of unsteady character with a different spectral-frequency composition. The efficiency criteria for the use of DVD in multi-storey buildings have been determined. The scope of vibration dampers depending on the dynamic building features and spectral-frequency composition of the seismic effect has been established. The impact of the stiffness degradation of the bonds between the building floors under seismic action on the performance of the DVD has been assessed. Recommendations for the main dimensions of building vibration dampers have been developed.

Keywords Increasing seismic resistance of buildings · Non-linear vibration dampener · Optimal dampener tuning · Generalized acceleration reduction factor

1 Introduction

The dynamics dampening theory of mechanical vibration is widely used in several applications to justify optimal combinations of settings to reduce the dynamic forces on various objects. The basic provisions of this theory in the linear formulation are quite well developed and tested in the practice of mechanical engineering, aviation, shipbuilding and other fields. There are known examples of the implementation of such devices in building practice [1–6] including applications for the reduction of dynamic loads on building structures, bridge abutments [7, 8] and other structures under non-stationary impacts of seismic nature, explosions and other man-made and natural impacts. Dynamic dampers in various designs are increasingly being used in high-rise buildings [9–13]. Probably the best known, both in terms of design

G. Bogdanova · A. Benin (✉)
Emperor Alexander I St. Petersburg State Transport University,
9 Moskovskiy ave., St. Petersburg 190031, Russian Federation
e-mail: nich@pgups.ru

and efficiency, is the current vibration damper represented by a huge ball-shaped counterweight installed in a 500-m tower in Taipei, China. This ball is 5.5 m in diameter and weighs almost 730 tons (Fig. 1). The purpose of this balloon is to dampen the vibration of the building caused by strong winds.

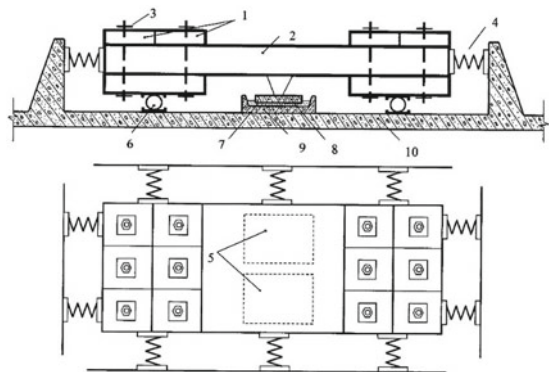
Nevertheless, such pendulum dampers are impractical and uneconomical to install on buildings of relatively low height. At the same time the seismic resistance of 9–25 storey buildings can be increased by installing non-linear dynamic vibration dampers in the form of reinforced concrete slabs. Figure 2 shows the author's design of a non-linear Dynamic Damper (Tuned Mass Dampers—TMD). The damper operating principle is as follows. When horizontal inertial forces occur due to seismic forces the damper is instantly activated by ball bearings and springs attached to the structure and the concrete damper slab. Increased vibration damping is ensured by the presence of dry friction dampers in whose considerable friction force of the concrete damper slab on the sand is realised.

The main parameters affecting the setting of the dynamic damper are its mass and natural frequency. The initial optimum tuning of the damper is carried out at the two lowest partial frequencies of the structure. They correspond to the longitudinal and transverse forms of vibration by selecting the damper weight and spring stiffness positioned at the mutually orthogonal sides of the construction.

Fig. 1 A pendulum vibration damper installed in a tower in Taipei (Photo from <https://trinixy.ru/119963-uni-kalnoe-ustroystvo-pozvolyyay-uschee-minimizirovat-raskac-hku-neboskrebov-11-foto-2-video.html>, accessed 20.04.2021)



Fig. 2 Dynamic vibration damper (patent RU14593U1): 1—removable concrete blocks; 2—concrete slab; 3—connecting elements (studs); 4—springs; 5—dry friction dampers; 6—supporting elements (rollers); 7—sand; 8—concrete slab dampers; 9—pallet; 10—building slab



However, when a structure is used for a long time as a result of local damage its stiffness decreases and, as a consequence, the natural vibration period of the structure increases resulting in detuning of the damper settings from the optimal ones. This can lead to a deterioration in the performance of the entire structure under subsequent seismic loads. The dependence of changes in the stiffness of various constructions over time based on the damage accumulation theory and empirical data is known. Therefore, by changing the damper mass, by removing individual concrete blocks and spring stiffness it is possible to reconfigure the damper to the new stiffness parameters of the construction. The dampener has been simplified by the use of dampers (dry friction dampers that do not require special devices, their frictional properties do not change during operation. The proposed dampers are cost-effective as they are made from materials commonly used in construction—concrete and sand. For the normal operation of the dry friction dampers it is only necessary to regularly check the sand availability in the pallets.

This paper provides a methodology for estimating the parameters of a multi-storey building with non-linear dynamic vibration dampers under seismic effects. The main aims and objectives were:

1. Performance of computational-theoretical analysis of the effectiveness of Dynamic Vibration Dampener (DVD) in high-rise buildings in order to identify optimal combinations of the main parameters of DVD under the impacts of non-stationary nature of various spectral-frequency composition; development of appropriate software;
2. Determination of performance criteria for DVD use in multi-storey buildings;
3. Establishment of the application area and performance assessment of DVD depending on the dynamic building performance and spectral-frequency composition of the seismic effect;
4. Evaluation of the first estimate of the degradation impact of the bond stiffness between the building storeys during a seismic impact on the performance of the DVD.
5. Recommendations for the selection of the main parameters of the DVD
6. The research was carried out by means of mathematical modelling. The calculation mathematical models used were the design diagrams of a multi-storey building in the form of a chain system with concentrated parameters. The degree of freedom corresponded to the number of storeys in the building. Such models take into account only the main dynamic characteristics of the real object while allowing to determine quite easily, in a first approximation, the areas of reasonable combinations of DVD parameters and the efficiency level in the dimension space of calculation pattern parameters.

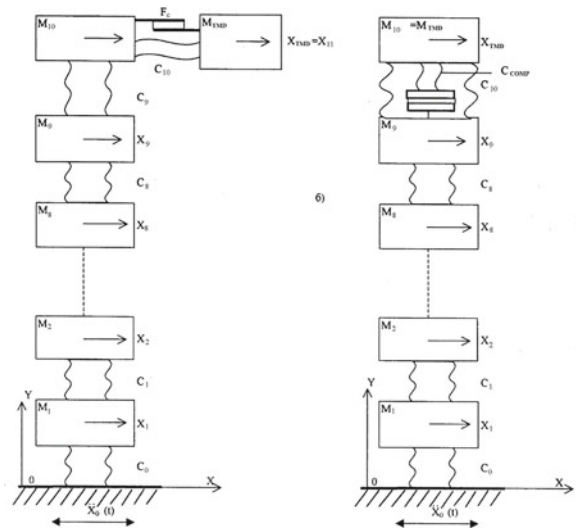
2 Patterns and Calculation Methods

The estimated patterns of 9-storey buildings shown in Fig. 3 a, b are considered. They represent a weightless rod with concentrated masses M_i . Each consisting of the slab mass between the storeys and half the masses of load-bearing walls and panels adjoining the storey.

The mass of the ground floor M_1 includes half the mass of the basement room, the mass of the tenth floor M_{10} includes the mass of the attic room. The mass linkages are assumed to be linear-elastic, with stiffness coefficients C_i , the damping in the building structures modelling the links between the storeys is taken into account according to the Voigt-Zeitlin hypothesis as equivalent linear-viscous friction. Two designs are considered for the dynamic dampener. In the first variant (Fig. 3, a) the DVD is made as the above described reinforced concrete mass (Fig. 2) installed at attic level or directly on the building roof. The springs acting as an elastic suspension have a stiffness factor of C_{10} . The second variant (Fig. 3, b) uses the mass of the attic building itself as a damper (M_{10} , mass setting the stiffness factor of the connection between the damper and the main part of the building C_{10} much lower than the stiffness factor of the connections between the storeys). This stiffness is reduced by selecting a special design of embedded elements at the panel fixing points at the floor level between the top floor and the attic of the building. In order to limit the large movements of the damper during high intensity seismic impacts an additional dissipation element made as a friction dampener with a deformation diagram (hysteresis characteristic) is introduced into the design of the DVD.

One of the options for such a damper could be a construction consisting of two reinforced concrete slabs with a layer of loose material pressed between them. The

Fig. 3 Settlement charts of a building with dynamic dampers: (a) DVD in the form of a separate element to be installed at the level of the slab or roof level of the building; b) DVD using the mass of the attic room



construction has fairly stable characteristics over time, easy and reliable operation and the possibility of adjusting the intensity of friction forces.

A diagram of the resistance force F_c developed in a damper with a hysteresis characteristic can be represented as

$$F_c = \begin{cases} -F[(X - XI) \cdot \zeta_{ld}] & \text{loading } c,lim \\ -F[(X_{max} - O_{ld}) \cdot \zeta_{unld}] & \text{unloading } (X_{max} - O, \text{ unloading}) \end{cases}_{c,lim} \quad (1)$$

where $F_{\frac{\pi}{2}c,lim}$ —s the limiting resistance force X — is the mutual displacement of the damper plates XI —is the value of the same displacement at the moment of transition from the loading to the unloading stage X_{max} —is the peak value of the same displacement achieved at the previous cycle of loading, ζ_{ld}, ζ_{unld} -, are the parameters determining the steepness of the deformation diagram at the loading and unloading stages respectively. In the case of bulk bed deformation the values of $F_{c,lim}, \zeta_{ld}$ and ζ_{unld} are related by the dependence: $\zeta_{unld} = K_p \cdot F_{ld,c,lim}$ where $K_p \geq 1$ —an empirical coefficient characterising the slope excess of the unloading front versus the slope angle of the tangent to the deformation diagram at the initial point; at $K_p = 1$ these angles are obviously equal.

Equations (1) show that the strain diagram has a different analytical representation under loading and unloading. More than that it has a “memory effect”, i.e. the diagram ordinates depend not only on the current values of coordinate X , but also on all preceding loading cycles determining the starting point of the next loading cycle on the diagram. In order to account for this circumstance relations (1) must be supplemented by appropriate switching conditions (changing the structure of the equations of motion).

The seismic action is specified in the form of a digitised instrumental record of the accelerogram of base motion during an earthquake. The parameters of the dynamic building response were evaluated for three accelerograms of different spectral-frequency composition [14]. The design envelope is rated $I = 9$. The predominant spectral period range of the computational package ranges from 0.1 to 2.6 s; thus, the selected computational accelerogram package covers virtually most of the known seismic impacts in spectral-frequency composition.

The considered settlement model represents in this case a system with 11 degrees of freedom (taking into account the dynamic damper of vibrations according to the first design scheme) and is described by the system of differential equations that it is expedient to present in the form of the first order formula. The system of equations of motion for the model in question is as follows:

$$\frac{dX_i}{dt} = V_i \quad (2)$$

$$\begin{aligned} \frac{dV_i}{dt} = & L_{i,i-1} \cdot X_{i-1} + L_{i,t} \cdot X_i + L_{i,i+1} \cdot X_{i+1} + D_{i,i-1} \cdot V_{i-1} \\ & + D_{i,i} \cdot V_i + D_{i,i+1} \cdot V_{i+1} - \ddot{X}_0(t) \quad (i = 1, 2, 3 \dots 9) \end{aligned} \quad (3)$$

$$\begin{aligned} \frac{dV_i}{dt} = & L_{i,i-1} \cdot X_{i-1} + L_{i,i} \cdot X_i + L_{i,i+1} \cdot X_{i+1} + D_{i,i-1} \cdot V_{i-1} \\ & + D_{i,i} \cdot V_i + D_{i,i+1} \cdot V_{i+1} + f_c - \ddot{X}_0(t) \quad (i = 10) \end{aligned} \tag{4}$$

$$\begin{aligned} \frac{dV_i}{dt} = & L_{i,i-1} \cdot X_{i-1} + L_{i,i} \cdot X_i + L_{i,i+1} \cdot X_{i+1} + D_{i,i-1} \cdot V_{i-1} \\ & + D_{i,i} \cdot V_i + D_{i,i+1} \cdot V_{i+1} - \frac{1}{\beta} f_c - \ddot{X}_0(t) \quad (i = 11) \end{aligned} \tag{5}$$

The following notations are introduced here:

$$\begin{aligned} L_{i,i-1} = \frac{C_{i-1}}{M_i}; L_{i,i} = -\frac{C_{i-1}+C_i}{M_i}; L_{i,i+1} = \frac{C_i}{M_i}; \beta = M_{11}/M_{10}; \\ D_{i,i-1} = \frac{B_{i-1}}{M_i}; D_{i,i} = -\frac{B_{i-1}+B_i}{M_i}; D_{i,i+1} = \frac{B_i}{M_i}; f_c = F_c/M_{10}. \end{aligned} \tag{6}$$

The coefficients $B_{i,i-1}$, $B_{i,i}$, $B_{i,i+1}$ characterising internal friction in the elastic coupling material are determined as a combination of the stiffness matrices and the inertial coefficient matrix (Rayleigh dissipation matrix) according to the relation:

$$|B| = \theta_1 \cdot |C| + \theta_2 \cdot |M| \tag{7}$$

For the second version of the DVD device the system of seismic vibration equations differs from the above only in the maximum value of index i , and in the value of stiffness coefficient C_9 that in this case is a variable value determining the partial frequency i.e. tuning of the damper. In addition for this version the damper mass was assumed constant and equal to the mass of the attic room.

In order to account for the stiffness degradation effect of the inter-storey connections the hypothesis of the stiffness degradation law [15] is adopted which may be represented in the form of a dependence:

$$C_i = C_{0i} \cdot \left[1 - K_{D,i} \cdot \sum_k \Delta_k \right] \tag{8}$$

Where C_i и C_{0i} —are, respectively, current and initial values of stiffness factor, $\Delta_k = X_i - X_{i-1}$ —increment modulus of mutual displacement of adjacent storey masses at k -step of integration of equation system KD, i – coefficient of degradation of bonds between adjacent storeys. Dependence (8) is the simplest; if we assume that the value of the degradation factor is the same for all building storeys (which is quite natural given the regular structure of multi-storey buildings) it can be seen that a single parameter KD is sufficient to account for the degradation phenomenon according to the adopted hypothesis. KD. This fact makes it possible to decide to a certain extent on the assignment of the KD degradation factor based on the results of field observations and surveys of this type of building subjected to seismic effects. In addition, as experience and field observations accumulate to refine this parameter it is possible to predict not only the change in the dynamic performance of a building under

a single seismic action but also to extend this prediction to cases of repeated seismic actions taking into account the accumulation of damage from previous earthquakes.

3 Methodology for Computational and Theoretical Studies

In order to estimate the numerical values of the dynamic response parameters of the computational building model the stepwise principle of finding a solution to the equation system (2–5) known in the literature as the Runge–Kutta method of fourth order was used. This method if certain conditions are met provides the necessary calculation accuracy is easy to algorithmise and allows the impact to be specified as a set of ordinates of an accelerogram digitised at a certain time step. This circumstance is particularly important when considering seismic effects which are generally defined in this way. In addition this method makes it possible to find solutions for non-linear differential equations with rather general requirements for the nature of non-linearities. In particular the presence of ambiguous characteristics, the possibility of changing the structure of the equations depending on the state of the system and stepwise changes in the parameters of the systems under study are allowed. It should also be noted that the computational programmes based on this method are very fast and that it is possible to present solutions in the form of time dependencies of the solutions found.

To determine the natural frequencies and shapes of the computational model in question a program based on the Gaussian method was compiled. This program was also used to estimate the range of possible values for the equivalent stiffness coefficients of the connections between storeys in the simplified calculation models. The geometric structure of modern multi-storey buildings including a large variety of elements (panels, slabs, walls, door and window openings, etc.) makes the calculation of equivalent stiffness coefficients very difficult when moving to a simpler model with a limited number of freedom degrees. Therefore, a technique was used based on comparing the results of in-situ building tests available in the literature regarding the assessment of the natural frequencies of buildings and the subsequent determination of equivalent stiffness coefficients in the computational model under consideration. According to these data for typical panel building structures the period of the fundamental tone is in the range 0.35...0.52 s (lower values correspond to longitudinal vibrations of the building in the symmetry plane parallel to the long side of the building, higher values correspond to transverse vibrations). In addition, several calculations were performed for buildings with a basic tone period of 0.25 and 1.0 s which can be matched to monolithic reinforced concrete buildings and flexible metal-framed buildings, respectively, when assessing the effectiveness of the DVD.

4 Performance Criteria for the Use of DVD for a Discrete Model

Ordinarily, when investigating the effectiveness of a seismic protection tool such as a DVD their effectiveness is assessed by comparing the inertial loads and the stress–strain characteristics of the design model in question before and after the application of such a tool. For systems with multiple degrees of freedom such as the calculation model considered in this study the same approach is taken whereby the absolute acceleration reduction factor for a given floor of a building, defined by the ratio, is taken as the efficiency criterion:

$$K_{W,i} = \frac{|W_{i,\max}^{lin}| - |W_{i,\max}|}{|W_{i,\max}^{lin}|} \quad (9)$$

where $|W_{i,\max}|$ —is the maximum modul value of the absolute acceleration of the they storey for the computed model of the building with the DVD.

$|W_{i,\max}^{lin}|$ —the same for the original calculation model of the building without DVD.

For a preliminary assessment of the efficiency of DVD the KW coefficient averaged over all storeys was also used as a generalised efficiency criterion defined by the ratio:

$$K_W = \frac{1}{N} \cdot \sum_{i=1}^N |W_{i,\max}^{lin}| - |W_{i,\max}| \cdot \frac{1}{W_{\max}^{lin}} \quad (10)$$

The KW coefficient makes it relatively easy to analyse the efficiency of DVD use in the variable range space and screen out combinations that are known to be inefficient. In addition, as calculations show the main contribution to the formation of absolute accelerations is made by the first form of vibration. Therefore, by the found value of KW and the weight function representing the set of normalized coefficients of the first proper form it is possible to pass from the value of the generalized coefficient KW to the reduction coefficient of absolute accelerations for this storey of calculation model with sufficient accuracy for practice.

The calculations also evaluated the relative mutual displacements between the storeys (including the damper mass displacement relative to the anchoring point of the DVD elastic bond), storey displacements relative to the foundation. For calculation variants with rigidity degradation the degree of degradation by storey was evaluated depending on the value of the degradation coefficient. Stiffness degradation was assessed by ratio:

$$\Delta C_i = \frac{c_{0i} - c_i}{c_{0i}} \cdot 100, \% \quad (11)$$

where ΔC_i is the relative amount of stiffness degradation in %. Obviously, the stiffness degradation value is directly related to the value of the set degradation coefficient KD. In order to select it, it is necessary to use the observation data of the changes in the free vibration period of the building as a result of the seismic effects that occurred during the preceding period of the building's use.

5 Calculation Agenda

The calculations were carried out as separate series with the number of variants in each series sufficient to reveal the dependence nature of the dynamic response parameters of the computational model on the seismic effect on the parameter being varied. The latter for the first DVD design scheme include the following:

- the relative mass value of the damper $b = M_{TMD}/M_{BLD}$;
- damper tuning parameter $\chi = \omega_{0TMD}/\omega_{0BLD}$ (ratio of the partial damper frequency to the first natural frequency of the building);
- intensity of inelastic drag forces developed by the friction damper included in the damper suspension design $\alpha = F_{c,lim}/[M_{11} \cdot g]$;
- the prevailing frequency or range of prevailing frequencies of the design seismic effect.

The bulk of the calculations are carried out for a building with the aforementioned natural vibration periods. In addition, a number of calculation options have been made for buildings with the same design scheme but with their own periods different from the adopted ones. These calculations make it possible to assess the change in the efficiency of DVD when the building's own vibration period is offset from the prevailing period of seismic action.

For the second design scheme of the DVD the adjustable damping factor χ (which in this case depends only on the stiffness factor of the elastic suspension), the inelastic drag force intensity of the friction dampener αl and the frequency composition of the seismic effect were used as varying parameters.

The calculations are performed for a suite of accelerograms with a fairly wide range of dominant frequencies on their spectrum. In addition, based on the parameter combinations selected as a result of these calculations verification calculations were also carried out. That allowed evaluating the dynamic response parameters of the model at different orientations of the seismic direction and the vibration plane of the building (vibrations in the transverse or longitudinal symmetry plane). For each option the values of the dynamic response parameters of the model are obtained including:

- the maximum absolute accelerations of masses for each storey $W_{i,max}$;
- maximum displacements of floor masses relative to the base $X_{i,max}$;
- maximum reciprocal displacements of adjacent masses $U_{i,max}$;

- the maximum displacements of the damper mass relative to the attachment point of its suspension elastic connection $U_{10,max}$;
- the value of the relative stiffness degradation of the inter-storey connections (for variants that take into account the stiffness degradation of the inter-storey connections);

Some calculation results are shown in Figs. 4, 5, 6.

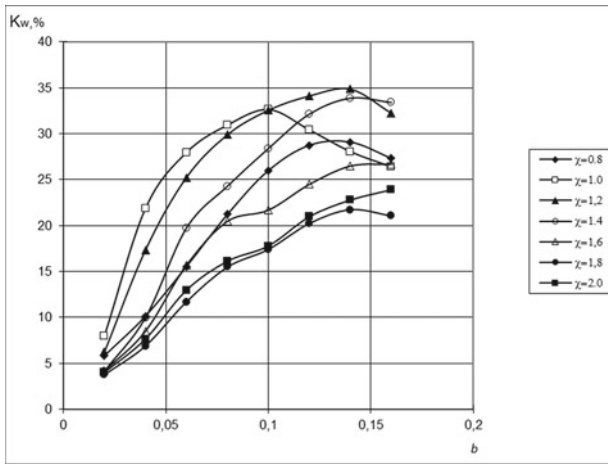


Fig. 4 Dynamic response characteristics of the design building model under seismic action (El-Centro accelerogram) as a function of the relative damper mass b for different values Damper tuning factor χ . Damper suspension friction coefficient $\alpha = 0.16$

Fig. 5 Dependencies of the generalised acceleration reduction coefficient for seismic impacts of different spectral-frequency composition. Primary tone period of a building without a damper $T_{01} = 0.25$ s, $\alpha = 0.16$, $\chi = 1.2$

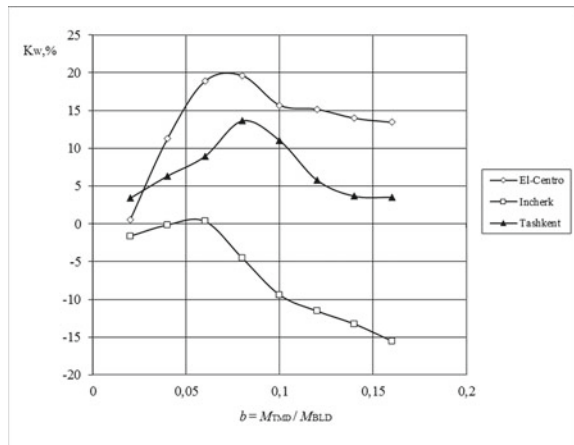
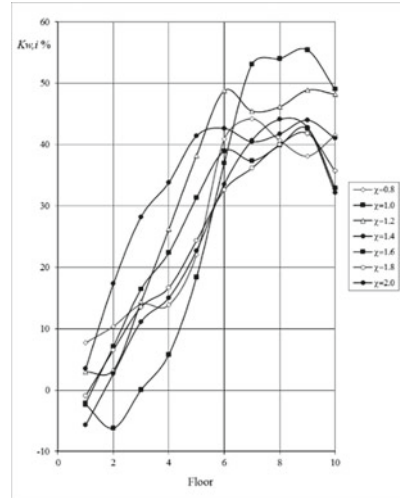


Fig. 6 Distribution dependencies of absolute acceleration reduction ratios by storey. El-Centro accelerogram, relative damper mass $b = 0.16$, friction parameter $\alpha = 0.16$



6 Results and Conclusions

The following conclusions can be drawn from the results:

1. The reduction of inertial loads is a function of a range of parameters including: the parameters of the building itself (primarily the natural frequency of the first tone), the seismic action (range of the predominant frequencies of the action spectrum), the parameters of the DVD (its mass, partial frequency and the intensity of the frictional forces created by the damping element introduced in the design of the DVD to limit the vibration amplitudes of the damper mass).
2. The best effect with DVD is achieved when the prevailing frequencies of the seismic action and the natural frequency of the building are the same or close with a tuning factor of $\chi = 1.1 \div 1.2$, a damper mass— f at least $0.1 \div 0.16$ of the building mass and a friction parameter $\alpha = 0.1 \div 0.12$. Under these conditions the generalized acceleration reduction factor can be as high as $30 \div 35\%$.
3. The possibility of different seismic wave propagation directions relative to the building and the occurrence of seismic effects with prevailing frequencies different from those assumed in the DVD calculation leads to a reduction in the efficiency of the DVD.
4. The reduction in inertial loads is not uniform across the floors of the building and increases as the floor number increases. In some cases there may be some increase in inertial loads on the lower floors of the building that might require reinforcing the load-bearing elements of the building on these stories.

References

1. Gutierrez Soto M, Hojjat A (2013) Tuned mass dampers. *Arch Comput Methods Eng* 20:419–431. <https://doi.org/10.1007/s11831-013-9091-7>
2. Gutierrez Soto M, Adeli H (2014) Optimum tuning parameters of tuned mass dampers for vibration. Control of irregular highrise building structures. *J Civ Eng Manag* 20(5):609–620.
3. Hoang N, Warnitchai P (2005) Design of multiple tuned mass dampers by using a numerical optimizer. *Earthquake Eng Struct Dynam* 34(2):125–144
4. Hamid Jafari N, Hamid Reza B, Amir Hossein H, Kaveh OAA (2020) The multiple tuned mass damper for passive control of structures by cuckoo algorithm. *Am J Eng Appl Sci* 13(3):358–367. <https://doi.org/10.3844/ajeassp.2020.358.367>
5. Albert YU, Dolgaya AA, Ivanova TV et al (2017) Seismic input models for tuned mass damper designing. *Mag Civ Eng* 8:98–105. <https://doi.org/10.18720/MCE.76.9>
6. Souza dos Santos MD, Fiuza Lima DV et al (2013) Vibration control of a gym floor using tuned mass dampers: a numerical analysis. *Mod Mech Eng* 3:9–16. <https://doi.org/10.4236/mme.2013.33A002>
7. Benin AV, Nesterova OP, Uzdin AM, Guan Y (2017) Evaluation of the reduction ratio of bridge piers. mathematical and computer simulation in mechanics of solids and structures – MCM 2017. Book of Abstracts
8. Benin A, Uzdin A, Prokopovich S, Nesterova O, Rutman Y, Guan Y (2020) On estimating the reduction factor of bridge piers. In: *E3S Web of conferences. Key trends in transportation innovation, KTTI 2019*, p 06012. <https://doi.org/10.1051/e3sconf/202015706012>
9. Teplyshev V, Mylnik A, Pushkareva M, Agakhanov M, Burova O (2018) Application of tuned mass dampers in high-rise construction/E3S. *Web Conf* 33:02016. <https://doi.org/10.1051/e3sconf/20183302016>
10. Tanaka H, Mak CY (1983) Effect of Tuned Mass Dampers on Wind Induced Response of Tall Buildings. *J Wind Eng Ind Aerodyn* 14:357–368
11. Sadek F, Mohraz B, Taylor AW, Chung RM (1997) A method of estimating the parameters of tuned mass dampers for seismic application. *Earthquake Eng Struct Dynam* 26(6):617–635
12. Picauly F, Priyosulistiy Hrc, Suhendro B, Triwiyono A (2014) Tuned Mass damper on reinforced concrete slab with additional “x-shaped metal” absorber. 2nd international conference on sustainable civil engineering structures and construction materials 2014 (SCESCM 2014). *Procedia Eng* 95:204 – 212. <https://doi.org/10.1016/j.proeng.2014.12.180>
13. Lin JL, Tsai KC, Yu YJ (2010) Coupled tuned mass dampers for the seismic control of asymmetric-plan buildings. *Earthq Spectra* 26(3):749–778
14. Nesterova O, Uzdin A, Fedorova M (2018) Features of tuned mass damper behavior under strong earthquakes. In: *AIP conference proceedings. 8th polyakhov’s reading: proceedings of the international scientific conference on mechanics*, p 030016. <https://doi.org/10.1063/1.5034596>
15. Benin AV, Nazarova S, Uzdin AM (2019) Designing scenarios of damage accumulation. *Adv Intell Syst Comput* 983:600–610. https://doi.org/10.1007/978-3-030-19868-8_57

Correction to: Modeling of Parameters of Laser Surfacing Zones and Determination of Tribotechnical Properties of Coatings Obtained by Laser Additive Technologies



Vladimir Biryukov 

Correction to:
Chapter “Modeling of Parameters of Laser Surfacing Zones and Determination of Tribotechnical Properties of Coatings Obtained by Laser Additive Technologies”
in: A. Mottaeva (ed.): *Technological Advancements in Construction*, Lecture Notes in Civil Engineering 180,
https://doi.org/10.1007/978-3-030-83917-8_46

In the original version of this book, the following belated correction has been incorporated in Chapter 46: The author name has been changed from “Biryukov Vladimir” to “Vladimir Biryukov”.

The updated version of this chapter can be found at
https://doi.org/10.1007/978-3-030-83917-8_46

Author Index

- Abirov, Rustam, 127
Akhmedov, Mashrap, 127
Akimov, Luka, 1, 13
Alaqabi, Mohammed, 391
Aleksandrova, Natalya, 71
Alekseeva, Ekaterina, 159
Antonov, Sergey, 543
Antonyan, Ashot, 245, 471
Aparin, Boris, 1
Arefyeva, Elena, 159
Arkulis, Mikhail, 109
- Badenko, Vladimir, 13
Balaev, Etibar, 503, 533
Bayramukov, Salis, 325
Bazlova, Tatiana, 521
Belikov, Artem, 313
Benin, Andrey, 553
Bespyatchuk, Daria, 359
Bezusov, Danil, 265
Biryukov, Vladimir, 511, 521
Bogdanova, Galina, 553
Bokov, Alexander, 279
Bolodyan, Galina, 335
Bormotov, Alexey, 61
Buslaeva, Irina, 303
- Cheng, Long, 193
Chernikova, Anna, 83
Chislov, Oleg, 265
- de Martino di Montegiordano, Davide, 13
De Mei, Kevin, 13
Demenkov, Peter, 313
Demina, Lyudmila, 457
- Dmitriev, Ivan, 543
Dolaeva, Zuriat, 325
Dubskiy, Gennadii, 109
- Eliseev, Vladimir, 503, 533
- Galkin, Aleksandr, 39
Gerasimov, Sergey, 255
Giyasov, Adham, 347
Golikov, Alexey, 47
Golovtsova, Irina, 203
Gorbashko, Elena, 203
Gorina, Larisa, 159
Gorodishenina, Anna, 171
Gorokhova, Anastasia, 61
Gradov, Oleg, 371, 521
Gravit, Marina, 335, 543
Guo, Meng, 193
Gura, Dmitry, 359
- Igumnova, Tatiana, 255
Ilina, Marina, 117
- Kalinin, Aleksandr, 71
Kamynina, Nadezhda, 203
Kassenov, Dauren, 137
Kazan, Igor, 493
Khakhulin, Lev, 503
Khezhev, Tolya, 325
Komarova, Liudmila, 183
Komolov, Vasili, 313
Korolkov, Dmitry, 335
Kotyazhov, Andrey, 25
Kozhevnikova, Tatyana, 149
Krasnozhen, Sergei, 13

- Kravets, Alexandra, 265
Kurochkin, Ivan, 117
Kuzmina, Svetlana, 83
- Lapin, Vladimir, 137
Larin, Oleg, 279
Lazarev, Yuri, 171
Lazareva, Margarita, 1
Li, Valeriy, 457
Lisienkova, Liubov, 183
Litvinov, Artem, 47
Loginova, Elena, 235
Logunova, Oxana, 109
Lukina, Galina, 417
Lvov, Vladimir, 13
Lysova, Natalia, 217
- Magomedova, Natalya, 265
Makhov, Vladimir, 493
Makish, Nurakhmet, 137
Manzhula, Ilya, 149
Matveev, Yury, 391
Matyakubov, Alisher, 289
Meshalkin, Evgeny, 543
Michailov, Aleksandr, 493
Mingareeva, Elena, 1
Morozov, Ilya, 99
Myasnikova, Nina, 217
- Nosov, Vladimir, 25
Nosova, Liudmila, 183
- Orekhov, Feodor, 371
Orlov, Dmitry, 493
Osennyaya, Anna, 359
Osipov, Nikolay, 13
Ostrovaia, Anastasia, 13
- Pankov, Vladimir, 39
Peshekhonov, Alexey, 83
Petrochenko, Marina, 171
Pirogova, Oksana, 381
Plotnikov, Dmitrii, 217
Plotnikov, Vladimir, 381
Polyakov, Pavel, 47
- Ponimatkina, Liudmila, 279
Popova, Ulyana, 417
Portnyagin, Denis, 235
Princ, Anton, 521
Prolygin, Aleksandr, 71
- Raupov, Dilmurod, 289
Rubailo, Tatyana, 171
Rudakova, Irina, 83
- Samarin, Sergey, 359
Sanzharova, Natalia, 1
Selivanov, Oleg, 117
Semenov, Anatolii, 217
Semenova, Maria, 417
Seregin, Nikolai, 481
Shchukin, Alexey, 543
Sirina, Nina, 405, 433
Sukhacheva, E., 1
Sun, Yaojia, 193
Syssoeva, Elena, 99
- Tagiev, Ruslan, 47
Terleev, Vitaly, 1, 13
Titova, Alexandra, 203
Tokmazov, Georgy, 109
Trubitsina, Galina, 109
- Vaganova, Olga, 25
Vasileva, Anastasia, 417
Vlasenko, Sergey, 457
- Yaitskov, Ivan, 47
Yakovleva, Lena, 303
Yerzhanov, Syrymgali, 137
Yusufova, Agakhanum, 381
- Zadayanchuk, Nina, 47
Zadorozhniy, Vyacheslav, 265
Zengin, Başak, 447
Zhang, Jiyun, 193
Zhichkin, Kirill, 25
Zhichkina, Lyudmila, 25
Zubkov, Valerii, 225, 405, 433